UNIVERSITAT DE BARCELONA

Precision Oncology Strategy and Personalized Medicine for the Treatment of Malignant Peripheral Nerve Sheath Tumor

Sara Ortega Bertran

Precision Oncology Strategy and Personalized Medicine for the Treatment of Malignant Peripheral Nerve Sheath Tumor

Estratègia d'Oncologia de Precisió i Medicina Personalitzada per al Tractament del Tumor Maligne de la Beina del Nervi Perifèric

Doctoral thesis submitted by
Sara Ortega Bertran
to obtain the doctoral degree
for the University of Barcelona (UB)

This thesis was developed under the joint supervision of
Dr. Conxi Lázaro García and **Dr. Juana Fernández Rodríguez**
at the Bellvitge Biomedical Research Institute (IDIBELL) and
the Catalan Institute of Oncology (ICO)

Biomedicine Doctoral Program
Faculty of Medicine and Health Sciences, University of Barcelona (UB)
Tutor: Dr. **Francesc Viñals Canals**

Dr. Conxi Lázaro Garcia Dr. Juana Fernández Rodríguez Dr. Francesc Viñals Canals

Sara Ortega Bertran

Barcelona, 2025

A vosaltres, avis…

ABSTRACT

Introduction: Malignant peripheral nerve sheath tumors (MPNSTs) are aggressive soft tissue sarcomas with an unfavorable prognosis and a low five-year survival rate. Approximately 50% of cases occur in patients with Neurofibromatosis type 1 (NF1), while the rest are sporadic or related to prior radiation exposure. Currently, there are no effective treatments, highlighting the urgent need for new therapeutic strategies. The pathogenesis of MPNSTs is driven by the inactivation of key tumor suppressor genes, such as *NF1*, *CDKN2A*, and *EED/SUZ12* (components of the Polycomb Repressive Complex 2, PRC2).

This doctoral thesis focuses on three main objectives: (i) Expanding the preclinical MPNST platform developed by our research group by characterizing new *in vitro* and *in vivo* models; (ii) Identifying a novel therapeutic combination based on a precision medicine strategy targeting the loss of NF1, CDKN2A, and PRC2; (iii) Implementing a feedback system based on tumor genomic analysis and preclinical drug testing to inform tumor molecular boards (MTBs) in clinical decision-making and treatment personalization in MPNST patients.

Methods: Patient-derived models, including cell lines and orthotopic xenografts (PDOX), were developed and validated through in-depth characterization at multiple levels. A high-throughput screening of 28 inhibitors targeting MEK, CDK, and BET was performed, evaluating 147 drug combinations. The most promising combinations were validated *in vitro* and subsequently tested *in vivo*. Additionally, a personalized medicine strategy was implemented, which included comprehensive genomic analysis of patient tumors to guide precision oncology treatments using PDOX models.

Results: The generated models faithfully reproduced the main genomic and histological features of the original tumors. Functional characterization of the cell lines revealed differences in proliferation, colony formation capacity, migration, and tumorigenic potential. Notably, the NF1-18B cell line displayed two distinct subpopulations with different ploidy states (<3n and 4n) and differential functional behavior *in vitro*. Moreover, the SP-10 cell line represents one of the few documented sporadic MPNST models with classic genomic and histological features.

Among the evaluated co-treatments, the combination of Arry-162 (MEK inhibitor) and I-BET151 (BET inhibitor) was the most effective, achieving a 65% reduction in tumor volume in the sporadic model and completely halting tumor growth in the NF1-related model.

Furthermore, the triple combination of Arry-162 + I-BET151 + Ribociclib (CDK inhibitor) enhanced this effect, achieving an average tumor reduction of 85% in the sporadic model.

The personalized medicine strategy illustrated two clinical cases: one NF1 patient who developed two independent MPNSTs, and one sporadic case with multiple metastatic relapses. In the latter, the combination of MEK and BET inhibitors showed the highest efficacy, achieving a 60% tumor reduction. As a result, the MTB decided to administer this treatment to the patient to prevent further relapses. Moreover, genomic analysis of samples at different stages of MPNST progression revealed genomic stability across primary tumors, relapses, and metastases.

Conclusions: We successfully expanded the preclinical MPNST platform, which enabled the identification of a promising triple therapeutic combination (MEK-BET-CDK) and the development of a personalized medicine strategy that supports clinical decision-making based on functional models and molecular analysis. These advances pave the way for more targeted and effective treatments for MPNST patients.

Keywords: MPNST, Neurofibromatosis type 1, PDOX, precision oncology, personalized medicine.

RESUMEN

Introducción: Los tumores malignos de la vaina del nervio periférico (MPNST, por sus siglas en inglés) son sarcomas agresivos de tejidos blandos con pronóstico desfavorable y una baja tasa de supervivencia a cinco años. Alrededor del 50% de los casos se presentan en pacientes con Neurofibromatosis tipo 1 (NF1), mientras que el resto son esporádicos o están relacionados con exposición previa a radioterapia. Actualmente no existen tratamientos efectivos, lo que subraya la necesidad urgente de nuevas estrategias terapéuticas. La patogénesis de los MPNST está impulsada por la inactivación de genes supresores tumorales clave, como *NF1, CDKN2A* y *EED/SUZ12* (componentes del complejo represivo de Polycomb 2, PRC2).

Esta tesis doctoral se centra en tres objetivos principales: (i) Ampliar la plataforma preclínica de MPNST que ha generado nuestro grupo mediante la caracterización de nuevos modelos *in vitro* e *in vivo*; (ii) identificar una nueva combinación terapéutica basada en una estrategia de medicina de precisión dirigida a la pérdida de *NF1*, *CDKN2A* y *PRC2*; (iii) implementar un sistema de retroalimentación basado en el análisis genómico tumoral y la evaluación preclínica de fármacos para informar a los comités moleculares de tumores (MTB, por sus siglas en inglés) en la toma de decisiones clínicas y la personalización de tratamientos en pacientes con MPNST.

Métodos: Se desarrollaron modelos derivados de pacientes, incluyendo líneas celulares y xenoinjertos ortotópicos (PDOX) a partir de pacientes, que fueron validados y caracterizados con profundidad a diferentes niveles. Se realizó un cribado de alto rendimiento de 28 inhibidores dirigidos a MEK, CDK y BET, evaluando 147 combinaciones. Las combinaciones más prometedoras se validaron *in vitro* y posteriormente *in vivo*. Además, se implementó una estrategia de medicina personalizada que incluyó un análisis genómico exhaustivo de los tumores de los pacientes para guiar tratamientos de oncología de precisión utilizando modelos PDOX.

Resultados: Los modelos generados reprodujeron las principales características genómicas e histológicas de los tumores originales. Además, la caracterización funcional de las líneas celulares reveló diferencias en proliferación, capacidad de formación de colonias, migración y potencial tumorigénico. Cabe destacar que la línea celular NF1-18B presentó dos subpoblaciones distintas con diferente estado de ploidia (< 3n y 4n) y comportamiento funcional diferencial *in vitro*. Por otro lado, la línea celular SP-10 representa uno de los pocos

modelos esporádicos de MPNST documentados con características genómicas e histológicas clásicas.

Entre los co-tratamientos evaluados, la combinación de Arry-162 (inhibidor de MEK) e I-BET151 (inhibidor de BET) fue la más eficaz, logrando una reducción del volumen tumoral del 65% en el modelo esporádico y deteniendo completamente el crecimiento tumoral en el modelo relacionado con NF1. Además, la combinación triple de Arry-162 + I-BET151 + Ribociclib (inhibidor de CDK), potenció este efecto, logrando una reducción tumoral promedio del 85% en el modelo esporádico.

La estrategia de medicina personalizada ilustró dos casos clínicos: un paciente con NF1 que desarrolló dos MPNST independientes y un caso esporádico con múltiples recaídas metastásicas. En este último, la combinación de inhibidores de MEK y BET mostró la mayor eficacia, logrando una reducción tumoral del 60%. En consecuencia, el MTB decidió administrar este tratamiento al paciente para prevenir posibles recaídas. Además, el análisis genómico de las muestras en distintas etapas de la progresión de los MPNSTs reveló estabilidad genómica entre el tumor primario, las recaídas y las metástasis.

Conclusiones: Se amplió con éxito la plataforma preclínica de MPNST, lo que permitió identificar una combinación terapéutica triple prometedora (MEK-BET-CDK) y desarrollar una estrategia de medicina personalizada que apoya decisiones clínicas basadas en modelos funcionales y análisis moleculares. Estos avances abren el camino hacia tratamientos más dirigidos y eficaces para pacientes con MPNST.

Palabras clave: MPNST, NF1, PDOX, oncología de precisión, medicina personalizada.

RESUM

Introducció: Els tumors malignes de la beina del nervi perifèric (MPNST) són sarcomes agressius de teixits tous amb un pronòstic desfavorable i una baixa taxa de supervivència a cinc anys. Aproximadament el 50% dels casos es presenten en pacients amb Neurofibromatosi tipus 1 (NF1), mentre que la resta són esporàdics o estan relacionats amb l'exposició prèvia a radioteràpia. Actualment no existeixen tractaments efectius, el que subratlla la necessitat urgent de noves estratègies terapèutiques. La patogènesi dels MPNST està impulsada per la inactivació de gens supressors tumorals clau, com *NF1*, *CDKN2A* i *EED/SUZ12* (components del complex repressiu de Polycomb 2, PRC2).

Aquesta tesi doctoral es centra en tres objectius principals: (i) Ampliar la plataforma preclínica de MPNST desenvolupada pel nostre grup mitjançant la caracterització de nous models *in vitro* i *in vivo*; (ii) Identificar una nova combinació terapèutica basada en una estratègia de medicina de precisió dirigida a la pèrdua de NF1, *CDKN2A* i PRC2; (iii) Implementar un sistema de retroalimentació basat en l'anàlisi genòmic tumoral i l'avaluació preclínica de fàrmacs per informar els comitès moleculars de tumors (MTB) en la presa de decisions clíniques i la personalització de tractaments en pacients amb MPNST.

Mètodes: Es van desenvolupar models derivats de pacients, incloent línies cel·lulars i xenoinjerts ortotòpics (PDOX), que es van validar i caracteritzar profundament a diferents nivells. Es va realitzar un cribratge d'alt rendiment de 28 inhibidors dirigits a MEK, CDK i BET, avaluant 147 combinacions. Les combinacions més prometedores es van validar *in vitro* i posteriorment *in vivo*. A més, es va implementar una estratègia de medicina personalitzada que incloïa un anàlisi genòmic exhaustiu dels tumors dels pacients per guiar els tractaments d'oncologia de precisió utilitzant models PDOX.

Resultats: Els models generats van reproduir les principals característiques genòmiques i histològiques dels tumors originals. A més, la caracterització funcional de les línies cel·lulars va revelar diferències en proliferació, capacitat de formació de colònies, migració i potencial tumorigènic. Cal destacar que la línia cel·lular NF1-18B va presentar dues subpoblacions distintes amb diferents estats de ploïdia (< 3n i 4n) i comportament funcional diferencial *in vitro*. D'altra banda, la línia cel·lular SP-10 representa un dels pocs models esporàdics de MPNST documentats amb característiques genòmiques i histològiques clàssiques. Entre els co-tractaments avaluats, la combinació de Arry-162 (inhibidor de MEK) i I-BET151 (inhibidor de BET) va ser la més eficaç, aconseguint una reducció del volum tumoral del 65% en el model esporàdic i aturant completament el creixement tumoral en el model relacionat amb NF1. A

més, la combinació triple de Arry-162 + I-BET151 + Ribociclib (inhibidor de CDK) va potenciar aquest efecte, aconseguint una reducció tumoral mitjana del 85% en el model esporàdic.

L'estratègia de medicina personalitzada va il·lustrar dos casos clínics: un pacient amb NF1 que va desenvolupar dos MPNST independents i un cas esporàdic amb múltiples recaigudes metastàtiques. En aquest últim, la combinació d'inhibidors de MEK i BET va mostrar la major eficàcia, aconseguint una reducció tumoral del 60%. Com a resultat, el MTB va decidir administrar aquest tractament al pacient per prevenir possibles recaigudes. A més, l'anàlisi genòmic de les mostres en diferents etapes de la progressió dels MPNST va revelar estabilitat genòmica entre el tumor primari, les recaigudes i les metàstasis.

Conclusions: S'ha ampliat amb èxit la plataforma preclínica d'MPNSTs, el que ha permès identificar una combinació terapèutica triple prometedora (MEK-BET-CDK) i desenvolupar una estratègia de medicina personalitzada que dona suport a la presa de decisions clíniques basades en models funcionals i anàlisis moleculars. Aquests avenços obren el camí per a tractaments més dirigits i eficaços per als pacients amb MPNST.

Paraules clau: MPNST, NF1, PDOX, oncologia de precisió, medicina personalitzada.

Table of contents

TABLE OF CONTENTS

List of Figures and Tables

LIST OF FIGURES AND TABLES

Introduction

Materials & Methods

Results

Abbreviations

ABBREVIATIONS

18F-FDG-PET/CT	[(18)F] Fluorodeoxyglucose-positron emission tomography/computed tomography
2-D	Two-dimensional
3-D	Three-dimensional
ANNUBP	Atypical neurofibromatous neoplasms of uncertain biologic potential
ATCC	American Type Culture Collection
B2B	Bench-to-bedside
BAF	B-allele frequency
BCA	Bicinchoninic acid assay
BET	Extra-terminal domain
BETi	Extra-terminal domain inhibitor
BSA	Bovine serum albumin
CAF	Cancer-associated fibroblast
CALM	*Café-au-lait* macules
cAMP	Cyclic adenosine monophosphate
CDK4/6i	Cyclin dependent kinase 4/6 inhibitor
CDK	Cyclin dependent kinase
CDKi	Cyclin dependent kinase inhibitor
cDNA	Complementary DNA
CDX	Cell line-derived xenografts
cfDNA	Cell-free DNA
CI	Combination index
CN	Copy-number
cNF	Cutaneous neurofibromas
CNG	Copy number gain
CNN-LOH	Copy number neutral LOH
CNS	Central nervous system
CNV	Copy number variation
CRC	Curve response class

CRISPR	Clustered Regularly Interspaced Short Palindromic Repeats
CTG	CellTiter-Glo
DAB	3,3'-diaminobenzidine
DAPI	4,6-diamino-2-phenilindole
DBSumNeg	Delta Bliss Sum negative
DMEM	Dulbecco's modified Eagle's medium
DMSO	Dimethyl sulfoxide
DNA	Deoxyribonucleic acid
EC_{50}	Half-maximal effective concentration
ECM	Extracellular matrix
E-HSA	Excess HSA
ERK	Extracellular signal-regulated kinase
Fa	Fraction affected
FBS	Fetal bovine serum
FDA	Food and drug administration
FFPE	Formalin-fixed and paraffin-embedded
FLINT	Fluorescence due to substrate cleavage in enzymatic reactions
FRET	Energy transfer between a donor and acceptor molecule
Fu	Fraction unaffected
GAPDH	Glyceraldehyde 3-phosphate dehydrogenase
GEMM	Genetically engineered modified mouse
GRD	GTPase-activating protein-related domain
H&E	Hematoxylin and Eosin
H3K27	Histone 3 lysine 27
H3K27Ac	Histone 3 lysine 27 acetylation
H3K27me3	Histone H3 lysine 27 trimethylation
HDACi	Histone deacetylase inhibitors
HED	Human equivalent dose
HPF	High power field
HRP	Horseradish peroxidase

HSA	Highest single agent
HTS	High-throughput screening
IC_{50}	Half-maximal inhibitory concentration
IF	Immunofluorescence
IHC	Immunohistochemistry
iPSC	Induced pluripotent stem cells
KO	Knockout
LOF	Loss of function
LOH	Loss of heterozygosity
MAPK	Mitogen-activated protein kinase
MAXR	Maximum response
MEK	Methyl ethyl ketone
MEKi	Methyl ethyl ketone inhibitor
MIPE	Mechanism Interrogation PlatE
miRNA	microRNA
MPNST	Malignant peripheral nerve sheath tumor
MRI	Magnetic resonance imaging
MTB	Molecular Tumor Board
MTD	Maximum tolerated dose
mTORi	Mammalian target of rapamycin inhibitor
MTT	3-(4,5-dimetrhylthiaziol-2-yl)-2,5-diphenyl-tetrazolium bromide
NC	Neural crest
NCATS	National Center for Advancing Translational Sciences
NF	Neurofibromatosis
NF1	Neurofibromatosis type 1
NF2	Neurofibromatosis type 2
NIH	National Institutes of Health
NK	Natural killer
NOAEL	No observed adverse effect levels
NOD	Non-obese diabetic

NRE	Normalized relative expression
NRSTS	Non-rhabdomyosarcoma soft tissue sarcoma
NSG	NOS SCID gamma
O/N	Overnight
OS	Overall survival
P/S	Penicillin/Streptomycin
PBS	Phosphate buffered saline
PBS-T	Phosphate buffered saline Tween
PCA	Principal component analysis
PD	Pharmacodynamics
PDOX	Patient-derived orthothopical xenografts
PDT	Population doubling time
PDX	Patient-derived xenograft
PFA	Paraformaldehyde
PFS	Progression-free survival
PI3K	Phosphatidylinositol-3 kinase
PK	Pharmacokinetics
PKA	Protein kinase A
PKC	Protein kinase C
pNF	Plexiform neurofibroma
PNS	Peripheral nervous system
PR	Partial response
PRC2	Polycomb repressive complex 2
qRT-PCR	Quantitative real-time polymerase chain reaction
RLU	Relative luminescence unit
RNA-seq	RNA sequencing
RT	Room temperature
RTK	Receptor tyrosine kinase
SC	Schwann cell
SCID	Severe combined immunodeficiency

SCNA	Somatic copy number alterations
SCNG	Somatic copy number gain
SD	Stabilized disease
SDS	Sodium dodecyl sulfate
sgRNA	Single guide RNA
SNP-array	Single nucleotide polymorphism array
SNW	Schwannomatosis
STR	Short tandem repeat
STS	Soft-tissue sarcoma
SV	Structural variant
TME	Tumor microenvironment
TSG	Tumor suppressor gene
WB	Western Blot
WES	Whole exome sequencing
WGS	Whole genome sequencing
Wnt	Wingless-related integration site
WT	Wild type
ZIP	Zero Interaction Potency

GENE AND PROTEIN ABBREVIATIONS

AKT	Alpha serine/threonine-protein kinase
ATRX	ATRX Chromatin Remodeler
AURKA	Aurora kinase A
BET	Bromodomain and extra-terminal motif
BIM	Bcl-2-like protein 11
BIRC5	Baculoviral IAP Repeat Containing 5
BRAF	Serine/threonine-protein kinase B-raf
BRD2	Bromodomain containing 2
BRD3	Bromodomain containing 3
BRD4	Bromodomain containing 4
BRDT	Bromodomain testis associated
CD34	CD34 Molecule
CDK2	Cyclin dependent kinase 2
CDK4	Cyclin dependent kinase 4
CDK6	Cyclin dependent kinase 6
CDKN2A	Cyclin-dependent kinase inhibitor 2A
Dhh	Desert hedgehog
E2F	E2 transcription factor
EED	Embryonic Ectoderm Development
EGFR	Epidermal growth factor receptor
ERK	Extracellular signal-regulated kinase
ERBB2	Erb-B2 Receptor Tyrosine Kinase 2
ERBB3	Erb-B2 Receptor Tyrosine Kinase 3
EWSR1	EWS RNA Binding Protein 1
EZH1	Enhancer of zeste 1 polycomb repressive complex 2 subunit
EZH2	Enhancer of zeste 2 polycomb repressive complex 2 subunit
FAK	Focal adhesion kinase
Foxn1	Forkhead box N1 (mouse)
GFAP	Glial fibrillary acidic protein

HGF	Hepatocyte growth factor
HMMR	Hyaluronan Mediated Motility Receptor
IL2rg	Interleukin 2 receptor subunit gamma (mouse)
KIT	KIT proto-oncogene, receptor tyrosine kinase
Lats1	Large tumor suppressor kinase 1 (mouse)
Lats2	Large tumor suppressor kinase 2 (mouse)
LMNA	Lamin A/C
LZTR1	Leucine-zipper-like transcriptional regulator 1
MAPK	Mitogen-activated protein kinase
MDM2	Murine double minute 2
MEK	Mitogen activated protein kinase
MET	MET Proto-Oncogene, Receptor Tyrosine Kinase
MMP-2	Matrix Metallopeptidase 2
MMP-9	Matrix Metallopeptidase 9
MTAP	Methyltioadenosine phosphorylase
mTOR	mammalian Target of Rapamycin
MYC	MYC proto-oncogene, bHLH transcription factor
NF1	Neurofibromin 1
NF2	Moesin-ezrin-radixin like (MERLIN) tumor suppressor
NGFR	Nerve Growth Factor Receptor
NRAS	Neuroblastoma RAS viral oncogene homolog
NTRK	Neurotrophic receptor tyrosine kinase
NTRK1	Neurotrophic receptor tyrosine kinase 1
NTRK3	Neurotrophic receptor tyrosine kinase 3
P75NTR	p75 neurtophin receptor
PAK	p21 (RAC1) activated kinase 1
PD-1	Programmed cell death 1
PDGFR	Platelet-derived growth factor receptor alpha
PD-L1	Programmed cell death ligand 1
PRDM1	PR/SET Domain 1

Prkdc	Protein kinase, DNA-activated, catalytic subunit (mouse)
PTEN	Phosphatase and tensin homolog
RAF	Raf proto-oncogene, Serine/Threonine kinase
RB1	Retinoblastoma
ROS1	ROS Proto-Oncogene 1
S100B	S100 calcium binding protein B
SHP-2	Src homology region 2
SMARCB1	SWI/SNF related matrix-associated actin-dependent regulator of chromatin subfamily B member 1
SNRNP70	Small Nuclear Ribonucleoprotein U1 Subunit 70
SOX10	SRY-box Transcription Factor 10
SOX2	SRY-box Transcription Factor 2
SOX9	SRY-box Transcription Factor 9
SUZ12	SUZ12 polycomb repressive complex 2 subunit
TERT	Telomerase reverse transcriptase
TJP1	Tight Junction Protein 1
TOP2A	DNA topoisomerase II
TP53	Tumor protein p53
TP73	Tumor protein p73
TPPP	Tubulin Polymerization Promoting Protein
TWIST1	Twist family basic helix-loop-helix transcription factor 1
TYK2	Tyrosine kinase 2
VEGF	Vascular endothelial growth factor
VEGFR	Vascular endothelial growth factor receptor
VEZF1	Vascular Endothelial Zinc Finger 1
WEE1	WEE G2 checkpoint kinase

Introduction

INTRODUCTION

I1. Neurofibromatosis type 1 (NF1)

Neurofibromatosis type 1 (NF1, or von Recklinghausen disease) is one of the most common autosomal dominant diseases, with an estimated prevalence of 1 in 3,000 individuals in the general population (Riccardi 1981, Kallionpää, Uusitalo et al. 2018, Lee, Chopra et al. 2023). It is caused by pathogenic mutations in the *NF1* gene, which encodes for the protein neurofibromin, which negatively regulates the RAS pathway to control cell growth and survival. Approximately half of the cases are attributed to familial inheritance, while the remaining half are due to *de novo* mutations (Riccardi 1981, Upadhyaya, Kluwe et al. 2008), affecting equally to both sexes and all ethnic groups. NF1 is the most prevalent disorder within the Neurofibromatosis (NF) group, which also encompasses all forms of Schwannomatosis (SNW), including *NF2*-related Schwannomatosis (*NF2*-SWN), *LZTR1*-SWN, and *SMARCB1*-SWN, each defined by its underlying genetic mutation (Evans, Mostaccioli et al. 2022, Plotkin, Messiaen et al. 2022). Additionally, because of its important role in the RAS pathway, it is classified as a RASopathty, a group of genetic disorders caused by germline mutations affecting one of the genes of the RAS/MAPK pathway, which plays an important role in the regulation of cell cycle, senescence, apoptosis, and cell differentiation (Cimino and Gutmann 2018).

NF1 is a multisystemic disease with a broad spectrum of clinical manifestations (Figure I1) and a high variability in the symptoms observed among patients, even from a family carrying the same germline *NF1* mutation (Carey, Laub et al. 1979, Easton, Ponder et al. 1993, Legius, Messiaen et al. 2021). This phenotypic diversity results from the involvement of various tissues, including the skin, bones, central nervous system (CNS), and peripheral nervous system (PNS) (Sabbagh, Pasmant et al. 2009, Sabbagh, Pasmant et al. 2013, Carton, Evans et al. 2023).

Most patients with NF1 have pigmented lesions, with 99% having *café-au-lait* macules (CALMs) and 85% having axillary or inguinal freckles. Other characteristic features include Lisch nodules (present in 95% of patients) and skeletal abnormalities (such as scoliosis or tibial pseudarthrosis, but less present) (Gutmann, Ferner et al. 2017, Legius, Messiaen et al. 2021) (Figure I1). Due to its high expression in the nervous system, *NF1* mutations cause cognitive impairment and are associated with learning difficulties and a higher incidence of Attention Deficit Hyperactivity Disorder and Autism Spectrum Disorder (Hyman, Shores et al. 2005, Gutmann, Ferner et al. 2017). Less frequently, patients present cardiovascular diseases (like

hypertension, stroke, and congenital heart disease), seizures or pulmonary diseases (Friedman 1998 - "Updated 2022", Ferner and Gutmann 2013, Carton, Evans et al. 2023).

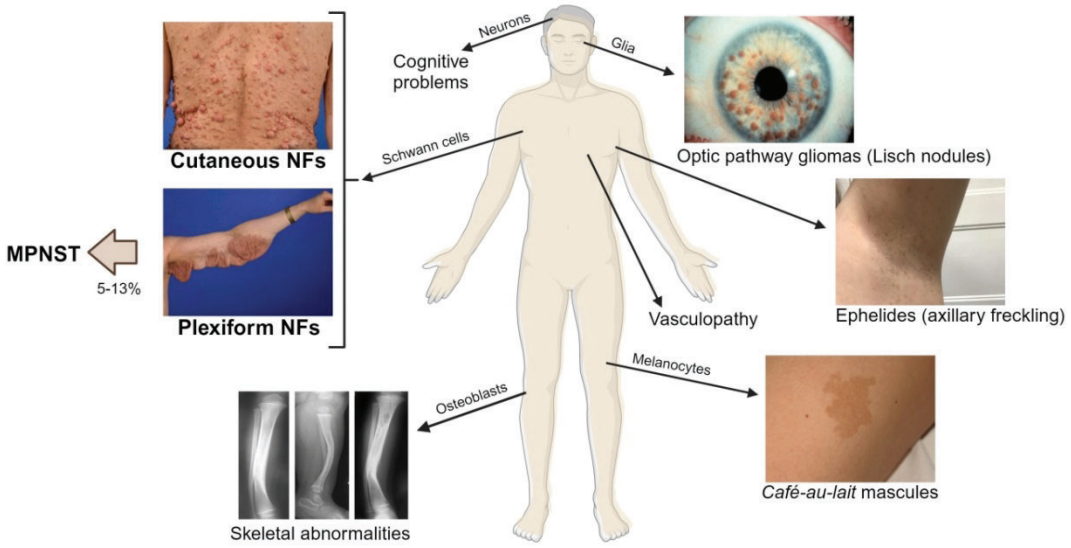

Figure I1. Clinical manifestations in NF1 patients. NF1 patients exhibit a broad range of symptomatology affecting multiple cell types and tissues. The diagram illustrates key features, including cutaneous and plexiform NFs (Kluwe et al., 2007), MPNST, skeletal abnormalities (Elefteriou et al., 2009), cognitive problems, optic pathway gliomas (Lisch nodules, Gutmann et al., 2017), axillary freckling (Upadhyaya et al., 2010), *café-au-lait* macules (Ozarslan et al., 2021), and vasculopathy. The figure also highlights the involvement of Schwann cells, neurons, glia, melanocytes, and osteoblasts in the disease pathway. NFs: Neurofibromas; MPNST: Malignant Peripheral Nerve Sheath Tumor. Adapted from (Upadhyaya 2010) and image created with Biorender.

Nearly 100% of patients have various types of neurofibromas caused by somatic inactivation of the second wild-type (WT) copy of the *NF1* gene in the Schwann cell (SC) lineage (Serra, Rosenbaum et al. 2000, Carton, Evans et al. 2023). There are several types of neurofibromas:

- Cutaneous neurofibromas (cNF) are benign SCs tumors that may appear in almost every nerve of the body during adolescence and adulthood (Figure I1). cNFs are present in nearly all NF1 patients (~99%) and are slow-growing, cell-circumscribed tumors of variable sizes located in the dermis (Gutmann, Ferner et al. 2017, Ortonne, Wolkenstein et al. 2018). They tend to increase in number with age (reaching the thousands in the most severe patients) and grow fast during puberty and pregnancy, indicating that hormones may play an important role (Duong, Bastuji-Garin et al. 2011). There is heterogeneity in the features of the cNF as they may be from 1-2 mm to a few centimeters, and with variable consistency. cNF tumor cells are characterized by the expression of S100B and SOX10 markers, both neural crest (NC)-derived markers (Rodriguez, Folpe et al. 2012). The main treatment for cNFs is surgical resection (Chamseddin, Hernandez et al. 2019), although this is not always feasible and entails a risk of scarring or tumor regrowth. Recently, a Phase II clinical trial has been carried out

to test the topical gel NFX-179 (Sarin, Kincaid et al. 2023), a MEK inhibitor, on cNF in NF1 patients, exhibiting promising results (NCT04435665).

- Plexiform neurofibromas (pNFs) (Figure I1) are detected in approximately 30% of patients with NF1 through physical examination, increasing to 50% when magnetic resonance imaging (MRI) is performed (Mautner, Asuagbor et al. 2008, Fisher, Blakeley et al. 2022). Although benign, these congenital tumors can cause pain, disfigurement, and functional impairment of adjacent nerves and tissues, growing mainly during childhood and adolescence (Zhang, Wang et al. 2014). The cellular components of pNFs are similar to those of cNFs; however, the tumor involves multiple nerve fascicles, generating a large tumor mass that extends through various tissue layers (Gutmann, Ferner et al. 2017). Pain management and surgery have been the main therapeutic options for patients, although it may be challenging due to the involvement of nervous structures. In addition, Selumetinib, a MEK inhibitor, is the only approved drug by the Food and Drug Administration (FDA) to treat pNFs as it has been described to shrink the tumor volume. Other MEK inhibitors, such as mirdametinib, have also shown efficacy in recent clinical trials (Weiss, Wolters et al. 2021). The most concerning feature of pNFs is their potential for malignant transformation into Malignant Peripheral Nerve Sheath Tumors (MPNSTs) (Fisher, Blakeley et al. 2022).
- Atypical neurofibromatous neoplasm with unknown biological potential (ANNUBP): these benign tumors are the intermediate step of transformation to malignancy between pNFs and MPNSTs. ANNUBP presents hypercellularity and nuclear atypia, with an increased mitotic rate compared with pNFs, losing the known histology of benign neurofibromas (Magro, Broggi et al. 2022). Moreover, they usually present a lower or complete absence of S100B and SOX10 marker expression (Miettinen, Antonescu et al. 2017).

In addition to benign neurofibromas, NF1 is a tumor predisposition syndrome that exposes patients to multisystem tumor complications at a very early age, with an average of cancer diagnosis of 39 years. The most common NF1-associated tumor types are optic gliomas (Listernick, Charrow et al. 1994, Carton, Evans et al. 2023), breast cancer (Evans, Kallionpää et al. 2020), gastrointestinal stromal tumors (Miettinen, Fetsch et al. 2006), phaeochromocytomas, paragangliomas, glomus tumors of the digits and a specific type of leukemia (Carton, Evans et al. 2023).

The onset timing of these clinical manifestations and the severity of the features may vary from person to person, affecting the individuals from birth, and increasing in severity and

frequency with age (Ferner 2007). The genotype-phenotype correlations of the *NF1* gene remain complex, though some associations have been identified. NF1 patients with type 1 microdeletions tend to exhibit more aggressive clinical features, including an increased risk of MPNST, a higher burden of neurofibromas, and more severe cognitive impairments (De Raedt, Brems et al. 2003, Bettegowda, Upadhayaya et al. 2021).. Additionally, specific NF1 missense variants (p.Met1149, p.Arg1276, and p.Lys1423) have been linked to distinct phenotypes (Koczkowska, Callens et al. 2020, Legius, Messiaen et al. 2021). The p.Arg1276 variant is associated with symptomatic spinal neurofibromas, p.Lys1423 with externally visible plexiform neurofibromas, and p.Met1149 with a milder presentation. Moreover, p.Arg1276 and p.Lys1423 carriers often exhibit Noonan-like features, including cardiovascular anomalies

It is therefore a multidisciplinary disease that has a significant impact on patients' quality of life. As symptoms also worsen over the years, the follow-up, monitoring and management of patients with NF1 is important. It requires a multidisciplinary approach and specific guidance tailored to the specific risks and natural history of the disease.

I2. Malignant Peripheral Nerve Sheath Tumors (MPNSTs)

MPNST is a rare type of non-rhabdomyosarcoma soft tissue sarcoma (NRSTS), accounting for 3 to 10% of all soft-tissue sarcomas (STS) (Cai, Tang et al. 2020). The prevalence in the general population is approximately 1 in 100,000, affecting both genders equally (Ducatman, Scheithauer et al. 1986, Evans, Baser et al. 2002, Ferner and Gutmann 2002, Uusitalo, Rantanen et al. 2016) while this percentage increases to 10-15% in patients with NF1. Notably, about 50% of MPNST cases occur in NF1 patients, while 40-45% cases are sporadic and 10-15% is associated with prior radiation therapy (Evans, Baser et al. 2002, LaFemina, Qin et al. 2013).

MPNSTs are frequently located in the proximal regions of the lower and upper extremities, as well as the pelvis, often arising at the confluence of major nerve roots and bundles. These include peripheral nerves, sciatic nerves, the brachial and sacral plex, and spinal nerve roots (Magro, Broggi et al. 2022). Surgical resection remains the mainstay of treatment, but achieving complete removal of tumors is often challenging due to their large size, proximity to complex nerves and the low chance of achieving negative resection margins (Porter, Prasad et al. 2009, Dunn, Spiliopoulos et al. 2013, Kim, Lu et al. 2020, Yao, Zhou et al. 2023). Prognosis has remained poor, with 5-year overall survival (OS) rates around 50% in patients who have undergone curative surgery of their tumor, and even lower rates (15-20%) in those with advanced and metastatic disease (Martin, Lamba et al. 2019). Furthermore, these tumors exhibit a recurrence rate of approximately 40%, requiring aggressive treatment to control

them (Cai, Tang et al. 2020). MPNSTs are characterized by invasive growth and a high metastatic potential (30-40%), with metastatic sites including mainly the lungs, but also the bones, lymph nodes, and liver (Anghileri, Miceli et al. 2006, Acem, Martin et al. 2021, Imura, Outani et al. 2021).

Poor prognostic factors include large tumor size, advanced disease stage, older age, poor response to chemotherapy, and the presence of relapsed tumors or distant metastases (Stucky, Johnson et al. 2012, Fan, Yang et al. 2014, Yuan, Xu et al. 2017, Yao, Zhou et al. 2023). Another important factor is the delay in diagnosis. Because of the heterogeneity of these tumors, biopsy sometimes fails to identify the malignancy, and therefore imaging technologies play a fundamental role. MRI is widely used, although the most accurate technique for diagnosing MPNST is [(18)F]-fluorodeoxyglucose positron emission tomography/computed tomography (18F-FDG-PET/CT) (Warbey, Ferner et al. 2009, Geitenbeek, Martin et al. 2022); nevertheless, it is not always easy to distinguish between pNFs (the benign precursor tumor) and MPNSTs using PET/CT. Liquid biopsy has also been used to monitor patients for early detection of MPNST. It has recently been reported that this technique is able to differentiate between cell-free DNA (cfDNA) of pNFs and MPNST, which has a shorter fragmentation profile and higher genomic instability (Szymanski, Sundby et al. 2021, Cortes-Ciriano, Steele et al. 2023). To improve the early detection of MPNSTs in NF1 patients, it is also crucial the clinical surveillance to detect persisting pain, rapid tumor enlargement or change in the texture of pNF that may indicate malignant transformation (Friedman 1998 - "Updated 2022")

Specific histologic criteria for MPNSTs have not been fully established. There are four described subtypes of MPNST: classic MPNST (being the most common), epithelioid MPNST, perineural MPNST, and malignant melanotic nerve sheath tumor (Magro, Broggi et al. 2022). These tumors can also be classified as low or high-grade based on tumor differentiation, mitotic activity, and necrosis (Knight, Knight et al. 2022). High-grade tumors accounts for the 90% of classic MPNSTs and presents a fibrosarcoma-like fascicular spindle-cell histological pattern, with high hypercellularity, high mitotic activity (higher than 10 high power fields (HPF) units), diffuse cytological atypia, and sites of tumor necrosis (Miettinen, Antonescu et al. 2017, Belakhoua and Rodriguez 2021, Knight, Knight et al. 2022); contrary, low-grade classic MPNSTs present a lower mitotic rate (3-9 HPF units) and no necrosis areas (Grobmyer, Reith et al. 2008). However, these histological features are similar to those of other soft-tissue sarcomas or melanomas, thus making the diagnosis of MPNST challenging, especially in sporadic cases (Creus-Bachiller, Fernández-Rodríguez et al. 2023, Magallón-Lorenz, Terribas et al. 2023).

Besides, there are no specific markers that uniquely distinguish MPNSTs from other tumor types with overlapping histological features (Le Guellec, Decouvelaere et al. 2016, Sahm, Reuss et al. 2018, Yao, Zhou et al. 2023).

Over the progression from pNF to MPNSTs, the malignant cells lose the expression of SC lineage markers such as S100B, SOX10, p75, or the endothelial marker CD34 (Fanburg-Smith and Miettinen 2001, Miettinen, Antonescu et al. 2017). Moreover, due to the recurrent inactivation of the Polycomb Repressive Complex 2 (PRC2), the loss of expression of histone H3 lysine 27 trimethylation (H3K27me3) is also unique in MPNSTs compared to the benign tumor. On the other hand, there are markers that are described as overexpressed in MPNSTs including Nestin (which is an intermediate filament), SOX2, SOX9, and EGFR (Holtkamp, Malzer et al. 2008, Miller, Jessen et al. 2009, Pekmezci, Reuss et al. 2015, Magallón-Lorenz, Terribas et al. 2023). Recently, Endoglin, a glycoprotein involved in angiogenesis, tumor growth and metastasis, has been described as a novel biomarker for MPNSTs (González-Muñoz, Di Giannatale et al. 2023).

I3. Genetic and Genomic MPNST Landscape

From a genomic perspective STSs are traditionally classified into two broad categories: those with few genomic structural alterations driven by specific translocations or activating mutations, and those with highly rearranged and complex karyotypes (Taylor, Barretina et al. 2011, Abeshouse A 2017). MPNSTs belong to the latter group, characterized by extensive somatic copy number alterations (SCNAs) and relatively few point mutations (Serra, Gel et al. 2020, Cortes-Ciriano, Steele et al. 2023). Among other works (Lee, Teckie et al. 2014, Abeshouse A 2017, Sohier, Luscan et al. 2017), Brohl et al. (2017) quantified between 7 and 472 point variants in MPNSTs, with a median of 63 (Brohl, Kahen et al. 2017). Due to the high proportion of structural variants, MPNSTs exhibit a highly rearranged and hyperploid genome (Abeshouse A 2017, Brohl, Kahen et al. 2017, Sohier, Luscan et al. 2017, Magallón-Lorenz, Terribas et al. 2023).

Recurrent genetic alterations in MPNST primarily involve the inactivation of five tumor suppressor genes (TSGs), as reported in various studies. These include *NF1*, which is inactivated in an average of 85% of cases (ranging from 62% to 100%), *CDKN2A* (72% on average, ranging from 58% to 100%), *SUZ12* (50% on average, ranging from 28% to 88%), *EED* (25% on average, ranging from 2% to 37%), and *TP53* (40% on average, ranging from 21% to 50%) (De Raedt, Beert et al. 2014, Lee, Teckie et al. 2014, Zhang, Wang et al. 2014, Brohl, Kahen et al. 2017, Sohier, Luscan et al. 2017, Magallón-Lorenz, Fernández-Rodríguez et al.

2021, Cortes-Ciriano, Steele et al. 2023). Additionally, although less frequent, other TSGs are mutated such as *RB1*, encoding the cell cycle negative regulator Retinoblastoma (Brohl, Kahen et al. 2017), *PTEN*, which participates in the downregulation of pro-survival cell signaling (Bradtmöller, Hartmann et al. 2012, Stefano and Giovanni 2019), *HMMR*, which regulates mitotic assembly (Mantripragada, Spurlock et al. 2008), and *ATRX*, a chromatin regulator involved in cell senescence (Lu, Eulo et al. 2018).

Conversely, MPNSTs also exhibit oncogene overexpression, particularly of receptor tyrosine kinases (RTKs) such *as EGFR, ERBB2, c-KIT, and MET*, which frequently show somatic copy-number gains (SCNGs) (Kim, Stewart et al. 2017). Other oncogenes with amplifications or activating mutations include *BRAF* (specifically in sporadic tumors) (Hirbe, Pekmezci et al. 2014, Kao, Wakeman et al. 2022), *AURKA* (Mohan, Castellsague et al. 2013), *SOX9* (Carbonnelle-Puscian, Vidal et al. 2011), *TWIST1* (Miller, Rangwala et al. 2006), and *NRAS* (Fernández-Rodríguez, Creus-Bachiller et al. 2022).

The MPNST genome exhibits more copy number gains (CNGs) than losses, along with extensive loss of heterozygosity (LOH) (Nakagawa, Yoshida et al. 2006, Serra, Gel et al. 2020, Cortes-Ciriano, Steele et al. 2023, Magallón-Lorenz, Terribas et al. 2023). Recurrent CNG regions involve oncogenes located on chromosomes 7 (*TWIST1, EGFR, HGF, MET*), 8 (*MYC*), 12 (*ERBB3, CDK4*), and 17 (*ERBB2, SOX9, TOP2A, BIRC5*). LOH, including copy-number neutral LOH (CNN-LOH), is a key mechanism for complete inactivation of TSGs such as *NF1, TP53, EED*, and *SUZ12* (Castellsagué, Gel et al. 2015, Magallón-Lorenz, Terribas et al. 2023). Recurrent CN losses affect TSGs on chromosomes 1 (*TP73*), 10 (*PTEN*), 11 (*EED*), and 17 (*NF1, SUZ12, TP53*), with the 9p21.3 locus (*CDKN2A/B, MTAP*) being the most commonly deleted (Brohl, Kahen et al. 2017, Pemov, Li et al. 2020, Høland, Berg et al. 2023).

Recurrent translocations and gene fusions have not been consistently identified in MPNSTs, although isolated cases have been reported. A recent study has described a case of NF1-related MPNST with *NTRK* rearrangement (Hiemcke-Jiwa, Meister et al. 2022). Another study reported a sporadic MPNST patient with an *NTRK3* gene fusion (*SNRNP70-NTRK3*) (Kobayashi, Makise et al. 2023), while two other cases describing oncogenic gene fusions such as *TJP1-ROS1* and *EWSR1-VEZF1* (Benini, Gamberi et al. 2020, Li, Liu et al. 2020). Within our research group, we identified an MPNST patient carrying an *NTRK1-LMNA* fusion gene. Given that NTRK-associated fusions, including *LMNA-NTRK1*, have been described in mesenchymal tumors such as Lipofibromatosis-Like Neural Tumors (Brčić, Godschachner et al. 2021, Panse, Reisenbichler

et al. 2021), which closely resemble low-grade MPNSTs, the possibility of misdiagnosis in this case cannot be ruled out(Creus-Bachiller, Fernández-Rodríguez et al. 2023).

3.1. Molecular model of MPNST generation in the NF1 context

In the context of NF1, pre-existing benign pNFs may progress to malignant transformation, undergoing an intermediate stage as a pre-malignant tumor known as ANNUBP (Figure I2) (Nielsen, Stemmer-Rachamimov et al. 1999, Miettinen, Antonescu et al. 2017). The genetic events that drive the progression of pNF-ANNUBP-MPNST are summarized in three important steps (Zhang, Murray et al. 2020):

1. pNFs develop due to bi-allelic inactivation of *NF1* gene (Pemov, Li et al. 2017), resulting in hyperactivation of the RAS-MAPK pathway. No other recurrent gross genomic alterations or point mutations have been identified in pNFs (Pemov, Li et al. 2017, Carrió, Mazuelas et al. 2019).
2. ANNUBPs develop within the pNF and the *CDKN2A*-containing genomic region inactivation, often caused by structural variants (SV), constituting a bottleneck for MPNST formation (Lee, Teckie et al. 2014, Abeshouse A 2017, Brohl, Kahen et al. 2017, Sohier, Luscan et al. 2017, Magallón-Lorenz, Fernández-Rodríguez et al. 2021).
3. In addition to the complete inactivation of *NF1* and *CDKN2A*, MPNSTs harbor mutations in other TSGs, the most common being *SUZ12* or *EED*, two components of the PRC2 (De Raedt, Beert et al. 2014, Brohl, Kahen et al. 2017, Sohier, Luscan et al. 2017, Magallón-Lorenz, Terribas et al. 2023). Dysfunction of PRC2 leads to loss of the epigenetic mark H3K27me3 and subsequent gene de-repression, which drives malignant transformation. *TP53* is also mutated in some MPNSTs, although compared to other cancer types, it is relatively rare in agreement with other sarcomas (Lee, Teckie et al. 2014, Abeshouse A 2017, Brohl, Kahen et al. 2017, Sohier, Luscan et al. 2017).

Overall, classic MPNST are characterized by recurrent inactivation of *NF1*, *CDKN2A*, and *EED/SUZ12* (Magallón-Lorenz, Fernández-Rodríguez et al. 2021).

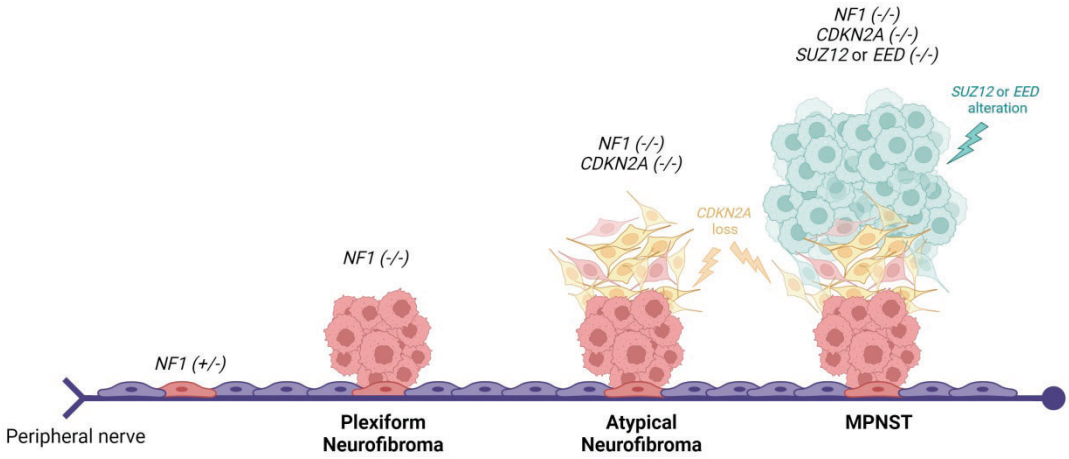

Figure I2. Genetic model of the pNF-ANNUBP-MPNST progression. *NF1* heterozygous mutated Schwann cells begin to overgrowth after complete inactivation of the gene, generating pNF (cells marked in red). As a second step, somatic bi-allelic inactivation of *CDKN2A* is recurrently found in ANNUBPs (cells marked in yellow), which may start accumulating mutations and copy-number alterations that result in the inactivation of other tumor suppressor genes like PRC2 subunits, evolving into MPNSTs (cells marked in green). Adapted from Zhang X et al. (2020) and image created with Biorender.

The microenvironment is believed to play a crucial role in cancer initiation. However, the specific interactions between microenvironmental cells and incipient cancer cells during tumor onset remain challenging to characterize. While the tumor microenvironment (TME) of MPNSTs has not been extensively studied, significant differences have been observed between the microenvironment of pNFs and MPNSTs. These differences suggest that certain cellular components and molecular factors within the TME may contribute additional growth signals, cytokines, or chemokines that accelerate MPNST progression (Peltonen, Marttala et al. 1981, Brockman, Scherer et al. 2022).

pNFs are benign tumors composed of a high proportion of neoplastic SC, fibroblasts, mast cells, and M2-polarized macrophages (Peltonen, Marttala et al. 1981, Walker and Upadhyaya 2018). Although immune cell recruitment occurs, there is no significant inflammatory response (Fletcher, Pundavela et al. 2020).

In contrast, MPNSTs are characterized by the transformation of neoplastic SC into a highly proliferative and aggressive phenotype. The TME of MPNSTs represents a very small percentage of these and contains a greater proportion of mesenchymal cells, activated cancer-associated fibroblasts (CAFs), and immunosuppressive immune cells (Cero, House et al. 2025). This immunosuppressive environment is marked by low or absent expression of PD-L1 and PD-1, infiltration of M2 macrophages, regulatory T cells, and reduced levels of cytotoxic CD8+ T cells, which collectively contribute to immune evasion (Shurell, Singh et al. 2016, Dancsok, Gao et al. 2020). Additionally, cytokine receptor interleukin-13 (IL-13R) is overexpressed in MPNSTs, enabling cancer cells to avoid cell death by binding to IL-13 without activating the α1 receptor (Mo, Chen et al. 2013, Mrowczynski, Payne et al. 2019).

The extracellular matrix (ECM) in pNFs is rich in collagen and proteoglycans, creating a relatively well-structured and less aggressive TME (Peltonen, Marttala et al. 1981). In contrast, the ECM in MPNSTs is highly degraded and remodeled, which enhances cell migration and invasion (Brockman, Scherer et al. 2022). MPNSTs overexpress MMP-2 and MMP-9, key matrix metalloproteinases involved in tumor dissemination (Brockman, Scherer et al. 2022).

Regarding angiogenesis, pNFs exhibit minimal vascularization, whereas MPNSTs display increased angiogenesis with elevated expression of VEGF (vascular endothelial growth factor), facilitating tumor progression (Gesundheit, Parkin et al. 2010). MPNSTs also undergo a metabolic shift toward aerobic glycolysis, promoting proliferation and resistance to hypoxia (Gesundheit, Parkin et al. 2010).

3.2. Differences between NF1-associated and sporadic MPNSTs

Sporadic MPNSTs are typically diagnosed in individuals between 30 and 50 years of age, with a mean age of 41 (Valentin, Le Cesne et al. 2016, Czarnecka 2018). In contrast, NF1-associated MPNSTs generally occur in younger patients, between 20 and 44 years old (Evans, Baser et al. 2002, Kolberg, Høland et al. 2013). However, pediatric onset is also possible, particularly in the context of NF1 (Friedrich, Hartmann et al. 2007). MPNSTs can metastasize widely in NF1 compared to MPNSTs in the general population (van Noesel, Orbach et al. 2019).

Clinically, NF1-related MPNSTs are associated with a worse prognosis than sporadic cases, though the underlying reasons remain unclear (Evans, Baser et al. 2002, Hwang, Hahn et al. 2017). This poorer prognosis aligns with a reduced chemotherapeutic response, with response rates ranging from 17.6-17.9% in NF1-associated cases compared to 44-55.3% in sporadic cases (Carli, Ferrari et al. 2005, Higham, Steinberg et al. 2017).

Despite differing clinical backgrounds, the histology of MPNSTs in both groups is very similar (Zhou, Coffin et al. 2003), with some difference reported as that NF1-associated tumors had a significantly higher cell density ($p < 0.001$) whereas sporadic tumors were characterized by a marked pleomorphism as compared to NF1 tumors ($p < 0.01$) (Hagel, Zils et al. 2007).

Gene expression profiling reveals significant similarities between NF1-associated and sporadic MPNSTs, with only minor differences (Watson, Perry et al. 2004). While PRC2 dysfunction is found in 70% of NF1-associated MPNST and 92% of sporadic cases (Lee, Teckie et al. 2014, Cleven, Al Sannaa et al. 2016, Prieto-Granada, Wiesner et al. 2016), the percentage of *NF1* and *CDKN2A* TSG inactivation is similar in both settings (Lee, Teckie et al. 2014). Still, unique genetic features have been identified in sporadic MPNSTs, such as mutations in the promoter

region of *TERT*, which encodes a subunit of the telomerase enzyme (Dubbink, Bakels et al. 2014). Additionally, differential expression of several microRNAs (miRNA) distinguishes NF1-associated and sporadic MPNSTs (Amirnasr, Verdijk et al. 2020).

The pathogenic mechanisms leading to MPNSTs may differ between NF1-related and sporadic cases (Longo, Brosius et al. 2021). In NF1-associated MPNSTs, tumorigenesis follows as well-characterized progression: an initial germline *NF1* mutation predisposes individuals to a secondary inactivating event, leading to the formation of benign pNFs, which can undergo malignant transformation. In contrast, sporadic MPNSTs arises *de novo*, without a known benign precursor, and their tumorigenic process remains poorly understood (Somatilaka, Sadek et al. 2022).

I4. Recurrent Altered Pathways in MPNSTs

4.1. *NF1* Inactivation: Upregulation of RAS Pathway

MPNSTs have inactivated the *NF1* gene, which is a TSG located on chromosome 17 (17q11.2) (Viskochil, Buchberg et al. 1990, Wallace, Marchuk et al. 1990) and covers a genomic size of 350 kb, being one of the largest genes in the genome (Li, O'Connell et al. 1995). The *NF1* gene has been reported to contain either 57–58 coding exons (according to Ensembl) or 61 exons (as noted in NCBI and UCSC Genome Browser). Among them, five undergo alternative splicing: 9a, 10a, 23a, 43, and 48a (Shen, Harper et al. 1996) and it has one of the highest mutation rates described.

NF1 encodes neurofibromin, a 280 kDa protein (Gutmann, Wood et al. 1991), which is highly conserved among mammals and is ubiquitously expressed in various tissue, such as thyroid gland, pancreas, liver, stomach, among others. Neurofibromin is primarily localized in the cytoplasm, although nuclear localization has been reported (Gutmann, Wood et al. 1991, Kaufmann, Müller et al. 2002)

Recent studies have revealed that neurofibromin forms high-affinity dimers, although the implications of this structure in the protein function are only beginning to be understood (Young, Goldstein de Salazar et al. 2023). There are some domains of neurofibromin that have been extensively described and characterized; however, its large size suggests that the full picture of its function remains partially unknown (Carnes, Kesterson et al. 2019, Sherekar, Han et al. 2020). The most important function of neurofibromin lies in the GTPase-activating protein-related domain (GRD) (Xu, O'Connell et al. 1990, Bergoug, Doudeau et al. 2020). Through the GRD domain, neurofibromin hydrolyses the active form of the RAS oncogenic

protein (RAS-GTP) to its inactive form (RAS-GDP) (Ballester, Marchuk et al. 1990, Bos, Rehmann et al. 2007, Ratner and Miller 2015), thus negatively regulating this pathway (Figure I3).

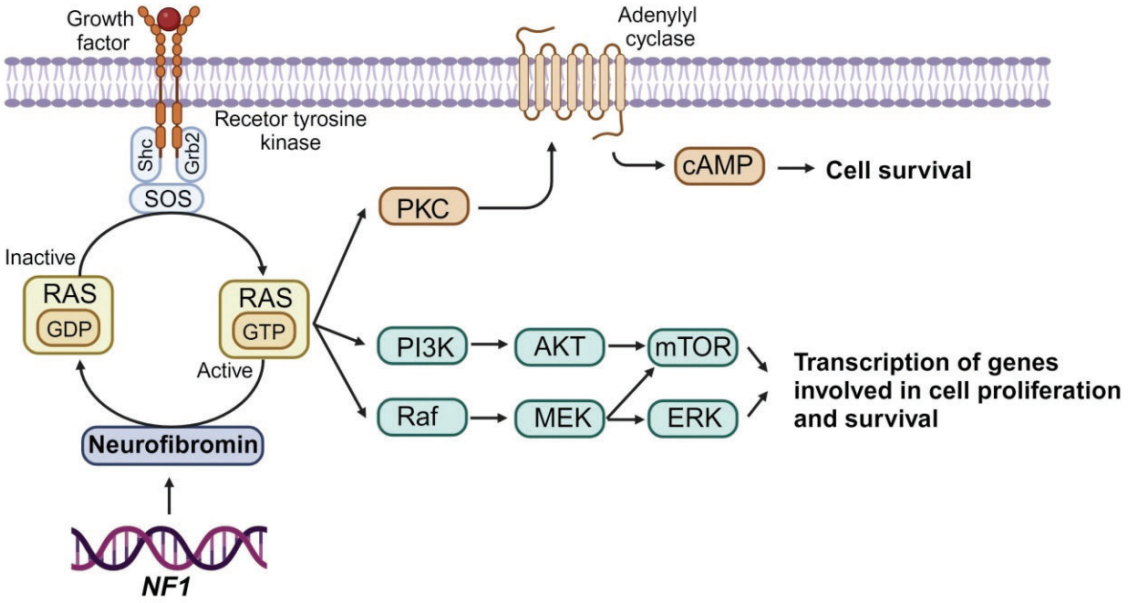

Figure I3. Schematic representation of RAS pathway. Neurofibromin regulates cell growth and survival through several downstream signaling effectors by accelerating the conversion of active GTP-bound RAS to its inactive GDP-bound form. RAS signaling can be activated by receptor tyrosine kinases (RTKs) following the binding of growth factors, which results in increased AKT and/or MEK activity and, subsequently, greater cell proliferation and/or survival. In addition, RAS controls the generation of cyclic AMP (cAMP) through protein kinase C (PKC). Depending on the cell type, RAS signaling might differentially use these downstream effectors, resulting in different cellular consequences. ERK, extracellular signal-regulated kinase; mTOR, mechanistic target of rapamycin. Adapted from Gutmann D.H. et al. (2017) and image created with Biorender.

When neurofibromin is not correctly expressed due to inactivating mutations in the *NF1* gene, the downstream effects on cellular signaling contribute significantly to tumorigenesis and other pathological conditions. The degradation of neurofibromin, usually through the ubiquitin-proteosome pathway (Cichowski, Santiago et al. 2003), results in the overexpression of active RAS (Carroll 2012), which recruits and activates the serine/threonine protein kinase RAF that consequently activates MEK1/2 and ERK1/2. The latter phosphorylates downstream effectors, driving the expression of genes involved in cell cycle progression, proliferation, and differentiation. Moreover, loss of neurofibromin also promotes upregulation of the PI3K/AKT/mTOR signaling pathway, a key pathway that controls cell growth, metabolism, and survival.

Besides these two major pathways, neurofibromin also regulates the generation of cyclic AMP (cAMP), adding another layer of dysregulation to cellular processes (Machado Almeida, Lago Solis et al. 2021). When neurofibromin is inactive or absent, there is a reduction of cAMP levels, disrupting signaling mediated by protein kinase A (PKA) and other downstream effectors, which are critical for controlling cell growth, differentiation, and survival. This

protein has been described to participate in axon length, growth cone diameter, and survival of CNS neurons. The deregulation of this pathway has been linked to the neurodevelopmental disorders associated with the NF1 (Brown, Gianino et al. 2010).

4.2. *CDKN2A* Inactivation: Cell Cycle Disruption

The *CDKN2A* gene is one of the two major genes in the *CDKN2A/B* locus. It is located on chromosome 9 at position 9p21.3 and has 10 exons. *CDKN2A* is not constitutively activated; its activation occurs in response to specific signals during the cell cycle, particularly in situations of stress or cell damage. *CDKN2A* encodes for two proteins, $P16^{INK4a}$ and $p14^{ARF}$, which share part of the exon 2, but each has a different and unique first exon, giving them a different open reading frame (Serrano 2000, Kim and Sharpless 2006) (Figure I4). $p14^{ARF}$ binds to MDM2, blocking the ubiquitinization and degradation of p53 and arresting the cell cycle when its needed. $p16^{INK4a}$ works by binding to CDK4 and CDK6, preventing the formation of the CDK4/Cyclin D1 complex and the phosphorylation of Retinoblastoma (pRB), which inhibits the release of the transcription factor E2F to the nucleus. As a result, the cell cycle is arrested, therefore, the main function of *CDKN2A* is the regulation of the cell cycle, together with its implication in replicative senescence, apoptosis, and stem-cell self-renewal (Gil and Peters 2006).

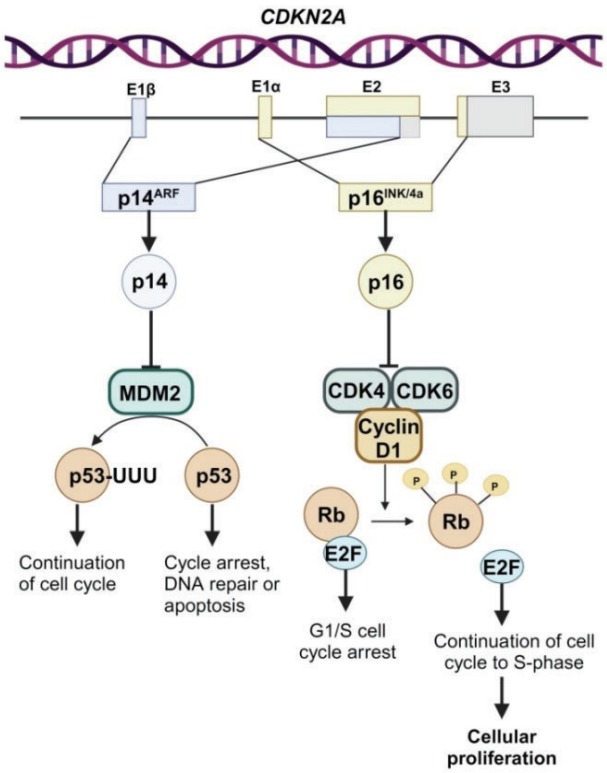

Figure I4. Schematic representation of the locus and signaling pathways regulated by $P16^{INK4a}$ and $p14^{ARF}$. $P14^{ARF}$ coding exons are represented in blue color, while $p16^{INK4a}$ exons are represented in yellow color. These proteins regulated negatively cell cycle. Adapted from Di Lorenzo, S.et al. (2016) and image created with Biorender.

In the event of *CDKN2A* loss, cell division is promoted through the induction of S phase of the cell cycle (Wagner and Gil 2020). In addition, inactivation of *CDKN2A* also causes degradation of the *TP53* product, thereby reducing cell apoptosis (Gil and Peters 2006). Inactivation of *CDKN2A* in MPNSTs occurs mostly through genomic translocations, many of which in a 500bp intronic hotspot near exon 2 of the gene (Beert, Brems et al. 2011, Magallón-Lorenz, Fernández-Rodríguez et al. 2021).

In addition to its involvement in MPNSTs, a comprehensive study linked *CDKN2A* gene to a broad panel of tumors, including lung, breast, ovarian, pancreatic, and prostate; observing point mutations in 5% of cases and making this gene one of the most recurrently inactivated in cancer (Kan, Jaiswal et al. 2010).

4.3. *EED/SUZ12* Inactivation (PRC2): Loss of Methylation of Histone 3 Lysine 27

As mentioned in Section 3.1, the inactivation of the PRC2 is a major driver in the tumorigenic process from an ANNUBP to an MPNST. The recurrent altered components of PRC2 in MPNST are *SUZ12* or *EED*, located on chromosome 17 (position 17q11.2) and chromosome 11 (position 11q14.2), respectively (De Raedt, Beert et al. 2014, Lee, Teckie et al. 2014, Patel, Liao et al. 2014, Zhang, Wang et al. 2014). These two components, together with *EZH1/EZH2,* form the core of the PRC2, which main function is to repress gene expression by methylating the Lysine 27th residue of histone 3 (H3K27) (Lee, Teckie et al. 2014) (Figure I5A). This complex is a crucial epigenetic regulator during early development, maintaining a specific gene expression pattern in each cell type (Simon and Kingston 2009, Margueron and Reinberg 2011, Zhang, Murray et al. 2020). While tri-methylation (H3K27me3) is the most extensively studied PRC2 epigenetic marker, mono- and di-methylation are also present across the genome, although their effects are less well understood.

Overall, genetic alterations affecting PRC2 have been reported in several cancer cell types (Zhan, Hardin et al. 2002). In the MPNST context, the inactivation of *SUZ12* and *EED* genes is mutually exclusive. Loss of *SUZ12* or *EED* triggers significant epigenetic changes, including increased global levels of H3K27 acetylation (H3K27Ac), which mediates the recruitment of Bromodomain 4 (BRD4) to chromatin (Figure I5B) (Filippakopoulos, Picaud et al. 2012). BRD4 is a key member of the bromodomain and extra-terminal domain (BET) family of epigenetic reader proteins, alongside BRD2, BRD3, and BRDT. BET proteins such as BRD4 bind to acetylated histones using their BD1 and BD2 bromodomains and promote the recruitment of transcriptional machinery to open chromatin regions (Wu and Chiang 2007, Zhang, Murray et al. 2020). Consequently, lack of PRC2 activates the transcription of genes associated with

tumorigenesis, such as c-*MYC* or members of the RAS pathway (Figure I5C) (De Raedt, Beert et al. 2014).

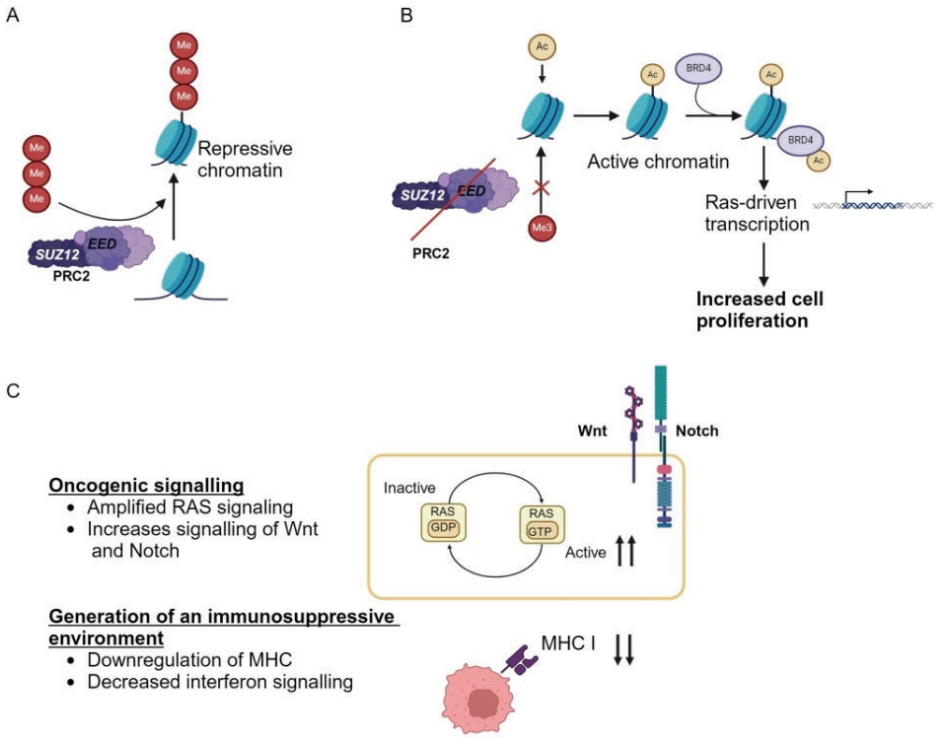

Figure I5. Molecular model showing gene transcription activation on MPNSTs due to PRC2 dysfunction. A. Histone 3 methylation by PRC2 leads to a repression of gene expression. **B.** Mutated *EED* or *SUZ12* in MPNSTs lead to loss of methylation and subsequent acetylation at Histone 3, which recruits BRD4 and opens the chromatin for expression of oncogenes like *RAS*, resulting in malignancy. **C.** Summary of the most notorious molecular changes in signaling pathways due to PRC2 inactivation in MPNSTs. MHC: Major Histocompatibility Complex. Adapted from Zhang X. et al. (2020) and image created with Biorender.

PRC2 deficiency has been associated with overexpression of components of the *Wnt* pathway, which is involved in several biological processes and has been implicated in the oncogenesis of various tumors (Figure I5C). The Notch pathway is another oncogenic pathway that has been implicated in PRC2 (Figure I5C). In this case, activation of Notch receptors leads to the formation of a complex that can recruit PRC2 to repress certain genes. However, when PRC2 is deficient, this repression can be disrupted, resulting in the activation of genes that contribute to oncogenesis (Zhang, Murray et al. 2020). In addition, loss of PRC2 in MPNST may also lead to immune evasion, allowing tumor cells to evade recognition and elimination by immune cells (Figure I5C) (Zhang, Murray et al. 2020, Brockman, Scherer et al. 2022). In particular, Zhang X. et al. (2020), observed that decreased PRC2 activity may result in reduced MHC class I antigen presentation, which is critical for CD8+ T cell activation (Zhang, Murray et al. 2020).

Finally, it has been described that inactivation of PRC2 in MPNST significantly affects chromatin organization, leading to genomic instability (Liu 2022, Angelico, Mazzucchelli et al. 2024). PRC2

plays a critical role in maintaining higher-order chromatin structures, such as chromatin compaction and long-range interactions, which are essential for transcriptional repression. Its loss disrupts these regulatory mechanisms, increasing chromatin accessibility and facilitating the accumulation of DNA damage, thereby promoting genomic instability (Liu 2022). In addition, inactivation of PRC2 has been associated with increased chromosomal rearrangements, loss of transposable element control, and higher mutation rates, further contributing to the aggressive nature of MPNST (Liu 2022, Angelico, Mazzucchelli et al. 2024).

4.4. TP53 Inactivation

TP53 gene is located on the short arm of chromosome 17 (17p13.1) and encodes a 393 amino acid protein called p53. Initially, *TP53* was thought to be an oncogene, as high levels of p53 conferred significant tumorigenic potential in rat embryonic fibroblasts (Parada, Land et al. 1984). Subsequent studies led to a re-evaluation of *TP53*, showing that *TP53* complementary DNA (cDNA) from non-tumoral cells did not transform them, while inhibited the growth of tumor cells (Lane and Benchimol 1990). Further research demonstrated that overexpression of *TP53* gene effectively suppressed the transforming effects of oncogenes, such as *MYC* and *RAS*, confirming *TP53*'s role as a TSG (Donehower, Harvey et al. 1992). The p53 protein is activated as a response to cellular stress DNA damage, oncogene activation, ribosomal stress, or hypoxia, inducing cell cycle arrest, apoptosis, and senescence (Hainaut and Hollstein 2000). In MPNST context, the inactivation of *TP53* is associated with reduced patient survival and poorer response to neo-adjuvant chemotherapy (Halling, Scheithauer et al. 1996, Zou, Smith et al. 2009, Høland, Kolberg et al. 2018).

Although the *TP53* gene is mutated in more than half of human cancers, its role in MPNST formation is controversial and relatively unknown compared to other sarcomas (Abeshouse A 2017). However, in 1999 Cichowski, et al. created the first genetically engineered mouse model (GEMM) of MPNST by combining *Nf1* and *Tp53* knock-out, which generated MPNST-like tumors (Cichowski, Shih et al. 1999), suggesting a possible involvement of *TP53* in the tumorigenic process.

I5. Preclinical Models for MPNST

Preclinical models are essential to improve our understanding of MPNST biology and to evaluate therapeutic strategies for patients. The key requirement to generate useful models is that they accurately replicate the primary characteristics of the human tumors they represent, enabling a reliable correlation between treatment response in the model and clinical outcome

in patients (Dhandapani and Goldman 2017). The preclinical models are divided in two general subgroups: *in vitro* and *in vivo* models. *In vitro* models are primarily cultured cell-based research platforms (2-D or 3-D), whereas *in vivo* models involve live animals (White, Swier et al. 2018, Somatilaka, Sadek et al. 2022). Both can be generated from primary, metastatic or recurrent MPNSTs. The characteristics of each model are summarized in Table I1.

Table I1. Main features of *in vitro* (2-D and 3-D cell cultures) and *in vivo* (CDX, GEM, and PDX) models

	Main features	2D Cell Culture	3D Cell Culture	CDX	GEM	PDX
		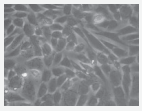	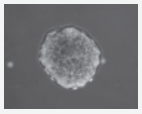		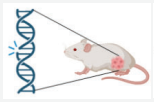	
Main features of the model	**Complexity**	Monoculture	Monoculture organoids or multiple cell type spheroids	Human tumor derived from a monoculture with mouse TME	Mouse tumor generated with mouse TME	Human tumor derived from patient with human/mouse TME
	Manipulation	Easy	Complex	Easy	Complex	Complex
	Data reproducibility	Favorable	Favorable	Unsuited	Unsuited	Unsuited
	Set-up time	Short	Medium	Large, tumor type dependent	Large	Very large, tumor type dependent
	Monitored environment	Yes	Yes	No	No	No
Patient's tumor features recapitulation	**Immune microenvironment**	No	No	No, immuno-compromised mice are used	Yes	No, immuno-compromised mice are used
	Genetics/Genomics	Same as the patient but loss of tumor genetic heterogeneity	Same as the patient but loss of tumor genetic heterogeneity	Same as the patient but loss of tumor genetic heterogeneity	Same patient genetic mutations but loss of genome complexity	Same genetic, genomic complexity and heterogeneity
	Tumor cell heterogeneity	Low	Moderate	Moderate	High	High
Usefulness of the model	**High througput screening**	Most suitable	Suitable	Unsuitable	Unsuitable	Unsuitable
	Personalized treatments	Suitable	Suitable	Suitable	Unsuitable	Most suitable
	Drug resistance	Suitable	Suitable	Suitable	Suitable	Suitable
	Metastasis studies	Unsuitable	Unsuitable	Suitable	Suitable	Suitable
	Discovery of molecular tumor drivers/targets	Suitable	Suitable	Unsuitable	Most suitable	Unsuitable

CDX: Cell-Derived Xenograft; GEM: Genetically Engineered Mouse; PDX: Patient-Derived Xenograft

5.1. MPNST *In Vitro* Models

The development of *in vitro* models is a fundamental tool for advancing the understanding of cancer biology. These models have been widely used in the MPNST context to study the molecular pathogenesis of TSGs and other relevant genes (Somatilaka, Sadek et al. 2022), to analyze gene expression for the identification of novel biomarkers and tumor drivers (Miller, Rangwala et al. 2006), and in preclinical studies to evaluate new therapeutic approaches (Fernández-Rodríguez, Creus-Bachiller et al. 2022). The most used *in vitro* models are 2-D, although in recent years the generation of 3-D models has been promoted.

5.1.1. 2-Dimensional (2-D) MPNST Cell Models

According to the *Cellosaurus* online database of cancer cell lines (version 51, updated December 2024), 44 different MPNST cell lines have been established and characterized by various laboratories (https://www.cellosaurus.org/). However, only five of these are available in public cell banks, such as the American Type Culture Collection (ATCC). While detailed information is lacking for many of these 44 lines, their analysis reflects the heterogeneity observed in MPNST tumors. The collection includes cell lines derived from both primary tumors and metastases or recurrent cases, representing both male and female patients, with ages ranging from 8 to 86 years.

The most widely used MPNST cell lines are the NF1-related S462 (Frahm, Mautner et al. 2004), sNF96.2 (Li, Rao et al. 2004), ST88-14 (Glover, Stein et al. 1991), NF90-8 (Glover, Stein et al. 1991), NMS-2 (Imaizumi, Motoyama et al. 1998), and sNF02.2 (Li, Rao et al. 2004); and the sporadic STS26T (Dahlberg, Little et al. 1993), HS-Sch-2 (Sonobe, Takeuchi et al. 2000), and HS-PSS. The main issue regarding the use of these cell lines is that they have not been extensive genomically characterized using sequencing techniques like whole exome sequencing (WES) or whole genome sequencing (WGS) while being used as models for many years (Williams and Largaespada 2020). One recent study analyzed eight of these commonly used MPNST cell lines using genomic, epigenomic, and molecular approaches and reported that sporadic cell lines STS26T, HS-Sch-2, and HS-PSS may be wrongly identified as MPNST, as there is evidence that they may be derived from a melanoma, a desmoplastic melanoma, and an epithelioid inflammatory myofibroblastic sarcoma, respectively (Magallón-Lorenz, Terribas et al. 2023). This study highlighted the importance of performing genetic analysis on patient's tumors as a diagnostic tool and better clinical management, especially in sporadic cases. Besides, the use of misidentified cell lines over the years for the testing of new therapies for MPNST may have led to unreliable preclinical results.

MPNST cell lines present diverse morphology, ranging from an elongated spindle-shaped to a polygonal shape (Oyama, Kito et al. 2020, Bhalla, Landers et al. 2022). They exhibit a wide range of population doubling times (PDTs), reflecting the heterogeneous functional features of these models, with values ranging from 16 to 96 hours depending on the cell line, as reported in *Cellosaurus* and other studies (Bhalla, Landers et al. 2022). MPNST cell lines are generally highly invasive, which correlates with the aggressive nature of MPNSTs in patients, and this ability is greater in sporadic cells than in NF1-related (Oyama, Kito et al. 2020). In addition, most of these cell lines are able to generate tumors in mice, becoming valuable tools in

preclinical studies. MPNST cell lines can retain the expression of tumor biomarkers, such as expression of SOX9 and absence of SOX10 and S100B (Miller, Jessen et al. 2009, Miettinen, Antonescu et al. 2017, Magallón-Lorenz, Terribas et al. 2023).

These models are particularly valuable for high-throughput drug screening, allowing the testing of a large number of compounds efficiently (Fernández-Rodríguez, Creus-Bachiller et al. 2022). Additionally, they play a crucial role in pharmacogenomics studies, enabling the assessment of differential drug sensitivity across various cell lines. Beyond drug testing, these models are also instrumental in the development of gene-editing techniques, such as CRISPR-Cas9 and synthetic lethality approaches, which help identify key genetic drivers of the disease and potential therapeutic targets Cas9 (Barretina, Caponigro et al. 2012).

5.1.2. 3-Dimensional (3-D) MPNST Model

2-D cell cultures are prone to genetic drift and are not representative of human tumor complexity because they cannot mimic the tumor microenvironment and the natural cell interactions (cell-cell and cell-matrix). For this reason, three-dimensional (3-D) cultures are becoming increasingly popular to close the gap between cell and animal models. Moreover, this system is more suitable for the optimal translation of preclinical results to clinical trials (Habanjar, Diab-Assaf et al. 2021).

In cNF and pNF studies, iPSC-differentiated cells are often cultured in 3-D low-attachment plates as spheroids or organoids (Huch and Koo 2015). Spheroids are scaffold-free or hydrogel-supported 3-D cell cultures, while organoids are self-organizing structures derived from stem cells, closely resembling their tissue of origin (Huch and Koo 2015). Spheroids can be homotypic (single-cell type) or heterotypic (multiple cell types), with the latter providing a more physiologically relevant model for studying tumor or organ behavior *in vivo* (Weydert, Lal-Nag et al. 2020).

In the MPNST context, 3-D models are still under development. There is only one study from Larsson et al. (2023) that has reported the creation of tumor microtissues using cells derived from Patient Derived Xenograft (PDX)-MPNSTs tumors. The study compared the effect of three known compounds in their PDX-derived microtissues and in PDX mouse models, observing that their 3-D-tissues better predict the *in vivo* drug response (Larsson, Bhatia et al. 2023). However, this study recognizes several limitations, thus these 3-D-models are still in an early stage of development.

5.2. MPNST *In Vivo* Mouse Models

The mouse (*Mus musculus*) is currently the most widely used animal species in scientific experimentation due to its reproductive characteristics, size and easy manipulation (Somatilaka, Sadek et al. 2022). Moreover, the mouse genome was fully sequenced in 2002 and there is extensive knowledge about conserved gene regions between mouse and human genomes (Waterston, Lindblad-Toh et al. 2002). Murine models are useful for the study of human cancer; for instance, factors involved in malignancy, invasion and metastasis, as well as the prediction of drug response and toxicity to evaluate the use of novel treatments in humans. Besides mice, zebrafish, flies (*Drosophila*), and even pigs, among others, have been used as models to study NF1 and MPNST (White, Swier et al. 2018, Somatilaka, Sadek et al. 2022).

There are several types of mouse models, but the two most widely used are GEMMs, which are genetically modified mice that generate tumors through mutations in specific genes, and xenografts, generated by engraftment of tumor cell lines or patient's tumor fragments in immunocompromised mice.

5.2.1. Genetically Engineered Mouse Models

GEMMs are powerful tools in cancer research, enabling precise genome modifications through the deletion or overexpression of specific genes. These alterations typically involve key driver genes implicated in tumor malignancy (Somatilaka, Sadek et al. 2022). Over the years, various MPNST-GEMMs have been developed using different gene-editing technologies, including germline knockouts, conditional knockouts, and, more recently, the CRISPR/Cas9 system.

The first MPNST-GEMM models were generated using germline knockout approaches, with *Nf1* being the most frequently inactivated gene for inducing tumor development. However, complete inactivation of both *Nf1* alleles in mice is lethal, leading to embryonic death due to cardiovascular and NC abnormalities (Brannan, Perkins et al. 1994). To circumvent this, the most widely used model, NPcis, was developed. This model carries germline cis-heterozygous loss of function (LOF) mutations in both *Nf1* and *Trp53* ($Nf1^{+/-}$; $p53^{+/-}$) (Cichowski, Shih et al. 1999, Vogel, Klesse et al. 1999). However, a key limitation of this model is that *Trp53* inactivation is not among the most common genetic alterations in human MPNSTs, unlike *Cdkn2a* and components of the PRC2 complex (*Suz12/Eed*), which may limit its ability to replicate the transcriptomic landscape of human tumors (Williams and Largaespada 2020).

To address this issue, Joseph et al. developed a mouse model harboring mutations in *Nf1* and *Cdkn2a* (*Nf1*$^{+/-}$; *p16*^{Ink4a}/*p19*^{Arf}*-/-)* (Joseph, Mosher et al. 2008). Additionally, De Raedt et al. generated two GEM models targeting PRC2 inactivation: one with germline heterozygous mutations in *Nf1* and *Suz12* (*Nf1*$^{+/-}$; *Suz12*$^{+/-}$), mimicking the genetic conditions found in NF1 microdeletion patients, and another model incorporating a heterozygous mutation in *Trp53* (*Nf1*$^{+/-}$; *p53*$^{+/-}$; *Suz12*$^{+/-}$), which accelerates MPNST development compared to the NPcis model, albeit with a higher incidence of gliomas (De Raedt, Beert et al. 2014).

Other GEMMs have been developed to study key pathways involved in MPNST pathogenesis, including RTKs such as *EGFRWa2/+* (Ling, Wu et al. 2005, Keng, Rahrmann et al. 2012, Wu, Patmore et al. 2014, Peacock, Pridgeon et al. 2018), growth factors (Huijbregts, Roth et al. 2003), and the Hippo pathway regulators *Lats1/Lats2* (Wu, Deng et al. 2018).

Beyond germline knockouts, conditional knockout models using the Cre-Lox system and tissue-specific promoters have been developed. In this system, Cre recombinase expression leads to excision of loxP-flanked target genes, enabling temporal and spatial control of gene depletion. This approach has been used to create various MPNST models, such as *Dhh-Cre*, *Periostin-Cre*, and *GFAP-Cre*, which induce gene deletion in embryonic SC lineage (Inoue, Janke et al. 2021). Additionally, viral infection methods have been employed to induce mutations in specific tissues (Hirbe, Dahiya et al. 2016).

In 2017, Huang et al. successfully applied CRISPR-Cas9 technology to generate MPNST-GEM models, a technique widely used in other cancers, including pancreatic, liver, and lung cancer. Despite the heterogeneity of sarcomas, Huang et al. developed a GEMM incorporating mutations in *Nf1* (sgRNANf1) and *Trp53* (sgRNATrp53) (Huang, Chen et al. 2017). Their study demonstrated that CRISPR-generated MPNST models closely resemble human tumors in terms of histology, growth kinetics, copy number variations (CNVs), and mutational load, highlighting CRISPR's potential as a more efficient alternative to conventional gene-editing methods.

GEMMs offer several advantages, including the ability to track tumor development from early stages and investigate specific genes involved in tumor pathogenesis. Additionally, these models allow tumors to grow within an intact immune system, better mirroring human physiological responses at a systemic level (Richmond and Su 2008, Clohessy and Pandolfi 2015).

However, GEMMs also present limitations. They can target only a limited number of genes, making it difficult to replicate the full genomic complexity of MPNSTs, including aneuploidy

and large structural variants (Richmond and Su 2008, Mohamad, Plante et al. 2021). Tumor development is often slow and unpredictable, making these models costly and time-consuming to establish and maintain (Clohessy and Pandolfi 2015). Additionally, since the tumors originate in mice, drug response correlations between these models and human patients can be limited (Lin 2008).

Another significant limitation of GEMMs is the lack of standardized criteria for tumor identification and classification. In 2004, a study established histological criteria for defining high-grade (Grade III) GEMM-PNSTs, which include hypercellularity, nuclear atypia, increased mitotic activity, and the presence of necrotic or hemorrhagic regions (Stemmer-Rachamimov, Louis et al. 2004). Furthermore, tumors should arise from a peripheral nerve, exhibit S100B positivity, and demonstrate invasive behavior in adjacent tissues (Stemmer-Rachamimov, Louis et al. 2004). However, not all models meet these criteria, and most fail to recapitulate the complex genetic alterations that drive human MPNST pathogenesis (Mohamad, Plante et al. 2021).

5.2.2. Xenograft MPNST Mouse Model

Xenografts models are *in vivo* systems where the human samples are implanted into immunodeficient mice. These models can be generated by engraftment of tumor cell lines (Cell line Derived Xenograft, CDX) or a piece of a patient tumor (PDX). The immunodeficient mice strains used possess genetic mutations that impair the immune system function, allowing the human tumor cells to grow without being rejected. There are three main strains of immunodeficient mouse (Morgan 2012, Chen, Liao et al. 2022):

- Nude mice: These mice have a mutation in the *Foxn1* gene, which is crucial for the development of thymic epithelial cells. The phenotype is a severely underdeveloped thymus, leading to a significant reduction in mature T cells and a characteristic lack of body hair.
- Non-obese diabetic/severe combined immunodeficiency (NOD/SCID) mice: These mice harbor a mutation in the *Prkdc* gene, which encodes a protein kinase essential for DNA repair. The mutation disrupts the development of functional T and B cells, resulting in a profound deficiency of the immune system.
- NOD/SCID gamma (NSG) mice: In combination with the NOD/SCID mutation, these mice have a mutation in the *IL2rg* gene, which encodes the common gamma chain, an important component in multiple cytokine receptors, leading to a deficiency in natural killer (NK) cells and a complete absence of T and B cells. NSG mice exhibit the most

severe immunodeficient phenotype, as they lack multiple cytokines signaling pathways and possess defects in innate immunity.

Beside the strain used for the models, the xenografts can also be classified according to the location of the human tumor or cells engraftment leading to two main groups: subcutaneous and orthotopic. In subcutaneous xenograft models, samples are implanted directly under the skin of the mice. This approach is advantageous because the procedure to implant the tumors is less challenging, and the resulting tumors are easier to palpate and measure as they grow. In orthotopic xenograft model, samples are implanted at the site corresponding to their origin in the patient. For MPNSTs, this would typically involve engraftment along the sciatic nerve of the mouse (Castellsagué, Gel et al. 2015). Orthotopic models are a valuable resource because they provide a TME that closely resembles the original tumor site in patients. This setup also better preserves the tumor's biological properties, as it has a faster growth (more similar to what happens in the patient) and metastatic potential, which allows for more clinically relevant results (Kim, Evans et al. 2009, Ruggeri, Camp et al. 2014). Less frequently, engraftments may also be performed into the intracapsular fat pad (Liu, Wu et al. 2023).

The xenograft models are crucial for studying MPNSTs as they allow researchers to investigate tumor growth, metastasis, and response to therapies. However, they also have limitations, such as the lack of a fully functional immune system. This may lead to potential differences in tumor biology due to the host mouse environment and precludes the use of immunological drugs as a preclinical strategy. In addition, the immunodeficient mice strains are more sensitive to infections with virus or bacteria, which may influence tumor growth or the sensitivity to drug treatments side-effects (Besselsen, Franklin et al. 2008, Jin, Yoshimura et al. 2023). Additionally, significant limitation of this model is the potential mismatch between human tumor receptors and murine ligands, which can impede efficient tumor growth proliferation in the xenograft setting (Clohessy and Pandolfi 2015).

5.2.2.1. Cell-Derived Xenograft (CDX) Models

CDX consists of injecting cell lines derived from patient into the mouse. These cancer cells have been adapted to grow outside their original tumor microenvironment (Liu, Wu et al. 2023). These models are preferred because the highly aggressive nature of MPNST cells facilitates their growth in immune-deficient mice. However, it has been described that the proliferative capacity of the MPNST tumor cells in xenografts models can vary significantly, depending on the number of cell culture passages they have undergone prior to implantation (Oyama, Kito et al. 2020). They provide a relatively straightforward and reproducible system for studying

tumor biology, drug response, and the mechanisms underlying tumor progression. Several widely used MPNST cell lines has been used for CDX models generation, although the most used MPNST is S462 (Jessen, Miller et al. 2013, Gu, Wang et al. 2022, Kohlmeyer, Lingo et al. 2023).

The main limitation of this model is that tumor heterogeneity is lost, as well as tumor microenvironment populations, due to tumor grows in an immuno-compromised system (Liu, Wu et al. 2023). In addition, tumor cell lines cultured *in vitro* often acquire genetic alterations that may arise from adaptation to the artificial conditions of cell culture (Siolas and Hannon 2013). These alterations may lead to differences in tumor behavior compared to primary tumors, including variations in growth rate, invasiveness, and response to therapies.

5.2.2.2. Patient-Derived Xenograft (PDX) Models

PDX consists of engrafting a piece of tumor from a patient into the mouse. PDX models are considered the most suitable *in vivo* system for recapitulating human tumor biology, primarily because they better maintain the heterogeneous composition of the original tumors, including not only cancer cells but also TME components such as the ECM, stromal cells, and immune cells. However, after the first passage the human stromal component of the tumor is replaced by murine cells (Castellsagué, Gel et al. 2015, Blomme, Van Simaeys et al. 2018). The preservation of the TME is critical for accurately modeling the tumorigenic process and predicting responses to treatments, making PDX models also valuable for drug testing (Abdolahi, Ghazvinian et al. 2022). PDX is highly relevant for studying tumor biology, including therapeutic resistance and tumor evolution. Moreover, PDX models enable the study of human-specific drug responses, aiding in the identification of predictive biomarkers for treatment efficacy and resistance.

Despite these advantages, PDX have been underused for MPNST modeling. Most of preclinical MPNST studies were performed with PDX engrafted subcutaneously (Bhola, Banerjee et al. 2010, Ramkissoon, Chaney et al. 2019, Dehner, Moon et al. 2021, Kohlmeyer, Lingo et al. 2023, Larsson, Bhatia et al. 2023). There are few studies using patient-derived orthotopic xenografts (PDOX) (Mohan, Castellsague et al. 2013, Castellsagué, Gel et al. 2015, Fernández-Rodríguez, Morales La Madrid et al. 2020, Fernández-Rodríguez, Creus-Bachiller et al. 2022). In this field, our group successfully has generated several MPNST-PDOX models, engrafting both sporadic and NF1-related tumors (Creus-Bachiller, Fernández-Rodríguez et al. 2023). However, one of the main limitations of this models is that the efficiency of engraftment is highly variable between tumors (Richmond and Su 2008).

Personalized Medicine Strategy Using PDX

PDX models are valuable for the implementation of personalized medicine strategies, providing a platform for testing and developing individualized therapeutic strategies (Clohessy and Pandolfi 2015). This model supports clinical decision making by enabling the generation of patient-specific model, often referred to as mouse 'avatar'. As shown in Figure I6, tumor tissue from a patient is engrafted into immunodeficient mice while the patient receives conventional therapy or undergoes surgery; then the tumor is expanded in the mice. During this period, genomic analysis is performed to identify key genetic alterations. Based on these findings, treatments targeting deregulated pathways in tumors are selected and tested in the 'avatar' mice. The preclinical results are then reported to a molecular tumor board (MTB), which uses the data to inform clinical decisions and allows a personalized treatment plan that can be implemented when the patient experiences disease progression, recurrence, or metastasis, (Abdolahi, Ghazvinian et al. 2022).

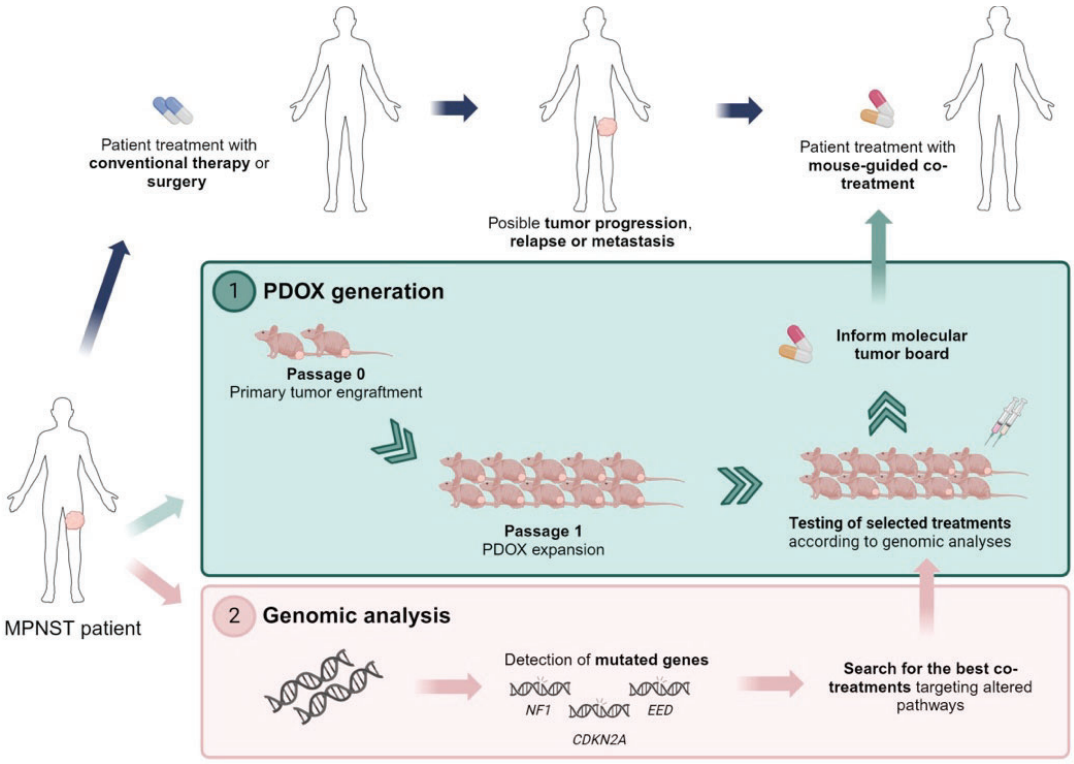

Figure I6. Schematic representation of a personalized medicine strategy. Patient-derived tumor tissue is transplanted into immunodeficient mice and expanded while the patient undergoes treatment. Genomic analysis identifies key alterations, guiding targeted therapies tested in 'avatar' mice. Preclinical results inform clinical decisions through a molecular tumor board, enabling personalized treatment for disease progression or recurrence. Adapted from Fernández-Rodríguez et al. (2020) and image created with Biorender.

Despite its potential, the use of PDX models in personalized medicine faces several challenges. A major limitation is the time required to execute this procedure. In addition, the high

economic costs associated with establishing and maintaining PDX models limit their widespread use (Abdolahi, Ghazvinian et al. 2022).

In 2015, our group reported the case of personalized medicine strategy applied to a 14-year-old MPNST patient. The patient's tumor was engrafted into mice, generating 'avatars' that underwent the same therapeutic regimen as the patient. After genetic analyses, drug combinations were selected and tested in the mice, leading to the identification of effective treatments for the patient (Fernández-Rodríguez, Morales La Madrid et al. 2020).

I6. Clinical Treatments for MPNSTs

6.1. First-line Treatment for MPNST Patients

Treatment options for MPNST patients are limited, so there is a high medical need for novel treatments to improve patient's prognosis. Currently, complete surgical resection with wide negative margins is the optimal approach, though it is often impractical due to tumor size, location, or metastases (Dunn, Spiliopoulos et al. 2013). Post-surgery, adjuvant radiotherapy is recommended for large or aggressive tumors, as it significantly reduces local recurrence, even though it does not improve OS. However, radiotherapy carries the risk of inducing secondary sarcomas (Wang, Zhang et al. 2015).

In cases where surgery is not feasible, chemotherapy remains a key treatment option. Doxorubicin, an anthracycline drug that intercalates DNA and inhibits DNA topoisomerase II (TOP2A), remains the first-line treatment. However, some studies, such as that by Kroep et al. (2011), suggested that the combination regimen of Doxorubicin and Ifosfamide, an alkylating agent that inhibits DNA replication, may provide better outcomes than monotherapy (Kroep, Ouali et al. 2011). However, this combination does not enhance OS and is associated with worse side effects (Kolberg, Høland et al. 2013, Zehou, Fabre et al. 2013), and a high percentage of tumors are resistant to this treatment (Peacock, Cherba et al. 2013, Amirnasr, Verdijk et al. 2017).

Neoadjuvant chemotherapy is sometimes used to reduce tumor size in large (>5 cm) or painful tumors, enabling surgical resection in selected cases (Carli, Ferrari et al. 2005, Kroep, Ouali et al. 2011, Shurell-Linehan, DiPardo et al. 2019). Epirubicin, another DNA-intercalating drug, has shown promise as a neoadjuvant option with reduced toxicity compared to Doxorubicin (Hirbe, Cosper et al. 2017). Adjuvant chemotherapy following tumor resection has demonstrated benefits in controlling recurrence, metastases, and improving OS, particularly for larger tumors where surgical margins may be compromised (Frustaci, Gherlinzoni et al. 2001, Yao, Zhou et al.

2023). Altogether, a multidisciplinary approach involving surgery, chemotherapy, and radiotherapy offers the best possible outcomes for MPNST patients, though the prognosis remains challenging.

Nowadays precision oncology has emerged as a useful strategy to identify targeted therapies against deregulated pathways in tumors. To this end, as the understanding of the molecular pathogenesis of MPNST is increasing, several preclinical and clinical trials testing targeted compounds have been already conducted.

6.2. From Bench to Bedside (B2B)

B2B research refers to the process of translating basic science discoveries into clinical applications. The B2B model typically follows a linear pathway, starting with observations made in the laboratory or the clinic and progressing through various stages of development, culminating in success or failure in clinical trials (Clohessy and Pandolfi 2015, Tsimberidou, Kahle et al. 2023):

- Preclinical studies: This stage is crucial for preliminarily evaluating efficacy, toxicity, pharmacokinetic, and safety. The initial assessment of new drug treatments for cancer primarily relies on human cell lines. Following these *in vitro* assessments, *in vivo* studies are conducted, often involving PDXs or GEMMs to better predict human response to the treatment. Several factors influence the evaluation of a drug's effect before its clinical application. These include pharmacokinetics (PK) such as absorption, distribution, metabolism, and excretion; or pharmacodynamics (PD), such as mechanism of action and interaction with biological targets; and preclinical studies assessing efficacy and safety, such as maximum tolerated doses assays (MTD) (Maertens, McCurrach et al. 2017). Additionally, genetic variations, patient-specific factors, and potential drug interactions play crucial roles. Finally, collaboration between academic laboratories, the pharmaceutical industry and foundations can facilitate access to resources and knowledge, thus improving the process of translating potential treatments into clinical trials (Maertens, McCurrach et al. 2017).

  At this stage, understanding the concept of interspecies dose extrapolation is essential for transitioning to clinical trials. Interspecies allometric scaling, which considers differences in body surface area relative to animal weight, is the commonly studied method for converting doses from animal models to human studies (Reigner and Blesch 2002). An empirical approach used for this purpose is the dose-by-factor method, which employs the no observed adverse effect levels (NOAEL) from preclinical

toxicological studies to estimate the human equivalent dose (HED) (Contrera, Matthews et al. 2004). The HED is calculated using the following formula:

$$HED\ \left(\frac{mg}{kg}\right) = Animal\ does\ \left(\frac{mg}{kg}\right) x\ \left(\frac{Animal\ Km}{Human\ Km}\right)$$

The correction factor K_m is determined by dividing the average body weight (kg) of the species by its body surface area (m^2). The K_m factor is constant for each species (Nair and Jacob 2016). This methodology is crucial for ensuring safe and effective dose translation from animal models to human clinical trials, thereby enhancing the reliability and relevance of preclinical studies.

- Phase 0 clinical trial: Involving a small cohort of participants (usually 10 to 15 individuals), these trials administer very low doses of the drug. The primary goals are to determine if the drug behaves as expected based on preclinical studies, such as whether it reaches cancer cells, how it is metabolized in the body, and the response of cancer cells.
- Phase I clinical trial: These trials typically recruit a small number of patients (20 to 50 individuals), often those with advanced cancer. The main focus is on evaluating the drug's safety, tolerability, and side effects, alongside pharmacokinetic and, if feasible, pharmacodynamics studies.
- Phase II clinical trial: Conducted on a larger group of patients (ranging from tens to over a hundred), these trials may include individuals with the same type of cancer or various types. The objectives are to determine the optimal dosage, further investigate side effects, and evaluate the treatment's efficacy. Phase II studies can be subdivided into Phase IIA, focusing on dose requirements, and Phase IIB, emphasizing drug efficacy.
- Phase III clinical trial: These are large-scale, randomized trials involving hundreds or thousands of patients, typically focusing on a single type of cancer. The goal is to compare the new treatment with the current standard treatment or a placebo, often over a period of 6 to 12 months.
- Phase IV clinical trial: Conducted after a drug has been approved and marketed, these trials involve medium to large groups of patients, usually with the same cancer type. They aim to collect additional information about long-term benefits and side effects.

The timeline for this process is highly variable; as it often takes between 10 to 15 years or more to complete all phases of clinical trials and reach the licensing stage (Clohessy and Pandolfi 2015, Tsimberidou, Kahle et al. 2023). However, this duration can vary significantly based on several factors, including:

- Type of cancer: Rare cancers may take longer to progress through clinical trials due to limited patient populations and less accumulated knowledge.
- Type of treatment: Novel treatment modalities, particularly those involving new drug delivery methods, may require additional time for development and validation.
- Type of trial: Prevention trials, which often require longer follow-up periods to observe outcomes, typically take longer than trials for acute treatment.
- Number of patients needed: The required sample size can impact the speed of patient recruitment and, consequently, the duration of the trial.
- Follow-up period: Long-term follow-up is sometimes necessary to assess the safety and efficacy of new treatments fully.
- Unforeseen issues during the treatment: Unexpected challenges, such as adverse side effects or difficulties in drug formulation, can delay the approval process.

These factors contribute to the complexity and variability of the drug development timeline, making the B2B process highly unpredictable. Additionally, approximately 90% of anticancer therapies fail in early clinical trials (Ledford 2011).

Assessing the toxicity of a drug is a critical process that involves several steps and methodologies and is considered during preclinical and clinical trials (Maertens, McCurrach et al. 2017, Tsimberidou, Kahle et al. 2023). The most common methods for assessing drug toxicity are:

1. **Preclinical cell culture studies:**
    a. Cell toxicity testing: Parameters such as cell viability, apoptosis (programmed cell death), and other cytotoxic effects can be measured.
2. **Preclinical animal studies:**
    a. Acute toxicology: toxicity is assessed after a single dose of the drug in animal models by observing immediate adverse effects and determining the median lethal dose (LD_{50}).
    b. Chronic toxicology: The drug is administered over a prolonged period to observe long-term effects, including changes in behavior, body weight, and organ function.
    c. Organ-specific studies: The effects of the drug on specific organs and systems (such as the liver, kidneys, and heart) are analyzed through biomarker, imaging, and histopathological analysis.

d. Biomarker analysis: During and after animal studies, biological samples (blood, urine, tissue) are analyzed for biomarkers of toxicity, such as elevated liver enzymes, creatinine levels, and other indicators of tissue or functional damage.
e. PK and PD studies: This evaluates how the drug is absorbed, distributed, metabolized and excreted in the body and how it interferes with biological processes. Inappropriate dosing can lead to toxicity, which is assessed by detailed PK/PD studies.

3. Evaluation in clinical trials:

a. As a drug advances to clinical trials, participants are monitored for adverse effects using established toxicity scales, such as the Toxicity Grade (CTCAE) scale, which rates the severity of side effects.
b. Toxicity data review: Data collected from preclinical studies and clinical trials are reviewed by ethics committees and regulatory agencies, such as the FDA, to ensure that the drug meets safety standards prior to approval for general use.

For a drug to advance to clinical trials, it must demonstrate significant tumor regression *in vivo*. Unfortunately, most drugs investigated for MPNSTs only show tumor growth inhibition rather than regression, limiting their progression to clinical trials. The rarity of these tumors complicates the conduct of large, randomized trials, leading to prolonged timelines for completing each trial phase (Sobczuk, Teterycz et al. 2020). To date, the majority of clinical trials involving MPNST patients are in Phase I or II stages (Kandi and Vadakedath 2023). In trials of investigational agents, patients with unresectable MPNST have a median OS of less than 5 months and a progression-free survival (PFS) of less than 2 months (Kim, Stewart et al. 2017).

In certain cases, some patients may be unable to participate in clinical trials but face a serious, life-threatening condition for which no standard treatment is available. These patients can be considered for an investigational treatment under compassionate use, also known as expanded access. Compassionate use allows patients to receive potentially promising cancer therapies that have not yet completed clinical trials or received regulatory approval, offering them a potential option when no other treatments are available. In MPNSTs, especially in pediatric patients, this alternative is currently being used.

6.2.1. Preclinical Trials of MEK, CDK4/6, and BET Inhibitors in MPNSTs

Several drugs have been tested in preclinical trials that target deregulated molecular pathways in MPNSTs. Significant attention has been focused on pathways associated with frequently

inactivated TSGs in MPNSTs: MEK inhibitors (MEKi), CDK inhibitors (CDKi), and BET inhibitors (BETi). To date, direct inhibitors of p53 have not been used in MPNSTs, as studies have focused on the use of inhibitors of downstream molecules affected by p53 disruption. Nevertheless, p53 status may alter the effect of drugs targeting the mTOR pathway, as an interaction between p53 and PI3K/AKT/mTOR has been reported (Cui, Qu et al. 2021).

In addition to inhibitors against these TSGs, compounds targeting overexpressed oncogenic proteins such as RTKs have also been tested in MPNSTs. Multi-kinase inhibitors like Imatinib Mesylate (c-KIT and PDGFR inhibitor), Sunitinib (VEGFR, c-KIT, and PDGFR inhibitor), Sorafenib (VEGFR, PDGFR, and B-RAF inhibitor), Cabozantinib (c-MET and VEGFR inhibitor), and Erlotinib (EGFR inhibitor) have reduced cell viability *in vitro*, but only exhibited cytostatic effects *in vivo* (Aoki, Nabeshima et al. 2007, Mahller, Vaikunth et al. 2007, Torres, Zhu et al. 2011, Ohishi, Aoki et al. 2013, Patwardhan, Surriga et al. 2014, Wu, Deng et al. 2018). Notably, our group published in 2015 a study demonstrating tumor shrinkage using Sorafenib in combination with Rapamycin (mTOR inhibitor) or Doxorubicin (Castellsagué, Gel et al. 2015), while in 2016 another study achieved 36-63% tumor volume regression using Cabozantinib in combination with Mirdametinib (MEK inhibitor) (Lock, Ingraham et al. 2016).

In addition to RTKs, another important oncoprotein that has been targeted in MPNST is the mitotic kinase AURKA. Alisertib (AURKA inhibitor) has shown reduced tumor growth rate *in vivo* in two independent studies in PDX models (Patel, Eaves et al. 2012, Mohan, Castellsague et al. 2013). Finally, inhibitors of the *Wnt* pathway (Watson, Rahrmann et al. 2013), JAK/STAT3 pathway (Wu, Patmore et al. 2014), and survivin have been also tested (Ghadimi, Young et al. 2012), but only achieving a cytostatic effect without tumor volume.

6.2.1.1. MEK Inhibitors (MEKi)

As mentioned in Section 3, recurrent inactivation of *NF1* in MPNSTs leads to the up-regulation of RAS-related pathways (RAF/MEK/ERK and PI3K/AKT/mTOR). In fact, evidence proves that MEK/ERK pathways is more overexpressed than AKT/mTOR, as increased levels of phosphorylated MEK (p-MEK) and ERK (p-ERK) were detected in 93.4% and 81.3% of MPNSTs compared to the 58.2% and 47.3% of tumors with increased phosphorylation in AKT and mTOR, respectively (Endo, Yamamoto et al. 2013). Thus, the MAPK pathway is a highly relevant therapeutic target (Zou, Smith et al. 2009). The most used compounds to inhibit the MAPK pathway are MEKi, which have already shown promising therapeutic efficacy in pNFs (Jessen, Miller et al. 2013). Table I2 summarizes all preclinical studies using MEKis in MPNSTs conducted since 2013. Single agent therapies, such as Mirdametinib, have been shown to

reduce cell viability and exhibit cytostatic effects *in vivo* in a S462-derived xenograft model (Jessen, Miller et al. 2013, Gu, Wang et al. 2022). However, some studies have reported tumor resistance to single treatment with MEKi due to the over-activation of RTKs (Grit, Pridgeon et al. 2020, Wang, Pollard et al. 2021).

Instead, combination therapy has shown improved efficacy. For example, the combination of Mirdametinib with JQ1 (BET inhibitor) resulted in a significant tumor regression in GEMMs (De Raedt, Beert et al. 2014), while the combination with Everolimus (mTOR inhibitor) prolonged survival in mouse models (Watson, Anderson et al. 2014). Other effective combinations include Mirdametinib with AZD8055 (mTOR inhibitor), Frax1036 (PAK inhibitor), and Deucravacitinib (TYK2 inhibitor), all exhibiting synergism *in vitro* and reduced tumor growth *in vivo* (Varin, Poulain et al. 2016, Semenova, Stepanova et al. 2017, Borcherding, Amin et al. 2023). Furthermore, the combination of Mirdametinib with anti-ENG (Endoglin inhibitor) tested *in vivo* in two CDX models effectively reduced tumor cell growth and angiogenesis (González-Muñoz, Di Giannatale et al. 2023).

Other MEKis have been tested including Trametinib in combination with MET inhibitors (Capmatinib), mTOR inhibitors (GSK2126458 and BMS777607), or FAK/SRC inhibitors showing additive or synergistic effects in various cell lines, and cytostatic or additive effect in CDX models (Peacock, Pridgeon et al. 2018, Wang, Pollard et al. 2021, Gu, Wei et al. 2022). Interestingly, none of them has achieved a relevant tumor reduction.

Table I2. Summary of MEKi-based treatments tested preclinically as monotherapy or in combination

				In vitro		*In vivo*	
Single vs Combination	**MAPK pathway inhibition**	**Study**	**Treatment**	**Cell line model**	**Outcome**	**Mouse model**	**Outcome**
Single Agent	MEK	Jessen et al. (2013)	Mirdametinib	STS26T, S462, ST88-14, T265	Decrease in cell viabilty except for STS26T	S462-derived xenograft	Cytostatic effect. Decrease in tumor growth
	MEK	Gu et al.(2022)	8 MEKi (Trametinib, Binimetinib, Selumetinib, Mirdametinib, etc.)	S462	Decrease in cell viabilty	S462-derived xenograft	Cytostatic effect. Complete tumor growth inhibition
Combination	MEK + BRD4	De Raedt et al. (2014)	Mirdametinib + JQ1	90-8TL	Synergistic decrease in cell viabilty	GEMM	Tumor regression (70%)
	MEK + mTOR	Watson et al. (2014)	Mirdametinib + Everolimus	STS26T, S462, S462TY ST88-14, T265	Synergistic decrease in cell viabilty; apoptosis activation	GEMM	Increased mouse survival
	MEK + mTOR	Varin et al. (2016)	Mirdametinib + AZD8055	STS26T, 90-8TL, ST88-14, sNF96.2	Synergistic decrease in cell viabilty	NA	NA
	MEK + PAK	Semenova et al. (2017)	Mirdametinib + Frax1036	STS26T, ST88-14, S462TY	Synergistic decrease in cell viabilty	STS26T and S462-derived xenograft	Cytostatic effect. Decrease in tumor growth
	MEK + MET	Peacock et al. (2018)	Trametinib + Capmatinib	NA	NA	GEMM	Cytostatic effect. Complete tumor growth inhibition
	MEK + mTOR	Wang et al. (2021)	Trametinib + GSK2126458	STS26T, ST88-14, NF90.8, NF94.3, NF96.2, NF10.1, NF11.1, JH-2-002, JH-2-009, JH-2-031	Decrease in cell viability	NA	NA
	MEKi + mTOR	Wang et al. (2021)	Trametinib + BMS777607 / Capmatinib	ST88-14	Additive activity	PDX JH-2-009 and NF11.1 resistent	Additive effect
	MEK + FAK/SRC	Gu et al. (2022)	Trametinib + SRCi	S462, S462TY, ST88-14	Synergistic decrease in cell viabilty	NA	NA
	MEK + TYK2	Borcherding et al. (2023)	Mirdametinib + Deucravacitinib	JW23.3, JH-2–002, MPNST-724	Synergistic decrease in cell viabilty; apoptosis activation	Three cell line-derived xenografts	Cytostatic effect. Decrease in tumor growth
	MEK + Endoglin	González-Muñoz et al. (2023)	Mirdametinib + anti-ENG antibody	NA	NA	Two cell line-derived models	Cytostatic effect. Decrease in tumor growth

6.2.1.2. CDK4/6 Inhibitors (CDKi)

Another important recurrent genetic alteration in MPNST is the inactivation of the *CDKN2A* gene. The downregulation of $p16^{INK4a}$ leads to the formation of the CDK4/6-Cyclin D1 complex, which promotes cell cycle progression. Consequently, treatment with CDK4/6 inhibitors may be effective for the regulation of the cell cycle in MPNSTs (Gil and Peters 2006). CDKis preclinical trials for MPNSTs are summarized in Table I3.

Table I3. Summary of CDKi-based treatments tested preclinically as monotherapy or in combination

				In vitro		*In vivo*	
Single vs Combination	**CDK inhibition**	**Study**	**Treatment**	**Cell line model**	**Outcome**	**Mouse model**	**Outcome**
Single Agent	CDK4/6	Kohlmeyer et al. (2020)	Palbociclib	STS26T, S462, sNF96.2	Decrease in cell viabilty	S462-derived xenograft	Cytostatic effect. Complete tumor growth inhibition
Combiantion	CDK4/6 + CDK2	Kohlmeyer et al. (2020)	Palbociclib + Dinaciclib	S462	Synergistic decrease in cell viabilty	sNF96.2-derived xenograft	Cytostatic effect. Complete tumor growth inhibition
	CDK4/6 + MEK	Kohlmeyer et al. (2023)	Palbociclib + Mirdametinib	S462	Synergistic decrease in cell viabilty; apoptosis activation	S462-derived xenograft	Tumor regression, but acquires resistance with time
	CDK4/6i + MEK + PD-L1	Kohlmeyer et al. (2023)	Palbociclib + Mirdametinib + anti-PD-L1 antibody	NA	NA	GEMM	Sustained tumor regression
	CDK4/6 + SHP2	Wang et al. (2023)	Ribociclib + TNO155	NA	NA	Three cell line-derived xenografts	Cytostatic effect. Reduction in tumor growth

Most of studies using this type of inhibitors were performed within the last five years, as the role of *CDKN2A* in the tumorigenic process was not identified as early as the *NF1*. Briefly, Kohlmeyer et al. (2020) used the CDKi Palbociclib in monotherapy in both *in vitro* and *in vivo* MPNST models. Although the three cell lines tested showed sensitivity to Palbociclib, particularly those with higher CDK4 levels, a limited cytostatic effect was observed in the S462-derived CDX model. Moreover, drug resistance to CDKi monotherapy remains a significant clinical challenge, prompting the exploration of rational combination therapies. Consequently, Kohlmeyer's team combined CDK4/6i with another CDKi targeting CDK2 (Dinaciclib), exhibiting greater efficacy *in vivo* reducing tumor growth and increasing the proportion of active RB (Kohlmeyer, Kaemmer et al. 2020). More recently, the same group combined Palbociclib with Mirdametinib (MEKi), achieving highly synergistic anti-proliferative activity *in vitro* and inducing tumor shrinkage in PDX models over several days of treatment, although the tumors eventually acquired drug resistance (Kohlmeyer, Lingo et al. 2023). To solve this problem, they tested a triple combination of CDK4/6i and MEKi with anti-PD-L1 therapy, eradicating tumors in some animals, and proposed this combination as a preclinical rationale for MPNST clinical trials (Kohlmeyer, Lingo et al. 2023).

Moreover, another group combined the CDK4/6i Ribociclib with the SHP-2 inhibitor TNO155. This combination suppressed MPNST cell growth *in vitro* by inhibiting the cell cycle; and induced apoptosis and reduced tumor growth in three CDX models, although the combined effect was not significantly higher from treatment with TNO155 alone (Wang, Calizo et al. 2023).

6.2.1.3. BET Inhibitors (BETi)

Targeting epigenetic or chromatin regulators has emerged as another attractive alternative anti-cancer strategy. BET proteins play a critical role in maintaining tumorigenesis by regulating gene expression programs of both oncogenes and TSGs, thus they have been proposed as druggable targets (Cooper, Patel et al. 2019). Among these chromatin regulators, the BET bromodomain protein BRD4 has received considerable attention due to its role in various cancers (Baude, Lindroth et al. 2014). In MPNSTs, BRD4 recruitment occurs as a result of mutations in PRC2, highlighting BRD4 as a potential therapeutic target (De Raedt, Beert et al. 2014).

BETi works by competitively binding to BET bromodomains and thereby impeding the BRD4 fusion with oncogenic regions in the chromatin. This displacement leads to squamous differentiation and specific anti-proliferative effects in BRD4-dependent cell lines and PDX models (Filippakopoulos, Qi et al. 2010).The efficacy of BETi as single agents is limited, with studies reporting only modest decreases in cell viability *in vitro* (Patel, Liao et al. 2014, Amirnasr, Verdijk et al. 2017) (Table I4). Although BETi monotherapy efficacy is limited, De Raedt et al. (2014) demonstrated that the combination of JQ1 (BETi) with Mirdametinib (MEKi) resulted in a remarkable 70% tumor volume regression in GEMMs (De Raedt, Beert et al. 2014) (Table I4).

Table I4. Summary of BETi-based treatments tested preclinically as monotherapy or in combination

				In vitro		*In vivo*	
Single vs Combination	**BET inhibition**	**Study**	**Treatment**	**Cell line model**	**Outcome**	**Mouse model**	**Outcome**
Single Agent	BRD4	Patel et al. (2014)	JQ1	Genetically modified skin-derived precursors	Decrease in cell viabilty	Cell line- derived allograft	Cytostatic effect. Complete tumor growth inhibition
	BRD4	Amirnasr et al. (2017)	JQ1	STS26T, ST88-14, sNF96.2, T265, 90-8TL	Low sensitivity to treatment	NA	NA
Combination	BRD4 + MEK*	De Raedt et al. (2014)	JQ1 + Mirdametinib	90-8TL	Synergistic decrease in cell viabilty	GEMM	Tumor regression (70%)
	BRD4 + KIF11	Terribes et al. (2020)	JQ1 + ARRY-520	ST88-14, S462	Synergistic decrease in cell viabilty	NA	NA

*The combination is also listed in the Table 2.

Although BETi have shown promise in treating MPNSTs, their clinical development has been hindered by significant toxicities, particularly thrombocytopenia, which prevent achieving effective therapeutic doses (Cooper, Patel et al. 2019). Consequently, there are limited preclinical studies focusing on this class of inhibitors, with all centered on JQ1, a well-known BET inhibitor (To, Xing et al. 2023).

Beyond BET inhibitors, PRC2 inactivation in MPNST induces global epigenomic reorganization, increasing susceptibility to histone deacetylase inhibitors (HDACi) (Wojcik, Marchione et al. 2019). HDACi trigger p21 expression, leading to cell cycle arrest and apoptosis activation, while also inhibiting tumor angiogenesis (Kim and Bae 2011). The HDACi Abexinostat, combined with Chloroquine (an autophagy inhibitor), effectively blocked tumor growth and enhanced HDACi-induced apoptosis (Lopez, Torres et al. 2011). Similarly, Vorinostat paired with Rapamycin (mTORi) reduced tumor volume by 40–70% through oxidative stress induction. Additional HDACi, including Panobinostat, Entinostat, Nexturastat A, and Romidepsin, were tested in vitro, with Panobinostat showing the strongest response. Its combination with Sapanisertib (mTORi) further reduced tumor size *in vivo* (Malone, Emerson et al. 2017). Finally, our group tested Panobinostat in various PDX models but observed high toxicity (Fernández-Rodríguez, Creus-Bachiller et al. 2022).

6.2.2. Clinical Trials in MPNST Patients

The National Cancer Institute's database (ClinicalTrials.gov) reports all ongoing and completed clinical trials. To date, 101 clinical trials have been registered for sarcomas, including some for MPNSTs patients only or with other tumors patients. As mentioned in Section 6.2, all clinical trials are phase I or II (Kandi and Vadakedath 2023) due to recruitment challenges in rare tumors. The first clinical trials with MPNST patients were performed using single agents, mostly RTK inhibitors such as Erlotinib, Sorafenib, and Dasatinib, although other targets have been tested including AURKA (Alisertib), mTOR (Sapanisertib), and PD-1 (Pembrolizumab) (Table I5). Most of these clinical trials showed limited clinical response, mostly stabilized disease (SD) in a percentage of patients, while a high proportion was non-responsive and presented tumor progression. Specifically, Alisertib, Pazopanib, and Sapanisertib were the most effective, with 50-70% of patients achieving PFS, SD and even a small percentage (between 4 to 20%) of partial response (PR) (Table I5) (Dickson, Mahoney et al. 2016, Nishida, Urakawa et al. 2021).

Table I5. Summary of clinical trials of single agent including MPNST patients

	Study	Treatment	Target	Phase	Participants (n)	Outcome	Side effects	Reference
Completed	NCT00068367	Erlotinib	EGFR	II	24	Inactive. No response in 19 patients	6 patients with grade 3 of toxicity	Albritton et al. (2006)
	NCT00245102	Sorafenib	VEGFR, PDGFR, BRAF	II	147 (12 MPNSTs)	25% of patients had SD	SD in 27 patients, PR in 9	Maki et al. (2009)
	NCT00464620 (SARC009)	Dasatinib	c-KIT, PDGFRβ, c-SRC	II	366 (14 MPNSTs)	Inactive. 3 patients with 2 months of PFS	86 patients had a total of 127 serious AE	Schuetze et al. (2010)
	NCT01653028	Alisertib	AURKA	II	72 (10 MPNSTs)	Failed RR, although 60% of patients had 12 weeks of PFS	At least 40% of patients with grade 3 and 4 of AE	Dickson et al. (2019)
	NCT02601209	Pazopanib hydrochloride	ITK, PDGFR, c-KIT	I/II	58	2.1% of patients had PFS, 2 patients had PR and 23 had SD	38 patients with grade 3 of AE	Nishida et al. (2021)
		Sapanisertib	mTOR	I/II	56	2% of patients had PFS, 2 patients had PR and 14 had SD	28 patients with grade 3 of AE	NA
	NCT02691026	Pembrolizumab	anti-PD-1 (immunotherapy)	II	8	Cancelled due to slow enrollment (2015-2020)	NA	NA
Ongoing	NCT05107037	TQ-B3234	MAPK	I	120	SC on 2024-12	NA	NA
	NCT04917042	Tazemetostat	EZH2 (PRC2)	II	24 (recruiting)	SC on 2025-09	NA	NA
	NCT05245500	MRTX1719	PRMT5 MTA complex	I/II	370 (recruiting)	SC on 2026-04	NA	NA
	NCT04222413	Metarrestin	Perinuclear compartment inhibitor	I	98 (recruiting)	SC on 2027-12	NA	NA
	NCT05985161	Selinexor	exportin-1 (XPO1)	II	36 (recruiting)	SC on 2029-08	NA	NA
	NCT03618381	EGFR806 (immunotherapy)	CAR T-cells (EGFR receptor)	I	44 (recruiting)	SC on 2040-06	NA	NA

AE: Adverse Events; SC: Study completion; SD: Stabilized disease; PR: Partial response; RR: Response rate; PFS: Progression-free survival; DP: Disease progression; NA: Not applicable.

Due to the low clinical benefit of single agent treatments, there is a growing emphasis on clinical trials exploring combination therapies to enhance efficacy and prevent drug resistance. Most trials involving drug combinations are based on precision oncology strategies to target deregulation pathways in the patient's tumors. Notably, three clinical trials (highlighted in purple in Table I6) specifically test drugs targeting the three most recurrently inactivated TSGs in MPNSTs (*NF1*, *CDKN2A*, and PRC2). The first trial, NCT03009201, used the combination of CDK4/6 inhibitor Ribociclib with DNA intercalating agent Doxorubicin, and concluded that 2 patients achieve PR, and five were PFS at 18 weeks. The second, NCT03433183, used the combination of the MEKi Selumetinib with mTOR inhibitor Sirolimus, both targets being upregulated in MPNST due to *NF1* mutations. This trial concluded in mid-2024, although its results have not yet been published. The third trial, NCT05253131, began last year and tests a combination of MEKi Selumetinib with a BETi to target PRC2 inactivation and Durvalumab (a PD-L1 inhibitor) (Table I6). MEK combined with BET inhibitors have shown significant efficacy in preclinical studies (De Raedt, Beert et al. 2014). This regimen also includes Durvalumab, which helps to counteract the immunosuppressive microenvironment by blocking inhibitory signals to the immune system. One recent study have demonstrated the potential of immune checkpoint inhibitors like Pembrolizumab (anti PD-1) in achieving complete remission in an MPNST patient (Larson, Russ et al. 2022). This innovative therapy is expected to become more prevalent in future treatments.

Table I6. Summary of clinical trials using combined therapies including MPNST patients

	Study	Treatment	Target	Phase	Participants (n)	Outcome	Side effects	Reference
Completed	NCT00304083 (SARC006)	Doxorubicin hydrochloride + Ifosfamide / Etoposide + Ifosfamide	DNA replication and damage	II	48	SD in 27 patients, PR in 9	13 patients with serious AE	Higham et al. (2017)
	NCT00837148	Sorafenib + Dacarbazine	VEGFR, PDGFR, BRAF + DNA alkylating	II	37 (4 MPNSTs)	Inactive	High hematologic toxicity effects	D'Adamo et al. (2019)
	NCT01661283 (SARC016)	Bevacizumab + Everolimus	VEGF + mTOR	II	25	Inactive. Only 3 patients with clinical benefit	5 patients with grade 3 AE	Widemann et al. (2019)
	NCT02008877 (SARC023)	Sirolimus + Ganetespib	mTOR + Hsp90	I/II	20	Inactive. Only 1 patient with PR	Acceptable toxicity in patients	Kim et al. (2020)
	NCT03009201	Ribociclib + Doxorubicin	CDK4/6 + DNA intercalating	I	16	2 patients with PR and five were PFS at 18 weeks	More than half patients presented grade 3 AE	Davis et al. (2020)
	NCT01532687	Gemcitabine + Pazopanib	DNA and RNA disruption + ITK, PDGFR, c-KIT	II	29	Clinical benefits in 66% of patients (4.5% had PFS)	At least 41% of patients with grade 3 of AE	Ryan et al. (2020)
	NCT00720174	Cixutumumab + Doxorubicin Hydrochloride	IGF-1R + DNA intercalating	I	30	5 patients has PR and 26 patients were PFS at 5.3 months	7 patients with grade 2, 3, and 4 of AE	Chugh et al. (2015)
	NCT03433183 (SARC031)	Selumetinib + Sirolimus	MEK + mTOR	II	21	No results posted	NA	NA
	NCT02584647	Pexidartinib + Sirolimus	c-Kit + mTOR	I/II	43	Clinical benefits in 67% of patients (3 patients had PR and 9 patients SD)	5 patients presented grade 2 or higher of AE	Manji et al. (2021)
Ongoing	NCT03611868	APG-115 + Pembrolizumab	MDM2 + anti-PD-1 (immunotherapy)	I/II	230 (24 MPNSTs, recruiting)	SC on 2025-03. In 2022, reported results of 12 MPNST patients with 40% of clinical benefits	NA	McKean et al. (2022)
	NCT03719430	Doxorubicin + APX005M	DNA intercalating + CD40 agonist	II	27	SC on 2025-12	NA	NA
	NCT04420975	BO-112 + Nivolumab	Viral mimetic particle + anti-PD-1 (immunotherapy)	I	14	SC on 2026-01	NA	NA
	NCT04872543	Cedazuridine + Decitabine	DNA methyltransferase	II	25 (recruiting)	SC on 2026-04	NA	NA
	NCT02834013	Nivolumab + Ipilimumab	anti-PD-1 + anti-CTLA-4 (immunotherapy)	II	818	SC on 2026-05	NA	NA
	NCT04465643	Nivolumab + Ipilimumab	anti-PD-1 + anti-CTLA-4 (immunotherapy)	I	18 (recruiting)	SC on 2026-08	NA	NA
	NCT06277154	MASCT-I + Doxorubicin + Ifosfamide	MASCT + DNA intercalating	II	148	SC on 2027-02	NA	NA
	NCT05253131	Selumetinib + BET inhibitor + Durvalumab	MEK + BET + anti-PD-L1 (immunotherapy)	II	41	SC on 2030-12	NA	De Raedt et al. (Abstract, 2018)

Combinations involving MEKi, CDKi or BETi are highlighted in purple. AE: Adverse Events; SC: Study completion; SD: Stabilized disease; PR: Partial response; PFS: Progression-free survival; NA: Not applicable.

One of the most effective treatments, which presented clinical benefits in several patients (including SD in 27 patients and PR in 9 patients), was Doxorubicin + Ifosfamide (NCT00304083), the standard-of-care chemotherapy for MPNST patients (Table I6).

Several other combination therapy trials are ongoing, though detailed outcomes are not yet available. For instance, the clinical trial NCT02584647, completed in 2024, evaluated the efficacy of combining Pexidartinib, a multikinase inhibitor, with Sirolimus (mTOR inhibitor) in patients with unresectable sarcomas and MPNSTs. This study reported clinical benefits in 12 out of 18 patients, including SD in nine patients and PR in three, and conclude by proposing to further investigation this combination to determine clinical efficacy (Manji, Van Tine et al. 2021). Another notable trial, NCT03611868, explored the combination of the MDM2 inhibitor APG-115 and Pembrolizumab. Preliminary results indicate clinical benefits in 40% of MPNST patients, with no reported side effected (McKean 2022).

I7. High-Throughput Screening Strategies

High-Throughput Screening (HTS) is a powerful approach for drug discovery that gained widespread popularity since the early 1990s (Szymański, Markowicz et al. 2012). It has become a standard method in the pharmaceutical industry for identifying potential therapeutic compounds. Essentially, HTS involves the rapid screening of a large number of biological modulators and effectors against specific targets, as well as the assessment interactions between compounds (Shinn, Chen et al. 2019). It is used to screen different types of libraries, including combinatorial chemistry, genomics, protein, and peptide libraries (Szymański, Markowicz et al. 2012).

One of the main advantages of HTS is its ability to process thousands of compounds, with some systems capable of handling up to 100,000 assays per day (Szymański, Markowicz et al. 2012, Shinn, Chen et al. 2019). This high capacity significantly reduces the time and cost associated with drug development. In addition, HTS methods are used to characterize the metabolic, pharmacokinetic, and toxicological profiles of new drugs (Inglese, Auld et al. 2006). Originally, 96-well plates were the most used, but these have been largely replaced by higher density formats, such as 384-well and even 1536-well plates, for which the working volume ranges from 2.5 to 10 µL, with 5 µL per well-being a common standard (Mayr and Fuerst 2008, Szymański, Markowicz et al. 2012).

HTS assays can measure a variety of biological outcomes, including enzyme inhibition, receptor binding, cell viability, and reporter gene expression (Szymański, Markowicz et al. 2012). These assays are often miniaturized and automated, using robotic systems for rapid and precise handling (Shinn, Chen et al. 2019). The most used HTS formats in the pharmaceutical industry include cell-based assays using cellular microarrays and 2-D cell monolayer cultures (Kasibhatla, Gourdeau et al. 2004). Cellular microarrays allow for the multiplexed interrogation of living cells and subsequent analysis of cellular responses (Chen and Davis 2006).

Several read-outs are used to assess the efficacy of compounds. The most important is cell viability, which measures the effect of increasing concentrations of compounds on tumor cell viability, generating dose-response curves. From these data, the half-maximal inhibitory concentration (IC_{50}) value is calculated, which indicates the concentration required to reduce the cell viability by half, as a measure of drug potency. Similarly, the half-maximal effective concentration (EC_{50}) is the concentration of a drug that produces a half-maximal response (Sebaugh 2011, Berrouet, Dorilas et al. 2020). Other parameters that can be measured include

apoptosis induction, cell and nuclear morphology, DNA content, and cytoskeletal rearrangements (Rausch 2006).

Fluorescence-based methods are also commonly used in HTS to detect molecular biological activity and molecular interactions. This methodology involve the detection of fluorescence released due to substrate cleavage in enzymatic reactions (FLINT) or energy transfer between a donor and an acceptor molecule (FRET) (Macarrón and Hertzberg 2011). Moreover, HTS is also instrumental in the assessment of compound toxicity. By simultaneously assessing cytotoxicity and efficacy, researchers can identify safe and effective drug candidates (Lee, Kumar et al. 2008).

Once the screening is performed, data analysis is based on the identification of 'hits', which are compounds that exhibit the desired activity. The 'hits' are distinguished by comparing the response of each compound to control samples. After initial identification, 'hits' undergo further validation and testing, including retesting and additional assays to confirm their activity and specificity. This iterative process ensures that only the most promising compounds advance through the drug development pipeline (Szymański, Markowicz et al. 2012).

HTS has been used extensively in many cancer types to find novel treatments, including colorectal cancer (Bialkowska and Yang 2012), pediatric cancer (Mayoh, Mao et al. 2023) and breast cancer (Abdulkareem, Bhat et al. 2022). In 2022, our group used this HTS technique to screen a collection of compounds from the National Center for Advancing Translational Sciences (NCATS) Mechanism Interrogation PlatE (MIPE) library, both as single agents and in combination (Fernández-Rodríguez, Creus-Bachiller et al. 2022). After *in vitro* and *in vivo* validation of the most potent compounds found in the HTS screen, we report a combination, MK-1775 (WEE1 kinase inhibitor) with Doxorubicin, which significantly reduced tumor growth rate in two PDOX models (Fernández-Rodríguez, Creus-Bachiller et al. 2022).

I8. Models for Studding Drug-Drug Interactions

The use of drug combinations is increasing in many areas of research, aiming to enhance therapeutic effects while minimizing doses (Tang, Wennerberg et al. 2015). The effectiveness of a combination is assessed by comparing its impact to that of individual drugs, categorizing interactions as synergistic (greater than expected), additive (equal to the sum of individual effects), or antagonistic (less than expected) (Foucquier and Guedj 2015, Richards, Schwartz et al. 2020). However, defining additivity is complex, leading to various theoretical models to

assess drug interactions. These models are classified into effect-based and dose-effect based approaches (Foucquier and Guedj 2015, Duarte and Vale 2022).

a) **Effect-Based Approaches:** These methods evaluate drug interactions based on the effects of individual drug within a combination (Figure I7A):
   - **a.** Combination Subthresholding: Assumes synergy if the combination's effect significantly exceeds the sum of individual effects, assessed statistically ($p < 0.05$).
   - **b.** Highest Single Agent (HSA): Considers a combination synergistic when the drug combination induces a greater response than the highest single agent (Mathews Griner, Guha et al. 2014): HSA = max(EA, EB)
     where EA and EB represent the individual drug effects.
     An Excess HSA (E-HSA) value can be obtained with the difference between the value of the HSA and the value of the combination effect. Thus, if E-HSA > 0, the combination is antagonistic (less effective than expected); if E-HSA = 0, the combination is additive (matches the best single-agent effect); and if E-HSA < 0, the combination is synergistic (more effective than expected).
   - **c.** Response Additivity: Defines synergy as a response greater than the sum of individual drug effects.
   - **d.** Bliss Independence: Assumes independent drug actions, predicting combinations effects using the formula:

     $$\text{Expected effect} = E_A + E_B\,(100 - E_A)$$

     where E_A and E_B are the individual drug effects (Liu, Yin et al. 2018).

b) **Dose-Effect Based Approaches:** These models incorporate dose-response relationships to provide clearer definitions of synergy, additivity, and antagonism. It is proposed to surpass the limitations of the effect-based approach (Figure I7B):
   - a. Loewe Additivity: Assumes drugs with similar mechanisms can substitute for one another. Loewe model is represented using Isobolograms: the diagonal line is the additive effect, and deviations from the additivity line indicate synergy (bottom, <1) or antagonism (top, >1).
     The synergy is calculated using the formula:

     $$\frac{yA}{YA} + \frac{yB}{YB} = 1$$

where yA and yB are the doses in combination, and YA and YB are the doses required for the same effect individually (Lederer, Dijkstra et al. 2018, Ma and Motsinger-Reif 2019).

b. Zero Interaction Potency (ZIP): A hybrid of Bliss Independence and Loewe Additivity, ZIP evaluates synergy by analyzing dose-response curve shifts, assuming minimal interaction if responses remain unchanged in combination.

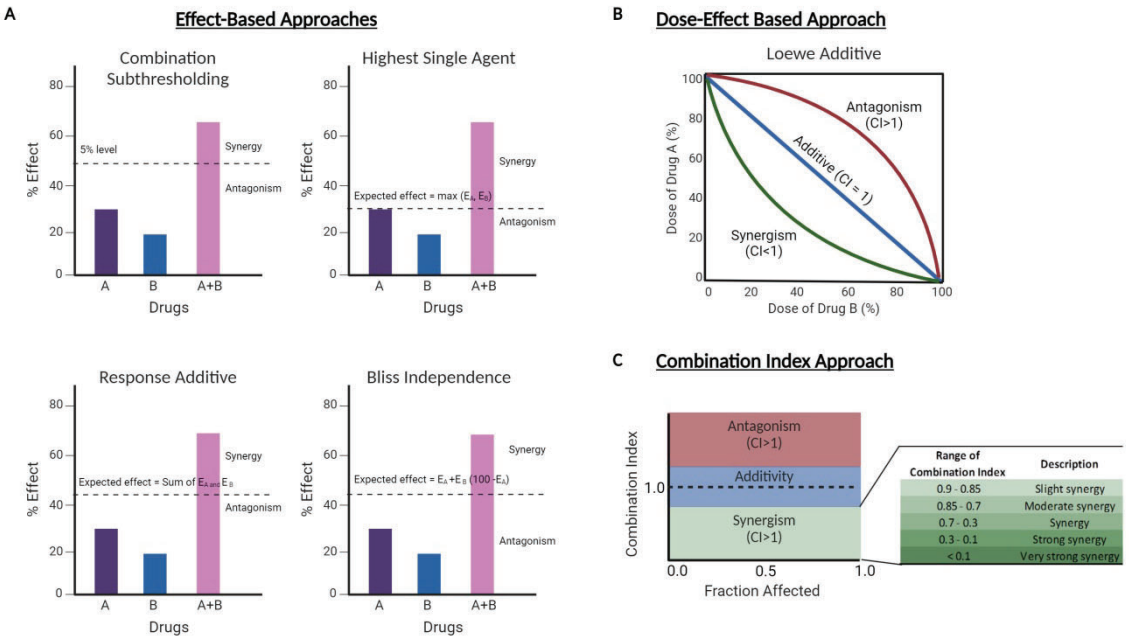

Figure I7. Graphic representation of the model for studying drug-drug interactions. A. Demonstration plots of the four effect-based approaches: Combination Subthresholding, Highest Single Agent, Response Additive, and Bliss Independence. Based on EA=30, EB=30, and EAB = 65. Adapted from Foucquier & Guedj (2015). **B.** Demonstration plot of dose-effect based approach: Loewe additive. Adapted from Foucquier & Guedj (2015). **C.** Fa-CI plot proposed by and Talalay, based on Loewe Additivity model. Fa indicates the observed effect and CI<1, CI1⁄41 and CI > 1 indicate synergism, additivity and antagonism, respectively. Adapted from Chou etl al. (2006).

Furthermore, another important metric for distinguish between synergy, additivity, and antagonism in drug combinations is the Combination Index (CI), a concept created by Chou and Talalay (Figure I7C) (Chou and Talalay 1984, Chou 2010). The CI is based on the Bliss Independence, Loewe Additive, and HSA models, making it a versatile tool for quantifying drug interactions. Its simplicity in equations, experimental design, and data analysis makes it efficient and economical, reducing the number of experimental animals or patients needed for drug combination clinical trials (Chou 2010). To understand CI, it is crucial to define the fraction affected (Fa) and its counterpart, the fraction unaffected (Fu). Fa represents the proportion of cells affected by the drug, ranging from 0 (no cell death) to 1 (100% cell death);

and Fu, therefore, is calculated as 1-Fa, representing the percentage of viable cells. The CI for a two-drug combination is calculated as follows:

$$CI = \frac{(D)1}{(Dx)1} + \frac{(D)2}{(Dx)2}$$

where (Dx)1 is the dose of drug D1 required to inhibit cell growth by x% when used alone, and (Dx)2 is the corresponding dose for drug D2. (D)1 and (D)2 are the doses of the respective drugs in combination that achieve the same level of inhibition (Duarte and Vale 2022).

CI values are plotted against Fa values to represent the nature of the drug interaction. CI values lower than 0.9 indicate synergism; CI values between 0.9 and 1.1 suggest additive effect and values higher than 1.1 indicate antagonism (Hernández, Padilla et al. 2013). In the oncology field, strong synergies are typically considered as those with low CI values at high Fa (greater than 0.8), demonstrating a strong effect on cell death (Chou 2010). In 2005, an updated software program called *CompuSyn* was introduced, based on the Chou-Talalay theory, to facilitate the calculation and interpretation of CI in drug combination studies (Figure I7C) (Chou 2010).

Hypothesis

HYPOTHESIS

Malignant peripheral nerve sheath tumors (MPNSTs) are aggressive soft tissue sarcomas and the leading cause of death in Neurofibromatosis Type 1 (NF1) patients. Due to their rarity and heterogeneity, current *in vitro* and *in vivo* models are insufficient to fully capture the diversity of these tumors. We aimed to expand our current pre-clinical MPNST platform by including new patient-derived orthotopic MPNST xenografts (PDOX) and cell lines. We reasoned that these models, by better representing MPNST variability, could provide a more accurate biological insight and the identification of more effective therapeutic strategies.

Currently, there is no effective treatment for MPNSTs. However, most MPNSTs exhibit inactivation of three key tumor suppressor genes: *NF1*, *CDKN2A*, and PRC2 components (*EED/SUZ12*), and inhibitors targeting these specific alterations already exist. We hypothesized that a dual or triple combination of these inhibitors could become an effective therapeutic strategy for this tumor type.

Given the lack of effective treatments for MPNST and the high heterogeneity of these tumors, we thought that a personalized medicine approach consisting in performing genome analysis-based precision oncology on tumor-specific PDX models, can provide valuable treatment options for a molecular tumor board in case of tumor progression.

Aims

AIMS

Main objective

The main goal of this thesis is to exploit therapeutic strategies targeting loss of function of the most frequently altered TSGs in MPNSTs, thereby advancing their potential application in precision oncology and personalized medicine.

Specific objectives

Objective 1: To expand the biological and genetic MPNST repertoire of our *in vitro* and *in vivo* preclinical platform for MPNST research

1. Develop and establish new pairs of *in vitro/in vivo* models.
2. Conduct a comprehensive characterization of the newly established MPNST cell lines and PDOX at functional, genomic, and histologic levels.

Objective 2: To evaluate the therapeutic potential of precision medicine strategies for MPNSTs

1. Perform high-throughput drug screening using compounds that target the three most recurrent altered TSGs (*NF1*, *CDKN2A*, and *EED/SUZ12*), including single agent and pairwise combinations.
2. Validate most synergistic combinations *in vitro* using a large panel of MPSNT cell lines.
3. Validate most synergistic pairwise combinations *in vivo*.
4. Assess the efficacy of a triple-drug combination.

Objective 3: To implement personalized medicine strategies to inform molecular tumor boards

1. Perform personalized medicine strategies for MPNSTs patients by genomic characterization and establishment of PDOX.
2. Conduct precision oncology treatments on tumor-specific PDOX models.

Materials & Methods

MATERIALS & METHODS

MM 1. Human Samples: Patients and Primary Tumors (MPNSTs)

This thesis majorly focuses on four MPSNST patients both NF1 derived and sporadic: NF1-16, NF1-18B, SP-10, and SP-12. Fresh tumor tissue was received for genomic characterization, cell line isolation and PDOX generation. Informed consent from all subjects was obtained from all subjects, covering genomic studies and the development of cell and mouse models for preclinical use.

Following tumor resection, tumor samples were analyzed by the pathology service according to the standard protocols. A portion of each tumor was placed in Dulbecco's modified Eagle's medium + GlutaMAX (DMEM, Gibco, Ref. 31966-021) with 10% Fetal Bovine Serum (FBS, Gibco, Ref. A5256701) and 1% Penicillin/Streptomycin solution (P/S, Gibco, Ref. MS028A) at room temperature (RT) and sent to the laboratory. Samples were then divided for various applications: 1) engraftment in immunodeficient (athymic or NSG) mice, 2) extraction of DNA, RNA, and/or protein, 3) cryopreservation in liquid nitrogen with FBS and 10% dimethyl sulfoxide (DMSO, Sigma-Aldrich, Ref. 67-68-5), and 4) establishment of a cell lines. In case where the available tumor tissue was insufficient, priority was given to engraftment and biomolecular extraction over cell line generation, as was the case of NF1-16 and SP-12.

MM 2. MPNST Cell Line Models

2.1. Cell Line Isolation Procedure

Two new cell lines, NF1-18B and SP-10, were established following this procedure:

1. Fresh tumors were cut into small fragments.
2. Tumor digestion was performed using DMEM medium supplemented with 10% FBS and 1% P/S, 100 U/ml collagenase (Sigma-Aldrich, Ref. C0130), and 1 U/ml dispase (Worthington Corporations, Ref. LS02100).
3. After 18-24h, cells were dissociated with a glass pipette and then the enzymes were removed by centrifuging and suspending with medium + 10% FBS + 1% P/S.
4. Single cells were obtained by filtering the digested tissue through a 40 µM filter (Merck, Ref. CLS352340) and seeded into 6-well plates (Corning).
5. Cells were cultured at 37ºC with 10% CO_2 for initial passages.
6. Cryopreservation in liquid nitrogen with FBS and 10% DMSO was performed every few passages to generate stocks for future experiments.

2.2. MPNST Established Cell Lines

Three MPNST cell lines (NF1-08-CL, NF1-09-CL, and SP-01-CL) were established in-house (Creus-Bachiller, Fernández-Rodríguez et al. 2023), and five were obtained from other laboratories: S462 (RRID: CVCL_1Y70; (Frahm, Mautner et al. 2004)), sNF96.2 (RRID: CVCL_K281; (Perrin, Li et al. 2007)), ST88-14 (RRID: CVCL_8916; (Fletcher, Kozakewich et al. 1991)), NF90-8 (RRID: CVCL_1B47; (Legius, Dierick et al. 1994)), and NMS-2 (RRID: CVCL_4662; (Imaizumi, Motoyama et al. 1998)). The human foreskin fibroblast (HFF-1) cell line (Banco de Células do Rio de Janeiro Cat. #0275, RRID: CVCL_3285) from ATCC (SCRC-1041) was used as controls in multiple assays. All cells were maintained in complete DMEM at 37°C with 5% CO_2 and passaged once a week. Cryopreservation in liquid nitrogen was performed periodically.

Mycoplasma contamination was tested before experimental use via PCR amplification of 16S rRNA from eight *Mycoplasma* species, using specific primers (5'-GGCGAATGGGTGAGTAACACG-3' and 5'-CGGATAACGCTTGCGACTATG-3'). PCR conditions were: 95ºC for 5 min, 35 cycles of [95ºC for 30 sec, 55ºC for 30 sec, 72ºC for 30 sec], followed by 72ºC for 7 min.

MM 3. Molecular Biology Techniques

3.1. DNA Isolation and Quantification

DNA from cell lines and tumor tissues was extracted using the Puregene Core Kit A (Qiagen, Ref. 1042601), following manufacturer's instructions, to perform Whole Genome Sequencing (WGS).

DNA extraction from cultured cell lines (procedure suitable for 3-4 x 10^6 cells):

a) Cells were trypsinized using 0.5% Trypsin-EDTA Solution (ThermoFisher Scientific, Ref. 15400-054).
b) Centrifugation was performed at 1250 rpm for 5 min.
c) Cells were washed with Phosphate Buffered Saline 1X (PBS 1X, Gibco, Ref. 14190-094).
d) A second centrifugation at 1250 rpm for 5 min was conducted.
e) The pellet was suspended in 50-100 µl of PBS 1X (adjusted according to cell number) and vortexed.
f) 600 µl of Cell Lysis Solution was added and vortexed.
a) 3 µl of RNasa A solution (Qiagen, Ref. 158922) was added, and mixed by inverting 25 times.
b) Incubation at 37ºC for 1h was performed.

g) The sample was incubated on ice for 1-3 min to cool.
h) 200 µl Protein Precipitation Solution was added and vortexed for 20 sec.
i) Centrifugation at 16,000 x *g* for 3 min was performed, followed by a 2 min incubation on ice.
j) The supernatant was collected.

DNA extraction from tissue (procedure suitable for 10-20 mg of tumor tissue):

a) Tumor tissue was cut into small pieces.
b) 600 µl of Cell Lysis Solution was added to a 2 ml Eppendorf tube.
c) One Tungsten Carbide Bead (Qiagen, Ref. 69997) was added.
d) Tissue was homogenized using TissueLyser II (Qiagen, Ref. 9003240) at 25 Hz for 30 sec. If necessary, the process was repeated at 20 Hz until complete homogenization.
e) 3 µl of Puregene Proteinase K (Qiagen, Ref. 158918) was added, and mixed inverting 25 times.
f) Incubation at 55ºC for 1h (up to 3h if needed) was performed.
g) 3 µl of RNasa A was added and mixed inverting 25 times.
h) Incubation at 37ºC for 1h.
i) The bead was removed.
j) 200 µl Protein Precipitation Solution was added and vortexed for 20 sec.
k) Centrifugation at 16,000 x *g* for 3 min was performed, followed by a 2 min incubation on ice.
l) The supernatant was collected.

Final steps for both DNA extraction protocols:

1. The supernatant was mixed with 1 ml ice-cold Isopropanol.
2. The tube was inverted until a visible DNA precipitate formed.
3. The precipitate was washed by sucking in ice-cold 70% ethanol 4-5 times.
4. The precipitate was suspended in 50 µl of distilled water (H_2Od).
5. Incubation at 37ºC overnight (O/N) was performed. If necessary, additional H_2Od was added until complete suspension of the DNA.

DNA quantity of each sample was measured with Qubit (Qubit™ dsDNA BR Assay Kit, Invitrogen, Ref. Q32850), and quality was evaluated with a NanoDrop 1000 Spectrophotometer (ThermoFisher Scientific). Quality was determined using the following parameters:

a) 260/280 ratio: Used to assess DNA and RNA purity. A ratio of ~1.8 indicates pure DNA, while a ratio of ~2.0 indicates pure RNA. Lower values suggest contamination with protein, phenol, or other impurities.
b) 260/230 ratio: A secondary measure of nucleic acid purity. Expected values range from 2.0-2.2. Lower values indicate potential contamination by substances absorbing at 230 nm.

Additionally, DNA integrity was evaluated using 1% agarose gel electrophoretic, with samples run at 120 V for 20 min.

3.2. DNA Purification

If NanoDrop values were outside the acceptable (~1.8 for 260/280 and 2.0-2.2 for 260/230), DNA purification was performed using the DNA Clean & Concentrator™ -5 kit (Zymo Research, Ref. D4014) according to the manufacturer's protocol:

1. DNA Binding Buffer (2-7 volumes) was added to each volume of DNA sample (2:1 ratio for genomic DNA >2 kb).
2. The mixture was transferred to a Zymo-Spin Column in a Collection Tube.
3. Centrifugation at 16,000 x *g* for 30 sec was performed.
4. The flow-through was discarded.
5. 200 µl DNA Wash Buffer was added to the column.
6. Centrifugation at 16,000 x *g* for 30 sec was performed.
7. 200 µl DNA Wash Buffer was added to the column.
8. Centrifugation at 16,000 x *g* for 30 sec was performed.
9. Approximately 20 µl DNA Elution Buffer was added to the column matrix, followed by incubation at RT for 1 min.
10. The column was transferred to a 1.58 ml microcentrifuge tube.
11. Centrifugation at 16,000 x *g* for 30 sec was performed.
12. DNA quantification was conducted using a NanoDrop 1000 Spectrophotometer.

3.3. Short Tandem Repeat Authentication

Short tandem repeat (STR) authentication was performed to confirm cell line identity and detect intra-species contamination in cultured human cell lines. DNA fingerprints were obtained using the AmpFISTR Identifiler Plus PCR Amplification kit (Applied Biosystems, Ref. 4427368) following the manufacturer's protocol.

The kit amplified 16 tetranucleotide STR loci and the gender-determining marker, Amelogenin, in a single PCR reaction using 33 primers: *D8S1179, D21S11, D7S820, CSF1PO, D3S1358, TH01, D13S317, D16S539, D2S1338, D19S433, vWA, TPOX, D18S51, AMEL, D5S818, and FGA*. This marker combination aligns with global database recommendations for identity testing. Allele calls were made from peak plots by comparing peaks to known fragment sizes using GeneMapper 4.0 (Applied Biosystems).

3.4. Whole Genome Sequencing and Analysis

WGS was performed at BGI (Shenzhen, China). In short, libraries were prepared following standard DNBseq protocols and sequenced on a BGISEQ-500 platform, generating a median of 881 million 150-bp paired-end reads per sample. Reads were mapped to the GRCh38 genome using BWA-MEM. WGS data were processed as described in Magallón-Lorenz et al. (2023). Small nucleotide variants were identified Strelka2 and annotated with Annovar. CN alterations were called using CNVkit with the recommended WGS settings.

A panel of normal samples was generated per CNVkit recommendations for comparison. The threshold method was applied to obtain exact CN profiles, and the Strelka2 germline results were used to detect LOH regions. To refine the thresholds, sample purity was calculated considering the 2n calling and a pseudo- B-allele frequency (BAF) obtained from the Strelka2 germline results using the loadSNPDataFromVCF function from the CopyNumberPlots R package (Bernat Gel 2024).

Based on this information, tumoral DNA purity was calculated with an in-house function, taking into account copy-neutral LOH regions or heterozygous loss regions and the pseudo-BAF output. Subsequently, ploidy was estimated, and the most accurate CNV calling for each sample was manually selected. Copy number alterations were plotted using the CopyNumberPlots (Bernat Gel 2024)and karyoploteR R packages.

3.5. RNA Isolation and Quantification

RNA isolation was performed for quantitative real-time polymerase chain reaction (qRT-PCR) and RNA sequencing (RNA-seq) analyses.

RNA extraction from cultured cell lines: Cells were treated in a step prior to RNA isolation:

a) Cells were scraped and lysed using 400 µl of TRI Reagent (Zymo Research, Ref. R2050-1-50) and incubated ON at -80ºC.
b) 400 µl of absolute ethanol was added.

RNA extraction from tumor tissue:

a) Tumor tissue was cut into small pieces.
b) 400 µl of TRI Reagent was added.
c) One Tungsten Carbide Bead was included.
m) Tissue was homogenized using TissueLyser II at 20 Hz for 30 sec. If needed, homogenization was repeated, not exceeding 2 min of shaking.
d) 400 µl of absolute ethanol was added.

Following lysis in TRI Regent, total RNA was extracted using Direct-zol RNA MiniPrep kit (Zymo Research, Ref. R2050):

1. Lysate was loaded into a Zymo-Spin IIC Column in a Collection Tube.
2. Centrifugation at 13,000 rpm for 1 min was performed.
3. 400 µl Direct-zol RNA PreWash was added, followed by centrifugation at 13,000 rpm for 1 min (repeated twice).
4. 75 µl of DNA Digestion buffer and 5 µl of DNAsa I were added.
5. Incubation at RT for 15 min was performed.
6. 700 µl of RNA Wash Buffer was added, followed by centrifugation at 13,000 rpm for 1 min (repeated twice).
7. The column was transferred to a new Eppendorf tube.
8. 50 µl H_2Od was added.
9. Centrifugation at 13,000 rpm for 1 min was performed.
10. RNA was quantified using NanoDrop 1000 Spectrophotometer. Quality assessment required a 260/280 ratio ~2.0 and a 260/230 ratio between 2.0 and 2.2.

Additionally, RNA integrity was evaluated using 1% agarose gel electrophoretic, with samples run at 120 V for 20 min.

RNA quality was assessed using the 2200 TapeStation Bioanalyzer (Agilent). This system evaluates RNA concentration and integrity with minimal sample input using electrophoresis and fluorescence detection. RNA fragments were separated by molecular weight, and fluorescence intensity correlates with RNA quantity, generating an electropherogram. The RNA Integrity Number (RINe) was calculated on a scale from 1 to 10, where 10 indicates intact RNA and 1 represents complete degradation. RNA with RIN < 6 was considered degraded, while samples with RIN > 7 were considered suitable for gene expression studies.

3.6. RNA Sequencing

RNA-seq libraries were prepared at BGI (Shenzhen, China) using DNBSEQ standard protocols. Data were aligned using Salmon v1.8.0 (RRID: SCR_017036; (Patro, Duggal et al. 2017)) against the UCSC refMrna and hg38 genome. Transcript-level estimates were imported into R (R v4.3.0 Bioconductor v3.17) and summarized to the gene level using tximport (RRID: SCR_016752; (Soneson, Love et al. 2015)). Genes with less than five counts in more than two samples were filtered out. A principal component analysis (PCA) plot was generated. Differentially expressed genes in PRC2-inactivated MPNST cell lines treated with I-BET151 were identified using DESeq2 (RRID: SCR_015687) with the Wald test and apeglm (RRID: SCR_015687). Genes with an adjusted P value <0.05 were considered differentially expressed. Heatmaps were created using the pheatmap package. The code used for generating the different bioinformatic analyses performed can be found at: https://github.com/miriammagallon/RNA-seq_Sara_MPNSTcl_treatments.

3.7. RT-qPCR

RT-qPCR was performed to amplify and quantify specific DNA regions. cDNA was synthesized from RNA samples by reverse transcription using the SuperScript™ III Reverse Transcriptase (Invitrogen™, Ref. 10432122):

1. RNA (1 µg) was mixed with H_2Od to a final volume of 11 µl.
2. 1 µl of random primers (provided in the kit) and 1 µl of dNTPs Mix (10 mM) were added.
3. The template-primer mixture was denatured by heating for 5 min at 65ºC in a thermal cycle with a heated lid.
4. The tube was immediately cooled on ice.
5. A reaction mix (x1) containing 4 µl of 5X First-Strand Buffer and 2 µl of 0,1 M DTT was added.
6. 1 µl of SuperScript™ III RT was added.
7. Incubation was performed for 10 min at 25ºC, followed by 50 min at 42ºC in the thermal cycler.
8. Reverse Transcriptase was inactivated by heating at 70ºC for 15 min, and samples were kept at 4ºC.
9. The sample was diluted 1:20 with $H_2$0d and stored at -20ºC.

After cDNA synthesis, qPCR was conducted as follows:

1. A reaction mix was prepared containing (x1) 5 µl of SYBR Green I Master kit (Roche, Ref. 04707516001), 3.2 µl of H_2Od, 0.4 µl (10 µM) of forward primer, and 0.4 µl (10 µM) of reverse primer.
2. 9 µl of the mix was added to a 384-well plate.
3. 1 µl of diluted cDNA was added.
4. The plate was sealed and centrifuged at 150 rcf for 10 min.
5. RT-qPCR was run using a LightCycler 480 real-time PCR system (Roche).
6. Gene expression was normalized to two selected reference genes (*EP300* and *TBP*) and expressed as Normalized Relative Expression (NRE). Primers used are listed in Table MM1.

Table MM1. Primers used for qPCR

Gene	Forward	Reverse	Source
MAFA	TCATCCGGCTCAAGCAGAAG	TGTACAGGTCCCGCTCTTTG	In-house design
TPPP	CAAAGGGAAGTCTTGCCGGA	CAAAGGGAAGTCTTGCCGGA	In-house design
ZDHHC11B	AGTGTGCGCCGAGATGGACA	GAGGCAGGAGGGGAATGAAG	In-house design
NGFR	TACATACCAAAGGGCACACG	CTGCCTGGACAGCGTGACGTT	In-house design
PRDM1	TACATACCAAAGGGCACACG	TGAAGCTCCCCTCTGGAATA	Guo H et al. 2022
ARHGDIB	AGTTGAGACAGAGGCACC	TCAGGGACTTCTGTGGTGGA	Zhang R et al. 2022
EP300	GCAGCCTGCAACTCCACT	GAGGATTTGATACCTGTCCTTCA	Mazuelas H et al. 2022
TBP	AGGAATTGAGGAAGTTGCTGAG	CGCTGGAACTCGTCTCACTA	Mazuelas H et al. 2022

3.8. Protein Extraction from Cell Lines and Tumor Samples

Cell line procedure:

1. Cells were trypsinized.
2. Cells were washed three times with PBS 1X, with centrifugation after each wash.
3. The pellet was suspended in RIPA lysis buffer (Table MM2) supplemented with protease inhibitor cocktail tablets (1 pill/10 ml, Roche, Ref. 04693), sodium pyrophosphate dibasic 200mM (150 µl/1 ml, Merck, Ref. P8135), and sodium orthovanadate 1M (2 µl/1 ml, Merck, Ref. S6508).
4. Incubation at 95ºC for 20 was performed.
5. Centrifugation at 16,000 x *g* at 4ºC for 10 min was conducted.
6. Protein quantification was performed using the Pierce Bicinchoninic acid assay (BCA) Protein Assay Kit (Thermo Fisher Scientific, Ref. 23225), following the manufacturer's instructions:

a. A standard curve was generated with seven Bovine serum albumin (BSA) concentrations (2, 1, 0.5, 0.25, 0.125, 0.0625, and 0 mg/ml).
b. 20 µl of each condition was plated in triplicate using a 1:4 protein dilution.
c. 200 µl of the reagent mixture (4 µl Reagent A + 196 µl Reagent B) was added per sample.
d. Incubation at 37ºC for 30 was performed.
e. Absorbance was measured using the VictorTM X5 2030 Multilabel Reader (PerkinElmer).
f. Protein concentration was determined using Excel and the standard curve.

Table MM2. RIPA Buffer components

Stock	Volume (mL)	[Final]	Source
5 M NaCl	5	150 mM	Sigma-Aldrich, Ref. S9625
0.5 M EDTA, pH 8.0	1	5 mM	Gibco, Ref. 15575-038
1 M Tris, pH 8.0	5	50 mM	Merck, Ref. GE17-1321-01
NP-40 (IGEPAL CA-630)	1	1.0%	Merck, Ref. 56741
10 % sodium deoxycholate	5	0.5%	Merck, Ref. D6750
10 % SDS	1	0.1%	TermoFisher, Ref. AM9823
H_2Od	84	-	-

Tumor tissue procedure:

1. A tumor sample (15-20 mg) was cut.
2. 200 µl RIPA buffer supplemented with protease inhibitor, sodium pyrophosphate dibasic, and sodium orthovanadate was added.
3. One Tungsten Carbide Bead was added.

n) Homogenization was performed using TissueLyser II at 25 Hz for 2 min. If tissue remained intact, homogenization was repeated but did not exceed 2 min.

4. Centrifugation at 16,000 x *g* at 4ºC for 10 min was conducted.
5. Protein quantification was performed using the Pierce BCA Protein Assay Kit, following the same steps described for cell lines.

3.9. Western Blot

Western Blot (WB) was used to detect specific proteins in cell lysates. Denatured proteins were separated by gel electrophoresis based on their molecular weight and transferred to a membrane. The membrane was incubated with primary antibody and secondary antibodies

conjugated to horseradish peroxidase (HRP), which catalyze a chemiluminescent reaction for protein detection.

1. A 12% 1.5 mm acrylamide gel (Bio-Rad, Ref. 1610185) was prepared:
    a. Resolver gel: 4 ml Resolver A*, 4 ml Resolver B*, 15 µl 10% APS (PanReac, Ref. A2941-0100), and 3 µl TEMED (Invitrogen, Ref. 15524-010).
    **Resolver A and Resolver B are the reagents in the kit.*
    b. Stacker gel: 1.5 ml Stacker A, 1.5 ml Stacker B, 15 µl 10% APS, and 3 µl TEMED.
    c. Polymerization was allowed for 30 min at RT.
    **Stacker A and Stacker B are the reagents in the kit.*
2. Protein samples were prepared by mixing 20 µg of protein with an equal volume of sample buffer: 960 µl 2X Laemmli Sample Buffer (Bio-Rad, Ref. 1610737) + 40 µl β-mercaptoethanol (Merck, Ref. 444203). The mixture was incubated at 85 ºC for 10 min.
3. Running buffer was prepared using a 1/10 dilution of TRIS-Glycine Buffer (1X) + 10 ml SDS 10% (Bio-Rad, Ref. 1610416) per liter.
    TRIS-Glycine Buffer (10X) was prepared: 30.28 g TRIS + 144.13 g Glycine (Sigma-Aldrich, Ref. G7126) + 1 L H_2Od.
4. 20 µl of the protein sample was loaded into each well of the 12% acrylamide gel. NZY color protein marker II (NZY tech, Ref. MB09003) was used as a molecular weight reference.
5. Electrophoresis was performed at 200 V for 1h.
6. Proteins were transferred using the Trans-Blot Turbo Transfer System (Bio-Rad, Ref. 1704150) and the Trans-Blot Turbo RTA Transfer Kit, Nitrocellulose (Bio-Rad, Ref. 170-4270), following the Bio-Rad TURBO program (3 min at 2.5 A constant current).
7. Membrane blocking was performed by rocking for 1h at RT:
    a. House-keeping proteins: 5% Skim Milk Powder (Sigma-Aldrich, Ref. 70166) in PBS 1X + 1% Tween20 (Merck, Ref. 655204) (PBS-T).
    b. Proteins of interest: 5% BSA Fraction V (Roche, Ref. 10735078001) in PBS 1X + PBS-T.
8. Membranes were incubated with primary antibodies in blocking solution (Table MM3) O/N at 4ºC.
9. Membranes were washed three times with PBS-T, rocking for 5 min at RT.
10. Secondary antibody incubation (HRP-conjugated) RT (Table MM3) was performed for 1h at.
11. Membranes were washed three times with PBS-T, rocking for 10 min at RT.

12. The revealed solution was prepared:
    a. Proteins with low expression: Super Signal West Femto chemiluminescent substrate kits (Thermo Fisher Scientific, Ref. 34095): 500 µl A + 500 µl B (buffers A and B included in the kit).
    b. Proteins with high expression (such as house-keeping proteins): 1 ml solution A + 3 µl solution B.
        i. Solution A: 1 ml of TRIS 1M pH=8.5, 22 µl of p-Coumaric acid (Sigma-Aldrich, Ref. C9008), 50 µl of Luminol (Sigma-Aldrich, Ref. A8511) and 9 ml H_2Od.
        ii. Solution B: 10 µl H_2O_2 (Merck, Ref. 108597) + 90 µl H_2Od.
13. 500 µl of the adequate revealed solution in each membrane was added.
14. Chemiluminescent detection was performed using ChemiDoc Imaging System (Bio-Rad, Ref. 12003153).
15. Protein expression was quantified using Image Lab and normalized to the loading control (tubulin, vinculin, or GAPDH). Values were normalized to the highest obtained expression level.

Table MM3. Antibodies used in the Western Blot (WB) assay

Protein Target	Primary / secondary	Company	Reference	Specie	Dilution
Phospho-p44/42 MAPK Erk1/2	Primary	Cell Signaling Technology	4376	Rabbit	1/1,000
Pan ERK	Primary	BD Biosciences	610124	Mouse	1/2,000
Phospho-Rb Ser780	Primary	Cell Signaling Technology	9307	Rabbit	1/1,000
Rb 4H1	Primary	Cell Signaling Technology	9309	Mouse	1/2,000
Anti-Wee1	Primary	Cell Signaling Technology	4936	Rabbit	1/1,000
c-Myc antibody [Y69]	Primary	Abcam	ab32072	Rabbit	1/1,000
Anti-Tubulin Polymerization Promoting	Primary	Abcam	ab92305	Rabbit	1/1000
Anti-p75 NGF Receptor antibody [EP1039Y]	Primary	Abcam	ab52987	Rabbit	1/1000
Blimp-1 Monoclonal Antibody (6D3)	Primary	ThermoFisher Scientific	14-5963-82	Mouse	1/1000
Bim (C34C5)	Primary	Cell Signaling Technology	2933	Rabbit	1/1,000
Tubulin	Primary	Sigma-Aldrich	V9264	Mouse	1/10,000
Vinculin	Primary	Sigma-Aldrich	T6074	Mouse	1/10,000
Anti-GAPDH	Primary	Abcam	ab9485	Rabbit	1/1000
Anti-Rabbit IgG (H+L), HRP	Secondary	Thermo Fisher Scientific	32460	Goat	1/10,000
Anti-Mouse IgG (H+L), HRP	Secondary	Thermo Fisher Scientific	32430	Goat	1/10,000

3.10. Cell Cycle Analysis Using Flow Cytometry

Flow cytometry was used to estimate the percentage of cells in the G1/S and G2/M phases of the cell cycle in fixed samples. The ploidy state of the cell culture was assessed, using fibroblasts as a diploid control.

1. Cells were trypsinized at 80% confluency, and 5 x 10^5 cells per condition were collected.
2. Cells were washed with PBS 1X + 1% FBS and centrifuged at 1250rpm for 5 min.
3. The pellet was suspended in 1 ml PBS 1X + 1% FBS.
4. Fixation was performed using 5 ml ice-cold 70% ethanol, followed by incubation at -20ºC for at least 24h.
5. Centrifugation at 800 x *g* for 5 min was conducted.
6. Cells were washed with PBS 1X - 1% FBS.
7. Centrifugation at 400 x *g* for 5 min was performed.
8. Cells were stained with 400 µl of PBS 1X + 1% FBS, 25 µl Propidium Iodide solution (0.0625 mg/ml; Sigma-Aldrich, Ref. R-P-4864), and 2.5 µl Ribonuclease A from bovine pancreas (10 µg/ml; Sigma-Aldrich, Ref. R-4642) for 30-45 min at 37ºC.
9. Up to 20,000 events per sample were analyzed using the Gallios Flow Cytometer (Beckman Coulter).

Cell cycle analysis was performed in IDIBELL Cytometry Service using ModFit LT V.3.3.11 software, with model fitting assessed by the Reduced Shi-Square (RCS) statistic.

3.11. Immunofluorescence

Immunofluorescence (IF) was used to visualize protein expression and localization. Proteins were detected using specific primary antibodies, followed by secondary antibodies conjugated with fluorochromes.

1. Cells were seeded in 12-well Corning® plates containing glass coverslips (12 mm Ø, ThermoFisher Scientific, Ref. 174950).
2. Once cells reached 80-90% confluency, the medium was removed, and cells were washed three times with PBS 1X.
3. Fixation was performed using 4% Paraformaldehyde (PFA) (ITW Reagents, Ref. 252931.1211) for 15 min at RT.
4. Cells were washed three times with PBS 1X 5 min at RT.
5. Permeabilization was carried out using PBS 1X + 0.1% Triton X-100 (Sigma-Aldrich, Ref. 9036-19-5) for 15 min at RT.

6. Blocking was performed in PBS 1X + 10% Goat Serum (Gibco, Ref. 11540526) for 30 min at RT.
7. Coverslips were removed from the plate and incubated with 100 µl of primary antibodies diluted in PBS 1X-1% Goat Serum in a humidified chamber O/N at 4ºC (Table MM4).
8. Coverslips were returned to the plate and washed three times with PBS 1X, rocking for 5 min at RT.
9. Secondary antibodies diluted in PBS 1X + 10% Goat Serum were applied for 1h at RT in a humidified chamber (Table MM4). From this step forward, cells were kept in the dark.

Table MM4. Antibodies used in the Immunofluorescence (IF) and Immunohistochemistry (IHC) assays

Antibody	Primary / secondary	Company	Reference	Specie	Dilution	Technique
SOX-9	Primary	Abcam	ab76997	Mouse	1:100	IF
Smooth muscle actin (SMA)	Primary	ThermoFisher Scientific	RB-9010-R7	Rabbit	1:100	IF
H3K27me3	Primary	Cell Signaling	9733	Rabbit	1:1500 1:200	IF IHC
SOX-10 (EP268)	Primary	Cell Marque	383R-14	Rabbit	1:50	IF, IHC
Vimentin	Primary	Life Technologies	180052	Mouse	1:200	IHC
Ki67	Primary	DAKO	M7240	Mouse	1:10	IHC
S100B	Primary	DAKO	Z031129	Rabbit	1:300	IHC
Anti-CD68	Primary	Ventana Medical Systems	790-2931	Mouse	Ready to use	IHC
Anti-CD163	Primary	Ventana Medical Systems	760-4437	Mouse	Ready to use	IHC
Alexa Fluor 488 anti-mouse	Secondary	Invitrogen	A11029	Goat	1:1000	IF
Alexa Fluor 568 anti-rabbit	Secondary	Invitrogen	A11036	Goat	1:1000	IF
EnVision + System-HRP Anti-mouse	Secondary	DAKO	K4001	Goat	Direct from Stock Solution	IHC
EnVision + System-HRP Anti-Rabbit	Secondary	DAKO	K4003	Goat	Direct from Stock Solution	IHC

10. Coverslips were returned to the plate and washed three times with PBS 1X, rocking for 5 min at RT.
11. Nuclear staining was performed using 4,6-diamino-2-phenilindole (DAPI) (1:1000, ThermoFisher Scientific, Ref. 62248) in PBS 1X, rocking for 10 min at RT.
12. Cells were washed five times with PBS 1X, rocking for 5 min at RT.
13. Coverslips were mounted on slides (Deltalab, Ref. D102440) using Immu-Mount (ThermoFisher Scientific, Ref. 9990402).

14. Images were acquired using a Nikon Eclipse 80i microscope, and image processing was conducted with NIS-Elements Microscope Imaging and Image J (Fiji).

3.12. Histological Procedures

3.12.1. Paraffin Embedding of Tissues

For long-term conservation and staining, tumor samples were formalin-fixed and paraffin-embedded (FFPE).

1. Tissues of interest were collected and placed in a cassette.
2. Fixation was performed using 4% PFA for 24h at RT.
3. Samples were washed with tap water for 30 min.
4. Dehydration steps were conducted as follows:
    a. 70% ethanol for 1h at RT.
    b. 96%-I ethanol (Alcoholes Gual S.A.) for 1h at RT.
    c. 96%-II ethanol for 1h at RT.
    d. 96%-III ethanol O/N at RT.
    e. Absolute ethanol-I (Alcoholes Gual S.A.) for 1h at RT.
    f. Absolute ethanol-II for 1h 30 min at RT.
    g. Absolute ethanol-III for 1h 30 min at RT.
5. Samples were immersed in xylene (PanReac, Ref. 251769.2714) for 1h 30 min at RT.
6. Samples were immersed in liquid paraffin O/N at 60ºC.
7. Liquid paraffin was poured into a hot metal mold, and the sample was placed within it.
8. The mold was cooled on a cold plate until solidified.

In this thesis, tumor cell lines were also embedded in paraffin to perform immunohistochemistry staining. The procedure for FFPE cell lines was as follows:

1. Cells were trypsinized.
2. Centrifugation at 1250 rpm for 5 min was performed, and the supernatant was aspirated.
3. The cell pellet was suspended in 100 µl of human plasma.
4. 100 µl of thrombospondin (Grifols, Barcelona, Spain) was added.
5. Gently shaking was performed to generate a cell clot.
6. The clot was wrapped with filter paper.
7. The clot was placed in a cassette.

8. Fixation was performed in 4% PFA O/N at RT, followed by the same steps as the tissue protocol.

3.12.2. Hematoxylin and Eosin Staining

Hematoxylin and eosin (H&E) staining was performed for structural visualization. Hematoxylin stained the nucleus (dark purple), while eosin stained the cytoplasm (pink) and extracellular matrix components.

1. Paraffin-embedded tissue sections (5 µm) were obtained using a microtome
2. Slides were heated at 80ºC for 10 min to melt the paraffin.
3. Rehydration was performed using following battery:
    a. Xylene I-IV for 10 min each.
    b. Absolute ethanol I-III for 5 min each.
    c. 96% ethanol I-III for 5 min each.
    d. 70% ethanol I for 5 min.
    e. 50% ethanol I for 5 min.
    f. Distilled water for 5 min.
4. Slides were stained with filtered hematoxylin (Merck, Ref. 1.09253) for 10 min and washed with tap water.
5. Acid differentiation was performed by dipping slides 9-10 times in 37% HCl until the solution turned red, followed by tap water wash.
6. Alkaline bluing was performed by dipping slides 9-10 times in 0.3% ammonia water [NH_3(aq)] 0.3% until the solution turned blue, followed by tap water wash.
7. Slides were stained with 0.25% eosin solution (Merck, Ref. 17372-87-1) for 1 min.
8. Dehydration was performed using the following battery:
    a. 96% ethanol I-II for 3 min each.
    b. Absolute ethanol I-II for 3 min each.
    c. Xylene I-IV for 3 min each.
9. Slides were mounted in DPX Mountant (Sigma-Aldrich, Ref. 3771).
10. Images were acquired using a Nikon Eclipse 80i vertical microscope.

3.12.3. Immunohistochemistry

Immunohistochemistry (IHC) was performed to identify specific tissue components using an antigen-antibody reaction tagged with a visible label. Proteins were detected using primary

antibodies, followed by secondary antibodies conjugated with a fluorochrome. IHC enabled the visualization of protein localization within cells and tissue context.

1. Paraffin-embedded tissue sections (3 µm) were obtained using a microtome.
2. Slides were heated at 80ºC for 10 min to melt the paraffin.
3. Rehydration was performed using following battery:
    a. Xylene I-IV for 5 min each.
    b. Absolute ethanol I-III for 5 min each.
    c. 96% ethanol I-III for 5 min each.
    d. 70% ethanol I for 5 min.
    e. 50% ethanol I for 5 min.
    f. Distilled water for 5 min.
4. Antigen retrieval was performed using citrate-based antigen retrieval (sodium citrate pH 6.0) at 110ºC for 15 min in a Decloaking Chamber™ NxGen (Biocare medical, Ref. DC2012), followed by cooling in buffer for 15 min.
5. Slides were washed three times with PBS-T at RT.
6. Endogenous peroxidase activity was blocked using a distillate water solution containing 3% H_2O_2 and 30% methanol (Alcoholes Gual S.A.) for 15 min at 4ºC.
7. Blocking was performed using PBS 1X + 5% Goat Serum for 1h at RT.
8. Primary antibody incubation was conducted O/N at 4ºC (Table MM4) followed by an additional 30 min at RT.
9. Slides were washed three times with PBS-T for 5 min at RT.
10. Incubation with secondary antibodies was performed for 1h at RT (Table MM4).
11. Slides were washed three times with PBS-T for 5 min at RT.
12. Liquid 3,3'-diaminobenzidine (DAB) Substrate Chromogen System (DAKO, Ref. K3468) was applied for antigen detection (maximum 10 min).
13. Slides were washed three times with H_2Od.
14. Counterstaining was performed by dipping slides in hematoxylin 3-10 times.
15. Dehydration was performed using the following battery:
    a. 70% ethanol I for 1 min.
    b. 96% ethanol I-II for 1 min each.
    c. Absolute ethanol I-II for 1 min each.
    d. Xylene I-IV for 10 min each.
16. Slides were mounted with DPX.
17. Images were acquired using a Nikon Eclipse 80i vertical microscope.

MM 4. *In Vitro* Cell Line Analysis

4.1. Cell Growth Curve

The growth rate of each cell line was assessed to determine the number of cells required for confluency after 10 days. Cell viability was measured using the MTT colorimetric assay [3-(4,5-dimetrhylthiaziol-2-yl)-2,5-diphenyl-tetrazolium bromide] (Sigma-Aldrich, Ref. #M2128-1), which is enzymatically reduced to formazan by viable cells, making dye intensity proportional to the number of living cells.

1. Cells were seeded in triplicate in 96-well plate (Thermo Fisher Scientific, Ref. 167008) at varying densities: 300, 500, 700, 900, 1100, 1300, 1500, 1700, and 2000 cells/well.
2. Cells were incubated for 10 days at 37ºC with 5% CO_2.
3. The MTT assay was performed:
    a. 0.5 mg/ml MTT (suspended in PBS 1X) was added to each well.
    b. Incubation was performed for 3h at 37ºC with 5% CO_2.
    c. The solution was removed by inverting the plate.
    d. 100 µl of a 1:3 glycine buffer (0.1 M NaCl and 0.1 M Glycine) and DMSO solution was added to each well.
    e. Incubation was conducted in the dark with rocking for 10 min.
    f. Absorbance was measured at 540 nm using the VictorTM X5 2030 Multilabel Reader (PerkinElmer).
4. The optimal cell concentration for PDT analysis was chosen so that absorbance was approximately 1 after 10 days.

4.2. Population Doubling Time

PDT was calculated to determine the time required for each cell line to double in number. PDT values were obtained from cell viability measurements using the MTT assay.

1. Cells were seeded in six replicates in 96-well plates, with 10 identical plates prepared. Cell densities were determined based on prior growth curve results: 1,100 cells/well for NF1-18B and 1,300 cells/well for SP-10.
2. The MTT assay was performed every 24h on a different plate (as described in Section 2.1 of M&M).
3. PDT values were calculated using an exponential growth equation in GraphPad Prism 7.

4.3. 2- Dimension Colony Formation

The 2-D colony formation assay was used to evaluate the ability of single adherent cells to survive and form colonies over time. Crystal violet staining was used to visualize colonies, with staining intensity proportional to the cell biomass attached to the plate.

1. 300 cells/well were seeded in 12-well Corning® plates.
2. Cells were cultured for 10 days at 37ºC with 5% $CO_{2.}$
3. The supernatant was aspirated.
4. Cells were rinsed once with 1 ml PBS 1X.
5. Fixation was performed using ice-cold 100% methanol for 10 min (kept in the freezer).
6. Cells were stained with an H_2Od solution containing 20% methanol and 0.1% crystal violet (Sigma-Aldrich, Ref. 61135-256) for 15 min at RT.
7. The crystal violet solution was removed, and cells were washed several times with H_2Od.
8. Cells were allowed to dry at RT.
9. Representative images of the 2-D colonies were captured without amplification.

4.4. Hanging-Drop Assay

The hanging drop assay was used to evaluate the ability of adherent cell lines to form 3-D clusters under non-adherent conditions.

1. 200 cells were seeded in a 20 µl drop of DMEM on the inverted lid of a 60 mm plate. 20 drops were seeded in each of three plates per cell line.
2. 5 ml of PBS 1X was added to the bottom of the plate.
3. The lid was inverted onto the PBS 1X-filled bottom chamber.
4. Cells were incubated at 37ºC with 5% $CO_{2.}$
5. Cells were imaged directly from the droplets on the lid at 24 and 48h using a Leica DM IL LED optical microscope at 10X magnification.

4.5. Wound-Healing Assay

The wound-healing (scratch) assay was used to evaluate 2-D cell migration. A gap was created in a confluent monolayer, and cell movement was tracked over time using microscopy.

1. 7 x 10^5 cells/ml (70 µl/well) were seeded into the culture insert (2 wells; Ibidi, Ref. 80209).
2. Cells were grown at 37ºC with 5% CO_2 for 24h until 100% confluency was reached.

3. Culture inserts were removed to create a wound gap.
4. Wound closure was monitored at 0, 4, 8, 12, and 24h.
5. Images were captured using a Leica DM IL LED optical microscope at 10X magnification.
6. Migration distance was measured using ImageJ software based on the remaining gap area.

MM 5. *In Vitro* High-Throughput Screening Strategy

5.1. Quantitative High-Throughput Screening in Single Agent

HTS was conducted at the NCATS, National Institutes of Health (NIH), in collaboration with Dr. Marc Ferrer's group. A total of 14 MEKi, 11 CDKi, and 3 BETi from the NIH Mechanism Interrogation Plate (MIPE) 4.0 library were tested in an 11-point dose-response format in three MPNST cell lines and one fibroblast cell line. Cell viability was measured using the CellTiter-Glo (CTG) luminescent assay after 48h, and compound activity was determined based on curve response class (CRC). The NCATS HTS protocol was as follows:

1. 1,000 cells per well were seeded into barcoded 1,536-well, solid-bottom white Greiner Bio-One tissue culture-treated plates (catalog #789173-F) using a Multidrop Combi dispenser (Thermo Fisher Scientific).
2. Drugs were dispensed to generate 11-point dose-response curves from a starting stock concentration of 10 mmol/L, decreasing to 46 µmol/L. A total of 23 nL of DMSO or drug was added per well using Kalypsys pintool.
3. Plates were incubated at 37 °C with 5% CO_2 and 95% humidity for 48h.
4. 3 µl of CTG luminescent assay reagent (Promega) was added per well using a Bioraptor Flying Reagent Dispenser (Aurora Discovery-BD).
5. Plates were incubated for 15 min at RT to stabilize the luminescent signal.
6. Luminescence was measured using a ViewLux (Perkin-Elmer) with a luminescent filter and a 10-second exposure time. Relative luminescence units (RLUs) were normalized to the median RLUs of DMSO-treated control wells, set as 100% viability.

HTS dose-response data were normalized and fitted using a custom NCATS grid-based algorithm to generate CRC scores, classifying compounds as active, inconclusive, or inactive based on (Figure MM1):

a) <u>High-quality active hits (CRC 1.1, 1.2, 2.1)</u>: These compounds exhibited well-defined dose-response relationships. Class 1.1 curves showed a strong fit ($R^2 \geq 0.9$), well-

defined asymptotes, and efficacy >80%. Class 2.1 curves had a single well-defined asymptote, while class 1.2 curves had moderate efficacy (30–80%).

b) Inconclusive results (CRC 2.2, 3): These compounds displayed incomplete or poorly fitted curves. Class 2.2 curves had moderate efficacy (30–80%) but lacked a strong fit, whereas class 3 curves were unreliable, showing weak responses or activity only at the highest doses.

c) Inactive compounds (CRC 4, 5): Class 4 curves showed no measurable effect, while class 5 curves could not be fitted.

The active compounds were selected for further study based on this classification.

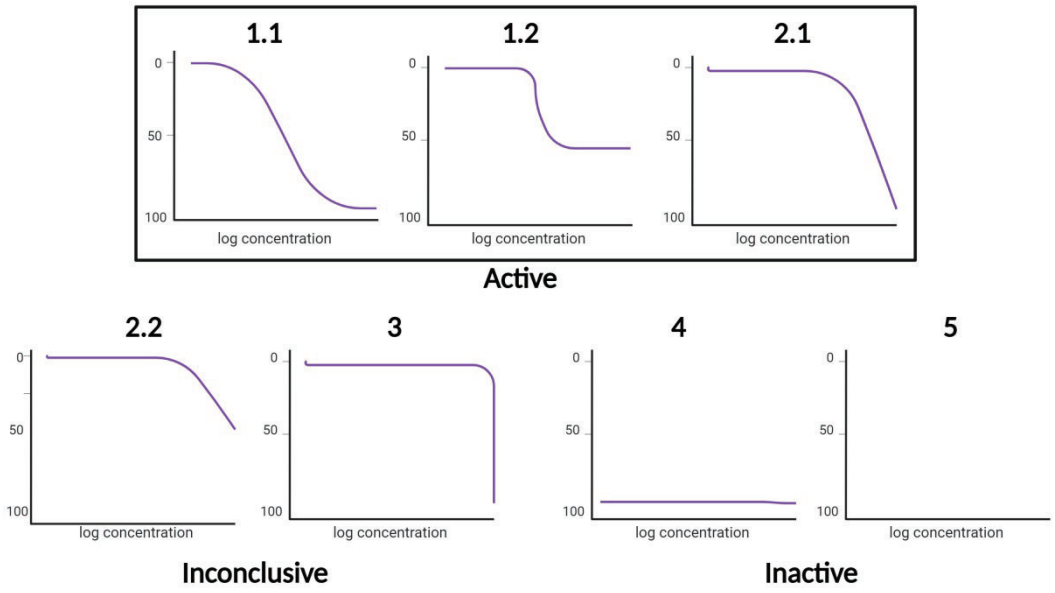

Figure MM1. Curve Response Classes from HTS. Active curves: 1.1, 1.2, and 2.1; inconclusive curves: 2.2 and 3; and inactive curves: 4 and 5.

5.2. Quantitative High-Throughput Screening in Pairwise Combination

147 co-treatments were screened for the 22 selected compounds in HTS in pairwise combinations at NCATS. A fixed 1:1 ratio of each compound was used to generate 10x10 concentration matrices, following the same protocol as for single compounds. Synergistic combinations were selected based on:

a) Visual inspection of 10x10 matrices, prioritizing those with effects at the lowest drug concentrations.

b) The E-HSA and the Delta Bliss Sum Negative (DBSumNeg) value obtained in HTS, with more negative values indicating greater synergy.

c) The clinical phase of the compounds, prioritizing those in advanced stages in clinical trials.

5.3. IC_{50} Calculation

To validate selected HTS combinations *in vitro,* the half-maximal inhibitory concentration (IC_{50}) was determined for all involved compounds (9 in total). IC_{50} is a quantitative measure of the concentration required to inhibit a biological process by 50%.

All compounds tested were provided by the NCATS Compound Management group in DMSO solutions at 10 mmol/L: MEK inhibitors (Trametinib, Selumetinib, Arry-162/Binimetinib), CDK inhibitors (Palbociclib, R-546, Flavopiridol), and BET inhibitors (I-BET151, JQ1), except for Riboclibib that was purchased from MedChemExpress (Ref. HY-15777).

1. Cells were seeded in 96-well plate in triplicate at densities optimized for 80-100% confluence at 72 hours: 8,000 cells/well for S462; 12,000 cells/well for NF1-08; 10,000 cells/well for sNF96.2; 3,500 cells/well for NF1-18B; 10,000 cells/well for NF1-09; 6,000 cells/well for SP-10; 9,000 cells/well for ST88-14; 6,000 cells/well for NF90-8; 5,000 cells/well for NMS-2.
2. Cells were incubated O/N at 37ºC with 5% CO_2.
3. Compounds were added in triplicates at five different concentrations:
    a. If tested at the micromolar scale: 0, 0.064, 0.32, 1.6, 8, and 40 µM.
    b. If tested at the nanomolar scale: 0, 0.1, 1, 10, 100, and 1000 nM.

    The same concentration of DMSO was added to the control wells.

4. Cells were incubated for 48h at 37ºC with 5% CO_2.
5. Cell viability was assessed using MTT assay (as described in Section 2.1 of M&M).
6. IC_{50} values were determined using Graphpad Prism 7 by applying a nonlinear regression (curve fitting) approach. Specifically, a dose-response inhibition model was used, where the logarithm of the inhibitor concentration was plotted against the normalized response with a variable slope. The wells containing only DMSO served as the 100% viability control, allowing for the normalization of the data and accurate estimation of the IC_{50} values.

5.4. Validation of Synergistic Combinations

Twenty-six combinations were tested to validate the synergy observed in HTS. The same protocol as for single compounds was used, with both drugs dispensed at a fixed 1:1 ratio

based on IC_{50} values. In previous works of our group (Fernández-Rodríguez, Creus-Bachiller et al. 2022), five concentrations are tested (1:3 dilutions): 10 x IC_{50}, 3.3 x IC_{50}, 1.1 x IC_{50}, 0.37 x IC_{50}, and 0.12 x IC_{50}. However, there are cases in which the calculation of 10 x IC_{50} is higher than the stock concentration (10 mM). In such cases, the dilution series was adjusted to ensure that the highest drug concentration used did not exceed the stock.

Synergy was assessed using CompuSyn software (RRID: SCR_022931), applying the Chou–Talalay method (Chou 2010).

- CI values lower than 0.9 indicated synergy.
- CI values between 0.9 and 1.1 indicated an additive effect.
- CI values higher than 1.1 indicated antagonism.
- Fa values represented the fraction of cell death, ranging from 0 (no cell death) to 1 (100% cell killing).

The most promising combinations had CI values below 0.9 and Fa values above 0.5.

MM 6. Animal Studies

All procedures complied with the Animal Care Committee guidelines of the *Generalitat de Catalunya* and were approved by the IDIBELL Ethics Committee (#PR213/13) and the IDIBELL Ethics committee for Animal experimentation (CEEA) (11831). Five-week-old male and female athymic nude mice (athymic nude *Foxn1*^{nu}, Envigo, RRID: IMSR_CRL:490) were housed in pathogen-free conditions with autoclaved bedding, food, and water under a 12h light/12h dark cycle.

6.1. PDOX Establishment

PDOX were generated following this procedure:

1. Human MPNST tumors were cut into 2-3 mm^3 fragments.
2. Mice were anesthetized with isoflurane (continuous flow of 1-3% isoflurane/oxygen mixture, 2 L/min).
3. Postoperative analgesia with meloxicam (20 µl/20g) was administered subcutaneously.
4. The skin over the biceps femoris muscle was disinfected with povidone-iodine and cut with scissors.
5. A small incision using a scissor in the biceps femoris muscle was made to expose the sciatic nerve.

6. Tumor fragments of 2-3 mm^3 were placed in the created pocket so that it remains in close contact with the sciatic nerve.
7. Muscle closure was performed with 7/0 polypropylene suture, and the skin was closed with surgical staples.
8. Analgesia with meloxicam (2 mg/kg) was administered subcutaneously once a day for two days.
9. Staples were removed after 10 days, and tumor growth was monitored weekly by palpation.

6.2. *In vivo* Tumorigeneicity

In vivo tumorigenicity assays were performed to evaluate the ability of a cell line to generate tumors *in vivo*.

1. 3 x 10^6 cells were counted and suspended in 100 µl of PBS 1X.
2. Cells were injected intramuscularly near the sciatic nerve in both legs of five-week-old female athymic nude mice.
3. Tumor formation was monitored weekly by palpation.
4. Once tumor growth was detected, measurements were taken twice a week using a caliper.
5. Tumor volume was calculated using the formula: v = (π/6 x L x W x W), where L is the length and W is the width.
6. When tumor reached 1.5 cm in diameter, mice were sacrificed, and tumors were extracted.
7. Tumors were cut into small fragments for cryopreservation in an FBS solution with 10% DMSO and/or engraftment into other mice (as described in Section 4.1 of M&M).

MM 7. *In Vivo* Drug Validation

7.1. Maximum Tolerated Dose

The Maximum Tolerated Dose (MTD) study determined the highest dose a compound could be administered without compromising animal health. Healthy, tumor-free athymic nude mice were used, with small groups per dose (N = 2). Mice were treated for three weeks, and body weight and general health (behavior and general condition) were monitored daily. At the end of treatment, mice were sacrificed.

7.2. *In Vivo* Compounds Doses

All the compounds' doses and solvents used for *in vivo* testing are listed in Table MM5.

Table MM5. Compound doses and solvents used *in vivo* in the PDOX models

	Selumetinib (MEKi)	Arry-162 / Binimetinib (MEKi)	Ribociclib (CDK4/6i)	I-BET151 (BETi)	MK-1775 / Adavosertib (WEE1i)	Panobinostat (HACi)	Docetaxel (chemotherapy)
Source	MedChemExpress						Our hospital pharmacy
Reference	HY-50706	HY-1520	HY-15777	HY-13235	HY-10993	HY-10224	-
Administration Route	Oral	Oral	Oral	Intraperitoneal	Oral	Intraperitoneal	Intravenous
Dosage	45 mg/kg	15 mg/kg	90 mg/kg	25 mg/kg	50 mg/kg	5 mg/kg	15 mg/kg
Schedule	Twice daily 5 day On/2 day Off	Twice daily 5 day On/2 day Off	5 day On/2 day Off	3 non-consecutive days/week	5 day On/2 day Off	3 non-consecutive days/week	Once week
Solvent	Saline solution	1% carboximethyl cellulose (CMC) + 0.5% Tween80, 98.5% saline solution	0.5% methyl cellulose (MC), 99.5% saline solution	5% Tween80, 5% DMSO, 90% saline solution	0.5% methyl cellulose (MC), 99.5% saline solution	5% Dextrose 99.5%, 2% DMSO, H_2Od	Saline solution

The solvents used for each compound, specified in Table MM5, were acquire from: Carboximethylcellulose sodium salt (CMC, Sigma-Aldrich, Ref. C5678), Methyl cellulose (MC, Sigma-Aldrich, Ref. M6385), Tween80 (Sigma-Aldrich, Ref. P4780), Dextrose 99.5% (D-(+)-Glucose >99.5%, Sigma-Aldrich, Ref. G8270), saline solution (B/Braun, Ref. 3545180).

7.3. PDOX Treatments

Different combinations were tested *in vivo* in different PDOX models.

1. Tumors were engrafted in five-week-old athymic nude mice (as described in Section 4.1 of M&M).
2. Once tumors reached 1,000-1,500 mm^3, they were resected and re-engrafted into the sciatic nerve of new five-week-old mice for PDOX treatment.
3. Mice were randomized into treatment groups when tumor reached 300-500 mm^3 (5-10 mice per group, Table MM6).
4. Treatments lasted between two and three weeks, depending on the tumor size of the controls. If the tumor volume exceeded the permissible limit (1.5 cm in diameter), it was sacrificed, and the treatment was terminated.
5. Body weight was monitored daily, and tumors were measured twice a week using a caliper. Tumor volume was calculated using the formula: $v = (\pi/6 \times L \times W \times W)$, where L is the length and W is the width.
6. At the end of treatment, mice were sacrificed 4-5 hours after drug administration. Tumors were resected, weighed, and processed for FFPE or snap-freezing. In mice

treated with drug combinations, the kidneys, lungs, heart, spleen, and liver were also removed and processed for FFPE.

Table MM6. Summary of the number of mice and treatment groups planned for each of the eight *in vivo* treatments testing

PDOX Model		NF1-18B	NF1-18B	NF1-18B	SP-10	SP-10	SP-10	NF1-16C	SP-12B
Number of mice		55	26	26	69	15	23	21	25
Treatment groups / mice per group	Vehicle	Yes, n=10	Yes, n=5	*	Yes, n=12	Yes, n=5	Yes, n=8	Yes, n=5	Yes, n=5
	Single	3 groups, n=5	-	-	3 groups, n=9	-	-	-	-
	Double combination	3 groups, n=10	1 group, n=5	1 group, n=6	3 groups, n=10	1 group, n=10	1 group, n=7	4 groups, n=4	5 groups, n=4
	Triple combination	-	2 groups, n=8	1 group, n=8	-	-	1 group, n=8	-	-
Treatment time (in weeks)		2	4	3	2	3 + 3	3	3	3

*In this *in vivo* study, our intention was to compare the double and triple treatment, so we did not use a vehicle.

MM 8. Data Analyses, Quantification and Statistics

Statistical parameters, standard deviation, and statistical significance were reported in the figures and in the figure's legends. Graphpad Prism 9 software was used for statistical analysis and p-value<0.05 was considered significant (****p-value<0.0001, ***p-value<0.001, **p-value<0.01 and n.s. p-value>0.05). Statistical significance among groups was determined by:

a) Student's t-test (data fitting normal distribution) for comparing the means of two independent groups.
b) Mann Whitney U test (data not fitting normal distribution) for two-group comparison.
c) One-way ANOVA with Tukey's correction for multiple comparison testing.

Results

RESULTS

R1. Part I: Generation of New MPNST Preclinical Models: Establishment, Validation, and Comprehensive Characterization of Cell Lines and PDOXs

1.1. Patient Tumor Clinical and Genetic Information

Two MPNST patients underwent surgical tumor resection at *Hospital Infantil La Paz* (NF1-related tumor, NF1-18B) and *Hospital Universitari Germans Trias i Pujol* (sporadic tumor, SP-10). The NF1-18B tumor was removed from the leg of an 18-year-old male patient with NF1, and the SP-10 tumor was located on the ribs of a female patient without NF1, confirming it as a sporadic MPNST case (Table R1). After resection, a piece of tumor was digested to generate a cell line (as described in Section 2.2 of M&M), and another was engrafted near the sciatic nerve of athymic Nude mice to generate a PDOX model (as described in Section 6.1 of M&M).

WGS was used on patients' tumors to analyze the mutational status of the most frequently inactivated TSGs in MPNST: *NF1, CDKN2A, SUZ12, EED,* and *TP53* (Table R1). Both tumors exhibited the inactivation of *NF1, CDKN2A*, and PRC2, as described in "classic" MPNSTs (Magallón-Lorenz, Terribas et al. 2023). In addition, the NF1-18B tumor harbors the inactivation of *TP53*.

Table R1. Summary of patient' MPNSTs clinical and genetic information

	Clinical information			Genetic information				
						PRC2		
Tumor ID	**Gender**	**NF1/SP**	**Location**	***NF1***	***CDKN2A***	***SUZ12***	***EED***	***TP53***
NF1-18B	Male	NF1	Leg	NM_000267.3:c.1642-449A>G + LOH	chr9:g.21971512-chr16:g.67089579; chr9:g.21972486-chr16:g.67089702 (balanced translocation)	WT	NM_003797.5:c.184_268-160del (in homozygosis)	GRCh38(chr17):g.7675457_7680618dup + LOH
SP-10	Female	SP	Ribs	GRCh38(chr17):g.30922951_31318216del (in homozygosis)	GRCh38(chr9):g.21962354_22055781del (in homozygosis)	NM_015355.4: c.1874+1G>A + LOH	WT	WT

SP:Sporadic; NF1: Neurofibromatosis type 1; WT: wild type; LOH: Loss of heterogeneity; PRC2: Polycomb Repressive Complex 2

Moreover, STR authentication analysis was performed to rule out potential cross-contamination, confirming that the established cell lines and PDOXs retained the same microsatellite pattern as their respective patient tumors (Table R2).

Table R2. STR authentication analysis of patient primary tumor, cell lines and PDOX tumors.
In bold type a difference found between PDOX and primary tumor.

		NF1-18B			SP-10		
Microsatellite	**Chromosomal localization**	**PT**	**Cell line**	**PDOX**	**PT**	**Cell line**	**PDOX**
D8S1179	8	13	13	13	12	12	12
D21S11	21q11.2-q21	30	30	30	29, 33	29, 33	29, 33
D7S820	7q11.21-22	8	8	8	8	8	8
CSF1PO	5q33.3-34	10	10	10, **11**	12	12	12
D3S1358	3p	16	16	16	18	18	18
TH01	11p15.5	8	8	8	9	9	9
D13S317	13q22-31	8, 11	8,11	8, 11	12	12	12
D16S539	16q24-qter	10, 11	10, 11	10	10	10	10
D2S1338	2q35-37.1	17, 18	17, 18	17, 18	17	17	17
D19S433	19q12-13.1	15	15	15	14	14	14
vWA	12p12-pter	17	17	17	17	17	17
TPOX	2p23-2per	8, 10	8, 10	8, 10	8, 9	8, 9	8, 9
D18S51	18q21.3	15	15	15	15	15	15
AMEL	Xp22.1-22.3 Yp11.2	X,Y	X,Y	X,Y	X	X	X
D5S818	5q21-31	11	11	11	9, 10	9, 10	9, 10
FGA	4q28	22	22	22	20	20	20

PT: Primary tumor; PDOX: Patient-derived orthothopic xenograft

1.2. Characterization of the New Generated MPNST Cell Lines

We performed a comprehensive phenotypic and functional characterization to analyze the *in vitro* behavior of the newly generated MPNST cell lines.

1.2.1. Cell Cycle Analysis and Ploidy Variation

Flow cytometry-based cell cycle analysis was performed in the cell models to measure the ploidy variation of the tumors. The sporadic model SP-10 presents an aneuploidy state slightly above 2n, which was stable over the passages (Figure R1). In contrast, the NF1-18B cell line ploidy changed over successive passages: at low passages the ploidy was slightly above 2n (<3n), but at higher passage numbers (above 16) the ploidy state was tetraploid (4n) (Figure R1). We hypothesized that this change could be related to the presence of two distinct cell subpopulations in the primary tumor. Indeed, cell cycle analysis of the NF1-18B cell line at first passages revealed that the predominant subpopulation is the one between 2n and 3n (<3n), but the tetraploid subpopulation is also present in a smaller proportion. With continued passaging under *in vitro* culture conditions, the tetraploid subpopulation was progressively selected until "<3n" cells were completely lost (Figure R1). Going forward, we characterized the NF1-18B cell lines at different passages as if they were independent cell lines (NF1-18B <3n and NF1-18B 4n) to analyze different functional features.

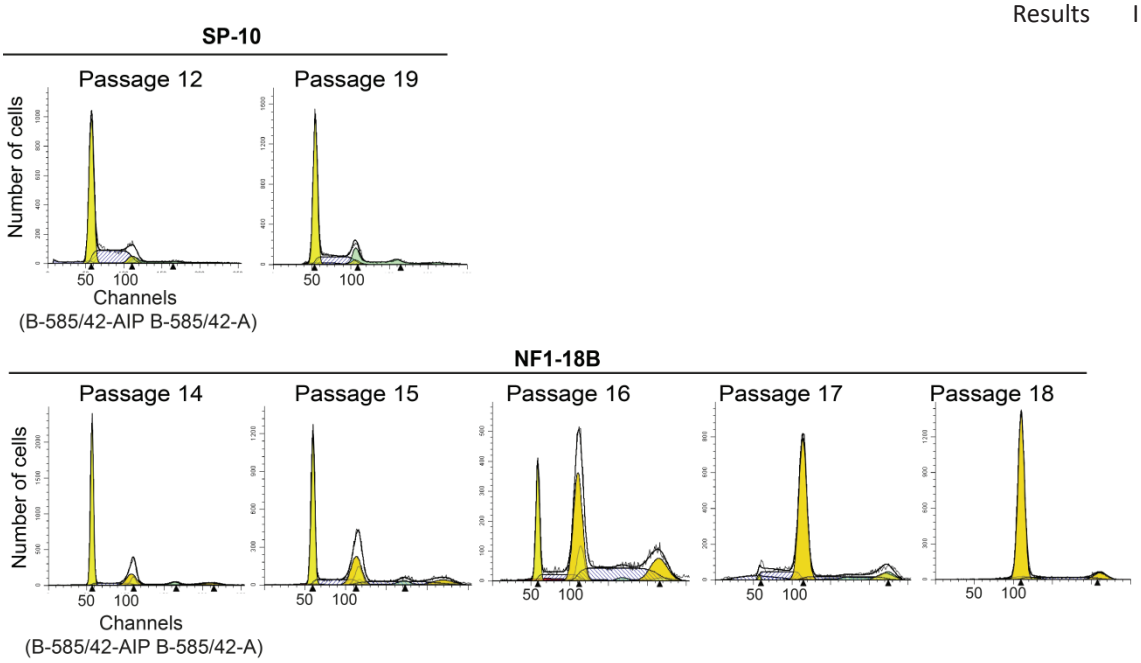

Figure R1. DNA content analysis of MPNST cell lines at different passages. The data are plotted as the number of cells versus DNA content. The X-axis represents fluorescence intensity measured in channels (B-585/42-AIP B-585/42-A), indicating flow cytometry analysis. In this type of assay, fluorescence intensity is directly proportional to the DNA content in cells, enabling the identification of different cell cycle phases based on DNA ploidy. A value of 50 on the X-axis corresponds to a population of cells with lower DNA content, representing the G1 phase of the cell cycle, while a value of 100 corresponds to a population with approximately twice the DNA content, representing the G2/M phase. The SP-10 cell line maintains an aneuploid state slightly above 2n at both low and high passages. The NF1-18B cell line exhibits an aneuploid state slightly above 2n at low passages and shifts to tetraploid at high passages.

1.2.2. Characterization Morphology and Marker Expression Analysis by Immunofluorescence

A first set of phenotypic analyses was performed to describe cell morphology and expression of MPNST's clinically relevant markers (SOX9, S100B, and H3K27me3) by immunofluorescence. The three cell lines (NF1-18B <3n, NF1-18B 4n and SP-10) exhibited a small, spindle-shaped to polygonal morphology, consistent with the morphology of MPNST cells *in vitro* (Figure R2).

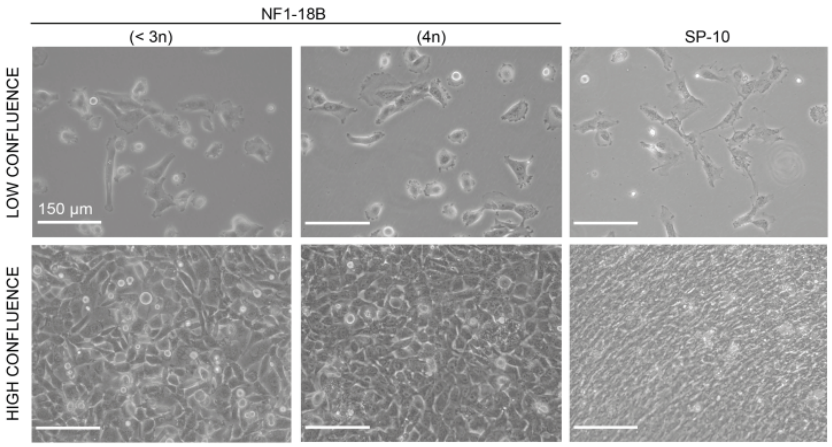

Figure R2. Representative images of NF1-18B ("<3n" and "4n") and SP-10 cell lines morphology at low and high confluence. The scale bar is 150 µm.

In addition, the three cell lines overexpressed SOX9 compared to non-tumoral cells (fibroblasts), as described in MPNSTs (Miller, Jessen et al. 2009, Magallón-Lorenz, Terribas et al. 2023), and did not exhibit expression of S100B or H3K27me3 (Figure R3), which are commonly lost in MPNSTs compared to their benign precursor (Magallón-Lorenz, Terribas et al. 2023). Interestingly, the cell lines' H3K27me3 marker expression is concordant with the mutational status of PRC2.

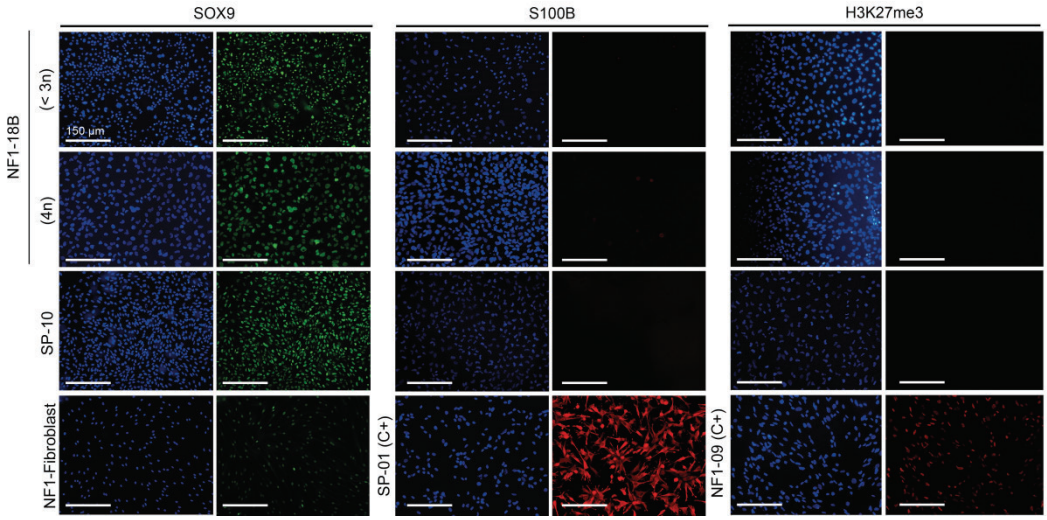

Figure R3. Representative immunofluorescence images of SOX9, S100B, and H3K27me3 markers expression. DAPI nuclear staining is shown in blue. Fibroblasts derivate from NF1 patient were used as basal expression of SOX9, SP-01 melanoma cell line was used as positive control for S100B, and NF1-09 MPNST cell line was used as positive control for H3K27me3 marker (Creus-Bachiller et al., 2023). C+: Positive control. The scale bar is 150 µm.

1.2.3. Proliferation, Colony Formation, and Cell Migration

The *in vitro* behavior of the MPNST cell lines was studied through proliferation, colony-formation and migration assays. First, the cell lines growth rate was evaluated by calculating the PDTs: 44h for NF1-18B <3n, 34h for NF1-18B 4n, and 29h for SP-10 (Figure R4A). Notably, the proliferation rate of the NF1-18B 4n cell line is higher than that of NF1-18B <3n.

We next evaluated the colony formation and migration capabilities, in which the NF1-18B 4n and SP-10 cell lines formed 2-D colonies, generated aggregates in the hanging drop assay to evaluate the cell-cell cohesion, and achieved 100% wound closure at 12h and 24h, respectively, in the wound healing assay (Figure R4B-D). In contrast, the NF1-18B <3n cell line did not form colonies or aggregates (cells remained loosely attached) and presented a low migration rate (Figure R4B-D).

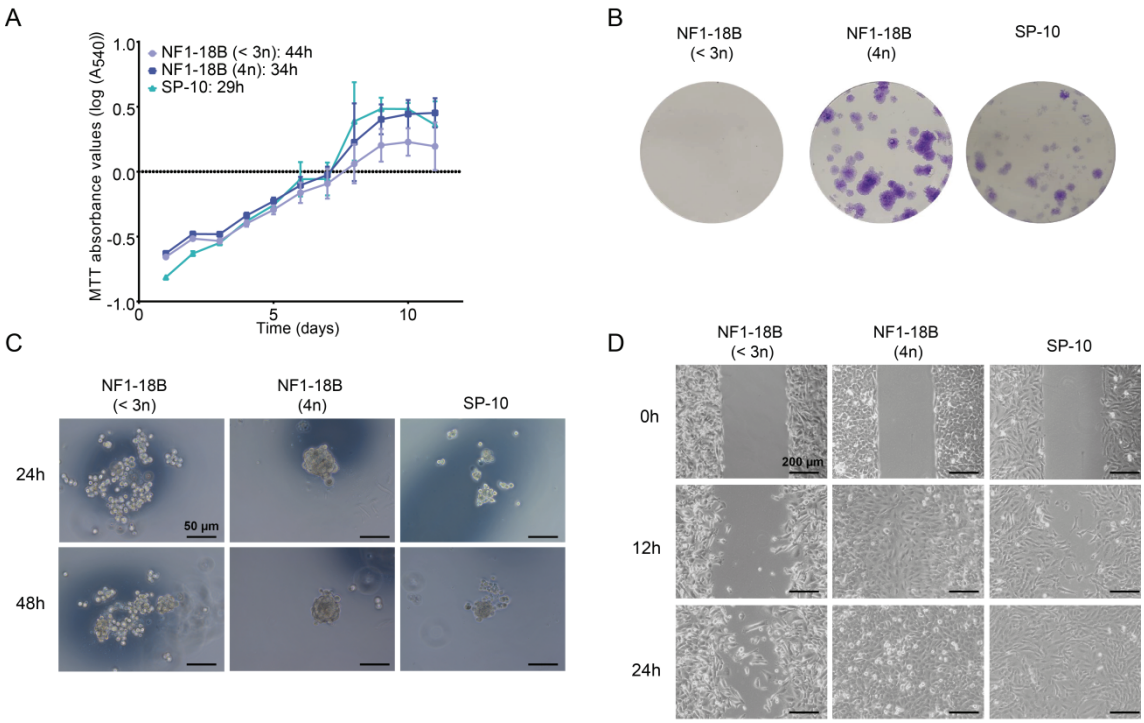

Figure R4. Characterization of the *in vitro* MPNST cell lines behavior. A. Cell growth curves of the three cell lines (NF1-18B "< 3n", NF1-18B "4n", and SP-10) plotted as MTT absorbance values every 24h. Growth curves were generated using the mean values (N=6) ± standard deviation (SD, error bars). **B.** Representative images of the 2-D colonies stained with crystal violet generated by the cell lines in a single well of a 12-well plate. Images were taken without amplification. **C.** Representative images of cell aggregates in the hanging drop assay. Images were taken at 24 and 48 hours. The scale bar is 50 µm. **D.** Representative images of the wound healing assay. Images of wound closure were taken at 0, 12, and 24 hours. The scale bar is 200 µm.

1.2.4. *In vivo* Tumorigenicity

Finally, we evaluated the tumorigenic capacity of the cell lines *in vivo* by injecting them near the sciatic nerve of athymic mice. The SP-10 cell line formed large tumors within six weeks after engraftment and the NF1-18B <3n cell line formed small tumors after four months, although they were only detected at the time of sacrifice (Figure R5A). Notably, the NF1-18B 4n cell line did not generate tumors, although it had a higher proliferation and migration rates *in vitro* compared to NF1-18B <3n cells. After tumors were resected from the mice, H&E staining revealed that the histologic features of the tumors generated by the cell lines were consistent with an MPNST, with high hypercellularity and mitotic activity, and exhibited a fibrosarcoma-like fascicular spindle cell histologic pattern (Figure R5A). In addition, both tumors showed high expression of the proliferation marker Ki67, indicating high proliferative capacity (Figure R5A).

We then wanted to compare the SP-10 tumor growth dynamic between the two main types of tumor engraftment procedures to generate PDXs: subcutaneous and orthotopic. Remarkable differences in growth rates were observed, as orthotopic tumors grew, on average, 7-fold faster than subcutaneously implanted tumors, confirming that orthotopic engraftments better recapitulate the aggressive tumor growth observed in the patient (Figure R5B).

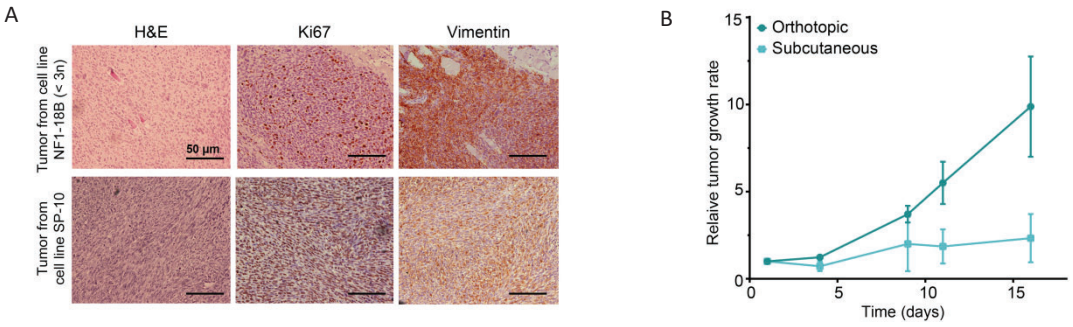

Figure R5. Histological and Growth Analysis of Tumors Derived from MPNST Cell Lines. A. Histological analysis of tumors derived from NF1-18B (<3 n) and SP-10 cell lines, stained with H&E, Ki67 (proliferation marker), and Vimentin (mesenchymal marker). NF1-18B "4n" did not generate tumors in mice. The scale bar is 50 µm. **B.** Relative tumor growth rate over two weeks in mice orthotopically and subcutaneously engrafted with a piece of SP-10 cell line-derived tumor. Growth curves were generated using the mean values (N=3) ± standard deviation (SD, error bars).

1.3. Newly Established Models Recapitulate Genetic and Histologic Features of the Patients Tumors

To validate our models, we performed WGS to compare the genetic characteristics of patient tumors with the generated PDOX and cell lines. The same mutations in *NF1*, *CDKN2A*, and PRC2 found in patient tumors were also found in the models (Table R1).

Furthermore, copy number (CN) variation profiles showed that the models recapitulated the major genomic features of the patient tumors, with minor differences. In the SP-10 tumor, few structural alterations, mainly CNG regions, and large areas of loss of heterozygosity (LOH) were observed in both the patient tumor and the models (Figure R6A), and a mean slightly higher than 2n was detected, concordant with the cell cycle analysis. In contrast, NF1-18B showed a higher proportion of genomic alterations and CNG regions (Figure R6B), in line with "classic" high-grade MPNSTs. In addition, the mean ploidy values of the two cell subpopulations were consistent with cell cycle analyses: 2.25n in the low passage cell line and 3.5n in the high passage. Interestingly, the ploidy value of the primary tumor is between these two values.

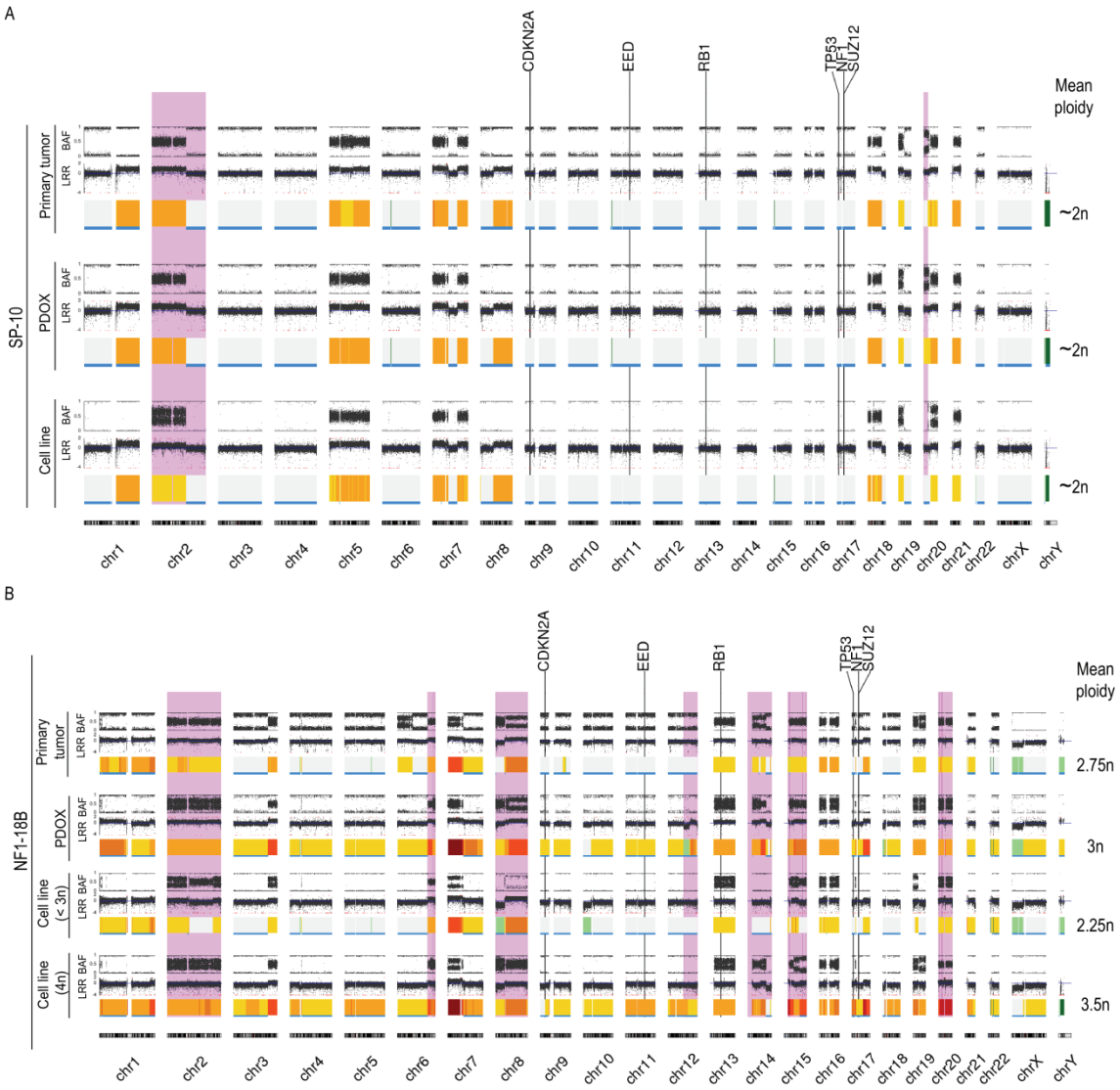

Figure R6. Patient-derived cell lines and PDOX recapitulate the major genomic features of primary SP-10 (A) and NF1-18B (B) tumors. Copy number (CN) variation profile represented by BAF and LRR of patient tumors, PDOX tumors, and cell lines. In the case of the NF1-18B cell line, the CN profile of the two NF1-18B cell line subpopulations ("< 3n" and "4n") is shown. CN variation is represented by a colored line below the LRR: gray for 2n region; yellow to red for chromosomal gain regions (>2n); and green to dark green for chromosomal loss regions (<2). LOH regions are shown in blue. Major genomic differences between the primary tumors and the models are highlighted in purple. A calculation of the mean ploidy value of the sample is shown on the right side. BAF: B-allele frequency; LRR: Log-R ratio; LOH: loss of heterozygosity.

We then also performed histologic analyses to compare patient tumor and the *in vivo* model. H&E showed that PDOX tumors highly recapitulated the histology of patient MPNSTs (Figure R7A).

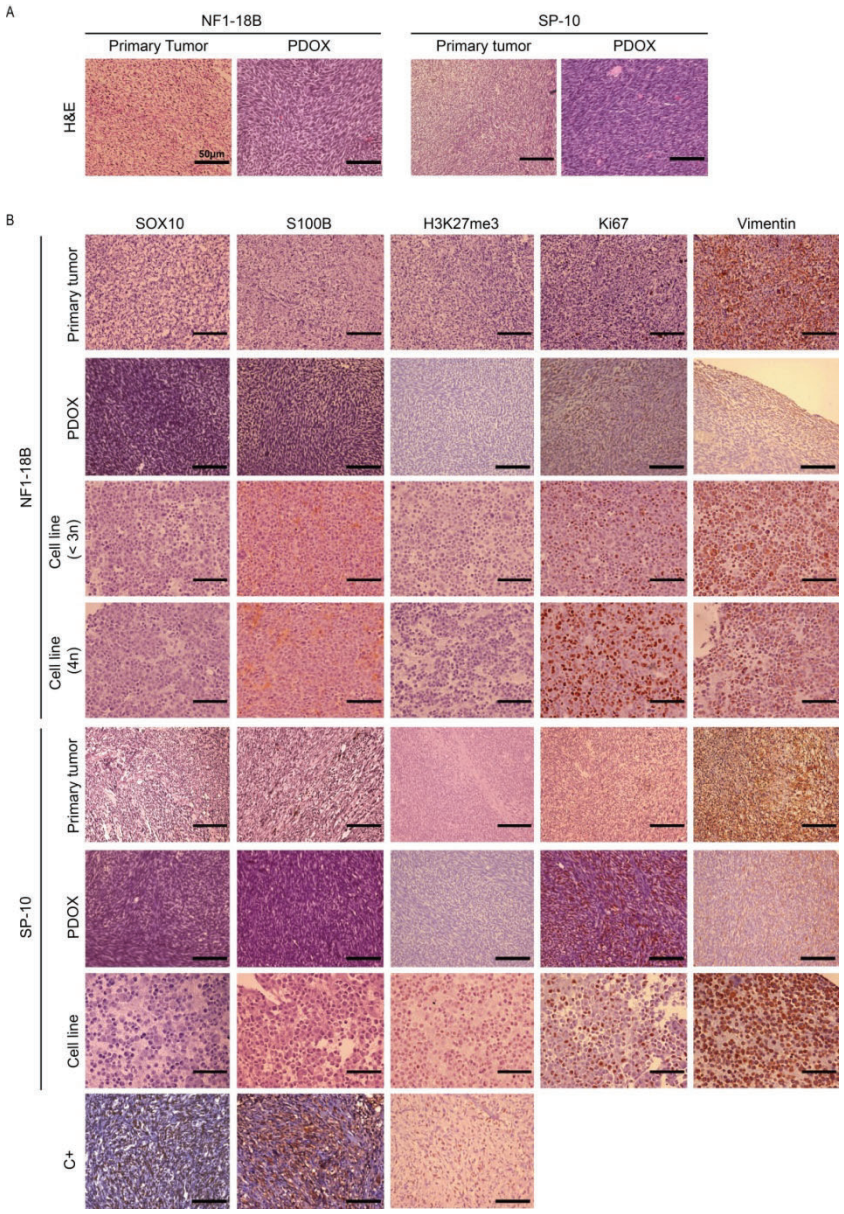

Figure R7. Cell lines and PDOX tumors recapitulate the main histological features of primary tumors. A. Representative images of Hematoxilin & Eosin (H&E) staining of primary and PDOX tumors. **B.** Representative images of immunostaining of SOX10, S100B, H3K27me3, Ki67, and Vimentin (positive mesenchymal lineage marker) markers in patient primary tumors, PDOX tumors, and cell lines. SP-01 melanoma cell line was used as positive control for S100B and SOX10, and NF1-09 MPNST cell line was used as positive control for H3K27me3 marker (Creus-Bachiller et al., 2023). The scale bar is 50 µm. C+: Positive control.

We also analyzed the expression of SOX10, S100B, and H3K27me3 markers in the primary tumors and the models. The lack of expression of these markers in the PDOXs tumors and cell models was consistent with primary tumors, although the SP-10 cell line showed focal expression of H3K27me3 (Figure R7B). The Ki67 marker was more highly expressed in both cell lines compared to the tumors, probably due to the cell culture conditions. Taken together, these results confirmed that the new PDOXs and cell models recapitulated the main genomic and histological features of the primary tumors.

R2. Part II: Precision Medicine Strategy for MPNSTs Using MEK, CDK, and BET Inhibitors in *In Vitro* and *In Vivo* Models

We performed a precision oncology strategy based on a high-throughput screening of MEKi (for the *NF1* gene loss), CDKi (for the *CDKN2A* gene loss), and BETi (for the PRC2 loss) using our MPNST preclinical platform of both *in vitro* and *in vivo* models.

2.1. High Throughput Screening of MEK, CDK, and BET Inhibitors as Single Agents in MPNST Cell Lines

We performed a HTS of 14 MEKi, 11 CDKi, and 3 BETi present in the NIH MIPE 4.0 library as single agents on three different NF1-related MPNST cell lines: S462, NF1-08, and NF1-09. The HTS of these drugs was conducted at NCATS-NIH

These cell lines were previously analyzed by WGS to assess the status of the most recurrently inactivated TSGs in MPNST. S462 and NF1-08 bore the inactivation of *NF1*, *CDKN2A*, and PRC2 (*SUZ12* or *EED*), concordant with "classic" MPNST models, whereas NF1-09 presented WT PRC2 function (Figure R8). In addition, NF1-09 bore a *PIK3CA* activating mutation (Figure R8).

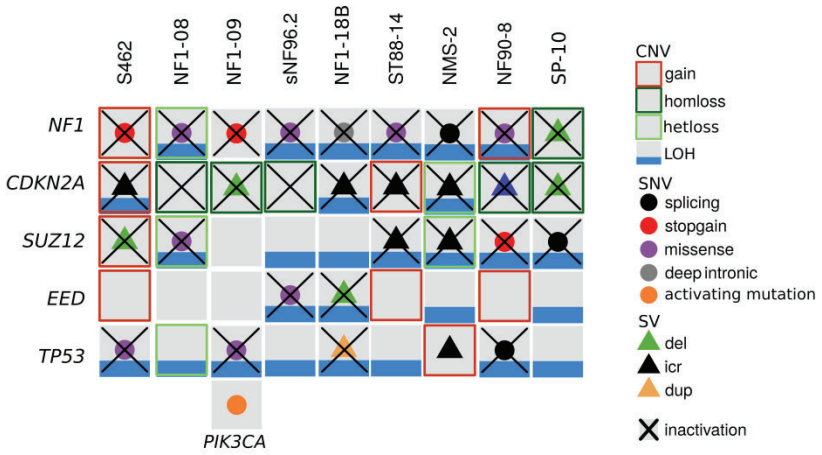

Figure R8. Mutational status of the MPNST most recurrently altered TSGs in the 9 tumor cell lines used in this project. The first three MPNST cell lines (S462, NF1-08 and NF-09) are the ones used for HTS. The other 6 MPNST lines will be used later in this project. A gray square represents WT gene and the bi-allelic inactivation of a gene is represented by a black cross. Copy number variation (CNV) in the genes is identified with colored squares: a blue line in the bottom part of the square indicates the presence of loss of heterozygosity (LOH); red square represents copy number gain (CN gain); dark green square indicated a homozygous CN loss of the gene; and light green square marks the heterozygous CN loss of the gene. The identification of the small nucleotide variant (SNV) types is represented with colored dots: a black dot indicates splicing variant, red dot indicates stop-gain variant, purple dot indicates missense variant, a grey dot indicates deep intronic variant, and orange dot indicates activating variant. The structural variants (SV) types are represented with colored small triangles: green for deletions (del), black for inter-chromosomal rearrangement (icr), and light orange for duplications (dup). Besides the TSGs, the tumor-specific mutated oncogene *PIK3CA* is also listed in the NF1-09 cell line. Genomic information that composes this figure was obtained from: Magallon-Lorenz et al. (2021) DOI:10.1007/s00439-021-02296-x; Magallon-Lorenz et al. (2023) DOI: 10.1016/j.isci.2023.106096; Creus-Bachiller et al. (2023) DOI: 10.1002/1878-0261.13534.

The compounds were incubated for 48 hours in the cell lines. Then, cell viability was measured using the CellTiter-Glo assay. The results provided from the NCATS included two key readouts (Figure R9):

- The CRC of the 28 drugs in each of the three MPNST cell lines. These dose-response curves were classified based on the criteria described in Materials and Methods Section 5.1: -1.1, -1.2, and -2.1 values represented active compounds.
- The percentage of cell viability at the maximum concentration tested, called as maximum response (MAXR).

Based on these two outputs, we select compounds that demonstrated anti-tumoral activity in at least two of the three cell lines. The MAXR data revealed a high degree of redundancy among inhibitors targeting the same molecular pathway in each cell line. The S462 and NF1-08 cell lines exhibited similar response to the three classes of inhibitors, whereas the NF1-09 model showed distinct sensitivity patterns, as it was slightly less sensitive to BETi and did not respond to MEKis, possibly due to the WT status of PRC2 and the presence of an activating mutation in the *PIK3CA* gene that activates the mTOR pathway, respectively.

Overall, most inhibitors exhibit a reduction of cell viability, although some compounds were inactive in all cell lines (e.g., MEKis: SL-327, U-0126, Refametinib, and PD-098059; CDKis: Purvalanol B and Indirubin). Considering these findings, we selected 22 out of the 28 agents for further evaluation in an all-versus-all pairwise combination screen (highlighted in bold in Figure R9).

Additionally, we included HFFs as a control to assess general toxicity. We observed that two CDKis, Fascaplysin and UCN-01, were toxic, as they also induced fibroblast cell death (Figure R9).

Inhibitor class	Compound	CRC class value S462	CRC class value NF1-08	CRC class value NF1-09	% MAXR value S462	% MAXR value NF1-08	% MAXR value NF1-09	% MAXR value HFF
MEKi	**ARRY-162**	2.1	1.1	1.2				
	AZD-8330	1.1	1.1	5				
	Hypothemycin	1.1	1.1	1.1				
	PD-0325901	2.1	1.1	5				
	PD-184352	1.2	2.1	2.2				
	PD-318088	2.1	1.1	5				
	Pimasertib	2.1	1.1	2.2				
	Selumetinib	2.1	1.1	2.2				
	TAK-733	1.1	1.1	2.2				
	Trametinib	1.1	1.1	2.2				
	SL-327	2.2	5	5				
	U-0126	2.2	2.2	5				
	Refametinib	2.2	2.1	5				
	PD-098059	5	3	5				
CDKi	**Cdk4/6 Inhibitor IV**	2.1	2.1	2.1				
	Fascaplysin	1.1	1.1	1.1				
	Palbociclib	2.1	2.1	2.1				
	PHA-690509	1.1	1.1	1.1				
	Purvalanol A	1.1	1.1	1.1				
	R-547	1.1	1.1	1.1				
	UCN-01	1.1	1.1	1.1				
	Milciclib	1.1	1.2	1.1				
	Flavopiridol	1.1	1.1	1.1				
	Purvalanol B	5	5	5				
	Indirubin	5	5	5				
BETi	**I-BET151**	1.2	1.2	1.2				
	I-BET762	1.2	1.2	5				
	JQ1	1.2	1.2	1.2				

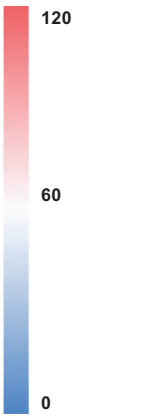

Active
Inconclusive
Inactive

Figure R9. High-throughput screening results of the single agent drug-testing of MEKi, CDKi, and BETi in three MPNST cell lines and one fibroblast cell line. In the left, the table displays the curve response class (CRC) classification values and maximum response (%MAXR) data for the 28 tested compounds in three MPNST cell lines (S462, NF1-08, and NF1-09). The CRC values are marked as follows: white square for active compounds (-1.1, -1.2, and -2.1 values), grey square for inconclusive compounds (2.2 and 3 scores), and green square for inactive compounds (5 score). In the right part, the heatmap represents a colored gradient of % MAXR values, where blue indicates low cell viability values, thus higher drug efficacy, and red indicates higher cell viability valued due to low drug efficacy. Human foreskin fibroblasts (HFFs) were included as a control to assess non-specific toxicity. The 22 compounds selected for testing in pairwise combinations are highlighted in bold.

2.2. Systematic Benchmarking of MEK, CDK, and BET Inhibitors Pairwise Combinations in MPNST Cell Lines

The next step was to perform a high-throughput screening also conducted at NCATS-NIH, of pairwise combinations of the 22 MEK, CDK, and MEK inhibitors selected in the single-agent treatments, to identify synergistic drug combinations. A total of 147 discrete 10 x 10 dose–response matrices were generated to test in the three MPNST cell lines, also using the CTG assay for cell viability readout after 48 hours of treatment. Two metrics were analyzed to measure the synergy between compounds: DBSumNeg values, Excess HSA values (E-HAS) (Appendix I). The more negative these two values are, the stronger the synergistic effect.

Additionally, a visual inspection of the matrices is also performed to validate the synergy measured by these values (Figure R10).

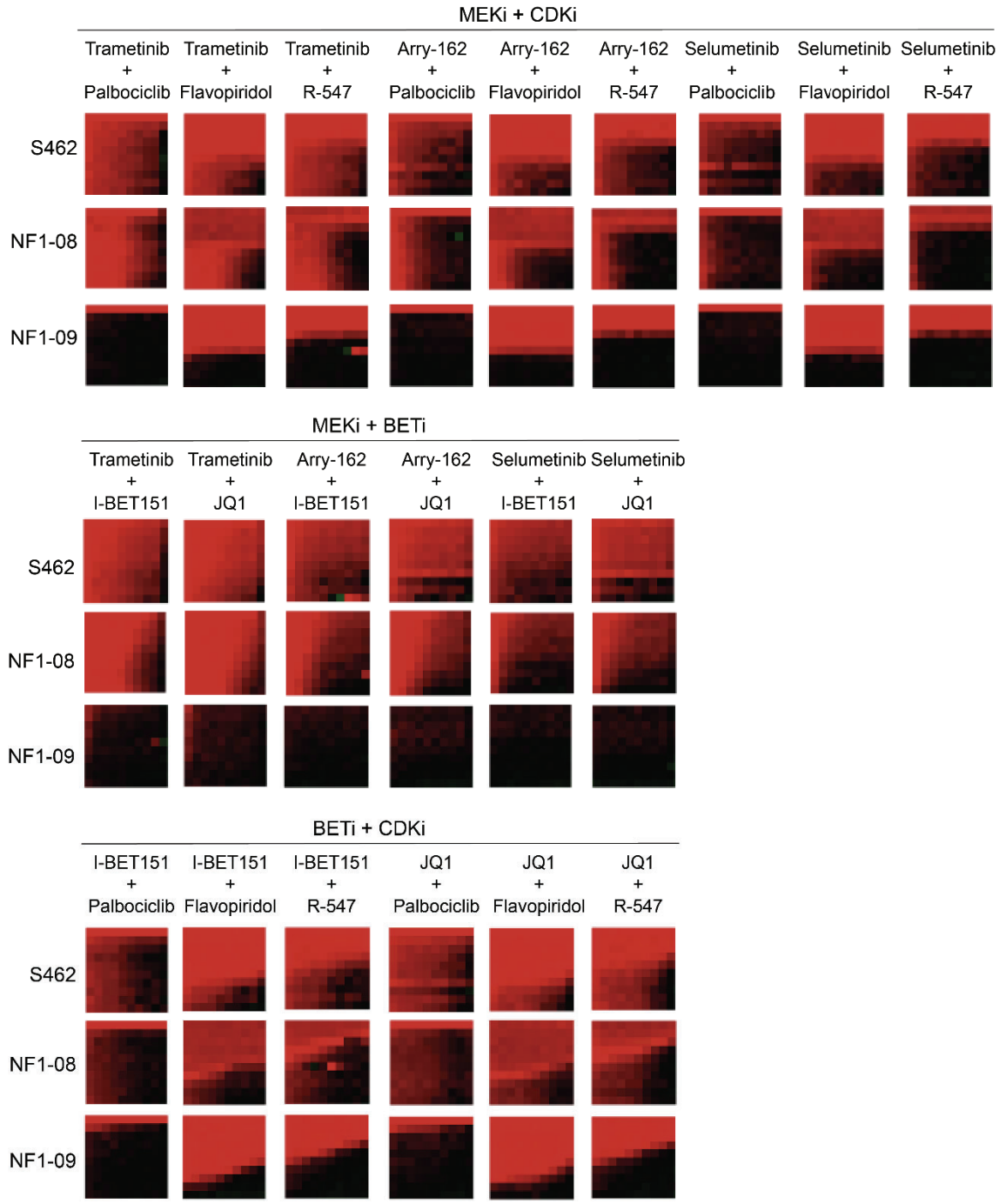

Figure R10. Heatmaps of the 21 pairwise 10x10 combination matrices screened in three MPNST cell lines. In red, the maximum effect of the compound is indicated (i.e., the minimum cell viability), while in black, no effect is observed (i.e., maximum cell viability). The X-axis represents one drug and the Y-axis another, with concentrations increasing from right to left (X-axis drug) and bottom to top (Y-axis drug).

Consistent with the single agent screening, a high degree of redundancy was observed among drug combinations targeting the same molecular pathways in each cell line. Based on combination synergy scores and the clinical development stage of each compound, we

selected 8 compounds to test 21 drug combinations for further validation *in vitro* in our laboratory: three MEKis (Arry-162, Selumetinib, and Trametinib), three CDKis (Palbociclib, R-547, and Flavopiridol), and two BETis (JQ1 and I-BET151) (Figure R10).

The DBSumNeg values of the 21 selected combinations in the three tested MPNST cell lines were all below 0, indicating the synergy of the compounds (Figure R11). In the NF1-08 cell line, the MEKi + BETi combination has the strongest effect, significantly reducing cell viability. In the NF1-09 cell line, the most effective combination is BETi + CDKi, showing the greatest decrease in viability. In the S462 cell line, all three treatments have a similar effect, leading to a comparable reduction in cell viability.

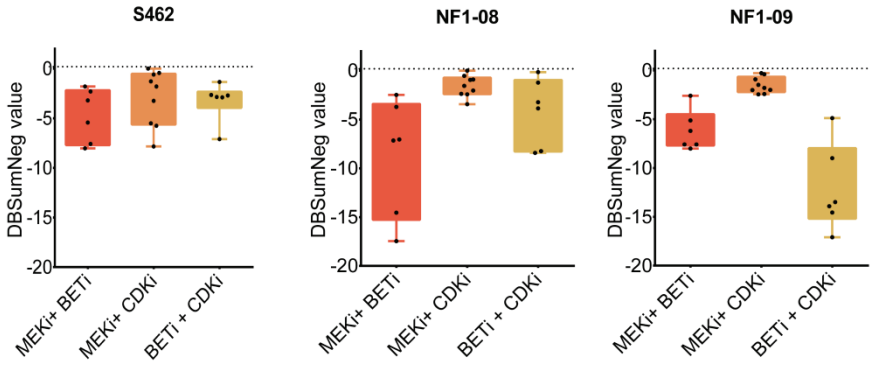

Figure R11. Delta Bliss Sum Negative (DBSumNeg) values of the 21 selected drug combinations in three MPNST cell lines. Each black dot indicates one single value from one combination.

2.3. Identification of the Three Most Synergistic Combinations of Selected MEKis, CDKis and BETis in a Panel of 9 MPNST Cell Lines

Next, we tested the 21 combinations selected from the HTS *in vitro* in our laboratory to validate their synergistic effect. As cell viability readout, we used MTT assay instead of the CTG assay. In addition to the selected HTS combinations, an additional CDKi was added for testing *in vitro*, Ribociclib (which was not part of the MIPE 4.0 library). This decision was based on its current use in clinical practice and the promising results obtained in a co-clinical pilot study performed in our laboratory. Therefore, five additional Ribociclib-based combinations were tested, resulting in a total of 26 combinations.

First the combinations were tested in three NF1-related MPNST cell lines (S462, NF1-08 and sNF96.2), all harboring mutations in *NF1*, *CDKN2A*, and PRC2 (Figure R8). The IC_{50} values of the nine compounds used in the combinations were calculated in the three MPNST cell lines to combine the drugs at a 1:1 ratio of the IC_{50}s (Table R3).

Table R3. IC_{50} values of the 9 compounds used for the *in vitro* validation in three MPNST cell lines

Inhibitor class	Compound	IC_{50} (µM) S462 8,000 cells/well	IC_{50} (µM) NF1-08 12,000 cells/well	IC_{50} (µM) sNF96.2 10,000 cells/well
CDKi	Palbociclib	16.18	26.97	17.60
	R-547	1.33	2.71	12.83
	Flavopiridol	0.2051	0.656	0.298
	Ribociclib	15.84	19.65	25.83
MEKi	Arry-162	3.92	6.59	7.22
	Selumetinib	11.27	8.84	18.96
	Trametinib	0.03214	1.14	0.096
BETi	JQ1	0.5276	1.18	1.17
	I-BET151	10.89	5.18	8.55

After determining the IC_{50} values for each compound and cell line, the 26 combinations were tested. CI was used to measure the synergistic effect and was calculated based on the dose-response curves.

In the S462 cell line, 23 out of 26 combinations had CI values below 0.9 at a Fa greater than 0.9 (Figure R12 and Table R4), validating a strong synergy of most combination in this cell line. In contrast, only 13 out of 26 combinations showed synergy in the NF1-08 cell line under the same conditions (Figure R13 and Table R4), while the 14 out of 26 combinations exhibited synergy in the sNF96.2 (Figure R14 and Table R4), demonstrating lower drug sensitivity than the S462 model. Notably, all MEKi + BETi combinations were synergistic in the three MPNST cell lines, whereas many MEKi-CDKi co-treatments failed to show synergy in NF1-08 and sNF96.2. These results are concordant with the IC_{50} values calculated, as CDKi had the highest IC_{50}s in the cell lines, thus being less potent.

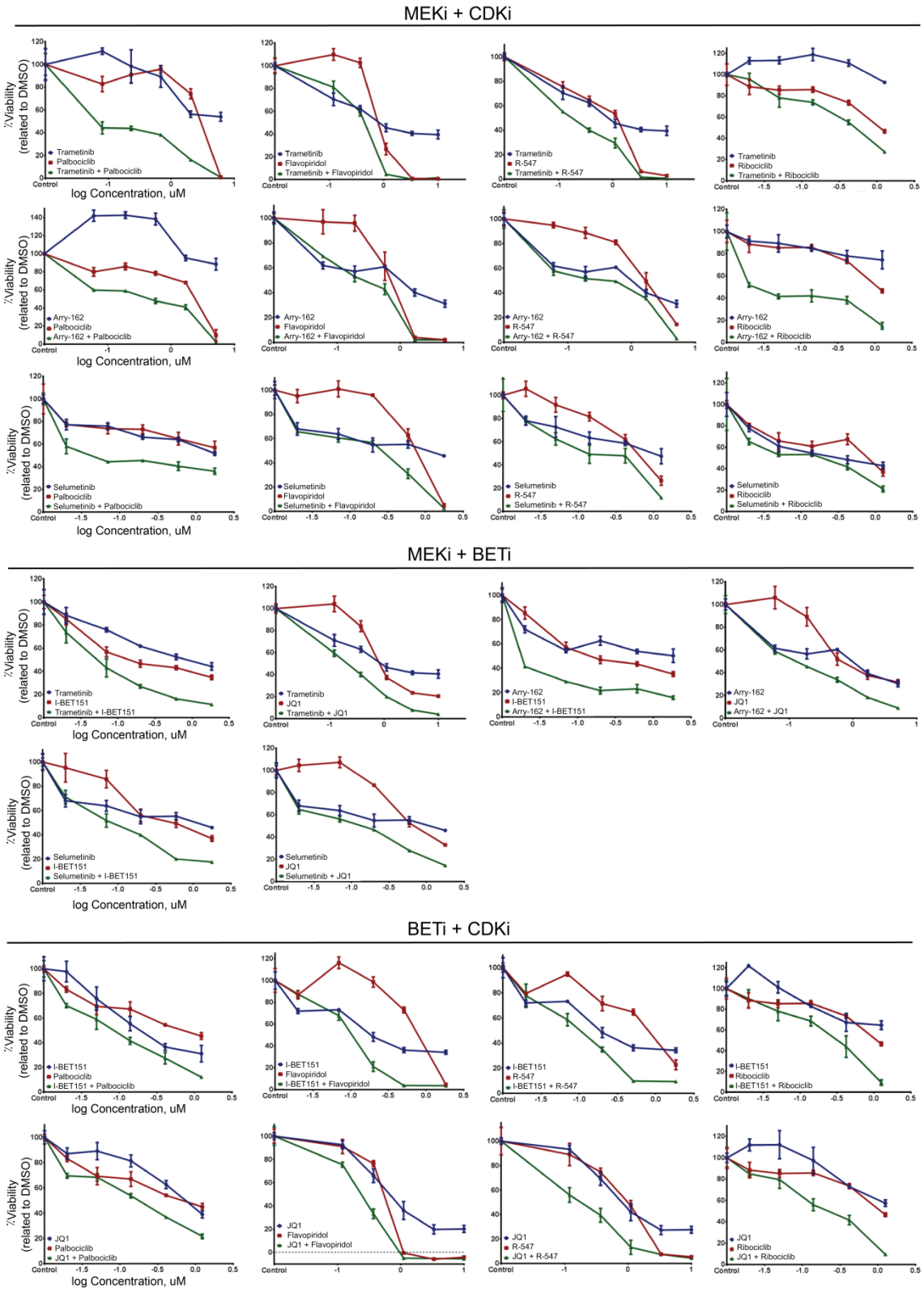

Figure R12. *In vitro* testing of the 26 combinations in the S462 MPNST cell line. Dose-response curves of single agents (in red and blue) and the combination (in green) generated using cell viability measure with MTT assay after 48 hours of treatment Combinations are classified according to the targeted pathways: MEKi + CDKi, MEKi + BETi, and BETi + CDKi.

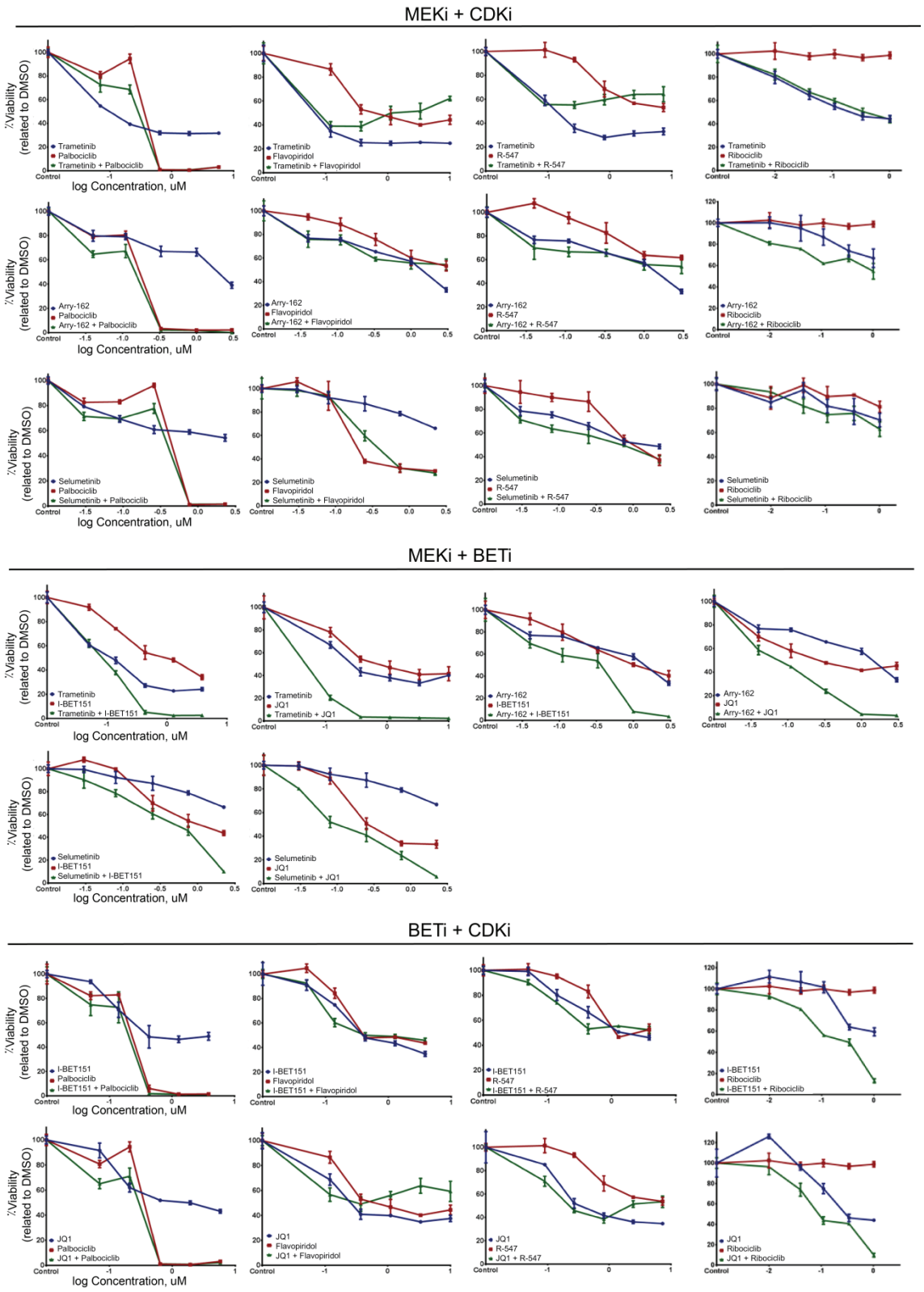

Figure R13. *In vitro* testing of the 26 combinations in the NF1-08 MPNST cell line. Dose-response curves of single agents (in red and blue) and the combination (in green) generated using cell viability measure with MTT assay after 48 hours of treatment Combinations are classified according to the targeted pathways: MEKi + CDKi, MEKi + BETi, and BETi + CDKi.

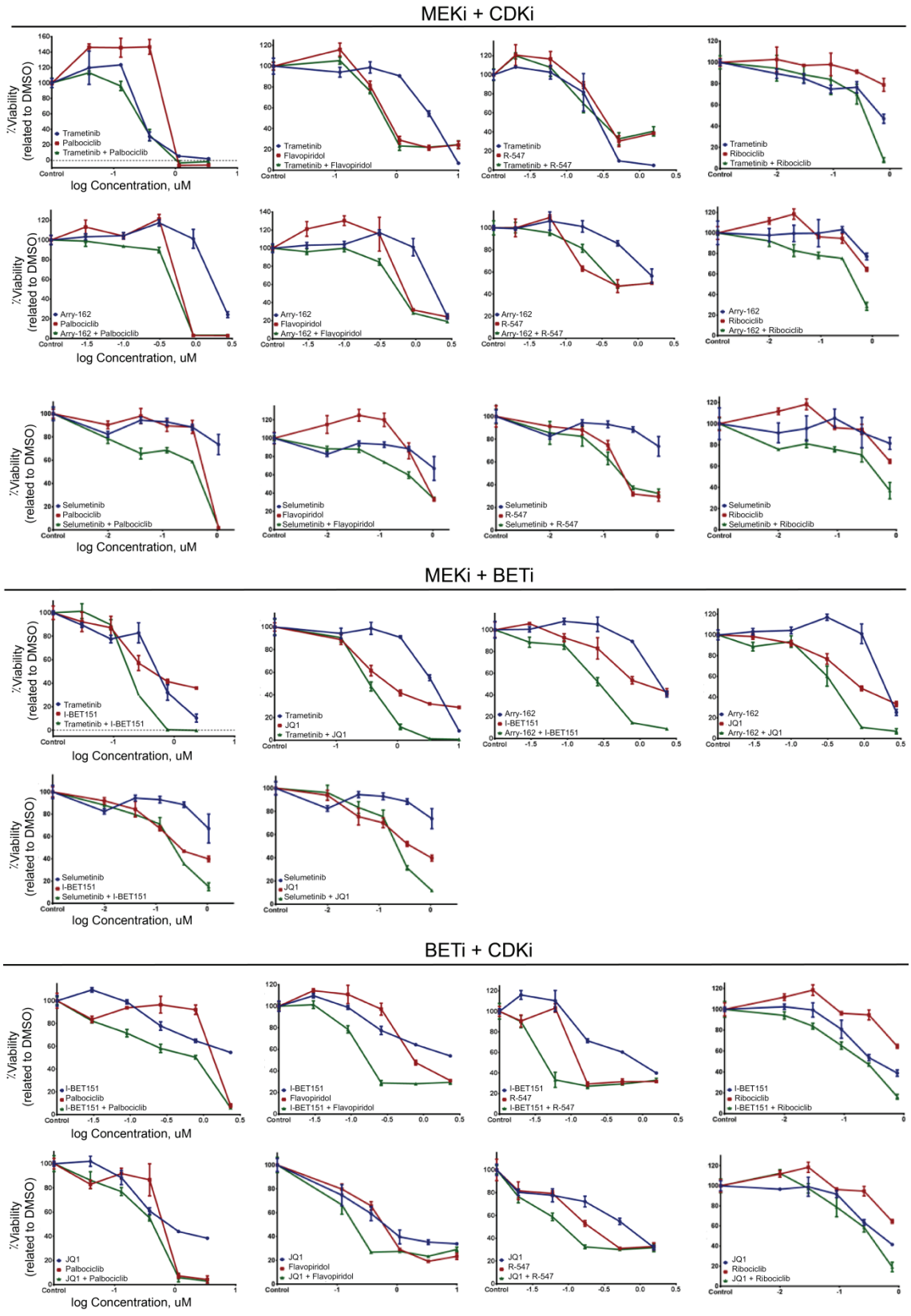

Figure R14. ***In vitro*** **testing of the 26 combinations in the sNF96.2 MPNST cell line.** Dose-response curves of single agents (in red and blue) and the combination (in green) generated using cell viability measure with MTT assay after 48 hours of treatment Combinations are classified according to the targeted pathways: MEKi + CDKi, MEKi + BETi, and BETi + CDKi.

Table R4. **Summary table of Combination Index values of the 26 combinations validated *in vitro* in three MPNST cell lines.** Synergy is evaluated using the CI values at Fraction affected (Fa) 0.5 and 0.9, and the range of synergistic Fa values.

					Combination Index								
					S462			NF1-08			sNF96.2		
ID combo	Compound A	Inhibitor class A	Compound B	Inhibitor class B	Fa 0.5	Fa 0.90	Range of synergistic Fa values	Fa 0.5	Fa 0.90	Range of synergistic Fa values	Fa 0.5	Fa 0.90	Range of synergistic Fa values
1	**Trametinib**	MEKi	**Palbociclib**	CDKi	0.16411	0.28638	0.05 - 0.97	3. 32058	0.06919	0.6 - 0.97	1. 31531	1. 30814	No synergy
2	**Trametinib**	MEKi	**Flavopiridol**	CDKi	0.36275	0.39579	0.4 - 0.97	4. 32381	*	No synergy	1. 43165	*	No synergy
3	**Trametinib**	MEKi	**R-547**	CDKi	0.55713	0.41969	0.4 - 0.97	12. 0156	*	No synergy	2. 95813	*	No synergy
4	**Trametinib**	MEKi	**Ribociclib**	CDKi	0.20983	0.03084	0.15 - 0.97	1. 28771	*	No synergy	0.21844	0.02336	0.25 - 0.97
5	**Trametinib**	MEKi	**I-BET151**	BETi	0.28431	0.07730	0.15 - 0.97	0.70429	0.03805	0.45 - 0.97	0.72502	0.16030	0.4 - 0.97
6	**Trametinib**	MEKi	**JQ1**	BETi	0.21046	0.51652	0.3 - 0.95	0.00379	2.14E-4	0.05 - 0.97	0.39298	0.10262	0.25 - 0.97
7	**Arry-162**	MEKi	**Palbociclib**	CDKi	0.21185	0.18904	0.05 - 0.97	0.77575	0.53243	0.4 - 0.97	0.73440	0.79545	0.05 - 0.97
8	**Arry-162**	MEKi	**Flavopiridol**	CDKi	0.61188	0.61337	0.45 - 0.97	4. 56571	*	0.05 - 0.25	0.69336	*	0.05 - 0.8
9	**Arry-162**	MEKi	**R-547**	CDKi	0.51272	0.35745	0.4 - 0.97	9. 27171	*	0.05- 0.35	1. 33361	*	No synergy
10	**Arry-162**	MEKi	**Ribociclib**	CDKi	0.01707	0.09042	0.05 - 0.97	3. 29449	*	0.05 - 0.4	0.15222	*	0.2 - 0.8
11	**Arry-162**	MEKi	**I-BET151**	BETi	0.01313	0.43829	0.1 - 0.9	0.25041	0.04032	0.25 - 0.97	0.32018	0.32070	0.05 - 0.97
12	**Arry-162**	MEKi	**JQ1**	BETi	0.34902	0.90443	0.35 - 0.9	0.19316	0.00400	0.35 - 0.97	0.32703	0.24503	0.05 - 0.97
13	**Selumetinib**	MEKi	**Palbociclib**	CDKi	0.07711	*	0.05 - 0.7	0.66230	0.78779	0.35 - 0.95	0.30467	0.62131	0.1 - 0.97
14	**Selumetinib**	MEKi	**Flavopiridol**	CDKi	0.21047	0.43105	0.4 - 0.97	1. 15974	*	0.05 - 0.3	0.35057	*	0.1 - 0.75
15	**Selumetinib**	MEKi	**R-547**	CDKi	0.38850	1. 09002	0.25 - 0.85	0.96660	*	0.05 - 0.5	0.92357	*	0.1 - 0.5
16	**Selumetinib**	MEKi	**Ribociclib**	CDKi	0.44119	0.15720	0.2 - 0.97	*	*	0.1 - 0.4	0.26747	*	0.05 - 0.65
17	**Selumetinib**	MEKi	**I-BET151**	BETi	0.23777	0.43540	0.35 - 0.97	0.40123	0.75440	0.05 - 0.95	0.45553	0.24581	0.15 - 0.97
18	**Selumetinib**	MEKi	**JQ1**	BETi	0.21564	*	0.35 - 0.85	0.32081	0.49124	0.05 - 0.97	0.48415	0.11744	0.3 - 0.97
19	**I-BET151**	BETi	**Palbociclib**	CDKi	0.37410	0.76654	0.15 - 0.9	0.74923	0.72971	0.25 - 0.97	0.28779	0.38079	0.5 - 0.97
20	**I-BET151**	BETi	**Flavopiridol**	CDKi	0.40201	0.13694	0.35 - 0.97	2. 21627	*	0.05 - 0.2	0.55226	0.62969	0.05 - 0.97
21	**I-BET151**	BETi	**R-547**	CDKi	0.43542	0.07764	0.35 - 0.97	2. 21626	*	0.05 - 0.2	0.39965	*	0.05 - 0.7
22	**I-BET151**	BETi	**Ribociclib**	CDKi	0.27561	0.22756	0.15 - 0.97	0.11523	0.17143	0.05 - 0.97	0.47481	0.81080	0.05 - 0.95
23	**JQ1**	BETi	**Palbociclib**	CDKi	0.37379	0.32170	0.1 - 0.97	0.52502	0.05041	0.4 - 0.97	0.81414	0.73177	0.15 - 0.95
24	**JQ1**	BETi	**Flavopiridol**	CDKi	0.57162	0.69814	0.05 - 0.97	0.10864	*	0.45 - 0.55	0.70983	*	0.05 - 0.6
25	**JQ1**	BETi	**R-547**	CDKi	0.37819	0.76103	0.05 - 0.95	2. 37075	*	No synergy	0.64636	*	0.05 - 0.7
26	**JQ1**	BETi	**Ribociclib**	CDKi	0.20561	0.20136	0.1 - 0.97	0.31226	0.35330	0.05 - 0.97	0.53495	0.29559	0.15 - 0.97

Note: light purple marks the combinations selected for additional validation to 6 MPNST cell lines; dark purple marks the combinations further validated *in vivo*. Abbreviations: Fa: Fraction affected. *No data due to the combination not reaching the Fa value.

Of the 26 combinations tested, the 12 most synergistic combinations were selected to evaluate toxicity in the HFF cell line (Figure R15). Only the combination of I-BET151 plus Palbociclib showed significant toxicity and was excluded from further investigation, leaving 11 promising potential combinations.

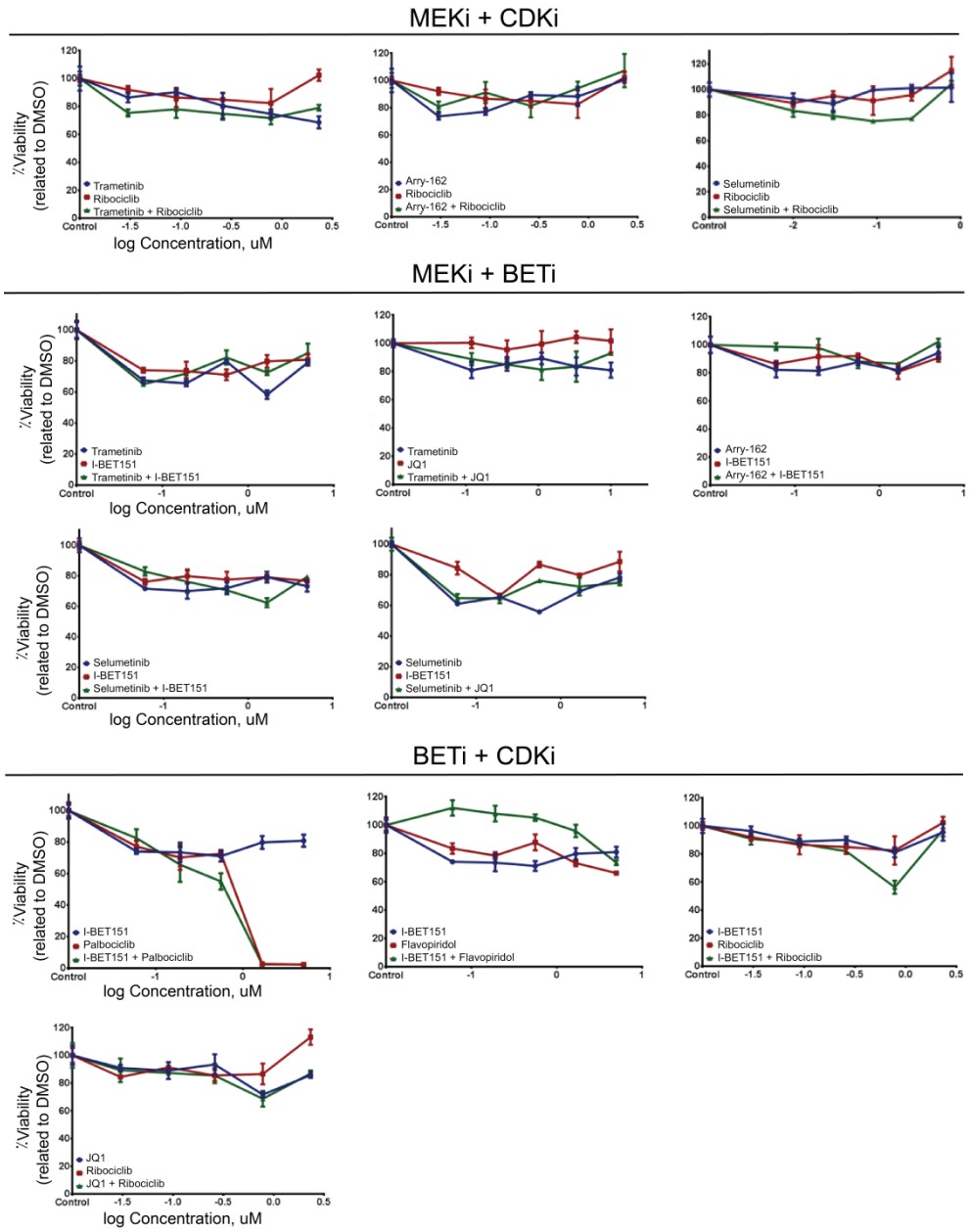

Figure R15. ***In vitro*** **testing of the 12 most synergistic combinations in HFF cell line.** Dose-response curves of single agents (in red and blue) and the combination (in green) generated using cell viability measure with MTT assay after 48 hours of treatment Combinations are classified according to the targeted pathways: MEKi + CDKi, MEKi + BETi, and BETi + CDKi. Only the combination of I-BET151 + Palbociclib present toxicity.

From the remaining 11 combinations, we selected two representative combinations for each inhibitor pair (MEKi-CDKi; MEKi + BETi; CDKi-BETi), resulting in six combinations for further validation in six additional MPNST cell lines: NF1-09, NF1-18B, ST88-14, NMS-2, NF90-8, SP-10. All the lines harbor mutations in *NF1, CDKN2A,* and PRC2, except for NF1-09, which retains a WT PRC2 status (Figure R8).

As performed before, the IC_{50} values of each of the seven drugs used in the selected six combinations were calculated in each of the additional six cell lines (Table R5). In some cases, the drug did not achieve 50% of cell viability reduction, thus the IC_{50} was not calculated (Table R5). In these cases, we used the highest IC_{50} obtained for that compound in another cell line.

Table R5. IC_{50} values of the 7 compounds used for *in vitro* validation in six MPNST cell lines: five NF1-associated (NF1-18B, NF1-09, ST88-14, NF90-8, and NMS-2) and one sporadic (SP-10).

		NF1-associated					Sporadic
Inhibitor class	**Compound**	**IC_{50} (µM) NF1-18B 3,500 cells/well**	**IC_{50} (µM) NF1-09 10,000 cells/well**	**IC_{50} (µM) ST88-14 9,000 cells/well**	**IC_{50} (µM) NF90-8 6,000 cells/well**	**IC_{50} (µM) NMS-2 5,000 cells/well**	**IC_{50} (µM) SP-10 6,000 cells/well**
CDKi	**Flavopiridol**	0.7143	0.375	NA	0.2568	0.0989	NA
	Ribociclib	10.33	8.185	NA	NA	18.29	2.319
MEKi	**Arry-162**	2.822	NA	22.63	NA	6.540	7.22
	Selumetinib	4.051	NA	1.010	NA	20.11	NA
	Trametinib	0.0134	NA	0.723	NA	0.2525	NA
BETi	**JQ1**	0.1108	1.113	6.492	3.339	1.452	0.2302
	I-BET151	1.09	9.892	10.48	NA	24.82	0.4650

NA: no IC_{50} value calculated due to compound not reaching 50% cell viability reduction

Once the IC_{50} values were calculated, we proceed to the combination testing in the additional MPNST cell lines. All the combinations exhibited synergistic effects across the different cell lines (Figure R16). Therefore, one representative compound from each inhibitor class was selected for testing drug combinations *in vivo* based on overall synergy and clinical development status: Arry-162 (MEKi, also known as Binimetinib), which is in clinical phase II for pNF, Ribociclib (CDKi), which is already FDA-approved, and I-BET151 (BETi), which is in the preclinical phase like most BETi.

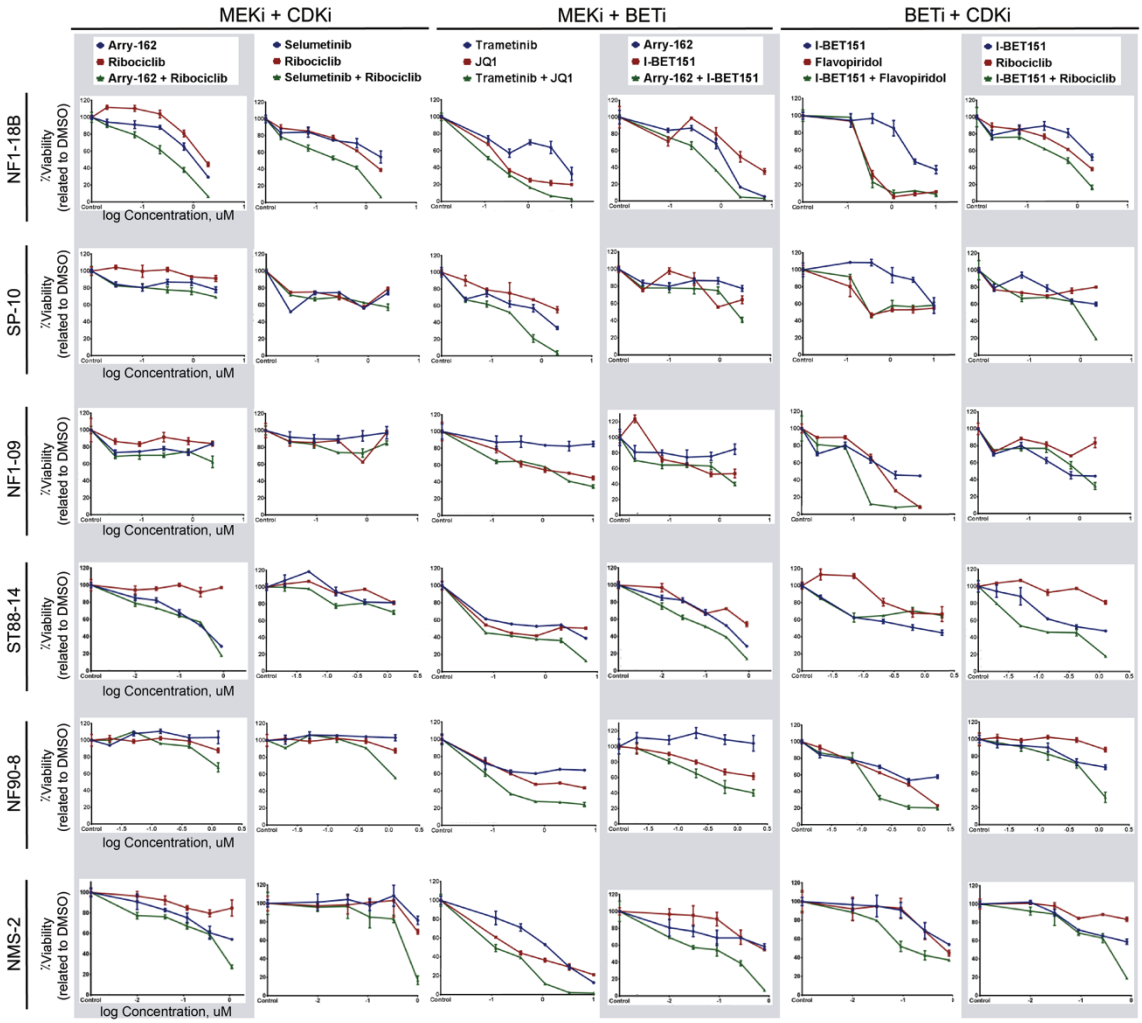

Figure R16. *In vitro* testing of the six most promising combinations in six MPNST cell lines. Dose-response curves of single agents (in red and blue) and the combination (in green) generated using cell viability measure with MTT assay after 48 hours of treatment, in six MPNST cell lines: NF1-18B, SP-10, NF1-09, ST88-14, NF90-9, and NMS-2. Each row is a different cell line (indicated on the left). Each column is a different combination (indicated at the top). The three combinations we chose for *in vivo* validation are shown in a gray box.

Figure R17 shows the CI values of the three combinations in the five tested doses for the nine MPNST lines. In many cases the doses tested exhibited a strong synergy (CI values below 0.5), as they reduced the cell viability by more than 50% (Fa values higher than 0.5). Among the tested combinations, Arry-162+I-BET151 demonstrated the highest degree of synergy.

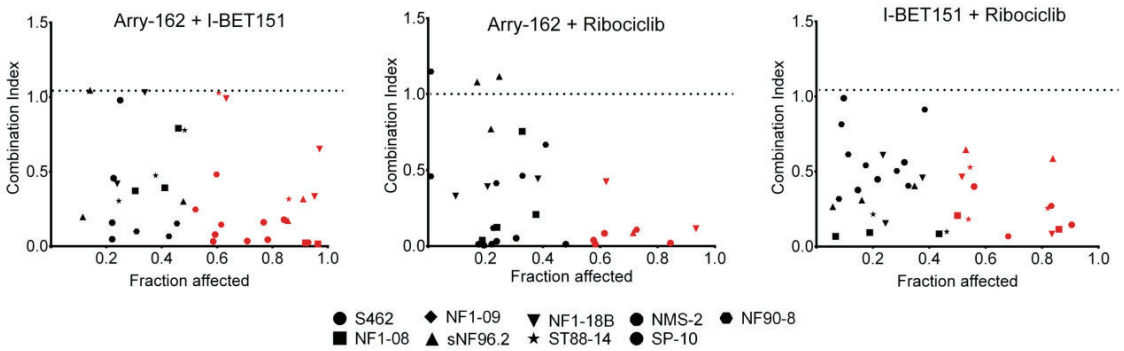

Figure R17. Synergistic effect of the three selected combinations of MEK, CDK, and BET inhibitors in 9 MPNST cell lines. CI plots of the three combinations represented as the CI values vs the Fraction affected (Fa)**.** Fa values represent the fraction of cell death by drug treatment, ranging from 0 (no cell death) to 1 (100% cell killing). Each dot shape represents one cell line, and 5 dots for each line represent the 5 tested drug concentrations. CI values lower than 0.9 indicate synergistic effect.Black dots represents combined effect below the 50% (Fa < 0.5), and red dots mark Fa greater than 0.5.

2.4. The MEKi + BETi Combination (Arry-162 + I-BET151) Induces *In Vivo* Tumor Shrinkage in Sporadic and NF1-Associated MPNST-PDOX

Before initiating *in vivo* treatment, we first determined the optimal dose for each compound to obtain the maximal anti-tumoral effect without toxicity. To achieve this, we performed a MTD assay, testing the drug combinations at different doses (16 conditions in total) in healthy, non-tumor bearing mice (Table R6). The mice weight was monitored daily to observed potential toxicity effects.

Table R6. Summary of the 16 dose combinations tested in the MTD assay

Compound 1	Dose (mg/kg)	Schedule (days a week)	Administration route	Compound 2	Dose (mg/kg)	Schedule (days a week)	Administration route
I-BET151	20	5	Intraperitoneal	Arry-162	5	5 x 2 times/day	Oral
I-BET151	20	5	Intraperitoneal	Arry-162	10	5 x 2 times/day	Oral
I-BET151	20	5	Intraperitoneal	Arry-162	15	5 x 2 times/day	Oral
I-BET151	30	5	Intraperitoneal	Arry-162	5	5 x 2 times/day	Oral
I-BET151	30	5	Intraperitoneal	Arry-162	10	5 x 2 times/day	Oral
I-BET151	30	5	Intraperitoneal	Arry-162	30	5	Oral
I-BET151	20	5	Intraperitoneal	Ribociclib	75	5	Oral
I-BET151	20	5	Intraperitoneal	Ribociclib	90	5	Oral
I-BET151	30	5	Intraperitoneal	Ribociclib	75	5	Oral
I-BET151	30	5	Intraperitoneal	Ribociclib	90	5	Oral
Arry-162	5	5 x 2 times/day	Oral	Ribociclib	75	5	Oral
Arry-162	5	5 x 2 times/day	Oral	Ribociclib	90	5	Oral
Arry-162	10	5 x 2 times/day	Oral	Ribociclib	75	5	Oral
Arry-162	10	5 x 2 times/day	Oral	Ribociclib	90	5	Oral
Arry-162	15	5 x 2 times/day	Oral	Ribociclib	75	5	Oral
Arry-162	15	5 x 2 times/day	Oral	Ribociclib	90	5	Oral

After three weeks of treatment, none of the tested conditions resulted in body weight reduction (Figure R18), thus the maximum tolerated dose for the compounds were: 15 mg/kg for Arry-162, 30 mg/kg for I-BET151, and 90 mg/kg for Ribociclib.

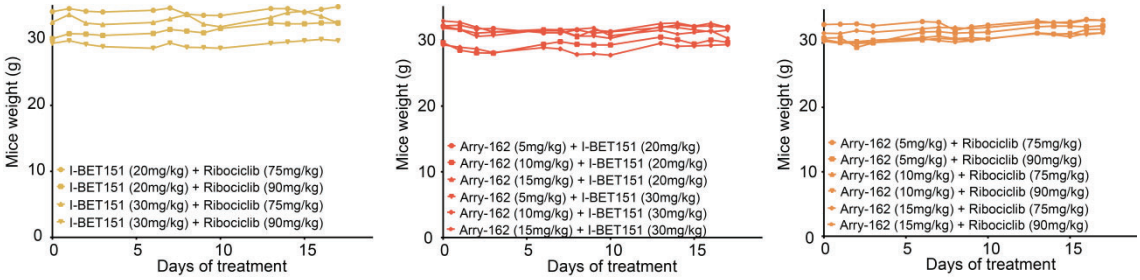

Figure R18. Mice weight evolution during the three weeks of treatments Each line represents the mean of two mice.

We then evaluated the three selected combinations (Arry-162 + I-BET151, Arry-162 + Ribociclib and I-BET151 + Ribociclib) in two MPNST-PDOX models: one NF1-associated (NF1-18B) and one sporadic (SP-10). Both were previously generated and characterized in Results Part I.

NF1-Associated NF1-18B PDOX Model. For the NF1-associated PDOX model, we adjusted the I-BET151 dose based on our previous experience comparing nude mice with or without tumors (Fernández-Rodríguez, Creus-Bachiller et al. 2022). Instead of the 30 mg/kg, daily dose used in the MTD assay, we administered 25 mg/kg three times per week. After two weeks of treatment, the Arry-162 + I-BET151 combination produced the most significant therapeutic response, slowing tumor growth and even reducing tumor volume in half of the treated mice (Figure R19A-B). At the end of the treatment, this combination resulted in a 75% reduction in tumor weight compared to controls, confirming the tumor volume measurements (Figure R19C-D).

The other two combinations (Arry-162 + Ribociclib and I-BET151 + Ribociclib) also reduced tumor growth rates but did not arrest tumor growth. Importantly, none of the tested combinations induced toxicity, as no reduction in body weight was observed over the two-week treatment period (Figure R19E).

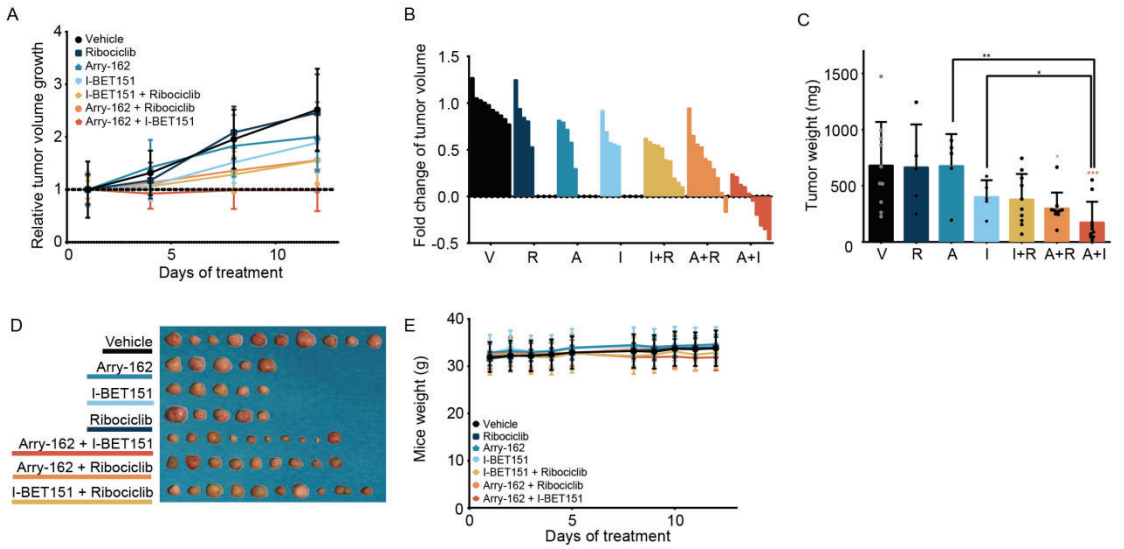

Figure R19. ***In vivo*** **testing of the three selected combinations in the NF1-associated NF1-18B PDOX mouse model.** **A.** Relative tumor volume growth of the NF1-18B PDOX mouse model during the 2 weeks of treatment in each group. **B.** Waterfall plot of the tumor volume fold change of each mouse tumor per treatment group at the end of the experiment. Each bar represents one mouse. **C.** Tumor weight at the end of the experiment (Mann–Whitney test). Each black dot indicates one single value. **D.** Photographs of the collected tumors at the end of the experiment. **E.** Mice weight evolution during the 2 weeks of treatment. Mann–Whitney test: ***, P value ≤ 0.001; **, P value ≤ 0.01; *, P value ≤ 0.05. A, Arry-162; A + I, Arry-162 + I-BET151; A + R, Arry-162 + Ribociclib; I, I-BET151; I + R, I-BET151 + Ribociclib; R, Ribociclib; V, vehicle.

To evaluate the molecular drug effect, we performed western blot to examine the expression of signaling pathways or biomarkers of treatment response (Figure R20). MEKi (Arry-162) activity was assessed by phospho-ERK (p-ERK) levels, CDK4/6i activity by phospho-RB (p-RB) and WEE1 expression, and BETi response by MYC expression. Both Arry-162-based combinations significantly reduced p-ERK levels compared to vehicle-treated controls, confirming MAPK pathway inhibition. Similarly, both Ribociclib-containing combinations reduced p-RB/RB ratio and WEE1 levels, indicating an effect on cell cycle regulation. Finally, MYC expression was significantly reduced in the Arry-162 + I-BET151 combination, while the I-BET151 + Ribociclib also showed a reduction, through it was not statistically significant (Figure R20).

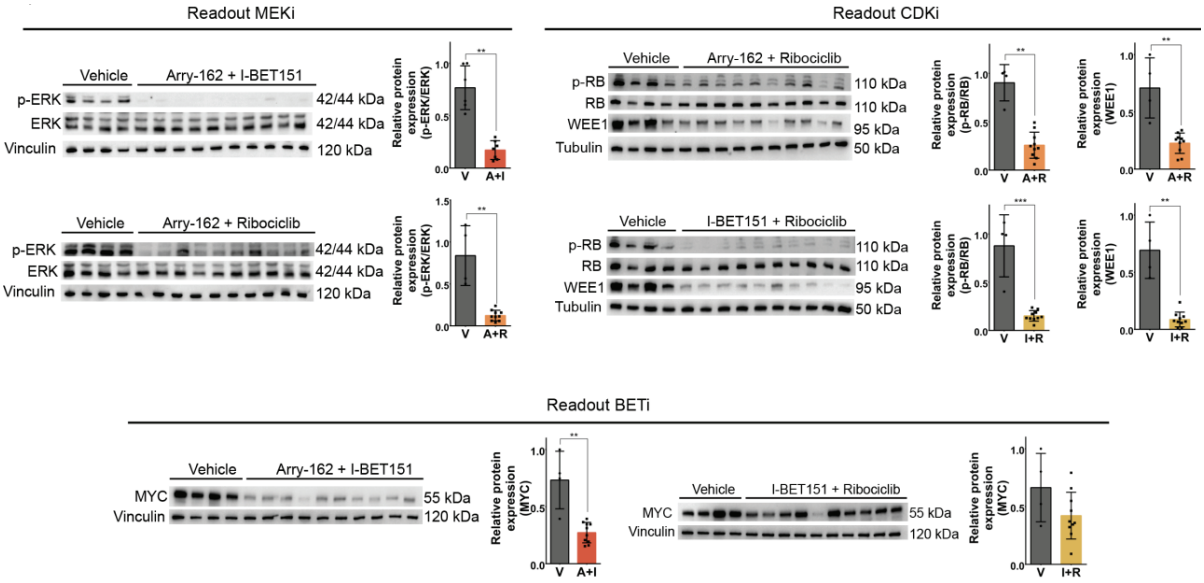

Figure R20. **Molecular target analyses of compounds used for *in vivo* validation in the N1-related PDOX model (NF1-18B).** Western blot analysis and quantification of molecular readouts for the three compounds used: Arry-162 (p-ERK/ERK), Ribociclib (p-RB/RB and WEE1), and I-BET151 (MYC). Each protein was normalized to their expression levels of Vinculin or Tubulin. Mann–Whitney test: **, P value ≤ 0.01; *, P value ≤ 0.05. A + I, Arry-162 + I-BET151; A + R, Arry-162 + Ribociclib; I + R, I-BET151 + Ribociclib; V, vehicle.

Sporadic SP-10 PDOX model. Since no toxicity was observed with I-BET151 in the NF1-associated PDOX model, we initially administered 30 mg/kg daily. However, during the first week, both I-BET151-containing combinations caused mild toxicity, as indicated by mice weight loss (Figure R21E). Consequently, we adjusted the dosage to match the NF1-associated model (25 mg/kg, three times per week) for the second week, which led to weight recovery (Figure R21E).

In this model, the Arry-162 + I-BET151 combination also yielded the most effective response, reducing tumor volume by 65% after two weeks of treatment (Figure R21A-B). This drug response is even higher than the one observed in the NF1-derived model. Tumor weight at the end of the experiment was reduced by 90% compared to the vehicle-treated control group (Figure R21C-D). In the other hand, the other two combinations also slowed tumor growth, but they did not lead to tumor shrinkage, similar to the results in the first model.

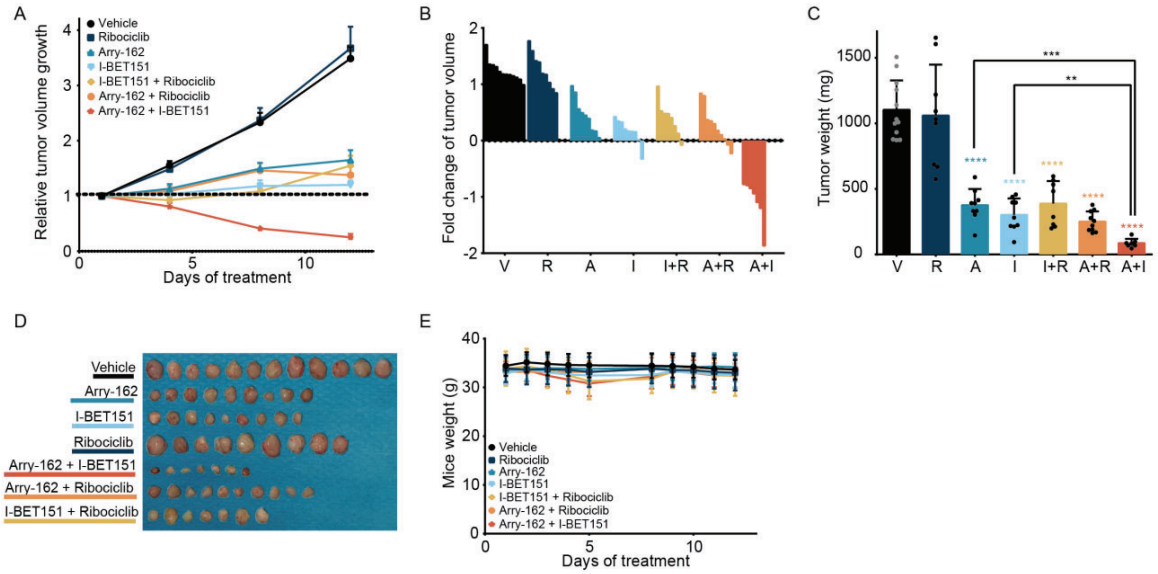

Figure R21. *In vivo* testing of the three selected combinations in the sporadic SP-10 PDOX mouse model. **A.** Relative tumor volume growth of the SP-10 PDOX mouse model during the 2 weeks of treatment in each group. **B.** Waterfall plot of the tumor volume fold change of each mouse tumor per treatment group at the end of the experiment. Each bar represents one mouse. **C.** Tumor weight at the end of the experiment (Mann–Whitney test). Each black dot indicates one single value. **D.** Photographs of the collected tumors at the end of the experiment. **E.** Plot of the mice weight during the 2 weeks of treatment. Mann–Whitney test: ****, P value ≤ 0.0001; ***, P value ≤ 0.001; **, P value ≤ 0.01; *, P value ≤ 0.05. A, Arry-162; A + I, Arry-162 + I-BET151; A + R, Arry-162 + Ribociclib; I, I-BET151; I + R, I-BET151 + Ribociclib; R, Ribociclib; V, vehicle.

Additionally, we wanted to assess if tumor remaining in mice after treatment with Arry-162 + I-BET151 was able to regrowth. After three weeks of treatment, tumors had a mean volume of 500 mm^3, which increased to 1200 mm^3 following two weeks without treatment (Figure R22). Resuming treatment for additional three weeks led to a 50% tumor volume reduction (Figure R22).

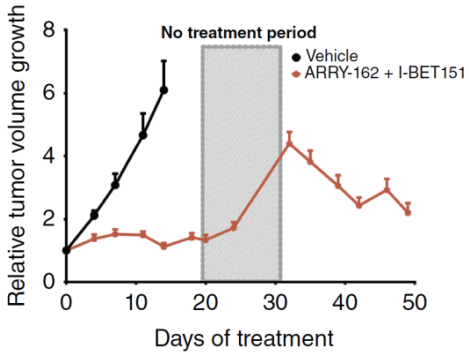

Figure R22. Sporadic PDOX model tumors treated with Arry-162 + I-BET151 regrowth after treatment. Relative tumor volume growth of the SP-10 PDOX mouse model during the regrowth experiment treated with Arry-162 + I-BET151.

Molecular analysis of drug activity in the sporadic PDOX model mirrored the findings in the NF1-associated model. All Arry-162-containing combinations significantly reduced p-ERK levels compared to vehicle-treated controls (Figure R23). Both Ribociclib-containing combinations decreased the p-RB/RB ratio and WEE1 levels, although the reduction of p-RB levels was not statistically significant in both combinations. Finally, MYC expression was significantly reduced in the Arry-162 + I-BET151 combination; however, this reduction was not statically significant in the I-BET151 + Ribociclib combination (Figure R23).

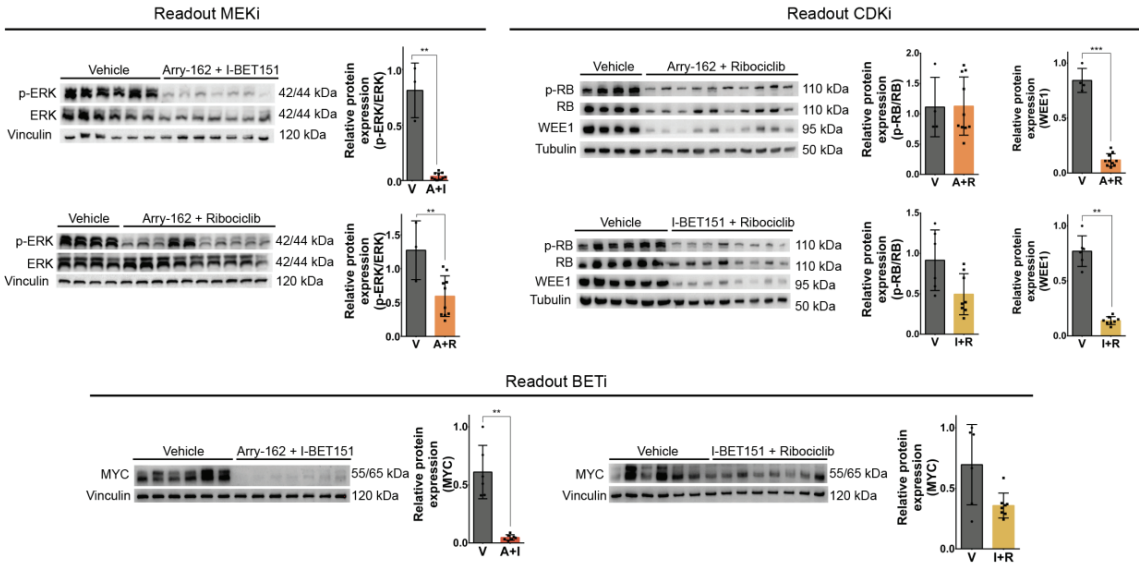

Figure R23. Molecular target analyses of compounds used for *in vivo* validation in the sporadic PDOX model (SP-10). Western blot analysis and quantification of molecular readouts for the three compounds used: Arry-162 (p-ERK/ERK), Ribociclib (p-RB/RB and WEE1), and I-BET151 (MYC). Each protein was normalized to their expression levels of Vinculin or Tubulin. Mann–Whitney test: ****, P value ≤ 0.0001; ***, P value ≤ 0.001; **, P value ≤ 0.01; *, P value ≤ 0.05; A + I, Arry-162 + I-BET151; A + R, Arry-162 + Ribociclib; I + R, I-BET151 + Ribociclib; V, vehicle.

2.5. Evaluating the Mechanism of the MEK + BET Inhibitors Co-Treatment in Tumor Response

After obtaining promising *in vivo* results with the MEKi + BETi combination, we sought to investigate the mechanism underlying PDOX tumor reduction. While the effect of MEKis on MAPK pathway is well characterized (as demonstrated in Figure R20 and Figure R23), the molecular impact of the BETis remain less defined. BETis are known to regulate transcription, but the specific genes involved, and their functional roles have not been fully elucidated.

To explore this, we performed RNA sequencing (RNA-seq) to assess gene expression changes induced by BETi alone or in combination with MEKi in PRC2 WT and PRC2-deficient MPNST cell lines. Specifically, we treated three PRC2 WT cell lines (NF1-09, HS-Sch-2 and STS-26T) with I-BET151, and three PRC2-deificient cell lines (S462, SP-10, and NF1-18B) with both I-BET151 and

the I-BET151 + Arry-162 combination. After 20 hours of treatment, RNA was extracted for bulk RNA-seq analysis (Figure R24).

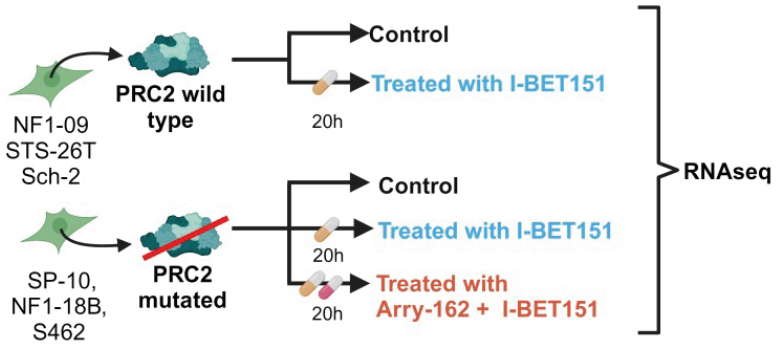

Figure R24. **Schematic representation of the experimental design to analyze changes in gene expression upon I-BET151 and Arry-162 + I-BET151 treatment**. Image created in BioRender.

PCA of the RNA-seq data (Figure R25A) revealed that global transcriptional variation among samples was primarily driven by PRC2 functional status, clearly separating PRC2-active from PRC2-inactive cell lines. Interestingly, the transcriptional perturbation induced by I-BET151 or the Arry-162 + I-BET151 combination in PRC2-mutated cell lines was relatively minor and similar to the effects observed in PRC2 WT cells treated with I-BET151 (Figure R25A).

Subsequent differential gene expression analysis comparing I-BET151-treated versus untreated PRC2-deficient cell lines identified a gene signature of upregulated and downregulated genes, with only a few being specific to PRC2-inactivated lines (Figure R25B). Among the most differentially expressed genes between treated and non-treated cells, we selected three for further validation: *TPPP* and *NGFR* (upregulated) and *PRDM1* (downregulated) (Figure R25C).

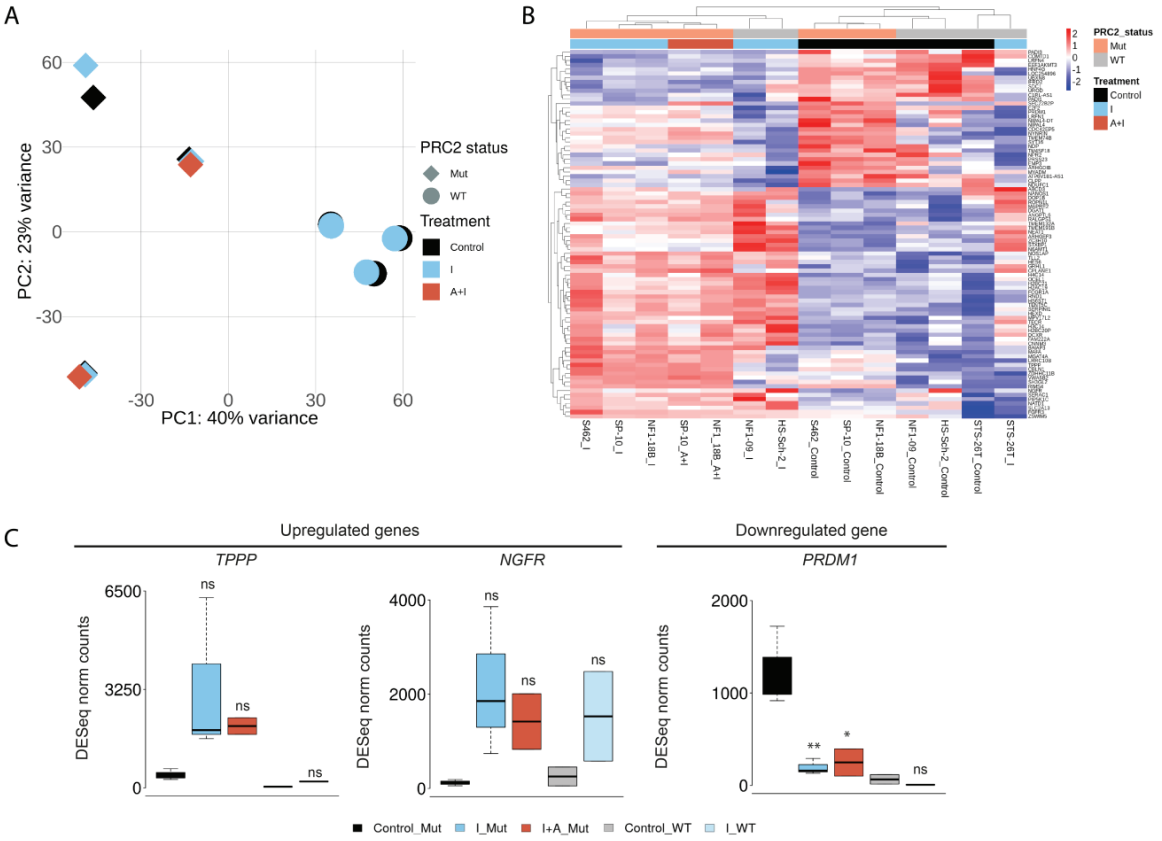

Figure R25. RNA-seq results of MPNST cell lines treated with I-BET151 and Arry-162 + I-BET151 combination. A. PCA plot showing the distribution of treated and untreated cell lines. The status of PRC2 is represented using different forms: diamond for PRC2-deficient samples and sphere for WT PRC2. Different treatments are represented in different colors: blue for single agent I-BET151 and orange for the combination. **B.** Heatmap representing differentially expressed genes of I-BET151 (I) treated vs. untreated cell lines for all cell lines. **C.** Boxplots representing the expression (DESeq normalize counts) of selected genes by group of samples (Tukey test, each group of treatment versus their control). Tukey test: I_Mut and A+I_Mut vs Control_Mut; and I_WT vs Control_WT. ** p-value≤0.01, * p-value≤0.05. Mut, PRC2-inactivated.

The expression of *TPPP*, *NGFR*, and *PRDM1* was analyzed by RT-qPCR (Figure R26A), and we observed the same trend as seen with RNA-seq: *TPPP* and *NGFR* were overexpressed when the cells were treated with I-BET151 or Arry-162 + I-BET151, whereas *PRDM1* was downregulated.

Next, we aimed to validate whether these findings were consistent at the protein level. To do so, we performed western blot analysis on PRC2-deficient cell lines following treatment (Figure R26B). We confirmed that the increased expression of *TPPP* and *NGFR* upon treatment was observed in two of the three analyzed MPNST cell lines (S462 and NF1-18B), although the effect was less pronounced (Figure R26B). However, *PRDM1* downregulation was not observed in the western blot assays (Figure R26B).

We then wanted to assess expression changes in these genes in the PDOX tumors treated with the three combinations *in vivo* to validate them as potential biomarkers of BETi response. Upregulation of *TPPP* and *NGFR,* along with *PRDM1* downregulation, was detected exclusively

in MEKi + BETi treated tumor from the NF1-associated PDOX model (NF-18B PDOX) but not from the sporadic model (SP-10 PDOX) (Figure R26C). Notably, the MEKi-CDKi and CDKi-BETi combinations also induced expression changes in these genes (Figure R26C). Overall, the inconsistencies between mRNA and protein levels analyses, as well as between *in vitro* and *in vivo* results, prevented us from establishing a marker for BETi treatment response. Also, these findings suggest that BETi's contribution to tumor reduction *in vivo* may not be directly linked to the transcriptional reversion of genes affected by PRC2 loss.

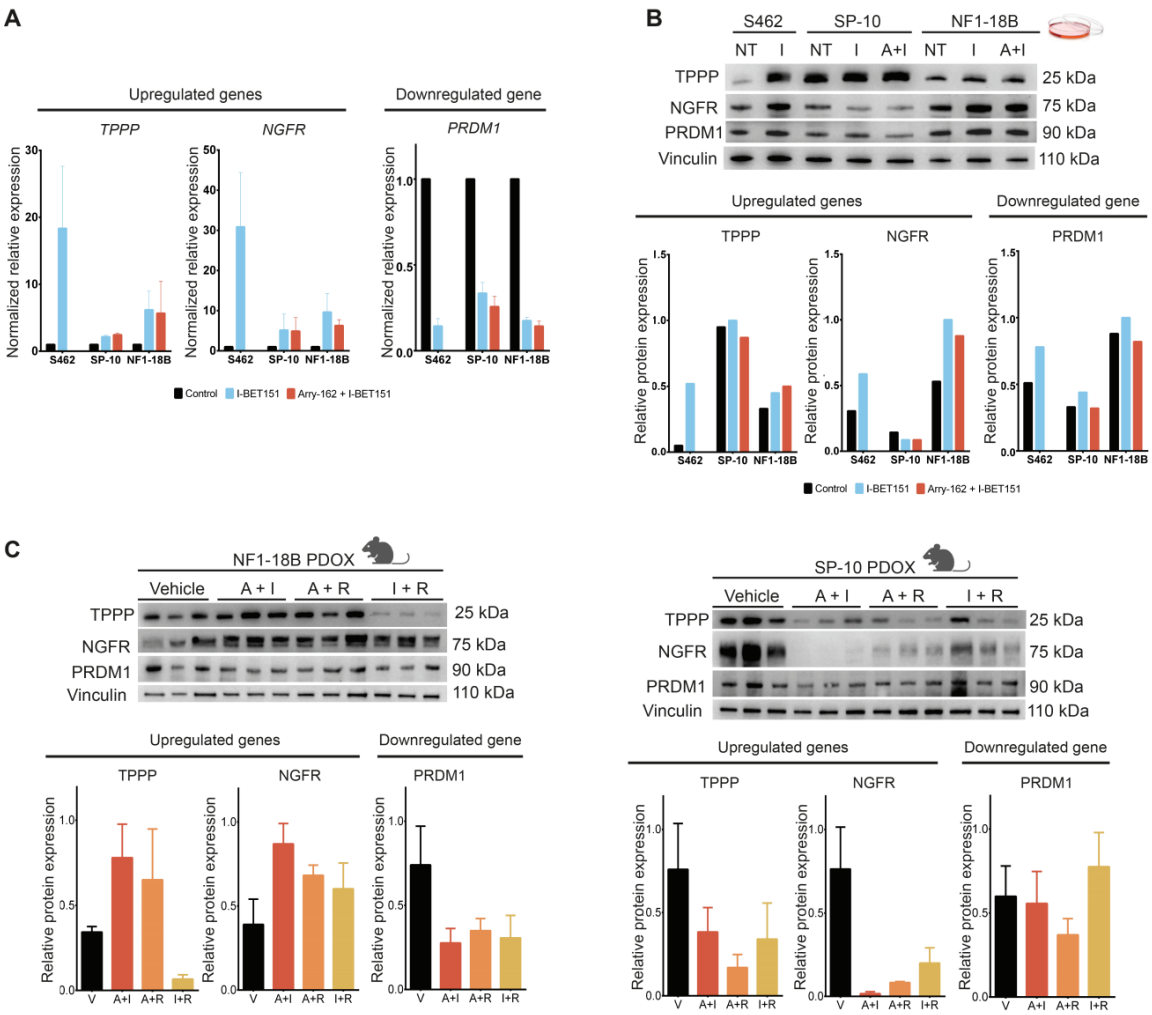

Figure R26. Expression analysis of potential biomarkers of BETi treatment response by RT-qPCR and western blot on cell lines and PDOX tumors. A. RT-qPCR analysis of *TPPP*, *NGFR*, and *PRDM1* expression in the PRC2-mutated cell lines, both non-treated (control) or treated with I-BET151 (I) or Arry-162 + I-BET151 (A+I). For SP-10 and NF1-18B Tukey test, for S462 Mann-Whitney test (each group of treatment versus their control). **B.** Protein expression analysis by Western blot and quantification of *TPPP*, *PRDM1*, and *NGFR* in three PRC2-mutated MPNST cell lines (S462, SP-10, and NF1-18B). **C.** Protein expression analysis by Western blot and quantification of *TPPP*, *PRDM1*, and *NGFR* in the NF1-18B and SP-10 PDOX models after co-treatments. Each protein was normalized to their expression levels of Vinculin. Untreated (control, NT), treated with I-BET151 (I), treated with Arry-162 + I-BET151 (A + I), treated with Arry-162 + Ribociclib (A + R), and treated with I-BET151 + Ribociclib (I + R).

Given these observations, we investigated alternative physiological mechanisms that could explain the MEKi + BETi combination's effect on tumor. We first analyzed the cell cycle in the

PRC2-deficient MPNST cell lines treated with MEKi + BETi using flow cytometry. We observed a decrease in the proportion of cells in the S-phase and an increase in the G_1-phase, indicative of cell cycle arrest due to MEKi + BETi co-treatment (Figure R27A).

To assess whether similar effects occurred *in vivo,* we performed H&E staining in PDOX tumors to evaluate the number of mitotic cells in treated versus untreated tumors (Figure R27B). Both sporadic and NF1-associated PDOX tumors exhibited a statistically significant reduction in the mitotic cell number across all three treatment conditions, with the most pronounced effect observed in MEKi + BETi-treated tumors. These results were consistent with the observed reduction in tumor growth rate *in vitro* but did not fully explain the tumor shrinkage seen in the sporadic model and in part of the NF1-associated PDOXs.

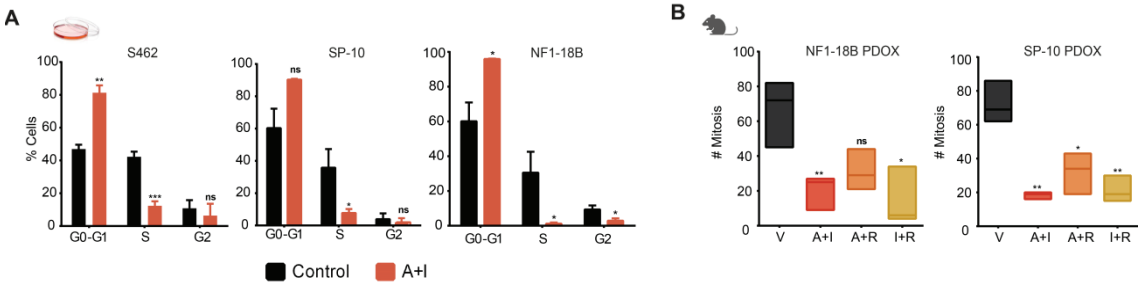

Figure R27. Cell cycle analysis of PRC2-deficient MPNST cell lines and PDOX tumors. A. Percentage of cells in each phase of the cell cycle in three MPNST cell lines (S462, SP-10, and NF1-18B) treated with DMSO (control) or with Arry-162 + I-BET151 (A + I). **B.** Number of mitoses in a 1.7 mm^2 area of a hematoxylin and eosin staining. A + I, Arry-162 + I-BET151; A + R, Arry-162 + Ribociclib; I + R, I-BET151 + Ribociclib; V, vehicle.

We next examined whether apoptosis played a role in tumor shrinkage by analyzing BIM expression (Patel, Liao et al. 2014) and caspase activation in the three MPNST cell lines. Both BETi and MEKi + BETi co-treatment led to a consistent increase in BIM expression in three independent MPNST cell lines (Figure R28A). Similar results were observed in treated versus untreated MPNST-PDOX tumors, with a pronounced increase in BIM expression in NF1-associated PDOX but a more modest increase in sporadic PDOX (Figure R28B). However, cleaved caspases 3, 7, and 9 were not detected in the cell lines and PDOX models treated with Arry-162 + I-BET151 (data not shown), suggesting that this combination is not apoptotic.

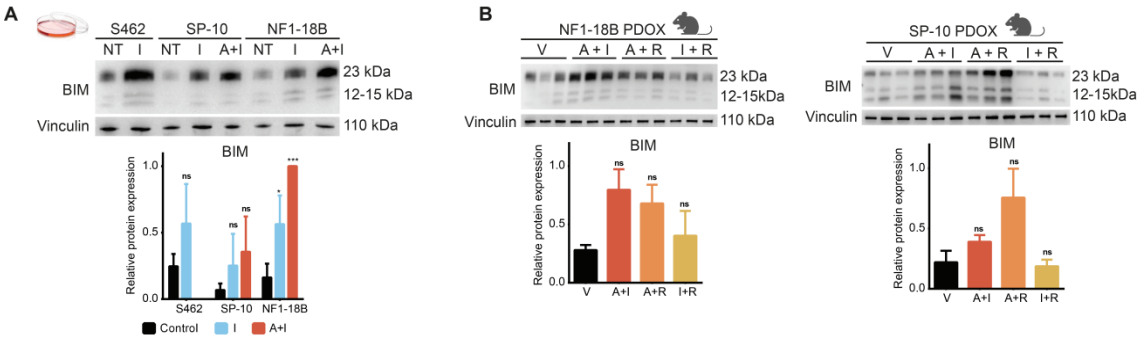

Figure R28. Analysis of BIM protein expression in MPNST cell lines and PDOX tumors. A. Western blot and quantification of BIM protein expression in three MPNST cell lines (S462, SP-10, and NF1-18B) DMSO-treated and treated with I-BET151 (I) or ARRY- 162 + I-BET151 (A+I). **B.** Western blot analyses and quantification of BIM protein expression in the PDOX tumors NF1-18B and SP-10 PDOX models after the three co-treatments (MEKi-BETi, CDKi-BETi, MEKi-CDKi). BIM was normalized to their expression levels of Vinculin. The Tukey test was used for the statistics, in which each treatment group was analyzed against its control: ***, P value ≤ 0.001; **, P value ≤ 0.01; *, P value ≤ 0.05. A + I, Arry- 162 + I-BET151; A + R, Arry-162 + Ribociclib; I, I-BET151; I + R, I-BET151 + Ribociclib; NT, no treatment; V, vehicle.

Given these findings, we hypothesize that the MEKi + BETi combination might exert its effects through modifications in the tumor microenvironment rather than through direct tumor cell-intrinsic mechanisms. Considering the compromised immune system of the athymic nude mice, with no mature T cells, but presenting viable macrophages, we performed a histological analysis using CD68 and CD163 stains to detect macrophage infiltration in the two MPNST-PDOX models from control and combination groups (Figure R29). All three co-treatments resulted in a loss of M2 macrophages (CD163-positive) in both MPNST-PDOX models, consistent with previous findings in genetically engineered mouse models (unpublished data of Dr. Thomas De Raedt).

The cytostatic effects, the activation of BIM, and the loss of M2 macrophages have been observed across all three co-treatments. Therefore, no specific mechanism has been identified thus far to fully explain the tumor reduction observed with the MEK-BET combination therapy.

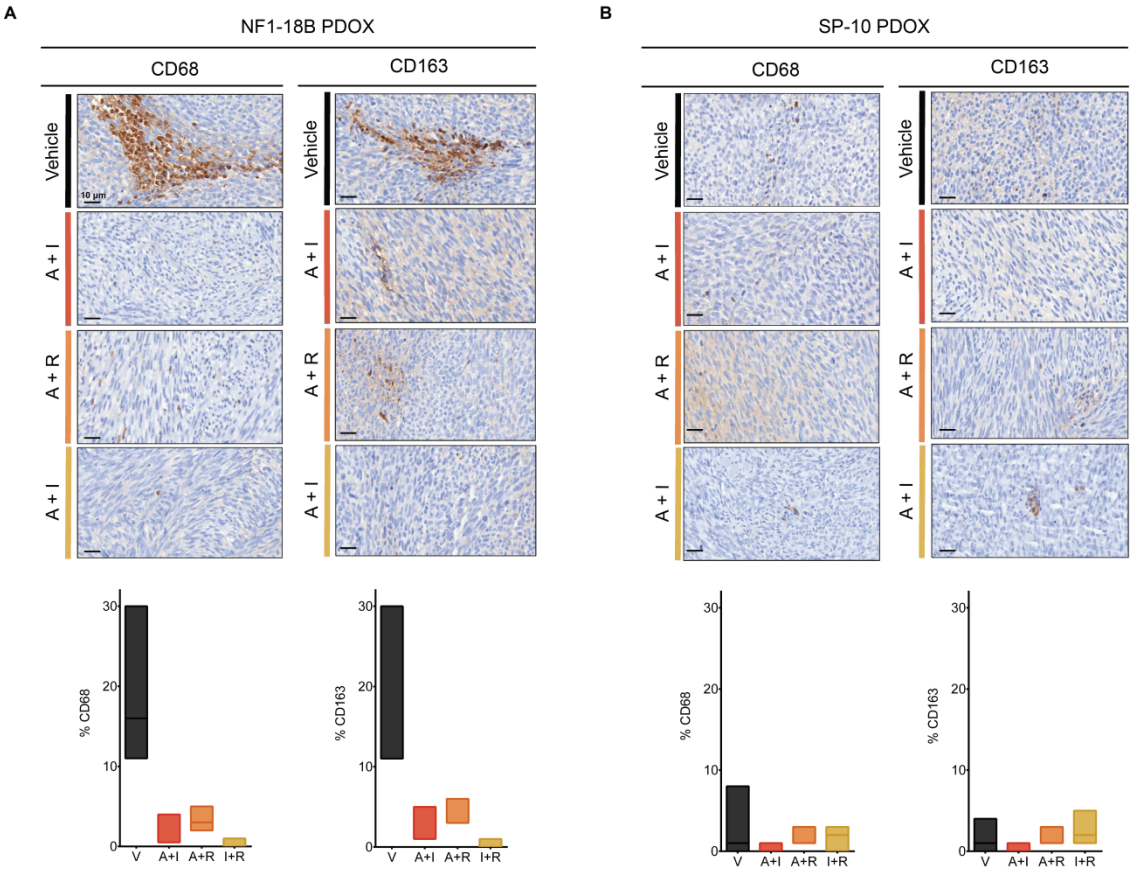

Figure R29. Analysis of macrophage infiltration in co-treated MPNST-PDOX tumors. A-B. Representative images of CD68 (Pan macrophages) and CD163 (M2) markers expression by immunohistochemistry and boxplots of expression quantification in NF1-18B and SP-10 PDOX tumors, respectively; untreated or treated with the three different combinations. A + I, Arry- 162 + I-BET151; A + R, Arry-162 + Ribociclib; I + R, I-BET151 + Ribociclib; V, vehicle. Mann–Whitney test (all groups analyzed against vehicle, nonsignificant).

2.6. The Triple Combination of MEK, BET, and CDK Inhibitors Further Increases the Reduction of Tumor Volume, Even Reaching Tumor Disappearance

Given the promising results obtained with the MEK + BET inhibitor combination, we conducted an additional *in vivo* experiment comparing the MEKi + BETi combination with the triple combination therapy including a CDKi: Arry-162 (MEKi) + I-BET151 (BETi) + Ribociclib (CDKi). We used the same two PDOX models as in previous experiments but initiated treatment when tumors were slightly smaller than in the prior MEKi + BETi assays. This adjustment allowed for a longer treatment period before vehicle-treated MPNST tumors reached maximum allowed size.

NF1-Associated PDOX Model. The triple combination therapy resulted in a 50% greater reduction in tumor volume compared to the MEKi + BETi combination after three weeks of treatment (Figure R30A-B). Tumor weight validate these findings: while vehicle-treated tumors had an average weight of 1,942 mg, tumors treated with MEKi + BETi averaged 310 mg, and

those receiving the triple therapy averaged 218 mg (Figure R30C-D). Importantly, no toxicity was observed throughout the three-week treatment period (Figure R30E).

At the end of treatment, four mice were monitored for tumor regrowth. Weekly measurements over one month revealed tumor regrowth in all four mice, starting just two weeks after treatment cessation (Figure R30F).

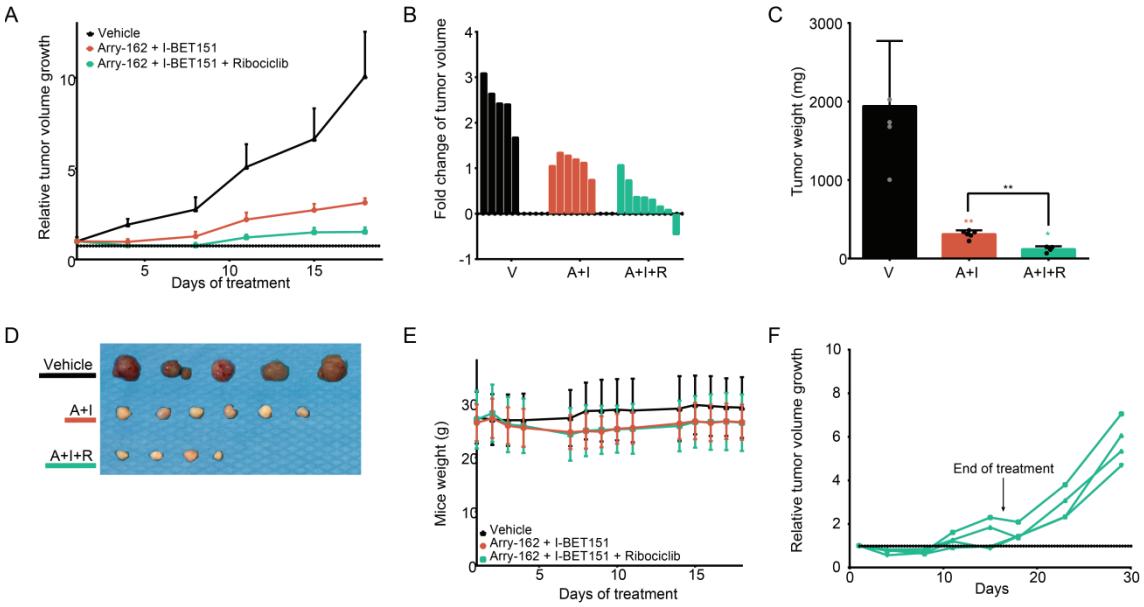

Figure R30. ***In vivo*** **testing of the triple combination of MEKi–BETi–CDKi in the NF1-related NF1-18B PDOX mouse model. A.** Relative tumor volume growth of the NF1-18B PDOX mouse model during the 3 weeks of treatment in each group. **B.** Waterfall plot of the tumor volume fold change of each mouse tumor per treatment group at the end of the experiment. Each bar represents one mouse. **C.** Tumor weight at the end of the experiment (Mann–Whitney test). Each black dot indicates one single value. **D.** Photographs of the collected tumors at the end of the experiment. **E.** Mice weight evolution during the 3 weeks of treatment. **F.** Tumor regrowth after the end of triple combination treatment. Relative tumor volume growth for four individual tumors is shown. Mann–Whitney test: **, P value ≤ 0.01; *, P value ≤ 0.05. A + I, Arry-162 + I-BET151; A + I + R, Arry-162 + I-BET151 + Ribociclib; V, vehicle.

Similar as the double treatments, we performed western blot analyses to assess expression of molecular targets. We analyzed vehicle-treated, MEKi + BETi- combination, and triple combination. In all cases, drugs –induced molecular targets inhibition (Figure R31). Notably, the reduction in pRB and WEE1 levels was significantly greater with the triple combination compared to the MEKi + BETi treatment.

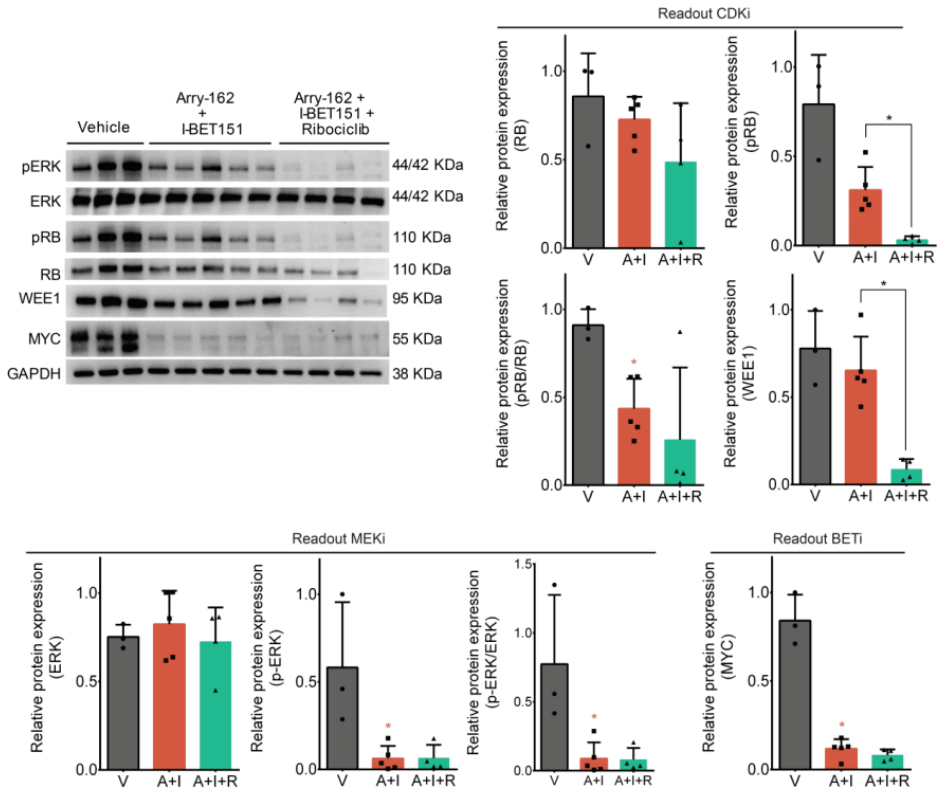

Figure R31. Analyses of the molecular targets of the triple treatment *in vivo* in NF1-18B MPNST PDOX. Western Blot and quantification of p-ERK/ERK (Arry-162), MYC (I-BET151) and pRB/RB and WEE1 (Ribociclib). Each protein of interest was normalized to their expression levels of GAPDH. Vehicle (V); Arry-162 + I-BET151 (A+I); Arry-162 + I-BET151 + Ribociclib (A+I+R). Mann–Whitney test: * p-value≤0.05.

Sporadic PDOX Model. The triple therapy led to an 85% reduction in tumor volume relative to baseline measurements (Figure R32A-B). Significant differences were also observed in final tumor weights: vehicle-treated tumors averaged 2,041 mg, MEKi + BETi-treated tumors averaged 122 mg, and tumors treated with the triple combination averaged just 29 mg (Figure R32C-D). Remarkably, in two of the eight mice treated with the triple combination for three weeks, tumors became undetectable by palpation. As with the NF1-18B model, no signs of toxicity were observed in the treated mice (Figure R32E).

To assess tumor regrowth after treatment cessation, we monitored four mice, including one of the two with no palpable tumor at the end of the treatment (Figure R32F). One mouse exhibited fast tumor regrowth 20 days post-treatment, while two others experienced slower regrowth (Figure R32F). Strikingly, the mouse with no palpable tumor showed no evidence of tumor recurrence even one month after treatment discontinuation (Figure R32F).

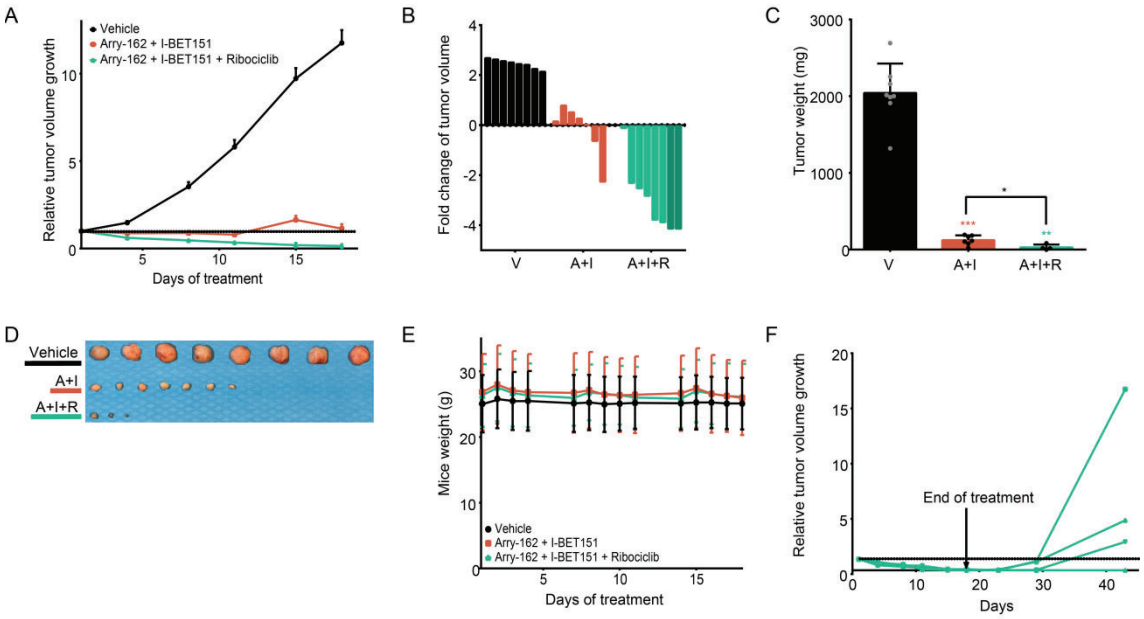

Figure R32. *In vivo* testing of the triple combination of MEKi–BETi–CDKi in the sporadic SP-10 PDOX mouse model. **A.** Relative tumor volume growth of the SP-10 PDOX mouse model during the 3 weeks of treatment in each group. **B.** Waterfall plot of the tumor volume fold change of each mouse tumor per treatment group at the end of the experiment. Each bar represents one mouse. **C.** Tumor weight at the end of the experiment (Mann–Whitney test). Each black dot indicates one single value. **D.** Photographs of the collected tumors at the end of the experiment. **E.** Plot showing mice weight during the 3 weeks of treatment. **F.** Analysis of tumor regrowth after the end of triple combination treatment. Relative tumor volume growth for four individual tumors is shown. Mann–Whitney test: ***, P value ≤ 0.001; **, P value ≤ 0.01; *, P value ≤ 0.05. A + I, Arry-162 + I-BET151; A + I + R, Arry-162 + I-BET151 + Ribociclib; V, vehicle.

In the mouse without palpable tumor after treatment, we performed H&E and Ki67 staining of the femoral bicep. We detected residual tumor tissue with Ki67-positive cells, indicating persistent proliferative activity (Figure R33).

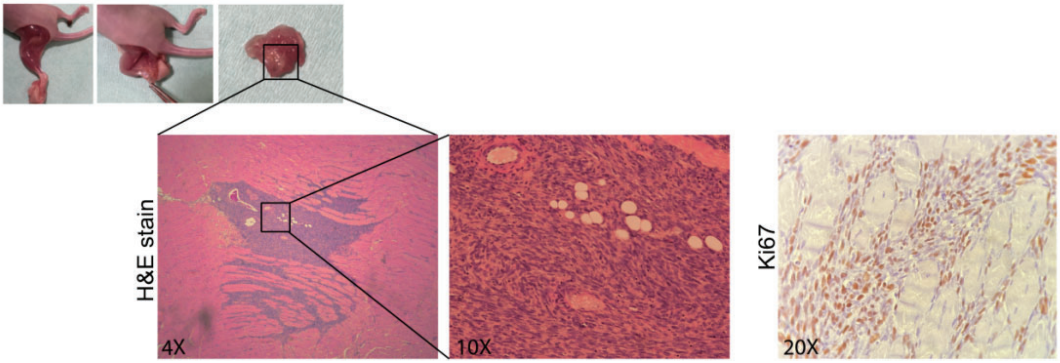

Figure R33. Hematoxylin and eosin and Ki67 staining of the femoral biceps of one of the mice without a palpable tumor. Image magnified 40X, 100X and 200X. H&E: Hematoxylin and eosin.

We also assessed molecular drug activity, as done in the NF1-associated model. In all cases, drugs –induced molecular targets inhibition (Figure R34), with a more pronounced and widespread inhibition in the sporadic PDOX model compared to the NF1-associated model.

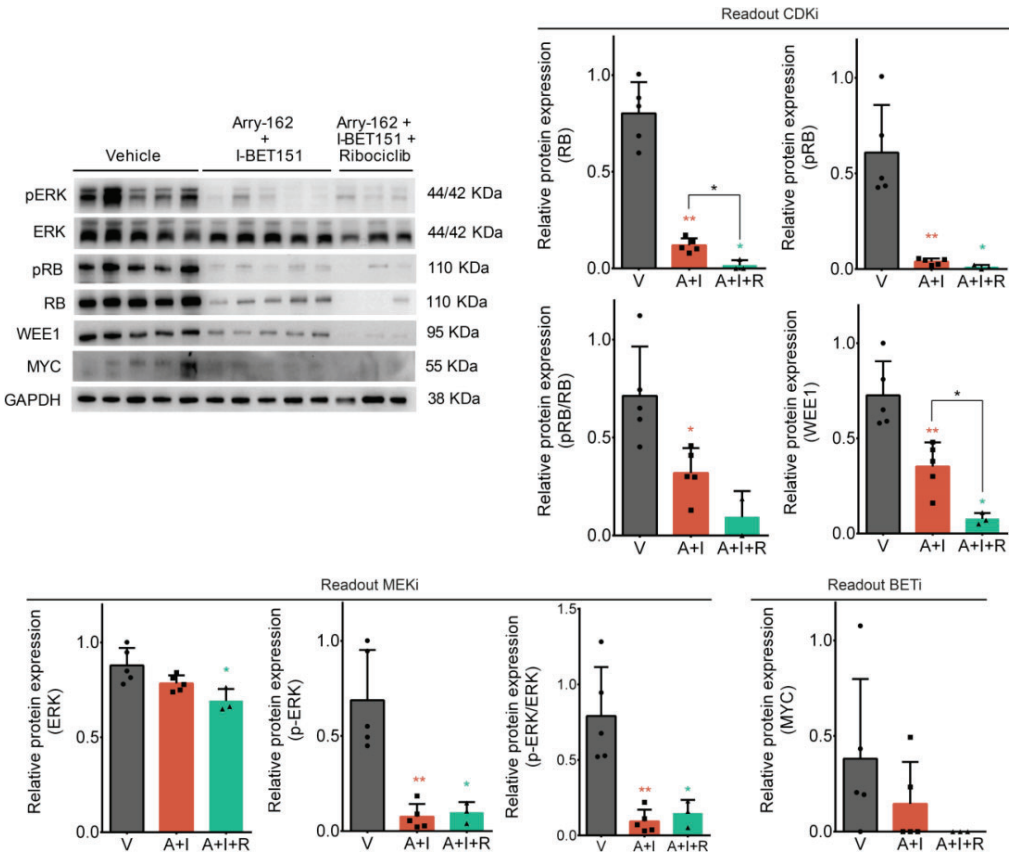

Figure R34. Analyses of the molecular targets of the triple treatment *in vivo* in SP-10 MPNST PDOX. Western Blot and quantification of p-ERK/ERK (Arry-162), MYC (I-BET151) and pRB/RB and WEE1 (Ribociclib). Each protein of interest was normalized to their expression levels of GAPDH. Vehicle (V); Arry-162 + I-BET151 (A+I); Arry-162 + I-BET151 + Ribociclib (A+I+R). Mann–Whitney test: ** p-value≤0.01, * p-value≤0.05.

R3. Part III: Personalized Medicine Strategy for MPNSTs: Using Precision Oncology on PDOX Models to Inform Tumor Boards

We propose a personalized medicine strategy for MPNST patients based on performing WGS-guided precision oncology to select targeted therapies and test them in MPNST-PDOX avatar model. After resection of the patient MPNST and pathological characterization, part of the tumor is used for genomic analysis by WGS, allowing the identification of key genetic alterations that serve as potential therapeutic targets. Pieces of the tumor are implanted in parallel into the sciatic nerve of nude mice to generate PDOX models and, after tumor expansion, to allow functional drug assays to be performed *in vivo*. Treatment responses guide the tumor molecular board about potential personalized therapeutic possibilities.

During this thesis, we have used a precision oncology strategy in two MPNST patients, as presented below.

3.1. Case 1: NF1 Patient that Developed Two Independent Primary MPNSTs

Clinical course (Figure R35). The patient is a 21-year-old boy bearing a *de novo* germline microdeletion in the *NF1* gene. At age 17, a tumor mass was detected in the cavum, and endonasal surgery was performed, leading to MPNST diagnosis (NF1-16A, Figure R35). A second surgical resection confirmed the absence of residual tumor tissue, and adjuvant proton radiation therapy was administered. Nine months later, a new nasal lesion was identified and resected (Relapse 1), coinciding with the detection of a second primary MPNST located in the right leg. Treatment with Selumetinib (MEKi) and Ribociclib (CDKi) was initiated but discontinued intermittently due to skin and gastrointestinal toxicity. During this period, a second nasal relapse (Relapse 2, NF1-16B) and a partial resection of the MPNST located in the leg (NF1-16C) was performed, followed by proton radiotherapy (Figure R35). Subsequent disease progression of the cavum lesion (Relapse 3) led to an additional nasal resection, adjuvant proton radiotherapy, and four cycles of chemotherapy (Ifosfamide + Doxorubicin). Treatment stopped at December 2022 and as of November 2024, the patient presents inactive disease in the residual leg and no lesion in the cavum.

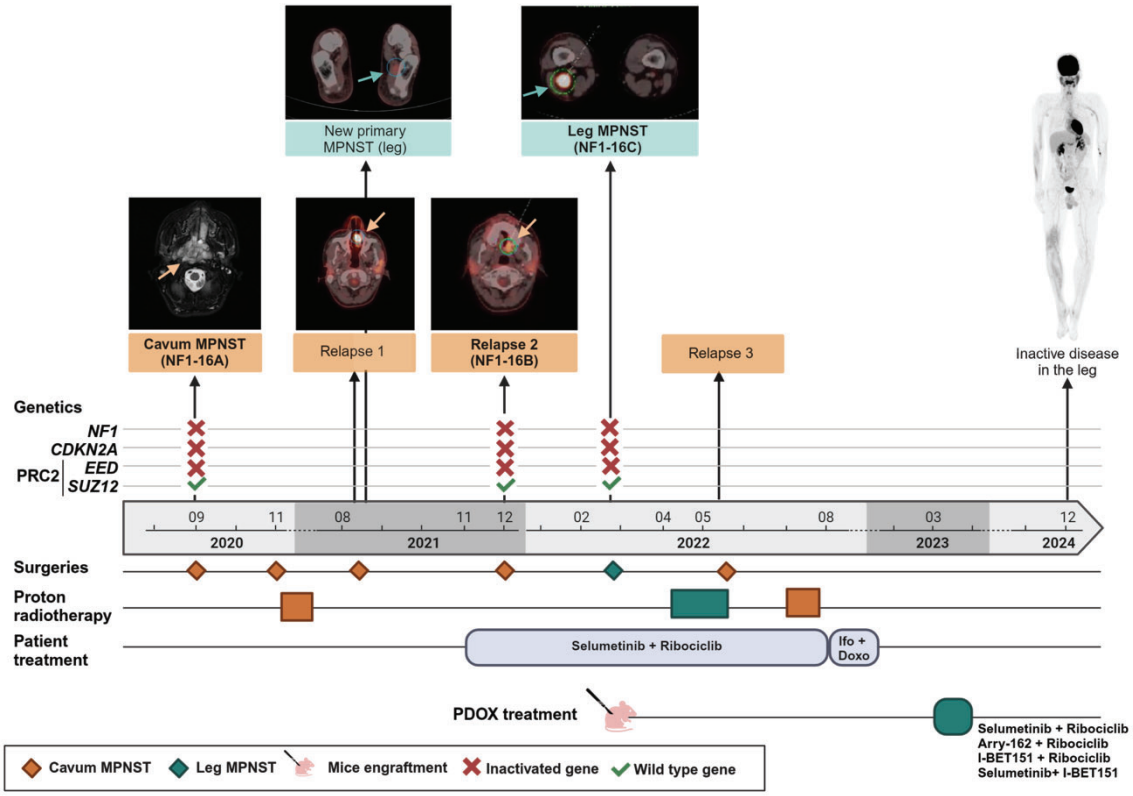

Figure R35. Timeline depicting the clinical course of the NF1-associated MPNST patient (NF1-16). This timeline illustrates the clinical progression, treatment interventions, and parallel research conducted on patient NF1-16 over time (in years and months). Orange indicates events related to the cavum MPNST, while green corresponds to the leg MPNST, emphasizing the distinction between tumor sites in the clinical course. The upper section includes Magnetic Resonance Image (MRI) and Positron Emission Tomography/Computed Tomography (PET/CT) scans showing from left to right: primary MPNST in the cavum (NF1-16A), relapse 1 in the cavum, the new primary tumor in the leg, relapse 2 in the cavum (NF1-16B), MPNST in the leg (NF1-16C), Hand, the last one presents the residual leg disease and no lesions in the cavum. PET/CT scans for relapse 3 (cavum) are not available. In the middle section of the figure, there is a brief genetic scheme of the main TSGs mutational status in NF1-16A, NF1-16B, and NF1-16C: a red cross denotes inactivating mutations, while green ticks indicate wild type gene Ifo + Doxo: Ifosfamide + Doxorubicin. Image created with BioRender.com.

Genomic analysis. WGS of the cavum primary tumor (NF1-16A) identified the triple inactivation of *NF1*, *CDKN2A*, and PRC2 (*EED* gene). Genomic characterization of the relapsed nasal tumor (NF1-16B) confirmed the same somatic mutations, and an almost identical genomic structure compared to the primary tumor, consistent with a local relapse (Table R7 and Figure R36).

Table R7. Genetic alterations identified in NF1-16 MPNST samples. NF1-16A and NF1-16B represent cavum samples, while NF1-16C corresponds to the leg tumor sample.

Sample	*NF1*		*CDKN2A*		*SUZ12*		*EED*	
	Allele 1 (germline)	Allele 2	Allele 1	Allele 2	Allele 1 (germline)	Allele 2	Allele 1	Allele 2
NF1-16A	NM_000267.3:c.-328016_60+8932del	NM_000267.3:c.4773-29458_*598163del ●	chr9:g.21971508_chr6:g.90608897 chr9:g.21972009_chr15:g.76637937 (translocation) ●	LOH	NM_015355.3:c.-640885_506-828del	WT	NM_003797.5:c.193del ●	LOH
NF1-16B	NM_000267.3:c.-328016_60+8932del	NM_000267.3:c.4773-29458_*598163del ●	chr9:g.21971508_chr6:g.90608897 chr9:g.21972009_chr15:g.76637937 (translocation) ●	LOH	NM_015355.3:c.-640885_506-828del	WT	NM_003797.5:c.193del ●	LOH
NF1-16C	NM_000267.3:c.-328016_60+8932del	NM_000267.3:c.289C>T ●	chr9:g.21971327_chr21:g.43894115 chr9:g.21971596_chr3:g.70516001 (translocation) ●	LOH	NM_015355.3:c.-640885_506-828del	WT	NM_003797.5:c.128del ●	LOH

The normalization of the variants was done with Mutalyzer 3. For translocations, we indicate the position of the breakpoints where they occur. The red dot indicates the same somatic mutations in the two sample, whereas the pink dot indicates other independent mutations affecting the genes in the NF1-16C sample

We also performed WGS of the MPNST developed in the leg (NF1-16C), revealing *NF1*, *CDKN2A*, and *EED* inactivation. However, the somatic mutations affecting these gens were different from the ones in the cavum. Moreover, the leg tumor NF1-16C presents a distinct genomic structure compared to the cavum NF1-16A (Table R7 and Figure R36). These findings confirmed that the tumor of the leg was an independent second primary MPNST, rather than a metastatic relapse of the MPNST of the cavum (Figure R36).

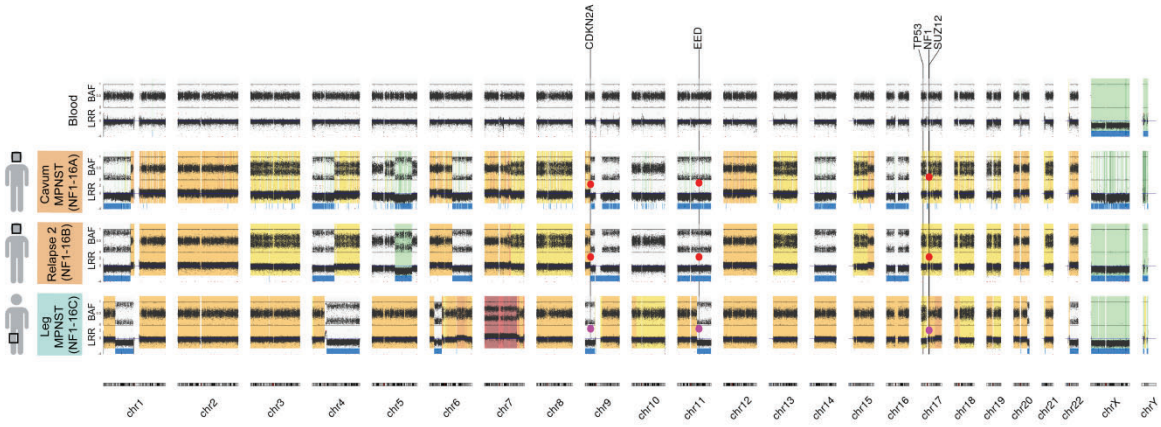

Figure R36. Copy number variation profiles of NF1-16A, NF1-16B, and NF1-16C tumors. B-allele frequency (BAF) and Log-R Ratio (LRR) No are represented. Yellow to red colors represent copy number gained regions, whereas light green indicates heterozygous loss. Loss of heterozygosity (LOH) is highlighted by a thick blue line. Inactivated genes are marked with a red circle; new mutations are marked with a pink circle.

PDOX generation and treatment. We tried to generate PDOX from NF1-16A and NF1-16B tumors, but they did not grow in the mouse. Instead, a PDOX model was generated from the recurrent leg tumor (NF1-16C). In anticipation of further relapses in the patient, the NF1-16C PDOX model was expanded and treated with four targeted drug combinations addressing *NF1*, *CDKN2A*, and PRC2 inactivations: i) Selumetinib (MEKi) plus Ribociclib (CDKi); ii) Arry-162 (MEKi) plus Ribociclib; iii) Selumetinib plus I-BET151 (BETi); iv) I-BET151 plus Ribociclib. In the Materials and Methods tables MM5 and MM6 the conditions used are described. All treatments significantly reduced tumor growth compared to controls (Figure R37A), with a

trend toward greater efficacy in BETi-containing regimens, achieving a 60% tumor weight reduction compared to 40% in the MEKi-CDKi combinations (Figure R37B). No signs of toxicity or body weight loss were observed in treated mice (Figure R37C). These findings were reported to the MTB, highlighting the potential clinical benefit of BETi-based combinations; however, none of these treatments have been administered to the patient due to his current stable disease state (Figure R35).

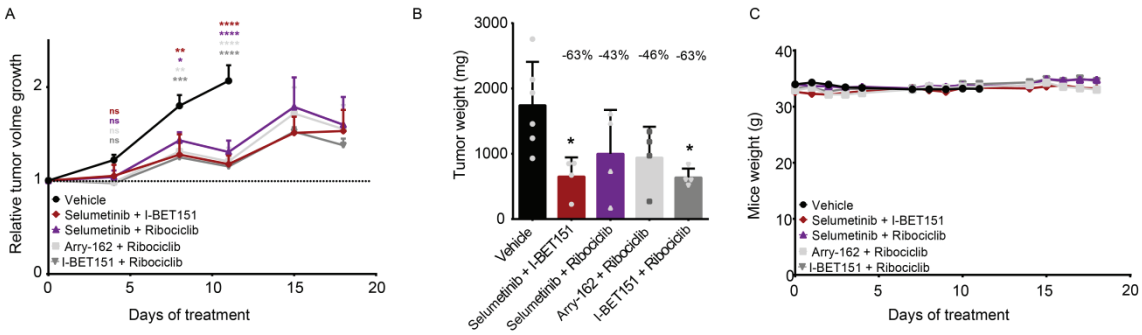

Figure R37. NF1-16C MPNST-PDOX treated with targeted drug combinations. A. Relative tumor volume growth of the NF1-16C PDOX mouse model during the three weeks of treatment in each group. **B.** Tumor weight at the end of the treatment (day 12 for vehicle group and day 18 for treatment groups). The percentages indicate the reduction in tumor weight compared to the control group. **C.** Mice weight evolution during the three weeks of treatment. The control group was sacrificed on day 12 due to mice reaching the tumor volume endpoint. Statistical Tukey test has been used: ****p-value≤0.0001, ***p-value≤0.001, ** p-value≤0.01, * p-value≤0.05.

3.2. Case 2: Sporadic MPNST Patient with Disease Progression Through Metastatic Relapses

Clinical course (Figure R38). SP-12 patient is a previously healthy 16-year-old female who first presented intermittent pain in the proximal right tibia at the age of 11. Imaging studies revealed a localized bone lesion, and biopsy confirmed the diagnosis of intraosseous MPNST (Figure R38). The tumor was surgically resected. Sixteen months later, a relapse was detected in the right femur (Metastatic relapse 1, SP-12A). Complete resection was performed, but another lesion (Metastatic relapse 2) occurred two months later, leading to treatment with seven cycles of chemotherapy (Ifosfamide and, later, Ifosfamide plus Doxorubicin) along with proton radiotherapy, achieving tumor remission. However, ten months later, another relapse (Metastatic relapse 3, SP-12B) was identified, prompting leg amputation. Subsequent metastatic relapses occurred in the sixth right rib (Metastatic relapse 4), requiring resection, followed by a relapse in the same location (Metastatic relapse 5, SP-12C), which was surgically removed and treated with radiotherapy.

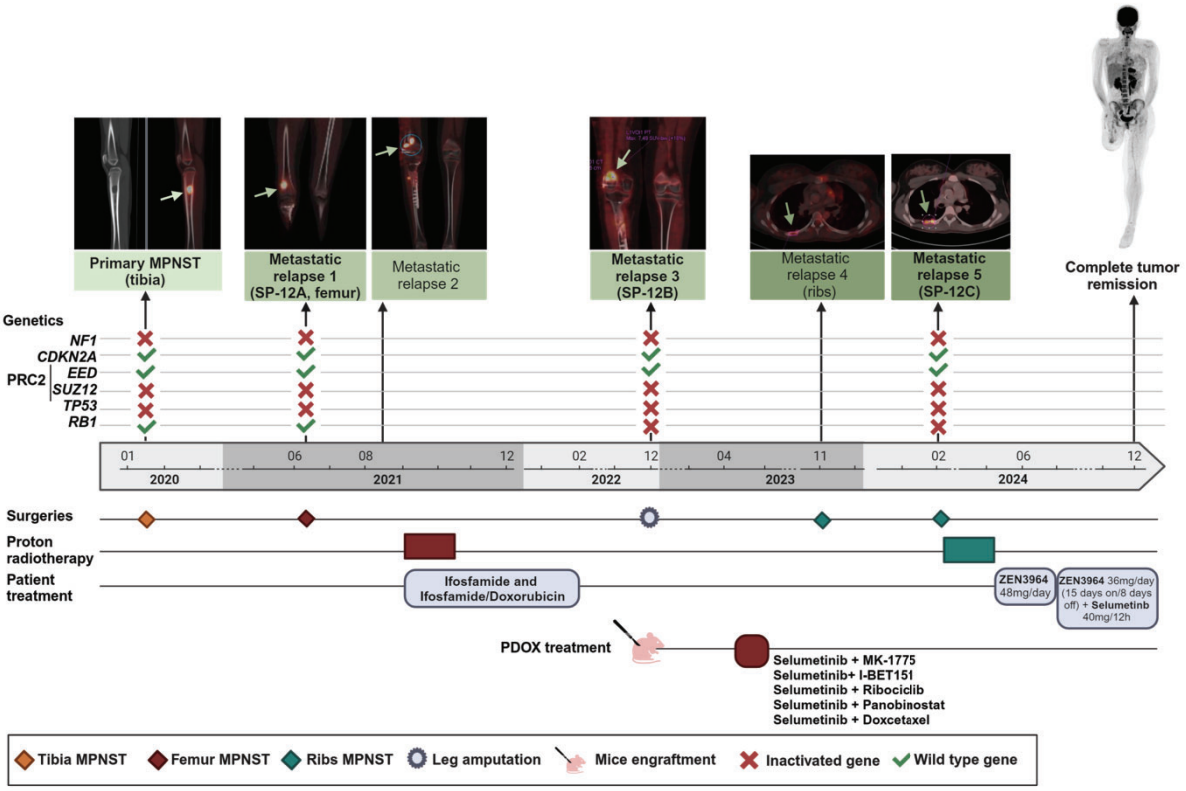

Figure R38. Timeline depicting the clinical course of the sporadic MPNST patient (SP-12). This timeline illustrates the clinical progression, treatment interventions, and parallel research conducted on patient SP-12 over time (in years and months). The upper section includes Magnetic Resonance Image (MRI) and Positron Emission Tomography/Computed Tomography (PET/CT) scans highlighting the PT and subsequent relapses: primary MPNST, metastatic relapse 1 (SP-12A), metastatic relapse 2, metastatic relapse 3 (SP-1B), metastatic relapse 4, metastatic relapse 5 (SP-12C), and eventual complete remission. The different shades of green in the lesions indicate different tumor locations: light green indicates tibia, medium green indicates femur, and dark green indicates ribs. Orange shows events associated with MPNST in the tibia, red in the femur, and green in the ribs. The multi-pointed star indicates the amputation of a patient's leg. Red X symbols denote TSG inactivating mutations, while green ticks indicate that the gene is wild type. Image created with BioRender.com.

Genomic analysis. Genomic characterization of the tibia primary tumor identified structural rearrangements leading to the inactivation of *NF1* and *SUZ12*, along with a homozygous deletion in *TP53* but no alteration of *CDKN2A* (Table R8 and Figure R39). WGS of the first metastatic relapse in the femur (SP-12A) confirmed these same pathogenic variants and a highly similar genomic structure compared to the tibial primary lesion, indicating a direct progression.

Table R8. Genetic alterations identified in SP-12 MPNST samples. Primary tumor, SP-12A, and SP-12B represent femur samples.

Sample	*NF1*		*SUZ12*		*TP53*		*RB1*	
	Allele 1	Allele 2	Allele 1	Allele 2	Allele 1	Allele 2	Allele 1	Allele 2
Primary tumor	chr17:g.31111528_34889876inv (inversion) ●	chr17:g.31113496_chr5:g.30005696 chr17:g.31204509_chr5:g.19101972 chr17:g.31217170_chr5:g.19092058 chr17:g.31281925_chr9:g.11755554 6 (translocation) ●	chr17:g.28881113_31990851inv (inversion) ●	chr17:g.32020025_33857484inv (inversion) ●	NM_001126115.1:c.168_175del ●	LOH	WT	WT
SP-12A	chr17:g.31111528_34889876inv (inversion) ●	chr17:g.31113496_chr5:g.30005696 chr17:g.31204509_chr5:g.19101972 chr17:g.31217170_chr5:g.19092058 chr17:g.31281925_chr9:g.11755554 6 (translocation) ●	chr17:g.28881113_31990851inv (inversion) ●	chr17:g.32020025_33857484inv (inversion) ●	NM_001126115.1:c.168_175del ●	LOH	WT	WT
SP-12B	chr17:g.31111528_34889876inv (inversion) ●	chr17:g.31113496_chr5:g.30005696 chr17:g.31204509_chr5:g.19101972 chr17:g.31217170_chr5:g.19092058 chr17:g.31281925_chr9:g.11755554 6 (translocation) ●	chr17:g.28881113_31990851inv (inversion) ●	chr17:g.32020025_33857484inv (inversion) ●	NM_001126115.1:c.168_175del ●	LOH	NM_000321.3:c.-198955_608-37del ●	LOH
SP-12C	chr17:g.31111528_34889876inv (inversion) ●	chr17:g.31113496_chr5:g.30005696 chr17:g.31204509_chr5:g.19101972 chr17:g.31217170_chr5:g.19092058 chr17:g.31281925_chr9:g.11755554 6 (translocation) ●	chr17:g.28881113_31990851inv (inversion) ●	chr17:g.32020025_33857484inv (inversion) ●	NM_001126115.1:c.168_175del ●	LOH	NM_000321.3:c.119del ●	LOH

The normalization of the variants was done with Mutalyzer 3. In the translocations, we indicate the position of the breakpoints where they occur. The red dot indicates inactivation of the gene, shared in several samples. The yellow and pink dot indicates an independent gene inactivation.

Later, analysis of the Metastatic relapse 3 still in the femur (SP-12B) and Metastatic relapse 5 located in the ribs (SP-12C) confirmed again the presence of the same somatic alterations in *NF1*, *TP53* and *SUZ12* and a highly similar genome structure compared to the primary tumor and to Metastatic relapse 1 (Figure R39), reinforcing a common origin. Notably, SP-12B and SP-12C acquired a *de novo* somatic inactivation of *RB1*, but with complete independent *RB1* mutations in each metastasis (Table R8 and Figure R39). This finding suggests that these two relapses originated from the primary tumor and independently acquired distinct *RB1* mutations. Furthermore, the copy-number profile across all four analyzed tumors was highly similar, providing additional evidence of a shared tumor origin (Figure R39) and demonstrating genomic stability across the different recurrences in this patient.

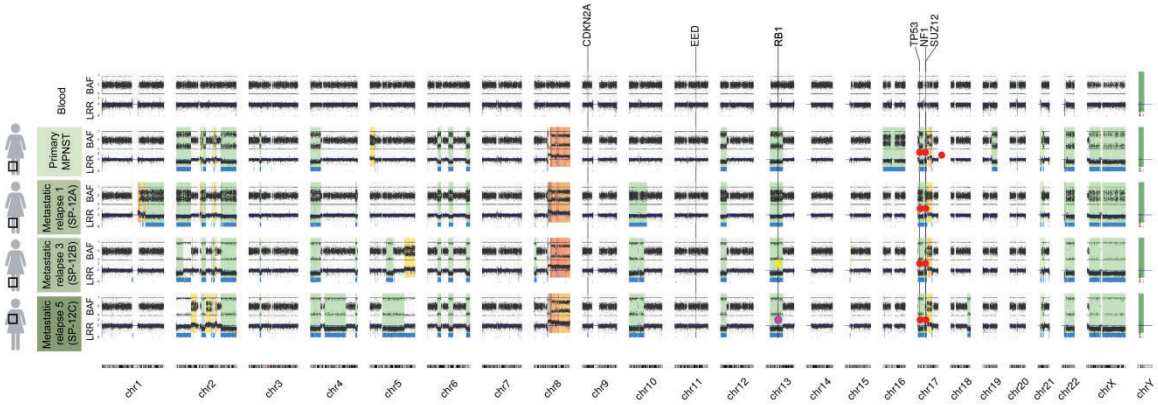

Figure R39. Copy number variation profiles of blood, primary tumor, Relapse 1 and 2 (SP-12A and SP-12B), and Metastasis Relapse 1 (SP-12C). Copy number profile from WGS data. B-allele frequency (BAF) and Log-R Ratio (LRR) are represented (see Methods for details). Warm colors represent copy number gain, whereas light green indicates heterogygous loss and dark green a homozygous loss. Loss of heterozygosity (LOH) is highlighted by a thick blue

line. The genomic location of MPNST-associated genes is indicated by a vertical black line with the gene symbol at the upper part of the graph. A red circle indicates an inactivated gene.

PDOX generation and treatment. In parallel, tumor fragments from both relapses (SP-12A and SP-12B) were engrafted in mice to generate PDOX models. Only the SP-12B tumor successfully grew after four months and was subsequently expanded. All selected treatment included the MEKi Selumetinib, due to *NF1* inactivation, in combination with various agents targeting the functional impact driven by identified mutations, such as MK-1775 (WEE1 inhibitor), for *TP53* inactivation, and I-BET151 (BETi), for PRC2 inactivation. MEKi was also combined with Ribociclib (CDKi), although no *CDKN2A* inactivation was identified, and with other previously identified compounds like Panobinostat (HDAC inhibitor, HDACi), and Docetaxel (microtubule depolymerization inhibitor).

After three weeks of *in vivo* treatment, all five combinations significantly reduced tumor growth compared to the control group, with Selumetinib + I-BET151 and Selumetinib + Docetaxel exhibiting the greatest efficacy, causing tumor volume shrinkage by a 58% and 45%, respectively (Figure R40A). On the last day of treatment, tumor weight exhibited a non-statistically significant trend towards higher tumor weight reduction in mice treated with Selumetinib+I-BET151 and Selumetinib + Docetaxel by more than 80% compared to 50-60% tumor weight reduction of the other treatments (Figure R40B).

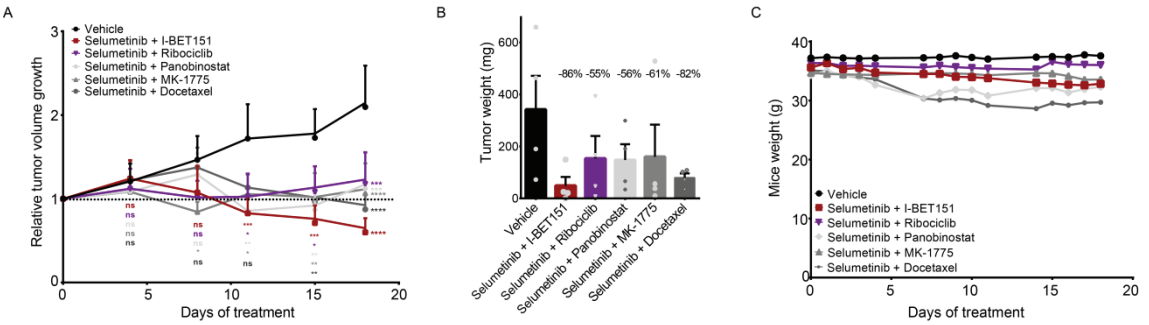

Figure R40. SP-12C MPNST-PDOX treated with targeted drug combinations. A. Relative tumor volume growth of the SP-12B PDOX mouse model during the three weeks of treatment in each group. **B.** Tumor weight at the end of the treatment. The percentages indicate the reduction in tumor weight compared to the control group. **C.** Mice weight evolution during the three weeks of treatment. Statistical Tukey test has been used: ****p-value≤0.0001, ***p-value≤0.001, ** p-value≤0.01, * p-value≤0.05.

However, Selumetinib + Docetaxel combination, alongside Selumetinib + Panobinostat, decreased mice weight around 18% and 11%, respectively (Table R9 and Figure R40C). The observed toxicity led to dose adjustments during the treatment period: Panobinostat was administered twice per week instead of three times and Docetaxel was not administered in the third week of treatment due to mouse tail necrosis. Following this dosage corrections, mice

weight remained stable for the rest of the treatment. Results on responses to drug treatments and toxicities were reported to the MTB to inform on potential other possibilities of treatment.

Table R9. Percentage of mice weight loss in the SP-12B PDOX model.

	% Mice weight reduction													
	Day 1	Day 2	Day 3	Day 4	Day 7	Day 8	Day 9	Day 10	Day 11	Day 14	Day 15	Day 16	Day 17	Day 18
Vehicle	-0,43	-0,05	0,16	0,00	-0,16	-0,38	-1,08	-0,32	0,43	-0,43	-0,70	-0,43	-1,51	-1,02
Selumetinib + I-BET151	-2,04	0,77	0,21	2,46	3,16	3,09	4,42	4,63	5,12	7,23	7,65	8,21	8,49	7,79
Selumetinib + MK-1775	0,58	0,81	0,92	1,09	0,29	0,12	0,35	0,63	1,21	0,17	0,29	1,61	3,40	3,30
Selumetinib + Ribociclib	-0,07	1,31	1,17	1,44	1,99	1,17	1,86	2,27	2,54	2,96	-0,62	0,55	0,76	0,89
Selumetinib + Panobinostat	-2,11	0,22	0,80	4,81	11,51	8,81	7,21	7,36	10,20	6,48	6,34	8,59	6,92	5,83
Selumetinib + Docetaxel	0,34	2,34	3,30	4,22	13,50	14,25	13,50	14,36	16,87	18,40	15,78	16,75	15,56	15,33

Values represent the average of mice in each group compared to day 0 of treatment. The red-green gradient represents the increase in body weight loss: the more red, the more body weight loss; the more green, the more body weight gain.

Based on these findings, the patient initiated compassionate use treatment with a combination of the MEKi and BETi provided by Alexion and Zenith Epigenetics, respectively. Given that BETis are not yet available in clinical practice, the patient was initially started on the BETi ZEN3964 (48 mg/day) as a monotherapy to assess tolerability. However, treatment was discontinued after six weeks due to grade 2 thrombocytopenia. The dose was subsequently reduced to 36 mg/day with a 15 days on/8 days off schedule, and Selumetinib (40 mg every 12 hours) was added to the regimen, which the patient tolerated well. Currently, eight months after surgery and radiotherapy, and with ongoing treatment using the two-inhibitor combination, the patient remains disease-free (Figure R38). The patient has not experienced a relapse during this period, contrasting with the short intervals between previous relapses.

Discussion

DISCUSSION

D1. *In-house* Preclinical Platform for MPNST Research

Since 2011 our group has developed a comprehensive preclinical platform integrating patient tumor samples, PDOX mouse models and tumor-derived cell lines (Castellsagué, Gel et al. 2015, Creus-Bachiller, Fernández-Rodríguez et al. 2023). This platform has been extensively characterized both genomically and histologically, serving as a versatile tool for screening new compounds (Fernández-Rodríguez, Creus-Bachiller et al. 2022), performing precision oncology strategies based on tumor-specific genomic alterations (Ortega-Bertran, Fernández-Rodríguez et al. 2024), and developing personalized treatment approaches through co-clinical studies (Fernández-Rodríguez, Morales La Madrid et al. 2020) (Figure D1).

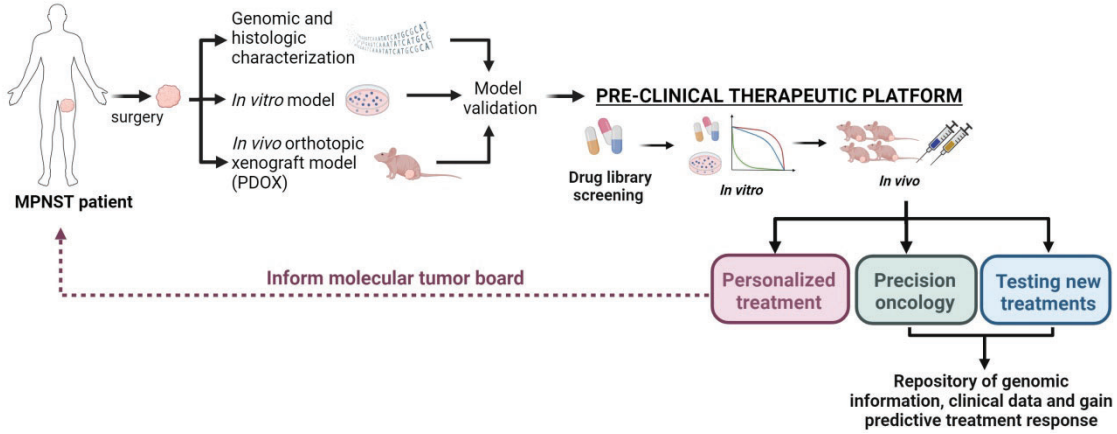

Figure D1: Workflow of the MPNST preclinical therapeutic platform developed by our group. Image created with Biorender.

Currently, the platform encompasses 41 pathologist-diagnosed MPNST samples from 29 patients (18 NF1-related, 11 sporadic), including 21 primary, 11 relapsed, and 2 metastatic tumors. We have successfully established 30 MPNST-PDOX models (16 NF1-related, 14 sporadic), achieving a 79% engraftment success rate —significantly improving upon the 50% reported for MPNST-PDX engraftments (Dehner, Moon et al. 2021). Additionally, we have developed five cell lines (three NF1-related and two sporadic). Therefore, we have generated five pairs of *in vitro/in vivo* models from the same patient: three already described in Creus-Bachiller et al. (2023) and two newly presented in Part I of the Results section of this thesis. A key advantage of this platform is its ability to capture the heterogeneity of MPNSTs by including classical MPNSTs cases with *NF1*, *CDKN2A*, and PRC2 inactivation, as well as MPNSTs that have a distinct TSG inactivation signature. Additionally, it encompasses tumors that are often mistaken for MPNSTs but belong to different entities, thereby reflecting their diverse clinical behavior.

The usefulness of this platform has been validated in multiple studies over the years. One of the earliest examples is a study published in 2013 by Mohan et al. in collaboration with our group, in which two PDOX models (MPNST-NF1-01 and MPNST-N1-02) were employed to evaluate MLN8237, an Aurora kinase A (AURKA) inhibitor, as a novel therapeutic strategy for MPNSTs (Mohan, Castellsague et al. 2013). Shortly after, Castellsagué et al. (2015) described the first characterization of four PDOX models from our platform (MPNST-NF1-01, MPNST-NF1-02, MPNST-SP-01, and MPNST-SP-02) and used them to assess the efficacy of drug combinations including Rapamycin, Sorafenib, and Doxorubicin, among others (Castellsagué, Gel et al. 2015). More recently, in 2023, our group published a comprehensive study characterizing six additional PDOX models and the first three tumor-derived cell lines established in our platform (MPNST-SP-01, MPNST-NF1-08, and MPNST-NF1-09) (article in Appendix IV) (Creus-Bachiller, Fernández-Rodríguez et al. 2023), which were used in a high-throughput screening strategy to identify novel drug combinations for MPNST treatment. This approach was published by Fernández-Rodríguez et al. (2022) and proposed Doxorubicin and MK-1775 (a WEE1 inhibitor) combination as a promising treatment for MPNSTs (article in Appendix IV) (Fernández-Rodríguez, Creus-Bachiller et al. 2022, Creus-Bachiller, Fernández-Rodríguez et al. 2023).

Ongoing efforts aim to expand the platform by incorporating additional PDOX models and improving the success rate of tumor-derived cell line isolation, which currently stands at 12.5% in our platform (5 out of 40 models). This rate is notably lower than the 25% reported for solid tumors (Kodack, Farago et al. 2017), likely due to limitations in the quantity of tumor samples received and the absence of an optimized protocol for establishing MPNST cell lines. Expanding the platform with more patient-derived models will enhance the representation of MPNST subtypes, facilitate a deeper exploration of therapeutic vulnerabilities, and increase the robustness of our preclinical findings. To address these challenges, we are actively working on optimizing protocols to improve cell line establishment and further strengthen our platform.

D2. Challenges in Expanding Preclinical *In Vitro* Models of the MPNST Platform

The development of MPNST models remains particularly challenging, mainly due to the tumor's low incidence. The *Cellosaurus* database, which compiles available MPNST cell lines, currently lists 44 MPNST-derived cell lines, from which only five are commercially accessible (ATCC, RIKEN or Roche). Furthermore, many of the models listed in *Cellosaurus* lack key information including NF1 status (sporadic vs. NF1-related) or tumor type (primary, relapse, or

metastatic). This scarcity of well-characterized preclinical models limits the validation of the studies or their translation to useful results in *in vivo* or in the clinics.

Additionally, the histological features of MPNST often overlap with those of other malignancies. Characteristics such as hypercellularity, spindle-shaped cells, scant cytoplasm, and hyperchromatic, elongated nuclei are also observed in other tumor types, including soft tissue sarcomas and melanomas (Yao, Zhou et al. 2023). Furthermore, certain markers overexpressed in MPNSTs, such as SOX9 and Nestin, are also overexpressed in both melanoma and MPNST (Bakos, Maier et al. 2010). Recently, studies have suggested that some of the most widely used sporadic MPNST cell lines may, in fact, belong to a different tumor entity (Le Guellec, Decouvelaere et al. 2016, Magallón-Lorenz, Terribas et al. 2023).

Given the challenges in distinguishing MPNST from other malignancies and the concerns regarding the authenticity of commonly used cell lines, this thesis has contributed to the MPNST scientific community by developing and characterizing two novel cell lines and PDOXs. One is derived from an NF1 patient, while the other represents the first well-characterized sporadic MPNST cell line confirmed as a genuine MPNST. These models have undergone extensive validation to ensure their genomic and histological fidelity to the primary tumors, reinforcing their relevance for preclinical research

2.1. Reproducing *In Vitro* Tumor Heterogeneity

A major challenge in developing MPNST models is the difficulty of capturing the significant intratumoral heterogeneity (Pemov, Li et al. 2020, Longo, Brosius et al. 2021). Remarkably, the NF1-18B cell line introduced in this thesis may address this issue, as it presents distinct cellular subpopulations within the culture. Specifically, two subpopulations with different ploidy states were identified by cell cycle analysis (Figure R1): one with a DNA content slightly exceeding 2n (< 3n) and another tetraploid (4n). Over successive passages, the culture gradually shifted from a predominance of “< 3n” cells to “4n” cells, suggesting a selective advantage of the tetraploid subpopulation under *in vitro* conditions. In addition, the two cell subpopulations of NF1-18B capture aspects of MPNST biology, with the "3n" line being less aggressive *in vitro* (non-colony forming, aggregate forming, and non-targeting), while the "4n" subpopulation had distinct biological characteristics, being more aggressive *in vitro* (with the ability to generate 2-D colonies, aggregate forming, and migration capacity) (Figures R4 and R5).

A similar phenomenon was previously observed in other cell lines, such as NF1-related cell line isolated in our group, NF1-09, where three distinct subpopulations (2n, 3n, and 4n) were found

(Creus-Bachiller, Fernández-Rodríguez et al. 2023). Nevertheless, in that study, no separate functional analyses were performed between these three subpopulations.

However, the isolation of such heterogeneity is largely a random process, as different tumor fragments may contain different subpopulations, and we could have used a more homogeneous fragment to generate the lines, which would have missed this heterogeneity. Furthermore, it remains unclear whether this change in subpopulation predominance also occurs *in vivo* or is an artifact of the *in vitro* culture conditions. This would require genomic analysis of PDX tumors over successive passages.

Recent analysis of a new PDOX model generated from an independent fragment of the same patient (NF1-18B) has shown a copy number profile similar to that of the < 3n line, allowing us to validate that these subpopulations were in the primary tumor (Appendix II).

2.2. Introduction of a Well-Characterized Genuine Sporadic MPNST Cell Line

As mentioned above, one of the important contributions of this thesis is the development and characterization of a genuine sporadic MPNST cell line (SP-10), faithfully recapitulating the genomic and molecular features of MPNST with a classical histology and TSG inactivation profile. This is particularly relevant given recent findings indicating that several widely used sporadic MPNST cell lines may originate from other tumor types (Le Guellec, Decouvelaere et al. 2016, Magallón-Lorenz, Terribas et al. 2023). Notably, STS-26T—one of the most commonly used cell lines in the MPNST filed—has been shown to derive from a melanoma rather than a MPNST, as it harbors the BRAF V600E mutation, a high mutational burden and a mutational signature that matches with COSMIC mutational signature 7 associated with skin cancers (Magallón-Lorenz, Terribas et al. 2023). Due to these evidence, STS-26T was excluded from this study.

Our research further reinforces these concerns, as a 2023 study from our group found that three out of four analyzed sporadic MPNST tumors (75%) lacked genomic features consistent with MPNST (Creus-Bachiller, Fernández-Rodríguez et al. 2023). Considering these findings, WGS has been proposed as a reliable approach to distinguish true MPNSTs when combined with pathology analysis (article in Appendix IV) (Magallón-Lorenz, Terribas et al. 2023). Accordingly, we applied WGS to our newly developed cell lines to assess all sorts of alterations, including structural variants, affecting key tumor suppressor genes. This analysis confirmed that both cell lines represent classic MPNSTs. Specifically, the sporadic SP-10 cell line harbors

inactivating alterations in *NF1*, *CDKN2A*, and *SUZ12/EED* (PRC2)—the TSG inactivation signature present in classic MPNSTs—validating its genuineness as a sporadic MPNST model.

D3. A Precision Oncology Approach for Targeting MPNST TSG Inactivation

The second main objective of this thesis was to use the models in our preclinical platform to evaluate the therapeutic potential of a precision medicine strategy targeting the inactivation of TSGs (*NF1*, *CDKN2A*, and PRC2) in MPNSTs. To our knowledge, this approach represents the first systematic effort to assess the efficacy of multiple MEK, CDK, and BET inhibitors for MPNSTs.

In this thesis we implemented a HTS strategy in collaboration with Dr. Marc Ferrer from NCATS to systematically and rapidly evaluate large panels of compounds for biological activity at the cellular, molecular, or pathway level (Chang, Oblinger et al. 2021, Fernández-Rodríguez, Creus-Bachiller et al. 2022). Specifically, we employed the MIPE 4.0 library (NIH-NCATS), which comprises small molecules with known mechanisms of action, including 767 preclinical investigational drugs, 420 agents in clinical trials, and 745 FDA-approved drugs (Chang, Oblinger et al. 2021). The inclusion of multiple redundant agents within each therapeutic class allowed the analysis of phenotype-mechanism associations and how the polypharmacology of individual drugs contributes to their observed effects. Our research group had previously applied a HTS strategy of the nearly 2,000 compounds of the MIPE 4.0 library, both as single agents and as pairwise combinations (Fernández-Rodríguez, Creus-Bachiller et al. 2022). In this study, we selected all MEK, CDK, and BET inhibitors from MIPE 4.0 library and tested them in three NF1-related MPNST cell lines (S462, NF1-08, and NF1-09) and a human fibroblast cell line for toxicity assessment. Overall, the HTS strategy analyzed the efficacy of 28 compounds as single agents and the synergy of 147 pairwise combinations of these three compound classes in 10 x 10 concentration matrices. We then selected 26 combinations for further validation of their synergy in our lab in a large panel of MPNST cell lines, to finally validate the three most promising combinations *in vivo* in two MPNST-PDOX models.

3.1. Rationale for Therapeutically Targeting Tumor Suppressor Gene Loss in Early MPNST Development

A precision medicine approach targeting TSG loss is a promising strategy for MPNST treatment due to the recurrence in the inactivation of the same TSGs during MPNST development. We hypothesized that MPNST generation can be divided in three phases. In the first phase, key TSGs such as *NF1*, *CDKN2A*, and PRC2 components *SUZ12/EED* are recurrently inactivated,

constituting an early event in classic MPNSTs, that constitute the largest proportion of diagnosed MPNSTs (Hirbe, Dahiya et al. 2015). In a second phase, a catastrophic event remodeling MPNST genome occurs, producing many structural rearrangements, LOH and CN alterations. Although the molecular mechanism behind these genomic events is not well-known, they could be important for tumor intra- tumor heterogeneity present in MPNSTs (Pemov, Li et al. 2020). Finally, a third phase, the tumor reaches a relatively stable state, preserving the genomic landscape, although minor modifications may still arise during MPNST progression.

The therapeutic advantage of the precision medicine strategy performed lies in the fact that since TSG inactivation is an early event, it affects all tumor cells bringing homogeneity to their therapeutic targeting. In contrast, drugs targeting other altered pathways occurring later in MPNST progression, may face significant challenges related to tumor heterogeneity according to the altered status, as these alterations may not be shared by all tumoral cells, increasing the likelihood of resistance mechanisms and reducing treatment efficacy. However, focusing on TSG loss also presents limitations, since subsequent positively selected genomic alterations may override the effects of the targeted therapies, requiring a broader therapeutic approach accounting for later stages of tumor evolution to achieve treatment response.

3.2. Robust Strategy with High Compound Redundancy

This study represents the first comprehensive comparison of all MEK (14), CDK (11), and BET (3) inhibitors included in the MIPE 4.0 library, encompassing both FDA-approved drugs and those in preclinical development. This broad analysis provides a robust understanding of the mechanisms of action of these compounds, offering valuable insights into their commonalities and specificities concerning therapeutic potential.

During *in vitro* validation, we observed a high degree of redundancy in the treatment response within each inhibitor class. Specifically, if a given MEK inhibitor was effective in a particular cell line, other MEK inhibitors exhibited a similar response in the same line. This redundancy across inhibitors of the same class was consistently observed throughout all validation phases.

In the initial HTS of single agents, for example, almost none MEK inhibitor was effective in the NF1-09 cell line, whereas most showed efficacy in S462 and NF1-08 (Figure R9). This trend persisted in the second phase of HTS, where MEK-BET inhibitor combinations failed to demonstrate synergy in NF1-09 (Figure R10). Finally, during the validation of 26 combinations in the laboratory, we observed nearly identical viability curves for inhibitors targeting the same

pathway (Figure R12, R13, R14, R16), further highlighting the functional redundancy within each inhibitor family.

3.3. Role of Additional Genetic Factors in Treatment Response

Despite the redundancy observed within each inhibitor class, we noted differences in treatment sensitivity across the nine MPNST cell lines used in this study, even though almost all of them harbor mutations in *NF1*, *CDKN2A,* and PRC2. The NF1-09 cell line stands out as the only one lacking inactivation of all three TSGs. Instead, it is WT for PRC2 and harbors an activating mutation in phosphoinositide 3-kinase (*PI3K*) (Figure R8). Our results suggest that this *PI3K* mutation may play a significant role in drug response, as NF1-09 exhibited resistance to MEKi. Previous studies have reported that tumor cells with WT *PI3K* tend to be sensitive to MEKi, whereas those harboring *PI3K* mutations are resistant (Halilovic, She et al. 2010). Furthermore, Kim et al. (2020) demonstrated the interconnection between *PIK3* and RAS pathways, showing that inhibition of one can lead to compensatory activation of the other, ultimately resulting in treatment failure (Kim, Lee et al. 2020). Most recently, Madsen et al. (2025) reported *PIK3CA* mutation enhances RAS interaction, increasing EGFR signaling and contributing to tumor heterogeneity and therapeutic resistance (Madsen, Le Marois et al. 2025).

In contrast, the remaining eight MPNST cell line all exhibited inactivation of the three TSGs, yet they displayed differential sensitivities to treatment, suggesting that drug response cannot be fully explained by these mutations alone. This highlights the potential role of additional genetic or genomic factors in shaping treatment efficacy.

To explore this hypothesis, we investigated the role of *TP53*, a gene known to play a critical role in MPNST pathogenesis and therapy resistance (Verdijk, den Bakker et al. 2010, Fernández-Rodríguez, Creus-Bachiller et al. 2022). Using CRISPR-Cas9, we silenced *TP53* in the ST88-14 MPNST cell line to assess its impact on drug response (results provided in Appendix III). Based on previous findings (Creus-Bachiller, Fernández-Rodríguez et al. 2023), we anticipated that *TP53* knockout (KO) clones would exhibit increased sensitivity to selected drug treatments, particularly to MK-1775 (a WEE1 inhibitor), given its synthetic lethality in *TP53*-mutant contexts. However, our results showed the opposite trend—homozygous *TP53* KO clones were less sensitive to all tested drug combinations compared to the parental ST88-14 WT cells. This suggests that complete loss of p53 may activate alternative survival pathways, potentially leading to therapy resistance rather than sensitization. Additionally, heterozygous

TP53 KO clones showed treatment responses similar to the parental line, indicating that a single functional *TP53* allele may retain partial tumor suppressor activity.

To develop a more comprehensive understanding of treatment response in MPNSTs, further investigations are needed to explore additional genes and pathways involved in drug sensitivity and resistance. This knowledge will not only enhance our understanding of the mechanisms driving drug susceptibility but also aid in identifying targeted therapies that can overcome resistance mechanisms, ultimately leading to more effective treatment strategies for MPNST patients.

3.4. Sequential Enhancement of Therapeutic Efficacy: From Single Agents to Triple Combination Therapy

A key finding of this study is the sequential improvement in therapeutic efficacy observed when progressing from single-agent treatments to dual and ultimately triple drug combinations. Our *in vivo* results demonstrate that while MEK and BET inhibitors exhibit some efficacy as monotherapies, their combination significantly enhances tumor response. Moreover, the addition of a CDK inhibitor further potentiates this effect, establishing the triple combination as the most effective strategy tested so far.

In our PDOX models, MEK-BET inhibition (Arry-162 + I-BET151) reduced tumor volume by 65% in the sporadic SP-10 model and stopped tumor growth in the NF1-18B model after two weeks of treatment. However, when incorporating the CDK inhibitor Ribociclib into the regimen, the triple combination (Arry-162 + I-BET151 + Ribociclib) achieved an 85% tumor reduction in the sporadic PDOX model and a 50% greater effect in NF1-related tumors compared to MEKi-BETi alone. These results underscore a clear stepwise enhancement in treatment efficacy with increasing drug complexity. Importantly, this escalation in therapeutic potency did not lead to significant toxicity in the treated mice, highlighting the feasibility of this strategy.

The combination of MEK and BET inhibitors has been previously explored in MPNST, with studies in GEMMs demonstrating significant tumor shrinkage of 67% (De Raedt, Beert et al. 2014, Echevarría-Vargas, Reyes-Uribe et al. 2018). These models have been instrumental in identifying promising therapeutic strategies and understanding tumor biology. However, PDOX models, derived from human tumors, offer complementary advantages by preserving the genetic heterogeneity and tumor microenvironment of patient samples, allowing for a more clinically relevant assessment of drug response (Mohamad, Plante et al. 2021). Contrarily, due to immunodeficiency constraints of our PDOX models, testing immunotherapy-based

approaches were not feasible. There is currently a clinical trial (NCT05253131) evaluating a triple combination of MEKi-BETi with a PD-L1 inhibitor in patients with MPNST.

As ongoing work in the group, we are trying to repeat this triple treatment in four more PDOX models (two sporadic and two NF1-related) to have a total of six models, to evaluate how general is this impressive therapeutic response in light of the existing MPNST diversity.

D4. MEKi-BETi Combination: Which Therapeutic Mechanism?

To elucidate the mechanism driving tumor reduction in PDOX models treated with MEKi-BETi combination, we conducted a series of analysis aimed at identifying potential cellular and microenvironmental contributors to this effect. Given that BETis are epigenetic modulators, our initial hypothesis was that this combination therapy might reverse the gene expression alterations associated with PRC2 loss. However, RNA-seq analysis of cells treated with BETi and MEKi-BETi revealed transcriptomic profiles remarkably similar to those of untreated controls (Figure R25). This unexpected finding suggests that the observed tumor reduction is unlikely to result from a direct transcriptional reversion of PRC2-related gene expression changes.

So, we went on to evaluate other potential aspects driving tumor reduction. We assumed that the combination was somehow eliciting cytotoxicity, because of the 65% reduction in sporadic tumors, although other groups have favored the view that BETi predominantly exerts cytostatic effects by inducing cell cycle arrest (Leal, Williams et al. 2017). To analyze that, we first analyzed the cell cycle in cells treated and amount of mitosis in tumors treated, and both showed significantly reduced tumor cell proliferation (Figure R27). The detection of apoptosis was complicated to interpret: meanwhile a significant BIM-dependent apoptosis was observed, we did not detect the implication of caspases in this process (Figure R28) (Gallagher, Mijatov et al. 2014, Patel, Liao et al. 2014). These findings suggest that the MEKi-BETi combination may elicit a combined response, with cytostatic effects evidenced by a clear reduction in proliferation, and cytotoxicity somehow related to BIM.

Other works have described that the use of BETis impacts the MPNSTs tumor microenvironment composition. Leal et al (2017) published that tumor shrinkage in murine models is caused by a reduction of cytokines production and the release of nitric oxide by macrophages (Leal, Williams et al. 2017); and unpublished data of Dr. Thomas De Raedt found a significant reduction in F4/80 and CD163 positive M2 macrophage population when tumors are treated with a MEKi-BETi combination. Moreover, in leukemia BETi treatment has been shown to enhance the efficacy of immunotherapy by reducing macrophage populations and

altering the immune landscape (Romine, MacPherson et al. 2023). Based on these findings, in our study we analyzed the macrophage population of treated PDOX tumors, detecting a non-significant reduction in the M2 macrophage population (Figure R29), but suggesting that immune modulation may contribute to PDOX tumor regression. The use of athymic mice has limited the research of other immune populations in the tumor microenvironment, that would require the use of humanized mice (Byrne, Alférez et al. 2017).

Nonetheless, further studies are warranted to fully elucidate the role of the tumor microenvironment in mediating the therapeutic effects of MEKi-BETi. Future investigations should expand beyond macrophage populations to evaluate the involvement of other immune cell subsets, such as natural killer (NK) cells, and assess cytokine profiles in treated versus untreated tumors. A comprehensive understanding of these interactions may pave the way for the development of more effective combination therapies that leverage both direct tumor-targeting and immune modulating strategies.

All these studies were conducted with dual therapy only, as the testing of triple therapy came later. Nevertheless, we could speculate that the effect of Ribociclib in this doublet regimen could provide a cytostatic effect, as this inhibitor has been described as having more cytostatic than cytotoxic functions (Wang, Calizo et al. 2023). In addition, the use of MEKi combined with CDK4/6i has been described to induce plasma cell-associated immune response and extended antitumor activity in MPNSTs, enhancing anti-PD-L1 therapy (Kohlmeyer, Lingo et al. 2023).

D5. Challenges in Translating Preclinical Findings to Clinical Trials

Translating preclinical findings into clinically effective treatments remains a major challenge in cancer research. While *in vitro* and *in vivo* models provide valuable insights, their inherent limitations can lead to discrepancies in treatment responses, complicating the prediction of clinical outcomes. This section discusses challenges associated with these models that we encountered, including inconsistencies in drug efficacy, toxicity assessment, and the optimization of *in vivo* treatment regimens.

5.1. Reproducibility Between *In Vitro* and *In Vivo* Drug Responses

During our co-treatment validation, we observed notable differences in drug responses among *in vitro* and *in vivo* models. The SP-10 model exhibited limited sensitivity to treatments *in vitro*, with only 2 out of the 6 tested combinations reducing cellular viability by at least 50% (Figure R16). In particular the Arry-162 + I-BET151 combination achieved only 60% of the reduction in

cell viability *in vitro*. However, in clear contrast, SP-10 PDX showed the best therapeutic response *in vivo* (Figure R21). Conversely, the NF1-18B model displayed strong *in vitro* sensitivity, achieving 100% reduction in viability across all six tested combinations -particularly with Arry-162 + I-BET15 (Figure R16). Yet, when tested *in vivo,* the same treatments led to varying degrees of tumor growth inhibition, with some combinations showing significant effects while others resulted in only partial responses (Figure R19).

Given that both *in vitro* and *in vivo* models were derived from the same patient tumor, we initially expected a higher degree of correlation in drug response, as they share an identical genetic background. However, such discrepancies are widely documented in cancer research (Ho, Pittet et al. 2022). Several factors likely contribute to these differences, including lack of a tumor microenvironment *in vitro*, which plays a crucial role in drug response, pharmacokinetic and pharmacodynamics factors exclusive to *in vivo* conditions, and resistance mechanisms mediated by stromal interactions, which cannot be replicated in 2-D cell culture (Mainardi, Mulero-Sánchez et al. 2018).

PDOX models better preserve tumor heterogeneity, histological architecture, and critical tumor-stroma interactions, making them a more accurate representation of *in vivo* tumor behavior (Kim, Stewart et al. 2017). In contrast, while *in vitro* cell lines are convenient for high-throughput drug screening, they undergo selective pressures that may lead to loss of cellular heterogeneity and thus fail to fully recapitulate *in vivo* drug responses. Therefore, it is essential to advance towards more complex 3-D models that better replicate the cellular and microenvironmental conditions of tumors *in vivo*. By incorporating key aspects of tumor architecture and interactions, these models can provide a more physiologically relevant platform for studying tumor biology and therapeutic responses.

Overall, while using matched *in vitro/in vivo* models from the same tumor is a valuable strategy to improve translational research, although some degree of discrepancy exists. This highlights the complementary nature of both approaches—with *in vitro* models serving as a convenient pre-screening tool, and *in vivo* models providing a more clinically relevant validation step in the drug development pipeline.

5.2. Widening the Therapeutic Efficacy vs Toxicity Window of Opportunity

Achieving an optimal balance between drug efficacy and toxicity is a key challenge in cancer treatment. This requires rigorous evaluation in both *in vitro* and *in vivo* models to refine therapeutic regiments while minimizing adverse effects.

5.2.1. *In vitro* Toxicity Assay

In vitro toxicity assays provide an initial assessment of potential off-target effects, allowing for an early elimination of highly toxic compounds before proceeding to *in vivo* drug testing. In our study, HFF fibroblasts were used as a non-tumor control to evaluate drug cytotoxicity. This strategy was crucial in identifying the combination of I-BET151 + Palbociclib as a treatment regimen with high toxicity, avoiding unnecessary *in vivo* testing (Figure R15).

Another example of using HFF cells as a toxicity control is described in another paper published by our group in 2022, where Panobinostat (HDACi) was used in combination with proteasome or mTORC1 inhibitors and showed significant toxicity in HFF cells, which was overlooked. When this combination was tested *in vivo*, it caused a high toxicity in mice (Fernández-Rodríguez, Creus-Bachiller et al. 2022).

5.2.2. *In vivo* Regimen Optimization

Determining the optimal *in vivo* dosing regimen is critical for ensuring therapeutic efficacy while minimizing toxicity. Achieving the right balance between anti-tumor activity and tolerable side effects requires careful dose fine-tuning and administration schedule adjustments. A key step in this process is performing a MTD assay before initiating *in vivo* testing. However, one major limitation of MTD assays is that they are typically conducted in healthy mice, which may tolerate higher drug doses than tumor-bearing mice due to disease-related metabolic differences.

A clear example of this dose-dependent toxicity challenge emerged during our *in vivo* validation of drug combinations in Part II of this thesis. We conducted an MTD assay for all tested compounds (Figure R18), and while Ribociclib and Arry-162 were well tolerated in both healthy and tumor-bearing mice, the case of I-BET151 was notably different. In healthy mice, 30 mg/kg (administered five days per week) was well tolerated. However, when applying this same dose to the SP-10 PDOX model, we observed significant weight loss and, in some cases, mortality (Figure R21E). As a result, we adjusted the regimen to 25 mg/kg, administered three times per week, which successfully reduced toxicity while maintaining efficacy. The toxicity of

I-BET151 was not unexpected, as it has been previously documented (Jing, Zhang et al. 2016, Yin, Guo et al. 2020). Anticipating potential adverse effects, we initially used a reduced dose in the NF1-18B PDOX model, prioritizing a cautious approach before testing higher doses.

Another example of dose-dependent toxicity and efficacy can be seen in the same Panobinostat study discussed above. When tested *in vivo* at 10 mg/kg, Panobinostat caused severe toxicity, whereas reducing the dose to 5 mg/kg made it well tolerated—but at the cost of losing its antitumor effects (Fernández-Rodríguez, Creus-Bachiller et al. 2022).

D6. Personalized Treatment Strategies and Molecular Tumor Board Integration

In Part III of this thesis, we present a personalized medicine approach that integrates comprehensive genomic analysis with PDOX model generation to provide additional possibilities to the treatment decisions need to be made for MPNST patients (Figure D1). By combining genomic profiling with preclinical testing, this strategy facilitates the identification of targeted therapies tailored to the molecular landscape of each tumor. We used this strategy for two MPNST patients -one NF1-related and one sporadic. The long clinical histories of these patients illustrate the significant challenges in identifying effective therapies (Figures R35 and R38).

In both cases, treatment selection was based on the well-established and supported principle that combination therapy is much more effective than monotherapy for MPNSTs. Consequently, we bypassed single agent testing and directly evaluated combination regimens predicted to be effective based on genomic analysis. In the NF1-associated case (NF1-16C), genomic profiling revealed inactivation of *NF1, CDKN2A* and PRC2, leading to the selection of Selumetinib + Ribociclib, Selumetinib + I-BET151, Arry-162 + I-BET151, and I-BET151 + Ribcoiclib for testing in the PDOX model. All four tested combinations successfully slowed tumor growth compared to the control (Figure R37). However, due to the stable nature of the patient's disease, none of these treatments have yet been administered (Figure R35).

In contrast, the sporadic case exhibited inactivation of *NF1*, PRC2, and *TP53*. This genomic profile guided the selection of MEKi to be combined with CDKi, BETi, WEE1 inhibitors (WEE1i), but also tried with additional potential treatments like HDAC inhibitors (HDACi), or the combination of MEKi with chemotherapy agents like Docetaxel. After three weeks of PDOX treatment, the MEKi-BETi combination resulted in a 65% tumor volume reduction (Figure R40), aligning with the regimen ultimately selected for precision medicine treatment in Part II. The MEKi-Docetaxel (chemotherapy) combination also demonstrated efficacy but caused

significant toxicity in mice, resulting in an 18% reduction in body weight. Before the preclinical results could be fully analyzed and reported to MTB, the patient experienced a metastatic relapse and TMB decided to treat the patient with the MEKi-BETi combination, which needed to be adjusted for several weeks due to side effects of BETi. Finally, the combination was possible to be provided. Eight months after surgery and radiotherapy of the metastatic relapse, and with ongoing treatment using the two-inhibitor combination, the patient remained disease-free (Figure R38).

6.1. Genomic Stability and Its Implications for MTB-Driven Treatment Strategies

A critical question related to the personalized treatment strategy adopted was whether recurrent or metastatic tumors would have the same sensitivity to therapy as the primary tumor, given that the tumor may change along progression. Genomic studies performed in multiple lesions across time in the two patients showed for the first time that MPNST genomes remain fairly stable in terms of global structure and tumor burden throughout disease progression (Figures R36 and R39). These results are in line with our view of MPNST formation in which the genome of MPNSTs achieves a fair stabilization after going through a catastrophic genomic event making tumors viable. This is the first demonstration of genomic stability in human MPNSTs, since prior evidence were limited to genomic analysis performed in PDX and cell line models along passages (Figure R6). However, new mutations can emerge during metastasis, as observed in our study with the independent inactivation of *RB1* in two different metastatic relapses (Godec, Jayasinghe et al. 2020) (Table R8).

The only published data on the genomic stability of human MPNSTs come from two studies of Angela Hirbe's group (Hirbe, Dahiya et al. 2015, Godec, Jayasinghe et al. 2020), which demonstrated that metastatic lesions share a clonal origin within the primary tumor. These studies suggest that metastatic potential is already present within the primary tumor (Godec, Jayasinghe et al. 2020) in agreement with our findings. The observed genomic stability along disease progression supports the idea that identified effective precision oncology treatments in the primary tumor may also be effective in later stages of disease. This underscores the importance of establishing PDOX models from primary tumors, as they may inform on the effectivity of treatments for future relapses without the need to test drugs in each lesion, also reducing the time needed for these studies.

6.2. Limitations of Our Personalized Treatment Strategy

Despite its potential, our personalized medicine approach is not exempt of limitations. One of the major limitations is the time required for obtaining *in vivo* pre-clinical information, a process that includes an initial PDOX generation phase (ranging from 2 to 5 months; sometimes longer), the expansion of the tumor PDX (approximately 1 month), and the treatment phase (1 additional month), lasting for about 6 months. This timeframe is heavily influenced by the tumor growth rate in mice, making this approach most suitable for patients with stable disease who are not in urgent need of treatment, providing potential opportunities in case of relapse. Furthermore, performing WGS to analyze the tumor's genomic landscape and identify altered pathways for targeted treatment selection is another time-consuming process. This can be partially overcome by using immunohistochemistry against the most frequently lost TSGs.

All these aspects challenge conducting previous *in vivo* studies to determine MTDs, particularly if an untested treatment is selected. The inability to conduct these preliminary toxicity studies may pose a significant obstacle when initiating treatment, as there is limited flexibility if unexpected toxicity arises, as observed in our experience with Selumetinib + Panobinostat or Selumetinib + Docetaxel, for instance.

Another limitation is the feasibility of real-time treatment adaptation. To fully replicate the patient's treatment history, mice would need to undergo the same therapeutic regimens to account for molecular adaptations induced by prior therapies. The rapid growth rate of these tumors together with the time constraints associated with a co-clinical pilot study further complicates efforts to model treatment-induced resistance in real time. Our group has been able to partially account for treatment resistance in a previous personalized medicine case (Fernández-Rodríguez, Morales La Madrid et al. 2020).

Drug availability in clinical practice is another limitation. In our study, combinations including a BETi showed the most promising results; however, BETi are not yet approved for clinical use. This delay in access to potentially effective therapies highlights the urgent need for expedited clinical trials and regulatory approvals to integrate innovative treatments into the standard care regimen for aggressive malignancies such as MPNSTs.

Finally, while our patients exhibited local relapses, they also developed metastasis, which our PDOX model was not designed to replicate. Developing a metastatic model requires the removal of the primary tumor followed by monitoring for metastatic progression, a process

that is difficult to achieve within the real-time constraints of co-clinical studies. Establishing a reliable metastatic PDOX model would be beneficial for better understanding tumor dissemination and testing therapies specifically targeting metastatic disease.

D7. Differential Sensitivity of Sporadic vs. NF1-Associated MPNSTs to Treatment

Another intriguing result derived from the *in vivo* experiments performed in this thesis is the different efficacy obtained using the same treatment combinations in sporadic and NF1-associated MPNST models. Sporadic PDOX models SP-10 and SP-12B exhibited substantial tumor volume reduction of 60% following Arry-162 + IBET151 treatment (Figures R21 and R40). In contrast, in the NF1-associated models NF1-18B and NF1-16C, the same treatment only reached tumor growth arrest, with a slight reduction in tumor volume in few cases of NF1-18B (Figures R19 and R37).

Preclinical data directly comparing treatment responses between these two MPNST subtypes remain limited. Most prior studies have primarily employed NF1-associated MPNST PDX models (e.g., S462, 90-8TL, sNF96.2, MPNST cell lines), precluding direct comparisons (Jessen, Miller et al. 2013, Yamashita, Baia et al. 2014, Kohlmeyer, Kaemmer et al. 2020). While the STS-26T PDX model has been occasionally used (Semenova, Stepanova et al. 2017), its classification as melanoma cell line (Magallón-Lorenz, Terribas et al. 2023) renders its results non-comparable.

Clinically, retrospective studies also support our observed differences in treatment response. One study reported a lower chemotherapy response rate in NF1-associated MPNSTs (17.9%) compared to sporadic cases (44%) (Higham, Steinberg et al. 2017). Another study (abstract only; Davis E. et al 2019) reported an OS of 24.5 months for NF1-associated MPNSTs, compared to 48 months for sporadic cases.

The underlying reasons for this discrepancy remain unclear. A study by Watson et al. (2017) suggested that the poorer prognosis in NF1-associated MPNSTs may be attributed to factors such as larger tumor size, unfavorable truncal location, and lower rates of negative resection margins compared to sporadic tumors (Watson, Al Sannaa et al. 2017). However, our mentioned discrepancies between *in vitro* and *in vivo* results, particularly for NF1-associated MPNSTs, opens the possibility of a different response of sporadic vs NF1-associated MPNST tumoral cells to the effects of tumor microenvironment upon combination treatments. Further investigations are needed to elucidate the molecular and microenvironmental differences that contribute to these distinct treatment responses.

D8. Integrating Genomic Insights, Preclinical Models, and Clinical Collaboration: A Comprehensive Approach to Precision Oncology

This thesis highlights the importance of the synergy between the characterization of MPNST genomics, the establishment of patient-derived models, and the translation of preclinical data to the MTB for widening the options of treatment for specific MPNST cases. By developing robust and genuine preclinical models of classic MPNSTs, we have tested novel treatment approaches targeting tumor-specific molecular vulnerabilities such as the triple combination of MEK, CDK and BET inhibitors, achieving tumor shrinkage in two PDOX models.

Our preclinical findings have also actively contributed to discussions with MTBs in a personalized medicine strategy, demonstrating how patient's tumor genomic profiling guiding precision oncology strategies combined with preclinical drug testing in PDOX avatar models improves clinical decision-making.

By combining basic research, tumor modeling, preclinical studies, and clinical collaboration, this work exemplifies a comprehensive approach for precision oncology. It underscores the value of continuous interaction between research and clinical teams, ensuring that molecular insights translate into actionable therapeutic strategies. Ultimately, this thesis provides a framework for improving treatment selection and testing, and for closing the gap between laboratory discoveries and clinical applications.

Conclusions

CONCLUSIONS

1. Our preclinical MPNST platform, which integrates patient-derived cell lines and PDOX mouse models, is a robust and versatile tool for the evaluation of novel therapeutic agents, the testing of precision oncology strategies and the implementation of real-time co-clinical personalized medicine approaches in MPNST patients.

2. We expanded the preclinical MPNST platform by establishing two new MPNST-derived cell lines and two PDOX models from the same MPNSTs, one from an NF1 patient (NF1-18B) and the other from a sporadic tumor (SP-10), constituting two *in vitro/in vivo* models. Remarkably, the SP-10 cell line is to date, one of the few existing well-characterized and genuine sporadic MPNST models. Genomic and histological analyses confirm that these models faithfully recapitulate the features of their primary tumors, maintaining their genomic and phenotypic stability along model generation and expansion.

3. In this study we represent the first robust and systematic high-throughput screening approach to evaluate the efficacy of targeting the loss of *NF1*, *CDKN2A*, and *EED*/*SUZ12* genes, by using a large panel of MEK, CDK, and BET inhibitors alone and in combinations. *In vitro* validation confirmed the synergy of selected drug combinations, revealing functional redundancy among inhibitors of the same class. However, other genetic or genomic factors beyond the triple TSG inactivation also have an influence on treatment response.

4. The combination of Arry-162 (MEK inhibitor, MEKi) and I-BET151 (BET inhibitor, BETi) show the best treatment response among the *in vivo* tested pairs of inhibitor classes. This co-treatment leads to a 65% reduction in tumor volume in the sporadic PDOX model and induces tumor growth arrest in the NF1-related PDOX. Treatment withdrawal allows tumor regrowth, although sensitivity to the combination is retained.

5. Triple combination of Arry-162 (MEKi), I-BET151 (BETi) and Ribociclib (CDKi) further enhances treatment efficacy *in vivo*. This regimen outperforms MEKi-BETi co-treatment, achieving up to an 85% tumor volume reduction in the sporadic PDOX model, with an apparent complete remission for some tumors. In the NF1-related MPNST PDOX model, which is more resistant to treatment than the sporadic model, the therapeutic efficacy is improved by 50%.

6. The mechanism of action of BETi treatment does not seem related to a transcriptional change of bromodomain-regulated genes. MEKi-BETi co-treatment elicits a combined response involving a significant reduction in tumor cell proliferation and an effect through tumor immune microenvironment, possibly by reducing the proportion of M2 macrophages. Further studies are needed to fully elucidate the mechanisms underlying the anti-tumor effects of both the MEKi-BETi and the MEKi-BETi-CDKi regimens.

7. We have developed a strategy for co-clinical personalized medicine for MPNSTs, consisting in performing *in vivo* precision oncology treatments, guided by MPNST genomic analysis, on PDOX generated from the same patient's MPNSTs. We applied this strategy in two MPNST patients, providing molecular tumor boards with novel therapeutic opportunities. The combination of MEK and BET inhibitors demonstrated the highest efficacy among the different tested treatments, achieving a 60% tumor reduction in the sporadic MPNST case, which is currently being treated with this therapeutic regime.

8. Local and metastatic MPNST recurrences along disease progression show a fair degree of genomic stability, supporting the validity of our personalized medicine strategy based on targeting initial but homogeneous genetic alterations in MPNSTs, such us the TSG inactivation profile.

Bibliography

BIBLIOGRAPHY

A

Abdolahi, S., Z. Ghazvinian, S. Muhammadnejad, M. Saleh, H. Asadzadeh Aghdaei and K. Baghaei (2022). "Patient-derived xenograft (PDX) models, applications and challenges in cancer research." J Transl Med **20**(1): 206.

Abdulkareem, N. M., R. Bhat, R. T. Powell, S. Chikermane, S. Yande, L. Trinh, H. Y. Abdelnasser, et al. (2022). "Screening of GPCR drugs for repurposing in breast cancer." Front Pharmacol **13**: 1049640.

Abeshouse A , et al. (2017). "Comprehensive and Integrated Genomic Characterization of Adult Soft Tissue Sarcomas." Cell **171**(4): 950-965.e928.

Acem, I., E. Martin, W. J. van Houdt, M. A. J. van de Sande, D. J. Grünhagen, C. Verhoef and Monaco Collaborators (2021). "The Association of Metastasis Pattern and Management of Metastatic Disease with Oncological Outcomes in Patients with Malignant Peripheral Nerve Sheath Tumors: A Multicenter Cohort Study." Cancers (Basel) **13**(20).

Amirnasr, A., R. M. Verdijk, P. F. van Kuijk, P. Kartal, A. L. M. Vriends, P. J. French, M. E. van Royen, et al. (2020). "Deregulated microRNAs in neurofibromatosis type 1 derived malignant peripheral nerve sheath tumors." Sci Rep **10**(1): 2927.

Amirnasr, A., R. M. Verdijk, P. F. van Kuijk, W. Taal, S. Sleijfer and E. A. C. Wiemer (2017). "Expression and inhibition of BRD4, EZH2 and TOP2A in neurofibromas and malignant peripheral nerve sheath tumors." PLoS One **12**(8): e0183155.

Angelico, G., M. Mazzucchelli, G. Attanasio, G. Tinnirello, J. Farina, M. Zanelli, A. Palicelli, et al. (2024). "H3K27me3 Loss in Central Nervous System Tumors: Diagnostic, Prognostic, and Therapeutic Implications." Cancers (Basel) **16**(20).

Anghileri, M., R. Miceli, M. Fiore, L. Mariani, A. Ferrari, C. Mussi, L. Lozza, et al. (2006). "Malignant peripheral nerve sheath tumors: prognostic factors and survival in a series of patients treated at a single institution." Cancer **107**(5): 1065-1074.

Aoki, M., K. Nabeshima, K. Koga, M. Hamasaki, J. Suzumiya, K. Tamura and H. Iwasaki (2007). "Imatinib mesylate inhibits cell invasion of malignant peripheral nerve sheath tumor induced by platelet-derived growth factor-BB." Lab Invest **87**(8): 767-779.

B

Bakos, R. M., T. Maier, R. Besch, D. S. Mestel, T. Ruzicka, R. A. Sturm and C. Berking (2010). "Nestin and SOX9 and SOX10 transcription factors are coexpressed in melanoma." Exp Dermatol **19**(8): e89-94.

Ballester, R., D. Marchuk, M. Boguski, A. Saulino, R. Letcher, M. Wigler and F. Collins (1990). "The NF1 locus encodes a protein functionally related to mammalian GAP and yeast IRA proteins." Cell **63**(4): 851-859.

Barretina, J., G. Caponigro, N. Stransky, K. Venkatesan, A. A. Margolin, S. Kim, C. J. Wilson, et al. (2012). "The Cancer Cell Line Encyclopedia enables predictive modelling of anticancer drug sensitivity." Nature **483**(7391): 603-607.

Baude, A., A. M. Lindroth and C. Plass (2014). "PRC2 loss amplifies Ras signaling in cancer." Nat Genet **46**(11): 1154-1155.

Beert, E., H. Brems, B. Daniëls, I. De Wever, F. Van Calenbergh, J. Schoenaers, M. Debiec-Rychter, et al. (2011). "Atypical neurofibromas in neurofibromatosis type 1 are premalignant tumors." Genes Chromosomes Cancer **50**(12): 1021-1032.

Belakhoua, S. M. and F. J. Rodriguez (2021). "Diagnostic Pathology of Tumors of Peripheral Nerve." Neurosurgery **88**(3): 443-456.

Benini, S., G. Gamberi, S. Cocchi, A. Righi, T. Frisoni, A. Longhi and M. Gambarotti (2020). "Identification of a novel fusion transcript EWSR1-VEZF1 by anchored multiplex PCR in malignant peripheral nerve sheath tumor." Pathol Res Pract **216**(1): 152760.

Bergoug, M., M. Doudeau, F. Godin, C. Mosrin, B. Vallée and H. Bénédetti (2020). "Neurofibromin Structure, Functions and Regulation." Cells **9**(11).

Bernat Gel, M. M. (2024). *CopyNumberPlots: Create Copy-Number Plots using karyoploteR functionality* . R package version 1.22.0.

Berrouet, C., N. Dorilas, K. A. Rejniak and N. Tuncer (2020). "Comparison of Drug Inhibitory Effects ([Formula: see text]) in Monolayer and Spheroid Cultures." Bull Math Biol **82**(6): 68.

Besselsen, D. G., C. L. Franklin, R. S. Livingston and L. K. Riley (2008). "Lurking in the shadows: emerging rodent infectious diseases." ILAR J **49**(3): 277-290.

Bettegowda, C., M. Upadhayaya, D. G. Evans, A. Kim, D. Mathios, C. O. Hanemann and R. I. Collaboration (2021). "Genotype-Phenotype Correlations in Neurofibromatosis and Their Potential Clinical Use." Neurology **97**(7 Suppl 1): S91-S98.

Bhalla, A. D., S. M. Landers, A. K. Singh, J. P. Landry, M. G. Yeagley, G. S. B. Myerson, C. B. Delgado-Baez, et al. (2022). "Experimental models of undifferentiated pleomorphic sarcoma and malignant peripheral nerve sheath tumor." Lab Invest.

Bhola, P., S. Banerjee, J. Mukherjee, A. Balasubramanium, V. Arun, Z. Karim, K. Burrell, et al. (2010). "Preclinical in vivo evaluation of rapamycin in human malignant peripheral nerve sheath explant xenograft." Int J Cancer **126**(2): 563-571.

Bialkowska, A. B. and V. W. Yang (2012). "High-throughput screening strategies for targeted identification of therapeutic compounds in colorectal cancer." Future Oncol **8**(3): 259-272.

Blomme, A., G. Van Simaeys, G. Doumont, B. Costanza, J. Bellier, Y. Otaka, F. Sherer, et al. (2018). "Murine stroma adopts a human-like metabolic phenotype in the PDX model of colorectal cancer and liver metastases." Oncogene **37**(9): 1237-1250.

Borcherding, D. C., N. V. Amin, K. He, X. Zhang, Y. Lyu, C. Dehner, H. Bhatia, et al. (2023). "MEK Inhibition Synergizes with TYK2 Inhibitors in NF1-Associated Malignant Peripheral Nerve Sheath Tumors." Clin Cancer Res **29**(8): 1592-1604.

Bos, J. L., H. Rehmann and A. Wittinghofer (2007). "GEFs and GAPs: critical elements in the control of small G proteins." Cell **129**(5): 865-877.

Bradtmöller, M., C. Hartmann, J. Zietsch, S. Jäschke, V. F. Mautner, A. Kurtz, S. J. Park, et al. (2012). "Impaired Pten expression in human malignant peripheral nerve sheath tumours." PLoS One **7**(11): e47595.

Brannan, C. I., A. S. Perkins, K. S. Vogel, N. Ratner, M. L. Nordlund, S. W. Reid, A. M. Buchberg, et al. (1994). "Targeted disruption of the neurofibromatosis type-1 gene leads to developmental abnormalities in heart and various neural crest-derived tissues." Genes Dev **8**(9): 1019-1029.

Brockman, Q. R., A. Scherer, G. R. McGivney, W. R. Gutierrez, A. P. Voigt, A. L. Isaacson, E. A. Laverty, et al. (2022). "PRC2 loss drives MPNST metastasis and matrix remodeling." JCI Insight **7**(20).

Brohl, A. S., E. Kahen, S. J. Yoder, J. K. Teer and D. R. Reed (2017). "The genomic landscape of malignant peripheral nerve sheath tumors: diverse drivers of Ras pathway activation." Sci Rep **7**(1): 14992.

Brown, J. A., S. M. Gianino and D. H. Gutmann (2010). "Defective cAMP generation underlies the sensitivity of CNS neurons to neurofibromatosis-1 heterozygosity." J Neurosci **30**(16): 5579-5589.

Brčić, I., T. M. Godschachner, M. Bergovec, J. Igrec, H. Till, H. Lackner, S. Scheipl, et al. (2021). "Broadening the spectrum of NTRK rearranged mesenchymal tumors and usefulness of pan-TRK immunohistochemistry for identification of NTRK fusions." Mod Pathol **34**(2): 396-407.

Byrne, A. T., D. G. Alférez, F. Amant, D. Annibali, J. Arribas, A. V. Biankin, A. Bruna, et al. (2017). "Interrogating open issues in cancer precision medicine with patient-derived xenografts." Nat Rev Cancer **17**(4): 254-268.

C

Cai, Z., X. Tang, H. Liang, R. Yang, T. Yan and W. Guo (2020). "Prognosis and risk factors for malignant peripheral nerve sheath tumor: a systematic review and meta-analysis." World J Surg Oncol **18**(1): 257.

Carbonnelle-Puscian, A., V. Vidal, I. Laurendeau, L. Valeyrie-Allanore, D. Vidaud, I. Bièche, K. Leroy, et al. (2011). "SOX9 expression increases with malignant potential in tumors from patients with neurofibromatosis 1 and is not correlated to desert hedgehog." Hum Pathol **42**(3): 434-443.

Carey, J. C., J. M. Laub and B. D. Hall (1979). "Penetrance and variability in neurofibromatosis: a genetic study of 60 families." Birth Defects Orig Artic Ser **15**(5B): 271-281.

Carli, M., A. Ferrari, A. Mattke, I. Zanetti, M. Casanova, G. Bisogno, G. Cecchetto, et al. (2005). "Pediatric malignant peripheral nerve sheath tumor: the Italian and German soft tissue sarcoma cooperative group." J Clin Oncol **23**(33): 8422-8430.

Carnes, R. M., R. A. Kesterson, B. R. Korf, J. A. Mobley and D. Wallis (2019). "Affinity Purification of NF1 Protein-Protein Interactors Identifies Keratins and Neurofibromin Itself as Binding Partners." Genes (Basel) **10**(9).

Carrió, M., H. Mazuelas, Y. Richaud-Patin, B. Gel, E. Terribas, I. Rosas, S. Jimenez-Delgado, et al. (2019). "Reprogramming Captures the Genetic and Tumorigenic Properties of Neurofibromatosis Type 1 Plexiform Neurofibromas." Stem Cell Reports **12**(2): 411-426.

Carroll, S. L. (2012). "Molecular mechanisms promoting the pathogenesis of Schwann cell neoplasms." Acta Neuropathol **123**(3): 321-348.

Carton, C., D. G. Evans, I. Blanco, R. E. Friedrich, R. E. Ferner, S. Farschtschi, H. Salvador, et al. (2023). "ERN GENTURIS tumour surveillance guidelines for individuals with neurofibromatosis type 1." EClinicalMedicine **56**: 101818.

Castellsagué, J., B. Gel, J. Fernández-Rodríguez, R. Llatjós, I. Blanco, Y. Benavente, D. Pérez-Sidelnikova, et al. (2015). "Comprehensive establishment and characterization of orthoxenograft mouse models of malignant peripheral nerve sheath tumors for personalized medicine." EMBO Mol Med **7**(5): 608-627.

Cero, C., J. S. House, V. Verdi, J. L. Ferguson, D. D. Jima, A. A. Selmek, O. M. Patania, et al. (2025). "Profiling the cancer-prone microenvironment in a zebrafish model for MPNST." Oncogene **44**(3): 179-191.

Chamseddin, B. H., L. Hernandez, D. Solorzano, J. Vega and L. Q. Le (2019). "Robust surgical approach for cutaneous neurofibroma in neurofibromatosis type 1." JCI Insight **5**(11).

Chang, L. S., J. L. Oblinger, A. E. Smith, M. Ferrer, S. P. Angus, E. Hawley, A. M., et al. (2021) Brigatinib causes tumor shrinkage in both NF2-deficient meningioma and schwannoma through inhibition of multiple tyrosine kinases but not ALK. PLoS One **16**(7): e0252048.

Chen, D. S. and M. M. Davis (2006). "Molecular and functional analysis using live cell microarrays." Curr Opin Chem Biol **10**(1): 28-34.

Chen, J., S. Liao, Z. Xiao, Q. Pan, X. Wang, K. Shen, S. Wang, et al. (2022). "The development and improvement of immunodeficient mice and humanized immune system mouse models." Front Immunol **13**: 1007579.

Chou, T. C. (2010). "Drug combination studies and their synergy quantification using the Chou-Talalay method." Cancer Res **70**(2): 440-446.

Chou, T. C. and P. Talalay (1984). "Quantitative analysis of dose-effect relationships: the combined effects of multiple drugs or enzyme inhibitors." Adv Enzyme Regul **22**: 27-55.

Cichowski, K., S. Santiago, M. Jardim, B. W. Johnson and T. Jacks (2003). "Dynamic regulation of the Ras pathway via proteolysis of the NF1 tumor suppressor." Genes Dev **17**(4): 449-454.

Cichowski, K., T. S. Shih, E. Schmitt, S. Santiago, K. Reilly, M. E. McLaughlin, R. T. Bronson and T. Jacks (1999). "Mouse models of tumor development in neurofibromatosis type 1." Science **286**(5447): 2172-2176.

Cimino, P. J. and D. H. Gutmann (2018). "Neurofibromatosis type 1." Handb Clin Neurol **148**: 799-811.

Cleven, A. H., G. A. Al Sannaa, I. Briaire-de Bruijn, D. R. Ingram, M. van de Rijn, B. P. Rubin, M. W. de Vries, et al. (2016). "Loss of H3K27 tri-methylation is a diagnostic marker for malignant peripheral nerve sheath tumors and an indicator for an inferior survival." Mod Pathol **29**(9): 1113.

Clohessy, J. G. and P. P. Pandolfi (2015). "Mouse hospital and co-clinical trial project--from bench to bedside." Nat Rev Clin Oncol **12**(8): 491-498.

Contrera, J. F., E. J. Matthews, N. L. Kruhlak and R. D. Benz (2004). "Estimating the safe starting dose in phase I clinical trials and no observed effect level based on QSAR modeling of the human maximum recommended daily dose." Regul Toxicol Pharmacol **40**(3): 185-206.

Cooper, J. M., A. J. Patel, Z. Chen, C. P. Liao, K. Chen, J. Mo, Y. Wang and L. Q. Le (2019). "Overcoming BET Inhibitor Resistance in Malignant Peripheral Nerve Sheath Tumors." Clin Cancer Res **25**(11): 3404-3416.

Cortes-Ciriano, I., C. D. Steele, K. Piculell, A. Al-Ibraheemi, V. Eulo, M. M. Bui, A. Chatzipli, et al. (2023). "Genomic Patterns of Malignant Peripheral Nerve Sheath Tumor (MPNST) Evolution Correlate with Clinical Outcome and Are Detectable in Cell-Free DNA." Cancer Discov **13**(3): 654-671.

Creus-Bachiller, E., J. Fernández-Rodríguez, M. Magallón-Lorenz, S. Ortega-Bertran, S. Navas-Rutete, C. Romagosa, T. M. Silva, et al. (2023). "Expanding a precision medicine platform for malignant peripheral nerve sheath tumors: New patient-derived orthotopic xenografts, cell lines and tumor entities." Mol Oncol.

Cui, D., R. Qu, D. Liu, X. Xiong, T. Liang and Y. Zhao (2021). "The Cross Talk Between p53 and mTOR Pathways in Response to Physiological and Genotoxic Stresses." Front Cell Dev Biol **9**: 775507.

Czarnecka, A. M. (2018). Malignant peripheral nerve sheath tumour (MPNST). M. Z. Paweł Sobczuk , Mateusz Spałek , Piotr Rutkowski. Oncology in Clinical Practice. **14**.

D

Dahlberg, W. K., J. B. Little, J. A. Fletcher, H. D. Suit and P. Okunieff (1993). "Radiosensitivity in vitro of human soft tissue sarcoma cell lines and skin fibroblasts derived from the same patients." Int J Radiat Biol **63**(2): 191-198.

Dancsok, A. R., D. Gao, A. F. Lee, S. E. Steigen, J. Y. Blay, D. M. Thomas, R. G. Maki, et al. (2020). "Tumor-associated macrophages and macrophage-related immune checkpoint expression in sarcomas." Oncoimmunology **9**(1): 1747340.

De Raedt, T., E. Beert, E. Pasmant, A. Luscan, H. Brems, N. Ortonne, K. Helin, et al. (2014). "PRC2 loss amplifies Ras-driven transcription and confers sensitivity to BRD4-based therapies." Nature **514**(7521): 247-251.

De Raedt, T., H. Brems, P. Wolkenstein, D. Vidaud, S. Pilotti, F. Perrone, V. Mautner, et al. (2003). "Elevated risk for MPNST in NF1 microdeletion patients." Am J Hum Genet **72**(5): 1288-1292.

Dehner, C., C. I. Moon, X. Zhang, Z. Zhou, C. Miller, H. Xu, X. Wan, et al. (2021). "Chromosome 8 gain is associated with high-grade transformation in MPNST." JCI Insight **6**(6).

Dhandapani, M. and A. Goldman (2017). "Preclinical Cancer Models and Biomarkers for Drug Development: New Technologies and Emerging Tools." J Mol Biomark Diagn **8**(5).

Dickson, M. A., M. R. Mahoney, W. D. Tap, S. P. D'Angelo, M. L. Keohan, B. A. Van Tine, M. Agulnik, et al. (2016). "Phase II study of MLN8237 (Alisertib) in advanced/metastatic sarcoma." Ann Oncol **27**(10): 1855-1860.

Donehower, L. A., M. Harvey, B. L. Slagle, M. J. McArthur, C. A. Montgomery, J. S. Butel and A. Bradley (1992). "Mice deficient for p53 are developmentally normal but susceptible to spontaneous tumours." Nature **356**(6366): 215-221.

Duarte, D. and N. Vale (2022). "Evaluation of synergism in drug combinations and reference models for future orientations in oncology." Curr Res Pharmacol Drug Discov **3**: 100110.

Dubbink, H. J., H. Bakels, E. Post, E. C. Zwarthoff and R. M. Verdijk (2014). "TERT promoter mutations and BRAF mutations are rare in sporadic, and TERT promoter mutations are absent in NF1-related malignant peripheral nerve sheath tumors." J Neurooncol **120**(2): 267-272.

Ducatman, B. S., B. W. Scheithauer, D. G. Piepgras, H. M. Reiman and D. M. Ilstrup (1986). "Malignant peripheral nerve sheath tumors. A clinicopathologic study of 120 cases." Cancer **57**(10): 2006-2021.

Dunn, G. P., K. Spiliopoulos, S. R. Plotkin, F. J. Hornicek, D. C. Harmon, T. F. Delaney and Z. Williams (2013). "Role of resection of malignant peripheral nerve sheath tumors in patients with neurofibromatosis type 1." J Neurosurg **118**(1): 142-148.

Duong, T. A., S. Bastuji-Garin, L. Valeyrie-Allanore, E. Sbidian, S. Ferkal and P. Wolkenstein (2011). "Evolving pattern with age of cutaneous signs in neurofibromatosis type 1: a cross-sectional study of 728 patients." Dermatology **222**(3): 269-273.

E

Easton, D. F., M. A. Ponder, S. M. Huson and B. A. Ponder (1993). "An analysis of variation in expression of neurofibromatosis (NF) type 1 (NF1): evidence for modifying genes." Am J Hum Genet **53**(2): 305-313.

Echevarría-Vargas, I. M., P. I. Reyes-Uribe, A. N. Guterres, X. Yin, A. V. Kossenkov, Q. Liu, G. Zhang, et al. (2018). "Co-targeting BET and MEK as salvage therapy for MAPK and checkpoint inhibitor-resistant melanoma." EMBO Mol Med **10**(5).

Endo, M., H. Yamamoto, N. Setsu, K. Kohashi, Y. Takahashi, T. Ishii, K. Iida, et al. (2013). "Prognostic significance of AKT/mTOR and MAPK pathways and antitumor effect of mTOR inhibitor in NF1-related and sporadic malignant peripheral nerve sheath tumors." Clin Cancer Res **19**(2): 450-461.

Evans, D. G., M. E. Baser, J. McGaughran, S. Sharif, E. Howard and A. Moran (2002). "Malignant peripheral nerve sheath tumours in neurofibromatosis 1." J Med Genet **39**(5): 311-314.

Evans, D. G., S. Mostaccioli, D. Pang, M. Fadzil O Connor, M. Pittara, N. Champollion, et al. (2022). "ERN GENTURIS clinical practice guidelines for the diagnosis, treatment, management and surveillance of people with schwannomatosis." Eur J Hum Genet **30**(7): 812-817.

Evans, D. G. R., R. A. Kallionpää, M. Clementi, E. Trevisson, V. F. Mautner, S. J. Howell, L. Lewis, et al. (2020). "Breast cancer in neurofibromatosis 1: survival and risk of contralateral breast cancer in a five country cohort study." Genet Med **22**(2): 398-406.

F

Fan, Q., J. Yang and G. Wang (2014). "Clinical and molecular prognostic predictors of malignant peripheral nerve sheath tumor." Clin Transl Oncol **16**(2): 191-199.

Fanburg-Smith, J. C. and M. Miettinen (2001). "Low-affinity nerve growth factor receptor (p75) in dermatofibrosarcoma protuberans and other nonneural tumors: a study of 1,150 tumors and fetal and adult normal tissues." Hum Pathol **32**(9): 976-983.

Ferner, R. E. (2007). "Neurofibromatosis 1 and neurofibromatosis 2: a twenty first century perspective." Lancet Neurol **6**(4): 340-351.

Ferner, R. E. and D. H. Gutmann (2002). "International consensus statement on malignant peripheral nerve sheath tumors in neurofibromatosis." Cancer Res **62**(5): 1573-1577.

Ferner, R. E. and D. H. Gutmann (2013). "Neurofibromatosis type 1 (NF1): diagnosis and management." Handb Clin Neurol **115**: 939-955.

Fernández-Rodríguez, J., E. Creus-Bachiller, X. Zhang, M. Martínez-Iniesta, S. Ortega-Bertran, R. Guha, C. J. Thomas, et al. (2022). "A High-Throughput Screening Platform Identifies Novel Combination Treatments for Malignant Peripheral Nerve Sheath Tumors." Mol Cancer Ther **21**(7): 1246-1258.

Fernández-Rodríguez, J., A. Morales La Madrid, B. Gel, A. Castañeda Heredia, H. Salvador, M. Martínez-Iniesta, C. Moutinho, et al. (2020). "Use of patient derived orthotopic xenograft models for real-time therapy guidance in a pediatric sporadic malignant peripheral nerve sheath tumor." Ther Adv Med Oncol **12**: 1758835920929579.

Filippakopoulos, P., S. Picaud, M. Mangos, T. Keates, J. P. Lambert, D. Barsyte-Lovejoy, I. Felletar, et al. (2012). "Histone recognition and large-scale structural analysis of the human bromodomain family." Cell **149**(1): 214-231.

Filippakopoulos, P., J. Qi, S. Picaud, Y. Shen, W. B. Smith, O. Fedorov, E. M. Morse, et al. (2010). "Selective inhibition of BET bromodomains." Nature **468**(7327): 1067-1073.

Fisher, M. J., J. O. Blakeley, B. D. Weiss, E. Dombi, S. Ahlawat, S. Akshintala, A. J. Belzberg, et al. (2022). "Management of neurofibromatosis type 1-associated plexiform neurofibromas." Neuro Oncol **24**(11): 1827-1844.

Fletcher, J. A., H. P. Kozakewich, F. A. Hoffer, J. M. Lage, N. Weidner, R. Tepper, G. S. Pinkus, et al. (1991). "Diagnostic relevance of clonal cytogenetic aberrations in malignant soft-tissue tumors." N Engl J Med **324**(7): 436-442.

Fletcher, J. S., J. Pundavela and N. Ratner (2020). "After." Neurooncol Adv **2**(Suppl 1): i23-i32.
Foucquier, J. and M. Guedj (2015). "Analysis of drug combinations: current methodological landscape." Pharmacol Res Perspect **3**(3): e00149.

Frahm, S., V. F. Mautner, H. Brems, E. Legius, M. Debiec-Rychter, R. E. Friedrich, W. T. Knöfel, et al. (2004). "Genetic and phenotypic characterization of tumor cells derived from malignant peripheral nerve sheath tumors of neurofibromatosis type 1 patients." Neurobiol Dis **16**(1): 85-91.

Friedman, J. (1998 - "Updated 2022"). Neurofibromatosis 1. Seattle (WA), University of Washington, Seattle.

Friedrich, R. E., M. Hartmann and V. F. Mautner (2007). "Malignant peripheral nerve sheath tumors (MPNST) in NF1-affected children." Anticancer Res **27**(4A): 1957-1960.

Frustaci, S., F. Gherlinzoni, A. De Paoli, M. Bonetti, A. Azzarelli, A. Comandone, P. Olmi, et al. (2001). "Adjuvant chemotherapy for adult soft tissue sarcomas of the extremities and girdles: results of the Italian randomized cooperative trial." J Clin Oncol **19**(5): 1238-1247.

G

Gallagher, S. J., B. Mijatov, D. Gunatilake, J. C. Tiffen, K. Gowrishankar, L. Jin, G. M. Pupo, et al. (2014). "The epigenetic regulator I-BET151 induces BIM-dependent apoptosis and cell cycle arrest of human melanoma cells." J Invest Dermatol **134**(11): 2795-2805.

Geitenbeek, R. T. J., E. Martin, L. H. Graven, M. P. G. Broen, M. H. M. E. Anten, J. A. J. van der Pol, C. Verhoef and W. Taal (2022). "Diagnostic value of." J Neurooncol **156**(3): 559-567.

Gesundheit, B., P. Parkin, M. Greenberg, S. Baruchel, C. Senger, J. Kapelushnik, C. Smith and G. L. Klement (2010). "The role of angiogenesis in the transformation of plexiform neurofibroma into malignant peripheral nerve sheath tumors in children with neurofibromatosis type 1." J Pediatr Hematol Oncol **32**(7): 548-553.

Ghadimi, M. P., E. D. Young, R. Belousov, Y. Zhang, G. Lopez, K. Lusby, C. Kivlin, et al. (2012). "Survivin is a viable target for the treatment of malignant peripheral nerve sheath tumors." Clin Cancer Res **18**(9): 2545-2557.

Gil, J. and G. Peters (2006). "Regulation of the INK4b-ARF-INK4a tumour suppressor locus: all for one or one for all." Nat Rev Mol Cell Biol **7**(9): 667-677.

Glover, T. W., C. K. Stein, E. Legius, L. B. Andersen, A. Brereton and S. Johnson (1991). "Molecular and cytogenetic analysis of tumors in von Recklinghausen neurofibromatosis." Genes Chromosomes Cancer **3**(1): 62-70.

Godec, A., R. Jayasinghe, J. S. A. Chrisinger, B. Prudner, T. Ball, Y. Wang, D. Srihari, et al. (2020). "Whole exome sequencing reveals the maintained polyclonal nature from primary to metastatic malignant peripheral nerve sheath tumor in two patients with NF1." Neurooncol Adv **2**(Suppl 1): i75-i84.

González-Muñoz, T., A. Di Giannatale, S. García-Silva, V. Santos, S. Sánchez-Redondo, C. Savini, O. Graña-Castro, C. Blanco-Aparicio, et al. (2023). "Endoglin, a Novel Biomarker and Therapeutical Target to Prevent Malignant Peripheral Nerve Sheath Tumor Growth and Metastasis." Clin Cancer Res **29**(18): 3744-3758.

Grit, J. L., M. G. Pridgeon, C. J. Essenburg, E. Wolfrum, Z. B. Madaj, L. Turner, J. Wulfkuhle, et al. (2020). "Kinome Profiling of NF1-Related MPNSTs in Response to Kinase Inhibition and Doxorubicin Reveals Therapeutic Vulnerabilities." Genes (Basel) **11**(3).

Grobmyer, S. R., J. D. Reith, A. Shahlaee, C. H. Bush and S. N. Hochwald (2008). "Malignant Peripheral Nerve Sheath Tumor: molecular pathogenesis and current management considerations." J Surg Oncol **97**(4): 340-349.

Gu, Y., W. Wang, Y. Li, H. Li, Z. Guo, C. Wei, M. Long, et al. (2022). "Preclinical Assessment of MEK Inhibitors for Malignant Peripheral Nerve Sheath Tumors Reveals Differences in Efficacy and Adaptive Response." Front Oncol **12**: 903177.

Gu, Y., C. Wei, M. Chung, H. Li, Z. Guo, M. Long, Y. Li, et al. (2022). "Concurrent inhibition of FAK/SRC and MEK overcomes MEK inhibitor resistance in Neurofibromatosis Type I related malignant peripheral nerve sheath tumors." Front Oncol **12**: 910505.

Gutmann, D. H., R. E. Ferner, R. H. Listernick, B. R. Korf, P. L. Wolters and K. J. Johnson (2017). "Neurofibromatosis type 1." Nat Rev Dis Primers **3**: 17004.

Gutmann, D. H., D. L. Wood and F. S. Collins (1991). "Identification of the neurofibromatosis type 1 gene product." Proc Natl Acad Sci U S A **88**(21): 9658-9662.

H

Habanjar, O., M. Diab-Assaf, F. Caldefie-Chezet and L. Delort (2021). "3D Cell Culture Systems: Tumor Application, Advantages, and Disadvantages." Int J Mol Sci **22**(22).

Hagel, C., U. Zils, M. Peiper, L. Kluwe, S. Gotthard, R. E. Friedrich, D. Zurakowski, et al. (2007). "Histopathology and clinical outcome of NF1-associated vs. sporadic malignant peripheral nerve sheath tumors." J Neurooncol **82**(2): 187-192.

Hainaut, P. and M. Hollstein (2000). "p53 and human cancer: the first ten thousand mutations." Adv Cancer Res **77**: 81-137.

Halilovic, E., Q. B. She, Q. Ye, R. Pagliarini, W. R. Sellers, D. B. Solit and N. Rosen (2010). "PIK3CA mutation uncouples tumor growth and cyclin D1 regulation from MEK/ERK and mutant KRAS signaling." Cancer Res **70**(17): 6804-6814.

Halling, K. C., B. W. Scheithauer, A. C. Halling, A. G. Nascimento, S. C. Ziesmer, P. C. Roche and P. C. Wollan (1996). "p53 expression in neurofibroma and malignant peripheral nerve sheath tumor. An immunohistochemical study of sporadic and NF1-associated tumors." Am J Clin Pathol **106**(3): 282-288.

Hernández, J. L., L. Padilla, S. Dakhel, T. Coll, R. Hervas, J. Adan, M. Masa, et al. (2013). "Therapeutic targeting of tumor growth and angiogenesis with a novel anti-S100A4 monoclonal antibody." PLoS One **8**(9): e72480.

Hiemcke-Jiwa, L. S., M. T. Meister, E. Martin, M. P. Dierselhuis, L. M. Haveman, R. W. J. Meijers, B. B. J. Tops, et al. (2022). "NTRK rearrangements in a subset of NF1-related malignant peripheral nerve sheath tumors as novel actionable target." Acta Neuropathol.

Higham, C. S., S. M. Steinberg, E. Dombi, A. Perry, L. J. Helman, S. M. Schuetze, J. A. Ludwig, et al. (2017). "SARC006: Phase II Trial of Chemotherapy in Sporadic and Neurofibromatosis Type 1 Associated Chemotherapy-Naive Malignant Peripheral Nerve Sheath Tumors." Sarcoma **2017**: 8685638.

Hirbe, A. C., P. F. Cosper, S. Dahiya and B. A. Van Tine (2017). "Neoadjuvant Ifosfamide and Epirubicin in the Treatment of Malignant Peripheral Nerve Sheath Tumors." Sarcoma **2017**: 3761292.

Hirbe, A. C., S. Dahiya, D. Friedmann-Morvinski, I. M. Verma, D. W. Clapp and D. H. Gutmann (2016). "Spatially- and temporally-controlled postnatal p53 knockdown cooperates with embryonic Schwann cell precursor Nf1 gene loss to promote malignant peripheral nerve sheath tumor formation." Oncotarget **7**(7): 7403-7414.

Hirbe, A. C., S. Dahiya, C. A. Miller, T. Li, R. S. Fulton, X. Zhang, S. McDonald, et al. (2015). "Whole Exome Sequencing Reveals the Order of Genetic Changes during Malignant Transformation and Metastasis in a Single Patient with NF1-plexiform Neurofibroma." Clin Cancer Res **21**(18): 4201-4211.

Hirbe, A. C., M. Pekmezci, S. Dahiya, A. J. Apicelli, B. A. Van Tine, A. Perry and D. H. Gutmann (2014). "BRAFV600E mutation in sporadic and neurofibromatosis type 1-related malignant peripheral nerve sheath tumors." Neuro Oncol **16**(3): 466-467.

Ho, W. W., M. J. Pittet, D. Fukumura and R. K. Jain (2022). "The local microenvironment matters in preclinical basic and translational studies of cancer immunology and immunotherapy." Cancer Cell **40**(7): 701-702.

Holtkamp, N., E. Malzer, J. Zietsch, A. F. Okuducu, J. Mucha, C. Mawrin, V. F. Mautner, et al. (2008). "EGFR and erbB2 in malignant peripheral nerve sheath tumors and implications for targeted therapy." Neuro Oncol **10**(6): 946-957.

Huang, J., M. Chen, M. J. Whitley, H. C. Kuo, E. S. Xu, A. Walens, Y. M. Mowery, et al. (2017). "Generation and comparison of CRISPR-Cas9 and Cre-mediated genetically engineered mouse models of sarcoma." Nat Commun **8**: 15999.

Huch, M. and B. K. Koo (2015). "Modeling mouse and human development using organoid cultures." Development **142**(18): 3113-3125.

Huijbregts, R. P., K. A. Roth, R. E. Schmidt and S. L. Carroll (2003). "Hypertrophic neuropathies and malignant peripheral nerve sheath tumors in transgenic mice overexpressing glial growth factor beta3 in myelinating Schwann cells." J Neurosci **23**(19): 7269-7280.

Hwang, I. K., S. M. Hahn, H. S. Kim, S. K. Kim, K. H. Shin, C. O. Suh, C. J. Lyu and J. W. Han (2017). "Outcomes of Treatment for Malignant Peripheral Nerve Sheath Tumors: Different Clinical Features Associated with Neurofibromatosis Type 1." Cancer Res Treat **49**(3): 717-726.

Hyman, S. L., A. Shores and K. N. North (2005). "The nature and frequency of cognitive deficits in children with neurofibromatosis type 1." Neurology **65**(7): 1037-1044.

Høland, M., K. C. G. Berg, I. A. Eilertsen, B. Bjerkehagen, M. Kolberg, K. Boye, O. C. Lingjærde, T. K. Guren, N. Mandahl, E. van den Berg, et al. (2023). "Transcriptomic subtyping of malignant peripheral nerve sheath tumours highlights immune signatures, genomic profiles, patient survival and therapeutic targets." EBioMedicine **97**: 104829.

Høland, M., M. Kolberg, S. A. Danielsen, B. Bjerkehagen, I. A. Eilertsen, M. Hektoen, N. Mandahl, et al. (2018). "Inferior survival for patients with malignant peripheral nerve sheath tumors defined by aberrant TP53." Mod Pathol **31**(11): 1694-1707.

I

Imaizumi, S., T. Motoyama, A. Ogose, T. Hotta and H. E. Takahashi (1998). "Characterization and chemosensitivity of two human malignant peripheral nerve sheath tumour cell lines derived from a patient with neurofibromatosis type 1." Virchows Arch **433**(5): 435-441.

Imura, Y., H. Outani, S. Takenaka, N. Yasuda, S. Nakai, T. Nakai, T. Wakamatsu, et al. (2021). "Clinical Outcomes and Prognostic Factors for Patients with Malignant Peripheral Nerve Sheath Tumour." Sarcoma **2021**: 8335290.

Inglese, J., D. S. Auld, A. Jadhav, R. L. Johnson, A. Simeonov, A. Yasgar, W. Zheng and C. P. Austin (2006). "Quantitative high-throughput screening: a titration-based approach that efficiently identifies biological activities in large chemical libraries." Proc Natl Acad Sci U S A **103**(31): 11473-11478.

Inoue, A., L. J. Janke, B. L. Gudenas, H. Jin, Y. Fan, J. Paré, M. R. Clay, et al. (2021). "A genetic mouse model with postnatal." Neurooncol Adv **3**(1): vdab129.

J

Jessen, W. J., S. J. Miller, E. Jousma, J. Wu, T. A. Rizvi, M. E. Brundage, D. Eaves, et al. (2013). "MEK inhibition exhibits efficacy in human and mouse neurofibromatosis tumors." J Clin Invest **123**(1): 340-347.

Jin, J., K. Yoshimura, M. Sewastjanow-Silva, S. Song and J. A. Ajani (2023). "Challenges and Prospects of Patient-Derived Xenografts for Cancer Research." Cancers (Basel) **15**(17).

Jing, Y., Z. Zhang, P. Ma, S. An, Y. Shen, L. Zhu and G. Zhuang (2016). "Concomitant BET and MAPK blockade for effective treatment of ovarian cancer." Oncotarget **7**(3): 2545-2554.

Joseph, N. M., J. T. Mosher, J. Buchstaller, P. Snider, P. E. McKeever, M. Lim, S. J. Conway, et al. (2008). "The loss of Nf1 transiently promotes self-renewal but not tumorigenesis by neural crest stem cells." Cancer Cell **13**(2): 129-140.

K

Kallionpää, R. A., E. Uusitalo, J. Leppävirta, M. Pöyhönen, S. Peltonen and J. Peltonen (2018). "Prevalence of neurofibromatosis type 1 in the Finnish population." Genet Med **20**(9): 1082-1086.

Kan, Z., B. S. Jaiswal, J. Stinson, V. Janakiraman, D. Bhatt, H. M. Stern, P. Yue, et al. (2010). "Diverse somatic mutation patterns and pathway alterations in human cancers." Nature **466**(7308): 869-873.

Kandi, V. and S. Vadakedath (2023). "Clinical Trials and Clinical Research: A Comprehensive Review." Cureus **15**(2): e35077.

Kao, E. Y., K. M. Wakeman, Y. Wu, J. M. Gross, E. Y. Chen, R. W. Ricciotti, Y. J. Liu and J. G. Mantilla (2022). "Prevalence and detection of actionable BRAF V600 and NRAS Q61 mutations in malignant peripheral nerve sheath tumor by droplet digital PCR." Hum Pathol **129**: 90-97.

Kasibhatla, S., H. Gourdeau, K. Meerovitch, J. Drewe, S. Reddy, L. Qiu, H. Zhang, et al. (2004). "Discovery and mechanism of action of a novel series of apoptosis inducers with potential vascular targeting activity." Mol Cancer Ther **3**(11): 1365-1374.

Kaufmann, D., R. Müller, O. Kenner, W. Leistner, C. Hein, W. Vogel and B. Bartelt (2002). "The N-terminal splice product NF1-10a-2 of the NF1 gene codes for a transmembrane segment." Biochem Biophys Res Commun **294**(2): 496-503.

Keng, V. W., E. P. Rahrmann, A. L. Watson, B. R. Tschida, C. L. Moertel, W. J. Jessen, T. A. Rizvi, et al. (2012). "PTEN and NF1 inactivation in Schwann cells produces a severe phenotype in the peripheral nervous system that promotes the development and malignant progression of peripheral nerve sheath tumors." Cancer Res **72**(13): 3405-3413.

Kim, A., Y. Lu, S. H. Okuno, D. Reinke, O. Maertens, J. Perentesis, M. Basu, et al. (2020). "Targeting Refractory Sarcomas and Malignant Peripheral Nerve Sheath Tumors in a Phase I/II Study of Sirolimus in Combination with Ganetespib (SARC023)." Sarcoma **2020**: 5784876.

Kim, A., D. R. Stewart, K. M. Reilly, D. Viskochil, M. M. Miettinen and B. C. Widemann (2017). "Malignant Peripheral Nerve Sheath Tumors State of the Science: Leveraging Clinical and Biological Insights into Effective Therapies." Sarcoma **2017**: 7429697.

Kim, H. J. and S. C. Bae (2011). "Histone deacetylase inhibitors: molecular mechanisms of action and clinical trials as anti-cancer drugs." Am J Transl Res **3**(2): 166-179.

Kim, M. J., S. J. Lee, J. H. Ryu, S. H. Kim, I. C. Kwon and T. M. Roberts (2020). "Combination of KRAS gene silencing and PI3K inhibition for ovarian cancer treatment." J Control Release **318**: 98-108.

Kim, M. P., D. B. Evans, H. Wang, J. L. Abbruzzese, J. B. Fleming and G. E. Gallick (2009). "Generation of orthotopic and heterotopic human pancreatic cancer xenografts in immunodeficient mice." Nat Protoc **4**(11): 1670-1680.

Kim, W. Y. and N. E. Sharpless (2006). "The regulation of INK4/ARF in cancer and aging." Cell **127**(2): 265-275.

Knight, S. W. E., T. E. Knight, T. Santiago, A. J. Murphy and A. H. Abdelhafeez (2022). "Malignant Peripheral Nerve Sheath Tumors-A Comprehensive Review of Pathophysiology, Diagnosis, and Multidisciplinary Management." Children (Basel) **9**(1).

Kobayashi, H., N. Makise, A. Shinozaki-Ushiku, L. Zhang, Y. Ishibashi, M. Ikegami, Y. Tsuda, et al. (2023). "Dramatic response to entrectinib in a patient with malignant peripheral nerve sheath tumor harboring novel SNRNP70-NTRK3 fusion gene." Genes Chromosomes Cancer **62**(1): 47-51.

Koczkowska, M., T. Callens, Y. Chen, A. Gomes, A. D. Hicks, A. Sharp, E. Johns, et al. (2020). "Clinical spectrum of individuals with pathogenic NF1 missense variants affecting p.Met1149, p.Arg1276, and p.Lys1423: genotype-phenotype study in neurofibromatosis type 1." Hum Mutat **41**(1): 299-315.

Kodack, D. P., A. F. Farago, A. Dastur, M. A. Held, L. Dardaei, L. Friboulet, F. von Flotow, et al. (2017). "Primary Patient-Derived Cancer Cells and Their Potential for Personalized Cancer Patient Care." Cell Rep **21**(11): 3298-3309.

Kohlmeyer, J. L., C. A. Kaemmer, C. Pulliam, C. K. Maharjan, A. M. Samayoa, H. J. Major, K. E. Cornick, et al. (2020). "RABL6A Is an Essential Driver of MPNSTs that Negatively Regulates the RB1 Pathway and Sensitizes Tumor Cells to CDK4/6 Inhibitors." Clin Cancer Res **26**(12): 2997-3011.

Kohlmeyer, J. L., J. J. Lingo, C. A. Kaemmer, A. Scherer, A. Warrier, E. Voigt, J. A. Raygoza Garay, et al. (2023). "CDK4/6-MEK Inhibition in MPNSTs Causes Plasma Cell Infiltration, Sensitization to PD-L1 Blockade, and Tumor Regression." Clin Cancer Res **29**(17): 3484-3497.

Kolberg, M., M. Høland, T. H. Agesen, H. R. Brekke, K. Liestøl, K. S. Hall, F. Mertens, et al. (2013). "Survival meta-analyses for >1800 malignant peripheral nerve sheath tumor patients with and without neurofibromatosis type 1." Neuro Oncol **15**(2): 135-147.

Kroep, J. R., M. Ouali, H. Gelderblom, A. Le Cesne, T. J. A. Dekker, M. Van Glabbeke, P. C. W. Hogendoorn and P. Hohenberger (2011). "First-line chemotherapy for malignant peripheral nerve sheath tumor (MPNST) versus other histological soft tissue sarcoma subtypes and as a prognostic factor for MPNST: an EORTC soft tissue and bone sarcoma group study." Ann Oncol **22**(1): 207-214.

L

LaFemina, J., L. X. Qin, N. H. Moraco, C. R. Antonescu, R. C. Fields, A. M. Crago, M. F. Brennan and S. Singer (2013). "Oncologic outcomes of sporadic, neurofibromatosis-associated, and radiation-induced malignant peripheral nerve sheath tumors." Ann Surg Oncol **20**(1): 66-72.

Lane, D. P. and S. Benchimol (1990). "p53: oncogene or anti-oncogene?" Genes Dev **4**(1): 1-8.

Larson, K., A. Russ, H. Arif-Tiwari, D. Mahadevan, A. Elliott, A. Bhattacharyya and H. Babiker (2022). "Pembrolizumab Achieves a Complete Response in an NF-1 Mutated, PD-L1 Positive Malignant Peripheral Nerve Sheath Tumor: A Case Report and Review of the Benchmarks." J Immunother **45**(4): 222-226.

Larsson, A. T., H. Bhatia, A. Calizo, K. Pollard, X. Zhang, E. Conniff, J. F. Tibbitts, et al. (2023). "Ex vivo to in vivo model of malignant peripheral nerve sheath tumors for precision oncology." Neuro Oncol.

Le Guellec, S., A. V. Decouvelaere, T. Filleron, I. Valo, C. Charon-Barra, Y. M. Robin, P. Terrier, et al. (2016). "Malignant Peripheral Nerve Sheath Tumor Is a Challenging Diagnosis: A Systematic Pathology Review, Immunohistochemistry, and Molecular Analysis in 160 Patients From the French Sarcoma Group Database." Am J Surg Pathol **40**(7): 896-908.

Leal, A. S., C. R. Williams, D. B. Royce, P. A. Pioli, M. B. Sporn and K. T. Liby (2017). "Bromodomain inhibitors, JQ1 and I-BET 762, as potential therapies for pancreatic cancer." Cancer Lett **394**: 76-87.

Lederer, S., T. M. H. Dijkstra and T. Heskes (2018). "Additive Dose Response Models: Explicit Formulation and the Loewe Additivity Consistency Condition." Front Pharmacol **9**: 31.

Ledford, H. (2011). "Translational research: 4 ways to fix the clinical trial." Nature **477**(7366): 526-528.

Lee, M. Y., R. A. Kumar, S. M. Sukumaran, M. G. Hogg, D. S. Clark and J. S. Dordick (2008). "Three-dimensional cellular microarray for high-throughput toxicology assays." Proc Natl Acad Sci U S A **105**(1): 59-63.

Lee, T. J., M. Chopra, R. H. Kim, P. C. Parkin and C. Barnett-Tapia (2023). "Incidence and prevalence of neurofibromatosis type 1 and 2: a systematic review and meta-analysis." Orphanet J Rare Dis **18**(1): 292.

Lee, W., S. Teckie, T. Wiesner, L. Ran, C. N. Prieto Granada, M. Lin, S. Zhu, et al. (2014). "PRC2 is recurrently inactivated through EED or SUZ12 loss in malignant peripheral nerve sheath tumors." Nat Genet **46**(11): 1227-1232.

Legius, E., H. Dierick, R. Wu, B. K. Hall, P. Marynen, J. J. Cassiman and T. W. Glover (1994). "TP53 mutations are frequent in malignant NF1 tumors." Genes Chromosomes Cancer **10**(4): 250-255.

Legius, E., L. Messiaen, P. Wolkenstein, P. Pancza, R. A. Avery, Y. Berman, J. Blakeley, et al. (2021). "Revised diagnostic criteria for neurofibromatosis type 1 and Legius syndrome: an international consensus recommendation." Genet Med **23**(8): 1506-1513.

Li, J., L. Liu, Q. Zhang, Y. Huang, Y. Zhang, X. Gan, S. Liu, et al. (2020). "A novel TJP1-ROS1 fusion in malignant peripheral nerve sheath tumor responding to crizotinib: A case report." Medicine (Baltimore) **99**(26): e20725.

Li, Y., P. O'Connell, H. H. Breidenbach, R. Cawthon, J. Stevens, G. Xu, S. Neil, et al. (1995). "Genomic organization of the neurofibromatosis 1 gene (NF1)." Genomics **25**(1): 9-18.

Li, Y., P. K. Rao, R. Wen, Y. Song, D. Muir, P. Wallace, S. J. van Horne, et al. (2004). "Notch and Schwann cell transformation." Oncogene **23**(5): 1146-1152.

Lin, J. H. (2008). "Applications and limitations of genetically modified mouse models in drug discovery and development." Curr Drug Metab **9**(5): 419-438.

Ling, B. C., J. Wu, S. J. Miller, K. R. Monk, R. Shamekh, T. A. Rizvi, G. Decourten-Myers, et al. (2005). "Role for the epidermal growth factor receptor in neurofibromatosis-related peripheral nerve tumorigenesis." Cancer Cell **7**(1): 65-75.

Listernick, R., J. Charrow, M. Greenwald and M. Mets (1994). "Natural history of optic pathway tumors in children with neurofibromatosis type 1: a longitudinal study." J Pediatr **125**(1): 63-66.

Liu, Q., X. Yin, L. R. Languino and D. C. Altieri (2018). "Evaluation of drug combination effect using a Bliss independence dose-response surface model." Stat Biopharm Res **10**(2): 112-122.

Liu, X. (2022). "PRC2, Chromatin Regulation, and Human Disease: Insights From Molecular Structure and Function." Front Oncol **12**: 894585.

Liu, Y., W. Wu, C. Cai, H. Zhang, H. Shen and Y. Han (2023). "Patient-derived xenograft models in cancer therapy: technologies and applications." Signal Transduct Target Ther **8**(1): 160.

Lock, R., R. Ingraham, O. Maertens, A. L. Miller, N. Weledji, E. Legius, B. M. Konicek, et al. (2016). "Cotargeting MNK and MEK kinases induces the regression of NF1-mutant cancers." J Clin Invest **126**(6): 2181-2190.

Longo, J. F., S. N. Brosius, I. Znoyko, V. A. Alers, D. P. Jenkins, R. C. Wilson, A. J. Carroll, et al. (2021). "Establishment and genomic characterization of a sporadic malignant peripheral nerve sheath tumor cell line." Sci Rep **11**(1): 5690.

Lopez, G., K. Torres, J. Liu, B. Hernandez, E. Young, R. Belousov, S. Bolshakov, et al. (2011). "Autophagic survival in resistance to histone deacetylase inhibitors: novel strategies to treat malignant peripheral nerve sheath tumors." Cancer Res **71**(1): 185-196.

Lu, H. C., V. Eulo, A. J. Apicelli, M. Pekmezci, Y. Tao, J. Luo, A. C. Hirbe and S. Dahiya (2018). "Aberrant ATRX protein expression is associated with poor overall survival in NF1-MPNST." Oncotarget **9**(33): 23018-23028.

M

Ma, J. and A. Motsinger-Reif (2019). "Current Methods for Quantifying Drug Synergism." Proteom Bioinform **1**(2): 43-48.

Macarrón, R. and R. P. Hertzberg (2011). "Design and implementation of high-throughput screening assays." Mol Biotechnol **47**(3): 270-285.

Machado Almeida, P., B. Lago Solis, L. Stickley, A. Feidler and E. Nagoshi (2021). "Neurofibromin 1 in mushroom body neurons mediates circadian wake drive through activating cAMP-PKA signaling." Nat Commun **12**(1): 5758.

Madsen, R. R., A. Le Marois, O. N. Mruk, M. Voliotis, S. Yin, J. Sufi, X. Qin, et al. (2025). "Oncogenic PIK3CA corrupts growth factor signaling specificity." Mol Syst Biol **21**(2): 126-157.

Maertens, O., M. E. McCurrach, B. S. Braun, T. De Raedt, I. Epstein, T. Q. Huang, J. O. Lauchle, et al. (2017). "A Collaborative Model for Accelerating the Discovery and Translation of Cancer Therapies." Cancer Res **77**(21): 5706-5711.

Magallón-Lorenz, M., J. Fernández-Rodríguez, E. Terribas, E. Creus-Batchiller, C. Romagosa, A. Estival, D. Perez Sidelnikova, et al. (2021). "Chromosomal translocations inactivating CDKN2A support a single path for malignant peripheral nerve sheath tumor initiation." Hum Genet **140**(8): 1241-1252.

Magallón-Lorenz, M., E. Terribas, S. Ortega-Bertran, E. Creus-Bachiller, M. Fernández, G. Requena, I. Rosas, et al. (2023). "Deep genomic analysis of malignant peripheral nerve sheath tumor cell lines challenges current malignant peripheral nerve sheath tumor diagnosis." iScience **26**(2): 106096.

Magro, G., G. Broggi, G. Angelico, L. Puzzo, G. M. Vecchio, V. Virzì, L. Salvatorelli and M. Ruggieri (2022). "Practical Approach to Histological Diagnosis of Peripheral Nerve Sheath Tumors: An Update." Diagnostics (Basel) **12**(6).

Mahller, Y. Y., S. S. Vaikunth, M. A. Currier, S. J. Miller, M. C. Ripberger, Y. H. Hsu, R. Mehrian-Shai, et al. (2007). "Oncolytic HSV and erlotinib inhibit tumor growth and angiogenesis in a novel malignant peripheral nerve sheath tumor xenograft model." Mol Ther **15**(2): 279-286.

Mainardi, S., A. Mulero-Sánchez, A. Prahallad, G. Germano, A. Bosma, P. Krimpenfort, C. Lieftink, et al. (2018). "SHP2 is required for growth of KRAS-mutant non-small-cell lung cancer in vivo." Nat Med **24**(7): 961-967.

Malone, C. F., C. Emerson, R. Ingraham, W. Barbosa, S. Guerra, H. Yoon, L. L. Liu, et al. (2017). "mTOR and HDAC Inhibitors Converge on the TXNIP/Thioredoxin Pathway to Cause Catastrophic Oxidative Stress and Regression of RAS-Driven Tumors." Cancer Discov **7**(12): 1450-1463.

Manji, G. A., B. A. Van Tine, S. M. Lee, A. G. Raufi, I. Pellicciotta, A. C. Hirbe, J. Pradhan, et al. (2021). "A Phase I Study of the Combination of Pexidartinib and Sirolimus to Target Tumor-Associated Macrophages in Unresectable Sarcoma and Malignant Peripheral Nerve Sheath Tumors." Clin Cancer Res **27**(20): 5519-5527.

Mantripragada, K. K., G. Spurlock, L. Kluwe, N. Chuzhanova, R. E. Ferner, I. M. Frayling, J. P. Dumanski, et al. (2008). "High-resolution DNA copy number profiling of malignant peripheral nerve sheath tumors using targeted microarray-based comparative genomic hybridization." Clin Cancer Res **14**(4): 1015-1024.

Margueron, R. and D. Reinberg (2011). "The Polycomb complex PRC2 and its mark in life." Nature **469**(7330): 343-349.

Martin, E., N. Lamba, U. E. Flucke, C. Verhoef, J. H. Coert, Y. M. H. Versleijen-Jonkers and I. M. E. Desar (2019). "Non-cytotoxic systemic treatment in malignant peripheral nerve sheath tumors (MPNST): A systematic review from bench to bedside." Crit Rev Oncol Hematol **138**: 223-232.

Mathews Griner, L. A., R. Guha, P. Shinn, R. M. Young, J. M. Keller, D. Liu, I. S. Goldlust, et al. (2014). "High-throughput combinatorial screening identifies drugs that cooperate with ibrutinib to kill activated B-cell-like diffuse large B-cell lymphoma cells." Proc Natl Acad Sci U S A **111**(6): 2349-2354.

Mautner, V. F., F. A. Asuagbor, E. Dombi, C. Fünsterer, L. Kluwe, R. Wenzel, B. C. Widemann and J. M. Friedman (2008). "Assessment of benign tumor burden by whole-body MRI in patients with neurofibromatosis 1." Neuro Oncol **10**(4): 593-598.

Mayoh, C., J. Mao, J. Xie, G. Tax, S. O. Chow, R. Cadiz, K. Pazaky, et al. (2023). "High-Throughput Drug Screening of Primary Tumor Cells Identifies Therapeutic Strategies for Treating Children with High-Risk Cancer." Cancer Res **83**(16): 2716-2732.

Mayr, L. M. and P. Fuerst (2008). "The future of high-throughput screening." J Biomol Screen **13**(6): 443-448.

McKean, M. (2022). "Newly updated activity results of alrizomadlin (APG-115), a novel MDM2/p53 inhibitor, plus pembrolizumab: Phase 2 study in adults and children with various solid tumors." Journal of Clinical Oncology. **40**.

Miettinen, M., J. F. Fetsch, L. H. Sobin and J. Lasota (2006). "Gastrointestinal stromal tumors in patients with neurofibromatosis 1: a clinicopathologic and molecular genetic study of 45 cases." Am J Surg Pathol **30**(1): 90-96.

Miettinen, M. M., C. R. Antonescu, C. D. M. Fletcher, A. Kim, A. J. Lazar, M. M. Quezado, K. M. Reilly, et al. (2017). "Histopathologic evaluation of atypical neurofibromatous tumors and their transformation into malignant peripheral nerve sheath tumor in patients with neurofibromatosis 1-a consensus overview." Hum Pathol **67**: 1-10.

Miller, S. J., W. J. Jessen, T. Mehta, A. Hardiman, E. Sites, S. Kaiser, A. G. Jegga, et al. (2009). "Integrative genomic analyses of neurofibromatosis tumours identify SOX9 as a biomarker and survival gene." EMBO Mol Med **1**(4): 236-248.

Miller, S. J., F. Rangwala, J. Williams, P. Ackerman, S. Kong, A. G. Jegga, S. Kaiser, et al. (2006). "Large-scale molecular comparison of human schwann cells to malignant peripheral nerve sheath tumor cell lines and tissues." Cancer Res **66**(5): 2584-2591.

Mo, W., J. Chen, A. Patel, L. Zhang, V. Chau, Y. Li, W. Cho, et al. (2013). "CXCR4/CXCL12 mediate autocrine cell- cycle progression in NF1-associated malignant peripheral nerve sheath tumors." Cell **152**(5): 1077-1090.

Mohamad, T., C. Plante and J. P. Brosseau (2021). "Toward Understanding the Mechanisms of Malignant Peripheral Nerve Sheath Tumor Development." Int J Mol Sci **22**(16).

Mohan, P., J. Castellsague, J. Jiang, K. Allen, H. Chen, O. Nemirovsky, M. Spyra, et al. (2013). "Genomic imbalance of HMMR/RHAMM regulates the sensitivity and response of malignant peripheral nerve sheath tumour cells to aurora kinase inhibition." Oncotarget **4**(1): 80-93.

Morgan, R. A. (2012). "Human tumor xenografts: the good, the bad, and the ugly." Mol Ther **20**(5): 882-884.

Mrowczynski, O. D., R. A. Payne, A. J. Bourcier, C. Y. Mau, B. Slagle-Webb, G. Shenoy, A. B. Madhankumar, et al. (2019). "Targeting IL-13Rα2 for effective treatment of malignant peripheral nerve sheath tumors in mouse models." J Neurosurg **131**(5): 1369-1379.

N

Nair, A. B. and S. Jacob (2016). "A simple practice guide for dose conversion between animals and human." J Basic Clin Pharm **7**(2): 27-31.

Nakagawa, Y., A. Yoshida, K. Numoto, T. Kunisada, D. Wai, N. Ohata, K. Takeda, et al. (2006). "Chromosomal imbalances in malignant peripheral nerve sheath tumor detected by metaphase and microarray comparative genomic hybridization." Oncol Rep **15**(2): 297-303.

Nielsen, G. P., A. O. Stemmer-Rachamimov, Y. Ino, M. B. Moller, A. E. Rosenberg and D. N. Louis (1999). "Malignant transformation of neurofibromas in neurofibromatosis 1 is associated with CDKN2A/p16 inactivation." Am J Pathol **155**(6): 1879-1884.

Nishida, Y., H. Urakawa, R. Nakayama, E. Kobayashi, T. Ozaki, K. Ae, Y. Matsumoto, et al. (2021). "Phase II clinical trial of pazopanib for patients with unresectable or metastatic malignant peripheral nerve sheath tumors." Int J Cancer **148**(1): 140-149.

O

Ohishi, J., M. Aoki, K. Nabeshima, J. Suzumiya, T. Takeuchi, A. Ogose, M. Hakozaki, et al. (2013). "Imatinib mesylate inhibits cell growth of malignant peripheral nerve sheath tumors in vitro and in vivo through suppression of PDGFR-β." BMC Cancer **13**: 224.

Ortega-Bertran, S., J. Fernández-Rodríguez, M. Magallón-Lorenz, X. Zhang, E. Creus-Bachiller, A. P. Diazgranados, I. Uriarte-Arrazola, et al. (2024). "Triple Combination of MEK, BET, and CDK Inhibitors Significantly Reduces Human Malignant Peripheral Nerve Sheath Tumors in Mouse Models." Clin Cancer Res.

Ortonne, N., P. Wolkenstein, J. O. Blakeley, B. Korf, S. R. Plotkin, V. M. Riccardi, D. C. Miller, et al. (2018). "Cutaneous neurofibromas: Current clinical and pathologic issues." Neurology **91**(2 Suppl 1): S5-S13.

Oyama, R., F. Kito, M. Takahashi, E. Hattori, R. Noguchi, Y. Takai, M. Sakumoto, et al. (2020). "Establishment and characterization of patient-derived cancer models of malignant peripheral nerve sheath tumors." Cancer Cell Int **20**: 58.

P

Panse, G., E. Reisenbichler, M. Snuderl, W. L. Wang, W. Laskin and G. Jour (2021). "LMNA-NTRK1 rearranged mesenchymal tumor (lipofibromatosis-like neural tumor) mimicking pigmented dermatofibrosarcoma protuberans." J Cutan Pathol **48**(2): 290-294.

Parada, L. F., H. Land, R. A. Weinberg, D. Wolf and V. Rotter (1984). "Cooperation between gene encoding p53 tumour antigen and ras in cellular transformation." Nature **312**(5995): 649-651.

Patel, A. J., C. P. Liao, Z. Chen, C. Liu, Y. Wang and L. Q. Le (2014). "BET bromodomain inhibition triggers apoptosis of NF1-associated malignant peripheral nerve sheath tumors through Bim induction." Cell Rep **6**(1): 81-92.

Patel, A. V., D. Eaves, W. J. Jessen, T. A. Rizvi, J. A. Ecsedy, M. G. Qian, B. J. Aronow, et al. (2012). "Ras-driven transcriptome analysis identifies aurora kinase A as a potential malignant peripheral nerve sheath tumor therapeutic target." Clin Cancer Res **18**(18): 5020-5030.

Patro, R., G. Duggal, M. I. Love, R. A. Irizarry and C. Kingsford (2017). "Salmon provides fast and bias-aware quantification of transcript expression." Nat Methods **14**(4): 417-419.

Patwardhan, P. P., O. Surriga, M. J. Beckman, E. de Stanchina, R. P. Dematteo, W. D. Tap and G. K. Schwartz (2014). "Sustained inhibition of receptor tyrosine kinases and macrophage depletion by PLX3397 and rapamycin as a potential new approach for the treatment of MPNSTs." Clin Cancer Res **20**(12): 3146-3158.

Peacock, J. D., D. Cherba, K. Kampfschulte, M. K. Smith, N. R. Monks, C. P. Webb and M. Steensma (2013). "Molecular-guided therapy predictions reveal drug resistance phenotypes and treatment alternatives in malignant peripheral nerve sheath tumors." J Transl Med **11**: 213.

Peacock, J. D., M. G. Pridgeon, E. A. Tovar, C. J. Essenburg, M. Bowman, Z. Madaj, J. Koeman, et al. (2018). "Genomic Status of." Cancer Res **78**(13): 3672-3687.

Pekmezci, M., D. E. Reuss, A. C. Hirbe, S. Dahiya, D. H. Gutmann, A. von Deimling, A. E. Horvai and A. Perry (2015). "Morphologic and immunohistochemical features of malignant peripheral nerve sheath tumors and cellular schwannomas." Mod Pathol **28**(2): 187-200.

Peltonen, J., T. Marttala, T. Vihersaari, S. Renvall and R. Penttinen (1981). "Collagen synthesis in cells cultured from v. Recklinghausen's neurofibromatosis." Acta Neuropathol **55**(3): 183-187.

Pemov, A., H. Li, R. Patidar, N. F. Hansen, S. Sindiri, S. W. Hartley, J. S. Wei, et al. (2017). "The primacy of NF1 loss as the driver of tumorigenesis in neurofibromatosis type 1-associated plexiform neurofibromas." Oncogene **36**(22): 3168-3177.

Pemov, A., H. Li, W. Presley, M. R. Wallace and D. T. Miller (2020). "Genetics of human malignant peripheral nerve sheath tumors." Neurooncol Adv **2**(Suppl 1): i50-i61.

Perrin, G. Q., H. Li, L. Fishbein, S. A. Thomson, M. S. Hwang, M. T. Scarborough, A. T. Yachnis, et al. (2007). "An orthotopic xenograft model of intraneural NF1 MPNST suggests a potential association between steroid hormones and tumor cell proliferation." Lab Invest **87**(11): 1092-1102.

Plotkin, S. R., L. Messiaen, E. Legius, P. Pancza, R. A. Avery, J. O. Blakeley, D. Babovic-Vuksanovic, et al. (2022). "Updated diagnostic criteria and nomenclature for neurofibromatosis type 2 and schwannomatosis: An international consensus recommendation." Genet Med **24**(9): 1967-1977.

Porter, D. E., V. Prasad, L. Foster, G. F. Dall, R. Birch and R. J. Grimer (2009). "Survival in Malignant Peripheral Nerve Sheath Tumours: A Comparison between Sporadic and Neurofibromatosis Type 1-Associated Tumours." Sarcoma **2009**: 756395.

Prieto-Granada, C. N., T. Wiesner, J. L. Messina, A. A. Jungbluth, P. Chi and C. R. Antonescu (2016). "Loss of H3K27me3 Expression Is a Highly Sensitive Marker for Sporadic and Radiation-induced MPNST." Am J Surg Pathol **40**(4): 479-489.

R

Ramkissoon, A., K. E. Chaney, D. Milewski, K. B. Williams, R. L. Williams, K. Choi, A. Miller, et al. (2019). "Targeted Inhibition of the Dual Specificity Phosphatases DUSP1 and DUSP6 Suppress MPNST Growth via JNK." Clin Cancer Res **25**(13): 4117-4127.

Ratner, N. and S. J. Miller (2015). "A RASopathy gene commonly mutated in cancer: the neurofibromatosis type 1 tumour suppressor." Nat Rev Cancer **15**(5): 290-301.

Rausch, O. (2006). "High content cellular screening." Curr Opin Chem Biol **10**(4): 316-320.

Reigner, B. G. and K. S. Blesch (2002). "Estimating the starting dose for entry into humans: principles and practice." Eur J Clin Pharmacol **57**(12): 835-845.

Riccardi, V. M. (1981). "Von Recklinghausen neurofibromatosis." N Engl J Med **305**(27): 1617-1627.

Richards, R., H. R. Schwartz, M. E. Honeywell, M. S. Stewart, P. Cruz-Gordillo, A. J. Joyce, B. D. Landry and M. J. Lee (2020). "Drug antagonism and single-agent dominance result from differences in death kinetics." Nat Chem Biol **16**(7): 791-800.

Richmond, A. and Y. Su (2008). "Mouse xenograft models vs GEM models for human cancer therapeutics." Dis Model Mech **1**(2-3): 78-82.

Rodriguez, F. J., A. L. Folpe, C. Giannini and A. Perry (2012). "Pathology of peripheral nerve sheath tumors: diagnostic overview and update on selected diagnostic problems." Acta Neuropathol **123**(3): 295-319.

Romine, K. A., K. MacPherson, H. J. Cho, Y. Kosaka, P. A. Flynn, K. H. Byrd, J. L. Coy, et al. (2023). "BET inhibitors rescue anti-PD1 resistance by enhancing TCF7 accessibility in leukemia-derived terminally exhausted CD8." Leukemia **37**(3): 580-592.

Ruggeri, B. A., F. Camp and S. Miknyoczki (2014). "Animal models of disease: pre-clinical animal models of cancer and their applications and utility in drug discovery." Biochem Pharmacol **87**(1): 150-161.

S

Sabbagh, A., E. Pasmant, A. Imbard, A. Luscan, M. Soares, H. Blanché, I. Laurendeau, et al. (2013). "NF1 molecular characterization and neurofibromatosis type I genotype-phenotype correlation: the French experience." Hum Mutat **34**(11): 1510-1518.

Sabbagh, A., E. Pasmant, I. Laurendeau, B. Parfait, S. Barbarot, B. Guillot, P. Combemale, et al. (2009). "Unravelling the genetic basis of variable clinical expression in neurofibromatosis 1." Hum Mol Genet **18**(15): 2768-2778.

Sahm, F., D. E. Reuss and C. Giannini (2018). "WHO 2016 classification: changes and advancements in the diagnosis of miscellaneous primary CNS tumours." Neuropathol Appl Neurobiol **44**(2): 163-171.

Sarin, K. Y., J. Kincaid, B. Sell, J. Shahryari, M. A. J. Duncton, E. Morefield, W. Sun, et al. (2023). "Development of a MEK inhibitor, NFX-179, as a chemoprevention agent for squamous cell carcinoma." Sci Transl Med **15**(717): eade1844.

Sebaugh, J. L. (2011). "Guidelines for accurate EC50/IC50 estimation." Pharm Stat **10**(2): 128-134.

Semenova, G., D. S. Stepanova, C. Dubyk, E. Handorf, S. M. Deyev, A. J. Lazar and J. Chernoff (2017). "Targeting group I p21-activated kinases to control malignant peripheral nerve sheath tumor growth and metastasis." Oncogene **36**(38): 5421-5431.

Serra, E., B. Gel, J. Fernández-Rodrígues and C. Lázaro (2020). Genomics of Peripheral Nerve Sheath Tumors Associated with Neurofibromatosis Type 1. Springer Nature.

Serra, E., T. Rosenbaum, U. Winner, R. Aledo, E. Ars, X. Estivill, H. G. Lenard and C. Lázaro (2000). "Schwann cells harbor the somatic NF1 mutation in neurofibromas: evidence of two different Schwann cell subpopulations." Hum Mol Genet **9**(20): 3055-3064.

Serrano, M. (2000). "The INK4a/ARF locus in murine tumorigenesis." Carcinogenesis **21**(5): 865-869.

Shen, M. H., P. S. Harper and M. Upadhyaya (1996). "Molecular genetics of neurofibromatosis type 1 (NF1)." J Med Genet **33**(1): 2-17.

Sherekar, M., S. W. Han, R. Ghirlando, S. Messing, M. Drew, D. Rabara, T. Waybright, et al. (2020). "Biochemical and structural analyses reveal that the tumor suppressor neurofibromin (NF1) forms a high-affinity dimer." J Biol Chem **295**(4): 1105-1119.

Shinn, P., L. Chen, M. Ferrer, Z. Itkin, C. Klumpp-Thomas, C. McKnight, S. Michael, et al. (2019). "High-Throughput Screening for Drug Combinations." Methods Mol Biol **1939**: 11-35.

Shurell, E., A. S. Singh, J. G. Crompton, S. Jensen, Y. Li, S. Dry, S. Nelson, et al. (2016). "Characterizing the immune microenvironment of malignant peripheral nerve sheath tumor by PD-L1 expression and presence of CD8+ tumor infiltrating lymphocytes." Oncotarget **7**(39): 64300-64308.

Shurell-Linehan, E., B. J. DiPardo, I. A. Elliott, D. S. Graham, M. A. Eckardt, S. M. Dry, S. D. Nelson, et al. (2019). "Pathologic Response to Neoadjuvant Therapy is Associated With Improved Long-term Survival in High-risk Primary Localized Malignant Peripheral Nerve Sheath Tumors." Am J Clin Oncol **42**(5): 426-431.

Simon, J. A. and R. E. Kingston (2009). "Mechanisms of polycomb gene silencing: knowns and unknowns." Nat Rev Mol Cell Biol **10**(10): 697-708.

Siolas, D. and G. J. Hannon (2013). "Patient-derived tumor xenografts: transforming clinical samples into mouse models." Cancer Res **73**(17): 5315-5319.

Sobczuk, P., P. Teterycz, A. M. Czarnecka, T. Świtaj, H. Koseła-Paterczyk, K. Kozak, S. Falkowski and P. Rutkowski (2020). "Systemic Treatment for Advanced and Metastatic Malignant Peripheral Nerve Sheath Tumors-A Sarcoma Reference Center Experience." J Clin Med **9**(10).

Sohier, P., A. Luscan, A. Lloyd, K. Ashelford, I. Laurendeau, A. Briand-Suleau, D. Vidaud, et al. (2017). "Confirmation of mutation landscape of NF1-associated malignant peripheral nerve sheath tumors." Genes Chromosomes Cancer **56**(5): 421-426.

Somatilaka, B. N., A. Sadek, R. M. McKay and L. Q. Le (2022). "Malignant peripheral nerve sheath tumor: models, biology, and translation." Oncogene **41**(17): 2405-2421.

Soneson, C., M. I. Love and M. D. Robinson (2015). "Differential analyses for RNA-seq: transcript-level estimates improve gene-level inferences." F1000Res **4**: 1521.

Sonobe, H., T. Takeuchi, M. Furihata, T. Taguchi, A. Kawai, Y. Ohjimi, H. Iwasaki, et al. (2000). "A new human malignant peripheral nerve sheath tumour-cell line, HS-sch-2, harbouring p53 point mutation." Int J Oncol **17**(2): 347-352.

Stefano, S. and S. Giovanni (2019). "The PTEN Tumor Suppressor Gene in Soft Tissue Sarcoma." Cancers (Basel) **11**(8).

Stemmer-Rachamimov, A. O., D. N. Louis, G. P. Nielsen, C. R. Antonescu, A. D. Borowsky, R. T. Bronson, D. K. Burns, et al. (2004). "Comparative pathology of nerve sheath tumors in mouse models and humans." Cancer Res **64**(10): 3718-3724.

Stucky, C. C., K. N. Johnson, R. J. Gray, B. A. Pockaj, I. T. Ocal, P. S. Rose and N. Wasif (2012). "Malignant peripheral nerve sheath tumors (MPNST): the Mayo Clinic experience." Ann Surg Oncol **19**(3): 878-885.

Szymanski, J. J., R. T. Sundby, P. A. Jones, D. Srihari, N. Earland, P. K. Harris, W. Feng, et al. (2021). "Cell-free DNA ultra-low-pass whole genome sequencing to distinguish malignant peripheral nerve sheath tumor (MPNST) from its benign precursor lesion: A cross-sectional study." PLoS Med **18**(8): e1003734.

Szymański, P., M. Markowicz and E. Mikiciuk-Olasik (2012). "Adaptation of high-throughput screening in drug discovery-toxicological screening tests." Int J Mol Sci **13**(1): 427-452.

T

Tang, J., K. Wennerberg and T. Aittokallio (2015). "What is synergy? The Saariselkä agreement revisited." Front Pharmacol **6**: 181.

Taylor, B. S., J. Barretina, R. G. Maki, C. R. Antonescu, S. Singer and M. Ladanyi (2011). "Advances in sarcoma genomics and new therapeutic targets." Nat Rev Cancer **11**(8): 541-557.

To, K. K. W., E. Xing, R. C. Larue and P. K. Li (2023). "BET Bromodomain Inhibitors: Novel Design Strategies and Therapeutic Applications." Molecules **28**(7).

Torres, K. E., Q. S. Zhu, K. Bill, G. Lopez, M. P. Ghadimi, X. Xie, E. D. Young, et al. (2011). "Activated MET is a molecular prognosticator and potential therapeutic target for malignant peripheral nerve sheath tumors." Clin Cancer Res **17**(12): 3943-3955.

Tsimberidou, A. M., M. Kahle, H. H. Vo, M. A. Baysal, A. Johnson and F. Meric-Bernstam (2023). "Molecular tumour boards - current and future considerations for precision oncology." Nat Rev Clin Oncol **20**(12): 843-863.

U

Upadhyaya, M. (2010). "Neurofibromatosis type 1: diagnosis and recent advances." Expert Opin Med Diagn **4**(4): 307-322.

Upadhyaya, M., L. Kluwe, G. Spurlock, B. Monem, E. Majounie, K. Mantripragada, M. Ruggieri, et al. (2008). "Germline and somatic NF1 gene mutation spectrum in NF1-associated malignant peripheral nerve sheath tumors (MPNSTs)." Hum Mutat **29**(1): 74-82.

Uusitalo, E., M. Rantanen, R. A. Kallionpää, M. Pöyhönen, J. Leppävirta, H. Ylä-Outinen, V. M. Riccardi, et al. (2016). "Distinctive Cancer Associations in Patients With Neurofibromatosis Type 1." J Clin Oncol **34**(17): 1978-1986.

V

Valentin, T., A. Le Cesne, I. Ray-Coquard, A. Italiano, G. Decanter, E. Bompas, N. Isambert, et al. (2016). "Management and prognosis of malignant peripheral nerve sheath tumors: The experience of the French Sarcoma Group (GSF-GETO)." Eur J Cancer **56**: 77-84.

Van Noesel, M. M., D. Orbach, B. Brennan, A. Kelsey, I. Zanetti, G. L. de Salvo, M. N. Gaze, et al. (2019). "Outcome and prognostic factors in pediatric malignant peripheral nerve sheath tumors: An analysis of the European Pediatric Soft Tissue Sarcoma Group (EpSSG) NRSTS-2005 prospective study." Pediatr Blood Cancer **66**(10): e27833.

Varin, J., L. Poulain, M. Hivelin, P. Nusbaum, A. Hubas, I. Laurendeau, L. Lantieri, et al. (2016). "Dual mTORC1/2 inhibition induces anti-proliferative effect in NF1-associated plexiform neurofibroma and malignant peripheral nerve sheath tumor cells." Oncotarget **7**(24): 35753-35767.

Verdijk, R. M., M. A. den Bakker, H. J. Dubbink, W. C. Hop, W. N. Dinjens and J. M. Kros (2010). "TP53 mutation analysis of malignant peripheral nerve sheath tumors." J Neuropathol Exp Neurol **69**(1): 16-26.

Viskochil, D., A. M. Buchberg, G. Xu, R. M. Cawthon, J. Stevens, R. K. Wolff, M. Culver, et al. (1990). "Deletions and a translocation interrupt a cloned gene at the neurofibromatosis type 1 locus." Cell **62**(1): 187-192.

Vogel, K. S., L. J. Klesse, S. Velasco-Miguel, K. Meyers, E. J. Rushing and L. F. Parada (1999). "Mouse tumor model for neurofibromatosis type 1." Science **286**(5447): 2176-2179.

W

Wagner, V. and J. Gil (2020). "Senescence as a therapeutically relevant response to CDK4/6 inhibitors." Oncogene **39**(29): 5165-5176.
Walker, J. A. and M. Upadhyaya (2018). "Emerging therapeutic targets for neurofibromatosis type 1." Expert Opin Ther Targets **22**(5): 419-437.

Wallace, M. R., D. A. Marchuk, L. B. Andersen, R. Letcher, H. M. Odeh, A. M. Saulino, J. W. Fountain, et al. (1990). "Type 1 neurofibromatosis gene: identification of a large transcript disrupted in three NF1 patients." Science **249**(4965): 181-186.

Wang, D., Q. Zhang, B. L. Eisenberg, J. M. Kane, X. A. Li, D. Lucas, I. A. Petersen, et al. (2015). "Significant Reduction of Late Toxicities in Patients With Extremity Sarcoma Treated With Image-Guided Radiation Therapy to a Reduced Target Volume: Results of Radiation Therapy Oncology Group RTOG-0630 Trial." J Clin Oncol **33**(20): 2231-2238.

Wang, J., A. Calizo, L. Zhang, J. C. Pino, Y. Lyu, K. Pollard, X. Zhang, et al. (2023). "CDK4/6 inhibition enhances SHP2 inhibitor efficacy and is dependent upon restoration of RB function in malignant peripheral nerve sheath tumors." bioRxiv.

Wang, J., K. Pollard, A. Calizo and C. A. Pratilas (2021). "Activation of Receptor Tyrosine Kinases Mediates Acquired Resistance to MEK Inhibition in Malignant Peripheral Nerve Sheath Tumors." Cancer Res **81**(3): 747-762.

Warbey, V. S., R. E. Ferner, J. T. Dunn, E. Calonje and M. J. O'Doherty (2009). "[18F]FDG PET/CT in the diagnosis of malignant peripheral nerve sheath tumours in neurofibromatosis type-1." Eur J Nucl Med Mol Imaging **36**(5): 751-757.

Waterston, R. H., K. Lindblad-Toh, E. Birney, J. Rogers, J. F. Abril, P. Agarwal, R. Agarwala, et al. (2002). "Initial sequencing and comparative analysis of the mouse genome." Nature **420**(6915): 520-562.

Watson, A. L., L. K. Anderson, A. D. Greeley, V. W. Keng, E. P. Rahrmann, A. L. Halfond, N. M. Powell, et al. (2014). "Co-targeting the MAPK and PI3K/AKT/mTOR pathways in two genetically engineered mouse models of schwann cell tumors reduces tumor grade and multiplicity." Oncotarget **5**(6): 1502-1514.

Watson, A. L., E. P. Rahrmann, B. S. Moriarity, K. Choi, C. B. Conboy, A. D. Greeley, A. L. Halfond, et al. (2013). "Canonical Wnt/β-catenin signaling drives human schwann cell transformation, progression, and tumor maintenance." Cancer Discov **3**(6): 674-689.

Watson, K. L., G. A. Al Sannaa, C. M. Kivlin, D. R. Ingram, S. M. Landers, C. L. Roland, J. N. Cormier, et al. (2017). "Patterns of recurrence and survival in sporadic, neurofibromatosis Type 1-associated, and radiation-associated malignant peripheral nerve sheath tumors." J Neurosurg **126**(1): 319-329.

Watson, M. A., A. Perry, T. Tihan, R. A. Prayson, A. Guha, J. Bridge, R. Ferner and D. H. Gutmann (2004). "Gene expression profiling reveals unique molecular subtypes of Neurofibromatosis Type I-associated and sporadic malignant peripheral nerve sheath tumors." Brain Pathol **14**(3): 297-303.

Weiss, B. D., P. L. Wolters, S. R. Plotkin, B. C. Widemann, J. H. Tonsgard, J. Blakeley, J. C. Allen, et al. (2021). "NF106: A Neurofibromatosis Clinical Trials Consortium Phase II Trial of the MEK Inhibitor Mirdametinib (PD-0325901) in Adolescents and Adults With NF1-Related Plexiform Neurofibromas." J Clin Oncol **39**(7): 797-806.

Weydert, Z., M. Lal-Nag, L. Mathews-Greiner, C. Thiel, H. Cordes, L. Küpfer, P. Guye, et al. (2020). "A 3D Heterotypic Multicellular Tumor Spheroid Assay Platform to Discriminate Drug Effects on Stroma versus Cancer Cells." SLAS Discov **25**(3): 265-276.

White, K. A., V. J. Swier, J. T. Cain, J. L. Kohlmeyer, D. K. Meyerholz, M. R. Tanas, J. Uthoff, et al. (2018). "A porcine model of neurofibromatosis type 1 that mimics the human disease." JCI Insight **3**(12).

Williams, K. B. and D. A. Largaespada (2020). "New Model Systems and the Development of Targeted Therapies for the Treatment of Neurofibromatosis Type 1-Associated Malignant Peripheral Nerve Sheath Tumors." Genes (Basel) **11**(5).

Wojcik, J. B., D. M. Marchione, S. Sidoli, A. Djedid, A. Lisby, J. Majewski and B. A. Garcia (2019). "Epigenomic Reordering Induced by Polycomb Loss Drives Oncogenesis but Leads to Therapeutic Vulnerabilities in Malignant Peripheral Nerve Sheath Tumors." Cancer Res **79**(13): 3205-3219.

Wu, J., D. M. Patmore, E. Jousma, D. W. Eaves, K. Breving, A. V. Patel, E. B. Schwartz, et al. (2014). "EGFR-STAT3 signaling promotes formation of malignant peripheral nerve sheath tumors." Oncogene **33**(2): 173-180.

Wu, L. M. N., Y. Deng, J. Wang, C. Zhao, R. Rao, L. Xu, W. Zhou, et al. (2018). "Programming of Schwann Cells by Lats1/2-TAZ/YAP Signaling Drives Malignant Peripheral Nerve Sheath Tumorigenesis." Cancer Cell **33**(2): 292-308.e297.

Wu, S. Y. and C. M. Chiang (2007). "The double bromodomain-containing chromatin adaptor Brd4 and transcriptional regulation." J Biol Chem **282**(18): 13141-13145.

X

Xu, G. F., P. O'Connell, D. Viskochil, R. Cawthon, M. Robertson, M. Culver, D. Dunn, et al. (1990). "The neurofibromatosis type 1 gene encodes a protein related to GAP." Cell **62**(3): 599-608.

Y

Yamashita, A. S., G. S. Baia, J. S. Ho, E. Velarde, J. Wong, G. L. Gallia, A. J. Belzberg, et al. (2014). "Preclinical evaluation of the combination of mTOR and proteasome inhibitors with radiotherapy in malignant peripheral nerve sheath tumors." J Neurooncol **118**(1): 83-92.

Yao, C., H. Zhou, Y. Dong, A. Alhaskawi, S. Hasan Abdullah Ezzi, Z. Wang, et al. (2023). "Malignant Peripheral Nerve Sheath Tumors: Latest Concepts in Disease Pathogenesis and Clinical Management." Cancers (Basel) **15**(4).

Yin, M., Y. Guo, R. Hu, W. L. Cai, Y. Li, S. Pei, H. Sun, et al. (2020). "Potent BRD4 inhibitor suppresses cancer cell-macrophage interaction." Nat Commun **11**(1): 1833.

Young, L. C., R. Goldstein de Salazar, S. W. Han, Z. Y. S. Huang, A. Merk, M. Drew, J. Darling, et al. (2023). "Destabilizing NF1 variants act in a dominant negative manner through neurofibromin dimerization." Proc Natl Acad Sci U S A **120**(5): e2208960120.

Yuan, Z., L. Xu, Z. Zhao, S. Xu, X. Zhang, T. Liu, S. Zhang and S. Yu (2017). "Clinicopathological features and prognosis of malignant peripheral nerve sheath tumor: a retrospective study of 159 cases from 1999 to 2016." Oncotarget **8**(62): 104785-104795.

Z

Zehou, O., E. Fabre, L. Zelek, E. Sbidian, N. Ortonne, E. Banu, P. Wolkenstein and L. Valeyrie-Allanore (2013). "Chemotherapy for the treatment of malignant peripheral nerve sheath tumors in neurofibromatosis 1: a 10-year institutional review." Orphanet J Rare Dis **8**: 127.

Zhan, F., J. Hardin, B. Kordsmeier, K. Bumm, M. Zheng, E. Tian, R. Sanderson, et al. (2002). "Global gene expression profiling of multiple myeloma, monoclonal gammopathy of undetermined significance, and normal bone marrow plasma cells." Blood **99**(5): 1745-1757.

Zhang, M., Y. Wang, S. Jones, M. Sausen, K. McMahon, R. Sharma, Q. Wang, et al. (2014). "Somatic mutations of SUZ12 in malignant peripheral nerve sheath tumors." Nat Genet **46**(11): 1170-1172.

Zhang, X., B. Murray, G. Mo and J. F. Shern (2020). "The Role of Polycomb Repressive Complex in Malignant Peripheral Nerve Sheath Tumor." Genes (Basel) **11**(3).

Zhou, H., C. M. Coffin, S. L. Perkins, S. R. Tripp, M. Liew and D. H. Viskochil (2003). "Malignant peripheral nerve sheath tumor: a comparison of grade, immunophenotype, and cell cycle/growth activation marker expression in sporadic and neurofibromatosis 1-related lesions." Am J Surg Pathol **27**(10): 1337-1345.

Zou, C., K. D. Smith, J. Liu, G. Lahat, S. Myers, W. L. Wang, W. Zhang, et al. (2009). "Clinical, pathological, and molecular variables predictive of malignant peripheral nerve sheath tumor outcome." Ann Surg **249**(6): 1014-1022.

Appendix I

Pairwise Combination Results from High Throughput Screening

		DBSumNeg CTG 48 hrs			Excess HSA CTG 48 hrs		
Compound A	**Compound B**	**S462**	**NF1-08**	**NF1-09**	**S462**	**NF1-08**	**NF1-09**
7-Hydroxystaurosporine	Trametinib	-8,0824	-4,19902	-7,11454	-1363,23056	-782,43759	-642,28925
Palbociclib	Trametinib	-5,51799	-3,43283	-2,46192	-695,18369	-689,90351	-235,26766
Fascaplysin	Trametinib	-0,74882	-1,32439	-2,13479	-251,24419	-404,18682	-212,34471
PHA-690509	Trametinib	-0,41057	-0,09636	-2,85445	-239,34005	149,67266	-167,09474
Flavopiridol	Trametinib	-1,28785	-0,90509	-2,00313	-335,59103	152,93509	-175,88391
I-BET762	Trametinib	-10,46594	-8,32873	-7,31591	-1679,71321	-1216,39138	-731,31086
Purvalanol A	Trametinib	-4,5645	-1,69792	-6,34459	-670,01254	-264,24572	-635,52555
R-547	Trametinib	-0,60587	0	-2,42525	-395,58195	749,20328	381,48549
Cdk4/6 Inhibitor IV	Trametinib	-3,23592	-2,70326	-3,33544	-321,23797	-142,70357	-188,39296
I-BET151	Trametinib	-5,43886	-2,48306	-7,5919	-1168,8805	-429,97159	-715,76655
PHA-848125	Trametinib	-4,76842	-0,0825	-3,81661	-952,56981	350,49749	-513,30006
JQ1	Trametinib	-2,30951	-3,7107	-7,58536	-1156,74701	-814,59486	-911,90631
7-Hydroxystaurosporine	AZD-8330	-10,92957	-4,71942	-5,80004	-1481,12091	-777,54623	-453,52252
Palbociclib	AZD-8330	-5,57852	-4,82644	-3,27763	-830,23694	-691,38091	-326,01317
Fascaplysin	AZD-8330	-0,86841	-1,19469	-1,1601	-185,42204	-324,02273	-81,38799
PHA-690509	AZD-8330	-0,64632	-0,57715	-1,00041	-268,46716	-19,62543	91,33696
Flavopiridol	AZD-8330	-1,51343	-2,298	-0,55706	-283,19336	23,24276	5,92829
I-BET762	AZD-8330	-8,87696	-11,08734	-4,89256	-1510,13335	-1372,81564	-463,02414
Purvalanol A	AZD-8330	-5,88665	-1,46504	-6,10327	-704,72993	-41,35355	-607,25689
R-547	AZD-8330	-1,36547	-0,6037	-1,17373	-288,40402	613,88051	-76,30175
Cdk4/6 Inhibitor IV	AZD-8330	-2,32665	-2,94196	-3,58724	-87,65201	-252,21744	-320,9962
I-BET151	AZD-8330	-7,87149	-4,76312	-3,8564	-1435,33491	-737,52249	-243,33641
PHA-848125	AZD-8330	-3,78645	-2,0735	-2,40611	-890,22659	27,01386	-268,73763
JQ1	AZD-8330	-2,06549	-3,45259	-4,74073	-1045,5376	-848,55097	-526,82076
7-Hydroxystaurosporine	I-BET762	-2,39541	-2,08252	-1,58348	-541,51907	-452,85549	101,87193
Palbociclib	I-BET762	-4,10276	-2,58569	-5,09338	-527,50737	-425,84241	-480,47233
Fascaplysin	I-BET762	-2,11618	-1,71031	-0,51445	-550,78084	95,84609	180,27048
PHA-690509	I-BET762	-1,5724	-0,72744	-3,68592	-331,4669	-92,50433	-308,62774
Flavopiridol	I-BET762	-6,55905	-5,95682	-13,01892	-793,53977	-723,96152	-1270,65994
Purvalanol A	I-BET762	-5,80872	-6,23677	-7,88826	-724,61642	-855,29532	-788,82609
R-547	I-BET762	-7,78084	-10,5025	-12,23703	-1010,22326	-1000,76828	-1190,66861
Cdk4/6 Inhibitor IV	I-BET762	-3,45165	-3,12846	-1,84193	-419,47225	-311,22241	136,70662
PHA-848125	I-BET762	-3,01693	-1,90849	-12,19251	-863,67095	-733,39211	-1277,83956
7-Hydroxystaurosporine	Hypothemycin	-3,68474	-2,06237	-6,92822	-602,83328	-398,1542	-707,15358
Palbociclib	Hypothemycin	-3,25776	-3,1058	-0,9731	-230,89397	-374,40619	325,55414
Fascaplysin	Hypothemycin	-0,00186	-0,14634	-0,38293	169,64825	-157,18327	106,06271
PHA-690509	Hypothemycin	-1,29819	-4,92482	-2,14599	-17,26772	-506,41666	-223,30197
Flavopiridol	Hypothemycin	-0,4641	-5,68182	-2,03778	11,02964	-598,3386	-180,2999
I-BET762	Hypothemycin	-4,94283	-8,77499	-4,00052	-804,91289	-1282,25763	-377,4021
Purvalanol A	Hypothemycin	-0,60937	-2,91156	-2,46999	-134,69605	-628,45878	-226,97198
R-547	Hypothemycin	-2,07028	-1,59373	-2,39986	-328,8016	94,09647	-159,45557
Cdk4/6 Inhibitor IV	Hypothemycin	-3,57518	-10,23971	-2,66829	-317,21214	-1099,28425	-84,14079
I-BET151	Hypothemycin	-5,57252	-6,45793	-8,60896	-843,45183	-1022,21259	-834,4945
PHA-848125	Hypothemycin	-3,49696	-1,39341	-6,86081	-626,4952	155,49832	-757,71265
JQ1	Hypothemycin	-4,14233	-2,33428	-6,96755	-951,56556	-775,4215	-609,22194
7-Hydroxystaurosporine	Mirdametinib	-9,25126	-2,63626	-4,49392	-1301,16037	-548,63764	-418,90103
Palbociclib	Mirdametinib	-4,58846	-0,3701	-1,04578	-484,46652	160,93044	49,45268
Fascaplysin	Mirdametinib	-0,11442	0	-1,65682	-37,40937	228,99596	-148,95924
PHA-690509	Mirdametinib	-3,34296	-4,07841	-4,14293	-521,99233	-416,28829	-356,27008
Flavopiridol	Mirdametinib	-0,86693	-3,77766	-0,60461	-205,56036	-298,85141	58,55586
I-BET762	Mirdametinib	-6,90786	-12,99063	-5,02317	-1394,39808	-1676,79639	-459,81662
Purvalanol A	Mirdametinib	-1,21172	-3,14659	-2,92444	-349,82546	-652,34183	-254,76208
R-547	Mirdametinib	-1,99111	-1,18345	-2,54366	-375,11091	340,35017	-244,09663
Cdk4/6 Inhibitor IV	Mirdametinib	-4,48191	-7,26272	-4,10382	-540,93217	-800,14797	-414,62582
I-BET151	Mirdametinib	-6,98951	-9,27957	-9,71462	-1262,7743	-1297,93539	-981,33101
PHA-848125	Mirdametinib	-1,6535	-1,06566	-7,56388	-585,50853	10,25063	-698,83647
JQ1	Mirdametinib	-6,15981	-8,44843	-6,23266	-1433,80179	-1402,57757	-597,41769
7-Hydroxystaurosporine	I-BET151	-2,65948	-1,24086	-1,22801	-319,61889	-311,60124	109,95261
Palbociclib	I-BET151	-1,34703	-1,2199	-4,8943	4,6733	-48,53579	-414,07805
Fascaplysin	I-BET151	-0,58456	-0,40888	-1,3288	-240,88237	-24,63195	-100,64818
PHA-690509	I-BET151	-6,31724	-3,59247	-7,42496	-793,25747	398,45014	-732,99056
Flavopiridol	I-BET151	-7,10755	-3,86437	-13,48899	-847,9486	-547,3937	-1299,31229
Purvalanol A	I-BET151	-1,39162	-6,25994	-7,65621	-8,92966	-954,90399	-756,40198
R-547	I-BET151	-2,6598	-8,42046	-14,56049	-528,82499	-907,67501	-1403,59871
Cdk4/6 Inhibitor IV	I-BET151	-4,3082	-4,46089	-4,06296	-498,236	-561,03361	-374,42422
PHA-848125	I-BET151	-5,65369	-3,27774	-10,11204	-899,53466	-683,83196	-988,42673
7-Hydroxystaurosporine	PD-318088	-13,62393	-4,64528	-2,48777	-1621,53984	-739,92918	-133,20553
Palbociclib	PD-318088	-5,04265	-2,81042	-2,85058	-832,5885	-445,45316	-236,13992
Fascaplysin	PD-318088	-1,77881	-0,20287	-1,14021	-354,3594	108,79278	-102,50452
PHA-690509	PD-318088	-2,15787	-1,06217	-0,59446	-355,96054	-34,68871	162,86521
Flavopiridol	PD-318088	-0,97842	-0,91187	-0,88828	-161,02909	-143,85097	-7,95882
I-BET762	PD-318088	-2,41755	-4,81458	-4,47305	-866,06461	-952,82194	-387,21846
Purvalanol A	PD-318088	-2,18752	-5,87388	-2,77209	-16,69538	-779,89585	-272,51928

I Appendix I

		DBSumNeg CTG 48 hrs			Excess HSA CTG 48 hrs		
Compound A	**Compound B**	**S462**	**NF1-08**	**NF1-09**	**S462**	**NF1-08**	**NF1-09**
R-547	PD-318088	-0,69753	-2,32899	-1,7325	91,62832	-166,27937	-161,83568
Cdk4/6 Inhibitor IV	PD-318088	-1,62556	-12,52801	-0,43569	17,62304	-1419,53223	1932,90156
I-BET151	PD-318088	-0,30435	-7,25193	-4,17191	-601,66429	-1153,60406	-417,19101
PHA-848125	PD-318088	-6,51389	-4,92698	-3,71241	-900,40002	-550,03783	-297,58192
JQ1	PD-318088	-12,02192	-13,59357	-7,23348	-1555,9459	-1919,46535	-705,19725
7-Hydroxystaurosporine	ARRY-162	-10,57345	-5,11667	-1,94838	-573,11743	-902,5997	-48,67707
Palbociclib	ARRY-162	-7,84467	-0,94665	-1,79789	-1130,1026	-131,03212	7,79482
Fascaplysin	ARRY-162	-0,79399	-0,65268	-0,49945	-249,97359	-62,53627	-10,30488
PHA-690509	ARRY-162	-1,83267	-0,97892	-0,58436	-417,70049	34,39436	13,64249
Flavopiridol	ARRY-162	-0,44017	-0,52931	-0,40212	-144,83638	35,49545	107,72921
I-BET762	ARRY-162	-0,98799	-4,18771	-2,61581	-884,00327	-887,31924	-159,53608
Purvalanol A	ARRY-162	-1,72317	-5,65228	-4,42891	-78,04324	-677,41647	-446,3769
R-547	ARRY-162	-1,80223	-2,42522	-1,48817	-300,70524	-63,00909	-131,35045
Cdk4/6 Inhibitor IV	ARRY-162	-3,91372	-12,05907	-2,46909	-380,94158	-1323,01551	-228,91134
I-BET151	ARRY-162	-3,20492	-7,05045	-5,12789	-15,10049	-856,86469	-502,83394
PHA-848125	ARRY-162	-6,15507	-5,91452	-4,48519	-1022,77996	-724,21173	-419,33716
JQ1	ARRY-162	-8,03762	-14,54331	-8,01418	-1352,60718	-1845,98112	-796,20266
7-Hydroxystaurosporine	AZD 6244; Selumetinib	-11,64742	-5,15283	-3,01867	-1484,1306	-700,04113	470,67105
Palbociclib	AZD 6244; Selumetinib	-5,76309	-2,03705	-2,01961	-862,72453	-382,00169	-138,36432
Fascaplysin	AZD 6244; Selumetinib	-1,4101	-1,21334	-0,64686	-252,62484	-155,90188	63,47541
PHA-690509	AZD 6244; Selumetinib	-2,45493	-1,32152	-0,73813	-514,50636	-110,5314	7,54587
Flavopiridol	AZD 6244; Selumetinib	-0,00111	-2,37397	-0,28833	33,07521	-451,02399	201,94979
I-BET762	AZD 6244; Selumetinib	-1,20004	-4,41124	-4,26256	-805,42906	-862,56797	-401,81926
Purvalanol A	AZD 6244; Selumetinib	-4,67116	-8,39442	-3,47437	-491,10333	-891,31753	-293,97404
R-547	AZD 6244; Selumetinib	-3,25441	-1,55688	-0,92361	-352,95515	-21,66424	-56,52964
Cdk4/6 Inhibitor IV	AZD 6244; Selumetinib	-3,03199	-10,67577	-5,69834	-402,65757	-1155,83484	-560,13304
I-BET151	AZD 6244; Selumetinib	-1,80608	-7,15712	-2,60176	-709,15988	-958,0251	-234,1224
PHA-848125	AZD 6244; Selumetinib	-6,82205	-5,85195	-3,48196	-935,90867	-825,62309	-315,04822
JQ1	AZD 6244; Selumetinib	-7,58991	-17,46421	-6,2024	-1209,28912	-2024,75749	-619,22402
7-Hydroxystaurosporine	TAK-733	-7,99985	-5,46482	-4,85736	-1146,31665	-855,2142	-357,28492
Palbociclib	TAK-733	-3,72261	-3,44114	-1,87101	-806,85258	-448,67194	-164,90066
Fascaplysin	TAK-733	-2,13737	-0,35521	-0,98389	-319,61136	-128,00048	-60,66565
PHA-690509	TAK-733	-2,48088	-1,10538	-0,88618	-295,67728	81,36	37,60309
Flavopiridol	TAK-733	-0,20007	-0,97976	-0,38386	-148,11816	136,815	121,56999
I-BET762	TAK-733	-1,90147	-2,43637	-4,45388	-802,77615	-610,38051	-415,23669
Purvalanol A	TAK-733	-2,91496	-3,91252	-5,94655	-352,39547	-472,35015	-595,43216
R-547	TAK-733	-1,42566	-2,36599	-2,3324	-382,99783	113,76345	-186,36669
Cdk4/6 Inhibitor IV	TAK-733	-3,61207	-9,94078	-4,66141	-487,04958	-1097,29275	-462,03786
I-BET151	TAK-733	-1,44665	-7,39369	-7,48638	-883,28896	-1125,21404	-758,09952
PHA-848125	TAK-733	-5,31104	-3,74193	-5,37343	-944,70522	-381,64001	-540,41725
JQ1	TAK-733	-6,7756	-12,23172	-10,33132	-1369,40337	-1634,65293	-1034,56356
7-Hydroxystaurosporine	Pimasertib	-6,67439	-6,75056	-5,52062	-1218,16226	-1042,86017	-403,05462
Palbociclib	Pimasertib	-1,64947	-2,53623	-1,928	-608,50888	68,40888	-147,69726
Fascaplysin	Pimasertib	-1,68488	-0,83005	-1,57567	-313,95687	-118,89725	-181,26317
PHA-690509	Pimasertib	-0,78186	-0,19209	-1,65258	-278,60673	228,99502	-120,41066
Flavopiridol	Pimasertib	-0,39937	-1,30478	-0,38099	-74,06057	83,15863	10,44202
I-BET762	Pimasertib	-1,05231	-3,00222	-7,5006	-721,28604	-782,05584	-763,58119
Purvalanol A	Pimasertib	-3,63029	-5,43742	-5,42343	-377,44146	-704,82553	-543,78245
R-547	Pimasertib	-2,13177	-1,28631	-1,8423	-367,29762	134,04926	-153,93881
Cdk4/6 Inhibitor IV	Pimasertib	-2,64394	-10,15225	-3,28405	-268,73309	-1118,82517	-319,3174
I-BET151	Pimasertib	-2,54015	-9,81615	-7,41542	-1020,78903	-1362,26971	-741,54164
PHA-848125	Pimasertib	-6,14584	-3,74642	-4,77462	-1010,34001	-457,76178	-448,01648
JQ1	Pimasertib	-7,04619	-12,26813	-10,67905	-1244,96036	-1822,33792	-1067,90537
7-Hydroxystaurosporine	PD 184352	-9,74511	-5,53578	-8,42709	-1261,04043	-718,33037	-912,72844
Palbociclib	PD 184352	-2,45286	-1,00195	-1,67102	-322,07347	-90,41145	-103,88624
Fascaplysin	PD 184352	-4,07504	-0,5803	-3,74856	-500,46529	-30,17467	-389,19082
PHA-690509	PD 184352	-3,41849	-0,72074	-1,58873	-511,49232	403,56704	-134,04977
Flavopiridol	PD 184352	-0,40899	-2,39088	-1,11368	-101,30897	-294,76276	-22,83884
I-BET762	PD 184352	-1,07479	-2,24764	-4,0297	-287,81107	-534,34402	-322,69594
Purvalanol A	PD 184352	-2,71221	-5,76706	-4,18593	-279,44719	-586,56818	-433,92748
R-547	PD 184352	-2,15039	-1,98128	-2,89973	-299,80206	14,48526	-242,90283
Cdk4/6 Inhibitor IV	PD 184352	-4,14411	-7,49281	-2,06222	-394,29065	-789,22042	-206,52741
I-BET151	PD 184352	-0,75376	-8,66545	-4,70062	-452,5046	-898,3609	-473,58508
PHA-848125	PD 184352	-6,68012	-4,76984	-3,56752	-764,53054	-145,22684	-318,0707
JQ1	PD 184352	-5,65821	-10,95661	-5,79888	-818,31615	-1264,65127	-503,05199
7-Hydroxystaurosporine	JQ1	-3,797	-2,44197	-4,61836	-919,68943	-744,61901	-266,7378
Palbociclib	JQ1	-2,7117	-0,1461	-8,9935	-629,69093	-288,06101	-915,46811
Fascaplysin	JQ1	-2,70739	-0,3736	-2,55338	-407,17329	-240,9026	-214,08741
PHA-690509	JQ1	-4,27123	-0,85781	-11,71531	-727,30804	-60,76162	-1177,05087
Flavopiridol	JQ1	-2,90209	-3,2318	-13,91381	-490,79892	-500,06786	-1375,93443
Purvalanol A	JQ1	-1,04668	-0,40535	-8,25956	-31,55003	-36,78082	-938,50768
R-547	JQ1	-2,86235	-8,24145	-17,09687	-450,52405	-780,02551	-1690,14382
Cdk4/6 Inhibitor IV	JQ1	-0,72249	-2,04882	-3,03724	232,53944	-253,19817	-279,10213
PHA-848125	JQ1	-1,27789	-1,7249	-9,72637	-467,33264	-511,2548	-1010,17774

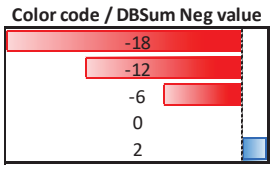

Selected combinations

Table AI-1: Table showing the DBSumNeg and Excess HSA values obtained at NIH-NCATS from viability (48 h) in the three MPNST cell lines tested (S462, NF1-08 and NF1-09). The 21 green rows indicate the combinations selected for future *in vitro* validation in the laboratory.

Table cited in Results Section 2.2.

Appendix II

Copy Number Profiles of NF1-18B Models

In this figure, we present the copy number **(**CN) profile of the newly generated PDOX_B model derived from NF1-18B. This profile is relevant because it allows us to validate that the "<3n" subpopulation, previously identified in the cell line and in PDOX_A (Figure R6), was already present in the primary tumor. The comparison with cell lines models derived from the same tumor confirms the stability of these genomic alterations and their conservation across different experimental systems. This finding is further discussed in *Discussion Section 2.1.*

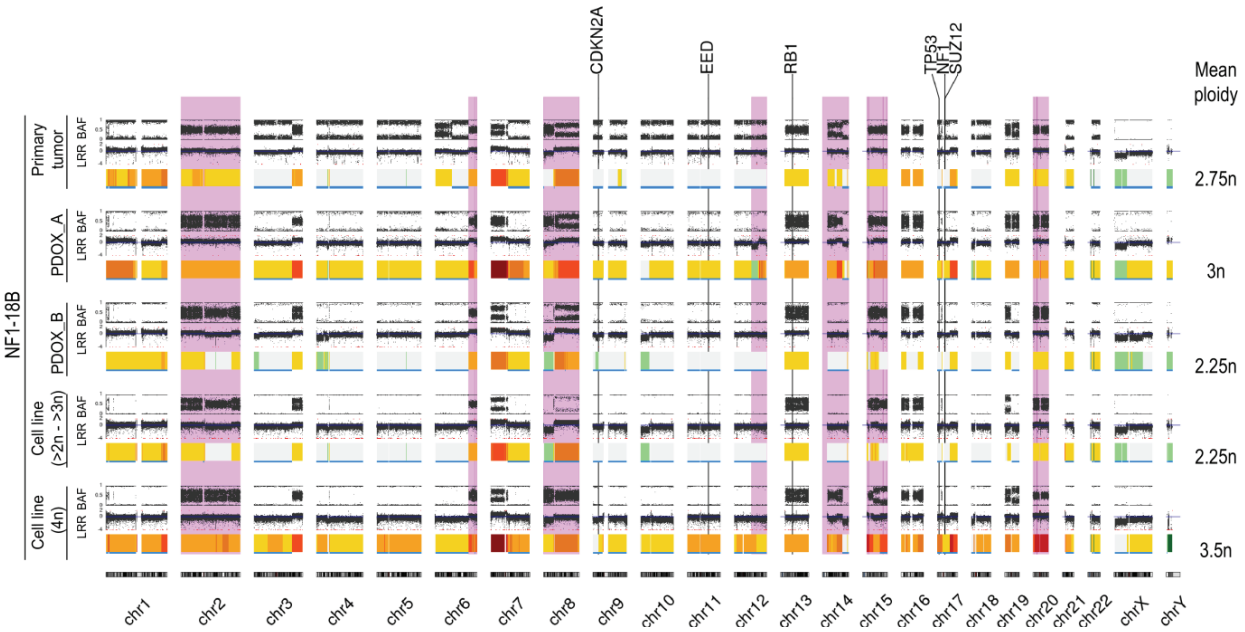

Figure AII-1. Patient-derived cell lines and PDOXs recapitulate the major genomic features of the primary NF1-18B tumor. Copy number (CN) variation profile represented by BAF and LRR of patient tumors, PDOX tumors, and cell lines. The CN profile of the two PDOXs generated from NF1-18B is shown: PDOX_A is in Figure R6 while here we present the CN profile of the newly generated PDOX_B. The CN profile of the two NF1-18B cell line subpopulations ("< 3n" and "4n") is also in Figure R6. CN variation is represented by a colored line below the LRR: gray for 2n region; yellow to red for chromosomal gain regions (>2n); and green to dark green for chromosomal loss regions (<2). LOH regions are shown in blue. Major genomic differences between the primary tumors and the models are highlighted in purple. A calculation of the mean ploidy of the sample is shown on the right side. BAF: B-allele frequency; LRR: Log-R ratio; LOH: loss of heterozygosity.

Appendix III

Impact of TP53 Inactivation on Drug Sensitivity in MPNST

Background

Malignant peripheral nerve sheath tumors (MPNSTs) are aggressive soft tissue sarcomas with a poor prognosis. Most of these tumors are characterized by the recurrent inactivation of three key tumor suppressor genes (TSGs): *NF1*, *CDKN2A*, and *EED/SUZ12* (components of the Polycomb Repressive Complex 2 complex) (Lee, Teckie et al. 2014, Magallón-Lorenz, Terribas et al. 2023). However, approximately 25% of tumors also harbor *TP53* mutations, pointing towards a functional role of this gene in the tumorigenic process (Legius, Dierick et al. 1994, Verdijk, den Bakker et al. 2010, Lemberg, Wang et al. 2020). While the precise contribution of *TP53* inactivation to MPNST pathogenesis remains unclear, one study has indicated that patients with *TP53* mutations may have a worse prognosis (Martin, Acem et al. 2020).

The role of *TP53* in MPNST development was first demonstrated in a genetically engineered mouse model (GEMM), in which the heterozygous inactivation of *Nf1* and *Tp53* led to the formation of MPNST-like tumors MPNST lesions (Cichowski, Shih et al. 1999, Verdijk, den Bakker et al. 2010). In addition to its role in the pathogenesis of MPNSTs, loss of *TP53* has recently been described to play a critical role in resistance to drug treatment in MPNSTs, complicating response to kinase inhibitors and affecting therapeutic efficacy at the preclinical level (Grit, McGee et al. 2024). It has also been reported that *TP53*-deficient patients have a poor response to neo-adjuvant chemotherapy (Karpinsky, Krawczyk et al. 2018).

One of the key findings of the high-throughput screening performed in this thesis (Results Part II) was the variable response to the same therapeutic agents (MEK, CDK, and BET inhibitors) across multiple MPNST cell lines, all of them harboring the inactivation of *NF1*, *CDKN2A*, and *EED/SUZ12*. These differences suggested that additional genetic alterations could influence drug response and help the tumor acquire drug resistance. We hypothesized that *TP53* status might play a role in modulating therapy response, as its inactivation is present in a subset of MPNSTs.

To assess this hypothesis, we generated a knockout in the *TP53* gene using CRIPSR-Cas9 in one MPNST cell line that has demonstrated a poor drug response in the *in vitro* validation (Results Part II). Our goal was to determine whether *TP53* inactivation alters the sensitivity to therapeutic agents, uncovering new drivers of MPNST drug resistance.

Materials & Methods

Cell line: The NF1-derived MPNST ST88-14 cell line (RRID: CVCL_8916) was used. Cells were maintained in complete DMEM at 37°C with 5% CO_2 and passaged weekly. Cryopreservation in liquid nitrogen was performed periodically.

Generation of the *TP53* Knockout cell line: The Architect Ribonucleic Protein (RNP)-based CRISPR-Cas9-eGFP genome editing system (Stem Cell Technologies), which utilizes a ribonucleoprotein complex (Cas9 protein + guide RNA) to target and edit specific DNA sequences, with eGFP serving as a fluorescent marker for tracking edited cells, was used to knockout the gene in the ST88-14 cell line. GFP-positive transfected cells were sorted using Fluorescence-activated Cell Sorting (FACS), and single-cell clones were expanded and analyzed by Sanger sequencing to detect *TP53* mutations. Transfection Protocol:

1. Day 1: 50,000 cells per well were seeded in a 24-well plate (Corning) with DMEM supplemented with 10% FBS and 1% P/S.
2. Day 2: Cells were transfected following these steps:
   2.1. The culture medium was removed and replaced with DMEM + 1% P/S (without FBS).
   2.2. Several mixtures were prepared to obtain the RNP Transfection Mix:
      a) Prepare **DMEM:F12+HEPES Solution** with 15mM. F12 Nut Mix (Gibco, Ref. 21765-029) and HEPES (Gibco, Ref. 15630-106).
      b) Prepare **guide RNA (gRNA) Mix** (for 4 wells):
         - 8 µl Annealing Buffer (StemCell, Ref. 76020)
         - 1 µl crRNA 200 µM (StemCell, Ref. 76010) (GCAGTCACAGCACATGACGG)
         - 1 µl tracrRNA 200 µM (StemCell, Ref. 76016)
         - 30 µl Nuclease-free water (StemCell, Ref. 79001)

         gRNA Mix was incubated in a thermocycler under the following conditions:

         - 95ºC 5 min
         - 60ºC 1 min
         - Cooled to RT

      c) Prepare **ArciTect Cas9 Nuclease Solution** (5 µM):

Component	µl per well
DMEM:F12 with 15mM HEPES	3.4
Cas9 eGFP (STEMCELL, ref. 76006)	1.6

d) Prepare **RNP Complex Mix** (5 µM) and incubate for 10 min at RT:

Component	µl per well
DMEM:F12 with 15mM HEPES	15.6
Guide RNA	9.8
Cas9 Nuclease	4.8

e) Prepare **Transfection Mix** (5 µM) and incubate for 10 min at RT:

Component	µl per well
DMEM:F12 with 15mM HEPES	28.8
TransLT-X2 (Mirus, ref. MIR 6004)	1.2

f) Prepare **RNP Transfection Mix** and incubate for 20 min at RT:

Component	µl per well
Transfection Mix	28
RNP Complex Mix	28

2.3. 50 µl of RNP Transfection Mix were added to each well.

3. Day 4 (48h post-transfection):
   3.1. Cells were trypsinized and suspended in 2 ml complete DMEM
   3.2. Cells were centrifuged at 1200 rpm for 5 min and suspended in 1 ml DMEM + 10% FBS + Normocin (Invivogen, Ref. ant-nr-05) (1:500).
   3.3. GFP-positive cells were sorted by FACS in the IGTP Cytometry core Facility to seed 1 cell/well in a 96-well plate. Moreover, 1 ml of the edited pool of cells was transferred to a 24-well plate.
4. Medium was changed every 3-4 days.
5. Once one cell clone had grown in the 96-well plate, it was expanded in a 24-well plate, then in a 12-well plate. Finally, half of the cells were cryopreserved, and the other half was used for DNA extraction.

PCR for *TP53* gene amplification:

1. DNA was extracted with Maxwell LEV (Promega) using the Maxwell RSC Cultured cells DNA kit (Promega, Ref. AS1620), following the manufacturer's instructions.
2. DNA quantification was performed using a NanoDrop 1000 Spectrophotometer.
3. PCR mix (x1 reaction):
   a. 5 µl Buffer Promega 5X (Promega, Ref. D230A)
   b. 1.5 µl MgCl2 25 mM (Promega, Ref. D112A)

c. 0.5 µl dNTPs 10 mM (ThermoFisher, Ref. R1191)
d. 1 µl Primer Forward *TP53* 10 mM (GCCAACTCTCTCTAGCTCGC)
e. 1 µl Primer Reverse *TP53* 10 mM (ACCCCAGTTGCAAACCAGAC)
f. 0.15 µl GoTaq 5U/ml Promega (Promega, Ref. D600B)
g. 100ng gDNA
h. Up to a final volume of 25 µl with H_20d

4. PCR mix was incubated in a thermocycler:
    a. 95ºC 2 min
    b. 34 cycles:
        i. 95ºC 30 sec
        ii. 60ºC 30 sec
        iii. 72ºC 30 sec
    c. 72ºC 15 min
    d. 4º
5. PCR product integrity was evaluated using a 2% agarose gel electrophoresis at 100 V for 30-40 min.

ExoSAP Cleanup: ExoSAP was used PCR purification, removing primers and nucleotides from PCR products before sequencing.

1. 1 µl ExoSAP (New England Biolabs: mix of Exonuclease I Ref. M0568 and Antarctic Phosphatase Ref. M0289) + 4 µl PCR product were mixed.
2. The Mix was incubated in a thermocycler protocol:
    a. 37ºC 30 min
    b. 80ºC 15 min
    c. 4ºC

DNA Sanger Sequencing: DNA sequencing was performed by STAB VIDA to analyze mutations in each clone. Samples were prepared as follows:

1. 3 µl ExoSAP product, 3 µl Primer Forward *TP53*, and 7 µl H_20d were mixed.
2. Sequences were analyzed using CLC workbench 8 software (Qiagen) and Benchling online software.

Reference sequence used was GeneBank: NC_000017.11, NM_000546.6, NP_000537.3. The normalization of the variants was done with Mutalyzer 3.

Gateway cloning: Gateway cloning is useful for efficiently transferring DNA fragments between different vectors using recombination, eliminating the need for restriction enzymes and ligases. In our thesis, we applied this technique to clones obtained via CRISPR-Cas9 to confirm whether they were heterozygous or homozygous.

Three clones (A3 and F1 *TP53* heterozygous clones, and G6 *TP53* homozygous clone) were further characterized using Gateway cloning to confirm gene modifications.

1. PCR mix for Cloning (attB) (x1 reaction):
    a. 2.5 µl Buffer Promega 5X
    b. 0.75 µl MgCl2 25 mM
    c. 0.25 µl dNTPs 10 mM
    d. 0.5 µl Primer Forward *TP53* 10 mM (GGGGACAAGTTTGTACAAAAAAGCAGGCTGCCAACTCTCTCTAGCTCGC)
    e. 0.5 µl Primer Reverse *TP53* 10 mM (GGGGACCACTTTGTACAAGAAAGCTGGGTACCCCAGTTGCAAACCAGAC)
    f. 0.075 µl GoTaq 5U/ml Promega
    g. 50 ng gDNA
    h. Up to a final volume of 12.5 µl with H_20d
2. PCR mix were incubated in a thermocycler:
    a. 95ºC 2 min
    b. 32 cycles:
        i. 95ºC 30 sec
        ii. 60ºC 30 sec
        iii. 72ºC 30 sec
    c. 72ºC 7 min
    d. 4º
3. BP reaction was prepared and incubated overnight at 25ºC:
    a. 1 µl attB-PCR product
    b. 2 µl pDONOR (ThermoFisher, Ref. 12536017)
    c. 5 µl TE Buffer (low)
    d. 2 µl (BP Clonase II enzyme) (ThermoFisher , Ref. 11789-020)
4. 2 µl Proteinase K Solution (ThermoFisher, Ref. 11789-020) was added and incubated at 37ºC for 10 min.
5. For each sample, 2 µl of BP reaction was added to 50 µl DH5α cells (Promega) on ice, followed by 30 min incubation on ice.
6. Heat-shock was performed for 30-40 sec at 42ºC, followed by 2 min incubation on ice.
7. 450 µl SOC medium was added and incubated for 30-60 min at 37ºC.
   SOC medium composition: Tryptone (Condalab, Ref. 1612.00), Yeast extract (Condalab, Ref. 1702.00), NaCl (Sigma Aldrich, Ref. 104936-0500), KCl (Merck, Ref. 1-04936-0500), MgCl2 (Merck, Ref. 1-05833-0250), Glucose (Sigma Aldrich, Ref. G7528-250G)
8. 100-200 µl of cells were plated in an LB agar Ampicillin petri dish and incubated overnight at 37ºC.
9. Six colonies per condition were selected for PCR confirmation.
10. PCR conditions and agarose gel electrophoresis were performed as previously described.

11. DNA was sent to STAB VIDA for sequencing.

Western Blot: This technique was used to analyze the p53 protein expression in the generated clones. The protocol is described in section 3.9 of the Materials and Methods. The antibody used is: p53 (7F5) Rabbit mAb (1:1000 dilution, Cell Signalling, Ref. 2527T). Vinculin expression was used as a loading control.

I*n vitro* compound testing: For *in vitro* testing, compounds were used according to the protocols described in sections 5.3 and 5.4 of the Materials and Methods as single agents (MK-1775, Ribociclib, and I-BET151), in combination (MK-1775 + Doxorubicin, MK-1775 + Arry-162, MK-1775 + I-BET151, MK-1775 + Ribociclib, and selumetinib + Ribociclib), and as a triple combination (MK-1775 + Arry-162 + I-BET151). All compounds tested were provided by the NCATS Compound Management group in DMSO solutions at 10 mmol/L.

In vivo Tumorigeneicity: This assay was used to analyze the tumorigenicity of the generated clones. The protocol is described in section 6.2 of the Materials and Methods.

Results

1. Generation of *TP53*-Edited ST88-14 MPNST Cell Line Clones

CRISPR-Cas9 editing of *TP53* in the ST88-14 MPNST cell line achieved an efficiency of 91.5% GFP+ cells, as determined by cell sorting. Consequently, a 96-well plate was seeded with a single GFP+ cell per well. The remaining GFP+ cell pool was plated in a 24-well plate and frozen for potential future use in generating additional clones. From the initial 96-well plate, 50 clones were obtained, expanded, and analyzed. Among them, only one was validated as homozygous (G6), while two were confirmed as heterozygous (A3 and F1). To increase the number of clones, the frozen pool was thawed, and a limiting dilution was performed to seed two additional 96-well plates, aiming for one cell per well. This yielded 50 additional clones, which were expanded and analyzed, leading to the validation of two new heterozygous clones (B3.1 and E1.1).

Table A1 summarizes the mutations detected in each clone through Sanger sequencing. The homozygous clone G6 exhibited a 7 base-pair (bp) deletion in both alleles. In contrast, the heterozygous clones A3, F1, and E1.1 carried deletions of 13 bp, 12 bp, and 29 bp, respectively. Meanwhile, the heterozygous clone B3.1 displayed a 1 bp insertion (Table AIII-1 and Figure AIII-1A).

Table AIII-1. Summary of genetic modifications identified in the generated clones of ST88-14 MPNT cell line

Clone	Allele	gDNA mutation	cDNA	Protein
G6	1	g.7675104_7675110del	c.503_509del	p.(His168ArgfsTer4)
	2	g.7675104_7675110del	c.503_509del	p.(His168ArgfsTer4)
A3	1	g.7675097_7675109del	c.502_514del	p.(His168LeufsTer2)
	2	WT	WT	WT
F1	1	g.7675099_7675110del	c.502_513del	p.(His168_Glu171del)
	2	WT	WT	WT
B3.1	1	g.7675103insA	c.508_509insT	p.(Thr170IlefsTer11)
	2	WT	WT	WT
E1.1	1	g.7675086_7675114del	c.498_526del	p.(Gln167ProfsTer4)
	2	WT	WT	WT

WT: wild type

No functional analysis of these newly generated knockout lines was performed. However, the morphology of all clones remained consistent with that of the parental cell line, showing the characteristic MPNST structure defined by small, spindle-shaped to polygonal cell morphology (Figure AIII-1A). The *in vitro* behavior of all clones was very similar, except for the growth rate of clones A3 and F1, which was slower.

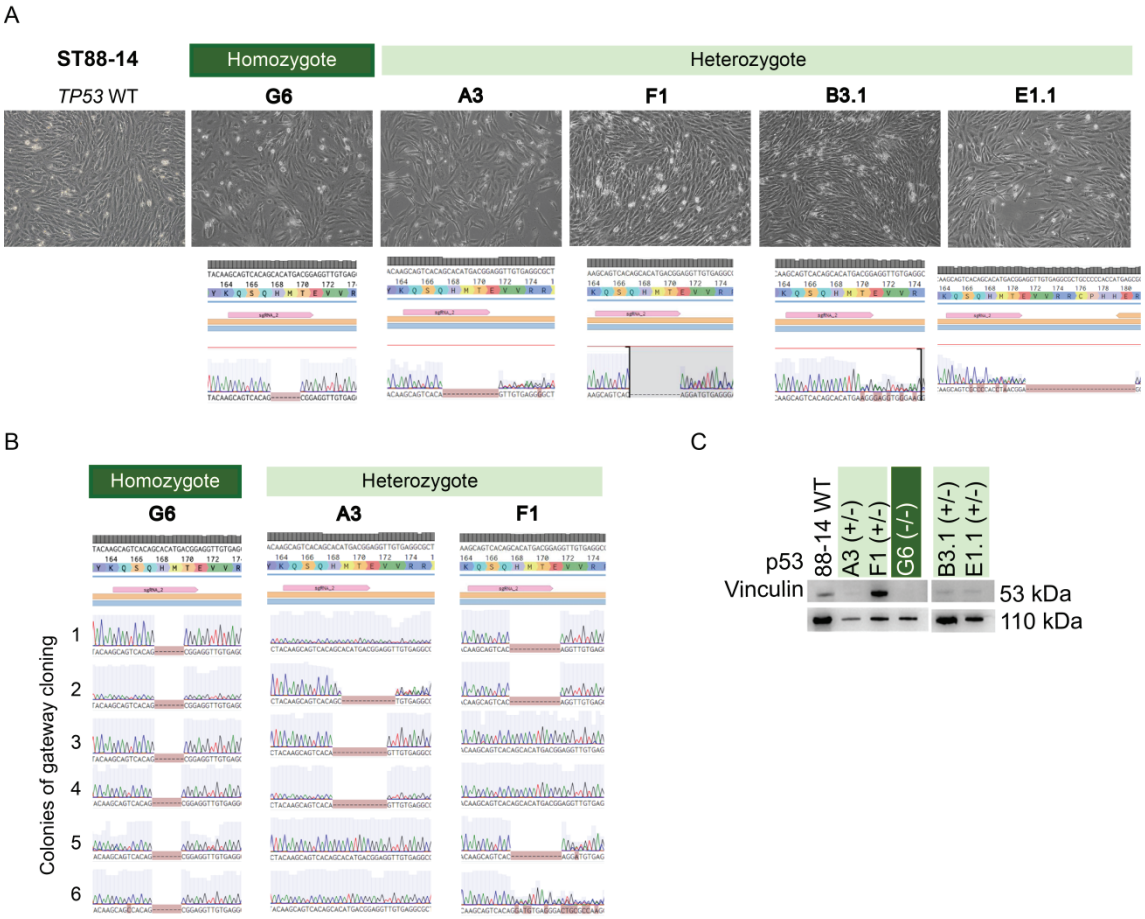

Figure AIII-1. Generation and characterization of *TP53*-edited ST88-14 MPNST cell clones. A. Morphological images and Sanger sequencing of the original ST88-14 cell line and five *TP53*-edited clones. Sequence images were generated using Benchling sequence alignments. **B.** Validation of the mutation by Gateway cloning of six single colonies from three selected clones (G6, A3 and F1). **C.** Western blot analyses of p53 protein expression in parental ST88-14 cells and the five clones. Vinculin was used as a loading control. The homozygous clone is indicated in dark green and the heterozygous clones in light green.

To further validate the mutations, we performed Gateway cloning on three selected clones (G6, A3, and F1). Sanger sequencing revealed that 100% of colonies derived from the G6 clone carried the same mutation, validating its homozygosity. In contrast, for the A3 and F1 clones, the 50% of colonies retained the wild-type sequence, while the other 50% harbored the mutation; thereby confirming the heterozygous status of these variants (Figure AIII-1B).

Following mutation validation, we performed functional analyses to assess p53 expression in the clones via Western blotting (Figure AIII-1C). Compared to the parental ST88-14 cells, the heterozygous clones (A3, B3.1 and E1.1) exhibited a marked reduction in p53 protein levels, although residual expression was still detectable. In contrast, the homozygous G6 clone displayed a complete loss of p53 expression. Notably, the heterozygous F1 clone exhibited increased p53 levels. This observation suggests that the 12-base pair deletion present in F1

may result in a missense mutation that may lead to the production of a more stable but aberrant p53 protein.

2. Drug Sensitivity of *TP53*-Edited ST88-14 MPNST Cell Line Clones

To investigate the role of *TP53* in drug resistance, we treated the edited clones and the parental ST88-14 cell lines using MK-1775 (WEE1 inhibitor), Ribociclib (CDK inhibitor), and I-BET151 (BET inhibitor) as single agents (Figure AIII-2A). MK-1775 was selected based on prior findings from our research group, which demonstrated that *TP53*-mutant cell lines exhibit increased sensitivity to MK-1775, whereas *TP53* wild-type cell lines are resistant (Fernández-Rodríguez, Creus-Bachiller et al. 2022). Ribociclib and I-BET151 were selected due to not being effective in the parental ST88-14 cell line (as described in the Part II of this thesis), displaying an IC_{50} of 10.48 µM in the case of the BET inhibitor and Ribociclib failing to reach 50% of cell death in the culture. However, after the edited cell clones treatment, we observed that both the parental and mutant clones exhibited similar responses to these agents (Figure AIII-2A): MK-1775 was effective, whereas Ribociclib and I-BET151 were largely ineffective in all clones.

Even though the results of the single agent treatment were not significant, we also assessed the impact of *TP53* inactivation on sensitivity to combination therapies. The MK-1775 plus Doxorubicin combination was included as it was also analyzed in the study by Fernández-Rodríguez et al. (2022). Other MK-1775 combinations were explored to identify potential novel therapeutic approaches; while the selumetinib plus Ribociclib combination was tested due to the lack of effect observed in the *in vitro* validation described in Results, Part II. The five heterozygous clones exhibited drug sensitivities similar to the parental line across all tested combinations, with only minor differences. In contrast, the homozygous G6 clone displayed lower sensitivity to all five drug combinations compared to the ST88-14 WT cell line (Figure AIII-2B).

Finally, we tested the triple drug combination of MK-1775 + Arry-162 + I-BET151 and observed a similar trend to the dual-drug combinations: the homozygous G6 clone was the least sensitive to the treatment (Figure AIII-2B).

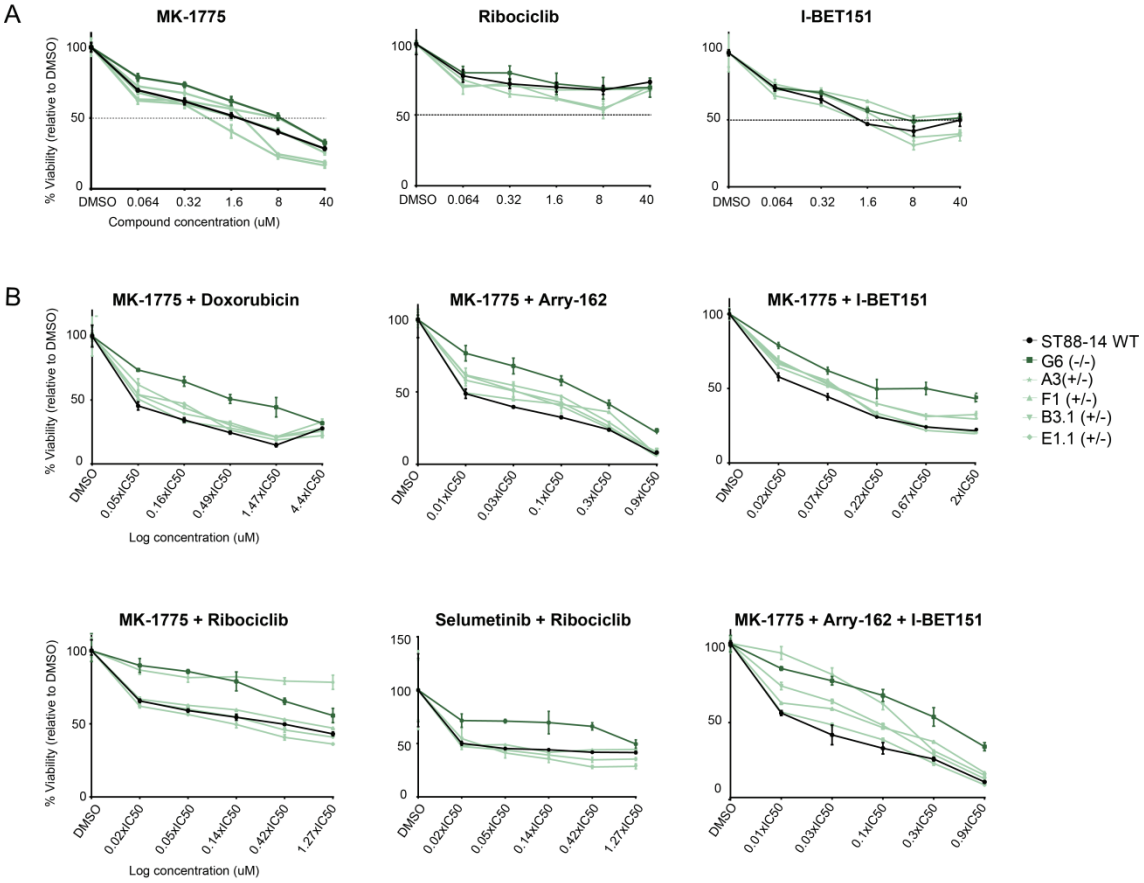

Figure AIII-2. Drug sensitivity of *TP53*-edited ST88-14 MPNST cell clones. A. Cell viability for single agent treatments. Clones and parental ST88-14 cells were tested with MK-1775, Ribociclib, and I-BET151 at increasing drug concentrations using MTT viability assay. Clone A3 was not used for Ribociclib or I-BET151 testing. **B.** Drug combinations treatments were performed at 1:1 ratio of IC_{50} values. In all cases, viability was assessed by MTT assay in the parental ST88-14 WT and all clones except the combination Selumetinib + Ribociclib, which was not tested in clone A3. The legend applies to all panels.

3. *In vivo* Tumorigenic Potential of *TP53*-Edited ST88-14 MPNST Cell Clones

Given the suspected role of *TP53* in tumorigenesis, we sought to evaluate the *in vivo* tumorigenic capacity of the *TP53*-edited clones in comparison to the parental ST88-14 WT cell line. Previous studies have reported that ST88-14 WT cells fail to form tumors *in vivo* (Creus-Bachiller, Fernández-Rodríguez et al. 2023), making them a suitable control for assessing potential changes in tumorigenicity following *TP53* editing.

To this end, we engrafted orthotopically (near the sciatic nerve) the cell lines into immunodeficient mice and monitored them over a period of six months post-engraftment. Body weight was recorded throughout the study as an indicator of systemic toxicity, with no significant weight loss observed in any group. However, we do not have any results for this part of the experiment as it is still ongoing.

Discussion

TP53 is a well-known TSG frequently mutated in many cancers, including MPNSTs (Legius, Dierick et al. 1994, Verdijk, den Bakker et al. 2010, Lemberg, Wang et al. 2020), where its inactivation has been associated with increased tumor aggressiveness (Cichowski, Shih et al. 1999) and therapy resistance (Creus-Bachiller, Fernández-Rodríguez et al. 2023). In this study, we aimed to explore the role of *TP53* loss in MPNST drug response by generating *TP53*-mutated ST88-14 clones via CRISPR-Cas9.

Based on previous findings (Creus-Bachiller, Fernández-Rodríguez et al. 2023), we expected that *TP53* knockout clones would exhibit increased sensitivity to selected drug treatments, particularly to MK-1775 (WEE1 inhibitor), given its known effectivity in *TP53*-mutant cancer cell lines. However, our results showed the opposite trend—the homozygous *TP53* knockout clone (G6) was less sensitive to all tested drug combinations compared to the parental ST88-14 WT cells. Additionally, heterozygous clones showed responses similar to the parental line, indicating that a single functional allele still retain tumor suppressor activity.

A major limitation of this study is that all experiments were conducted in a single cell line (ST88-14). It will be important to use other MPNST cell lines to determine whether they may have different behavior in the presence of TP53 mutations. Another important limitation is that we were only able to generate one homozygous *TP53* knockout clone (G6). The limited number of homozygous clones makes it difficult to draw strong conclusions about the true impact of *TP53* loss in MPNSTs. Future studies should aim to increase the number of homozygous *TP53* knockout clones to confirm whether the observed reduced drug sensitivity is reproducible across multiple clones.

Other limitation of this study is the few number of compounds tested, which prevents drawing definitive conclusions about the role of *TP53* in drug response. Only three drugs were evaluated: MK-1775, I-BET151, and Ribociclib. MK-1775 was included as a positive control due to its known association with *TP53* inactivation in previous studies (Fernández-Rodríguez, Creus-Bachiller et al. 2022). I-BET151, on the other hand, is not directly linked to the *TP53* pathway, making it uncertain whether *TP53* mutations alone would influence sensitivity. However, it was tested because the parental line showed no response to it, and we wanted to explore potential differences. Finally, the relationship between *TP53* status and sensitivity to CDK4/6 inhibitors has been reported in some articles (Knudsen and Witkiewicz 2017). Although this interaction is complex and not yet well characterized, we decided to use Ribociclib to see if we could observe differences. Given these constraints, further studies should expand the

range of tested compounds to gain a more comprehensive understanding of the impact of *TP53* inactivation on drug sensitivity.

References

Cichowski, K., T. S. Shih, E. Schmitt, S. Santiago, K. Reilly, et al. (1999). "Mouse models of tumor development in neurofibromatosis type 1." Science **286**(5447): 2172-2176.

Creus-Bachiller, E., J. Fernández-Rodríguez, M. Magallón-Lorenz, S. Ortega-Bertran, S. Navas-Rutete, et al. (2023). "Expanding a precision medicine platform for malignant peripheral nerve sheath tumors: New patient-derived orthotopic xenografts, cell lines and tumor entities." Mol Oncol.

Fernández-Rodríguez, J., E. Creus-Bachiller, X. Zhang, M. Martínez-Iniesta, S. Ortega-Bertran, et al. (2022). "A High-Throughput Screening Platform Identifies Novel Combination Treatments for Malignant Peripheral Nerve Sheath Tumors." Mol Cancer Ther **21**(7): 1246-1258.

Grit, J. L., L. E. McGee, E. A. Tovar, C. J. Essenburg, E. Wolfrum, et al. (2024). "p53 modulates kinase inhibitor resistance and lineage plasticity in NF1-related MPNSTs." Oncogene **43**(19): 1411-1430.

Karpinsky, G., M. A. Krawczyk, E. Izycka-Swieszewska, A. Fatyga, A. Budka, et al.(2018). "Tumor expression of survivin, p53, cyclin D1, osteopontin and fibronectin in predicting the response to neo-adjuvant chemotherapy in children with advanced malignant peripheral nerve sheath tumor." J Cancer Res Clin Oncol **144**(3): 519-529.

Knudsen, E. S. and A. K. Witkiewicz (2017). "The Strange Case of CDK4/6 Inhibitors: Mechanisms, Resistance, and Combination Strategies." Trends Cancer **3**(1): 39-55.

Lee, W., S. Teckie, T. Wiesner, L. Ran, C. N. Prieto Granada, et al. (2014). "PRC2 is recurrently inactivated through EED or SUZ12 loss in malignant peripheral nerve sheath tumors." Nat Genet **46**(11): 1227-1232.

Legius, E., H. Dierick, R. Wu, B. K. Hall, P. Marynen, et al. (1994). "TP53 mutations are frequent in malignant NF1 tumors." Genes Chromosomes Cancer **10**(4): 250-255.

Lemberg, K. M., J. Wang and C. A. Pratilas (2020). "From Genes to -Omics: The Evolving Molecular Landscape of Malignant Peripheral Nerve Sheath Tumor." Genes (Basel) **11**(6).

Magallón-Lorenz, M., E. Terribas, S. Ortega-Bertran, E. Creus-Bachiller, M. Fernández, et al. (2023). "Deep genomic analysis of malignant peripheral nerve sheath tumor cell lines challenges current malignant peripheral nerve sheath tumor diagnosis." iScience **26**(2): 106096.

Martin, E., I. Acem, D. J. Grünhagen, J. V. M. G. Bovée and C. Verhoef (2020). "Prognostic Significance of Immunohistochemical Markers and Genetic Alterations in Malignant Peripheral Nerve Sheath Tumors: A Systematic Review." Front Oncol **10**: 594069.

Verdijk, R. M., M. A. den Bakker, H. J. Dubbink, W. C. Hop, W. N. Dinjens and J. M. Kros (2010). "TP53 mutation analysis of malignant peripheral nerve sheath tumors." J Neuropathol Exp Neurol **69**(1): 16-26.

Appendix IV

Other Research Contributions During the PhD

A High-Throughput Screening Platform Identifies Novel Combination Treatments for Malignant Peripheral Nerve Sheath Tumors

Juana Fernández-Rodríguez[1,2,3], Edgar Creus-Bachiller[1,2,3], Xiaohu Zhang[4], Maria Martínez-Iniesta[5,2], Sara Ortega-Bertran[1,2], Rajarshi Guha[4], Craig J. Thomas[4], Margaret R. Wallace[6], Cleofe Romagosa[7,3], Lourdes Salazar-Huayna[7], Karlyne M. Reilly[8], Jaishri O. Blakely[9], Jordi Serra-Musach[5], Miguel Angel Pujana[5,2], Eduard Serra[10,3], Alberto Villanueva[5,2], Marc Ferrer[4], and Conxi Lázaro[1,2,3]

ABSTRACT

Malignant peripheral nerve sheath tumors (MPNST) are soft-tissue sarcomas that are the leading cause of mortality in patients with Neurofibromatosis type 1 (NF1). Single chemotherapeutic agents have shown response rates ranging from 18% to 44% in clinical trials, so there is still a high medical need to identify chemotherapeutic combination treatments that improve clinical prognosis and outcome. We screened a collection of compounds from the NCATS Mechanism Interrogation PlatE (MIPE) library in three MPNST cell lines, using cell viability and apoptosis assays. We then tested whether compounds that were active as single agents were synergistic when screened as pairwise combinations. Synergistic combinations *in vitro* were further evaluated in patient-derived orthotopic xenograft/orthoxenograft (PDOX) athymic models engrafted with primary MPNST matching with their paired primary-derived cell line where synergism was observed. The high-throughput screening identified 21 synergistic combinations, from which four exhibited potent synergies in a broad panel of MPNST cell lines. One of the combinations, MK-1775 with Doxorubicin, significantly reduced tumor growth in a sporadic PDOX model (MPNST-SP-01; sevenfold) and in an NF1-PDOX model (MPNST-NF1–09; fourfold) and presented greater effects in *TP53* mutated MPNST cell lines. The other three combinations, all involving Panobinostat (combined with NVP-BGT226, Torin 2, or Carfilzomib), did not reduce the tumor volume *in vivo* at noncytotoxic doses. Our results support the utility of our screening platform of *in vitro* and *in vivo* models to explore new therapeutic approaches for MPNSTs and identified that combination MK-1775 with Doxorubicin could be a good pharmacologic option for the treatment of these tumors.

Introduction

Malignant peripheral nerve sheath tumors (MPNST) are aggressive neoplasms that account for 2% to 5% of soft-tissue sarcomas diagnosed annually (1). MPNSTs are encountered in three different clinical settings: associated with Neurofibromatosis type 1 (NF1; 40%–50%), sporadic cases (40%–47%), and associated with sites of previous radiation therapy (10%–13%; ref. 2). In patients with NF1, MPNSTs are the major malignant tumors associated with this autosomal dominant genetic disorder (3) and usually arise from a preexisting plexiform neurofibroma. The lifetime risk is 8% to 15% (4) and it is the leading cause of mortality in patients with NF1. These tumors have a poor prognosis, and multiple centers have reported that the 5-year disease-free survival rates of patients with MPNST are between 30% to 60% (2). Complete surgical excision with wide negative margins is the primary treatment option for local MPNST disease (3, 5). However, the success of surgical excision is limited by tumor infiltration, which results in a high relapse rate, and often is not feasible due to location, size, and metastases (5). Currently, there are no single-agent effective chemotherapeutic treatments for MPNSTs. Clinical trials of typical cytotoxic drugs have shown response rates ranging from 18% to 44%, with some stability as well (6). Doxorubicin and Ifosfamide have traditionally been used as the chemotherapy regimen for MPNSTs. However, a 10-year institutional review showed no correlation between chemotherapy and patient survival (7). The role of adjuvant radiation is not conclusive but is often recommended for high-grade lesions (8). To identify new therapeutic options for MPNST, the research directs towards the understanding of the underlying biology of these tumors and the generation of suitable preclinical models (2).

[1]Hereditary Cancer Program, Catalan Institute of Oncology, Hospitalet de Llobregat, Barcelona, Spain. [2]Program in Molecular Mechanisms and Experimental Therapy in Oncology (Oncobell), IDIBELL, Hospitalet de Llobregat, Barcelona, Spain. [3]Centro de Investigación Biomédica en Red de Cáncer (CIBERONC), Spain. [4]Division of Preclinical Innovation, National Center for Advancing Translational Sciences, NIH, Rockville, Maryland. [5]Procure Program, Catalan Institute of Oncology, Hospitalet de Llobregat, Barcelona, Spain. [6]Department of Molecular Genetics & Microbiology, University of Florida College of Medicine, Gainesville, Florida. [7]Department of Pathology, Vall d'Hebron University Hospital, Barcelona, Spain. [8]Pediatric Oncology Branch, Center for Cancer Research, National Cancer Institute, NIH, Bethesda, Maryland. [9]Neurofibromatosis Therapeutic Acceleration Program (NTAP), Department of Neurology, Johns Hopkins University School of Medicine, Baltimore, Maryland. [10]Hereditary Cancer Group, The Institute for Health Science Research Germans Trias i Pujol (IGTP) - PMPPC, Badalona, Barcelona, Spain.

Note: Supplementary data for this article are available at Molecular Cancer Therapeutics Online (http://mct.aacrjournals.org/).

J. Fernández-Rodríguez and E. Creus-Bachiller contributed equally to this article

J. Fernández-Rodríguez and E. Creus-Bachiller are the co-first authors of this article.

Corresponding Author: Conxi Lázaro, Hereditary Cancer Program, Catalan Institute of Oncology, IDIBELL and CIBERONC, Av. Gran Via 199-203, Hospitalet de Llobregat 08908, Spain. Phone: 349-3260-7145; E-mail: clazaro@iconcologia.net; and Marc Ferrer, National Center for Advancing Translational Sciences, NIH, 9800 Medical Center Drive, Rockville, MD 20850. Phone: 240-515-4118. E-mail: marc.ferrer@nih.gov

Mol Cancer Ther 2022;21:1246–58

doi: 10.1158/1535-7163.MCT-21-0947

NF1 inactivation is necessary but not sufficient for MPNST development, and mutations in other driver genes have been reported (*TP53*, *CDKN2A*, and *SUZ12*, and *EED* from Polycomb Repressive Complex 2; ref. 9, 10). The increasing knowledge of altered molecular pathways in MPNST suggested targeted therapies as potential treatments to block these dysregulated signaling pathways (2). Despite the advances, clinical trials, so far, have produced low response rates and have shown that the outcome for unresectable MPNST is poor (11). For this reason, there is a high medical need to identify therapeutic combinations that help overcome resistance and result in durable responses in patients with MPNST. Current technologies allow for rapid screening of multiple cancer cell lines against large libraries of compounds as simple agents (12, 13). These technological advances also allow for the screening of a large number of drug combinations in an unbiased manner, to identify synergistic compound combinations that promote tumor reduction and/or increased survival *in vivo* (14). Previous reports have used high-throughput screening methods to identify drug sensitivities in NF1 and Neurofibromatosis type 2 (NF2) tumors (15–17). *In vivo* models are critical to assessing the efficacy and therapeutic index of potential drug treatments suggested from *in vitro* screening. The current MPNST animal models available include xenograft models produced by the injection of MPNST cells, genetically engineered mouse models (GEMM), and patient-derived orthoxenografts (PDOX) in which a small portion of the patient's tumor is engrafted, without previous culturing near the sciatic nerve of athymic or NSG mice (11).

Here, we screened the National Center for Advancing Translational Sciences (NCATS) oncology-focused collection [Mechanism Interrogation PlatE (MIPE)] of 1,912 mechanistically annotated small molecules on three MPNST cell lines. The library includes approved and preclinical/clinical development drugs for cancer treatment. The aim is to test whether the compounds identified as active as single agents had a synergistic effect when added as pairwise combinations. The most synergistic combinations in a panel of MPNST cell lines were tested in our PDOX mouse models.

Materials and Methods

Cell lines

The establishment of the MPNST-SP-01, MPNST-NF1–08, and MPNST-NF1–09 cell lines at the Catalan Institute of Oncology is described in a manuscript under preparation. Supplementary Table S1 summarizes clinical and molecular data from the patients and tumors from which the three cell lines were isolated. MPNST-SP-01 was already presented in a previous work from our group (18). All molecular features of the primary tumors were confirmed in the derived cell lines. STS-26T (19), HS-PSS, HS-sch2 (20), S462 (21), and sNF96.2 (22) cell lines were previously established in other laboratories. The Human Foreskin Fibroblast (HFF) cell line was purchased from ATCC. Cells were maintained in DMEM growth medium with 10% FBS (Gibco) and 100 μg/mL penicillin and 100 μg/mL streptomycin (BioWest) under standard incubator conditions. All cell lines are validated as *Mycoplasma* negative before starting the *in vitro* validation and were retested every 2 months.

MIPE Compound Library

The MIPE 4.0 library of approved and investigational drugs included 1,912 individual small molecules (17). It encompasses a small-molecule modulator of over 400 specific gene targets, cellular pathways, or genotypes. Within well-explored targets, there are multiple, redundant agents incorporated as a means to inform the on-target nature of phenotype-to-mechanism data associations and to explore instances where a phenotype is the result of the specific polypharmacology of an individual drug.

Quantitative High-Throughput Screen

The screening method used in this study in the MPNST-SP-01, S462, and sNF96.2 cell lines was similar to that previously described (12, 23). Briefly, compounds in the MIPE library were transferred to columns 5–48, and controls were added in columns 1–4 of a 1536-well assay plate. Column 1 contained media only, column 2 contained cells with added DMSO, while columns 3 and 4 contained the protease inhibitor Bortezomib or the antibiotic Salinomycin in DMSO (final concentration 10 μmol/L). Compounds were tested once as 11-point dose-response starting at a stock concentration of 10 mmol/L (the highest final compound concentration was 46 μmol/L) and diluted threefold with DMSO, as described previously (24). Relative luminescence units (RLU) for each well were normalized to the median RLUs from the DMSO control wells as 100% viability, and median RLUs from control wells with media only as 0% viability.

Curve Response Class

The activity of the compounds was determined based on their curve response class (CRC), in which normalized data is fitted to 4-parameter dose-response curves using a custom grid-based algorithm to generate a CRC score for each compound dose-response (25). CRC values of −1.1, −1.2, −2.1, are considered the highest quality hits; CRC values of −1.3, −1.4, −2.3, −2.2, −2.4, and −3 are considered inconclusive hits; and a CRC value of 4 is considered inactive compounds.

Target enrichment analysis

Given a selection of compounds, we used the annotated target for these compounds and computed the enrichment for each target class, compared with the background, using Fisher exact test (26). For this test, the background was defined as all the targets annotated in the MIPE collection. The *P* value from the test was adjusted for multiple hypothesis testing using the Benjamini-Hochberg method (27).

Compound Combination Matrix Screening

For the combination matrix screen with the selected compounds, protocols were as described before (12, 28). Briefly, compounds were pre-plated using an acoustic dispenser ATS-100 (EDC Biosystems, Fremont, CA). A total of 5 nL of each compound solubilized in DMSO, as well as DMSO control wells, were dispensed with threefold dilutions to generate 6 × 6 dose-response matrices, first, followed by confirmatory retesting using twofold dilutions in 10 × 10 dose-response matrices. 5 μL of a cell suspension (500 cells/well) were added directly to the plates immediately after compounds were pre-plated. Two sets of plates were screened. The first one was for cell proliferation assays, where cells were incubated with the compounds for 48 hours, and proliferation was quantified by adding CellTiter-Glo reagent. RLU was measured with the Viewlux (Perkin Elmer) after 15 minutes incubation at room temperature. The second plate was used for an apoptosis assay, incubating cells with the compounds for 16 hours and adding the Caspase-Glo 3/7 reagent to measure apoptosis.

In vitro validation of compound combinations

The IC_{50} of all compounds used in the 21 combinations selected was calculated for MPNST-SP-01 or S462 cells. First, 10,000 cells/well of MPNST-SP-01 cells or 8,000 cells/well of S462 were seeded in 96-well plates (Corning) and incubated overnight. Then, compounds in

DMSO were added to the wells in three replicates. Two series of dilutions were performed at two concentration ranges depending on the potency of the compound. Stocks were prepared at 10 mmol/L, and compounds were 10-fold diluted from 1,000 nmol/L to 0.1 nmol/L or fivefold diluted from 40 μmol/L to 0.064 μmol/L, using DMSO. After 48 hours of incubation with the drugs, cell viability was analyzed using MTT (Sigma-Aldrich). Briefly, 14 μL of MTT (0.5 mg/mL) were added to each well. After 2 hours of incubation at 37°C, media was removed from the wells and 100 μL of glycine buffer solution (25 μL of buffer 0.1 mol/L NaCl and 0.1 mol/L Glycine with 75 μL of DMSO) was added. Plates were shaken for 15 minutes and the absorbance levels were read in the VictorTM X5 2030 Multilabel Reader (PerkinElmer). The IC_{50} was calculated using GraphPad Prism Version 6 (La Jolla, CA). The percentage of cell viability was calculated by normalizing the values to DMSO control wells as 100% viability. Later, the four chosen synergistic combinations were tested in six additional MPNST cell lines, for which individual IC_{50} of compounds was also calculated.

For combination assays, compounds were added to wells in three replicates as single treatments or in combination at a fixed 1:1 ratio of the IC_{50} of both compounds, and threefold dilutions were performed from $10 \times IC_{50}$ concentration to $0.12 \times IC_{50,}$ for each compound. After 48 hours of incubation, cell viability was measured by MTT, and combination index (CI) values for the combinations were calculated using CompuSyn Software, based on Chou-Talalay calculations (29). When CI is lower than 0.9 at high values of fraction affected of cells (Fa), we labeled the combination as synergistic. Fa value represents the fraction of cell death by drug treatment, ranging from 0 (no cell death) to 1 (100% cell killing). CI values between 0.9 and 1.1 are indicative of an additive effect and when values are higher than 1.1, the compounds are antagonistic (30).

Apoptosis analysis

MPNST-SP-01 and S462 cells were seeded (75,000 cells/mL and 60,000 cells/mL, respectively) in 6-well plates and incubated overnight. Cells were then treated with single compounds or combinations. Combinations with Panobinostat were tested at a fixed 1:1 ratio of the IC_{50} and MK-1775 with Doxorubicin was combined at a 1:1 ratio of $3 \times IC_{50}$ to visualize the differences in apoptosis activation between the combination and individual treatments. After 24 hours of incubation, apoptosis activation was evaluated using the Annexin V APC Dead cell kit and SYTOX Green (ThermoScientific) to stain annexin-positive cells, according to the manufacturer's protocol. Samples were analyzed by FACSCanto II (BD Biosciences) flow cytometer. The apoptotic index was calculated as the mean percentage of apoptotic cells in 10^4 cells measured in each of three independent experiments. Alternatively, apoptosis was determined by the percentage of cells in the sub-G_1 cell-cycle phase using flow cytometric analysis. After treatment, cells were fixed in ice-cold 70% ethanol and left for 24 hours at –20°C. Ethanol-fixed cells were centrifuged at $800 \times g$, washed, and resuspended in citrate-phosphate buffer (Na_2HPO_4 0.2 mol/L and citric acid 0.1 mol/L at a ratio 192:8, pH 7.8) for 30 minutes. Cells were centrifuged at $400 \times g$ and incubated in PBS supplemented with 1% FBS, 0.2 mg/mL RNAse (Sigma-Aldrich), and 60 μg/mL propidium iodide (Sigma-Aldrich) for 45 minutes at 37°C. 10,000 to 20,000 cells per sample of three experiments were measured to determine the percentage of cells at the sub-G_1 phase of the cell cycle. The percentage of cells in the G_1, S, and G_2–M phases was also calculated.

Dosage test

We adjusted the dosages and the administration schemes for the different compounds (Supplementary Table S2), using athymic nude 6-week-old male mice, in which no tumor was engrafted. Treatments lasted for 3 weeks and the mice body weight was daily measured to analyze potential toxicity. Carfilzomib and Doxorubicin were obtained from our hospital pharmacy. NVP-BGT226 (S2749), Torin 2 (S2817), and Panobinostat (S1030) were purchased from Selleckchem and MK-1775 (ref. 31; Adavorsetib, HY-10993) from MedChemExpress.

In vivo drug treatment

Before drug treatments, an early-passage (P2–P4) MPNST-SP-01 or MPNST-NF1–09 PDOX tumor had to be expanded. To do this, each tumor was implanted in five mice. When tumors reached 1,000 to 1,500 mm^3, mice were sacrificed; tumors were harvested and cut into small fragments and engrafted near the sciatic nerve of 60 athymic nude male 6-week-old mice. Once tumors reached 300 to 500 mm^3, mice were randomly distributed into treatment groups ($n = 5$–10/group): (i) single compound 1; (ii) single compound 2; (iii) combination compounds 1+2; and (iv) control receiving solvents of compounds 1+2. The final tumor weight plot from MPNST-NF1–09 PDOX model presented less than 5 points in some groups due to mice left to perform regrowth testing. Dosages and treatment schedules are specified in Supplementary Table S3. The study received IDIBELL IRB (#PR213/13) and IDIBELL Animal Ethics Experimentation Committee (CEEA-IDIBELL; #9111) approval. Combinations in which we did not observe tumor reduction by day 18 were further tested until day 25. Twenty-four hours after the last dose, mice were sacrificed and tumors extracted. Tumors were measured using a caliper twice a week, and volume was calculated using the formula "$v = (w^2 L/2)$", where l is the longest diameter and w the width. Changes in tumor volume were quantified as the "increased tumor volume" since day 0, where each measurement is calculated following the formula "increased tumor volume = tumor volume day X – tumor volume day 0". The interaction between follow-up time (in days) and treatment was used to assess the effect of each treatment in terms of volume change compared with the control group.

Protein extraction and Western blot analysis

Protein was extracted from control tumors ($n = 4$) and tumors treated with the combinations ($n = 6$) using RIPA buffer supplemented with protease inhibitor (cOmplete Tablets, Roche). Briefly, 15 to 20 mg of tissue was homogenized in RIPA using TissueLyser II (Qiagen) and centrifuged at $16{,}000 \times g$ at 4°C for 10 minutes. Proteins in the supernatant were quantified with the Pierce BCA Protein Assay Kit (ThermoScientific), using BSA as a standard.

For Western blot, equivalent amounts of protein (20 μg) were separated on 12% Acrylamide gels (TGX Stain-Free FastCastAcrylamide Kit, Bio-Rad). Before transference, gels were activated for 45 seconds by UV radiation using ChemiDoc Touch Imaging System (Bio-Rad), so that proteins could fluorescence when exposed to UV. Proteins were then transferred to nitrocellulose membranes from the Trans-Blot Turbo RTA Transfer Kit (Bio-Rad) using an established protocol from the Trans-Blot Turbo Transfer System (Bio-Rad). After transference, total protein from each lane was detected by exposing the membrane to UV. Then, membranes were blocked using 5% BSA (Roche) for 1h. Primary antibodies against Cdk1 (77055S), phospho-Cdk1^{Tyr15} (9111T), Caspase-3 (9662S), Cleaved Caspase-3 (9661S), Histone H3 (9715S), Acetyl-Histone H3^{Lys18} (9675S), SAPK/JNK (9252T), phospho-SAPK/JNK$^{Thr183/Tyr185}$ (4668T), p70S6 Kinase (9202S), and phospho-p70^{Thr389} S6 Kinase (9234S) were purchased from Cell Signaling Technology, diluted 1:1,000 in 5% BSA, and incubated overnight at 4°C. Membranes were probed with secondary antibody Stabilized Peroxidase Conjugated Goat Anti-Rabbit (Thermo

Scientific), diluted 1:1,000 in 5% BSA, and incubated at room temperature for 1 hour. Finally, detection of proteins was conducted using SuperSignal West Femto Chemiluminescent substrate kits (Pierce Biotechnology Inc., Rockford, IL). Quantification analyses were carried out by the Image Lab program from Bio-Rad. Each protein of interest was normalized to the total protein of the lane to assess differences due to protein loading. Then, phosphorylated and acetylated proteins were also normalized to their levels of basal protein.

Statistical analyses

Statistical analyses were performed using Graphpad Prism 6. We calculated differences in terms of cell apoptosis activation between cells treated with combination of compounds and cells treated with single compounds or DMSO-control treated cells ($n = 3$ in each group), by using the unpaired t test with a significant level of 0.05. We also assessed differences in tumor volume and tumor weight between mice treated *in vivo* with combinations compared with single treatments and controls ($n = 7$–10 in each group) using the Mann–Whitney test with a significant level set at 0.05.

Data availability statement

A full list of compounds from the MIPE 4.0 library is available upon request.

Data from the 113 10×10 combination screening matrices for the three MPNST cell lines, performed by the NIH-NCATS, are found in the following web links:

MPNST-SP-01 Apoptosis 16 h https://tripod.nih.gov/matrix-client/rest/matrix/blocks/6341/table
MPNST-SP-01 Cell viability 48 h https://tripod.nih.gov/matrix-client/rest/matrix/blocks/6342/table
sNF96.2 Apoptosis 16 h https://tripod.nih.gov/matrix-client/rest/matrix/blocks/6343/table
sNF96.2 Cell viability 48 h https://tripod.nih.gov/matrix-client/rest/matrix/blocks/6344/table
S462Apoptosis 16 h https://tripod.nih.gov/matrix-client/rest/matrix/blocks/6345/table
S462Cell viability 48 h https://tripod.nih.gov/matrix-client/rest/matrix/blocks/6346/table

Results

High-throughput screening of the MIPE library as single agents

We screened the MIPE library using a quantitative high-throughput screen approach against three different MPNST cell lines, one sporadic established in our laboratory (MPNST-SP-01), and two NF1-related: S462 and sNF96.2. The assay used for the screen quantitated cellular ATP levels as a measure of cell viability/proliferation after 48 hours of treatment. From the dose-response screening, several hundred compounds were judged to be active based on CRC scores of –1.1, –1.2, and –2.1, for each cell line (480 active compounds at MPNST-SP-01 cell line, 507 at S462 and 410 at sNF96.2; refs. 24, 32). The CRC score is a measure of both potency (AC_{50}) and maximum response (MAXR), which is the percentage of activity at the maximum tested concentration (46 μmol/L). Differences between cell lines in the hierarchical clustering of the screening responses via MAXR (**Fig. 1A**) showed that the three MPNST cell lines had distinct pharmacologic vulnerabilities. Another parameter used to analyze the response of the drugs is the Area under the curve (AUC), which includes both the potency and efficacy of the compounds (33). When comparing the median AUC values of different compounds grouped by their mechanism of action (MOA) and target classes, while some mechanisms appear to have similar effects (e.g., tyrosine or serine/threonine kinase inhibitors), for other mechanisms (e.g., proteasome inhibitors or tubulin inhibitors) the response is quite different between cell lines (**Fig. 1B**). In general, the median AUC for each compound class is higher (less active) in the sporadic cell line compared with the NF1 cell lines. The redundancy in the number of compounds in each target class enabled us to perform target enrichment analysis for the active compounds in each cell line (**Fig. 1C**). There were only three target classes enriched (–log P value > 1) in all three cell lines (PIK3CA, CDK1, and PSMD1), and three targets enriched in two cell lines: TUBB for MPNST-SP-01 and S462; and histone deacetylase 1 (HDAC1) and MTOR for MPNST-SP-01 and sNF96.2. However, compounds targeting these enriched targets displayed different ranges of responses, as measured by AUC, among the three MPNST cell lines (**Fig. 1D**). We also performed a pharmacogenomic analysis and used exome sequencing data from the sporadic MPNST-SP-01 primary tumor, and found that the distance between somatic mutations and targets that were pharmacologically enriched was shorter than expected, including ERBB2, EGFR, PIK3CA, and PRKCA (**Fig. 1E**). The responses of compounds targeting these gene products were, in general, stronger for MPNST-SP-01 compared with the other two cell lines (**Fig. 1F**). On the basis of the target enrichment data, high-quality CRC, clinical relevance, and pathways of therapeutic interest, 25 compounds were selected to implement a pairwise all-versus-all matrix screen to explore synergistic activity in the MPNST-SP-01 and S462 cell lines and 50 compounds in sNF96.2 cell line.

Identification of synergistic compound combinations

The selected hits (75 among the three MPNST cell lines) were first screened in an all-versus-all, pairwise, 6 dose × 6 dose-response screening matrix. These experiments resulted in 300 discrete 6 × 6 matrices against MPNST-SP-01 and S462 cell lines, and 1,326 matrices against sNF96.2 cell line, using CellTiter-Glo ATP measurement as readout after 48 hours of treatment. Combinations that displayed synergy at selected concentrations, as quantitated by multiple metrics including the Bliss independence and the excess highest single agent (HSA) models, were advanced into 10 dose × 10 dose-response matrix experiments (12). For the 10 × 10 matrix screen, two sets of plates were generated, one for 48 hours treatment with CellTiter-Glo measurement, and the second for 16 hours treatment with Caspase-Glo to measure apoptotic cell death. A total of 113 10 × 10 dose-response pairwise combination matrices were generated and screened with all three MPNST cell lines (data in Materials and Methods). Hierarchical clustering analysis using the Delta Bliss Sum Negative (DBsumNeg) values for each matrix, with both the cell viability (**Fig. 2A**, left) and apoptosis (**Fig. 2A**, right) readouts, shows that synergies are stronger for the MPNST-SP-01 cell line at 48h, while they are weaker and similar between the S462 and sNF96.2 cell lines.

When selecting combinations with DBSumNeg values lower than –7, we observed different patterns of synergism among the three MPNST cell lines (**Fig. 2B**). For example, from the eighteen combinations that met this criterion for the MPNST-SP-01 cell line, seven included Panobinostat (HDAC inhibitor) combined with compounds targeting many different targets like Torin 2, NVP-BGT226, Carfilzomib, Fluvastatin, Lenvatinib, Obatoclax, and Doxorubicin. Interestingly, Panobinostat is not the compound driving most of the synergies for the other two MPNST cell lines. Moreover, five combinations including Doxorubicin (DNA damaging agent), and four including NVP-BGT226 (mTOR inhibitor) were observed for this cell line. On the other hand, from the eleven combinations that met the criterion for S462, four included Doxorubicin with NVP-BGT226, Englerin A,

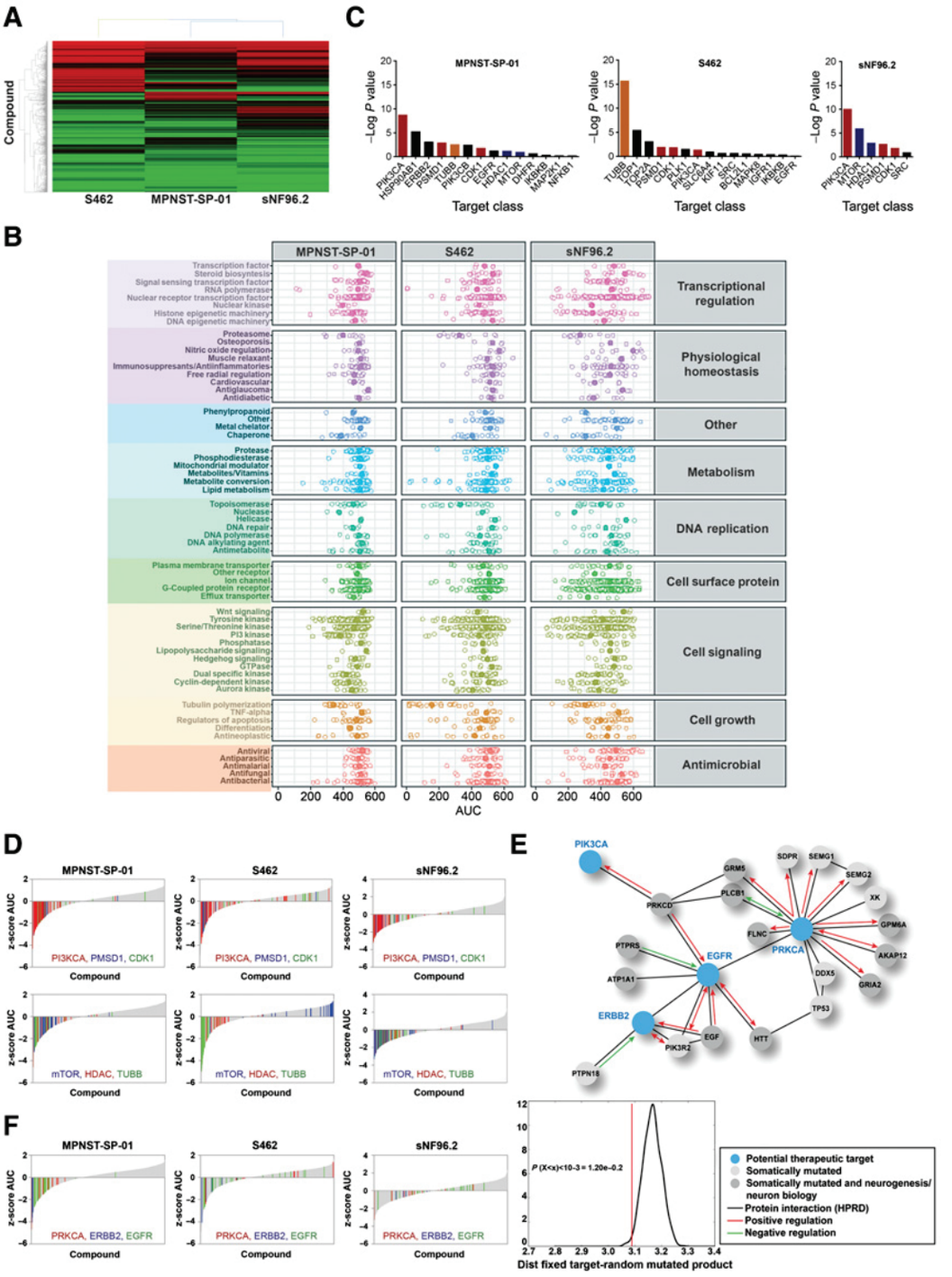

Figure 1.

Summary of single-agent screening against MPNST-SP-01, S462, and sNF96.2 cell lines. **A,** Heatmap plot of percent maximum response parameter (MAXR) measuring cell viability at 48 hours for all the compounds in the NCATS MIPE collection in the three MPNST cell lines. Red indicates a low percentage of cell viability, and the green represents a high percentage of cell viability. **B,** Cell viability responses to all MIPE library agents (as judged by AUCs) binned per mechanistic classes. **C,** Summary of the enriched MOA in the three MPNST cell lines. Red is MOA enriched in the three MPNST cell lines screened, orange is MOA enriched in two MPNST cell lines (MPNST-SP-01 and S462), blue is MOA enriched in the MPNST-SP-01 and sNF96.2 cell lines. **D,** Plot of z-scores AUC for each compound tested, highlighting MOA enriched in at least two different MPNST cell lines. **E,** Plot representing somatic mutations found in the MPNST-SP-01 and their distance to potential therapeutic targets. **F,** Plot of z-score AUC for each compound highlighting MOA related to somatic mutations in the MPNST-SP-01.

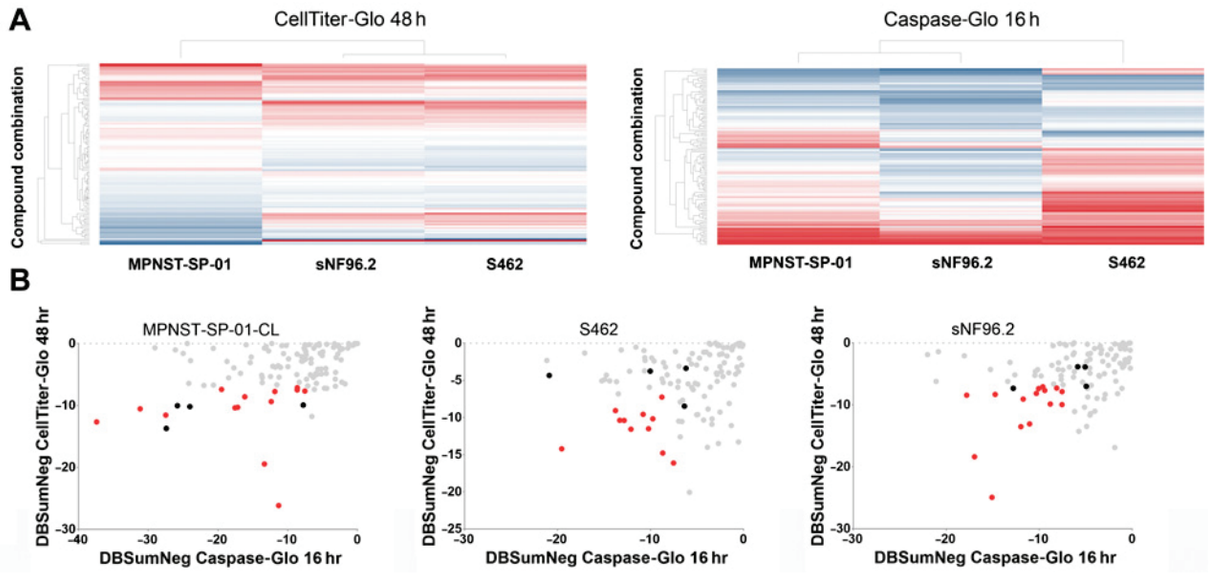

Figure 2.

Results from the drug combination screening. **A,** Heatmap plot from DBSumNeg value for viability (48 hours; left) and apoptosis (16 hours; right) readouts in the MPNST-SP-01, S462, and sNF96.2 cell lines. Blue combinations display low values of DBSumNeg parameter indicating the presence of synergism, and red indicates high values for the DBSumNeg parameter indicating no presence of synergism. **B,** Correlation between DBSumNeg values for cell viability at 48 hours and apoptosis at 16 hours. The four combinations selected for *in vivo* testing are highlighted in black, and in red combinations with DBSumNeg<-7 in both readouts.

Neratinib, and Torin 2; and from 16 combinations for sNF96.2, four combined Sirolimus (mTOR inhibitor) with AT-9283, Cabozantinib, Crizotinib, and CUDC-101 (Supplementary Table S4).

Doxorubicin combined with MK-1775 and Panobinostat combined with NVP-BGT226, Torin 2, and Carfilzomib are synergistic in MPNST cell lines

The selection of synergistic combinations for further validation was focused on those combinations showing synergism in at least two of the three MPNST cell lines (MPNST-SP-01, S462, and sNF96.2), based on the DBSumNeg values. Also, visual inspection of the 10 × 10 matrices was taken into account when the DBSumNeg value was not a clear indication of synergism (Supplementary Fig. S1).

Twenty-one combinations were further tested *in vitro* to obtain a CI for each treatment according to dose-response curves. Synergy was observed in 13 of the 21 combinations, where CI was lower than 0.9 at Fa values higher than 0.8 (ref. 29; **Table 1**; Supplementary Fig. S2). From these combinations, the most synergistic ones were Panobinostat combined with Torin 2, NVP-BGT226, and Carfilzomib. We also selected the combination of MK-1775 with Doxorubicin because, even though the treatment did not kill cells beyond Fa = 0.85, the response of the combined compounds in terms of cell viability was notably increased compared with the individual drugs. These four combinations exhibited low DBSumNeg (**Table 1**) and excess HSA values (**Fig. 3A**) and synergistically decreased cell viability in the MPNST-SP-01, S462, and sNF96.2 cell lines compared with individual treatments (**Fig. 3B** and **C**). We then tested the four combinations in a broad panel of MPNST cell lines: three sporadic (STS26T, HS-PSS, and HS-sch2) and two NF1-derived cell lines (MPNST-NF1–08 and MPNST-NF1–09). We observed a synergistic effect in almost all the MPNST cell lines, independent of their *NF1* status (Supplementary Fig. S3). In addition, the combinations were also tested in a fibroblastic cell line, HFFs, to evaluate general cell toxicity. Synergism was observed in all the combinations containing Panobinostat, but at higher concentrations than in the MPNST cell lines, indicating that tumor cells are more sensitive to the treatment, but also pointing to potential cytotoxicity. On the contrary, MK-1775 with Doxorubicin did not show synergism in the HFF cell line (Supplementary Fig. S3).

Combined treatments induce apoptosis

To gain further insight into the nature of these four compound combinations, we investigated their synergistic effect on the activation of apoptosis by measuring *in vitro* the percentage of annexin-positive cells and the fraction of cells at the sub-diploid (sub-G_1) phase, both as apoptosis readouts. We observed that Panobinostat combinations presented a significantly higher percentage of annexin-positive cells than individual treatments, confirming a potent apoptotic response in both cell lines. The combination MK-1775 with Doxorubicin showed an increased apoptotic response after treatment at high doses of the combined compounds in both cell lines (**Fig. 4A**). We observed that the combined treatment and the single compounds caused a greater apoptotic response in the S462 cell line, proving that this cell line is more sensitive to the treatments (**Fig. 4A**). The fraction of cells in the sub-G_1 phase in the four combinations treatment was also significantly higher, confirming the synergy at the apoptotic level (**Fig. 4B**). The apoptosis results obtained from annexin staining or phase sub-G_1 analyses presented a good correlation in both cell lines (except for MPNST-SP-01 treated with MK-1775 plus Doxorubicin). Moreover, the percentage of cells in the G_1/S/G_2 phases of the cell cycle was calculated to evaluate changes in the cell-cycle progression due to the treatments (**Fig. 4C**). The most notable change was observed when using MK-1775 (Wee1 kinase inhibitor) as a single treatment, due to its effect on the cell cycle via G_2–M checkpoint inactivation, as we observed a decreasing proportion of cells in the G_1 phase, which results in S-phase accumulation (31). Panobinostat also promotes cell-cycle arrest by blocking cells in the G_2–M phase before cell death, thus

Table 1. List of the 21 selected combinations (according to DBSumNeg values of the three screened MPNST cell lines) validated *in vitro* by CI values in MPNST-SP-01 or S462 cell lines.

	COMBO ID	Compound A	Target A	Compound B	Target B	DBSumNeg 48h			*In vitro* tested cell line	CI			Compounds interaction
						MPNST-SP-01	S462	sNF96.2		Fa 0.5	Fa 0.75	Fa 0.95	
1	4	AT-9283	Aurora-A/B Inhibitor	Englerin A	PKC Activator	−0.02	−20.7	−24.9	S462	46.25	*	*	AN Fa > 0.5
2	10	AT-9283	Aurora-A/B Inhibitor	NVP-BGT226	PI3K Inhibitor	−0.25	−8.48	−13.07	S462	0.77	0.48	0.40	S
3	11	AT-9283	Aurora-A/B Inhibitor	Neratinib	EGFR (HER1; erbB1) Inhibitor	−0.2	−10.17	−4.13	S462	0.65	0.71	0.84	S
4	13	AT-9283	Aurora-A/B Inhibitor	Thapsigargin	SERCA Inhibitor	−1.6	−8.12	−8.19	MPNST-SP-01	0.25	0.3	0.63	S
5	19	CUDC-101	EGFR Inhibitor	Carfilzomib	Proteasome Inhibitor	−0.78	−3.78	−3.9	MPNST-SP-01	0.67	0.6	0.52	S
6	27	Doxorubicin	Topoisomerase I Inhibitor	MK-1775	Wee1 Kinase Inhibitor	−9.93	−8.48	−7	S462	0.58	0.78	1.3	S
7	28	Doxorubicin	Topoisomerase II Inhibitor	Neratinib	EGFR (HER1; erbB1) Inhibitor	−0.49	−14.21	−18.38	S462	0.74	0.92	1.90	AD/AN Fa > 0.5
8	30	Doxorubicin	Topoisomerase II Inhibitor	Ponatinib	FGFR Inhibitor	−6.83	−10.55	−11.02	S462	1.03	0.92	1.36	AD
9	47	Ispinesib	Kinesin-Like Spindle Protein Inhibitor	Thapsigargin	SERCA Inhibitor	−0.74	−1.96	−1.89	S462	0.95	0.95	1.14	AD
10	53	Neratinib	EGFR (HER1; erbB1) Inhibitor	Obatoclax	Bcl-xL Inhibitor	−9.37	−7.15	−3.16	MPNST-SP-01	3.45	5.11	13.32	AN
11	58	NVP-BGT226	PI3K Inhibitor	Ponatinib	FGFR Inhibitor	−3.81	−4.26	−4.29	S462	0.53	0.47	0.6	S
12	61	NVP-BGT226	PI3K Inhibitor	Neratinib	EGFR (HER1; erbB1) Inhibitor	−1.63	−6.82	−8.32	S462	0.45	0.24	0.08	S
13	63	Panobinostat	HDAC Inhibitor	Carfilzomib	Proteasome Inhibitor	−13.7	−4.34	−7.33	MPNST-SP-01	0.48	0.56	0.76	S
14	71	Panobinostat	HDAC Inhibitor	MK-1775	Wee1 Kinase Inhibitor	−6.66	−0.92	−3.2	MPNST-SP-01	0.38	0.47	1.06	S
15	73	Panobinostat	HDAC Inhibitor	NVP-BGT226	PI3K Inhibitor	−10.03	−3.38	−3.89	MPNST-SP-01	0.24	0.20	0.17	S
16	74	Panobinostat	HDAC Inhibitor	Ponatinib	FGFR Inhibitor	−2.48	−1.53	−2.61	S462	1.62	1.42	1.15	AN
17	75	Panobinostat	HDAC Inhibitor	Topotecan hydrochloride	Topoisomerase I Inhibitor	−3.93	−0.3	−0.3	S462	1.21	1.24	1.31	AN
18	76	Panobinostat	HDAC Inhibitor	Torin-2	mTORC1 Inhibitor	−10.18	−3.77	−3.84	MPNST-SP-01	0.31	0.05	0.008	S
19	78	Panobinostat	HDAC Inhibitor	Cabozantinib	VEGFR-2 Inhibitor	−3.74	−4.9	−6.22	S462	0.84	0.53	0.32	S
20	84	Panobinostat	HDAC Inhibitor	Elesclomol	Copper Chelator	−2.77	−2.33	−0.39	S462	1.17	0.84	0.53	S Fa > 0.5
21	86	Sirolimus	mTOR inhibitor	Neratinib	EGFR (HER1; erbB1) Inhibitor	−6.51	−13.5	−14.27	S462	0.46	*	*	AN Fa > 0.5

Note: In orange, the combinations further validated *in vivo*.
Abbreviations: S, Synergism; AD, Additive; AN, Antagonism; HDAC, Histone deacetylase.
*No data due to the combination not reaching the Fa value.

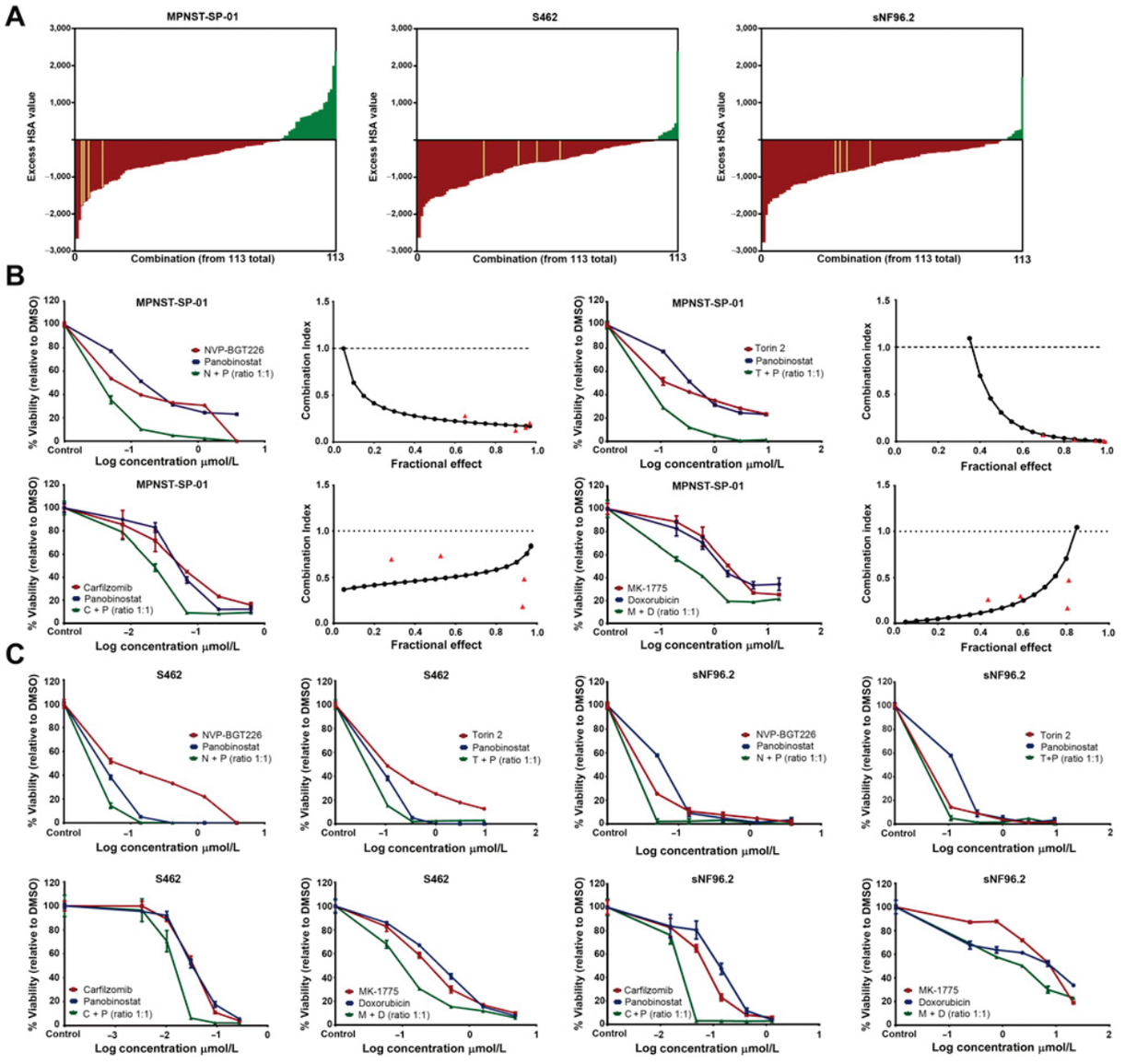

Figure 3.

Panobinostat combined with NVP-BGT226, Torin 2, and carfilzomib, and MK-1775 combined with doxorubicin are synergistic in three MPNST cell lines. **A,** Combination response blot representing 113 discrete drug synergy scores (as judged by the excess HSA metric) from the 10×10 matrix screen. Examples of high-ranking drug synergies are highlighted in orange, including the combination of MK-1775 with Doxorubicin and Panobinostat combined with Torin 2, NVP-BGT226, and Carfilzomib in the three MPNST cell lines screened. **B,** Single-agent and combined responses for the 4 combinations reported by the MTT viability assay (left) and CI plot (left) in the MPNST-SP-01 cell line. **C,** Single-agent and combined dose–response plots reported by cell viability assay for the 4 combinations in S462 and sNF96.2 cell lines.

observing a lower percentage of G_1 cells and increased levels of G_2 cells in the three combinations using this compound (34).

The combination of MK-1775 with doxorubicin reduces tumor growth in two PDOX mouse models engrafted with primary sporadic and NF1-derived MPNSTs

We further tested the four combinations *in vivo* in patient-derived orthotopic xenograft (orthoxenograft/PDOX) mouse models from our preclinical platform. Only MK-1775 with Doxorubicin reduced the tumor growth compared with control and individual treatments in two different PDOX-MPNST models: one sporadic PDOX (MPNST-SP-01) and one NF1-related PDOX model (MPNST-NF1–09). The treatment caused the final tumor volume in mice to be seven times lower than the vehicle in the sporadic model after eighteen days of treatment, and almost four times lower in the NF1-PDOX model (**Fig. 5A** and **B**). This reduction was validated through tumor weight measures once they were extracted from mice at the end of the treatment. In the sporadic model, tumor weight was almost two times

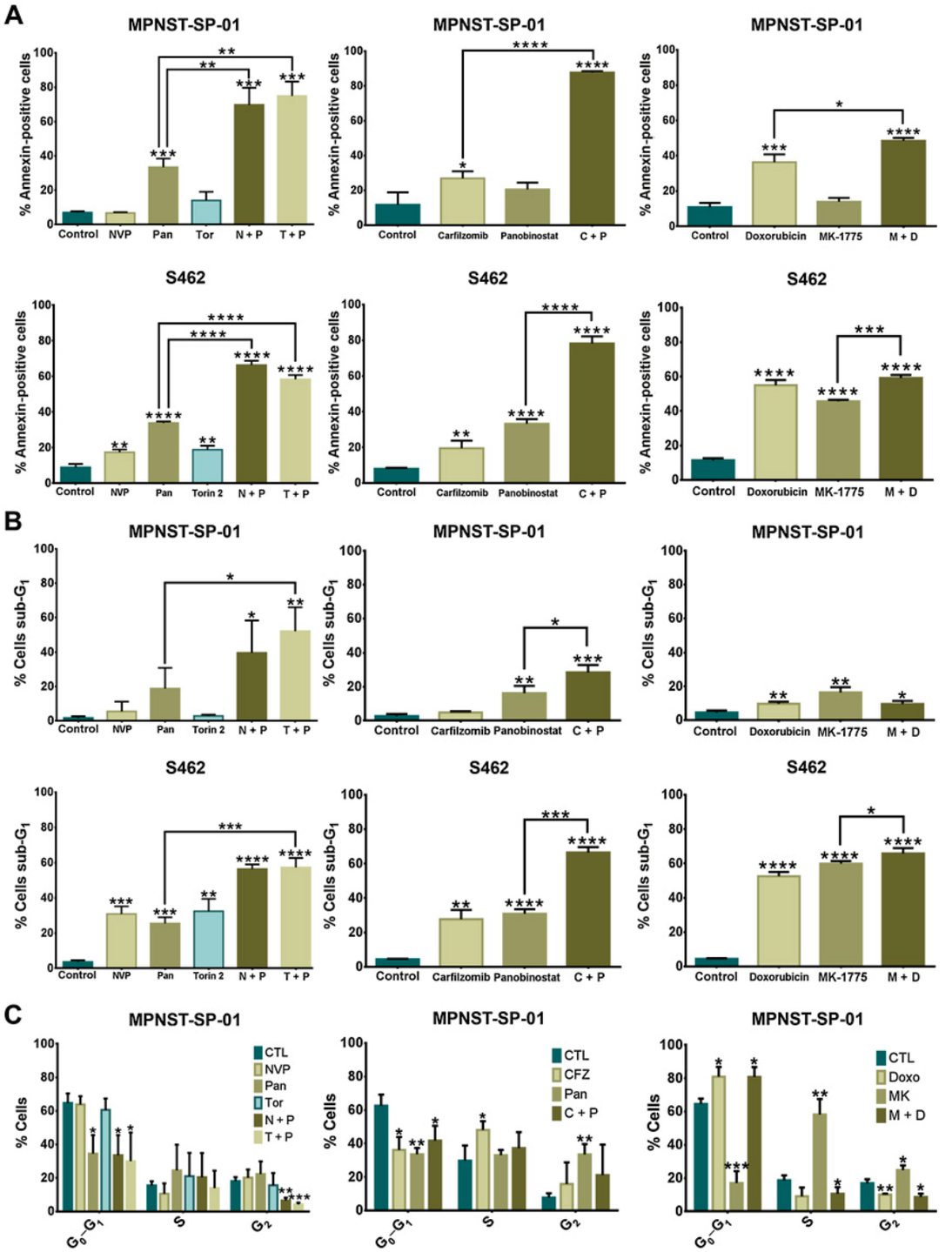

Figure 4.

Combined treatments induce apoptosis. **A,** Apoptosis measurement quantified as annexin-positive cells in MPNST-SP-01 and S462 cell lines treated with single and combined treatments MK-1775 with doxorubicin and NVP-BGT226/Torin 2/carfilzomib with panobinostat (unpaired *t* test). **B,** Apoptosis measurement quantified as the percentage of cells in the sub-G_1 phase in MPNST-SP-01 and S462 cell lines treated with the four combinations. **C,** Cell-cycle analyses in cells treated with single agents and combinations in the MPNST-SP-01 cell line. CTL, untreated cells; NVP, NVP-BGT226; Pan, panobinostat; Tor, Torin 2; CFZ, carfilzomib; Doxo, Doxorubicin; MK, MK-1775; N + P, NVP-BGT226 + panobinostat; T + P, Torin 2 + panobinostat; C + P, carfilzomib + panobinostat; M + D, MK-1775 + doxorubicin (unpaired *t* test). ****, $P \leq 0.0001$; ***, $P \leq 0.001$; **, $P \leq 0.01$; *, $P \leq 0.05$.

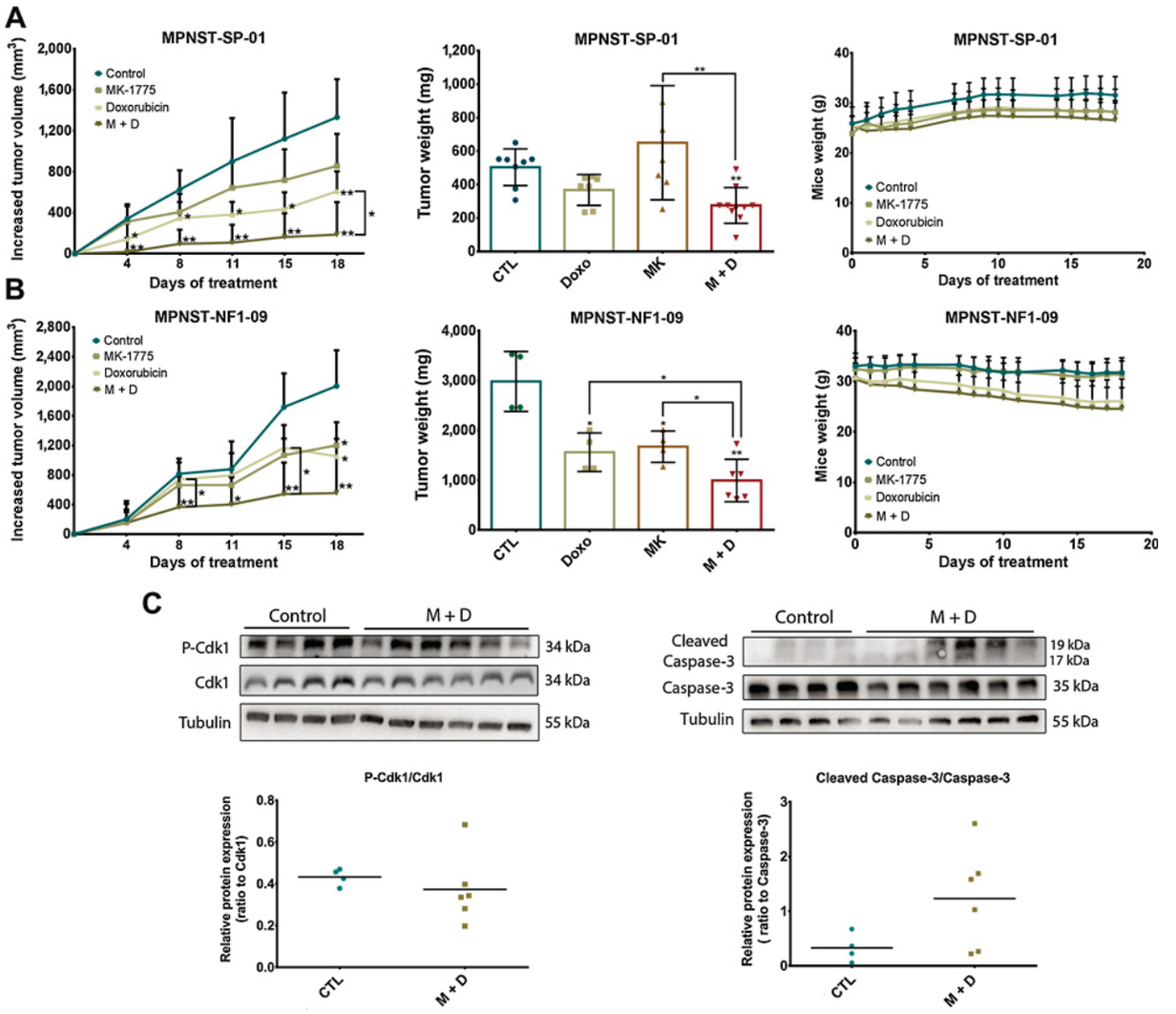

Figure 5.

In vivo testing of the combination MK-1775 with doxorubicin in two PDOX-MPNST mouse models for 18 days of treatment. **A,** Tumor reduction in the sporadic MPNST-SP-01 PDOX mouse model presented in two plots: the increased tumor volume since day 0 in each group during treatment (left panel), and tumor weight at the end of the experiment (middle panel). The toxicity effect was assessed by changes in mouse body weight (right panel) (Mann–Whitney test). **B,** Tumor reduction in the NF1-derived MPNST-NF1–09 PDOX mouse model presented in the same plots as **A** (Mann–Whitney test). The final tumor weight plot from MPNST-NF1–09 PDOX model presented less than 5 points in control and single treatments groups because several mice were left alive to study the regrowth of the tumor. However, all the mice were included in the plot representing tumor volume. **C,** Analyses of the molecular target of MK-1775 (P-Cdk1) and doxorubicin (cleaved caspase-3) by Western blot analysis. CTL, mice treated with vehicle; Doxo, mice treated with doxorubicin; MK, mice treated with MK-1775; M + D, mice treated with the combination MK-1775 and doxorubicin; **, $P \leq 0.01$; *, $P \leq 0.05$.

lower than control, and three times lower in the case of the NF1-related PDOX-MPNST. Moreover, treatment minimally reduced mice's body weight: approximately 10% in the NF1-related PDOX and no detectable weight loss in the sporadic model (**Fig. 5A** and **B**). In contrast, the three combinations selected with Panobinostat neither reduced the tumor volume nor the final tumor weight in the sporadic PDOX model (MPNST-SP-01) after 25 days of treatment (Supplementary Fig. S4A and S4B) at the tested doses, which were not toxic to the animals (Supplementary Fig. S4C). Higher doses of the compounds were tested, but toxicity was observed (Supplementary Table S2).

We also performed western blot to evaluate the expression of key molecular targets of the compounds in control tumors and tumors treated with the combinations. We observed a reduction of phosphorylation of Cdk1 (P-Cdk1) in some tumors treated with the combination MK-1775 with Doxorubicin due to the inactivation of Wee1 kinase activity by MK-1775 (31). Moreover, this combination caused higher levels of cleaved Caspase-3, which suggests activation of the apoptosis pathway due to DNA damage caused by Doxorubicin (**Fig. 5C**; ref. 35).

Some tumors treated using Panobinostat with Torin 2 and Panobinostat with NVP-BGT226 presented higher levels of acetylation of

Histone 3 than controls, due to Panobinostat working as a HDAC inhibitor (36). Also, phosphorylation of p70S6 kinase was reduced in treated tumors, as both Torin 2 and NVP-BGT226 inhibit mTOR kinase activity (37, 38). On the other hand, tumors treated with Panobinostat and Carfilzomib did not show an increase in Histone 3 acetylation or an increase in the phosphorylation of JNK proteins, as would be expected due to reactive oxygen species being produced by the proteasome disruption by Carfilzomib (Supplementary Fig. S4D; ref. 39). In general, results from Western blot were weak and not statistically significant, likely due to the compounds being washed out in the 24 hours between the last dose and tumor extraction.

Discussion

Our current study shows the results of a large-scale screening of 1,912 oncology-focused molecules on three MPNST cell lines (S462, sNF96.2, and MPNST-SP-01). This HTS approach has been successfully applied to find synergistic drug combinations for different cancers and has suggested new therapeutic options that worked *in vivo* (14, 28).

We found that the pharmacologic responses among the MPNST cell lines differed and that synergistic combinations in the sporadic cell line MPNST-SP-01 did not fully correlate with those in the NF1 lines, S462 and sNF96.2, probably due to the complex genomic landscape and genetic variability between different MPNSTs (40). Although most of the enriched targets identified have been previously suggested as possible therapeutic targets for MPNSTs (41–43), clinical trials using single agents have only so far shown response rates in the 18% to 44% range (6). It has been argued that cellular and molecular MPNST heterogeneity could limit the efficacy of single anticancer drugs in eliminating all the malignant cells in a tumor (44). There is much evidence that combination therapy could be superior to monotherapy because of the ability to target multiple pathways, minimizing drug resistance as cancer cells are frequently incapable of adapting to the simultaneous toxic effects. Moreover, if two compounds present synergism, the dose required for efficacy could be reduced (44). We, therefore, looked for synergistic combinations effective against MPNST cell lines. As a result of the single-agent MIPE library screening, some compounds were selected based on potency, efficacy, cellular target, and clinical relevance, and assayed in pairwise combinations to identify potential potent synergies. From the 21 *in vitro* selected combinations, four were identified as highly synergistic in a panel of MPNST cell lines: MK-1775 with Doxorubicin, Panobinostat with NVP-BGT226, Panobinostat with Torin 2, and Panobinostat with Carfilzomib. The combinations containing Panobinostat (a histone deacetylase inhibitor, HDACi) showed a potent apoptotic response in tumor cells but also exhibited cytotoxicity. Dual PI3K-mTOR inhibitors combined with HDACi have been effective in cell lines and mice models of medulloblastoma, non–small cell lung cancer, and breast cancer, among others (45–47). Moreover, there is also preclinical evidence of the effectiveness of mTOR and HDAC inhibitors for MPNSTs (48), in which the combined inhibition impinges on the thioredoxin pathway, triggering catastrophic oxidative stress and cell death, thus achieving tumor regression *in vivo*. In our study, none of the two combinations using HDAC and PI3K-mTOR inhibitors (Panobinostat with NVP-BGT226 or Torin 2) resulted in a reduction of tumor volume in our sporadic PDOX-MPNST model (MPNST-SP-01). We also tested Panobinostat *in vivo* with Carfilzomib (a proteasome inhibitor). This combination is in Phase I/II clinical trials (NCT01496118 and NCT01301807) for patients with relapsed and refractory multiple myeloma (49, 50). Also, it has been validated as synergistic in osteosarcoma cell lines *in vitro* (51). The combination triggers cell death through the accumulation of unfolded proteins that cannot be degraded by the proteosome or aggresome, in which HDAC-6 plays an important role (52). However, we did not observe the effect of this combination on tumor volume in our MPNST-SP-01 PDOX mouse model.

The observed differences in our *in vivo* experiments compared with the data in the literature could be due to the polypharmacology of the compounds, as well as to differences between tumor types. Another factor is the drug doses used in the different studies. We initially treated PDOX model MPNST-NF1–09 with 10 mg/kg of Panobinostat daily, as described previously (48), after assessing that combinations with Panobinostat at this dose were not toxic in non-engrafted nude mice (Supplementary Table S2). Contrary to expected, engrafted mice did not tolerate that dosage of Panobinostat. We then reduced the dose of Panobinostat to 5 mg/kg for testing in the MPNST-SP-01 PDOX model, which was well tolerated by the mice but did not produce tumor reduction. This difference in the tolerance may be due to the mouse strain; Malone et al used GEMMs on a C57BL6 background (48), which may tolerate higher doses than our nude mouse strain. Carfilzomib was also used at higher doses in other tumor types in C57BL6 mice (3–5 mg/kg), but such concentrations were lethal in our mouse model (53). We concluded that combinations that induce high levels of apoptosis *in vitro*, such as the three tested with Panobinostat, may not be good therapeutic approaches for MPNSTs, as toxicity may not allow the administration of the doses needed to effectively inhibit HDAC in nude mice PDOX models, therefore not achieving tumor reduction. It could be interesting to test these combinations in another mouse strain with higher drug tolerance.

The fourth combination validated in our panel of MPNST cell lines is MK-1775, a Wee1 inhibitor, with Doxorubicin, a DNA-damaging agent. Further analyses demonstrated that this combination is not as apoptotic as the combinations using Panobinostat. The combination of Wee1 inhibitors with DNA damaging agents has proved effective *in vitro* and *in vivo* for some other cancers. For instance, MK-1775 and Gemcitabine had synergy *in vitro* against MPNST (among other sarcomas cell lines) in other works (54) and reduced tumor volume in PDOX mouse models of pancreatic cancer, and MK-1775 with Cisplatin reduced tumor growth in gastric cancer (55, 56). This therapeutic approach has been described to be more effective in *TP53* mutated tumors, as the G_2–M checkpoint (which is disrupted by MK-1775) is the only one that prevents tumor cells from programmed death due to DNA damage caused by the other compound (31). *In vitro*, we observed that MK-1775 with Doxorubicin presented higher drug activity in the MPNST cell lines with *TP53* mutated (MPNST-SP-01, S462, MPNST-NF1–09, HS-sch2, and STS26T). Synergy was not observed in the wild-type *TP53* cell lines MPNST-NF1–08 and HS-PSS and sNF96.2 presented less synergy than the *TP53* mutated cell lines. *In vivo*, MK-1775 with Doxorubicin significantly reduced tumor growth compared with single treatments in two PDOX-MPNST models, one sporadic (MPNST-SP-01) and one NF1-related (MPNST-NF1–09), both *TP53* mutated. The effect in both primary tumors matched the effects seen in their isolated cell lines where synergism was validated. Specifically, mice treated with the combination showed a significant tumor growth reduction in the MPNST-SP-01 and MPNST-NF1–09 PDOX models compared with the control group. It has been described that NF1-derived MPNSTs may have a lower response rate to chemotherapy than sporadic tumors, which agrees with our results (6). Overall, this less apoptotic combination proved to be a better therapeutic approach for MPNSTs, as toxicity effects were not observed in mice at the doses used to achieve tumor growth reduction.

In conclusion, the data presented here clearly show the potential of our screening platform for the discovery of potential combination therapies and presented results suggesting the combination of MK-1775 with Doxorubicin as a potential therapy for MPNST treatment, especially for those with *TP53* mutated, although further studies on sequencing and dosing preclinically may yield more information that can assist in moving these combinations forward into the clinic.

Authors' Disclosures

J. Fernández-Rodríguez reports grants from Children's Boston Hospital, Carlos III National Health Institute, Government of Catalonia, Fundación Proyecto Neurofibromatosis; and grants from Fundació La Marató de TV3 during the conduct of the study. E. Creus-Bachiller reports grants from Children's Boston Hospital, Carlos III National Health Institute, Government of Catalonia, grants from Fundación Proyecto Neurofibromatosis (FPNF); and grants from Fundació La Marató de TV3 during the conduct of the study. K.M. Reilly reports grants from Neurofibromatosis Therapeutics Acceleration Program during the conduct of the study. J.O. Blakeley reports personal fees from TriAct; other support from SpringWorks Therapeutics, AstraZenica; and nonfinancial support from Bristol-Myers Squibb outside the submitted work. No disclosures were reported by the other authors.

Authors' Contributions

J. Fernández-Rodríguez: Conceptualization, formal analysis, supervision, validation, investigation, visualization, methodology, writing–original draft, writing–review and editing. **E. Creus-Bachiller:** Formal analysis, validation, investigation, visualization, methodology, writing–original draft, writing–review and editing. **X. Zhang:** Investigation, writing–review and editing. **M. Martínez-Iniesta:** Investigation, writing–review and editing. **S. Ortega-Bertran:** Investigation, writing–review and editing. **R. Guha:** Investigation, writing–review and editing. **C.J. Thomas:** Methodology, writing–review and editing. **M.R. Wallace:** Methodology, writing–review and editing. **C. Romagosa:** Funding acquisition, writing–review and editing. **L. Salazar-Huayna:** Investigation, writing–review and editing. **K.M. Reilly:** Methodology, writing–review and editing. **J.O. Blakeley:** Investigation, writing–review and editing. **J. Serra-Musach:** Investigation, writing–review and editing. **M.A. Pujana:** Methodology, writing–review and editing. **E. Serra:** Methodology, writing–review and editing. **A. Villanueva:** Conceptualization, supervision, funding acquisition, investigation, methodology, writing–original draft, writing–review and editing. **M. Ferrer:** Conceptualization, supervision, funding acquisition, visualization, methodology, writing–original draft, writing–review and editing. **C. Lázaro:** Conceptualization, supervision, funding acquisition, methodology, writing–original draft, writing–review and editing.

Acknowledgments

Work developed by J. Fernández-Rodríguez, E. Creus-Bachiller, M. Martínez-Iniesta, S. Ortega-Beltran, A.Villanueva, and C. Lázaro was supported by NFRI grant from Boston Children's Hospital and the Carlos III National Health Institute funded by FEDER funds – a way to build Europe – [PI19/00553, PI16/00563; PI16/01898; PI19/01320 and CIBERONC]; the Government of Catalonia [Pla estratègic de recerca i innovació en salut (2017SGR1282 and 2017SGR496)]; the Fundación Proyecto Neurofibromatosis (FPNF), and Fundació La Marató de TV3. Work developed by X. Zhang, R. Guha, C.J. Thomas, and M.Ferrer at NCATS was funded by the NIH Intramural Research Program and NTAP. L. Salazar-Huayna and C. Romagosa are supported by a grant from the "Programa d'impuls del talent i de l'ocupabilitat del PERIS 2016–2020".The authors thank CERCA Program/Generalitat de Catalunya for their institutional support. We thank all the patients and families with MPNST tumors, as well as all Spanish NF patients and NF associations for their continuing support, in particular the Spanish Asociación de Afectados de Neurofibromatosis (AANF) and the Associació Catalana de les Neurofibromatosis (ACNefi). We also wish to thank the ICO and IGTP Hereditary Cancer Program teams, as well as the members of the Spanish CSUR of Phakomatoses. We also want to thank Centres Científics i Tecnològics de la UB (CCiTUB) for assistance in the apoptosis and cell-cycle analyses.

Received November 23, 2021; revised March 9, 2022; accepted April 28, 2022; published first May 5, 2022.

References

1. Brennan MF, Antonescu CR, Moraco N, Singer S. Lessons learned from the study of 10,000 patients with soft-tissue sarcoma. Ann Surg 2014;260:416–21.
2. Longo JF, Weber SM, Turner-Ivey BP, Carroll SL. Recent advances in the diagnosis and pathogenesis of Neurofibromatosis type 1 (NF1)-associated peripheral nervous system neoplasms. Adv Anat Pathol 2018;25:353–68.
3. Ducatman BS, Scheithauer BW, Piepgras DG, Reiman HM, Ilstrup DM. Malignant peripheral nerve sheath tumors. A clinicopathologic study of 120 cases. Cancer 1986;57:2006–21.
4. Uusitalo E, Rantanen M, Kallionpää RA, Pöyhönen M, Leppävirta J, Ylä-Outinen H, et al. Distinctive cancer associations in patients with Neurofibromatosis type 1. J Clin Oncol 2016;34:1978–86.
5. Ferner RE, Gutmann DH. International consensus statement on malignant peripheral nerve sheath tumors in neurofibromatosis. Cancer Res 2002;62:1573–7.
6. Higham CS, Steinberg SM, Dombi E, Perry A, Helman LJ, Schuetze SM, et al. SARC006: Phase II trial of chemotherapy in sporadic and Neurofibromatosis type 1—associated chemotherapy-naive malignant peripheral nerve sheath tumors. Sarcoma 2017;2017:8685638.
7. Zehou O, Fabre E, Zelek L, Sbidian E, Ortonne N, Banu E, et al. Chemotherapy for the treatment of malignant peripheral nerve sheath tumors in neurofibromatosis 1: a 10-year institutional review. Orphanet J Rare Dis 2013;8:127.
8. Stucky CC, Johnson KN, Gray RJ, Pockaj BA, Ocal IT, Rose PS, et al. Malignant peripheral nerve sheath tumors (MPNST): the Mayo Clinic experience. Ann Surg Oncol 2012;19:878–85.
9. Sohier P, Luscan A, Lloyd A, Ashelford K, Laurendeau I, Briand-Suleau A, et al. Confirmation of mutation landscape of NF1-associated malignant peripheral nerve sheath tumors. Genes Chromosomes Cancer 2017;56:421–6.
10. Lee W, Teckie S, Wiesner T, Ran L, Granada CNP, Lin M, et al. PRC2 is recurrently inactivated through EED or SUZ12 loss in malignant peripheral nerve sheath tumors. Nat Genet 2014;46:1227–32.
11. Kim A, Stewart DR, Reilly KM, Viskochil D, Miettinen MM, Widemann BC. Malignant peripheral nerve sheath tumors state of the science: leveraging clinical and biological insights into effective therapies. Sarcoma 2017;2017:7429697.
12. Griner LAM, Guha R, Shinn P, Young RM, Keller JM, Liu D, et al. High-throughput combinatorial screening identifies drugs that cooperate with ibrutinib to kill activated B-cell–like diffuse large B-cell lymphoma cells. Proc Natl Acad Sci USA 2014;111:2349–54.
13. Mathews LA, Keller JM, Goodwin BL, Guha R, Shinn P, Mull R, et al. A 1,536-well quantitative high-throughput screen to identify compounds targeting cancer stem cells. J Biomol Screen 2012;17:1231–42.
14. Heske CM, Davis MI, Baumgart JT, Wilson K, Gormally MV, Chen L, et al. Matrix screen identifies synergistic combination of PARP inhibitors and nicotinamide phosphoribosyltransferase (NAMPT) inhibitors in Ewing sarcoma. Clin Cancer Res 2017;23:7301–11.
15. Guo J, Grovola MR, Xie H, Coggins GE, Duggan P, Hasan R, et al. Comprehensive pharmacological profiling of neurofibromatosis cell lines. Am J Cancer Res 2017;7:923–34.
16. Ferrer M, Gosline SJC, Stathis M, Zhang X, Guo X, Guha R, et al. Pharmacological and genomic profiling of Neurofibromatosis type 1 plexiform neurofibroma-derived Schwann cells. Sci Data 2018;5:180106.
17. Chang LS, Oblinger JL, Smith AE, Ferrer M, Angus SP, Hawley E, et al. Brigatinib causes tumor shrinkage in both NF2-deficient meningioma and schwannoma through inhibition of multiple tyrosine kinases but not ALK. PLoS One 2021;16:e0252048.
18. Castellsagué J, Gel B, Fernández-Rodríguez J, Llatjós R, Blanco I, Benavente Y, et al. Comprehensive establishment and characterization of orthoxenograft mouse models of malignant peripheral nerve sheath tumors for personalized medicine. EMBO Mol Med 2015;7:608–27.
19. Dahlberg WK, Little JB, Fletcher JA, Suit HD, Okunieff P. Radiosensitivity *in vitro* of human soft-tissue sarcoma cell lines and skin fibroblasts derived from the same patients. Int J Radiat Biol 1993;63:191–8.

20. Sonobe H, Takeuchi T, Furihata M, Taguchi T, Kawai A, Ohjimi Y, et al. A new human malignant peripheral nerve sheath tumour-cell line, HS-sch-2, harbouring p53 point mutation. Int J Oncol 2000;17:347–52.
21. Frahm S, Mautner VF, Brems H, Legius E, Debiec-Rychter M, Friedrich RE, et al. Genetic and phenotypic characterization of tumor cells derived from malignant peripheral nerve sheath tumors of Neurofibromatosis type 1 patients. Neurobiol Dis 2004;16:85–91.
22. Perrin GQ, Li H, Fishbein L, Thomson SA, Hwang MS, Scarborough MT, et al. An orthotopic xenograft model of intraneural NF1 MPNST suggests a potential association between steroid hormones and tumor cell proliferation. Lab Invest 2007;87:1092–102.
23. Ceribelli M, Kelly PN, Shaffer AL, Wright GW, Xiao W, Yang Y, et al. Blockade of oncogenic IκB kinase activity in diffuse large B-cell lymphoma by bromodomain and extraterminal domain protein inhibitors. Proc Natl Acad Sci USA 2014;111:11365–70.
24. Inglese J, Auld DS, Jadhav A, Johnson RL, Simeonov A, Yasgar A, et al. Quantitative high-throughput screening: a titration-based approach that efficiently identifies biological activities in large chemical libraries. Proc Natl Acad Sci USA 2006;103:11473–8.
25. Wang Y, Jadhav A, Southal N, Huang R, Nguyen DT. A grid algorithm for high throughput fitting of dose-response curve data. Curr Chem Genomics 2010;4:57–66.
26. Fisher R. On the interpretation of χ^2 from contingency tables, and the calculation of P. J Roy Statist Soc Ser C 1922;85:87–94.
27. Benjamini YHY. Controlling the false discovery rate: a practical and powerful approach to multiple testing. J R Stat Soc 1995;57:289–300.
28. Mott BT, Eastman RT, Guha R, Sherlach KS, Siriwardana A, Shinn P, et al. High-throughput matrix screening identifies synergistic and antagonistic antimalarial drug combinations. Sci Rep 2015;5:13891.
29. Chou TC. Drug combination studies and their synergy quantification using the Chou-Talalay method. Cancer Res 2010;70:440–6.
30. Hernández JL, Padilla L, Dakhel S, Coll T, Hervas R, Adan J, et al. Therapeutic targeting of tumor growth and angiogenesis with a novel anti-S100A4 monoclonal antibody. PLoS One 2013;8:e72480.
31. Hirai H, Iwasawa Y, Okada M, Arai T, Nishibata T, Kobayashi M, et al. Small-molecule inhibition of Wee1 kinase by MK-1775 selectively sensitizes p53-deficient tumor cells to DNA-damaging agents. Mol Cancer Ther 2009;8:2992–3000.
32. Noel T Southall AJ, Huang R, Nguyen T, Wang Y. Handbook of drug screening. Boca Raton, FL: CRC Press; 2009.
33. Atkinson KE. An introduction to numerical analysis. Hoboken, NJ: John Wiley & Sons; 1989.
34. Pettazzoni P, Pizzimenti S, Toaldo C, Sotomayor P, Tagliavacca L, Liu S, et al. Induction of cell-cycle arrest and DNA damage by the HDAC inhibitor panobinostat (LBH589) and the lipid peroxidation end product 4-hydroxynonenal in prostate cancer cells. Free Radic Biol Med 2011;50:313–22.
35. Eom YW, Kim MA, Park SS, Goo MJ, Kwon HJ, Sohn S, et al. Two distinct modes of cell death induced by doxorubicin: apoptosis and cell death through mitotic catastrophe accompanied by senescence-like phenotype. Oncogene 2005;24:4765–77.
36. Dias JNR, Aguiar SI, Pereira DM, André AS, Gano L, Correia JDG, et al. The histone deacetylase inhibitor panobinostat is a potent antitumor agent in canine diffuse large B-cell lymphoma. Oncotarget 2018;9:28586–98.
37. Liu Q, Xu C, Kirubakaran S, Zhang X, Hur W, Liu Y, et al. Characterization of Torin2, an ATP-competitive inhibitor of mTOR, ATM, and ATR. Cancer Res 2013;73:2574–86.
38. Chang KY, Tsai SY, Wu CM, Yen CJ, Chuang BF, Chang JY. Novel phosphoinositide 3-kinase/mTOR dual inhibitor, NVP-BGT226, displays potent growth-inhibitory activity against human head and neck cancer cells *in vitro* and *in vivo*. Clin Cancer Res 2011;17:7116–26.
39. Kuhn DJ, Chen Q, Voorhees PM, Strader JS, Shenk KD, Sun CM, et al. Potent activity of carfilzomib, a novel, irreversible inhibitor of the ubiquitin-proteasome pathway, against preclinical models of multiple myeloma. Blood 2007;110:3281–90.
40. Miller DT, Cortés-Ciriano I, Pillay N, Hirbe AC, Snuderl M, Bui MM, et al. Genomics of MPNST (GeM) Consortium: Rationale and study design for Multi-omic characterization of NF1-associated and sporadic MPNSTs. Genes 2020;11:387.
41. Brohl AS, Kahen E, Yoder SJ, Teer JK, Reed DR. The genomic landscape of malignant peripheral nerve sheath tumors: diverse drivers of Ras pathway activation. Sci Rep 2017;7:14992.
42. Lopez G, Bill KL, Bid HK, Braggio D, Constantino D, Prudner B, et al. HDAC8, a potential therapeutic target for the treatment of malignant peripheral nerve sheath tumors (MPNST). PLoS One 2015;10:e0133302.
43. Ghadimi MP, Lopez G, Torres KE, Belousov R, Young ED, Liu J, et al. Targeting the PI3K/mTOR axis, alone and in combination with autophagy blockade, for the treatment of malignant peripheral nerve sheath tumors. Mol Cancer Ther 2012;11:1758–69.
44. Chen SH, Lahav G. Two is better than one; toward a rational design of combinatorial therapy. Curr Opin Struct Biol 2016;41:145–50.
45. Pei Y, Liu KW, Wang J, Garancher A, Tao R, Esparza LA, et al. HDAC and PI3K antagonists cooperate to inhibit growth of MYC-driven medulloblastoma. Cancer Cell 2016;29:311–23.
46. Piao J, Chen L, Quan T, Li L, Quan C, Piao Y, et al. Superior efficacy of co-treatment with the dual PI3K/mTOR inhibitor BEZ235 and histone deacetylase inhibitor Trichostatin A against NSCLC. Oncotarget 2016;7:60169–80.
47. Chen L, Jin T, Zhu K, Piao Y, Quan T, Quan C, et al. PI3K/mTOR dual inhibitor BEZ235 and histone deacetylase inhibitor Trichostatin A synergistically exert antitumor activity in breast cancer. Oncotarget 2017;8:11937–49.
48. Malone CF, Emerson C, Ingraham R, Barbosa W, Guerra S, Yoon H, et al. mTOR and HDAC inhibitors converge on the TXNIP/Thioredoxin pathway to cause catastrophic oxidative stress and regression of RAS-Driven tumors. Cancer Discov 2017;7:1450–63.
49. Berdeja JG, Hart LL, Mace JR, Arrowsmith ER, Essell JH, Owera RS, et al. Phase I/II study of the combination of panobinostat and carfilzomib in patients with relapsed/refractory multiple myeloma. Haematologica 2015;100:670–6.
50. Kaufman JL, Mina R, Jakubowiak AJ, Zimmerman TL, Wolf JJ, Lewis C, et al. Combining carfilzomib and panobinostat to treat relapsed/refractory multiple myeloma: results of a Multiple Myeloma Research Consortium Phase I Study. Blood Cancer J 2019;9:3.
51. Yu D, Kahen E, Cubitt CL, McGuire J, Kreahling J, Lee J, et al. Identification of synergistic, clinically achievable, combination therapies for osteosarcoma. Sci Rep 2015;5:16991.
52. Afifi S, Michael A, Azimi M, Rodriguez M, Lendvai N, Landgren O. Role of histone deacetylase inhibitors in relapsed refractory multiple myeloma: a focus on vorinostat and panobinostat. Pharmacotherapy 2015;35:1173–88.
53. Hurchla MA, Garcia-Gomez A, Hornick MC, Ocio EM, Li A, Blanco JF, et al. The epoxyketone-based proteasome inhibitors carfilzomib and orally bioavailable oprozomib have anti-resorptive and bone-anabolic activity in addition to anti-myeloma effects. Leukemia 2013;27:430–40.
54. Kreahling JM, Foroutan P, Reed D, Martinez G, Razabdouski T, Bui MM, et al. Wee1 inhibition by MK-1775 leads to tumor inhibition and enhances efficacy of gemcitabine in human sarcomas. PLoS One 2013;8:e57523.
55. Rajeshkumar NV, De Oliveira E, Ottenhof N, Watters J, Brooks D, Demuth T, et al. MK-1775, a potent Wee1 inhibitor, synergizes with gemcitabine to achieve tumor regressions, selectively in p53-deficient pancreatic cancer xenografts. Clin Cancer Res 2011;17:2799–806.
56. Chen D, Lin X, Gao J, Shen L, Li Z, Dong B, et al. Wee1 inhibitor AZD1775 combined with cisplatin potentiates anticancer activity against gastric cancer by increasing DNA damage and cell apoptosis. Biomed Res Int 2018;2018:5813292.

iScience

CellPress
OPEN ACCESS

Article

Deep genomic analysis of malignant peripheral nerve sheath tumor cell lines challenges current malignant peripheral nerve sheath tumor diagnosis

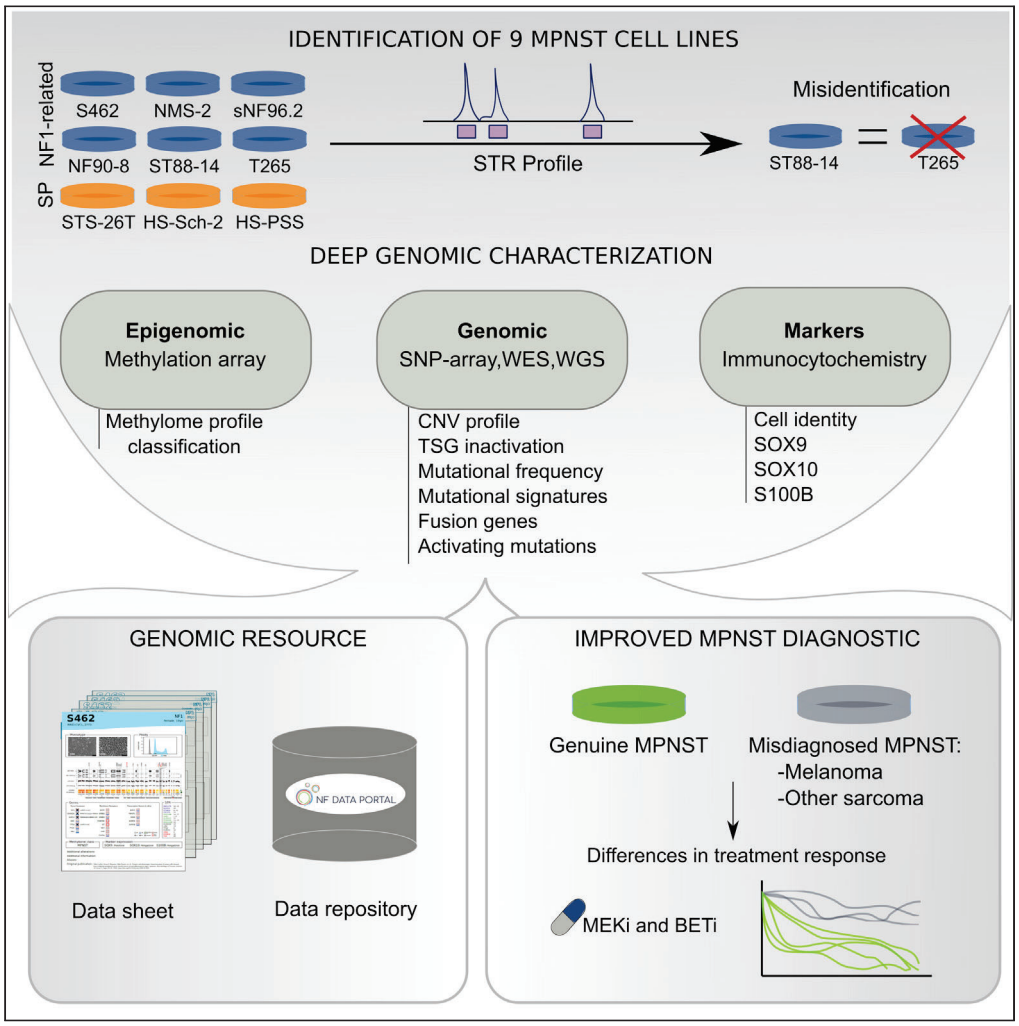

Miriam Magallón-Lorenz, Ernest Terribas, Sara Ortega-Bertran, ..., Meritxell Carrió, Bernat Gel, Eduard Serra

bgel@igtp.cat (B.G.)
eserra@igtp.cat (E.S.)

Highlights

A comprehensive genomic resource of widely used MPNST cell lines is presented

Genomic, epigenomic, and marker information improve MPNST differential diagnosis

Genomic analysis detected misidentified and misdiagnosed MPNST cell lines

Misdiagnosed cell lines exhibited a different drug-treatment response

Magallón-Lorenz et al., iScience 26, 106096
February 17, 2023
https://doi.org/10.1016/j.isci.2023.106096

iScience

CellPress
OPEN ACCESS

Article

Deep genomic analysis of malignant peripheral nerve sheath tumor cell lines challenges current malignant peripheral nerve sheath tumor diagnosis

Miriam Magallón-Lorenz,[1,20] Ernest Terribas,[1,20] Sara Ortega-Bertran,[2,3] Edgar Creus-Bachiller,[2,3,4] Marco Fernández,[5] Gerard Requena,[5] Inma Rosas,[6,7] Helena Mazuelas,[1] Itziar Uriarte-Arrazola,[1] Alex Negro,[6,7] Tereza Lausová,[8,9] Elisabeth Castellanos,[6,7] Ignacio Blanco,[6,10] George DeVries,[11] Hiroyuki Kawashima,[12] Eric Legius,[13] Hilde Brems,[13] Viktor Mautner,[14] Lan Kluwe,[14] Nancy Ratner,[15] Margaret Wallace,[16] Juana Fernández-Rodriguez,[2,3,4] Conxi Lázaro,[2,3,4] Jonathan A. Fletcher,[17] David Reuss,[8,9] Meritxell Carrió,[1] Bernat Gel,[1,18,19,*] and Eduard Serra[1,4,19,21,*]

SUMMARY

Malignant peripheral nerve sheath tumors (MPNSTs) are soft-tissue sarcomas of the peripheral nervous system that develop either sporadically or in the context of neurofibromatosis type 1 (NF1). MPNST diagnosis can be challenging and treatment outcomes are poor. We present here a resource consisting of the genomic characterization of 9 widely used human MPNST cell lines for their use in translational research. NF1-related cell lines recapitulated primary MPNST copy number profiles, exhibited *NF1*, *CDKN2A*, and *SUZ12/EED* tumor suppressor gene (TSG) inactivation, and presented no gain-of-function mutations. In contrast, sporadic cell lines collectively displayed different TSG inactivation patterns and presented kinase-activating mutations, fusion genes, altered mutational frequencies and COSMIC signatures, and different methylome-based classifications. Cell lines re-classified as melanomas and other sarcomas exhibited a different drug-treatment response. Deep genomic analysis, methylome-based classification, and cell-identity marker expression, challenged the identity of common MPNST cell lines, opening an opportunity to revise MPNST differential diagnosis.

INTRODUCTION

Malignant peripheral nerve sheath tumors (MPNSTs) are aggressive soft tissue sarcomas that arise from cells of the peripheral nervous system and account for 3-10% of all malignant soft tissue tumors.[1] Half of these tumors develop in the context of the tumor predisposition syndrome Neurofibromatosis type 1 (NF1) while the other half are sporadic neoplasms.[2,3] The MPNST incidence in the general population is 1 in 100,000[2–4] whereas the lifetime risk of an NF1 individual developing an MPNST is 10-15%.[2,5] Due to its invasive growth and propensity to metastasize, MPNSTs have a poor prognosis and are the leading cause of adult NF1-related mortality.[2,5] Like many soft tissue sarcomas, complete resection with wide margins is essential in MPNST therapy, followed by radiation and/or chemotherapy.[6–8]

MPNSTs are usually high-grade malignant spindle cell neoplasms arising in association with large peripheral nerves.[9] Their diagnosis can be challenging, especially outside of individuals with NF1, since MPNSTs are rare tumors and specific histological criteria have not been completely established.[10–12] In the context of NF1, MPNSTs often progress from a pre-existing benign plexiform neurofibroma, commonly through an intermediate discrete nodular tumor termed atypical neurofibroma or ANNUBP.[12,13] Although neurofibromas contain numerous S100B/SOX10-positive Schwann cells and CD34-positive fibroblasts, the expression of both markers is significantly reduced or absent in MPNSTs.[12]

MPNSTs contain hyperploid and highly rearranged genomes with a low mutation burden.[14–17] Several tumor suppressor genes (TSGs) are commonly mutated, including *NF1*, *CDKN2A*, and components of

[1]Hereditary Cancer Group, Germans Trias i Pujol Research Institute (IGTP), Can Ruti Campus, 08916 Badalona, Barcelona, Spain

[2]Hereditary Cancer Program, Catalan Institute of Oncology (ICO-IDIBELL), L'Hospitalet de Llobregat, 08098 Barcelona, Spain

[3]Program in Molecular Mechanisms and Experimental Therapy in Oncology (Oncobell), IDIBELL, Hospitalet de Llobregat, Barcelona, Spain

[4]Centro de Investigación Biomédica en Red de Cáncer (CIBERONC), Madrid, Spain

[5]Cytometry Core Facility, Germans Trias & Pujol Research Institute (IGTP), Badalona, Barcelona, Spain

[6]Clinical Genomics Research Group, Germans Trias i Pujol Research Institute (IGTP), Can Ruti Campus, 08916 Badalona, Barcelona, Spain

[7]Clinical Genomics Unit, Clinical Genetics Service, Northern Metropolitan Clinical Laboratory, Germans Trias i Pujol University Hospital (HGTP), Can Ruti Campus, 08916 Badalona, Barcelona, Spain

[8]Department of Neuropathology, Institute of Pathology, Heidelberg University Hospital, Heidelberg, Germany

[9]Clinical Cooperation Unit Neuropathology, German Cancer Research Center (DKFZ), German Consortium for Translational Cancer Research (DKTK), Heidelberg, Germany

Continued

the polycomb repressive complex 2 (PRC2), including *SUZ12* and *EED*. *TP53* is also frequently lost or mutated. MPNSTs also show recurrently altered chromosomal regions, particularly constituting somatic copy number gains (revised in Serra et al. 2020[18]). Complete loss of *CDKN2A*, often caused by structural alterations, seems to constitute a bottleneck for MPNST formation.[19,20]

Established cell lines are an important tool for gaining insight into cancer biology and treatment. However, there are also different caveats in their use as faithful and useful models, with issues including misidentification and cross-contamination and poor characterization of similarity to their tumor source.[21–24] There is no dedicated registry for MPNST cell lines, but according to Cellosaurus (https://web.expasy.org/cellosaurus/), around forty different MPNST cell lines may have been established by different laboratories, derived from both sporadic and NF1-related MPNSTs. Some of these MPNST cell lines are well distributed among labs[25,26] or deposited in global repositories (ATCC, RIKEN). These lines have been used as a primary tool for the identification of molecular pathways involved in MPNST pathogenesis,[27,28] and served, for instance, for the identification of MEK inhibitors as useful therapeutic agents.[29] Some can be engrafted in mice to generate genuine orthotopic MPNST tumors.[30,31] However, a systematic and comprehensive genomic characterization of these MPNST cell lines is still missing, limiting the use of these cell lines for precision medicine or pharmacogenomic studies.

In this work, we performed a deep genomic characterization of 8 commonly used MPNST cell lines,[25,26] identifying heterogeneity regarding the structure of the genome, the inactivation of tumor suppressor genes, the frequency of mutations, the mutational signatures, and the presence of gain-of-function mutations, especially among sporadic MPNST cell lines. This characterization challenged the identity of the sporadic MPNST cell lines studied and prompted us to use a methylome sarcoma classifier and to perform immunofluorescence of known cell identity markers. Our results, in addition to providing a valuable resource, uncover the necessity of systematically analyzing MPNSTs, combining pathology with genomic and molecular results, for improved differential diagnosis and classification of these malignancies.

RESULTS

A genomic resource for neurofibromatosis type 1-associated and sporadic malignant peripheral nerve sheath tumor cell lines

We started with 9 NF1-associated and sporadic MPNST cell lines for a short tandem repeat (STR) authentication analysis and a comprehensive genomic characterization. We first performed an interspecies PCR of all cell lines to identify any possible interspecies cross-contamination (Data S1). Then we performed a human STR authentication analysis to identify any possible cross-contamination or misidentification among cell lines of human origin (Table S1). All STR profiles matched the STR profiles published in Cellosaurus and ATCC when available. However, in this process, we identified the same STR profile for ST88-14 and T265 cell lines (Data S2) in all ST88-14- and T265-related samples provided by different laboratories. To find out which cell line was misidentified we analyzed the oldest ST88-14 and T265 stored vials in their original labs and more conclusively, the primary tumor from which the ST88-14 cell line was isolated (Data S2). We identified the ST88-14 cell line as the genuine cell line for that STR profile, *NF1* germline (c.1649dupT) mutation and somatic copy number alteration landscape, and dismissed the use of the T265 cell line, which we assume was misidentified at some point after its establishment and expansion. Note that ST88-14 *NF1* germline mutation is not correctly described in certain repositories and publications.

We performed a comprehensive genomic characterization of the remaining 8 MPNST cell lines. Table 1 summarizes information on patients and MPNSTs from which cell lines were established and on their *NF1* mutational status. It also provides a reference to the original description of each cell line. With them, we performed flow cytometry, SNP-array analysis, whole-exome sequencing, and whole-genome sequencing techniques. We compiled information about their ploidy, global copy-number profile and loss of heterozygosity (LOH) status, structural rearrangements, single nucleotide variants (SNVs), and mutational signatures, and summarized the mutational status of a set of selected MPNST-related genes. With all these data we elaborated a practical summary sheet for each cell line, containing the most relevant information (Data S3).

A plethora of different ploidies

We first intended to characterize the karyotype of each MPNST cell line by spectral karyotyping (SKY) and G-banding staining. Both techniques produced results difficult to summarize consistently (data not shown),

[10]Genetic Counseling Unit, Clinical Genetics Service, Northern Metropolitan Clinical Laboratory, Hospital Universitari Germans Trias i Pujol, Badalona, Spain

[11]Hines VA Hospital, Hines, IL 60141, USA

[12]Division of Orthopedic Surgery, Department of Regenerative and Transplant Medicine, Niigata University Graduate School of Medical and Dental Sciences, Palliative Care Team, Niigata University Medical and Dental Hospital, Niigata, Japan

[13]Department of Human Genetics, KU Leuven, Leuven, Belgium

[14]Department of Neurology, University Medical Center Hamburg-Eppendorf, Hamburg, Germany

[15]Division of Experimental Hematology and Cancer Biology, Cincinnati Children's Hospital Medical Center, Cincinnati, OH, USA

[16]Department of Molecular Genetics & Microbiology, and UF Health Cancer Center, University of Florida College of Medicine, Gainesville, FL, USA

[17]Department of Pathology, Brigham and Women's Hospital, Harvard Medical School, 20 Shattuck Street, Thorn 528, Boston, MA 02115, USA

[18]Departament de Fonaments Clínics, Facultat de Medicina i Ciències de la Salut, Universitat de Barcelona (UB), 08036 Barcelona, Spain

[19]Senior author

[20]These authors contributed equally

[21]Lead contact

*Correspondence: bgel@igtp.cat (B.G.), eserra@igtp.cat (E.S.)

https://doi.org/10.1016/j.isci.2023.106096

Table 1. General description of the eight MPNST cell lines analyzed

	S462	ST88-14	NF90-8	sNF96.2	NMS-2	STS-26T	HS-Sch-2	HS-PSS
Type of human MPNST	primary, grade IV	primary	primary, from PNF	primary	primary	metastasis, grade III/III	primary, low grade	UNK
MPNST localization	thigh	retroperitoneum	left forearm	leg	right thigh	left scapula	left thigh	prostate
NF1/Sp	NF1	NF1	NF1	NF1	NF1	Sp	Sp	Sp
Age of patient	19	24	17	27	30	51	54	UNK
Sex of patient	F	M	F	M	M	F	F	M
Original Reference	Frahm-2004	Fletcher-1991	Legius-1994	Perrin-2007	Imaizumi-1998	Dahlberg-1993	Sonobe-2000	n/a
NF1 constitutional pathogenic variant	c.6855C>A p.Y2264X Frahm-2004	c.1649dupT p.V551Gfs*7 Varin-2016	c.3904_3910del p.D1302Yfs*5 Wu-1999	c.3683delC p.N1229Mfs*11 Perrin-2007	**c.6999+1G>T (splice donor)**			
NF1 somatic pathogenic variant	LOH	LOH	LOH	LOH	**LOH**	**LOH**	**c.270_288del p.E91Nfs*6; c.3113+1G>A (splice donor)**	

MPNST: Malignant peripheral nerve sheath tumor; NF1/Sp: NF1-related/Sporadic MPNST; F:Female; M: Male; Bold annotations: mutations described in this article; LOH: Loss of Heterozygosity; UNK: Unknown.

possibly due to the high degree of variability when analyzing multiple metaphases from the same cell line and to the highly rearranged nature of MPNST genomes. Therefore, we decided to analyze the ploidy by propidium iodide staining analysis using flow cytometry (Figure 1A), which revealed a striking diversity among the 8 MPNST cell lines. Most of them exhibited ploidies higher than 2n, three clearly around 4n (S462, HS-Sch-2, STS-26T), yet two cell lines were 2n or less (sNF96.2, HS-PSS). In addition, two cell lines, NF90-8 and NMS-2, showed two cell populations with different ploidy, resembling the result of a genome duplication event in the population with higher ploidy (Figure 1A). STS-26T cell line was composed of two subpopulations with slightly different ploidies. The mean ploidy of each cell line was also calculated considering this diversity.

Malignant peripheral nerve sheath tumor cell lines faithfully recapitulate the genomic copy number profile of primary malignant peripheral nerve sheath tumors

Next, we performed a global copy number analysis using SNP-array data from the 8 MPNST cell lines. To verify whether these cell lines were capturing the copy number profiles present in primary MPNST tumors, we also analyzed SNP-array data from an independent set of primary MPNSTs previously analyzed,[19] and compared the genomic profiles of cell lines and tumors (Figure 1B). Taken together, the copy number profiles of the 8 MPNST cell lines recapitulated fairly well those present in primary MPNSTs. The most recurrently gained genomic regions were chromosomes 7, 8, and 17q; and chromosome 9p was the most recurrently lost genomic region. When we separated NF1-related and sporadic MPNSTs, NF1-related cell lines mostly maintained these profiles and recurrences, but the three sporadic cell lines (Figure 1B) differ substantially in many genomic regions (see for example shaded gray regions in Figure 1B).

We also performed a copy number analysis from all cell lines based on WGS data. In addition, we obtained a B-allele frequency (BAF)-like profile from variant-allele frequencies (VAF) and a log-R ratio (LRR) from coverage. We plotted them together with the resulting LOH determination and copy number calling from SNP-array comparing both independent sets of data (Figure 2; Data S4 for a high-resolution profile). The use of both technologies for generating the same data allowed the validation of the results with all cell lines displaying similar BAF and LRR profiles. It also underscored the difficulty of using copy number callers for analyzing the highly altered MPNST genomes, indicating the necessity of estimating copy number changes in MPNSTs by different means. In addition to its known hyperploid genome, our analysis identified a high degree of generalized LOH (e.g.: almost the entire genome of the sNF96.2 cell line), perhaps pointing to the inactivation of TSGs before the gain of chromosomal regions. Finally, it must be noted that the copy number profile of a given MPNST cell line differed a bit from lab to lab, in terms of a certain number of different genomic alterations. By comparing the genomic profiles of different batches of the same cell lines obtained from distinct labs, we found that despite being quite stable, genomes of MPNST cell lines can

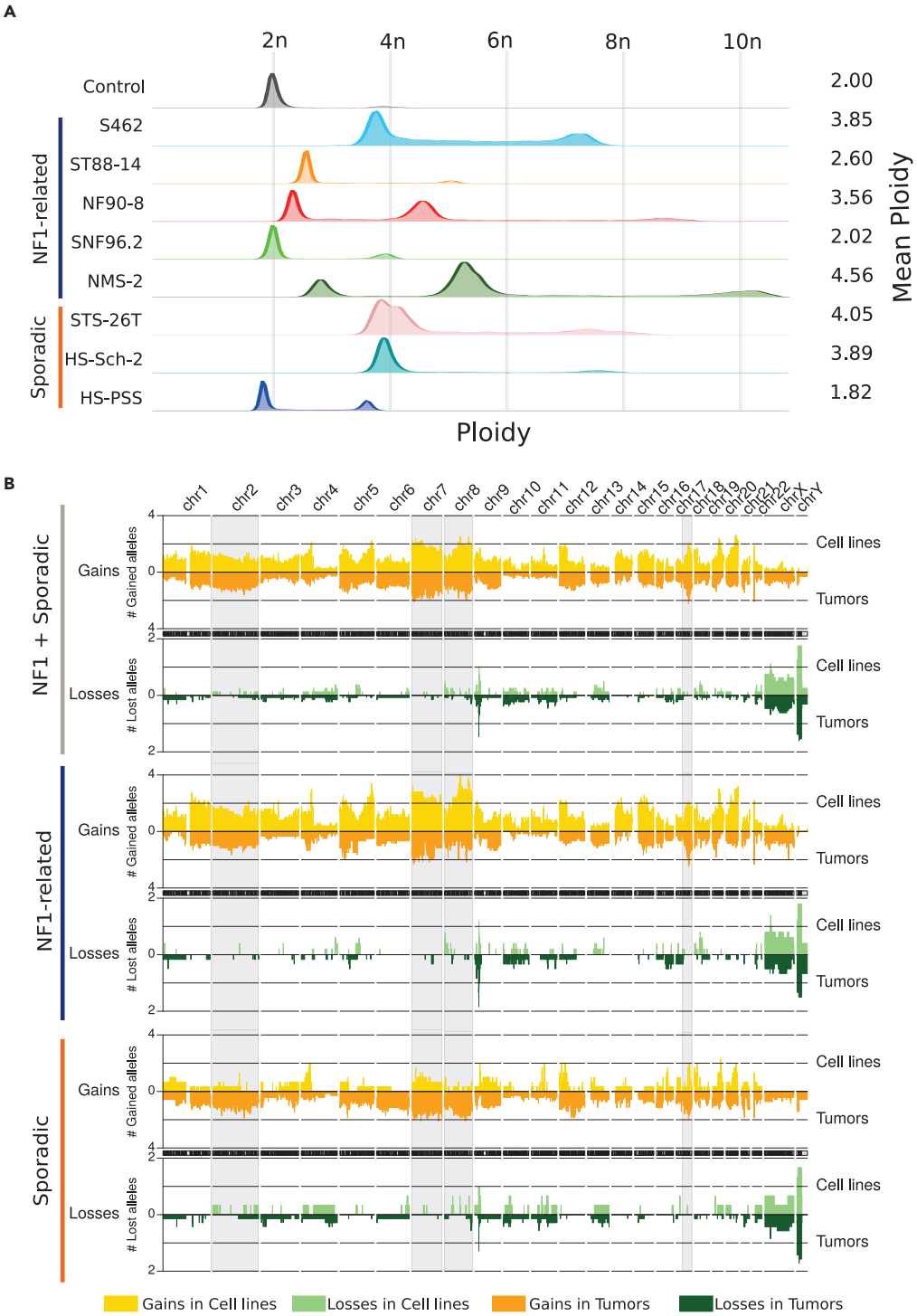

Figure 1. MPNST cell lines have different ploidies and recapitulate the genomic copy-number profile of primary MPNSTs

(A) Ploidy status of MPNST cell lines obtained by flow cytometry. Each row represents a cell line, with the mean ploidy shown on the right side. HFF were used as 2n control cells.

Figure 1. *Continued*
(B) Aggregated copy number profiles comparing MPNST cell lines and tumors. Y axis represents the mean number of gained (orange) or lost (green) alleles by sample type and Y axis genomic position. Cell lines are plotted in the upper part of each graph, represented by light colors, and tumors in the lower part, represented by dark colors and with inverted Y axis. Three different groups of samples are represented. From top to bottom: all MPNSTs; NF1-associated MPNSTs; and sporadic MPNSTs.

accumulate changes in chromosomal regions (Data S5). Part of this inter-laboratory variability could be removed after growing the cell line as a xenograft in mice[31] when growth selective pressure is applied.

Structural variants as key players for tumor suppressor gene inactivation

Ploidy and copy number profile comprise a partial description of the genomic status of MPNST cell lines. We also took advantage of WGS data to analyze the presence of structural variants, represented by different types of chromosomal rearrangements (Figure 3). This analysis revealed that in addition to being hyperploid, MPNST genomes were highly rearranged, adding an extra layer of complexity. Structural changes were spread over all chromosomes, although certain cell lines such as ST88-14 and HS-PSS showed some genomic regions with a high frequency of adjacent rearrangements. Importantly, as previously reported,[19] structural changes caused the inactivation of key MPNST TSGs, such as *CDKN2A*, PRC2 genes, and *TP53* (Data S6), that had been previously missed when WGS data was not available. Furthermore, WGS also facilitated the unexpected identification of a translocation resulting in the generation of a fusion gene EML4-ALK variant 5a[32] in the HS-PSS cell line, which was validated by RT-PCR, amplification, and sequencing (Data S6). The significant number of structural variants identified together with the copy number profiles and ploidy exhibited, demonstrates the complex genomic landscape of MPNST cell lines, with highly altered but also fairly stable genomes.

The limited importance of small genomic variants

In contrast to the rich number of gross structural alterations, fine-scale analysis of small variants, including single-nucleotide variants (SNVs) and small indels, uncovered a relatively moderate impact of these alterations in MPNSTs. We used WES and WGS data from all cell lines to call small variants. Since we did not have available non-tumoral tissue counterparts for these cell lines, we filtered the small variants to partially remove germline variants and obtain a call set enriched in somatic variants. The number of variants with a potential impact on protein function in this dataset was modest (Table S2), particularly for NF1-associated MPNST cell lines, which harbored a mean of 129 SNVs. We then used this quasi-somatic variant dataset to estimate the contribution of the COSMIC mutational signatures[33] in the variant profile of the MPNST cell lines (Figure 4A). This analysis did not identify a particular mutational mechanism prevalent in MPNSTs and showed a major contribution of clock-like signatures (signatures 1 and 5), comparable with previous observations in other sarcomas.[17] However, the STS-26T cell line in addition to exhibiting a higher number of mutations compared to the other cell lines (about two times the average of the rest of the cell lines), also presented an important contribution from signature 7, predominantly found in skin cancers (see later in discussion).

The functional impact of small variants in oncogenes and TSGs was also moderate. We identified some MPNST-related genes inactivated by pathogenic SNVs (Figure 4B and Table S3). In addition to germline *NF1* mutations, somatic mutations also affected *NF1*, as well as other genes including *TP53*, PRC2 genes, and *PTEN*. Remarkably, we did not identify gain-of-function mutations in oncogenes, except a *BRAF* V600E mutation in the STS-26T cell line. In contrast, we identified gains in genomic regions containing receptors, especially a highly gained region containing *PDGFRA* and *KIT* in two NF1-related cell lines (S462 and NF90-8) (Figure 4B). The most frequently inactivated gene in our set of cell lines was *CDKN2A*, a known bottleneck for MPNST development.[19,20] The fact that this gene was inactivated by a point mutation only in one cell line, exemplifies the relatively low functional impact of small variants compared to structural variants in MPNST initiation.

The combination of genome, methylome, and expression marker analysis, represent useful tools for a better differential diagnosis and classification of malignant peripheral nerve sheath tumors

This complete description of the genomic status of MPNST cell lines uncovered a fair degree of diversity among them, prompting us to question the MPNST identity of the sporadic cell lines and to perform a

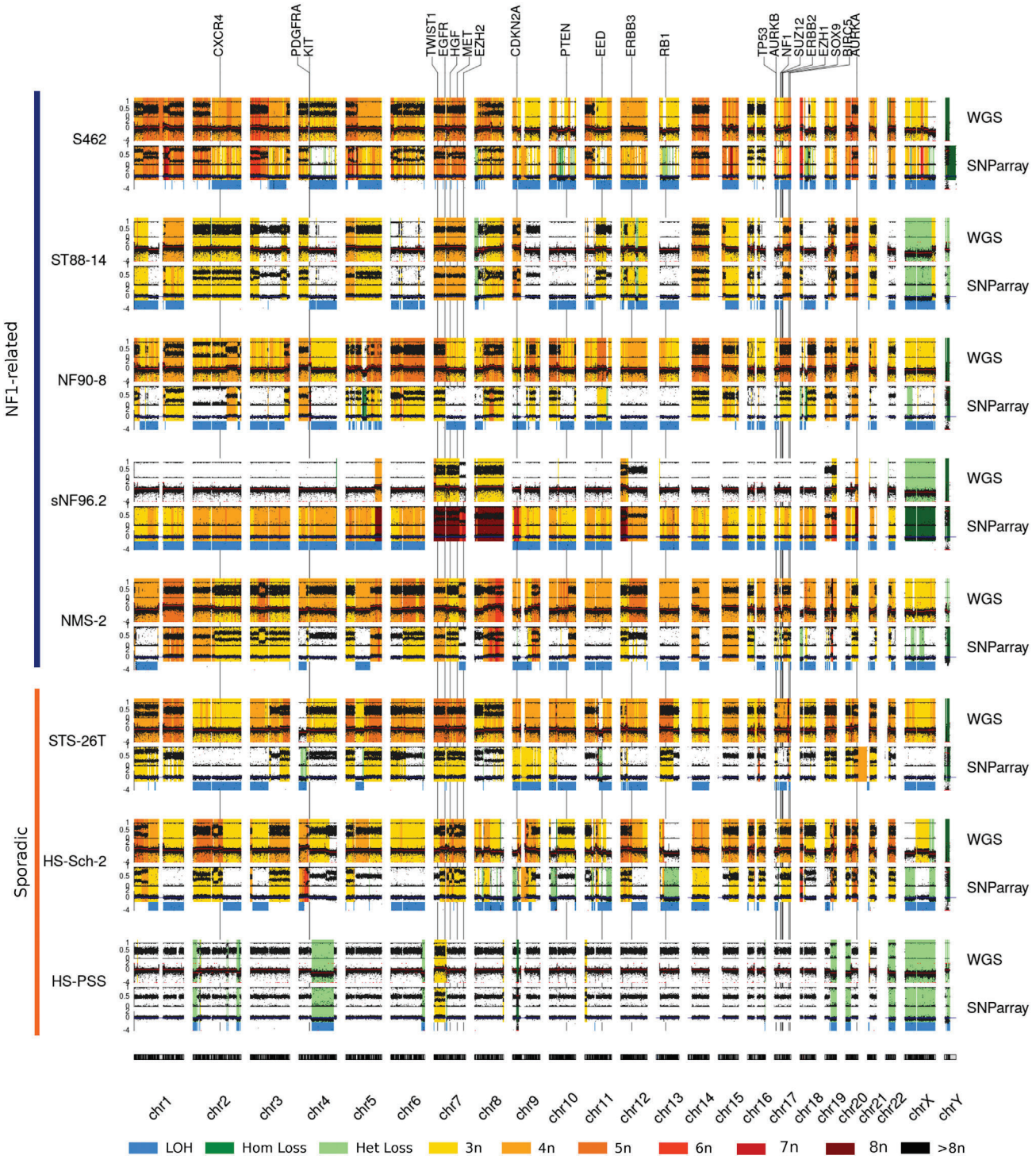

Figure 2. Global view of the copy number profiles of all MPNST cell lines studied

Copy number profiles from SNP-array and WGS data. For both technologies, B-allele frequency (BAF) and Log-R Ratio (LRR) are represented (see STAR Methods for details). Warm colors represent copy number gains, whereas light green indicates a heterozygous loss and dark green a homozygous loss. Loss of heterozygosity (LOH) detected by using SNP-array data is highlighted by a thick blue line. The genomic location of MPNST-associated genes is indicated by a vertical black line with the gene symbol at the upper part of the graph. See Data S3 for a high-resolution profile of each cell line, chromosome by chromosome.

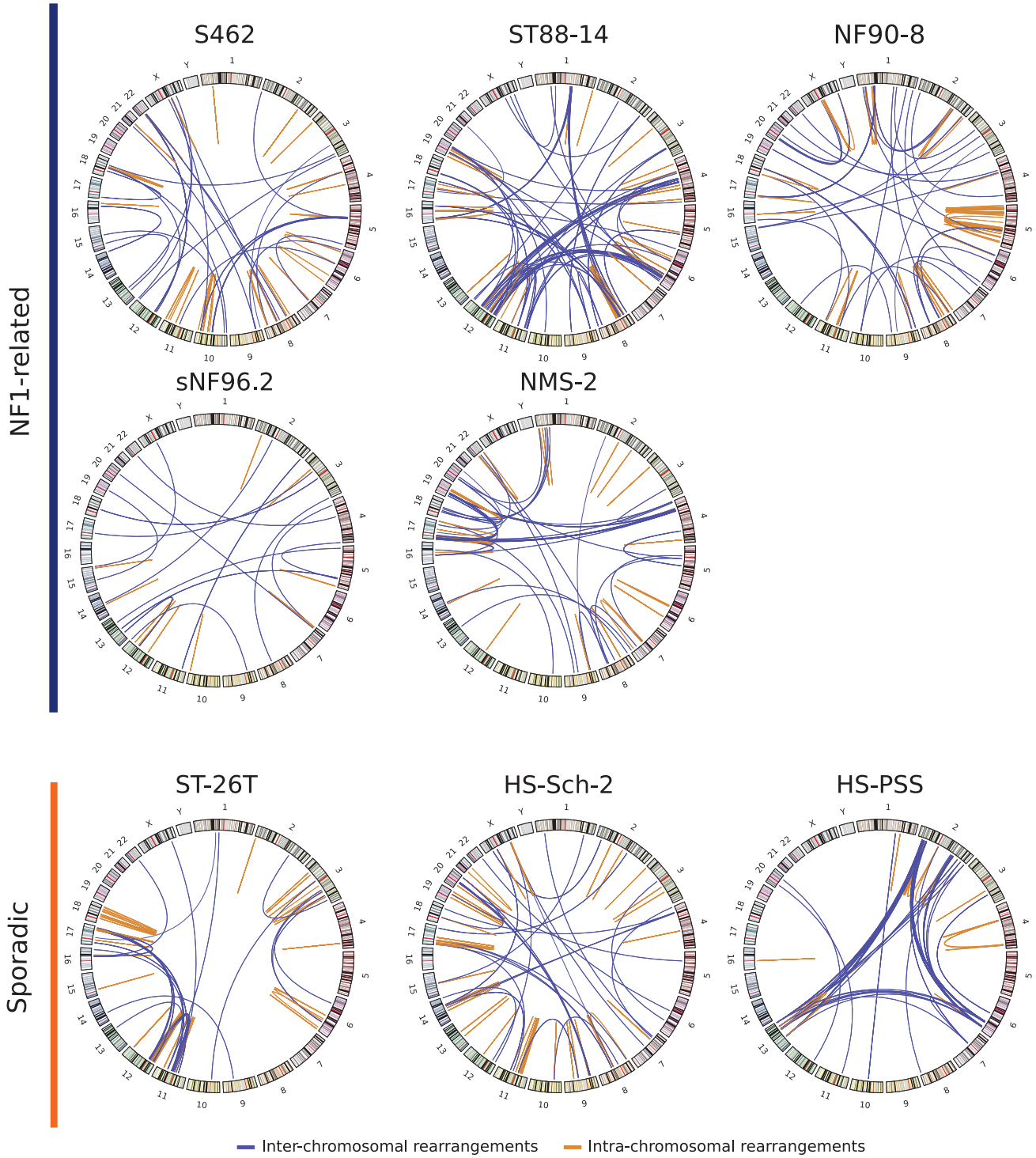

Figure 3. Structural rearrangements as key players for tumor suppressor gene inactivation

Circos plots showing the chromosomal rearrangements identified in the different MPNST cell lines. Blue lines represent inter-chromosomal rearrangements and orange lines intra-chromosomal rearrangements. These rearrangements were obtained using Lumpy and CliffHunteR on WGS data.

further characterization. Since sarcomas comprise a morphologically heterogeneous class of tumors and their diagnosis has been hampered by a high misclassification rate, we decided to perform methylome analysis of all cell lines in comparison to established reference cohorts of different peripheral nerve sheath

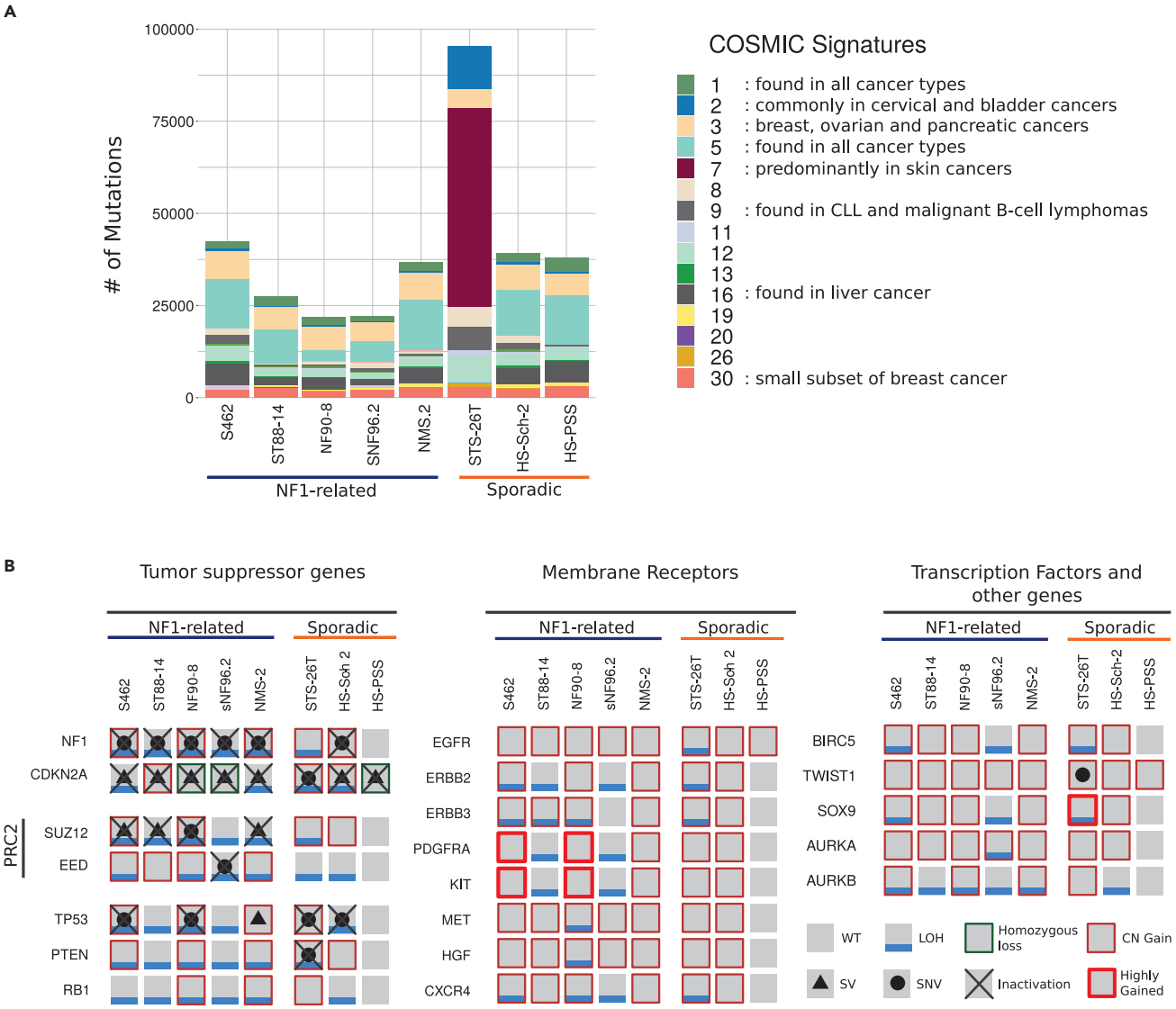

Figure 4. Small genomic variants have limited importance in altering MPNST-associated genes

(A) Mutation number and estimated contribution of COSMIC mutational signatures in MPNST cell lines. Each bar represents the total number of somatically enriched single nucleotide variants (SNVs) found in an MPNST cell line. Each color represents a different COSMIC mutational signature.

(B) Status of the commonly altered genes in MPNSTs. A gray square represents a wild type (WT) status of the gene; a blue line indicates the presence of loss of heterozygosity (LOH) detected by using SNP-array data; a black dot a small nucleotide variant affecting the gene; a black triangle indicates that the gene is affected by a structural variant (SV); copy number gain (CN gain) is represented by a thin red square; and a thick red square denotes a highly gained region affecting the gene. A homozygous loss of a gene is specified by a thin dark green square and the complete inactivation of a gene is represented by a black cross. Note that all NF1-related MPNST cell lines have the complete inactivation of *NF1*, *CDKN2A* and the *PRC2* complex. In addition, *CDKN2A* is also inactivated in sporadic cell lines.

and soft tissue tumors[34] to clarify whether there was a problem in the diagnosis of MPNSTs or on the identification and classification of different MPNST types. Figure 5A shows a dimension reduction using Uni-form Mani-fold Approximation and Projection (UMAP) analysis plot. While all NF1-related MPNST cell lines were located within the MPNST cluster, the sporadic cell lines lay within the melanoma cluster (STS-26T and HS-Sch-2 cell lines) or within the not fully characterized group of MPNST-like sarcomas (HS-PSS cell line). With these results, we decided to further characterize the 8 cell lines by performing immunostaining for 3 markers: SOX9, SOX10, and S100B. SOX9 is normally expressed in MPNSTs[28] and also in melanomas.[35] SOX10 and S100B are markers that define the neural crest-Schwann cell differentiation axis but also the neural crest-melanocytic path. Both markers are frequently reduced or absent in MPNSTs

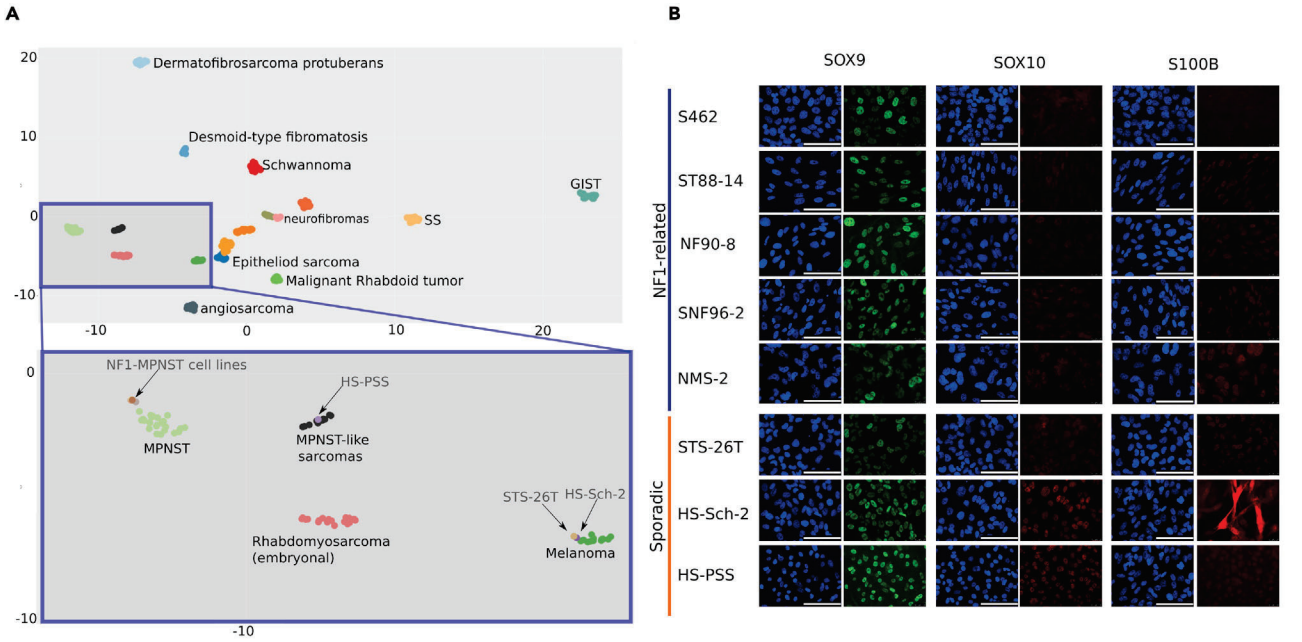

C

		Genomics							Methylome	Specific expression Markers			
		NF1	*CDKN2A*	PRC2	*TP53*	% Brkpnt affected Genome	# Small Nucleotide Variants	# exonic SNVs	Classification	*SOX9*	*SOX10*	*S100B*	Other important alterations
NF1-related	S462	-	-	-	-	5,20%	89048	144	MPNST	+	-	-	
	ST88-14	-	-	-	WT	8,00%	76741	103	MPNST	+	-	-	
	NF90-8	-	-	-	-	7,40%	66596	95	MPNST	+	-	-	
	SNF96-2	-	-	-	WT	2,70%	68616	97	MPNST	+	-	-	
	NMS-2	-	-	-	Het	5,70%	88557	117	MPNST	+	-	-	
Sporadic	STS-26T	WT	-	WT	-	5,40%	147141	262	Melanoma	+	-	-	BRAF: V600E; COSMIC signature 7
	HS-Sch-2	-	-	WT	-	5,60%	96259	162	Melanoma	+	+	+	
	HS-PSS	WT	-	WT	WT	3,40%	96824	137	MPNST-Like	+	+	-	Fusion gene: EML4-ALK

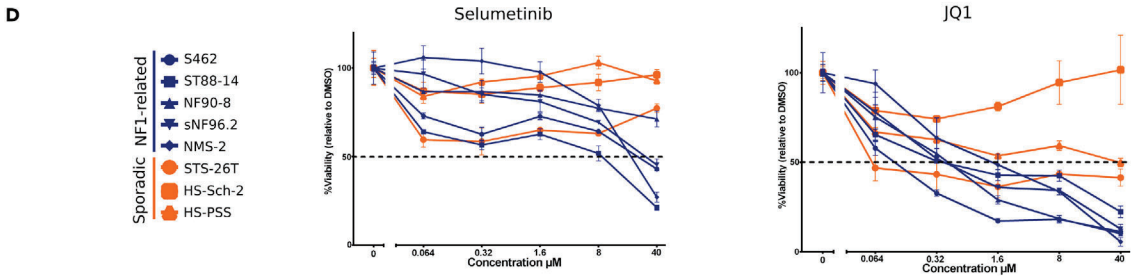

Figure 5. Genome, methylome, and marker analysis: useful tools for a better differential diagnosis and MPNST classification

(A) UMAP analysis of the methylome profile of the MPNST cell lines in comparison to different soft tissue tumor types.[34] The upper part of the plot provides a global view of the classification. Each dot represents a sample and every color is a different sarcoma type. The lower part of the graph is an inset magnification of a specific part containing all the MPNST cell lines analyzed. All NF1-related MPNST cell lines group within the MPNST methylation group (light green). HS-PSS cell line clustered with the MPNST-like sarcomas group (black) and STS-26T and HS-Sch-2 clustered together with the melanoma group (dark green).

(B) Immunofluorescence images showing expression of SOX9, SOX10, and S100B markers in the different cell lines. DAPI was used to stain nuclei. Scale bars: 100µm.

(C) Summary table of the genomic, methylome, and marker expression status of all MPNST cell lines. Genomics contains the status of *NF1*, *CDKN2A*, PRC2, and *TP53* genes (blue, complete gene inactivation (–); yellow wild type (WT); light green heterozygous deletion (Het)); percentage (%) of breakpoints affecting the genome +/– 1 mb; the number (#) of small nucleotide variants per sample; the # of exonic small nucleotide variants with a potential impact on protein function. Methylome contains the methylome-based classification of each cell line. Expression markers contain the expression of SOX9, SOX10, and

Figure 5. *Continued*

S100B identity markers (yellow for expression (+); blue for absence (−). The "other important information" column summarizes additional relevant information identified in each cell line.

(D) Cell viability assay upon treatment with different concentrations of Selumetinib and JQ1 of the NF1-related cell lines (blue) and the sporadic cell lines (orange). Each dot represents the mean of three independent experiments and error bars represent the standard deviation. The percentage of cell viability was calculated by normalizing the values to DMSO control cells.

according to the WHO classification,[36] lost in transitions of ANNUBP toward a low-grade MPNST[12] and also significantly downregulated/absent using expression analysis[28]; and data not shown). In contrast, SOX10 and S100B are frequently expressed in melanoma.[37] All cell lines stained positive for SOX9 (Figure 5B). All NF1-related cell lines stained negative for SOX10 and S100B, as did the STS-26T sporadic cell line. In contrast, HS-PSS and HS-Sch-2 sporadic cell lines stained positive for SOX10 and, in addition, HS-Sch-2 also stained positive for S100B (Figure 5B), moving them away from a classic MPNST identity.

Altogether, the fine landscape of genomic alterations, methylome-based classification, marker expression, and particular informative gain-of-function mutations, captured a fair degree of variability among MPNST cell lines (Figure 5C) uncovering the probable misidentification of some of the tumors from which the sporadic cell lines were isolated and also the need of a complete and systematic characterization of additional MPNST tumors and cell lines to better understand whether MPNSTs constitute a homogeneous group of tumors or there exist different types.

To investigate the impact of genomic differences identified genuine MPNST cell lines and the ones potentially misidentified (Figure 5C), we performed a drug response assay. We used a MEK inhibitor targeting the loss of the *NF1* gene (Selumetinib) and a BET inhibitor targeting the inactivation of PRC2 (JQ1), since both TSGs had different inactivation patterns in the two groups of cell lines (Figure 4B). Both compounds tested showed a higher impact on cell viability in NF1-related cell lines, compared to the sporadic ones (Figure 5D), highlighting the importance of correct diagnostics of MPNSTs.

DISCUSSION

We performed a deep genomic characterization of 9 of the most distributed and used MPNST cell lines[25] including cell lines banked in repositories (ATCC, RIKEN). Before this analysis, we performed authentication assays which resulted in discarding the T265 cell line since it exhibited the same STR profile as the ST88-14 and its matched primary MPNST (Data S2).

Despite the diverse ploidies exhibited by the MPNST cell lines, NF1-related cell lines faithfully reproduced the copy number profiles present in primary MPNST tumors, something that was not true for sporadic cell lines. These results reinforce the idea that despite the high degree of genomic alterations, MPNSTs contain quite stable genomes, as shown by comparing primary tumors with derived orthotopic PDX.[31] Our use of WGS was crucial for more complete detection of genomic alterations present in MPNSTs, due to the significant number of structural variants present.[19] This was especially important for detecting the inactivation of MPNST-related tumor suppressor genes (TSGs), particularly for *CDKN2A* and the PRC2-related genes (*SUZ12/EED*). The use of WGS also allowed the identification of fusion genes, such as EML4-ALK, generated by an inversion affecting both genes in the HS-PSS sporadic cell line. The presence of fusion genes is common in other types of soft tissue sarcomas that otherwise contain genomes with few genomic alterations. However, fusion genes are not common in the karyotypically complex MPNSTs.[38] In concordance with this idea, and supporting a non-MPNST identity, in addition to the EML4-ALK fusion gene, the HS-PSS cell line contained a ploidy close to 2n, containing only a few copy number alterations and structural changes (Figures 1A and Figures 2 and 3, and Data S4).

In contrast to the importance of somatic copy number alterations and structural rearrangements, MPNST cell lines exhibited a modest frequency of mutations, with moderate functional impact, mainly involving the inactivation of *TP53*. Notably, the frequency and the type of mutation signatures exhibited provided an important differential indicator. While all cell lines exhibited a similar number of mutations and similar mutational signatures, the STS-26T cell line contained a much higher number of mutations and an important contribution from mutational signature 7, predominantly found in skin cancers.

Genomic alterations or mutations constituting a gain-of-function were not common in NF1-related MPNST cell lines. In fact, we identified only two cell lines (S462 and NF90-8) with a highly gained region in

chromosome 4 containing the *PDGFRA* and *KIT* receptors, consistent with previous reports[39,40] but not, for instance, kinase-activating mutations or translocations, like those involving NTRK genes.[41] In contrast, we identified the *BRAF* V600E mutation in the STS-26T cell line and the already mentioned EML4-ALK fusion gene in the HS-PSS cell line.

Our deep genomic characterization (ploidy, copy number profile, structural variants, mutation frequencies, and signatures, presence of gain-of-function mutations, and altered MPNST-related genes) questioned the MPNST identity of the analyzed sporadic cell lines. Methylome-based classification[34] and immunofluorescence of cell identity markers (SOX9, SOX10, S100B) complemented genomic analysis. STS-26T cell line contained a functional PRC2 complex and the *BRAF* V600E mutation. It also exhibited a much higher mutation frequency than the other cell lines and an important COSMIC signature 7, predominantly present in skin cancers as previously described by Hayward et al. (2017).[42] Finally, a methylome classifier unequivocally classified it as a melanoma. Taking together our compiled evidence, in our opinion, the original diagnosis of a "malignant schwannoma"[43] if made today would probably be "melanoma." In this regard, it would be interesting to further analyze MPNSTs with *BRAF* V600E mutations described in the literature[44–46] using additional tools like mutation frequencies and signatures, methylome classifier, and cell identity marker expression. The HS-Sch-2 cell line showed a WT status for PRC2 genes but harbored the complete inactivation of *NF1* and *CDKN2A*. It was classified as melanoma by the methylome classifier and expressed the markers SOX10 and S100B. The expression of these two markers is lost in transitions from atypical neurofibromas to MPNSTs and is commonly significantly reduced or absent in MPNSTs.[12] The HS-Sch-2 cell line also stained negative for the melanoma marker Melan-A (data not shown). The combination of positive staining for SOX10 and S100B and negative staining for Melan-A is characteristic of desmoplastic melanoma,[47] which also commonly exhibits the complete inactivation of *NF1* and *CDKN2A*,[48,49] neurotropism and nerve infiltration,[50,51] the latter described in the original publication of this cell line.[52] Finally, HS-PSS also showed a WT status for PRC2 genes, was assigned to the provisional and not fully characterized "MPNST-like sarcoma" methylation group, was positive for SOX10, contained an almost unaltered genome proximal to 2n but harbored a translocation generating the fusion gene EML4-ALK. This fusion gene is associated with a type of sarcoma termed epithelioid inflammatory myofibroblastic sarcoma[53,54] which also contain a spindle cell component, being the most probable identity of the tumor from which HS-PSS was derived.

Preliminary data on drug treatment using these cell lines showed a different impact on cell viability between genuine MPNST cell lines and the ones potentially misidentified, highlighting the importance of correct MPNST diagnostics for better clinical management.

Despite the potential misdiagnosis of the three sporadic cell lines studied here, it is important to remark that these results do not imply that all sporadic MPNSTs (and derived cell lines) are not genuine MPNSTs. In fact, deep genomic analysis of primary MPNSTs (Magallón-Lorenz et al. in preparation), confirmed the existence of sporadic MPNSTs exhibiting the same genomic characteristics as the NF1-related MPNST cell lines reported here. Conversely, our results neither discard the misidentification of MPNSTs in the NF1 setting.

In summary, the new genomic and epigenomic characterization of MPNST cell lines provided in this work uncovered the misidentification of the commonly used NF1-related T265 MPNST cell line and, in addition, compiled multiple pieces of evidence to question the identity of the three sporadic MPNST cell lines analyzed here, proposing alternative identities for all of them: a melanoma for STS-26T; a desmoplastic melanoma for the HS-Sch-2 cell line; and an epithelioid inflammatory myofibroblastic sarcoma for the HS-PSS. These results may imply the need of determining the impact of their use in previous and probably current works being performed, considering the new information provided. It also alerts us, as a scientific community, that we need to improve the characterization and control of the cell lines and tissues we use in our research. But above all, it provides an opportunity to look ahead and improve our understanding of what is an MPNST and which types might exist. In this regard, a systematic combination by different laboratories of histological characterization together with these new ways of analyzing genomes and epigenomes opens the door to revising the manner we perform differential diagnostics of MPNSTs and related tumors.

Our results, in addition to generating a valuable resource for the study of new therapeutic strategies for MPNSTs, uncover the need to systematically analyze MPNSTs, combining pathology with genomic and

molecular techniques. Genomic analysis such as copy number profiles, structural variants, mutation frequencies and signatures, presence of gain-of-function mutations, and the inactivation of specific TSGs, together with methylome-based sarcoma classification and cell identity marker analysis, emerge as valuable tools for a better differential diagnosis and classification of MPNSTs.

Limitations of the study

Different limitations of this study exist. The cell lines used here may not completely represent the repertoire of recurrent genomic alterations present in MPNSTs due to their type and limited number. In addition, the use of established MPNST cell lines makes difficult the availability of the original MPNST for comparison purposes or of a normal pair tissue for the identification of a reliable set of somatic variants. Finally, all sporadic cell lines used here may be misclassified, which urges for the deep genomic characterization of additional MPNST cell lines.

ETHICS DECLARATIONS

This work has been approved by the Germans Trias i Pujol Hospital (HUGTiP) Ethics Committee.

STAR★METHODS

Detailed methods are provided in the online version of this paper and include the following:

- KEY RESOURCES TABLE
- RESOURCE AVAILABILITY
  - Lead contact
  - Materials availability
  - Data and code availability
- EXPERIMENTAL MODEL AND SUBJECT DETAILS
  - MPNST and other established cell lines
- METHOD DETAILS
  - DNA extraction
  - STR profiling
  - Calculation of cell ploidy by flow cytometry
  - *NF1* mutational status
  - SNP-array analysis
  - Whole-exome sequencing (WES) and whole-genome sequencing (WGS)
  - Selection of putatively pathogenic somatic variants using WES and WGS
  - Mutational signatures
  - Copy number variants (CNVs) from WGS
  - Structural variants and detection of fusion genes
  - DNA methylation and Uni-form Mani-fold Approximation and Projection (UMAP) analysis
  - Validation of inter-chromosomal rearrangements
  - Fusion gene validation
  - Immunocytochemical analysis
  - Cell viability assay
- QUANTIFICATION AND STATISTICAL ANALYSIS

SUPPLEMENTAL INFORMATION

Supplemental information can be found online at https://doi.org/10.1016/j.isci.2023.106096.

ACKNOWLEDGMENTS

We would like to thank Aurora Sánchez from the Molecular Genetics and Biochemistry Service, CDB, Hospital Clínic (Barcelona) and Marta Salido, Mar Rodríguez-Rivera and Blanca Espinet from the Molecular Cytogenetics Laboratory, IMIM-Hospital del Mar (Barcelona), for their initial effort in the MPNST cell line cytogenetic characterization using G-banding and SKY. We thank the IGTP core facilities and their staff for their contribution and technical support: High-Performance Computing; Translational Genomics Core Facility; High Content Genomics and Bioinformatics Core Facility. We would like to thank the constant support of the NF lay associations: Asociación de Afectados de Neurofibromatosis and ACNefi.

Funding

This work has been supported by the Instituto de Salud Carlos III National Health Institute funded by FEDER funds—a way to build Europe—[PI14/00577, PI17/00524, PI19/00553, PI20/00228]; Fundación Proyecto Neurofibromatosis (projects to CL and BG-ES); Fundació La Marató de TV3 (51/C/2019); the Government of Catalonia [2017-SGR-496], CERCA Program. MM-L is supported by Fundación Proyecto Neurofibromatosis.

AUTHOR CONTRIBUTIONS

Conception and design of the work: MM-L, ET, BG, and ES. Project supervision: BG and ES. Bioinformatic analysis and visualization: MM-L, BG. Experimental work acquisition, analysis and interpretation: ET, MM-L, MC, MAF, GR, IR, HM, IU-A, AN, JF-R, BG, and ES. Additional resources: JF, DR, and CL. Drug testing: SO, EC-B, and JF-R. Methylome analysis and sarcoma classifier: DR and TL. Writing original draft: MM-L, ET, BG, and ES. Writing, reviewing, editing, and scientific input: all authors. All authors also approved this version of the article.

DECLARATION OF INTERESTS

The authors declare that they have no competing interests.

Received: July 26, 2022
Revised: November 23, 2022
Accepted: January 26, 2023
Published: January 31, 2023

REFERENCES

1. Grobmyer, S.R., Reith, J.D., Shahlaee, A., Bush, C.H., and Hochwald, S.N. (2008). Malignant peripheral nerve sheath tumor: molecular pathogenesis and current management considerations. J. Surg. Oncol. *97*, 340–349. https://doi.org/10.1002/jso.20971.

2. Evans, D.G.R., Baser, M.E., McGaughran, J., Sharif, S., Howard, E., and Moran, A. (2002). Malignant peripheral nerve sheath tumours in neurofibromatosis 1. J. Med. Genet. *39*, 311–314. https://doi.org/10.1136/jmg.39.5.311.

3. Ferner, R.E., and Gutmann, D.H. (2002). International consensus statement on malignant peripheral nerve sheath tumors in neurofibromatosis. Cancer Res. *62*, 1573–1577.

4. Ducatman, B.S., Scheithauer, B.W., Piepgras, D.G., Reiman, H.M., and Ilstrup, D.M. (1986). Malignant peripheral nerve sheath tumors. A clinicopathologic study of 120 cases. Cancer *57*, 2006–2021. https://doi.org/10.1002/1097-0142(19860515)57:10<2006.

5. Uusitalo, E., Rantanen, M., Kallionpää, R.A., Pöyhönen, M., Leppävirta, J., Ylä-Outinen, H., Riccardi, V.M., Pukkala, E., Pitkäniemi, J., Peltonen, S., and Peltonen, J. (2016). Distinctive cancer associations in patients with neurofibromatosis type 1. J. Clin. Oncol. *34*, 1978–1986. https://doi.org/10.1200/JCO.2015.65.3576.

6. Anghileri, M., Miceli, R., Fiore, M., Mariani, L., Ferrari, A., Mussi, C., Lozza, L., Collini, P., Olmi, P., Casali, P.G., et al. (2006). Malignant peripheral nerve sheath tumors: prognostic factors and survival in a series of patients treated at a single institution. Cancer *107*, 1065–1074. https://doi.org/10.1002/cncr.22098.

7. Porter, D.E., Prasad, V., Foster, L., Dall, G.F., Birch, R., and Grimer, R.J. (2009). Survival in malignant peripheral nerve sheath tumours: a comparison between sporadic and neurofibromatosis type 1-associated tumours. Sarcoma *2009*, 756395. https://doi.org/10.1155/2009/756395.

8. Moretti, V.M., Crawford, E.A., Staddon, A.P., Lackman, R.D., and Ogilvie, C.M. (2011). Early outcomes for malignant peripheral nerve sheath tumor treated with chemotherapy. Am. J. Clin. Oncol. *34*, 417–421. https://doi.org/10.1097/COC.0b013e3181e9c08a.

9. Belakhoua, S.M., and Rodriguez, F.J. (2021). Diagnostic pathology of tumors of peripheral nerve. Neurosurgery *88*, 443–456. https://doi.org/10.1093/neuros/nyab021.

10. Rodriguez, F.J., Folpe, A.L., Giannini, C., and Perry, A. (2012). Pathology of peripheral nerve sheath tumors: diagnostic overview and update on selected diagnostic problems. Acta Neuropathol. *123*, 295–319. https://doi.org/10.1007/s00401-012-0954-z.

11. Le Guellec, S., Decouvelaere, A.-V., Filleron, T., Valo, I., Charon-Barra, C., Robin, Y.-M., Terrier, P., Chevreau, C., and Coindre, J.-M. (2016). Malignant peripheral nerve sheath tumor is a challenging diagnosis: a systematic pathology review, immunohistochemistry, and molecular analysis in 160 patients from the French sarcoma group Database. Am. J. Surg. Pathol. *40*, 896–908. https://doi.org/10.1097/PAS.0000000000000655.

12. Miettinen, M.M., Antonescu, C.R., Fletcher, C.D.M., Kim, A., Lazar, A.J., Quezado, M.M., Reilly, K.M., Stemmer-Rachamimov, A., Stewart, D.R., Viskochil, D., et al. (2017). Histopathologic evaluation of atypical neurofibromatous tumors and their transformation into malignant peripheral nerve sheath tumor in patients with neurofibromatosis 1—a consensus overview. Hum. Pathol. *67*, 1–10. https://doi.org/10.1016/j.humpath.2017.05.010.

13. Higham, C.S., Dombi, E., Rogiers, A., Bhaumik, S., Pans, S., Connor, S.E.J., Miettinen, M., Sciot, R., Tirabosco, R., Brems, H., et al. (2018). The characteristics of 76 atypical neurofibromas as precursors to neurofibromatosis 1 associated malignant peripheral nerve sheath tumors. Neuro Oncol. *20*, 818–825. https://doi.org/10.1093/neuonc/noy013.

14. Lee, W., Teckie, S., Wiesner, T., Ran, L., Prieto Granada, C.N., Lin, M., Zhu, S., Cao, Z., Liang, Y., Sboner, A., et al. (2014). PRC2 is recurrently inactivated through EED or SUZ12 loss in malignant peripheral nerve sheath tumors. Nat. Genet. *46*, 1227–1232. https://doi.org/10.1038/ng.3095.

15. Brohl, A.S., Kahen, E., Yoder, S.J., Teer, J.K., and Reed, D.R. (2017). The genomic landscape of malignant peripheral nerve sheath tumors: diverse drivers of Ras pathway activation. Sci. Rep. *7*, 14992. https://doi.org/10.1038/s41598-017-15183-1.

16. Sohier, P., Luscan, A., Lloyd, A., Ashelford, K., Laurendeau, I., Briand-Suleau, A., Vidaud, D., Ortonne, N., Pasmant, E., and Upadhyaya, M. (2017). Confirmation of mutation landscape of NF1-associated malignant peripheral

nerve sheath tumors. Genes Chromosomes Cancer *56*, 421–426. https://doi.org/10.1002/gcc.22446.

17. Abeshouse, A., Adebamowo, C., Adebamowo, S.N., Akbani, R., Akeredolu, T., Ally, A., Anderson, M.L., Anur, P., Appelbaum, E.L., Armenia, J., et al. (2017). Comprehensive and integrated genomic characterization of adult soft tissue sarcomas. Cell *171*, 950–965.e28. https://doi.org/10.1016/j.cell.2017.10.014.

18. Serra, E., Gel, B., Fernández-Rodríguez, J., and Lázaro, C. (2020). Genomics of peripheral nerve sheath tumors associated with neurofibromatosis type 1. In Multidisciplinary Approach to Neurofibromatosis Type 1, G. Tadini, E. Legius, and H. Brems, eds. (Springer International Publishing), pp. 117–147. https://doi.org/10.1007/978-3-319-92450-2_9.

19. Magallón-Lorenz, M., Fernández-Rodríguez, J., Terribas, E., Creus-Batchiller, E., Romagosa, C., Estival, A., Perez Sidelnikova, D., Salvador, H., Villanueva, A., Blanco, I., et al. (2021). Chromosomal translocations inactivating CDKN2A support a single path for malignant peripheral nerve sheath tumor initiation. Hum. Genet. *140*, 1241–1252. https://doi.org/10.1007/s00439-021-02296-x.

20. Beert, E., Brems, H., Daniëls, B., de Wever, I., van Calenbergh, F., Schoenaers, J., Debiec-Rychter, M., Gevaert, O., de Raedt, T., et al. (2011). Atypical neurofibromas in neurofibromatosis type 1 are premalignant tumors. Genes Chromosomes Cancer *50*, 1021–1032. https://doi.org/10.1002/gcc.20921.

21. Markovic, O., and Markovic, N. (1998). Cell cross-contamination in cell cultures: the silent and neglected danger. In Vitro Cell. Dev. Biol. Anim. *34*, 1–8. https://doi.org/10.1007/s11626-998-0040-y.

22. Langdon, S.P. (2003). Cancer Cell Culture (Humana Press). https://doi.org/10.1385/1592594069.

23. Reid, Y.A. (2011). Characterization and authentication of cancer cell lines: an overview. Methods Mol. Biol. *731*, 35–43. https://doi.org/10.1007/978-1-61779-080-5_4.

24. Allen, M., Bjerke, M., Edlund, H., Nelander, S., and Westermark, B. (2016). Origin of the U87MG glioma cell line: good news and bad news. Sci. Transl. Med. *8*, 354re3. https://doi.org/10.1126/scitranslmed.aaf6853.

25. Kim, A., Stewart, D.R., Reilly, K.M., Viskochil, D., Miettinen, M.M., and Widemann, B.C. (2017). Malignant peripheral nerve sheath tumors state of the science: leveraging clinical and biological insights into effective therapies. Sarcoma *2017*, 7429697–7429710. https://doi.org/10.1155/2017/7429697.

26. Pemov, A., Li, H., Presley, W., Wallace, M.R., and Miller, D.T. (2020). Genetics of human malignant peripheral nerve sheath tumors. Neurooncol. Adv. *2*, i50–i61. https://doi.org/10.1093/noajnl/vdz049.

27. Miller, S.J., Rangwala, F., Williams, J., Ackerman, P., Kong, S., Jegga, A.G., Kaiser, S., Aronow, B.J., Frahm, S., Kluwe, L., et al. (2006). Large-scale molecular comparison of human Schwann cells to malignant peripheral nerve sheath tumor cell lines and tissues. Cancer Res. *66*, 2584–2591. https://doi.org/10.1158/0008-5472.CAN-05-3330.

28. Miller, S.J., Jessen, W.J., Mehta, T., Hardiman, A., Sites, E., Kaiser, S., Jegga, A.G., Li, H., Upadhyaya, M., Giovannini, M., et al. (2009). Integrative genomic analyses of neurofibromatosis tumours identify SOX9 as a biomarker and survival gene. EMBO Mol. Med. *1*, 236–248. https://doi.org/10.1002/emmm.200900027.

29. Jessen, W.J., Miller, S.J., Jousma, E., Wu, J., Rizvi, T.A., Brundage, M.E., Eaves, D., Widemann, B., Kim, M.O., Dombi, E., et al. (2013). MEK inhibition exhibits efficacy in human and mouse neurofibromatosis tumors. J. Clin. Invest. *123*, 340–347. https://doi.org/10.1172/JCI60578.

30. Perrin, G.Q., Li, H., Fishbein, L., Thomson, S.A., Hwang, M.S., Scarborough, M.T., Yachnis, A.T., Wallace, M.R., Mareci, T.H., and Muir, D. (2007). An orthotopic xenograft model of intraneural NF1 MPNST suggests a potential association between steroid hormones and tumor cell proliferation. Lab. Invest. *87*, 1092–1102. https://doi.org/10.1038/labinvest.3700675.

31. Castellsagué, J., Gel, B., Fernández-Rodríguez, J., Llatjós, R., Blanco, I., Benavente, Y., Pérez-Sidelnikova, D., García-Del Muro, J., Viñals, J.M., Vidal, A., et al. (2015). Comprehensive establishment and characterization of orthoxenograft mouse models of malignant peripheral nerve sheath tumors for personalized medicine. EMBO Mol. Med. *7*, 608–627. https://doi.org/10.15252/emmm.201404430.

32. Takeuchi, K., Choi, Y.L., Soda, M., Inamura, K., Togashi, Y., Hatano, S., Enomoto, M., Takada, S., Yamashita, Y., Satoh, Y., et al. (2008). Multiplex reverse transcription-PCR screening for EML4-ALK fusion transcripts. Clin. Cancer Res. *14*, 6618–6624. https://doi.org/10.1158/1078-0432.CCR-08-1018.

33. Alexandrov, L.B., Kim, J., Haradhvala, N.J., Huang, M.N., Tian Ng, A.W., Wu, Y., Boot, A., Covington, K.R., Gordenin, D.A., Bergstrom, E.N., et al. (2020). The repertoire of mutational signatures in human cancer. Nature *578*, 94–101. https://doi.org/10.1038/s41586-020-1943-3.

34. Koelsche, C., Schrimpf, D., Stichel, D., Sill, M., Sahm, F., Reuss, D.E., Blattner, M., Worst, B., Heilig, C.E., Beck, K., et al. (2021). Sarcoma classification by DNA methylation profiling. Nat. Commun. *12*, 498. https://doi.org/10.1038/s41467-020-20603-4.

35. Rao, P., Fuller, G.N., and Prieto, V.G. (2010). Expression of sox-9 in metastatic melanoma-A potential diagnostic pitfall. Am. J. Dermatopathol. *32*, 262–266. https://doi.org/10.1097/DAD.0b013e3181b7fc8d.

36. Sahm, F., Reuss, D.E., and Giannini, C. (2018). WHO 2016 classification: changes and advancements in the diagnosis of miscellaneous primary CNS tumours. Neuropathol. Appl. Neurobiol. *44*, 163–171. https://doi.org/10.1111/nan.12397.

37. Szumera-Ciećkiewicz, A., Bosisio, F., Teterycz, P., Antoranz, A., Delogu, F., Koljenović, S., van de Wiel, B.A., Blokx, W., van Kempen, L.C., Rutkowski, P., et al. (2020). SOX10 is as specific as S100 protein in detecting metastases of melanoma in lymph nodes and is recommended for sentinel lymph node assessment. Eur. J. Cancer *137*, 175–182. https://doi.org/10.1016/j.ejca.2020.06.037.

38. Taylor, B.S., Barretina, J., Maki, R.G., Antonescu, C.R., Singer, S., and Ladanyi, M. (2011). Advances in sarcoma genomics and new therapeutic targets. Nat. Rev. Cancer *11*, 541–557. https://doi.org/10.1038/nrc3087.

39. Holtkamp, N., Okuducu, A.F., Mucha, J., Afanasieva, A., Hartmann, C., Atallah, I., Estevez-Schwarz, L., Mawrin, C., Friedrich, R.E., Mautner, V.F., and von Deimling, A. (2006). Mutation and expression of PDGFRA and KIT in malignant peripheral nerve sheath tumors, and its implications for imatinib sensitivity. Carcinogenesis *27*, 664–671. https://doi.org/10.1093/carcin/bgi273.

40. Zietsch, J., Ziegenhagen, N., Heppner, F.L., Reuss, D., von Deimling, A., and Holtkamp, N. (2010). The 4q12 amplicon in malignant peripheral nerve sheath tumors: consequences on gene expression and implications for sunitinib treatment. PLoS One *5*, 118588–e11910. https://doi.org/10.1371/journal.pone.0011858.

41. Brčić, I., Godschachner, T.M., Bergovec, M., Igrec, J., Till, H., Lackner, H., Scheipl, S., Kashofer, K., Brodowicz, T., Leithner, A., et al. (2021). Broadening the spectrum of NTRK rearranged mesenchymal tumors and usefulness of pan-TRK immunohistochemistry for identification of NTRK fusions. Mod. Pathol. *34*, 396–407. https://doi.org/10.1038/s41379-020-00657-x.

42. Hayward, N.K., Wilmott, J.S., Waddell, N., Johansson, P.A., Field, M.A., Nones, K., Patch, A.-M., Kakavand, H., Alexandrov, L.B., Burke, H., et al. (2017). Whole-genome landscapes of major melanoma subtypes. Nature *545*, 175–180. https://doi.org/10.1038/nature22071.

43. Dahlberg, W.K., Little, J.B., Fletcher, J.A., Suit, H.D., and Okunieff, P. (1993). Radiosensitivity in vitro of human soft tissue sarcoma cell lines and skin fibroblasts derived from the same patients. Int. J. Radiat. Biol. *63*, 191–198. https://doi.org/10.1080/09553009314550251.

44. Serrano, C., Simonetti, S., Hernández-Losa, J., Valverde, C., Carrato, C., Bagué, S., Orellana, R., Somoza, R., Moliné, T., Carles, J., et al. (2013). BRAF V600E and KRAS G12S mutations in peripheral nerve sheath tumours. Histopathology *62*, 499–504. https://doi.org/10.1111/his.12021.

45. Hirbe, A.C., Pekmezci, M., Dahiya, S., Apicelli, A.J., Van Tine, B.A., Perry, A., and Gutmann, D.H. (2014). BRAFV600E mutation in sporadic and neurofibromatosis type 1-related malignant peripheral nerve sheath tumors.

Neuro Oncol. *16*, 466–467. https://doi.org/10.1093/neuonc/not248.

46. Kaplan, H.G., Rostad, S., Ross, J.S., Ali, S.M., and Millis, S.Z. (2018). Genomic profiling in patients with malignant peripheral nerve sheath tumors reveals multiple pathways with targetable mutations. J. Natl. Compr. Cancer Netw. *16*, 967–974. https://doi.org/10.6004/jnccn.2018.7033.

47. Palla, B., Su, A., Binder, S., and Dry, S. (2013). SOX10 expression distinguishes desmoplastic melanoma from its histologic mimics. Am. J. Dermatopathol. *35*, 576–581. https://doi.org/10.1097/DAD.0b013e31827a0b98.

48. Wiesner, T., Kiuru, M., Scott, S.N., Arcila, M., Halpern, A.C., Hollmann, T., Berger, M.F., and Busam, K.J. (2015). NF1 mutations are common in desmoplastic melanoma. Am. J. Surg. Pathol. *39*, 1357–1362. https://doi.org/10.1097/PAS.0000000000000451.

49. Boada, A., Quer Pi-Sunyer, A., Richarz, N., and Jaka-Moreno, A. (2021). Update on the diagnosis and management of desmoplastic melanoma. Actas Dermo-Sifiliográficas *113*, 47–57. https://doi.org/10.1016/j.adengl.2021.11.003.

50. Chen, J.Y., Hruby, G., Scolyer, R.A., Murali, R., Hong, A., FitzGerald, P., Pham, T.T., Quinn, M.J., and Thompson, J.F. (2008). Desmoplastic neurotropic melanoma: a clinicopathologic analysis of 128 cases. Cancer *113*, 2770–2778. https://doi.org/10.1002/cncr.23895.

51. Frydenlund, N., and Mahalingam, M. (2015). Desmoplastic melanoma, neurotropism, and neurotrophin receptors - what we know and what we do not. Adv. Anat. Pathol. *22*, 227–241. https://doi.org/10.1097/PAP.0000000000000076.

52. Sonobe, H., Takeuchi, T., Furihata, M., Taguchi, T., Kawai, A., Ohjimi, Y., Iwasaki, H., Kaneko, Y., and Ohtsuki, Y. (2000). A new human malignant peripheral nerve sheath tumour-cell line, HS-sch-2, harbouring p53 point mutation. Int. J. Oncol. *17*, 347–352. https://doi.org/10.3892/ijo.17.2.347.

53. Jiang, Q., Tong, H.-X., Hou, Y.-Y., Zhang, Y., Li, J.-L., Zhou, Y.-H., Xu, J., Wang, J.-Y., and Lu, W.-Q. (2017). Identification of EML4-ALK as an alternative fusion gene in epithelioid inflammatory myofibroblastic sarcoma. Orphanet J. Rare Dis. *12*, 97. https://doi.org/10.1186/s13023-017-0647-8.

54. Xu, P., Shen, P., Jin, Y., Wang, L., and Wu, W. (2019). Epithelioid inflammatory myofibroblastic sarcoma of stomach: diagnostic pitfalls and clinical characteristics. Int. J. Clin. Exp. Pathol. *12*, 1738–1744.

55. Frahm, S., Mautner, V.-F., Brems, H., Legius, E., Debiec-Rychter, M., Friedrich, R.E., Knöfel, W.T., Peiper, M., and Kluwe, L. (2004). Genetic and phenotypic characterization of tumor cells derived from malignant peripheral nerve sheath tumors of neurofibromatosis type 1 patients. Neurobiol. Dis. *16*, 85–91. https://doi.org/10.1016/j.nbd.2004.01.006.

56. Fletcher, J.A., Kozakewich, H.P., Hoffer, F.A., Lage, J.M., Weidner, N., Tepper, R., Pinkus, G.S., Morton, C.C., and Corson, J.M. (1991). Diagnostic relevance of clonal cytogenetic aberrations in malignant soft-tissue tumors. N. Engl. J. Med. *324*, 436–442. https://doi.org/10.1056/NEJM199102143240702.

57. Legius, E., Dierick, H., Wu, R., Hall, B.K., Marynen, P., Cassiman, J.-J., and Glover, T.W. (1994). TP53 mutations are frequent in malignant NF1 tumors. Genes Chromosomes Cancer *10*, 250–255. https://doi.org/10.1002/gcc.2870100405.

58. Imaizumi, S., Motoyama, T., Ogose, A., Hotta, T., and Takahashi, H.E. (1998). Characterization and chemosensitivity of two human malignant peripheral nerve sheath tumour cell lines derived from a patient with neurofibromatosis type 1. Virchows Arch. *433*, 435–441. https://doi.org/10.1007/s004280050271.

59. Badache, A., and De Vries, G.H. (1998). Neurofibrosarcoma-derived Schwann cells overexpress platelet-derived growth factor (PDGF) receptors and are induced to proliferate by PDGF BB. J. Cell. Physiol. *177*, 334–342. https://doi.org/10.1002/(SICI)1097-4652.

60. Robinson, J.T., Thorvaldsdóttir, H., Winckler, W., Guttman, M., Lander, E.S., Getz, G., and Mesirov, J.P. (2011). Integrative genomics viewer. Nat. Biotechnol. *29*, 24–26. https://doi.org/10.1038/nbt.1754.

61. Li, H. (2013). Aligning sequence reads, clone sequences and assembly contigs with BWA-MEM. Preprint at arXiv. https://doi.org/10.6084/M9.FIGSHARE.963153.V1.

62. Kim, S., Scheffler, K., Halpern, A.L., Bekritsky, M.A., Noh, E., Källberg, M., Chen, X., Kim, Y., Beyter, D., Krusche, P., and Saunders, C.T. (2018). Strelka2: fast and accurate calling of germline and somatic variants. Nat. Methods *15*, 591–594. https://doi.org/10.1038/s41592-018-0051-x.

63. Wang, K., Li, M., and Hakonarson, H. (2010). ANNOVAR: functional annotation of genetic variants from high-throughput sequencing data. Nucleic Acids Res. *38*, e164. https://doi.org/10.1093/nar/gkq603.

64. Layer, R.M., Chiang, C., Quinlan, A.R., and Hall, I.M. (2014). LUMPY: a probabilistic framework for structural variant discovery. Genome Biol. *15*, R84. https://doi.org/10.1186/gb-2014-15-6-r84.

65. Talevich, E., Shain, A.H., Botton, T., and Bastian, B.C. (2016). CNVkit: genome-wide copy number detection and visualization from targeted DNA sequencing. PLoS Comput. Biol. *12*, e1004873. https://doi.org/10.1371/journal.pcbi.1004873.

66. Krzywinski, M., Schein, J., Birol, I., Connors, J., Gascoyne, R., Horsman, D., Jones, S.J., and Marra, M.A. (2009). Circos : an information aesthetic for comparative genomics. Genome Res. *19*, 1639–1645. https://doi.org/10.1101/gr.092759.109.19.

67. Gel, B., and Serra, E. (2017). karyoploteR: an R/Bioconductor package to plot customizable genomes displaying arbitrary data. Bioinformatics *33*, 3088–3090. https://doi.org/10.1093/bioinformatics/btx346.

68. Fantini, D., Vidimar, V., Yu, Y., Condello, S., and Meeks, J.J. (2020). MutSignatures: an R package for extraction and analysis of cancer mutational signatures. Sci. Rep. *10*, 18217–18312. https://doi.org/10.1038/s41598-020-75062-0.

69. Chiang, C., Layer, R.M., Faust, G.G., Lindberg, M.R., Rose, D.B., Garrison, E.P., Marth, G.T., Quinlan, A.R., and Hall, I.M. (2015). SpeedSeq : ultra-fast personal genome analysis and interpretation. Nat. Methods *12*, 6–10. https://doi.org/10.1038/nmeth.3505.

70. MacDonald, J.R., Ziman, R., Yuen, R.K.C., Feuk, L., and Scherer, S.W. (2014). The Database of Genomic Variants: a curated collection of structural variation in the human genome. Nucleic Acids Res. *42*, 986–992. https://doi.org/10.1093/nar/gkt958.

71. Varin, J., Poulain, L., Hivelin, M., Nusbaum, P., Hubas, A., Laurendeau, I., Lantieri, L., Wolkenstein, P., Vidaud, M., Pasmant, E., et al. (2016). Dual mTORC1/2 inhibition induces anti-proliferative effect in NF1-associated plexiform neurofibroma and malignant peripheral nerve sheath tumor cells. Oncotarget *7*, 35753–35767. https://doi.org/10.18632/oncotarget.7099.

72. Wu, R., López-Correa, C., Rutkowski, J.L., Baumbach, L.L., Glover, T.W., and Legius, E. (1999). Germline mutations in NF1 patients with malignancies. Genes Chromosomes Cancer *26*, 376–380. https://doi.org/10.1002/(SICI)1098-2264.

73. Popova, T., Manié, E., Stoppa-Lyonnet, D., Rigaill, G., Barillot, E., and Stern, M.H. (2009). Genome Alteration Print (GAP): a tool to visualize and mine complex cancer genomic profiles obtained by SNP arrays. Genome Biol. *10*, R128. https://doi.org/10.1186/gb-2009-10-11-r128.

74. Landrum, M.J., Lee, J.M., Benson, M., Brown, G.R., Chao, C., Chitipiralla, S., Gu, B., Hart, J., Hoffman, D., Jang, W., et al. (2018). ClinVar: improving access to variant interpretations and supporting evidence. Nucleic Acids Res. *46*, D1062–D1067. https://doi.org/10.1093/nar/gkx1153.

75. Li, Q., and Wang, K. (2017). InterVar: clinical interpretation of genetic variants by the 2015 ACMG-AMP guidelines. Am. J. Hum. Genet. *100*, 267–280. https://doi.org/10.1016/j.ajhg.2017.01.004.

76. Ng, P.C., and Henikoff, S. (2003). SIFT: predicting amino acid changes that affect protein function. Nucleic Acids Res. *31*, 3812–3814. https://doi.org/10.1093/nar/gkg509.

77. Adzhubei, I.A., Schmidt, S., Peshkin, L., Ramensky, V.E., Gerasimova, A., Bork, P., Kondrashov, A.S., and Sunyaev, S.R. (2010). A method and server for predicting damaging missense mutations. Nat. Methods *7*, 248–249. https://doi.org/10.1038/nmeth0410-248.

78. Schwarz, J.M., Rödelsperger, C., Schuelke, M., and Seelow, D. (2010). MutationTaster evaluates disease-causing potential of sequence alterations. Nat. Methods *7*, 575–576. https://doi.org/10.1038/nmeth0810-575.

79. Reva, B., Antipin, Y., and Sander, C. (2011). Predicting the functional impact of protein mutations: application to cancer genomics. Nucleic Acids Res. *39*, e118–e143. https://doi.org/10.1093/nar/gkr407.

80. Shihab, H.A., Gough, J., Cooper, D.N., Stenson, P.D., Barker, G.L.A., Edwards, K.J., Day, I.N.M., and Gaunt, T.R. (2013). Predicting the functional, molecular, and phenotypic consequences of amino acid substitutions using hidden markov models. Hum. Mutat. *34*, 57–65. https://doi.org/10.1002/humu.22225.

81. McInnes, L., Healy, J., and Melville, J. (2018). UMAP: Uniform Manifold approximation and projection for dimension reduction. Preprint at arXiv. https://doi.org/10.48550/arXiv.1802.03426.

STAR★METHODS

KEY RESOURCES TABLE

REAGENT or RESOURCE	SOURCE	IDENTIFIER
Antibodies		
Mouse IgG anti-Sox9	Abcam	Cat# ab76997 RRID:AB_2194156
Rabbit IgG anti-Sox10	Abcam	Cat# ab108408 RRID:AB_10859341
Rabbit IgG anti-S100B	DAKO	Cat# Z0311 RRID:AB_10013383
Goat anti-Mouse IgG (H + L) Alexa Fluor 488	Thermo Fisher Scientific	Cat# A-11001 RRID:AB_2534069
Goat anti-rabbit IgG (H + L) Alexa Fluor 568	Thermo Fisher Scientific	Cat# A-11011 RRID:AB_143157
Chemicals, peptides, and recombinant proteins		
DMEM	Biowest	Cat# L0106-500
FBS	Biowest	Cat# S181B-500
L-glutamine	Gibco	Cat# 25030024
Trypsin-EDTA 0.25%	Gibco	Cat# 25200–056
PBS	Biowest	Cat# L0615-500
DMSO	Sigma-Aldrich	Cat# 276855
JQ1	MedChemExpress	Cat# HY-13030
Selumetinib	Tocris	Cat# 6815
DAPI	Stemcell Technology	Cat# 75004
Paraformaldehyde	Santa Cruz Animal Health	Cat# sc-281692
Triton X-100	Sigma-Aldrich	Cat# X100
Vectashield	Vector Laboratories	Cat# H-1000-10
Critical commercial assays		
Maxwell 16 LEV simply RNA Purification Kit	Promega	Cat# AS1270
AmpFlSTR Identifiler Plus Amplification kit	Applied Biosystems	Cat# 4322288
Quant-iT™ PicoGreen® dsDNA Assay	Thermo Fisher Scientific	Cat# P7589
BigDye Terminator v.3.1 Sequencing Kit	Applied Biosystems	Cat# 4337455
MTT assay	Sigma-Aldrich	Cat# M2128-1G
Gentra Puregene Core Kit A	Qiagen	Cat# 153667
Deposited data		
WES and SNP-array data of 8 MPNST cell lines	Magallón-Lorenz et al. (2021)[19]	https://nf.synapse.org/ Synapse: syn22392179
WGS of 8 MPNST cell lines	This paper	https://nf.synapse.org/ Synapse: syn22392179

(*Continued on next page*)

Continued

REAGENT or RESOURCE	SOURCE	IDENTIFIER
Experimental models: Cell lines		
Human: S462 cell	Frahm et al. (2014)[55]	RRID: CVCL_1Y70
Human: ST88-14 cells	Fletcher et al. (1991)[56]	RRID: CVCL_8916
Human: NF90-8 cells	Legius et al. (1994)[57]	RRID: CVCL_1B47
Human: sNF96.2 cells	Perrin et al. (2007)[30] ATCC	CRL-2884; RRID: CVCL_K281
Human: NMS-2 cells	Imaizumi et al. (1998)[58] RIKEN	RCB2347; RRID: CVCL_4662
Human: T265 cells	Badache et al. (1998)[59]	RRID: CVCL_S805
Human: STS-26T cells	Dahlberg et al. (1993)[43]	RRID: CVCL_8917
Human: HS-Sch-2 cells	Sonobe et al. (2000)[52] RIKEN	RCB2230; RRID: CVCL_8718
Human: HS-PSS cells	RIKEN	RCB2362; RRID: CVCL_8717
Human: HFF-1	ATCC	SCRC-1041; RRID:CVCL_3285
Oligonucleotides		
Primers for interspecies PCR assay, see Supplementary Data S1, Table1	This paper	N/A
Primers for *CDKN2A* and *TP53* breakpoints, see Supplementary Data S6, Table1	This paper	N/A
Primers for *EML4-ALK* fusion gene	Takeuchi et al. (2008)[32]	https://doi.org/10.1158/1078-0432.CCR-08-1018
Software and algorithms		
CLC workbench 6 software	Qiagen	https://digitalinsights.qiagen.com/products-overview/discovery-insights-portfolio/analysis-and-visualization/qiagen-clc-main-workbench/
FlowJo	BD Bioscience	https://www.flowjo.com/
Integrative Genomic Viewer (IGV)	Robinson et al. (2011)[60]	https://software.broadinstitute.org/software/igv/
BWA-MEM	Li (2013)[61]	http://arxiv.org/abs/1303.3997
Strelka2	Kim et al. (2018)[62]	v2.9.10 https://github.com/Illumina/strelka/blob/v2.9.x/docs/userGuide/quickStart.md
annovar	Wang et al. (2014)[63]	v 20191024 https://annovar.openbioinformatics.org/en/latest/#annovar-documentation
Lumpy-smoove	Layer et al. (2014)[64]	Lumpy (v0.2.13)-smoove (v0.2.5) https://github.com/brentp/smoove
CNVkit	Talevich et al. (2016)[65]	v0.9.7 https://cnvkit.readthedocs.io/en/stable/
CliffHunteR	In-house software	https://github.com/TranslationalBioinformaticsIGTP/CliffHunteR
Circos	Connors et al. (2009)[66]	v0.69–8 http://circos.ca/
R	https://cran.r-project.org/	4.0.2
Bioconductor	https://bioconductor.org	3.11
CopyNumberPlots	https://doi.org/10.18129/B9.bioc.CopyNumberPlots	v1.4.0 https://bioconductor.org/packages/release/bioc/html/CopyNumberPlots.html

(*Continued on next page*)

Continued

REAGENT or RESOURCE	SOURCE	IDENTIFIER
KaryoploteR	Gel and Serra (2017)[67]	v1.14.0 http://bioconductor.org/packages/release/bioc/html/karyoploteR.html
mutSignatures	Fantini et al. (2020)[68]	v2.1.1 https://cran.r-project.org/web/packages/mutSignatures/index.html
umap	R package	v0.2.7.0 https://cran.r-project.org/web/packages/umap/index.html
Other		
H.sapiens NCBI reference genome GRCh38 with no ALT sequences	NCBI	https://ftp.ncbi.nlm.nih.gov/genomes/all/GCA/000/001/405/GCA_000001405.15_GRCh38/seqs_for_alignment_pipelines.ucsc_ids/GCA_000001405.15_GRCh38_no_alt_analysis_set.fna.gz
COSMIC Mutation Data	The Catalog Of Somatic Mutations In Cancer (COSMIC)	COSMIC v92
ICGC Somatic Mutations	International Cancer Genome Consortium (ICGC)	ICGC Release 28
Structural Variants problematic regions	Chiang et al. (2015)[69]	https://github.com/hall-lab/speedseq/blob/master/annotations/exclude.cnvnator_100bp.GRCh38.20170403.bed
Database of Genomic Variants (DGV)	MacDonald et al. (2014)[70]	https://genome.ucsc.edu/cgi-bin/hgTables

RESOURCE AVAILABILITY

Lead contact

Further information and requests for resources and reagents should be directed to and will be fulfilled by the lead contact, Eduard Serra (eserra@igtp.cat) and Bernat Gel (bgel@igtp.cat).

Materials availability

HS-Sch-2, HS-PSS, NMS-2 and HFF cell lines are commercially available. The other MPNST cell lines used in this study are available from the lead contact upon request.

Data and code availability

- WGS data generated in this paper, SNP-array and WES data of the 8 different MPNST cell lines data previously generated in Magallón-Lorenz et al. (2021),[19] are jointly deposited in a publicly accessible unified repository at Synapse (https://www.synapse.org/#!Synapse:syn22392179/wiki/605466) (https://doi.org/10.7303/syn22392179) and is part of the NF Data Portal (https://nf.synapse.org/).
- The code used in this paper is available on GitHub (https://github.com/TranslationalBioinformaticsIGTP/MPNSTcellLines) and archived on Zenodo (https://doi.org/10.5281/zenodo.7524265). CliffHunteR, an in-house software, is available on GitHub (https://github.com/TranslationalBioinformaticsIGTP/CliffHunteR) and also archived at Zenodo (https://doi.org/10.5281/zenodo.7524539).
- Any additional information required to analyze the data reported in this paper is available from the lead contact upon request.

EXPERIMENTAL MODEL AND SUBJECT DETAILS

MPNST and other established cell lines

In this study, we used a set of MPNST cell lines that contains some of the most frequently used MPNST cell lines together with a few which can be found in known repositories (ATCC, RIKEN). We studied six NF1-associated cell

lines: S462 (RRID:CVCL_1Y70),[55] ST88-14 (RRID:CVCL_8916),[56] NF90-8 (RRID:CVCL_1B47),[57] sNF96.2 (RRID:CVCL_K281),[30] NMS-2 (RRID:CVCL_4662),[58] and T265 (RRID:CVCL_S805),[59] although the latter was discarded as it was found to be misidentified; and three sporadic lines: STS-26T (RRID:CVCL_8917),[43] HS-Sch-2 (RRID:CVCL_8718)[52] and HS-PSS (RRID:CVCL_8717). Table 1 summarizes clinical information about patients and tumors from whom these cell lines were established. Human foreskin fibroblast (HFF-1, ATCC: SCRC-1041) were used as control cells for ploidy analysis. All cell lines were cultured under standard conditions (37°C and 5% CO2) with High Glucose DMEM with sodium pyruvate (Biowest) supplemented with 10% FBS (Biowest) and 2 mM L-glutamine (Gibco). They were passaged and harvested using trypsin-EDTA (Gibco).

METHOD DETAILS

DNA extraction

Total DNA was extracted from cell lines using the Gentra Puregene Kit (Qiagen). DNA was quantified with Nanodrop 1000 spectrophotometer (Thermo Scientific). For SNP array, whole exome and genome sequencing and methylome experiments, a fluorescence-based quantification of DNA was performed either by using the Quant-iT PicoGreen dsDNA Assay (Thermo Fisher Scientific) or a Qubit fluorometer (Life Technologies).

STR profiling

DNA fingerprinting of short tandem repeats (STRs) was conducted for all MPNST cell lines using the AmpFlSTR Identifiler Plus Amplification kit (Applied Biosystems) following the manufacturer's instructions. This kit is based on the analysis of 16 microsatellites, including the nine STRs used by the ATCC.

Calculation of cell ploidy by flow cytometry

About 1–2x10^6 cells from each cell line were trypsinized, washed with PBS, and fixed in ice-cold 70% ethanol for 2h at −20°C. Then, cells were washed with PBS and resuspended in a citrate-phosphate buffer for at least 30 min, up to 2h. Cells were then washed with PBS- 1% FBS and propidium iodide (PI) was added. Cells in PI solution were treated with DNAse-free RNAse A for 30–45 min at 37°C and were ready for flow cytometry analysis. All samples were analyzed on a FACSCanto II flow cytometer (BD Biosciences, San Jose CA) and a total of 10,000 single cells were analyzed for each sample. Aggregated cells were excluded by gating out on a biparametric plot with DNA content pulse area versus width. Data was analyzed using FlowJo software (BD Biosciences, San Jose, CA). HFF-1 were used as 2n control cells.

NF1 mutational status

Sanger sequencing was used to confirm previously described *NF1* constitutional pathogenic variant of the cell lines S462,[55] ST88-14,[71] NF90-8,[72] sNF96.2.[30] In this project, we identified the constitutional *NF1* pathogenic variant of NMS-2 cell line, and the *NF1* pathogenic variants present in the HS-Sch-2 cell line by whole-exome sequencing (see below) which were also confirmed by Sanger sequencing. We used specific primers targeting the mutation region in each case and the BigDye Terminator v.3.1 Sequencing Kit (Applied Biosystems). Sequences were generated with the ABI Prism 3100 Genetic Analyzer (Applied Biosystems) and analyzed with CLC Main Workbench 6 software.

SNP-array analysis

SNP-array data from the different cell lines and tumors was obtained from Magallon-Lorenz et al. (2021).[19] In short, the analysis was performed using Illumina BeadChips (Human660W-Quad, OmniExpress v1.0 and OmniExpress 1.2) at the IGTP High Content Genomics Core Facility. Raw data were processed with Illumina Genome Studio to extract B allele frequency (BAF) and log R ratio (LRR). We used GAP[73] to perform copy-number calling.

Whole-exome sequencing (WES) and whole-genome sequencing (WGS)

WES from the 8 MPNST cell lines was also previously analyzed in Magallón-Lorenz et al. (2021).[19] In short, the exome was captured using Agilent SureSelect Human All Exon V5 kit (Agilent, Santa Clara, CA, US) and sequenced in a HiSeq instrument (Illumina, San Diego, CA, US) at Centro Nacional de Analisis Genomicos (CNAG, Barcelona, Spain) to a median of 165.5 million 100 bp paired-end reads per sample. Sequencing reads were then mapped with BWA-MEM[61] against GRCh38 genome.

The whole genome of two cell lines (ST88–14 and S462) had already been sequenced for Magallón Lorenz et al. (2021).[19] The WGS of the other 6 cell lines were produced for this work at BGI (Shenzhen, China). In short, the 6 libraries were prepared following standard DNBseq protocols, sequenced in a BGISEQ-500 to a median of 881 million 150 bp paired-end reads per sample and mapped with bwa mem against the GRCh38 genome.

Selection of putatively pathogenic somatic variants using WES and WGS

Small nucleotide variants were called with strelka2[62] and annotated with annovar.[63] We filtered strelka2 results from WGS data to select potentially driver variants affecting protein function as follows: we selected exonic and splicing variants and removed all synonymous variants then, we filtered out variants with a population frequency (AF_popmax) higher than 1%, classified as benign in ClinVar,[74] annotated as benign or likely benign in Inter-Var automated,[75] present in 3 or more of the cell lines or classified as pathogenic in more than 5 out of 7 in-silico predictors (SIFT pred,[76] PolyPhen2 HDIV pred,[77] LRT pred, Mutation Taster pred,[78] Mutation Assessor pred,[79] FATHMM pred,[80] CLNSIG[74]) Then, we filtered out those variants with a variant allele frequency (VAF) lower than 0.1 as these variants were deemed as unlikely to be present in the original malignant cell. In addition, we removed non-frameshift deletion or insertion variants present in dbSNP and variants in highly variable genes (*MUC3A*, *MUC5AC*, *OR52E5*, *OR52L1*, *SMPD1*, *PRAMEF* and *LILR*). Finally, we filtered out the variants present in dbSNP except for those included in COSMIC somatic mutations (https://ftp.ncbi.nlm.nih.gov/snp/others/rs_COSMIC.vcf.gz) or the International Cancer Genome Consortium (ICGC) (https://ftp.ncbi.nlm.nih.gov/snp/others/snp_icgc.vcf.gz) variant lists. WES data was processed using the same approach and used to validate the variants identified in WGS data.

Mutational signatures

Raw variants called by Strelka2 in WGS data were also the basis for the mutational signature analysis. Since normal pairs were not available, we applied a series of filters to approximate a somatic callset: we filtered out the variants with a population frequency (AF_popmax) higher than 1%, called in more than one cell line, with a variant allele frequency (VAF) lower than 0.1 and, variants in highly variable genes (*MUC3A*, *MUC5AC*, *OR52E5*, *OR52L1*, *SMPD1*, *PRAMEF* and *LILR*). We also filtered out the variants in dbSNP except for those present in COSMIC and ICGC. We used this call set enriched in somatic variants with the mutSignatures[68] R package to estimate the contribution of each of the thirty COSMIC mutational signatures to the mutational profile of each cell line.

Copy number variants (CNVs) from WGS

We called copy-number alterations from WGS using CNVkit[65] with the recommended settings for WGS data with no matched normal pair (flat reference, difficult region black-list (https://github.com/Boyle-Lab/Blacklist/blob/master/lists/hg38-blacklist.v2.bed.gz), -no-edge option and 1000 bp bins). To obtain the exact copy number profile of each sample we used the threshold method with sample-specific thresholds defined considering the ploidy of each cell line obtained by flow cytometry. Summarized and per-cell line copy number profiles were plotted using the CopyNumberPlots (10.18129/B9.bioc.CopyNumberPlots) and karyoploteR[67] R packages.

Structural variants and detection of fusion genes

We used LUMPY[64] via Smoove (https://github.com/brentp/smoove) as a structural variant (SV) caller with parameters for small cohorts and excluding the problematic regions defined in https://github.com/hall-lab/speedseq/blob/master/annotations/exclude.cnvnator_100bp.GRCh38.20170403.bed.[60] We also used CliffHunteR (https://github.com/TranslationalBioinformaticsIGTP/CliffHunteR), an in-house developed sensitivity-oriented R package for breakpoint detection, and a thorough visual inspection using Integrative Genomic Viewer (IGV)[60] to detect breakpoints affecting tumor suppressor genes associated with MPNSTs (*NF1*, *CDKN2A*, *SUZ12*, *EED*, *TP53*, *PTEN*, *RB1*). To discard germline structural variants, we filtered out SVs present in the Database of Genomic Variants (DGV)[70] and the SVs with the same breakpoints in more than two MPNST cell lines. Inter-chromosomal and intra-chromosomal rearrangements were plotted using circos.[66] We defined the genome region affected by an SV as 1 Mb upstream and downstream of its breakpoints. To investigate the presence of known fusion genes, we crossed the SV breakpoints detected by LUMPY and CliffHunteR with the fusion genes in COSMIC (https://cancer.sanger.ac.uk/census).

DNA methylation and Uni-form Mani-fold Approximation and Projection (UMAP) analysis

DNA methylation profiles were generated using the Infinium MethylationEPIC (850k) BeadChip array (Illumina, San Diego, USA) according to the manufacturer's instructions. The data was processed as previously described.[34] The two-dimensional UMAP[81] embedding was created using the 20,000 most variable CpGs from the DNA methylation profiles of the cell lines and the reference cohorts of soft tissue tumors.[34] The UMAP analysis was performed using the R package umap (version 0.2.7.0) with default parameters except for n_neighbors = 8.

Validation of inter-chromosomal rearrangements

Inter-chromosomal rearrangements detected by LUMPY or CliffHunteR affecting genes commonly altered in MPNST were validated by PCR and Sanger sequencing. PCR primers, annealing temperatures and amplicon lengths are summarized in Data S6.

Fusion gene validation

EML4-ALK v5a fusion gene breakpoints were detected by LUMPY in HS-PSS cell line. EML4-ALK fusion gene was validated by RT-PCR and Sanger sequencing. Total RNA from HS-PSS cell line was extracted using the 16 LEV simplyRNA Purification Kit (Promega) following the manufacturer's instructions in the Maxwell 16 Instrument (Promega). RNA was quantified with a Nanodrop 1000 spectrophotometer (Thermo Scientific). RNA (0.5 μg) was reverse transcribed using the Superscript III reverse transcriptase enzyme (Life technologies) according to the manufacturer's instructions. PCR primers, annealing temperatures, and amplicon lengths were previously described by Takeuchi et al. (2008).[32]

Immunocytochemical analysis

Cells were fixed in 4% paraformaldehyde (PFA) (Santa Cruz Animal Health) in PBS for 15 min at room temperature, permeabilized with 0.1% Triton X-100 in PBS for 10 min, blocked in 10% FBS in PBS for 15 min, and incubated with the primary antibodies, SOX10, SOX9 and S100B overnight at 4°C. Secondary antibodies were Alexa Fluor 488- and Alexa Fluor 568- (Thermo Fisher Scientific). Nuclei were stained with DAPI (Stem Cell Technologies, 1:1000). Slides were mounted with Vectashield (Vector laboratories), and coverslips were secured with polish nail.

Cell viability assay

Compounds (Selumetinib and JQ1) were prepared at 10 mmol/L in DMSO, and were diluted 5-fold from 40 μmol/L to 0.064 μmol/L, with DMSO. Cells were seeded in 96-well plates (Corning) at a density between 2.000 and 10.000 cells/well. 24 h later, drugs were added in three replicates. After 48 h of incubation with the drugs, cell viability was analyzed using MTT assay (Sigma-Aldrich), following manufacturer's instructions. The percentage of cell viability was calculated by normalizing the values to DMSO control cells.

QUANTIFICATION AND STATISTICAL ANALYSIS

Bioinformatic analysis is thoroughly described in the method details section, including the exact software and statistical methods used. The meaning of value of n, and/or dispersion and precision measure (SEM) can be found in the Figure 5 legends.

Molecular Oncology

FEBS PRESS science publishing by scientists

Expanding a precision medicine platform for malignant peripheral nerve sheath tumors: New patient-derived orthotopic xenografts, cell lines and tumor entities

Edgar Creus-Bachiller[1,2], Juana Fernández-Rodríguez[1,2,3,4], Miriam Magallón-Lorenz[5], Sara Ortega-Bertran[1,2], Susana Navas-Rutete[1], Cleofe Romagosa[6], Tulio M. Silva[6], Maria Pané[7], Anna Estival[8], Diana Perez Sidelnikova[9], Mireia Morell[1,2,3], Helena Mazuelas[5], Meritxell Carrió[5], Tereza Lausová[10,11], David Reuss[10,11], Bernat Gel[5], Alberto Villanueva[2,12], Eduard Serra[4,5] and Conxi Lázaro[1,2,4]

1 Hereditary Cancer Program, Catalan Institute of Oncology, ICO-IDIBELL, Hospitalet de Llobregat, Barcelona, Spain
2 Program in Molecular Mechanisms and Experimental Therapy in Oncology (Oncobell), IDIBELL, Hospitalet de Llobregat, Barcelona, Spain
3 Mouse Lab, IDIBELL, Hospitalet de Llobregat, Barcelona, Spain
4 Centro de Investigación Biomédica en Red de Cáncer (CIBERONC), Madrid, Spain
5 Hereditary Cancer Group, Germans Trias i Pujol Research Institute (IGTP), Barcelona, Spain
6 Department of Pathology, Hospital Vall d'Hebron, Barcelona, Spain
7 Department of Pathology, HUB-IDIBELL, L'Hospitalet de Llobregat, Barcelona, Spain
8 Department of Medical Oncology, Catalan Institute of Oncology, Barcelona, Spain
9 Plastic Surgery Service HUB-IDIBELL, L'Hospitalet de Llobregat, Barcelona, Spain
10 Department of Neuropathology, Institute of Pathology, Heidelberg University Hospital, Heidelberg, Germany
11 Clinical Cooperation Unit Neuropathology, German Cancer Research Center (DKFZ), German Consortium for Translational Cancer Research (DKTK), Heidelberg, Germany
12 Procure Program, Catalan Institute of Oncology, Barcelona, Spain

Keywords
cellular models; MPNST; NF1; PDOX; treatment response; tumor entities

Correspondence
Conxi Lázaro, Hereditary Cancer Program, Catalan Institute of Oncology, IDIBELL and CIBERONC. Av. Gran Via 199-203, Hospitalet de Llobregat, Barcelona 08908, Spain
Tel: (+34) 93 2607145.
E-mail: clazaro@iconcologia.net

Eduard Serra, Hereditary Cancer Group, Germans Trias i Pujol Research Institute (IGTP), Can Ruti Biomedical Campus, Carretera de Can Ruti, Camí de les Escoles, Badalona, Barcelona 08916, Spain
Tel: (+34) 93 554 3067
E-mail: eserra@igtp.cat

Malignant peripheral nerve sheath tumors (MPNSTs) are aggressive soft-tissue sarcomas with a poor survival rate, presenting either sporadically or in the context of neurofibromatosis type 1 (NF1). The histological diagnosis of MPNSTs can be challenging, with different tumors exhibiting great histological and marker expression overlap. This heterogeneity could be partly responsible for the observed disparity in treatment response due to the inherent diversity of the preclinical models used. For several years, our group has been generating a large patient-derived orthotopic xenograft (PDOX) MPNST platform for identifying new precision medicine treatments. Herein, we describe the expansion of this platform using six primary tumors clinically diagnosed as MPNSTs, from which we obtained six additional PDOX mouse models and three cell lines, thus generating three pairs of *in vitro–in vivo* models. We extensively characterized these tumors and derived preclinical models, including genomic, epigenomic, and histological analyses. Tumors were reclassified after these analyses: three remained as MPNSTs (two being classic MPNSTs), one was a melanoma, another was a neurotrophic tyrosine receptor kinase (*NTRK*)-rearranged spindle cell neoplasm, and, finally, the last was an unclassifiable tumor bearing neurofibromin-2 (*NF2*) inactivation, a neuroblastoma

Abbreviations
ANNUBP, Atypical neurofibromatous with unknown biological potential; BAF, Biallelic frequency; CI, Combination Index; CN, Copy number; GAP, Genome Alteration Print; IC50, Half-maximal inhibitory dilution; ICGC, International Cancer Genome Consortium; IGV, Integrative Genome Viewer; LOH, Loss of heterozygosity; LRR, Log R ratio; MPNST, Malignant peripheral nerve sheath tumor; NF1, Neurofibromatosis type 1; PDOX, Patient-derived orthotopic xenograft; PDT, Population doubling time; PRC2, Polycomb repressive complex 2; SNV, Single nucleotide variant; SV, Structural variant; TSG, Tumor suppressor gene; UMAP, Uniform Manifold Approximation and Projection; VAF, Variant allele frequency; WES, Whole exome sequencing; WGS, Whole genome sequencing; WT, wild-type.

Edgar Creus-Bachiller and Juana Fernández-Rodríguez contributed equally to this work
Eduard Serra and Conxi Lázaro should be considered joint corresponding authors

(Received 16 June 2023, revised 7 August 2023, accepted 4 October 2023)

doi:10.1002/1878-0261.13534

RAS viral oncogene homolog (*NRAS*) oncogenic mutation, and a SWI/SNF-related matrix-associated actin-dependent regulator of chromatin (*SMARCA4*) heterozygous truncated variant. New cell lines and PDOXs faithfully recapitulated histology, marker expression, and genomic characteristics of the primary tumors. The diversity in tumor identity and their specific associated genomic alterations impacted treatment responses obtained when we used the new cell lines for testing compounds against known altered pathways in MPNSTs. In summary, we present here an extension of our MPNST precision medicine platform, with new PDOXs and cell lines, including tumor entities confounded as MPNSTs in a real clinical scenario. This platform may constitute a useful tool for obtaining correct preclinical information to guide MPNST clinical trials.

1. Introduction

Malignant peripheral nerve sheath tumors (MPNSTs) account for about 3–10% of all soft-tissue sarcomas [1]; half of them occur in patients with neurofibromatosis type 1 (NF1), an autosomal dominant genetic disorder with an incidence at birth of 1 : 2000–1 : 3000 [2,3]. The lifetime risk of developing an MPNST in NF1 patients is around 8–15% [4,5], constituting the leading cause of mortality in these patients [4,6]. In the NF1 clinical context, MPNSTs usually arise from preexisting benign plexiform neurofibromas (pNF), which can undergo premalignant transformation into atypical neurofibromas (ANNUBPs) before MPNST generation. ANNUBPs, in addition to *NF1* loss, harbor *CDKN2A* inactivation as a common genomic loss in the progression toward MPNSTs [7,8]. Malignant peripheral nerve sheath tumor cells contain highly rearranged and hyperploid genomes with a low mutation burden and few recurrent alterations [9]. A core MPNST tumor suppressor gene (TSG) mutational pattern consists of the recurrent inactivation of *NF1*, *CDKN2A*, and components of the polycomb repressive complex 2 (PRC2; *SUZ12* and *EED*); less frequently, *TP53* is also inactivated [10-12]. Interestingly, some drugs can target these pathways, such as MEK inhibitors (*NF1* loss), CDK4/CDK6 inhibitors (loss of *CDKN2A*), and BRD4 inhibitors (PRC2 loss of function), and some have been tested in preclinical [13,14] or clinical [15-17] contexts. However, clinical trials of typical cytotoxic drugs have shown response rates ranging from 18 to 44%, indicating that drug combinations will be required for efficient treatment [18]. Doxorubicin and ifosfamide have been used as the standard chemotherapy regimen for MPNSTs; however, a 10-year institutional review found no correlation between chemotherapy and patient survival [19]. Currently, complete surgical excision with clear margins is the standard treatment option for local MPNST disease [20,21]; nevertheless, its success is limited by tumor infiltration, resulting in a high relapse rate [21]. In addition, the diagnosis of MPNSTs may be challenging, especially in the sporadic context, which may contribute to low efficacy of MPNST treatments. Nowadays, specific histological criteria for MPNST diagnosis are lacking [22,23], and other tumor entities share histological characteristics with MPNSTs. The more usual MPNST histology includes the presence of spindle cells with a fascicular growth pattern and areas with high hypercellularity, sometimes called a 'classic' MPNST [24]. However, in many cases, MPNST histology may differ from this usual pattern.

In vitro and *in vivo* models are paramount to studying MPNST biology and testing new therapeutic approaches. At least 44 NF1 or sporadic MPNST cell lines from primary tumors, metastases, or mice tumors have been described (Cellosaurus version 45, updated in March 2023) [25,26]. Several *in vivo* tumor models have been developed to study MPNSTs, including xenograft models of patient-derived cells injected subcutaneously or orthotopically [25], genetically engineered mouse models (reviewed in [27]), and patient-derived xenografts [28-31]. Our laboratory previously reported the establishment and validation of four MPNST patient-derived orthotopic xenograft (PDOX) mouse models [32]. We also demonstrated that PDOX mouse models closely resemble primary tumors at different levels, histologically and molecularly [32].

Over several years, our group has collected a total of 43 primary, relapsed, and metastatic tumors clinically diagnosed as MPNSTs from NF1 and sporadic patients and have generated PDOX models from most of them for precision medicine preclinical studies and the discovery of new therapeutic treatments [33,34]. In this work, we enlarge our preclinical platform by characterizing, at the molecular and histological level, six primary tumors diagnosed as MPNSTs by clinical

pathology. Furthermore, we describe the establishment of six PDOX models and three cell lines directly derived from primary tumors, generating three cell line-PDOX model pairs from the same tumors. Finally, the established cell lines were used to test different known MPNST drugs, evidencing that both genomic status and misidentification of tumor entities are at least partially responsible for the observed heterogeneity in MPNST treatment response.

2. Materials and methods

2.1. Patients, animal, and cell models

2.1.1. Primary tumor acquisition and processing

Six primary tumors from different unrelated patients were identified and removed from January 2011 to March 2016 at different hospitals from the Barcelona area (Bellvitge, Vall Hebron, and Germans Trias i Pujol). Clinical data from the patients are summarized in Table S1. Five of the patients did not receive any treatment before surgery. Only one patient (SP-06) received neoadjuvant radiotherapy. After surgery, a piece of each tumor was stored in DMEM culture medium supplemented with 10% fetal bovine serum (FBS; Gibco, Waltham, MA, USA) at room temperature (RT) before being sent to our laboratory. Small pieces of each tumor were directly frozen in liquid nitrogen for DNA, RNA, and protein extraction; other fragments were frozen in FBS with 10% DMSO for cell culture establishment and mouse engraftment. Written informed consent was obtained from all subjects, and the study received IDIBELL IRB (#PR213/13) approval. The experimental protocols followed the Declaration of Helsinki.

2.1.2. Animal care conditions

Six-week-old male Athymic Nude-Foxn1^{nu} (Envigo, Indianápolis, IN, USA) mice weighing 18 to 22 g were used in this study. Animals were housed in a sterile environment, in cages with autoclaved bedding, food, and water. The mice were maintained on a daily 12-h light/12-h dark cycle.

2.1.3. Human tumor engraftment for PDOX generation and perpetuation

Fresh surgical specimens were implanted in athymic nude mice, as described previously [32]. Briefly, fresh surgical specimens were minced into small fragments 2–3 mm^3 in size, grafted close to the sciatic nerve, and grown surrounding the epineurium. The MPNST-PDOX procedure was approved by the campus Animal Ethics Committee and complied with AAALAC (Association for Assessment and Accreditation of Laboratory Animal Care International) procedures.

2.1.4. Establishment of cell lines from primary human tumors

Fresh tumors were minced into small fragments and digested with 100 U·mL^{-1} collagenase (C0130; Sigma-Aldrich, Burlington, MA, USA) and 1 U·mL^{-1} dispase (LS02100; Worthington Corporations, Lakewood, NJ, USA) in DMEM medium supplemented with 10% FBS and 100 µg·mL^{-1} Penicillin/Streptomycin (Bio-West, Nuaillé, France). After 18 h of incubation, digested tissue was filtered through a 40 µm filter to seed single cells in 6-well plates. Cell lines were initially maintained for 10 passages at 37 °C and 10% CO_2. Subsequently, cells were cultured at 5% CO_2. In this work, the following established cell lines were also used: NF1-derived 88-14 (RRID: CVCL_8916) [35] and S462 (RRID: CVCL_1Y70) [36], and sporadic STS-26T (RRID: CVCL_8917) [37]. All details regarding these three cell lines, as well as the laboratories originating and providing these cell lines, are described in Magallón-Lorenz et al. [38]. Cell lines were validated as *Mycoplasma* negative and were retested every 2 months. Cell lines have been authenticated in the past 3 years by performing short tandem repeat (STR) profile authentication.

2.2. Tumor-derived cell lines characterization

2.2.1. Morphological analysis

Cells were plated in 10 cm plates and grown to 30% or 90% confluency to observe their morphology at low and high confluence, respectively, using a Leica DM IL LED optical microscope through Leica Microsystems' contrast phase mode (Leica Biosystems, Deer Park, IL, USA).

2.2.2. STR authentication

DNA fingerprints were obtained using the AmpFLSTR Identifiler Plus PCR Amplification kit (Applied Biosystems, Waltham, MA, USA), according to the manufacturer's protocol. The combination of markers used is consistent with worldwide recommendations for identity testing. The kit amplifies 15 tetranucleotide STR loci and the gender-determining marker, amelogenin, in a single PCR amplification.

2.2.3. Fluorescence immunostaining

Cells were plated in 12-well Corning® (Corning, NY, USA) plates using coverslips (12 mm Ø) and fixed for 15 min in 4% paraformaldehyde when highly confluent. Then, cells were permeabilized in PBS 1x-0.1% Triton and blocked using PBS 1x-10% Goat serum for 30 min. Primary antibodies SOX9 (1 : 100, ab76997; Abcam, Cambridge, UK), smooth muscle actin (SMA, 1 : 100, RB-9010-R7; ThermoFisher Scientific, Waltham, MA, USA), EGFR (1 : 50, ab32562; Abcam), p75 (1 : 100, AB-N07; ATSbio, Carlsbad, CA), and S100B (1 : 1000, Z031129; Dako, Glostrup, Denmark) were diluted in PBS-1% Goat serum and incubated overnight at 4 °C. Secondary antibodies Alexa Fluor 488 goat anti-mouse (1 : 1000, A11029; Invitrogen, Waltham, MA, USA), Alexa Fluor 488 donkey anti-rabbit (1 : 1000, 711-545-152; Jackson ImmunoResearch, Philadelphia, PA, USA), and Alexa Fluor 568 goat anti-rabbit (1 : 1000, A11036; Invitrogen) were diluted in PBS-10% Goat serum and incubated for 1 h at RT. After washing three times with PBS 1x, DAPI diluted in PBS (1 : 1000, 62248; ThermoFisher Scientific) was added for 10 min and then washed three times, and finally, coverslips were mounted in ImmuMount (9990402; ThermoFisher Scientific). Images were acquired using a Nikon Eclipse 80i fluorescence microscope with NIS-Elements Microscope Imaging Software and analyzed using ImageJ Fiji software (Lexington, KY, USA).

2.2.4. Cell cycle

A total of 2.5×10^5 cells from a 50–60% confluent plate were fixed using 70% cold-ethanol and dyed with a mixture of PBS-1% FBS, propidium iodide (0.0625 $mg{\cdot}mL^{-1}$; Sigma-Aldrich), and RNAse A (10 $\mu g{\cdot}mL^{-1}$; Sigma-Aldrich) for 30–45 min at 37 °C. Samples were analyzed via a FACSCanto II (BD Bioscience, Franklin Lakes, NJ, USA) flow cytometer. Each cell line was analyzed in duplicate.

2.2.5. Growth kinetics and migration properties

2.2.5.1. Population doubling time

Population doubling times (PDTs) of cell lines were estimated using two different methodologies: dyeing cells with Trypan Blue (Sigma-Aldrich) to count living cells using an optical microscope or by using a colorimetric cell viability assay [3-(4,5-dimethylthiazol-2-yl)-2,5-diphenyl-tetrazolium bromide] (MTT). In the first approach, cell lines were seeded in triplicate in 6-well plates to reach 100% confluence after 7–8 days of culture. Living cells were counted every 24 h using a Fast Reader 102® (Biosigma, Cona, Italy). Population doubling time was calculated by the following formula: $PDT = (t_2 - t_1)/3.32x (\log n_2 - \log n_1)$, where t = time in days and n = number of cells. In the second approach using MTT, cell lines were seeded in six replicates in 96-well plates to reach 100% confluence after 7–8 days of culture. The MTT assay was performed every 24 h by adding 0.5 $mg{\cdot}mL^{-1}$ MTT (M2128; Sigma-Aldrich) to each well. After 2 h of incubation, the formazan precipitate generated by cells was diluted using a 1 : 3 solution of Glycine buffer (0.1 M NaCl and 0.1 M Glycine) and DMSO to each well. Absorbance was measured at 560 nm in a PowerWave XS microplate spectrophotometer (Biotek, Winooski, VT, USA), and PDTs were calculated using GraphPad Prism 6 (La Jolla, CA, USA).

2.2.5.2. Percentage of proliferating cells

Cells were seeded in a 12-well plate in duplicate. When cells reached 50–60% confluence, they were trypsinized and treated according to the Click-iT® EdU Flow Cytometry Assay Kit (C10425; ThermoFisher Scientific) manufacturer's instructions. A total of 20 000 events were analyzed from each sample using a FACS Canto II cytometer and ModFit LT V.3.3.11 software to obtain the percentage of proliferating cells.

2.2.5.3. Wound healing assay

Cells were seeded in culture inserts (80209; ibidi, Gräfelfing, Germany) to reach confluence after 24 h, and then, culture inserts were removed. Pictures were taken at 0, 4, 8, 12, and 24 h after removal using an optical microscope. Each cell line was seeded in triplicate, and analyses were performed using TScratch software [39]. Proliferation was not inhibited either pharmacologically or with serum deprivation.

2.2.5.4. Colony formation assay

Two-dimensional colony formation assay. A total of 300 cells/well were seeded in 12-well plates in duplicate. After 10 days, cells were fixed with methanol for 10 min and then stained with 0.1% crystal violet for 10 more minutes.

Three-dimensional colony formation assay. First, we plated a bottom layer of agar in 6-well plates, consisting of 1 mL of 1.6% SeaPlaque agar in DMEM, allowing it to solidify at RT for 5 min. Then, we plated the upper layer of 0.8% SeaPlaque agar in

DMEM containing 20 000 cells·mL^{-1}. Finally, we added 1 mL of DMEM supplemented with 10% FBS and 1% Penicillin/Streptomycin. After culturing for 14 days, cells were fixed and stained with a solution of 0.1% crystal violet in paraformaldehyde for 1 h. The cell lines were seeded in duplicate. Pictures of the colonies were taken using an optical microscope.

2.2.6. *In vivo* tumorigenicity

A total of 1×10^7 cells resuspended in 200 µL of PBS-Matrigel (ratio 1 : 1) were injected intramuscularly near the sciatic nerve of 6-week-old female athymic nude mice. Animals were monitored weekly, and when tumors reached 1 cm in diameter, they were resected. If tumors did not reach this size, they were resected after 3 months. The study received IDIBELL Animal Ethics Experimentation Committee (CEEA-IDIBELL) (#9111) approval.

2.3. Immunohistochemistry marker analyses

Paraffin-embedded tissues of human primary and passage one PDOX tumor sections (3 µm) were deparaffinized and gradually rehydrated. Endogenous peroxidases were blocked by incubation with hydrogen peroxide (H_2O_2 3% for 20 min), and antigen retrieval was performed by heating tissue sections for 20 min in citrate buffer (pH = 6). Blocking was performed by incubation for 20 min with 10% goat serum. The primary antibodies Vimentin (1 : 200, 180052; Life Technologies, Carlsbad, CA, USA), SOX10 (1 : 50, 383R-14; Cell Marque, Rocklin, CA, USA), H3K27me3 (1 : 200, 9733S; Cell Signalling, Danvers, MA, USA), CD34 (IR632; DAKO), S100B (1 : 300, Z0311; DAKO), and Ki-67 (1 : 10, M7240; DAKO) were incubated overnight at 4 °C following the manufacturer's guidelines. The secondary HPRT-conjugated antibody (EnVision; DAKO) was incubated at RT for 30 min. Finally, staining was conducted using diaminobenzidine (DAB; DAKO) for 10 min; nuclei were counterstained with hematoxylin. Images were taken using a Nikon Eclipse 80i vertical microscope. For immunohistochemistry of cell lines, a cell pellet was generated and incubated with equal volumes of human plasma and thrombospondin (Grifols, Barcelona, Spain), to generate a cell clot that could be embedded in paraffin.

2.4. Genomic analyses

Table S2 summarizes the different genomic analyses performed in the patient tumors and the PDOX and cell line models.

2.4.1. DNA and RNA extraction

The GentraPuregene Kit (Qiagen, Hilden, Germany) was used for DNA extraction from frozen human and PDOX tumors, according to the manufacturer's recommendations, after homogenization using TissueLyser II (Qiagen). DNA quality and quantity were assessed by agarose gel, NanoDrop, and Qubit.

For RNA extraction, Direct-zol RNA MiniPrep (R2050; Zymo Research, Irvine, CA, USA) and TRI reagent (R2050-1-50; Zymo Research) were used according to the manufacturer's protocol. RNA quality and quantity (RNA Integrity Number) were assessed by NanoDrop and 4200 TapeStation (Agilent Technologies, Santa Clara, CA, USA).

2.4.2. SNP array

SNP array was performed using BeadChip technology from Illumina (San Diego, CA, USA). All samples (primary tumors, PDOX tumors, and cell lines) were analyzed using HumanOmniExpress-24v1-1 (713 599 SNPs), except for those previously described in Castellsagué et al., [32], which were analyzed using Illumina OmniExpress for the SP-01 primary tumor and Illumina Omni1S for the SP-01 orthotopic xenograft tumor. Raw data were processed with Illumina Genome Studio to extract B allele frequency (BAF) and log R ratio (LRR) as described previously [32]. We used Genome Alteration Print (GAP) [40] to obtain the copy number (CN) profiles of the samples.

2.4.3. Whole exome sequencing (WES) and whole genome sequencing (WGS)

Whole exome sequencing was performed in primary tumors, the patient's constitutional DNA (except for SP-06), PDOX tumors at passage one, and cell lines (maximum passage 10). We used the Agilent SureSelect Human All Exon V5 kit (Agilent) according to the manufacturer's instructions. Paired-end sequencing was performed on a HiSeq2000 instrument (Illumina) using 150-base reads, and the analysis was performed as described previously [32].

The WGS, only performed in the primary tumors, was produced at BGI (Shenzhen, China). In short, the libraries were prepared following standard DNBseq protocols, sequenced in a BGISEQ-500 to a median of 881 million 150-bp paired-end reads per sample, and mapped with BWA-MEM [41] against the GRCh38 genome.

2.4.4. Selection of somatic variants using WES and WGS

Whole exome sequencing and WGS data were processed as described in [38]. In summary, small nucleotide variants were called with Strelka2 [42] and annotated with annovar [43]. We ran the somatic calling in those samples (4 individuals) where we had tumor-normal pair, and the germline calling in all samples followed by filters to enrich in somatic variants. For the somatic variant calling of Strelka2, we followed the developers' recommendations; thus, we first ran the Manta SV and indel caller [44] on the same set of samples, and then, we supplied Manta's candidate indels as input to Strelka2 somatic calling. We used these results to validate the ones obtained by the germline calling.

After running the Strelka2 germline calling in all samples (tumor and normal), we filtered Strelka2 results from WGS data to select potential driver variants affecting protein function by selecting exonic and splicing variants. Then, we filtered out variants with a population frequency (AF_popmax) higher than 1%, classified as benign in ClinVar [45], annotated as benign or likely benign in InterVar automated [46], present in more than 1 individual or classified as pathogenic in less than five out of seven in silico predictors (SIFT pred [47], PolyPhen2 HDIV pred [48], LRT pred, Mutation Taster pred [49], Mutation Assessor pred [49], FATHMM pred [50], and CLNSIG [45]). Then, we filtered out those variants with a variant allele frequency (VAF) lower than 0.1. In addition, we removed nonframeshift deletion or insertion variants present in dbSNP and variants in highly variable genes (*MUC3A*, *MUC5AC*, *OR52E5*, *OR52L1*, *SMPD1*, *PRAMEF*, and *LILR*). Finally, we filtered out the variants present in dbSNP except for those included in the Catalogue of Somatic Mutations in Cancer (COSMIC) (https://ftp.ncbi.nlm.nih.gov/snp/others/rs_COSMIC.vcf.gz) or the International Cancer Genome Consortium (ICGC) (https://ftp.ncbi.nlm.nih.gov/snp/others/snp_icgc.vcf.gz) variant lists. Whole exome sequencing data were processed using the same approach and used to validate the variants identified in WGS data. Moreover, we used Integrative Genomic Viewer (IGV) [51] for performing a manual inspection of TSGs associated with MPNSTs.

2.4.5. Mutational signatures

As previously described in Magallón-Lorenz et al. [38], raw variants called by Strelka2 in WGS data were used for the mutational signature analysis. Since normal pairs were not available, we applied a series of filters to approximate a somatic callset: we filtered out the variants with a population frequency (AF_popmax) higher than 1%, called in more than one cell line, with a VAF lower than 0.1, and variants in highly variable genes (*MUC3A*, *MUC5AC*, *OR52E5*, *OR52L1*, *SMPD1*, *PRAMEF*, and *LILR*). We also filtered out the variants in dbSNP except for those present in COSMIC and ICGC. We used this call set enriched in somatic variants with the mutSignatures (42) R package to estimate the contribution of each of the 30 COSMIC mutational signatures to the mutational profile of each cell line.

2.4.6. Structural variants detection from WGS

The structural variants (SVs) detection methodology was described previously by Magallón-Lorenz et al. [38]. LUMPY (41) was used via Smoove (https://github.com/brentp/smoove) as a SV caller with parameters for small cohorts and excluding the problematic regions defined in https://github.com/hall-lab/speedseq/blob/master/annotations/exclude.cnvnator_100bp.GRCh38.20170403.bed. We also used CliffHunteR (https://github.com/TranslationalBioinformaticsIGTP/CliffHunteR), an in-house developed sensitivity-oriented R package for breakpoint detection, and a thorough visual inspection using IGV to detect breakpoints affecting TSGs associated with MPNSTs (*NF1*, *CDKN2A*, *SUZ12*, *EED*, and *TP53*). To discard germline SVs, we filtered out SVs present in the Database of Genomic Variants (DGV) and the SVs with the same breakpoints in more than two tumors.

2.4.7. RNA sequencing

RNA-seq libraries were established and sequencing of primary tumors was performed at Centro Nacional de Análisis Genómicos (CNAG, Barcelona, Spain), pooling three samples per lane (paired-end, 2 × 100).

2.4.8. Fusion-gene detection from RNA-seq

We applied the default parameters of STAR-Fusion for the detection of fusion genes from RNA-seq. After obtaining the results, we performed bibliographic research for looking for potential fusion genes associated with disease.

2.4.9. Methylome profile and Uniform Manifold Approximation and Projection (UMAP) analysis

DNA methylation profiles were generated using the Infinium MethylationEPIC (850 k) BeadChip array

(Illumina) according to the manufacturer's instructions. The data were processed as described previously [52]. The two-dimensional UMAP embedding was created using the 20 000 most variable CpGs from the DNA methylation profiles of the cell lines and the reference cohorts of soft-tissue tumors 52. The UMAP analysis was performed using the R package umap (version 0.2.7.0) with default parameters except for *n*_neighbors = 8.

2.5. *In vitro* drug testing

The half-maximal inhibitory concentration (IC_{50}) of JQ1, MLN8237 (Alisertib), and PD-0325901 (Mirdametinib; Selleckchem, Houston, TX, USA) was calculated for each cell line, as we described previously [34]. Compounds (stock at 10 mM) were added in three replicates and subsequently diluted fivefold from 100 μM to 0.16 μM. The IC_{50} was calculated using GraphPad Prism Version 6. For combination assays, the following previously described protocols were performed [34]. Combination Index (CI) values for the combinations were calculated using CompuSyn software, based on Chou-Talalay calculations [53]. When CI was < 0.9 at high values of fraction affected of cells (fraction of cell death by treatments), we labeled the combination as synergistic [54].

3. Results

3.1. Expansion of the MPNST platform: From genuine MPNSTs to other clinically misclassified tumor entities

Six primary tumors (sporadic tumors SP-01, SP-04, SP-05, and SP-06; and NF1-derived NF1-08 and NF1-09) were identified and removed at the Bellvitge, Vall d'Hebron, and Germans Trias i Pujol hospitals. After surgery, the tumors were sent to the respective pathology services, analyzed following standard methodologies, and classified as MPNSTs, following the WHO classification of soft-tissue tumors and bone. In parallel, part of each tumor was sent to our laboratory and split for DNA extraction, PDOX engraftment in nude mice, and cell culture expansion (see Section 2).

To characterize the primary tumors, genomic, epigenomic, and histologic analyses were performed. We used WGS and WES to analyze the status of the most recurrent inactivated TSGs in MPNSTs: *NF1*, *CDKN2A*, and *SUZ12* and *EED* (from PRC2). In addition, we analyzed the status of genes unrelated to MPNSTs (Fig. 1A, Table 1). Only SP-04 and NF1-08 have classic MPNST genetic features like *NF1*, *CDKN2A*, and PRC2 inactivated [10-12]. NF1-09 presents MPNST genetic features such as the inactivation of *NF1*, *CDKN2A*, and also *TP53*, but with PRC2 active and an activating mutation in the *PIK3CA* gene. The other three sporadic tumor features distanced them further from classic MPNSTs: SP-01 only has *NF1* mutated, and SP-05 and SP-06 have only *CDKN2A* inactivated. Moreover, the SP-01 tumor presents an activating mutation in the *ERBB4* gene, which is described as a driver of *BRAF* wild-type (WT) melanomas [55,56], and SP-06 presents an oncogenic *NRAS* mutation, inactivation of *NF2*, and a truncating mutation in *SMARCA4* (in one allele; Fig. 1A, Table 1).

The mutational frequency and signatures of all tumors except SP-06 (in which we only performed WES) were analyzed using WGS. We observed that tumor SP-01 exhibited at least a ninefold higher mutation number compared with other primary tumors, mainly containing the SBS7 COSMIC mutational signature, characteristic of skin cancers [57]. The other tumors presented low mutation burden and no specific COSMIC signatures besides clock-like signature 5, which appears in most tumor types [57] (Fig. 1B).

Moreover, the methylome profile of the three cell lines obtained from tumors SP-01, NF1-08, and NF1-09 was compared with other sarcomas. Figure 1C presents a methylome profile classifier of several sarcomas using a UMAP plot [52]. Taking a closer view of the MPNST region, SP-01's methylome profile matched that of melanoma (like STS-26T, which was recently reclassified from an MPNST to a melanoma cell line [38]), tumor NF1-08 clustered with the classic MPNST group (as for ST88-14 and S462 cell lines), and NF1-09 clustered in the rather catchall MPNST-like sarcoma group (Fig. 1D, Table 1). This group of sarcomas is characterized by bearing an active PRC2, which generates a different methylation pattern compared with PRC2-inactivated tumors [58].

Finally, we analyzed several markers routinely clinically used for MPNST diagnosis: S100B and SOX10 (cell identity markers of the peripheral nervous system), H3K27me3 (epigenetic marker of PRC2 dysfunction), Vimentin (mesenchymal cell marker), Ki-67 (proliferation cell marker), and CD34 (fibroblast and endothelial marker). Only tumor SP-01 presented strong dual staining for S100B and SOX10, contrary to classic MPNSTs that present negative or focal expression [59], like S100B expression in the SP-04 tumor. We found a lack of H3K27me3 in four tumors, including SP-01 and SP-05 (Fig. 1E, Table 1), which are WT for *SUZ12* or *EED* (Fig. 1A), implying that PRC2 inactivation may be due to other genetic alterations unrelated to MPNSTs [12]. All samples were

positive for the soft-tissue tumor marker Vimentin, as expected, and the CD34 endothelial cell marker was negative in tumor cells, only marking vessels (Fig. S1).

Taken together, only SP-04 and NF1-08 fulfilled most genetic features of classic MPNSTs and evidence shows that three primary tumors may be misdiagnosed as MPNSTs (Table 1). Tumor suppressor gene profile inactivation, mutational burden and signatures, methylome profile classification, and positive expression of neural crest markers may indicate that SP-01 should be reclassified as a melanoma. In the case of tumors SP-05 and SP-06, besides the TSG inactivation pattern,

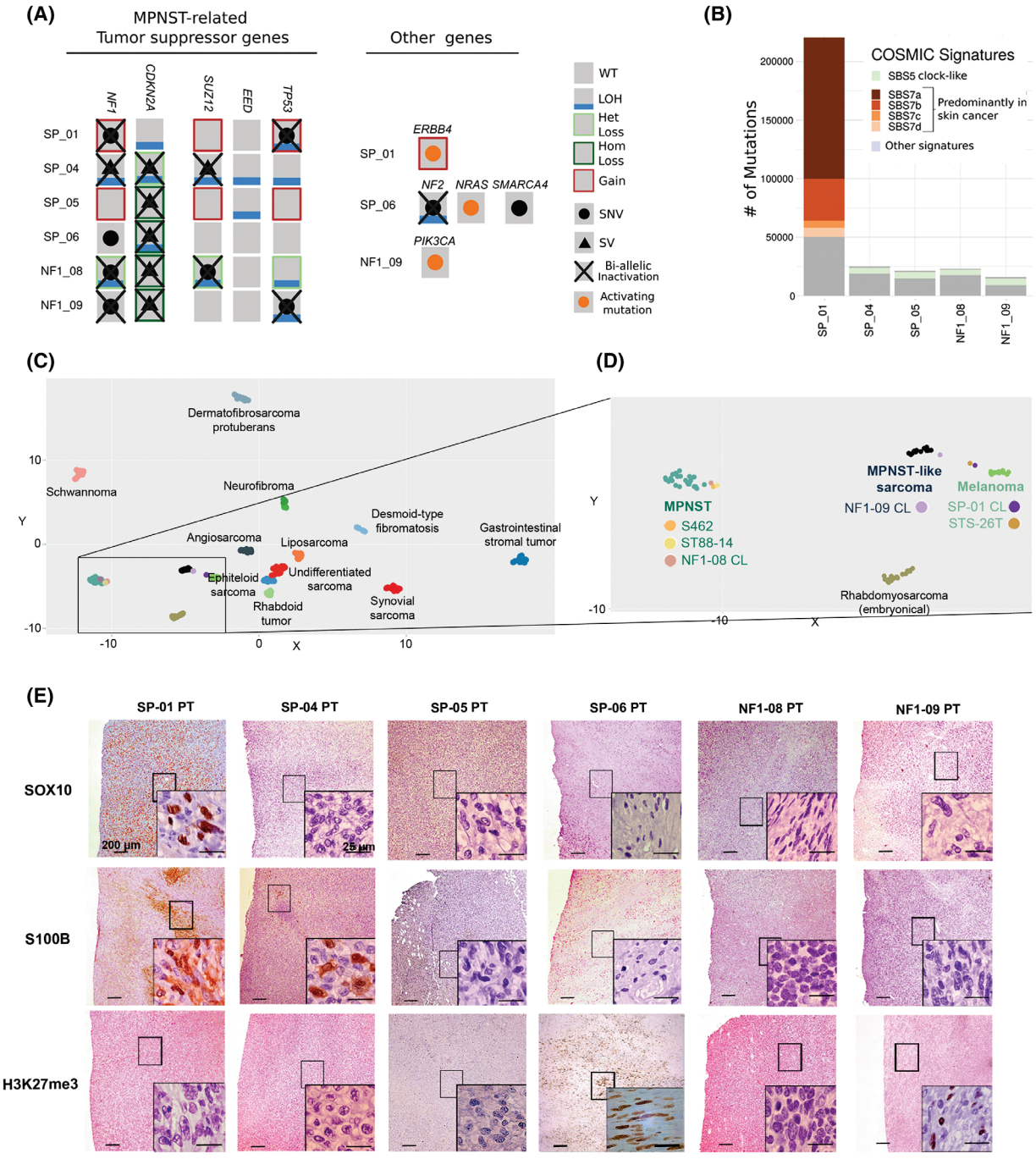

Fig. 1. Genomic, epigenomic, and histological characterization of primary tumors and diagnostic validation. (A) Genetic status of the most recurrent inactivated TSGs in MPNSTs using WGS and genes related to other tumor entities. A gray square represents a WT gene; a blue line indicates the presence of LOH; a black dot represents a single nucleotide variant (SNV) affecting the gene; an orange dot represents an activating SNV in the gene; a black triangle indicates a SV; a red square is for CN gain; a light green square is for heterozygous CN loss (Het loss) of the gene, and dark green is for homozygous CN loss (Hom loss); the complete biallelic inactivation of a gene is represented by a black cross. SP-06 tumor TSGs status was obtained using WES and SNP array. (B) Number of somatic SNVs and contribution of COSMIC mutational signatures in primary MPNSTs. SP-06 was not included as WGS was not performed on this tumor ($n = 1$). (C) UMAP plot representing methylome classification of multiple sarcomas. Each dot represents a tumor sample and each color a different sarcoma type [52]. (D) Inset amplification of the UMAP plot, showing the classification of the methylome profile of three cell lines derived from our primary tumors (SP-01, NF1-08, and NF1-09) and three other established control cell lines (S462, ST88-14, and STS-26T). The MPNST group is represented in blue, the MPNST-like group in black, and melanomas in green. Each cell line is represented by a unique color. CL: cell line. (E) Representative immunostaining of SOX10, S100B, and H3K27me3 in the patient's primary tumors ($n = 1$). PT: Primary tumor. Original magnifications are 40× and 600× in the inset magnified view, and scale bars are 200 μm and 25 μm, respectively.

they presented specific genetic features that do not correlate with MPNSTs. SP-05 tumor bore the fusion-gene *LMNA-NTRK1*, which was identified using WGS and confirmed by RNA sequencing. The fusion product was histologically validated by overexpression of *NTRK* as the tumor retained the kinase domain of *NTRK1* in exons 13 to 17 (Fig. S2). Currently, there are no recurrent fusion genes described in MPNSTs [60,61], potentially indicating that tumor SP-05 may be an *NTRK*-associated sarcoma. Finally, tumor SP-06 presented genetic alterations in genes *NF2*, *SMARCA4*, and *NRAS*, which may point to other tumor entities.

With all the genomic data generated, an independent pathologist analyzed the hematoxylin/eosin staining of the primary tumors not validated as classic MPNSTs (Fig. S3), confirming NF1-09 as a high-grade MPNST, SP-01 as a melanoma, SP-05 as an *NTRK*-associated spindle cell sarcoma, and SP-06 remained unclassifiable.

3.2. Expansion of the MPNST platform: Generation of PDOX models and new cell line models

From the six primary tumors, we were able to obtain PDOX models for each engrafted tumor and, in addition, three new cell lines, two from NF1-MPNST tumors (NF1-08 and NF1-09), and one from the sporadic tumor SP-01, a suspected melanoma. Moreover, a fourth cell line was generated from the SP-01 PDOX model (SP-01-OT; Fig. 2A). Remarkably, we obtained a total of three pairs of *in vitro*/*in vivo* models for primary tumors, only two of which were true MPNSTs, from the same patient. DNA microsatellite authentication analysis demonstrated that the newly generated cell lines and PDOX models matched blood and primary tumor profiles from patients (Table S3).

The mouse PDOX models presented the main histological features of the primary tumors, such as spindle cell hypercellularity with fusiform nuclei (Fig. S3). We performed a thorough histological characterization of PDOX models and cell lines, testing the same MPNST histological markers as in the primary tumors. We found a high correlation between primary tumors, PDOX tumors, and cell lines in terms of marker expression (Fig. 2B,C, Table 2, Fig. S1). The only differences were observed for Ki-67 staining: The tumor cell proliferation rate was similar independent of whether the tumor was primary or orthotopic (ranging from 10 to 30% of proliferating cells); however, it was slightly increased in cell lines (40 to 60%), probably due to the intrinsic nature of cell cultures (Fig. S1, Table 2).

Finally, in the process of obtaining tumor cell lines from tumors SP-04, SP-05, and SP-06, we observed only tumor-associated fibroblast isolation, evidenced by SMA-positive cells with diploid DNA content and no structural abnormalities in the genome (Fig. S4). These cell lines were also included in the platform for further characterization in the future.

3.3. New cell lines and PDOX models recapitulate the main genomic features of primary tumors

A thorough genomic characterization of PDOX models (at passage one) and cell lines was performed using SNP array and WES (Table S2), for validation against primary tumors.

A hallmark characteristic of MPNSTs is the presence of hyperploid and highly altered genomes [7]. Using SNP arrays, we analyzed the CN profile and allele ratios of primary tumors, PDOXs, and cell lines. The data proved that the genomic structure of tumors SP-04 and NF1-08 highly resembled that of classic

Table 1. Summary of genetic, epigenetic, and histological marker expression features of the six primary tumors. del, deletion; ger, germline; het, heterozygous; NA, not applicable; som, somatic. Red color shading indicates complete inactivation of the gene. Blue shading indicates positive validation of MPNST diagnosis.

			Genetics						Epigenetics	MPNST markers				
Tumor ID	Other aliases	Tumor (%)	*NF1*	*CDK2NA*	*SUZ12*	*EED*	*TP53*	Number of somatic exonic SNV	Cell line methylome classification	SOX10	S100B	H3K27me3	Additional alterations not related to MPNSTs	Potential tumor classification
SP-01	MPNST-SP-01	50	NM_000267.3: c.3520C > T: p.(Gln1174*) (som)[a] NM_000267.3: c.3888T > A: p.(Tyr1296*) (som)[a]	WT	WT	WT	NM_000546.6: c.949C > T: p.(Gln317*)[a] + LOH	1410	Melanoma	+	+	–	***ERBB4***:NM_005235:c.1834C > T: p.(Arg612Trp) (het) **COSMIC signature 7**	Melanoma
SP-04	MPNST-SP-04	89	SV: translocation-mediated inactivation (som) + LOH	SV: inversion-mediated del + LOH	NM_015355.2: c.1596-28_1616del + LOH	WT	WT	20	NA	–	(Focal +) –	–	NA	MPNST
SP-05	MPNST-SP-05	86	WT	SV: inversion-mediated del	WT	WT	WT	23	NA	–	–	–	***LMNA-NTRK1*** gene fusion	*NTRK*-rearranged spindle cell neoplasm
SP-06[b]	MPNST-SP-06	50	WT	SV: del[b] + LOH	WT	WT	WT	23	NA	–	–	+	***NRAS***:NM_002524.5: c.35G > C: p.(Gly12Ala) (het) ***NF2***: NM_000268: c.1157delA: p.(Lys387 Argfs*39) + LOH ***SMARCA4***: NM_003072: c.3121C > T: p.(Gln1041*) (het)	Unclassifiable
NF1-08	MPNST-NF1-08	95	NM_000267.3: c.701_730 + 10del (ger) + LOH	SV: inversion-mediated del	NM_015355.2: c.1236_1240del: p.(Glu415Glyfs*5)[a] + LOH	WT	WT	33	MPNST	–	–	–	NA	MPNST
NF1-09	MPNST-NF1-09	62	NM_000267.3: c.6792C > A: p.(Tyr2264*) (ger)[a] NM_000267.2: c.1186-5_1186-1del (som)	SV: inversion-mediated del	WT	WT	NM_000546.6: c.844C > T: p.(Arg282Trp)[a] + LOH	NA	MPNST-like	–	–	+	***PIK3CA***:NM_006218.4: c.1035T > A: p.(Asn345Lys) (het)	MPNST

[a]The SNV is present in the primary tumor, PDOX tumor, and cell line (in the case of SP-01, NF1-08, and NF1-09).
[b]SP-06 tumor data obtained from WES and SNP array.
Bold terms are highlight the genetic alterations not related to MPNSTs in the six analyzed primary tumors.

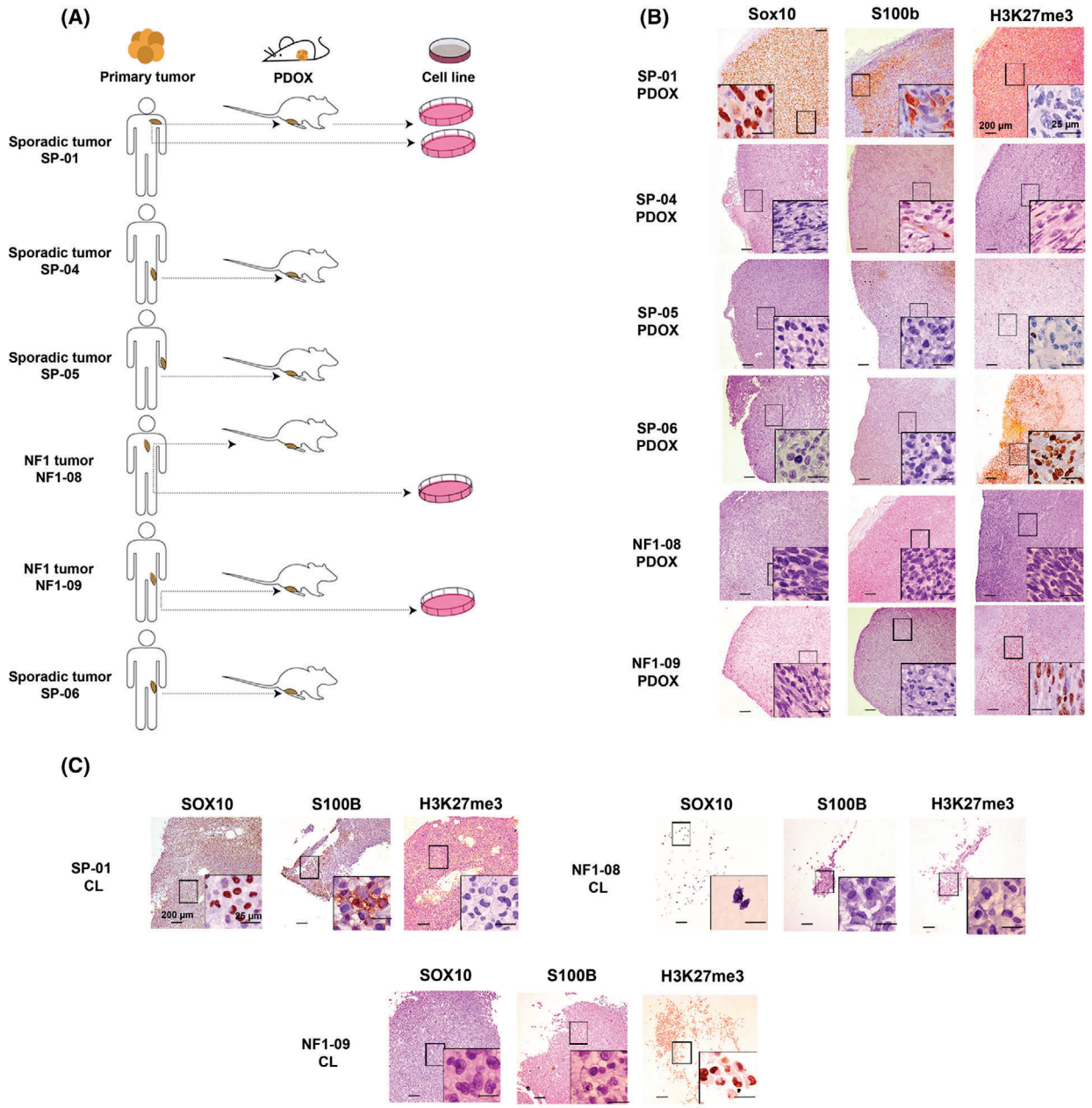

Fig. 2. Characterization of new PDOX and cell line models. (A) Scheme of the *in vitro/in vivo* models generated from the patient's tumors. Two cell lines were generated from the same patient, one from the primary tumor and the second from the PDOX tumor. (B) Representative histological stains of Sox10, S100b, and H3K27me3 in the six PDOX tumors ($n = 1$). Original magnifications are 40× and 600× in the inset magnified view, and scale bars are 200 µm and 25 µm, respectively. (C) Representative histological stains of SOX10, S100B, and H3K27me3 in the three cell lines derived from primary tumors ($n = 1$). CL: cell line. Magnifications are 40× and 600× in the inset magnified view, and scale bars are 200 µm and 25 µm, respectively.

MPNSTs, presenting gains of whole chromosomes or large chromosomal regions and a few losses of genetic material, alongside extended regions of loss of heterozygosity (LOH; Fig. 3A, Fig. S5) [38]. Tumors SP-01 and SP-05, potentially reclassified as other tumor entities, nonetheless, also presented similar classic MPNST genomic features. Contrarily, tumors NF1-09 and SP-06 presented less-altered genomes (Fig. S5).

Genome features from PDOX tumors and cell lines highly recapitulated the patient tumors, thus validating

Table 2. Summary table comparing histological marker expression in primary tumors (PTs), PDOX tumors (OTs), and cell lines (CL).

	SP-01			SP-04		SP-05		SP-06		NF1-08			NF1-09		
Marker	PT	OT	CL	PT	OT	PT	OT	PT	OT	PT	OT	CL	PT	OT	CL
SOX10	+	+	+	–	–	–	–	–	–	–	–	–	–	–	–
S100	+	+	+	– (Focal)	– (Focal)	–	–	–	–	–	–	–	–	–	–
H3K27me3	–	–	–	–	–	–	–	+	+	–	–	–	+	+	+
CD34	–	–	–	–	–	–	–	–	–	–	–	–	–	–	–
Vimentin	+	+	+	+	+	+	+	+	+	+	+	+	+	+	+
Ki-67 (%)	35	30	60	10	40	20	30	5	10	30	30	60	10	10	40

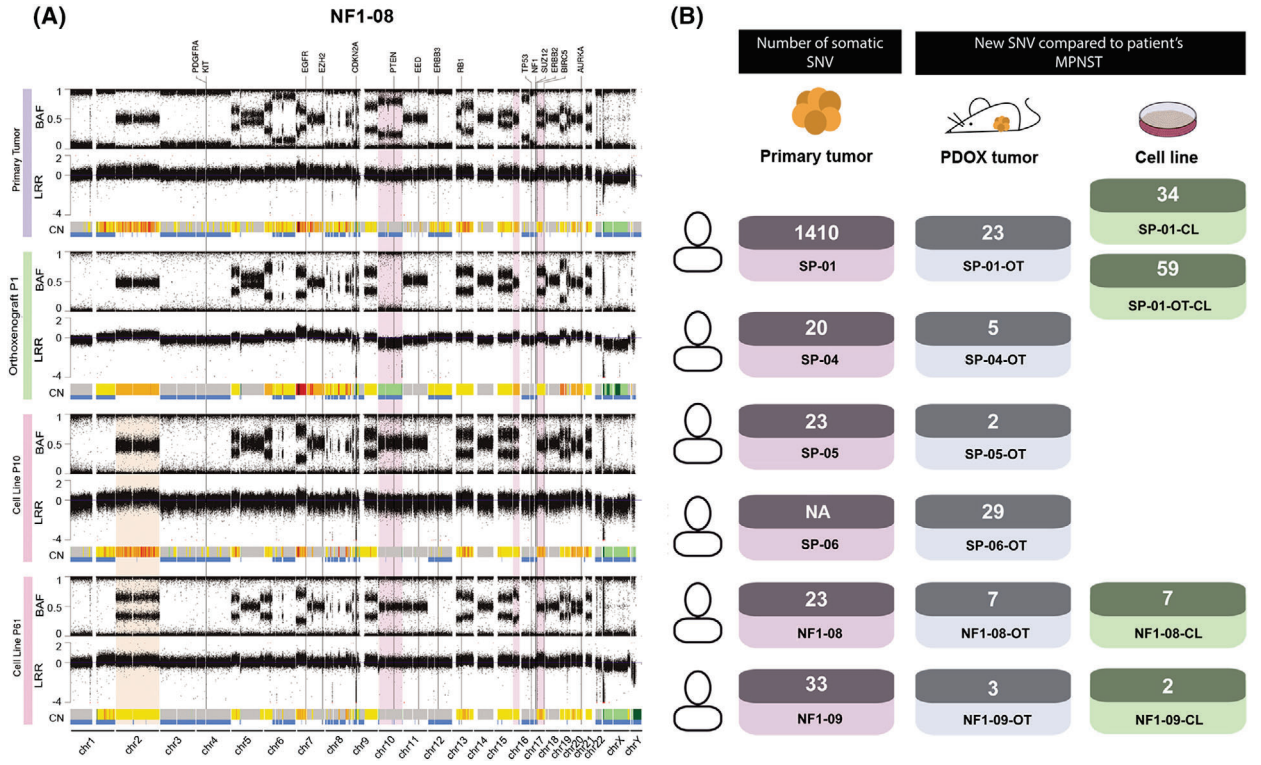

Fig. 3. Patient-derived orthotopic xenografts and cell lines recapitulate the main genetic and genomic features of primary tumors. (A) CN profile of primary tumor, orthoxenograft (PDOX) tumor, and cell line from patient NF1-08, representing that the models recapitulate the genomic hallmarks of the primary tumor. BAF and LRR profiles are represented. CN variations are represented by a colored line under each LRR: gray for 2n region; yellow to red for >2n, representing chromosomal gain; and green for <2n, representing chromosomal loss. LOH events are shown in blue. Genomic differences between primary and xenograft tumors are highlighted in purple, and differences between cell lines at low and high passage are marked in a cream color. (B) Number of somatic SNVs in the coding regions of primary tumors and models calculated using WES. The blood of patients was used as a control of constitutive DNA. New somatic SNVs were calculated in PDOX tumors and cell lines compared with primary tumors. The number of SNVs of primary tumor SP-06 was not analyzed due to the lack of blood sample from the patient. OT: PDOX tumor.

our models (Fig. 3A, Fig. S5). There were only a few differences, probably due to loss of signal from human stromal cells in the PDOX or cell lines. We found more differences between cell lines and primary tumors than PDOX and primary tumors, concordant with the intrinsic characteristics of cell culture conditions. Moreover, we checked the genome stability of cell lines through the passages. We found a high degree of genomic stability in all cases, except for cell line NF1-09 (Fig. 3A, Fig. S5). This cell line exhibited a different genomic structure profile in late passages compared with early passages, the latter being more similar to

primary and PDOX tumors. The changes observed in the passages could be explained by the selection of a specific subpopulation that seemed to exist in the primary tumor but in a small proportion. Remarkably, the cell line genome at high passage number bears a greater resemblance to the genomic features of MPNST [60] (Fig. S5).

Using WES, we were able to confirm the presence of all somatic single nucleotide variants (SNVs) identified in primary tumors, in their corresponding PDOX and derived cell lines (Table 1). We also quantified somatic SNVs and small indels in coding regions of primary tumors and matched PDOX models and cell lines, to analyze the genetic variation caused by new somatic variants in models compared with primary tumors. We performed a somatic calling of all samples, except for the SP-06 tumor as we did not have a normal counterpart. Excluding SP-01 (due to its higher mutation burden compared with other tumors), PDOX tumors at first passage, just after engraftment, presented a mean of ~ 9.2 (2–29) new somatic variants compared with primary tumors (Fig. 3B); cell lines, at low passage, presented a mean of ~ 4.5 (2–7) new variants. The SP-01 PDOX tumor only presented 23 new SNVs compared with the primary tumor, similar to the two cell lines derived from this tumor that showed a mean of ~ 46.5 (34–59) new SNVs (Fig. 3B). Altogether, the low number of new somatic variants detected in the engrafted tumors and cell lines with respect to their primary counterparts reinforces our observation that the models generated in this study faithfully recapitulate the genomic characteristics of the primary tumors, being quite stable genetically.

3.4. Tumor-derived cell lines exhibit heterogeneity in phenotypic and functional features

We performed a comprehensive characterization of the three cell lines (SP-01, NF1-08, and NF1-09) isolated from primary tumors. The first set of analyses aimed to describe the cells' phenotypic characteristics in the different cell cultures, as regards morphology (Fig. 4A), marker expression (Fig. 4B), and ploidy (Fig. 4C). Morphologically, the two cell lines from NF1-MPNST validated tumors (NF1-08 and NF1-09) were composed of small, polygonal cells that grew forming a monolayer without contact inhibition, similar to the morphology of other classic MPNST cell lines like S462 or ST88-14 (Fig. S6A). Regarding the expression of neural crest stem cell lineage markers (S100B and p75) and MPNST markers (SOX9 and EGFR) [62,63], these two cell lines were positive for SOX9 and EGFR expression and negative for S100B and p75 (only focal in the NF1-09 cell line), similar to MPNST control cell lines (S462 and ST88-14) [38] (Fig. 4B, Table 3, Fig. S6B). In the case of SP-01, cells presented Schwann cell characteristics such as bipolar or tripolar morphology with oval nuclei [64] and were positive for all four markers (Fig. 4A,B, Table 3), compatible with a melanoma cell line [65-68]. As for DNA content, different degrees of aneuploidy were observed across tumor cell lines. The NF1-08 cell line was between 2n and 3n, while SP-01 was triploid. In the case of NF1-09, cell cycle analysis proved that this cell line presented different subpopulations of tumor cells, with heterogeneity of ploidies (Fig. 4C, Table 3). The analyses of several isolated clones indicated the presence of three different cell subpopulations: one higher than 2n; a second nearly triploid; and a third completely tetraploid. The three subpopulations remained stable across multiple passages in culture (Fig. S6C).

We further characterized the three cell lines by performing a set of functional assays (summarized in Table 3): proliferation assays (calculating the PDT); *in vivo* tumor formation capacity (Fig. 4D); 2D and 3D *in vitro* colony formation capacity (Fig. 4E); and migration ability (wound healing assay; Fig. 4F). We compared the functional properties of the newly isolated cell lines with those already established (S462, ST88-14, and STS-26T).

We calculated the PDT using two different methodologies, Trypan Blue dye exclusion and MTT viability assay, obtaining similar results (Fig. 4D, Fig. S6D). Cell lines STS-26T, S462, SP-01, and NF1-09 had the highest proliferation rates with PDT values < 1, correlating with cell lines that generated tumors in athymic nude mice. Interestingly, these four cell lines all had the *TP53* gene inactivated (Fig. 4D, Table 3). Quantification of proliferating cells in cell lines ranged from 20 to 50%, where lower PDT represents higher rates of dividing cells, as expected (Table 3). Regarding colony formation capacity, only cell lines NF1-09, S462, and STS-26T formed colonies in 2D and 3D assays, also generating tumors when engrafted in mice (Fig. 4E, Fig. S6E, Table 3). Cell line SP-01 was also able to generate tumors *in vivo* (Table 3); however, it was not able to generate colonies in 2D and 3D (not shown). The migration ability also differed between cell lines, SP-01 and NF1-09 presenting a higher migration rate in the wound healing assay, similar to STS-26T and S462 (Fig. 4F, Fig. S6F, Table 3). Contrarily, NF1-08 had a much lower proliferation capacity, similar to ST88-14 (PDT values of 2–3 days) and the migration capacity was low, having 100% of open wound area at

12 h. Interestingly, both NF1-08 and ST88-14 cell lines did not generate 3D colonies. Moreover, these two cell lines, that were unable to form tumors *in vivo* after engraftment, bore a WT *TP53* (Table 3).

Remarkably, we obtained two cell line models from the same patient (SP-01), one from the primary tumor and the other from the PDOX (SP-01-OT). We characterized and compared the two cell lines (Fig. S7,

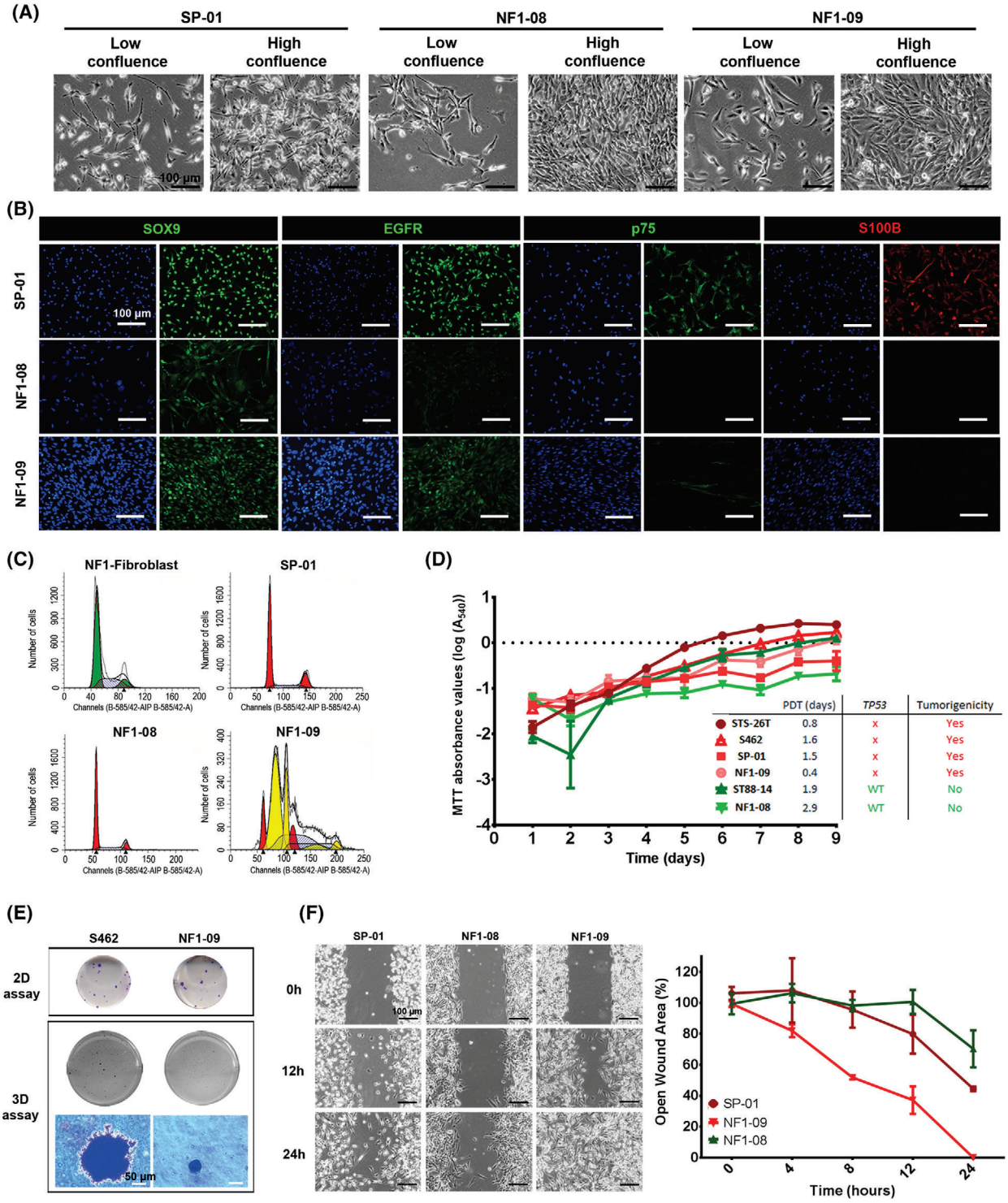

Fig. 4. Phenotypic and functional characterization of new established cell lines. (A) Representative morphology images of the newly generated cell lines at low and high confluence ($n = 1$). Images were taken by optical microscope at 100× magnification. The scale bar is 100 μm. (B) Representative immunofluorescence images of MPNSTs markers SOX9 and EGFR, and neural crest-Schwann cell lineage markers p75 and S100B ($n = 1$). Original magnification of images is 200×, and the scale bar is 100 μm. (C) DNA content analyses of the three cell lines (using fibroblasts derived from a NF1 patient as a diploid control), represented as the number of cells versus DNA quantity ($n = 2$). (D) Cell growth curves of the three newly generated cell lines and three control tumor cell lines (S462, ST88-14, and STS-26T), obtained using MTT viability assay. Growth curves are derived from mean values ± SD (error bars, $n = 6$). PDT values and *TP53* status correlate with the tumorigenic capacity of the cell lines. In red, cell lines that generate tumors in mice, with low PDT values and *TP53* inactivated. In green, cell lines that do not generate tumors, with high PDT values and active *TP53*. (E) Colony formation ability of cell lines. Representative images of 2D and 3D colonies generated by the new established cell line NF1-09 and control MPNST cell line S462; both generate tumors in mice ($n = 2$). Original magnification of images is 400×. The scale bar is 50 μm. (F) Wound healing assay of the three cell lines. Representative images of wound closing were captured at 0, 12, and 24 h (left) at 100× magnification. The migration ability of cells was represented as the percentage of open wound at 0, 4, 8, 12, and 24 h (right). Open wound curves are derived from mean values ± SD (error bars, $n = 3$). In red, cell lines that generate tumors in mice and, in green, cell lines that do not generate tumors. The scale bar is 100 μm.

Table 3), which presented similar features, indicating the utility of isolating cell lines from PDOX.

3.5. Different *in vitro* therapeutic responses between genuine MPNSTs and reclassified entities

Finally, the three newly generated cell lines derived from primary tumors and the S462 cell line (as a classic MPNST cell line control) were treated with three different compounds. Two of these targeted pathways deregulated due to the loss of specific TSGs in MPNSTs: the MEK inhibitor Mirdametinib (PD0325901), to compensate the activation of the Ras/MAPK pathway by *NF1* inactivation [14], and the bromodomain inhibitor JQ1 for PRC2 inactivation [13]. The third compound tested was the Aurora A kinase inhibitor (AURKAi) Alisertib (MLN8237), which was previously described to be a good treatment candidate for MPNSTs [69,70].

Classic MPNST cell lines (S462 and NF1-08) carrying the three recurrent inactivated TSGs (*NF1*, *CDKN2A*, and PRC2) were the most sensitive to the three compounds, which highly decreased cell viability. Surprisingly, for NF1-09, an MPNST that presents active PRC2, we observed that JQ1 was effective. Furthermore, although *NF1* is completely inactivated in this cell line, we observed a limited therapeutic response to MEKi, probably due to a potential bypass produced by the oncogenic *PIK3CA* mutation present in this cell line. Finally, the suspected melanoma cell line SP-01 presented a lower response to the three treatments, only reducing cell viability by half at the maximum concentrations of the compounds tested (Fig. 5A). Indeed, NF1-09 (nonclassic MPNST) and SP-01 (melanoma) presented higher IC_{50} values for Mirdametinib and Alisertib (> 100 μM) compared with NF1-08 (9.267 and 12.59, respectively) and S462 (0.98 and 3.872; Fig. 5A). We then wanted to test whether the compounds could be synergistic in combination in the S462 and NF1-08 cell lines, the only ones sensitive to the single treatments. Both cell lines presented synergistic effects with the three tested combinations, especially for JQ1 plus Mirdametinib, as observed by CI values <1 in a high fraction of affected cells (Fig. 5B). Taken together, we observed that treatment response was different when we used compounds directed against altered MPNST pathways in classic MPNST cell lines compared with other potential tumor entities, such as melanomas.

4. Discussion

More than 50% of MPNSTs arise in NF1 patients, being the main cause of early mortality in young patients with this genetic condition [6]. The low prevalence of MPNSTs in the general population hampers the development of therapeutic approaches designed *ad hoc* for this tumor type, making the use of *in vitro* and *in vivo* models paramount to moving toward precision and personalized therapeutic strategies. Malignant peripheral nerve sheath tumors may be difficult to diagnose as other tumor entities can mimic their morphology and marker expression patterns, especially outside the NF1 clinical context [22].

It was recently described that some cell lines commonly used by the scientific community as MPNST cell models, particularly sporadic models, may not be derived from MPNSTs but rather from other entities. This work has drawn attention to the potential heterogeneity of tumors placed under the MPNST umbrella, highlighting the potential utility of genomic and epigenetic information in guiding their differential diagnostics [38]. Thus, we aimed to enrich our precision medicine platform by reclassifying tumor entities that

Table 3. Summary table comparing phenotypic and functional features of MPNST expression in newly generated cell lines and established control cell lines. OT, PDOX tumor; PT, primary tumor; WT, wild-type.

	Expression of markers				Proliferation		Colony formation		Migration	Genetics		
	S100	p75	SOX9	EGFR	PDT (days) MTT	% Proliferating cells	2D-colony assay	3D-colony assay	% of open wound (12 h)	*TP53* status	DNA content	Tumorigenicity
Newly generated cell lines												
SP-01	+ + +	+ +	+ + +	+ + +	1.53	20.30	–	–	75.19	Inactivated	>2n	+
SP-01-OT	+ + +	+	+ + +	+ + +	2.72	17.75	–	–	55.52	Inactivated	>2n	–
NF1-08	–	–	+ +	+	2.90	9.85	–	–	100	WT	>2n	–
NF1-09	–	– (+ focal expression)	+ + +	+ + +	0.44	36.55	+	+	37.44	Inactivated	>2n, 3n and 4n (3 subpopulations)	+
Established cell lines												
STS-26T	–	–	+ + +	+ + +	0.80	53.95	+	+	19.72	Inactivated	4n	+
S462	–	–	+ + +	+ + +	1.61	42.40	+	+	79.46	Inactivated	>2n	+
88-14	–	–	+ + +	+ + +	1.59	35.75	+	–	17.59	WT	>2n	–

may be confounded using the current clinical tools to diagnose MPNSTs and may be more appropriately classified using genomic, epigenomic, and marker expression information. After the analyses of six primary tumors, we have classified two tumors as classic MPNSTs (the sporadic SP-04 and the NF1-related NF1-08) since both bore the complete inactivation of *NF1*, *CDKN2A*, and *SUZ12* [10,11,12,71,72] and displayed an MPNST-compatible genomic CN profile [10,11]. A third tumor, NF1-09, was classified as an MPNST although it has PRC2 active, which might account for the NF1-09-derived cell line clustering in the MPNST-like sarcoma group when using a methylome classifier. Moreover, these three MPNSTs presented few somatic SNVs (20–30), similar to other groups described in this tumor type (median of 40–60 variants) [10,11] and presented negative SOX10 and S100B staining, as expected [24,73,74,75]. A second analysis by an independent pathologist identified tumor NF1-09 as a high-grade MPNST.

Remarkably, the other three primary tumors, all sporadic (representing three out of four sporadic cases), after compiling genomic information and re-evaluation by an independent pathologist, were reclassified as a melanoma (SP-01), an *NTRK*-related spindle cell neoplasm (SP-05), and the third was discarded as an MPNST although further classification was inconclusive (SP-06). SP-01 highly mimicked MPNSTs histologically but expressed S100B, p75, and SOX10 neural crest markers, like melanomas [65,76], and presented a high mutation frequency, mostly associated with the skin cancer COSMIC mutational signature [77]. SP-05 presented genomic and histological features compatible with MPNSTs but bore an *NTRK*-associated gene fusion (*NTRK1-LMNA*). Gene fusions involving the *NTRK* gene family (*NTRK1*, *NTRK2*, and *NTRK3*) are usually described in a broad spectrum of mesenchymal tumors [78]. For instance, *LMNA-NTRK1* has been reported in Lipofibromatosis-Like Neural Tumors, which highly resemble low-grade MPNSTs [79,80]. A case report study detected this gene fusion within a subset of NF1-related MPNSTs [81]; however, the histological and molecular characterization of these tumors was scarce. Finally, according to genomic characteristics, tumor SP-06 is clearly distinct from classic MPNSTs (*NF2* inactivation, *NRAS* oncogenic mutation, and truncating mutation in *SMARCA4*). However, a second analysis by an independent pathologist was unable to provide a definitive identity, highlighting the difficulty in diagnosing MPNSTs and related tumors with overlapping histological characteristics. Other high-grade sarcomas can also mimic histological and marker expression patterns of MPNSTs, such as synovial

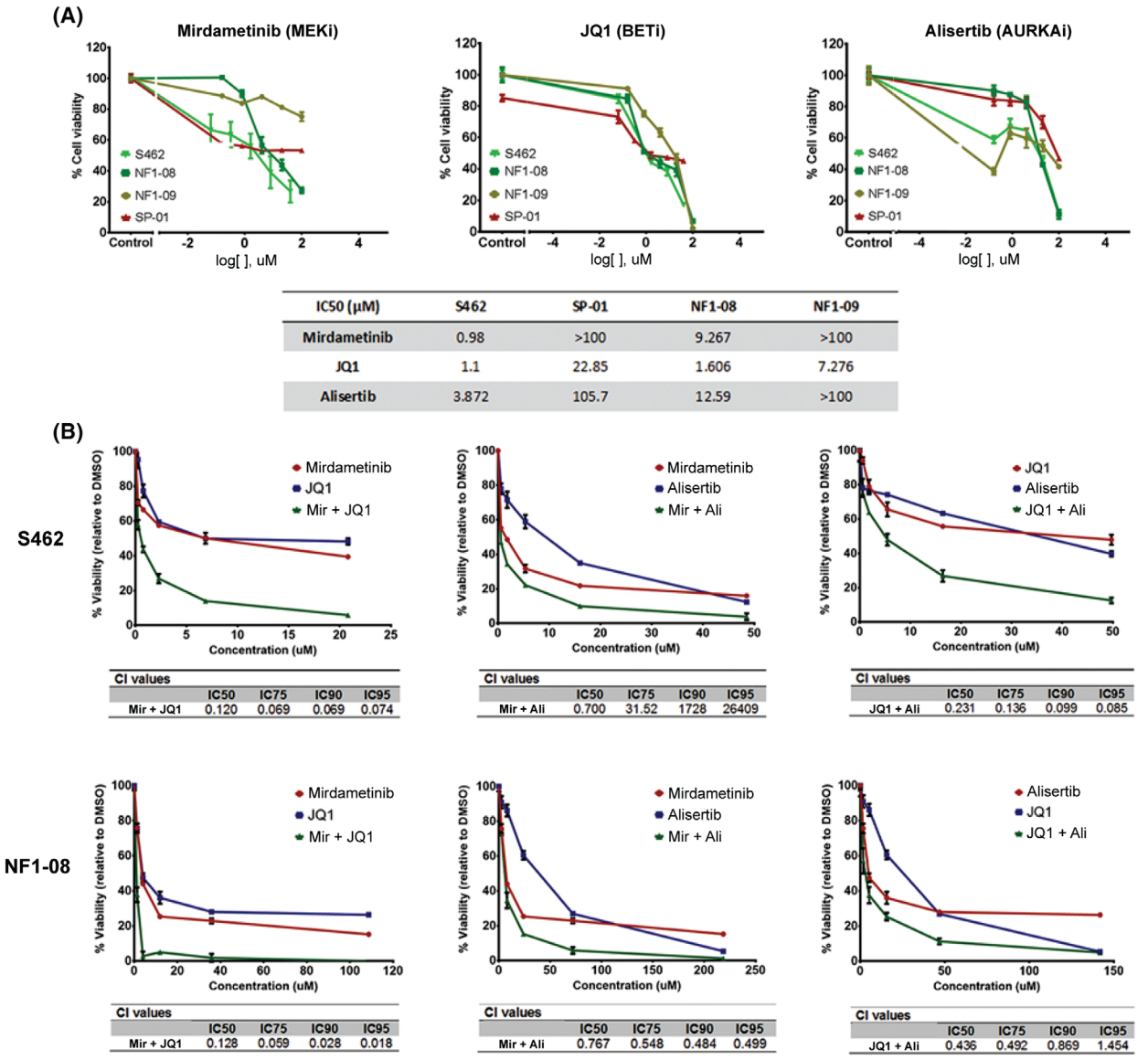

IC50 (μM)	S462	SP-01	NF1-08	NF1-09
Mirdametinib	0.98	>100	9.267	>100
JQ1	1.1	22.85	1.606	7.276
Alisertib	3.872	105.7	12.59	>100

CI values	IC50	IC75	IC90	IC95
S462 Mir + JQ1	0.120	0.069	0.069	0.074
S462 Mir + Ali	0.700	31.52	1728	26409
S462 JQ1 + Ali	0.231	0.136	0.099	0.085
NF1-08 Mir + JQ1	0.128	0.059	0.028	0.018
NF1-08 Mir + Ali	0.767	0.548	0.484	0.499
NF1-08 JQ1 + Ali	0.436	0.492	0.869	1.454

Fig. 5. Genuine and confounded MPNST cell lines exhibit different treatment responses. (A) Cell viability plots of cell lines treated singly with MEK inhibitor (MEKi) Mirdametinib, Aurora A kinase inhibitor (AURKAi) Alisertib, and BET inhibitor (BETi) JQ1, and IC50 values of the compounds for each cell line. Cell viability curves are derived from mean values ± SD (error bars, $n = 3$). In green, cell lines S462 and NF1-08 are classic MPNSTs; in khaki green, the NF1-09 cell line is an MPNST with active PRC2; and in red, the SP-01 cell line is derived from a melanoma. (B) Cell viability plots of NF1-08 and S462 cell lines treated with pairwise combinations of the three compounds, alongside CI values to evaluate the synergy of the combinations. Cell viability curves are derived from mean values ± SD (error bars, $n = 3$). Synergy is observed at CIs <1. Single treatments are marked in blue and red, and combination in green in the cell viability plot.

sarcoma, fibrosarcomatous dermatofibrosarcoma protuberans, myxofibrosarcoma, or spindle cell sarcomas [82]. Thus, two messages can arise from our work. First, the thorough genomic and histologic characterization of tumors applied in a larger number of samples may facilitate a correct diagnostic of tumors currently labeled as MPNSTs in the clinics. Second, we should reinterpret results obtained with newly rediagnosed models previously considered MPNSTs, such as the STS-26T cell line (recently reclassified as probably being a melanoma [38]) and used by many different laboratories; or the SP-01 cell line (also MPNST-SP-01 in previous works) [32,34], used in our group.

Our platform also includes cellular and mouse models from MPNSTs and confounded tumor entities. We have generated PDOXs from all six primary

tumors and cell lines from half of them (SP-01, NF1-08, and NF1-09). One of the main challenges was the generation of tumor-derived cell lines, which is normally difficult to achieve [83] and was not feasible for all primary tumors. Histological and genomic analyses validated that all derived PDOXs and cell lines genuinely represented their respective primary tumors. In the context of the primary tumors studied herein, PDOX generation seems more efficient than establishing 2D cell lines. Interestingly, after 2D establishment, only cell lines with *TP53* inactivated, among other features, had tumorigenic capacity in animal models, although further experiments will be required to elucidate any causal relationship. Altogether, there seem to be different molecular requirements for *in vitro* or *in vivo* model generation. The migration and growth capacities of the cells are also described as hallmarks of the tumor's potential invasion and metastatic capacity [84], being factors that may improve the ability of cells to generate tumors in mice. Beyond *TP53* status, we found a good correlation between *in vitro* and *in vivo* properties. Cell lines with high proliferation, invasion, and migration potential (NF1-09, SP-01, and the established cell lines S462 and STS-26 T), were those exhibiting tumor formation capacity.

Finally, we investigated potential differences in drug treatment response in our three isolated cell lines, which are representative of the clinical diversity of MPNSTs, with classic MPNST cell lines, an MPNST cell line with active PRC2, and a cell line from a tumor entity (melanoma) potentially misclassified as an MPNST. The cell lines were used for testing three targeted drug compounds for MPNSTs: a MEK inhibitor (Mirdametinib or PD0325901), a bromodomain inhibitor (JQ1), and an Aurora A kinase inhibitor (Alisertib or MLN8237). The sensitivity of the cell lines to the compounds was quite different, as expected, as we know that part of these differences arise because we are testing different entities with distinct genetic alterations. Only the classic MPNST cell line NF1-08 and the S462 cell line were sensitive to the three treatments. NF1-09, considered nonclassic MPNST, had differences in treatment response compared with the classic ones as it was resistant to AURKAi and MEKi treatments, although the latter could be related to the presence of an oncogenic mutation in *PIK3CA*, and it was sensitive to JQ1, despite being PRC2 WT. The cell line SP-01 was the most resistant to the three MPNST-directed treatments, as expected considering it is probably a melanoma cell line. In summary, part of the different responses to single treatments could be attributed to the genetic status of the cell lines; however, this is clearly not the only factor playing a role in drug response. For all combinations, co-treatment therapies in NF1-08 and S462 MPNST cell lines generated a synergistic effect, reinforcing this strategy [85].

5. Conclusions

In summary, here we present our MPNST precision medicine platform, an excellent tool for research and preclinical studies to reclassify clinically diagnosed MPNSTs. It is noteworthy that we have *in vitro* and *in vivo* pairs from the same primary tumor for two of the three true MPNSTs in this study. Moreover, the expansion of the MPNST platform to tumor entities that might be confounded in routine clinical diagnostics makes it more representative of a real clinical scenario and will constitute a useful tool to obtain correct preclinical information to guide successful clinical trials in humans. The clinical diversity of tumors, together with their specific genetic and genomic alterations, was translated into different response to treatments.

Acknowledgements

We thank CERCA Program/Generalitat de Catalunya for their institutional support [Pla estratègic de recerca i innovació en salut (PERIS_MedPerCan and URDCat projects), 2021SGR01112], the Carlos III National Health Institute funded by FEDER funds, a way to build Europe (PI19/00553, PI16/00563, PI16/01898, PI20/00228, and CIBERONC); the Fundación PROYECTO NEUROFIBROMATOSIS (FPNF), the Scientific Foundation Asociación Española Contra el Cáncer, and Fundació La Marató de TV3. We thank all the patients and families with MPNST tumors. We would like to thank all Spanish NF patients and NF associations for their continuing support and effort, in particular the Spanish Asociación de Afectados de Neurofibromatosis (AANF) and the Associació Catalana de les Neurofibromatosis (ACNefi). We also wish to thank the ICO and IGTP Hereditary Cancer Program teams, as well as the members of the Spanish CSUR of Phakomatoses. Finally, we want to thank the pathology unit of Hospital Universitari de Bellvitge and Vall Hebrón, for the assessment of histological staining and evaluation of tumors, and the Mouse Lab Unit of the IDIBELL for assistance with the mouse models. Biorender was used for figures generation.

Conflict of interest

The authors declare no conflict of interest.

Author contributions

EC-B, JF-R, ES, and CL were involved in study concept and design and original manuscript draft. EC-B, JF-R, MM-L, SO-B, SN-R, MP, MM, HM, MC, and AV were involved in experimental work acquisition, analysis, and interpretation. MM-L and BG were involved in bioinformatic analyses. TL and DR were involved in methylome analysis and sarcoma classifier. CR, AE, DPS were involved in clinical case contribution. CR, TMS, and MP were involved in pathology review. All authors were involved in review and editing of manuscript.

Peer review

The peer review history for this article is available at https://www.webofscience.com/api/gateway/wos/peer-review/10.1002/1878-0261.13534.

Data accessibility

The data that support the findings of this study are available from the corresponding author (clazaro@iconcologia.net) upon reasonable request. The methylome classifier data are available through a public web link (https://doi.org/10.7303/syn52387995).

References

1 Grobmyer SR, Reith JD, Shahlaee A, Bush CH, Hochwald SN. Malignant peripheral nerve sheath tumor: molecular pathogenesis and current management considerations. *J Surg Oncol*. 2008;**97**(4):340–9. https://doi.org/10.1002/jso.20971

2 Kallionpää RA, Uusitalo E, Leppävirta J, Pöyhönen M, Peltonen S, Peltonen J. Prevalence of neurofibromatosis type 1 in the Finnish population. *Genet Med*. 2018;**20**(9):1082–6. https://doi.org/10.1038/gim.2017.215

3 Kresak JL, Walsh M. Neurofibromatosis: a review of NF1, NF2, and schwannomatosis. *J Pediatr Genet*. 2016;**5**(2):98–104. https://doi.org/10.1055/s-0036-1579766

4 Evans DG, Baser ME, McGaughran J, Sharif S, Howard E, Moran A. Malignant peripheral nerve sheath tumours in neurofibromatosis 1. *J Med Genet*. 2002;**39**(5):311–4.

5 Uusitalo E, Rantanen M, Kallionpää RA, Pöyhönen M, Leppävirta J, Ylä-Outinen H, et al. Distinctive cancer associations in patients with neurofibromatosis type 1. *J Clin Oncol*. 2016;**34**(17):1978–86. https://doi.org/10.1200/JCO.2015.65.3576

6 Rasmussen SA, Yang Q, Friedman JM. Mortality in neurofibromatosis 1: an analysis using U.S. death certificates. *Am J Hum Genet*. 2001;**68**(5):1110–8. https://doi.org/10.1086/320121

7 Beert E, Brems H, Daniëls B, de Wever I, van Calenbergh F, Schoenaers J, et al. Atypical neurofibromas in neurofibromatosis type 1 are premalignant tumors. *Genes Chromosomes Cancer*. 2011;**50**(12):1021–32. https://doi.org/10.1002/gcc.20921

8 Higham CS, Dombi E, Rogiers A, Bhaumik S, Pans S, Connor SEJ, et al. The characteristics of 76 atypical neurofibromas as precursors to neurofibromatosis 1 associated malignant peripheral nerve sheath tumors. *Neuro Oncol*. 2018;**20**(6):818–25. https://doi.org/10.1093/neuonc/noy013

9 Abeshouse EA. Comprehensive and integrated genomic characterization of adult soft tissue sarcomas. *Cell*. 2017;**171**(4):950–965.e28. https://doi.org/10.1016/j.cell.2017.10.014

10 Sohier P, Luscan A, Lloyd A, Ashelford K, Laurendeau I, Briand-Suleau A, et al. Confirmation of mutation landscape of NF1-associated malignant peripheral nerve sheath tumors. *Genes Chromosomes Cancer*. 2017;**56**(5):421–6. https://doi.org/10.1002/gcc.22446

11 Brohl AS, Kahen E, Yoder SJ, Teer JK, Reed DR. The genomic landscape of malignant peripheral nerve sheath tumors: diverse drivers of Ras pathway activation. *Sci Rep*. 2017;**7**(1):14992. https://doi.org/10.1038/s41598-017-15183-1

12 Lee W, Teckie S, Wiesner T, Ran L, Prieto Granada CN, Lin M, et al. PRC2 is recurrently inactivated through EED or SUZ12 loss in malignant peripheral nerve sheath tumors. *Nat Genet*. 2014;**46**(11):1227–32. https://doi.org/10.1038/ng.3095

13 De Raedt T, Beert E, Pasmant E, Luscan A, Brems H, Ortonne N, et al. PRC2 loss amplifies Ras-driven transcription and confers sensitivity to BRD4-based therapies. *Nature*. 2014;**514**(7521):247–51. https://doi.org/10.1038/nature13561

14 Jessen WJ, Miller SJ, Jousma E, Wu J, Rizvi TA, Brundage ME, et al. MEK inhibition exhibits efficacy in human and mouse neurofibromatosis tumors. *J Clin Invest*. 2013;**123**(1):340–7. https://doi.org/10.1172/JCI60578

15 Dombi E, Baldwin A, Marcus LJ, Fisher MJ, Weiss B, Kim AR, et al. Activity of selumetinib in neurofibromatosis type 1-related plexiform neurofibromas. *N Engl J Med*. 2016;**375**(26):2550–60. https://doi.org/10.1056/NEJMoa1605943

16 Gross AM, Wolters PL, Dombi E, Baldwin A, Whitcomb P, Fisher MJ, et al. Selumetinib in children with inoperable plexiform neurofibromas. *N Engl J Med*. 2020;**383**(13):1290. https://doi.org/10.1056/NEJMx200013

17 Gross AM, Dombi E, Wolters PL, Baldwin A, Dufek A, Herrera K, et al. Long-term safety and efficacy of

selumetinib in children with neurofibromatosis type 1 on a phase 1/2 trial for inoperable plexiform neurofibromas. *Neuro Oncol*. 2023;**25**:1883–94. https://doi.org/10.1093/neuonc/noad086
18 Kim A, Pratilas CA. The promise of signal transduction in genetically driven sarcomas of the nerve. *Exp Neurol*. 2018;**299**:317–25. https://doi.org/10.1016/j.expneurol.2017.08.014
19 Zehou O, Fabre E, Zelek L, Sbidian E, Ortonne N, Banu E, et al. Chemotherapy for the treatment of malignant peripheral nerve sheath tumors in neurofibromatosis 1: a 10-year institutional review. *Orphanet J Rare Dis*. 2013;**8**:127. https://doi.org/10.1186/1750-1172-8-127
20 Ducatman BS, Scheithauer BW, Piepgras DG, Reiman HM, Ilstrup DM. Malignant peripheral nerve sheath tumors. A clinicopathologic study of 120 cases. *Cancer*. 1986;**57**(10):2006–21.
21 Ferner RE, Gutmann DH. International consensus statement on malignant peripheral nerve sheath tumors in neurofibromatosis. *Cancer Res*. 2002;**62**(5):1573–7.
22 Le Guellec S, Decouvelaere AV, Filleron T, Valo I, Charon-Barra C, Robin YM, et al. Malignant peripheral nerve sheath tumor is a challenging diagnosis: a systematic pathology review, immunohistochemistry, and molecular analysis in 160 patients from the French Sarcoma Group Database. *Am J Surg Pathol*. 2016;**40**(7):896–908. https://doi.org/10.1097/PAS.0000000000000655
23 James AW, Shurell E, Singh A, Dry SM, Eilber FC. Malignant peripheral nerve sheath tumor. *Surg Oncol Clin N Am*. 2016;**25**(4):789–802. https://doi.org/10.1016/j.soc.2016.05.009
24 Magro G, Broggi G, Angelico G, Puzzo L, Vecchio GM, Virzì V, et al. Practical approach to histological diagnosis of peripheral nerve sheath tumors: an update. *Diagnostics*. 2022;**12**(6). https://doi.org/10.3390/diagnostics12061463
25 Kim A, Stewart DR, Reilly KM, Viskochil D, Miettinen MM, Widemann BC. Malignant peripheral nerve sheath tumors state of the science: leveraging clinical and biological insights into effective therapies. *Sarcoma*. 2017;**2017**:7429697. https://doi.org/10.1155/2017/7429697
26 Bairoch A. The cellosaurus, a cell-line knowledge resource. *J Biomol Tech*. 2018;**29**(2):25–38. https://doi.org/10.7171/jbt.18-2902-002
27 Osum SH, Watson AL, Largaespada DA. Spontaneous and engineered large animal models of neurofibromatosis type 1. *Int J Mol Sci*. 2021;**22**(4). https://doi.org/10.3390/ijms22041954
28 Oyama R, Kito F, Takahashi M, Hattori E, Noguchi R, Takai Y, et al. Establishment and characterization of patient-derived cancer models of malignant peripheral nerve sheath tumors. *Cancer Cell Int*. 2020;**20**:58. https://doi.org/10.1186/s12935-020-1128-z
29 Williams KB, Largaespada DA. New model systems and the development of targeted therapies for the treatment of neurofibromatosis type 1-associated malignant peripheral nerve sheath tumors. *Genes (Basel)*. 2020;**11**(5). https://doi.org/10.3390/genes11050477
30 Hirbe AC, Dodd RD, Pratilas CA. Special Issue: genomics and models of nerve sheath tumors. *Gene*. 2020;**11**(9):1024. https://doi.org/10.3390/genes11091024
31 Larsson AT, Bhatia H, Calizo A, Pollard K, Zhang X, Conniff E, et al. Ex vivo to in vivo model of malignant peripheral nerve sheath tumors for precision oncology. *Neuro Oncol*. 2023. https://doi.org/10.1093/neuonc/noad097
32 Castellsagué J, Gel B, Fernández-Rodríguez J, Llatjós R, Blanco I, Benavente Y, et al. Comprehensive establishment and characterization of orthoxenograft mouse models of malignant peripheral nerve sheath tumors for personalized medicine. *EMBO Mol Med*. 2015;**7**(5):608–27. https://doi.org/10.15252/emmm.201404430
33 Fernández-Rodríguez J, Morales la Madrid A, Gel B, Castañeda Heredia A, Salvador H, Martínez-Iniesta M, et al. Use of patient derived orthotopic xenograft models for real-time therapy guidance in a pediatric sporadic malignant peripheral nerve sheath tumor. *Ther Adv Med Oncol*. 2020;**12**:1758835920929579. https://doi.org/10.1177/1758835920929579
34 Fernández-Rodríguez J, Creus-Bachiller E, Zhang X, Martínez-Iniesta M, Ortega-Bertran S, Guha R, et al. A high-throughput screening platform identifies novel combination treatments for malignant peripheral nerve sheath tumors. *Mol Cancer Ther*. 2022;**21**(7):1246–58. https://doi.org/10.1158/1535-7163.MCT-21-0947
35 Fletcher JA, Kozakewich HP, Hoffer FA, Lage JM, Weidner N, Tepper R, et al. Diagnostic relevance of clonal cytogenetic aberrations in malignant soft-tissue tumors. *N Engl J Med*. 1991;**324**(7):436–42. https://doi.org/10.1056/NEJM199102143240702
36 Legius E, Dierick H, Wu R, Hall BK, Marynen P, Cassiman JJ, et al. TP53 mutations are frequent in malignant NF1 tumors. *Genes Chromosomes Cancer*. 1994;**10**(4):250–5. https://doi.org/10.1002/gcc.2870100405
37 Dahlberg WK, Little JB, Fletcher JA, Suit HD, Okunieff P. Radiosensitivity in vitro of human soft tissue sarcoma cell lines and skin fibroblasts derived from the same patients. *Int J Radiat Biol*. 1993;**63**(2):191–8. https://doi.org/10.1080/09553009314550251
38 Magallón-Lorenz M, Terribas E, Ortega-Bertran S, Creus-Bachiller E, Fernández M, Requena G, et al. Deep genomic analysis of malignant peripheral nerve sheath tumor cell lines challenges current malignant peripheral nerve sheath tumor diagnosis. *iScience*.

2023;**26**(2):106096. https://doi.org/10.1016/j.isci.2023.106096
39 Gebäck T, Schulz MM, Koumoutsakos P, Detmar M. TScratch: a novel and simple software tool for automated analysis of monolayer wound healing assays. *Biotechniques*. 2009;**46**(4):265–74. https://doi.org/10.2144/000113083
40 Popova T, Manié E, Stoppa-Lyonnet D, Rigaill G, Barillot E, Stern MH. Genome Alteration Print (GAP): a tool to visualize and mine complex cancer genomic profiles obtained by SNP arrays. *Genome Biol*. 2009;**10**(11):R128. https://doi.org/10.1186/gb-2009-10-11-r128
41 Li H. Aligning sequence reads, clone sequences and assembly contigs with BWA-MEM, (in eng), *arXiv*: genomics. 2013.
42 Kim S, Scheffler K, Halpern AL, Bekritsky MA, Noh E, Källberg M, et al. Strelka2: fast and accurate calling of germline and somatic variants. *Nat Methods*. 2018;**15**(8):591–4. https://doi.org/10.1038/s41592-018-0051-x
43 Wang K, Li M, Hakonarson H. ANNOVAR: functional annotation of genetic variants from high-throughput sequencing data. *Nucleic Acids Res*. 2010;**38**(16):e164. https://doi.org/10.1093/nar/gkq603
44 Chen X, Schulz-Trieglaff O, Shaw R, Barnes B, Schlesinger F, Källberg M, et al. Manta: rapid detection of structural variants and indels for germline and cancer sequencing applications. *Bioinformatics*. 2016;**32**(8):1220–2. https://doi.org/10.1093/bioinformatics/btv710
45 Landrum MJ, Lee JM, Benson M, Brown GR, Chao C, Chitipiralla S, et al. ClinVar: improving access to variant interpretations and supporting evidence. *Nucleic Acids Res*. 2018;**46**:D1062–7. https://doi.org/10.1093/nar/gkx1153
46 Li Q, Wang K. InterVar: clinical interpretation of genetic variants by the 2015 ACMG-AMP guidelines. *Am J Hum Genet*. 2017;**100**(2):267–80. https://doi.org/10.1016/j.ajhg.2017.01.004
47 Ng PC, Henikoff S. SIFT: predicting amino acid changes that affect protein function. *Nucleic Acids Res*. 2003;**31**(13):3812–4. https://doi.org/10.1093/nar/gkg509
48 Adzhubei IA, Schmidt S, Peshkin L, Ramensky VE, Gerasimova A, Bork P, et al. A method and server for predicting damaging missense mutations. *Nat Methods*. 2010;**7**(4):248–9. https://doi.org/10.1038/nmeth0410-248
49 Schwarz JM, Rödelsperger C, Schuelke M, Seelow D. MutationTaster evaluates disease-causing potential of sequence alterations. *Nat Methods*. 2010;**7**(8):575–6. https://doi.org/10.1038/nmeth0810-575
50 Shihab HA, Gough J, Cooper DN, Stenson PD, Barker GLA, Edwards KJ, et al. Predicting the functional, molecular, and phenotypic consequences of amino acid substitutions using hidden Markov models. *Hum Mutat*. 2013;**34**(1):57–65. https://doi.org/10.1002/humu.22225
51 Robinson JT, Thorvaldsdóttir H, Winckler W, Guttman M, Lander ES, Getz G, et al. Integrative genomics viewer. *Nat Biotechnol*. 2011;**29**(1):24–6. https://doi.org/10.1038/nbt.1754
52 Koelsche C, Schrimpf D, Stichel D, Sill M, Sahm F, Reuss DE, et al. Sarcoma classification by DNA methylation profiling. *Nat Commun*. 2021;**12**(1):498. https://doi.org/10.1038/s41467-020-20603-4
53 Chou TC. Drug combination studies and their synergy quantification using the Chou-Talalay method. *Cancer Res*. 2010;**70**(2):440–6. https://doi.org/10.1158/0008-5472.CAN-09-1947
54 Hernández JL, Padilla L, Dakhel S, Coll T, Hervas R, Adan J, et al. Therapeutic targeting of tumor growth and angiogenesis with a novel anti-S100A4 monoclonal antibody. *PloS One*. 2013;**8**(9):e72480. https://doi.org/10.1371/journal.pone.0072480
55 Lau C, Killian KJ, Samuels Y, Rudloff U. ERBB4 mutation analysis: emerging molecular target for melanoma treatment. *Methods Mol Biol*. 2014;**1102**:461–80. https://doi.org/10.1007/978-1-62703-727-3_24
56 Lucas LM, Dwivedi V, Senfeld JI, Cullum RL, Mill CP, Piazza JT, et al. The Yin and Yang of ERBB4: tumor suppressor and oncoprotein. *Pharmacol Rev*. 2022;**74**(1):18–47. https://doi.org/10.1124/pharmrev.121.000381
57 Alexandrov LB, Kim J, Haradhvala NJ, Huang MN, Tian Ng AW, Wu Y, et al. The repertoire of mutational signatures in human cancer. *Nature*. 2020;**578**(7793):94–101. https://doi.org/10.1038/s41586-020-1943-3
58 Röhrich M, Koelsche C, Schrimpf D, Capper D, Sahm F, Kratz A, et al. Methylation-based classification of benign and malignant peripheral nerve sheath tumors. *Acta Neuropathol*. 2016;**131**(6):877–87. https://doi.org/10.1007/s00401-016-1540-6
59 Karamchandani JR, Nielsen TO, van de Rijn M, West RB. Sox10 and S100 in the diagnosis of soft-tissue neoplasms. *Appl Immunohistochem Mol Morphol*. 2012;**20**(5):445–50. https://doi.org/10.1097/PAI.0b013e318244ff4b
60 Pemov A, Li H, Presley W, Wallace MR, Miller DT. Genetics of human malignant peripheral nerve sheath tumors. *Neurooncol Adv*. 2020;**2**(Suppl 1):i50–61. https://doi.org/10.1093/noajnl/vdz049
61 Cortes-Ciriano I, Steele CD, Piculell K, al-Ibraheemi A, Eulo V, Bui MM, et al. Genomic patterns of malignant peripheral nerve sheath tumor (MPNST) evolution correlate with clinical outcome and are detectable in cell-free DNA. *Cancer Discov*. 2023;**13**(3):654–71. https://doi.org/10.1158/2159-8290.CD-22-0786
62 Du X, Yang J, Ylipää A, Zhu Z. Genomic amplification and high expression of EGFR are key targetable oncogenic events in malignant peripheral

nerve sheath tumor. *J Hematol Oncol*. 2013;**6**:93. https://doi.org/10.1186/1756-8722-6-93
63 Miller SJ, Jessen WJ, Mehta T, Hardiman A, Sites E, Kaiser S, et al. Integrative genomic analyses of neurofibromatosis tumours identify SOX9 as a biomarker and survival gene. *EMBO Mol Med*. 2009;**1**(4):236–48. https://doi.org/10.1002/emmm.200900027
64 Silva TP, Silva AC, Baruque Mda G, Oliveira RB, Machado MP, Sarno EN. Morphological and functional characterizations of Schwann cells stimulated with *Mycobacterium leprae*. *Mem Inst Oswaldo Cruz*. 2008;**103**(4):363–9. https://doi.org/10.1590/s0074-02762008000400009
65 Marsland M, Dowdell A, Jiang CC, Wilmott JS, Scolyer RA, Zhang XD, et al. Expression of NGF/proNGF and their receptors TrkA, p75. *Int J Mol Sci*. 2022;**23**(8):4260. https://doi.org/10.3390/ijms23084260
66 Bakos RM, Maier T, Besch R, Mestel DS, Ruzicka T, Sturm RA, et al. Nestin and SOX9 and SOX10 transcription factors are coexpressed in melanoma. *Exp Dermatol*. 2010;**19**(8):e89–94. https://doi.org/10.1111/j.1600-0625.2009.00991.x
67 Ohsie SJ, Sarantopoulos GP, Cochran AJ, Binder SW. Immunohistochemical characteristics of melanoma. *J Cutan Pathol*. 2008;**35**(5):433–44. https://doi.org/10.1111/j.1600-0560.2007.00891.x
68 Rákosy Z, Vízkeleti L, Ecsedi S, Vokó Z, Bégány Á, Barok M, et al. EGFR gene copy number alterations in primary cutaneous malignant melanomas are associated with poor prognosis. *Int J Cancer*. 2007;**121**(8):1729–37. https://doi.org/10.1002/ijc.22928
69 Patel AV, Eaves D, Jessen WJ, Rizvi TA, Ecsedy JA, Qian MG, et al. Ras-driven transcriptome analysis identifies aurora kinase A as a potential malignant peripheral nerve sheath tumor therapeutic target. *Clin Cancer Res*. 2012;**18**(18):5020–30. https://doi.org/10.1158/1078-0432.CCR-12-1072
70 Mohan P, Castellsague J, Jiang J, Allen K, Chen H, Nemirovsky O, et al. Genomic imbalance of HMMR/RHAMM regulates the sensitivity and response of malignant peripheral nerve sheath tumour cells to aurora kinase inhibition. *Oncotarget*. 2013;**4**(1):80–93. https://doi.org/10.18632/oncotarget.793
71 Magallón-Lorenz M, Fernández-Rodríguez J, Terribas E, Creus-Batchiller E, Romagosa C, Estival A, et al. Chromosomal translocations inactivating CDKN2A support a single path for malignant peripheral nerve sheath tumor initiation. *Hum Genet*. 2021;**140**(8):1241–52. https://doi.org/10.1007/s00439-021-02296-x
72 Lemberg KM, Wang J, Pratilas CA. From genes to -omics: the evolving molecular landscape of malignant peripheral nerve sheath tumor. *Genes*. 2020;**11**(6):691. https://doi.org/10.3390/genes11060691
73 Miettinen M, McCue PA, Sarlomo-Rikala M, Biernat W, Czapiewski P, Kopczynski J, et al. Sox10 – a marker for not only schwannian and melanocytic neoplasms but also myoepithelial cell tumors of soft tissue: a systematic analysis of 5134 tumors. *Am J Surg Pathol*. 2015;**39**(6):826–35. https://doi.org/10.1097/PAS.0000000000000398
74 Paratore C, Goerich DE, Suter U, Wegner M, Sommer L. Survival and glial fate acquisition of neural crest cells are regulated by an interplay between the transcription factor Sox10 and extrinsic combinatorial signaling. *Development*. 2001;**128**(20):3949–61.
75 Lucas CG, Vasudevan HN, Chen WC, Magill ST, Braunstein SE, Jacques L, et al. Histopathologic findings in malignant peripheral nerve sheath tumor predict response to radiotherapy and overall survival. *Neurooncol Adv*. 2020;**2**(1):vdaa131. https://doi.org/10.1093/noajnl/vdaa131
76 Gaspard M, Lamant L, Tournier E, Valentin T, Rochaix P, Terrier P, et al. Evaluation of eight melanocytic and neural crest-associated markers in a well-characterised series of 124 malignant peripheral nerve sheath tumours (MPNST): useful to distinguish MPNST from melanoma? *Histopathology*. 2018;**73**(6):969–82. https://doi.org/10.1111/his.13740
77 Alexandrov LB, Nik-Zainal S, Wedge DC, Aparicio SA, Behjati S, Biankin AV, et al. Signatures of mutational processes in human cancer. *Nature*. 2013;**500**(7463):415–21. https://doi.org/10.1038/nature12477
78 Brčić I, Godschachner TM, Bergovec M, Igrec J, Till H, Lackner H, et al. Broadening the spectrum of NTRK rearranged mesenchymal tumors and usefulness of pan-TRK immunohistochemistry for identification of NTRK fusions. *Mod Pathol*. 2021;**34**(2):396–407. https://doi.org/10.1038/s41379-020-00657-x
79 Panse G, Reisenbichler E, Snuderl M, Wang WL, Laskin W, Jour G. LMNA-NTRK1 rearranged mesenchymal tumor (lipofibromatosis-like neural tumor) mimicking pigmented dermatofibrosarcoma protuberans. *J Cutan Pathol*. 2021;**48**(2):290–4. https://doi.org/10.1111/cup.13772
80 Agaram NP, Zhang L, Sung YS, Chen CL, Chung CT, Antonescu CR, et al. Recurrent NTRK1 gene fusions define a novel subset of locally aggressive lipofibromatosis-like neural tumors. *Am J Surg Pathol*. 2016;**40**(10):1407–16. https://doi.org/10.1097/PAS.0000000000000675
81 Hiemcke-Jiwa LS, Meister MT, Martin E, Dierselhuis MP, Haveman LM, Meijers RWJ, et al. NTRK rearrangements in a subset of NF1-related malignant peripheral nerve sheath tumors as novel actionable target. *Acta Neuropathol*. 2022;**145**:149–52. https://doi.org/10.1007/s00401-022-02515-3
82 Cleven AH, al Sannaa GA, Briaire-de Bruijn I, Ingram DR, van de Rijn M, Rubin BP, et al. Loss of H3K27 tri-methylation is a diagnostic marker for malignant peripheral nerve sheath tumors and an indicator for an inferior survival. *Mod Pathol*. 2016;**29**(9):1113. https://doi.org/10.1038/modpathol.2016.103

83 Kodack DP, Farago AF, Dastur A, Held MA, Dardaei L, Friboulet L, et al. Primary patient-derived cancer cells and their potential for personalized cancer patient care. *Cell Rep*. 2017;**21**(11):3298–309. https://doi.org/10.1016/j.celrep.2017.11.051

84 Kusakawa S, Yasuda S, Kuroda T, Kawamata S, Sato Y. Ultra-sensitive detection of tumorigenic cellular impurities in human cell-processed therapeutic products by digital analysis of soft agar colony formation. *Sci Rep*. 2015;**5**:17892. https://doi.org/10.1038/srep17892

85 Chen SH, Lahav G. Two is better than one; toward a rational design of combinatorial therapy. *Curr Opin Struct Biol*. 2016;**41**:145–50. https://doi.org/10.1016/j.sbi.2016.07.020

Supporting information

Additional supporting information may be found online in the Supporting Information section at the end of the article.

Fig. S1. Histological stains of Ki-67, CD34, and Vimentin in the primary tumors and models.

Fig. S2. *LMNA-NTRK1* gene fusion in the SP-05 tumor.

Fig. S3. Hematoxylin–Eosin (H&E) stains of primary tumors and tumors from PDOX mice.

Fig. S4. Tumor-associated fibroblasts derived from three primary tumors.

Fig. S5. Copy number profile of primary tumor, orthoxenograft (PDOX) tumor, and cell line from tumors SP-01, SP-04, SP-05, SP-06, and NF1-09 (related to Fig. 3).

Fig. S6. Phenotypic and functional characterization of established control cell lines (related to Fig. 4).

Fig. S7. Comparison of the main phenotypic and functional features of the two cell lines derived from SP-01, one from the primary tumor and the other from the PDOX tumor (SP-01-0T).

Table S1. Clinical data from patients and preclinical models obtained.

Table S2. Summary of the genomic analyses performed in primary tumors, PDOX models, and cell lines.

Table S3. Short tandem repeat (STR) cell line authentication from new established cell lines.